

Said Zeghloul
Lotfi Romdhane
Med Amine Laribi *Editors*

Computational Kinematics

Proceedings of the 7th International
Workshop on Computational Kinematics
that was held at Futuroscope-Poitiers,
France, in May 2017

Mechanisms and Machine Science

Volume 50

Series editor

Marco Ceccarelli

LARM: Laboratory of Robotics and Mechatronics

DICeM: University of Cassino and South Latium

Via Di Biasio 43, 03043 Cassino (Fr), Italy

e-mail: ceccarelli@unicas.it

More information about this series at <http://www.springer.com/series/8779>

Saïd Zegloul · Lotfi Romdhane
Med Amine Laribi
Editors

Computational Kinematics

Proceedings of the 7th International
Workshop on Computational Kinematics
that was held at Futuroscope-Poitiers,
France, in May 2017

 Springer

Editors

Saïd Zegloul
Institut PPRIME, UPR 3346
University of Poitiers
Poitiers
France

Med Amine Laribi
SP2MI, Téléport 2
University of Poitiers
Poitiers
France

Lotfi Romdhane
American University of Sharjah, UAE,
on leave from the National School
of Engineering of Sousse
Sousse Erriadh
Tunisia

ISSN 2211-0984

Mechanisms and Machine Science

ISSN 978-3-319-60866-2

DOI 10.1007/978-3-319-60867-9

ISSN 2211-0992 (electronic)

ISSN 978-3-319-60867-9 (eBook)

Library of Congress Control Number: 2017944354

© Springer International Publishing AG 2018

This work is subject to copyright. All rights are reserved by the Publisher, whether the whole or part of the material is concerned, specifically the rights of translation, reprinting, reuse of illustrations, recitation, broadcasting, reproduction on microfilms or in any other physical way, and transmission or information storage and retrieval, electronic adaptation, computer software, or by similar or dissimilar methodology now known or hereafter developed.

The use of general descriptive names, registered names, trademarks, service marks, etc. in this publication does not imply, even in the absence of a specific statement, that such names are exempt from the relevant protective laws and regulations and therefore free for general use.

The publisher, the authors and the editors are safe to assume that the advice and information in this book are believed to be true and accurate at the date of publication. Neither the publisher nor the authors or the editors give a warranty, express or implied, with respect to the material contained herein or for any errors or omissions that may have been made. The publisher remains neutral with regard to jurisdictional claims in published maps and institutional affiliations.

Printed on acid-free paper

This Springer imprint is published by Springer Nature

The registered company is Springer International Publishing AG

The registered company address is: Gewerbestrasse 11, 6330 Cham, Switzerland

Preface

This book contains the Proceedings of the seventh International Workshop on Computational Kinematics (CK2017) sponsored by IFToMM, the International Federation for the Promotion of Mechanism and Machine Science.

CK 2017, IFToMM International Workshop on Computational Kinematics, is the seventh event of a series that started in 1993 as a specific conference on computational kinematics. The first event was held at the International Conference and Research Center for Computer Science (IBFI), Germany, in October 1993; the second was held at INRIA Sophia Antipolis, France, in September 1995; the third was held in Seoul, South Korea, 2001; the fourth was held at the University of Cassino, Italy, in May 2005; the fifth was held at the University of Duisburg-Essen, Germany, in May 2009; and the sixth was held in Barcelona, Spain, in May 2013.

The aim of CK workshop is to bring together researchers from the broad range of disciplines related to computational kinematics in an intimate, collegial, and stimulating environment, where they can present and exchange their newest scientific results.

The seventh CK workshop comes to Poitiers, taking place from 22 to 24, May 2017. The workshop received 78 papers. After peer-reviewed evaluation, 69 papers, from 24 different countries, have been accepted for presentation. The topics of the papers are related to computational kinematics, including kinematic design and synthesis, computational geometry in kinematics, motion analysis and synthesis, theory of mechanisms, mechanism design, kinematical analysis of serial and parallel robots, kinematical issues in biomechanics, kinematical motion analysis and simulation, geometric constraint solvers, deployable and tensegrity structures, robot motion planning, applications of computational kinematics, education in computational kinematics, and theoretical foundations of kinematics.

The community of kinematicians, thus, continues to exhibit its traditional vitality. The reader will find here a representative sample of the most modern techniques available nowadays for the solution of challenging problems arising in computational kinematics. In light of its contents, this book should be of interest to researchers, graduate students, and practicing engineers working in kinematics or related areas. The researchers gathering in Poitiers on the occasion of CK2017 will

continue to make this truth and to show how their results have an important impact in several different domains.

We thank the authors who have contributed with very interesting papers on several subjects, covering many areas linked to computational kinematics and additionally for their cooperation in revising papers in a short time in agreement with the reviewers' comments. We are grateful to the 65 reviewers for the time and efforts they spent in evaluating the papers with a tight schedule that has permitted the publication of this Proceedings volume in time for the workshop.

We thank the University of Poitiers, in particular, the Fundamental and Applied Science Faculty, for having hosted the CK 2017 event.

We also thank the support of International Federation for the Promotion of Mechanism and Machine Science (IFTOMM). The symposium received generous support from local sponsors, namely the University of Poitiers, the Grand Poitiers, the Nouvelle Aquitaine region, and the Aquitaine Robotics cluster, which were critical to make this workshop possible.

We thank the publisher Springer and its editorial staff for accepting and helping in the publication of this Proceedings volume within the book series on Mechanism and Machine Science (MMS).

Saïd Zegloul
Lotfi Romdhane
Med Amine Laribi

Contents

Applications

Inherently Balanced Double Bennett Linkage	3
Volkert van der Wijk	
3D Revolute Joint with Clearance in Multibody Systems	11
Narendra Akhadkar, Vincent Acary, and Bernard Brogliato	
Kinematics and Bifurcation of a Twofold-Symmetric Eight-Bar Linkage	19
Zhao Tang, Dimiter Zlatanov, and Jian Dai	
A Novel Kinematic Model of Spatial Four-bar Linkage RSPS for Testing Accuracy of Actual R-Pairs with Ball-bar	27
Zhi Wang, Delun Wang, Xiaopeng Li, Huimin Dong, and Shudong Yu	
Model Reduction Methods for Optimal Follow-the-Leader Movements of Binary Actuated, Hyper-redundant Robots	35
Svenja Tappe, Dairong Yu, Jens Kotlarski, and Tobias Ortmaier	
Kinematic Design of a Lighting Robotic Arm for Operating Room	44
J. Sandoval, L. Nouaille, G. Poisson, and Y. Parmantier	
Elastostatic Modelling of a Wooden Parallel Robot	53
Lila Kaci, Clement Boudaud, Sebastien Briot, and Philippe Martinet	
Towards an Autonomous Airborne Robotic Agent	62
Daniel Soto-Guerrero, José Gabriel Ramírez-Torres, and Jean-Pierre Gazeau	
Autonomous March Control for Humanoid Robot Animation in a Virtual Reality Environment	70
Víctor H. Andaluz, Santiago Guamán, and Jorge S. Sánchez	

Control Based on Linear Algebra for Mobile Manipulators	79
Victor H. Andaluz, Edison R. Sásig, William D. Chicaiza, and Paola M. Velasco	
Modeling and Kinematic Nonlinear Control of Aerial Mobile Manipulators.	87
Jessica S. Ortiz, Alex P. Erazo, Christian P. Carvajal, José A. Pérez, Luis E. Proaño, Franklin M. Silva M., and Víctor H. Andaluz	
Path Planning Based on Visual Feedback Between Terrestrial and Aerial Robots Cooperation	96
Jessica S. Ortiz, Crithian F. Zapata, Alex D. Vega, and Víctor H. Andaluz	
Biomechanics	
Dynamic Analysis and Control of a Hybrid Serial/Cable Driven Robot for Lower-Limb Rehabilitation.	109
Mourad Ismail, Samir Lahouar, and Lotfi Romdhane	
Kinematic Analysis of Active Ankle Using Computational Algebraic Geometry	117
Shivesh Kumar, Abhilash Nayak, Bertold Bongardt, Andreas Mueller, and Frank Kirchner	
Optimization of a Redundant Serial Spherical Mechanism for Robotic Minimally Invasive Surgery	126
Carl A. Nelson, Med Amine Laribi, and Said Zeghloul	
Kinematic Analysis for a Prostate Biopsy Parallel Robot Using Study Parameters	135
Iosif Birlescu, Paul Tucan, Bogdan Gherman, Calin Vaida, Nicolae Crisan, Corina Radu, Nicolae Plitea, and Doina Pislă	
Optimum Walking of the Bioloid Humanoid Robot on a Rectilinear Path	143
Gabriela Reyes, Jose Alfonso Pamanes, Jesus Edurado Fierro, and Victor Nunez	
A New Experimental Set-up for Training Multi-parameter Gaits.	152
Sami Bennour, Houssein Lamine, Baptiste Ulrich, Thomas Legrand, Brigitte Jolles, Julien Favre, and Lotfi Romdhane	
Cable Robots	
Comprehensive Dynamic Study of an Unloaded Walking Within a Cable-Based Gait Trainer.	165
Houssein Lamine, Sami Bennour, and Lotfi Romdhane	

A Cable-Driven Robot for Upper Limb Rehabilitation Inspired by the Mirror Therapy 174
 Lukas Tappeiner, Erika Ottaviano, and Manfred L. Husty

Computing Cross-Sections of the Workspace of Cable-Driven Parallel Robots with 6 Sagging Cables 182
 Jean-Pierre Merlet

Efficient Computation of the Workspace Boundary, Its Properties and Derivatives for Cable-Driven Parallel Robots 190
 Andreas Pott

Application of the Rigid Finite Element Method to the Simulation of Cable-Driven Parallel Robots 198
 Philipp Tempel, Andreas Schmidt, Bernard Haasdonk, and Andreas Pott

Cams/Gear

Evaluating the Knot Vector to Synthesize the Cam Motion Using NURBS 209
 T.T.N. Nguyen, S. Kurtenbach, M. Hüsing, and B. Corves

Kinematics of Biplanetary Epicyclic Gears 217
 J. Drewniak, A. Deptuła, T. Kądziołka, and S. Zawiślak

Optimization

Dynamic Synthesis of a Multibody System: A Comparative Study Between Genetic Algorithm and Particle Swarm Optimization Techniques 227
 Mohamed Amine Ben Abdallah, Imed Khemili, Med Amine Laribi, and Nizar Aifaoui

Robust Design Methodology of Topologically Optimized Components Under the Effect of Uncertainties 235
 Joshua Amrith Raj and Arshad Javed

Parallel Robots

Kinematic and Dynamic Modeling and Base Inertial Parameters Determination of the Quadrupteron Parallel Manipulator 249
 Behzad Danaei, Alaleh Arian, Mehdi Tale Masouleh, and Ahmad Kalhor

Forward Kinematics of the General Triple-Arm Robot Using a Distance-Based Formulation 257
 Nicolas Rojas and Federico Thomas

Parallel Manipulators in Terms of Dual Cayley-Klein Parameters 265
 G. Nawratil

An Approach for Type Synthesis of Overconstrained 1T2R Parallel Mechanisms	274
C. Dong, H. Liu, Q. Liu, T. Sun, T. Huang, and D.G. Chetwynd	
Transmission Quality Evaluation for a Class of Four-limb Parallel Schönflies-motion Generators with Articulated Platforms	282
Guanglei Wu, Shaoping Bai, and Stéphane Caro	
Study of Redundantly Actuated DELTA-Type Parallel Kinematic Mechanisms	291
Burkhard Corves, Seyed Amirreza Shahidi, Michael Lorenz, Sami Charaf Eddine, and Mathias Hüsing	
3-RRR Spherical Parallel Robot Optimization with Minimum of Singularities	299
Asma Jelassi, Abdelbadia Chaker, and Abdelfattah Mlika	
4haptic: A Dexterous 4 d.o.fs Haptic Device Based on Delta Architecture	307
Celestin Preault, Housseem Saafi, Med Amine Laribi, and Said Zeghloul	
Error Modelling and Sensitivity Analysis of a Planar 3-PRP Parallel Manipulator	315
Jayant K. Mohanta, Santhakumar Mohan, Mathias Huesing, and Burkhard Corves	
Determination of Workspace Volume of Parallel Manipulators Using Monte Carlo Method	323
Arkadeep Narayan Chaudhury and Ashitava Ghosal	
Kinematics of a 6-RUU Parallel Robots with Reconfigurable Platforms	331
Guanglei Wu and Huimin Dong	
On the Motion/Force Transmissibility and Constrainability of Delta Parallel Robots	340
Jan Brinker, Burkhard Corves, and Yukio Takeda	
A Geometrical Approach for the Singularity Analysis of a 3-RRS Parallel Manipulator	349
Halil Tetik and Gokhan Kiper	
The Collision-Free Workspace of the Tripteron Parallel Robot Based on a Geometrical Approach	357
Zolfa Anvari, Parnyan Ataei, and Mehdi Tale Masouleh	
A Novel 3T1R Parallel Manipulator 2PaRSS and Its Kinematics	365
Huiping Shen, Guowei Shao, Jiaming Deng, and Ting-li Yang	

Multi-objective Optimization of a Tripod Parallel Mechanism for a Robotic Leg 374
 Matteo Russo, Saioa Herrero, Oscar Altuzarra, and Marco Ceccarelli

Robust Optimization of the RAF Parallel Robot for a Prescribed Workspace 383
 M.A. Laribi, A. Mlika, L. Romdhane, and S. Zeghloul

Optimal Design of N-*UU* Parallel Mechanisms 394
 Yuanqing Wu and Marco Carricato

Robust Multi-objective Design Optimization of the 3-UPU TPM Based on the GA-Krawczyk Method 403
 S. El Hraiech, A.H. Chebbi, Z. Affi, and L. Romdhane

Planar Robots

Topology Optimization of a Reactionless Four-Bar Linkage 413
 Sebastien Briot and Alexandre Goldsztejn

Kinetostatic Analysis and Solution Classification of a Planar Tensegrity Mechanism 422
 P. Wenger and D. Chablat

Design Optimization and Accuracy Analysis of a Planar 2PRP-PRR Parallel Manipulator 432
 Santhakumar Mohan, Burkhard Corves, and Philippe Wenger

Operation Modes of the Planar 3-RRR Manipulator 441
 Aravind Baskar and Sandipan Bandyopadhyay

The Impact of Kinematic Redundancies on the Conditioning of a Planar Parallel Manipulator 449
 Joao Vitor C. Fontes, Hiparco L. Vieira, and Maira M. da Silva

Holistic Modular Multilayer Synthesis of Planar Linkages Using Parameterized Mass Properties 457
 S. Heinrich and M. Berger

Theoretical Kinematics

Motion Interpolation in Lie Subgroups and Symmetric Subspaces 467
 J.M. Selig, Yuanqing Wu, and Marco Carricato

Intrusion, Proximity and Stationary Distance 475
 Paul Zsombor-Murray

A Novel Geometric Analysis of the Kinematics of the 3-RPS Manipulator 483
 Teja Krishna Mamidi, Aravind Baskar, and Sandipan Bandyopadhyay

Constraint Equations of Inverted Kinematic Chains 491
 Thomas Stigger and Manfred L. Husty

Local and Full-Cycle Mobility Analysis of a 3-RPS-3-SPR Series-Parallel Manipulator 499
 Abhilash Nayak, Stéphane Caro, and Philippe Wenger

Application of Intersection Theory to Singularity and Motion Mode Analysis of Mechanisms. 508
 Samuli Piipponen, Andreas Müller, Eero Hyry, and Jukka Tuomela

Rational Parametrization of Linear Pentapod’s Singularity Variety and the Distance to It 516
 Arvin Rasoulzadeh and Georg Nawratil

Inverse Kinematics of Anthropomorphic Arms Yielding Eight Coinciding Circles. 525
 B. Bongardt

Optimal Synthesis of Overconstrained 6R Linkages by Curve Evolution. 535
 Tudor-Dan Rad and Hans-Peter Schröcker

The Instantaneous Screw Axis of Motions in the Kinematic Image Space 544
 Martin Pfurner and Josef Schadlbauer

A New Insight into the Coupler Curves of the RCCC Four-Bar Linkage 552
 Federico Thomas and Alba Pérez-Gracia

A Forward Kinematics Data Structure for Efficient Evolutionary Inverse Kinematics 560
 Sebastian Starke, Norman Hendrich, and Jianwei Zhang

Adaptation of the Geometric Model of a 6 dof Serial Robot to the Task Space 569
 Jose Gutiérrez, Helene Chanal, Severine Durieux, and Emmanuel Duc

Differentiation-Free Taylor Approximation of Finite Motion in Closed Loop Kinematics. 577
 J.J. de Jong, A. Müller, J. van Dijk, and J.L. Herder

A New Direct Position Analysis Solution for an Over-Constrained Gough-Stewart Platform. 585
 Luca Luzi, Nicola Sancisi, and Vincenzo Parenti Castelli

**A Study on Constraints Violation in Dynamic Analysis
of Spatial Mechanisms 593**
 P. Flores

**A Generalized and Analytical Method to Solve Inverse Kinematics
of Serial and Parallel Mechanisms Using Finite Screw Theory 602**
 T. Sun, S. F. Yang, T. Huang, and J. S. Dai

Applications

Inherently Balanced Double Bennett Linkage

Volkert van der Wijk^(✉)

Department of Precision and Microsystems Engineering,
Mechatronic System Design, Delft University of Technology,
Delft, The Netherlands
v.vanderwijk@tudelft.nl

Abstract. For fast moving mechanisms shaking force balance is important to reduce base vibrations. When mechanisms are force balanced, they are also gravity balanced which is important for reduced actuation effort and increased safety. It has been shown that from planar inherently balanced linkage architectures a variety of new and interesting force balanced mechanism solutions can be synthesized. The goal of this paper is to derive the balance conditions of one special solution consisting of two similar 4R four-bar linkages connected by a parallelogram, based on two sets of principal vectors. It is shown that also here the balance conditions can be derived from the linear momentum equations of each relative degree of freedom. Subsequently it is shown how the planar version can be transformed into a spatial version becoming an inherently balanced linkage of two similar Bennett linkages connected by a planar parallelogram. The balance conditions for both the planar and spatial version are exactly equal.

Keywords: Inherent force balance · Bennett linkage architecture · Mass motion · Principal vectors

1 Introduction

When mechanisms (i.e. robotic manipulators) move at high-speeds, base vibrations due to the dynamic reactions on the base (the so called shaking forces and shaking moments) are generally significant. These vibrations limit the performance of mechanisms which cannot run as fast and precise as desired. Contrary to common solutions to minimize the influence of base vibrations such as damping and advanced control, it is also possible to design a mechanism such that it does not produce any base vibrations at all. The mechanism then is designed dynamically (shaking force and shaking moment) balanced [2,3].

The main challenge in designing balanced mechanisms is to limit the increase of mass, inertia, and complexity of the design for an advantageous application [6]. Instead of balancing a pre-existing mechanism, an approach where dynamic balance forms the starting point of the design based on which suitable mechanism architectures are synthesized has shown to lead to a variety of new balanced mechanism. This approach is named inherent dynamic balancing [3].

The inherent dynamic balance approach is based on the method of principal vectors, describing the motion of link masses relative to the center of mass (CoM) of the complete linkage in a specific decoupled way. In [5] for the first time a ‘grand’ inherently balanced linkage architecture was presented, with the novelty that it is not based on solely one principal vector set, but on the combination of all possible principal vector sets. From this highly overconstrained but movable architecture it was shown that a variety of new and interesting balanced linkages could be found.

In this paper it is shown how the balance conditions can be derived of one of the inherently balanced mechanism solutions which is based on two principal vector sets. The mechanism consists of two similar four-bar linkages that are connected with a parallelogram. It is shown also how from this planar linkage a spatial inherently balanced double Bennett linkage is found.

First the planar linkage is explained and the force balance conditions are derived from the linear momentum equations of each DoF independently. Here one element in each closed chain is modeled mass equivalently. Subsequently it is shown how the spatial inherently balanced Bennett linkage architecture can be obtained from the planar version.

2 Planar Inherently Balanced Linkage with Two Similar Four-Bars

Figure 1 shows the basic inherently balanced linkage solution that was derived in [5] from the so called ‘grand 4R four-bar based inherently balanced linkage architecture’, a highly overconstrained but movable architecture including all principal vector links of the four different principal vector sets. The linkage is drawn to scale for a realistic impression and consists of eight links which are organized as two similar four-bar linkages $A_0A_1A_2A_3$ and $D_4B_7SB_6$ with solely revolute pairs. The four-bar linkages move synchronously for all motion which is induced by the parallelogram $A_0P_{12}D_4P_{43}$ of which $P_{12}D_4$ is part of link $P_{12}B_6$ and D_4P_{43} is part of link B_7P_{43} . The links of four-bar $A_0A_1A_2A_3$ have lengths l_i whereas the inner links have lengths a_2 , a_3 , a_4 , and a_5 . Joints P_{12} and P_{43} , which are two principal points, are located at a distance a_1 and a_6 from A_0 , respectively as illustrated. The parameters a_i are principal dimensions of two different sets of principal vectors in the grand architecture. The conditions for similarity of the two four-bars can be described as:

$$\frac{l_1}{a_2 - a_1} = \frac{l_2}{a_3} = \frac{l_3}{a_4} = \frac{l_4}{a_5 - a_6} \quad (1)$$

with $a_2 - a_1 = |B_7D_4|$ and $a_5 - a_6 = |B_6D_4| = h_4$. Each link i has a mass m_i of which the CoM is located along the lines through the joints (i.e. all links are assumed mass symmetric with respect to these lines) defined by parameters e_i for the outer four-bar and by p_i for the inner four-bar as illustrated. The common CoM of all links together is in joint S for all motion of the linkage. By choosing joint S as the pivot with the base, the common CoM is stationary for which for all motion the linkage is shaking force balanced and gravity balanced. About S the linkage has two-degree-of-freedom (2-DoF) motion.

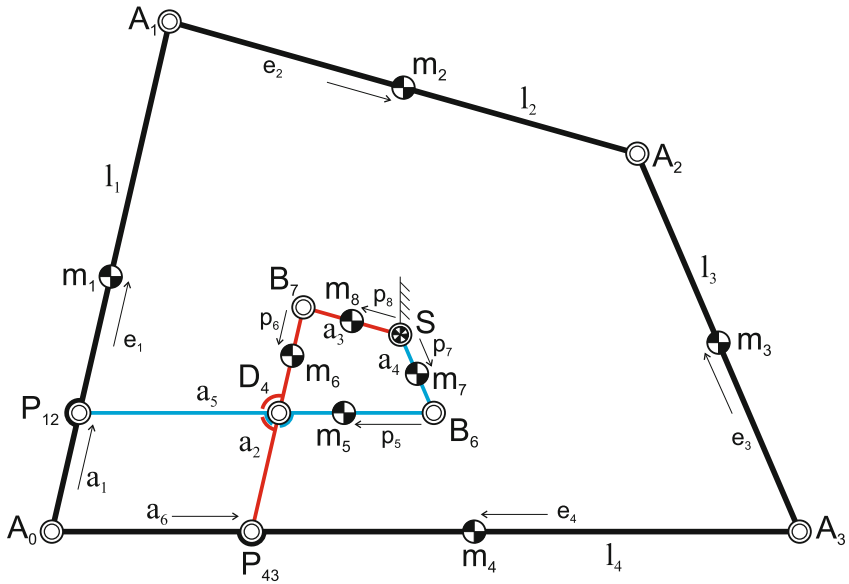


Fig. 1. Inherently balanced 2-DoF planar 4R four-bar based linkage with 8 links from [5], drawn to scale for a realistic impression. Four-bar $A_0A_1A_2A_3$ is similar to four-bar $D_4B_7SB_6$ and moves synchronously for all motion with the common CoM S stationary in the base pivot.

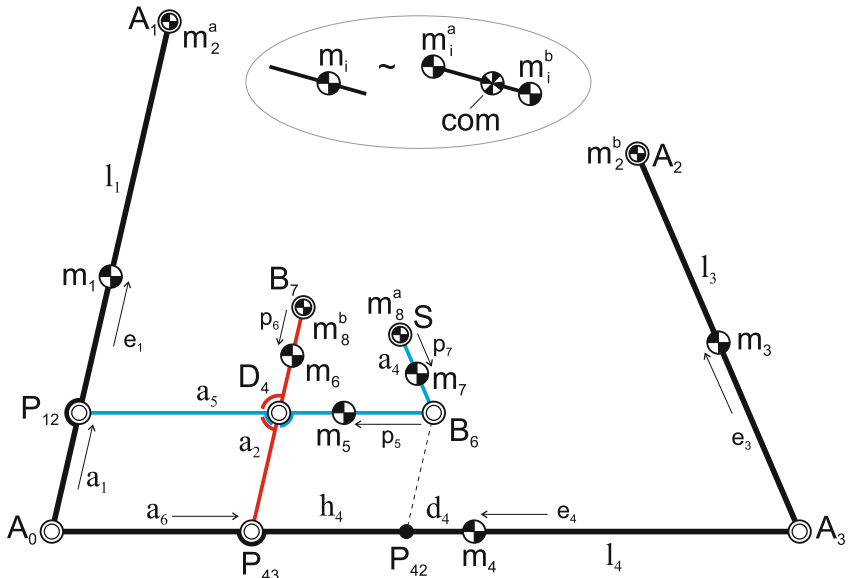


Fig. 2. To derive the force balance conditions, links A_1A_2 and SB_7 are modeled with equivalent masses m_2^a , m_2^b , m_8^a , and m_8^b in joints A_1 , A_2 , S , and B_7 , respectively. The closed chains then are modeled as mass equivalent open chains.

Also for a mechanism based on multiple sets of principal vectors such as the mechanism under investigation, the force balance conditions or conditions for which the common CoM is in joint S for all motion can be derived from the linear momentum equations of each relative DoF individually as explained in [3,4]. Then first one element in each closed loop is modeled mass equivalently as shown in Fig. 2 to obtain an open-loop mass equivalent linkage. The mass m_2 of link A_1A_2 is modeled with equivalent masses m_2^a and m_2^b in joints A_1 and A_2 , respectively, with the conditions for mass equivalence $m_2^a + m_2^b = m_2$ and $m_2^a e_2 = m_2^b (l_2 - e_2)$. Similarly for link SB_7 the mass m_8 can be modeled with equivalent masses m_8^a and m_8^b in joints S and B_7 , respectively, with the conditions for mass equivalence $m_8^a + m_8^b = m_8$ and $m_8^a p_8 = m_8^b (a_3 - p_8)$.

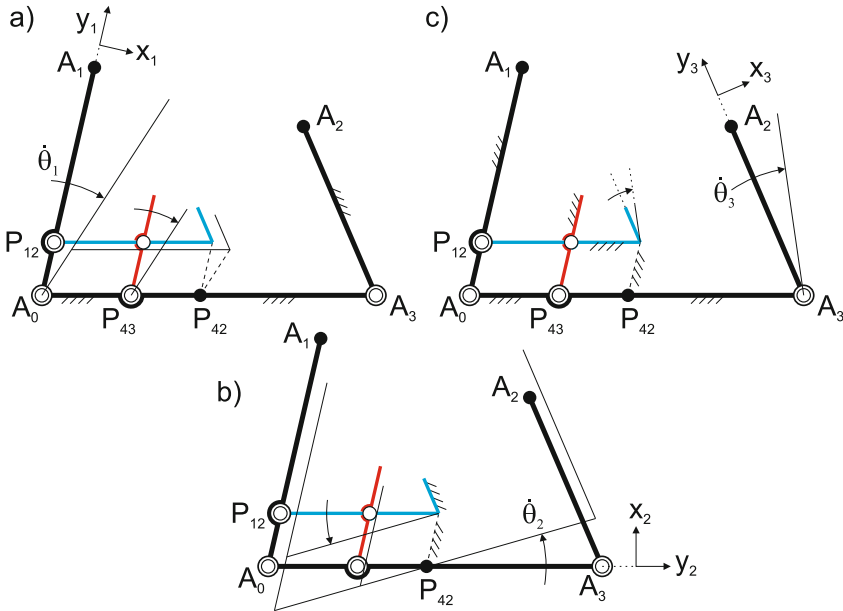


Fig. 3. The force balance conditions are derived from the linear momentum equations of each relative motion individually: (a) DoF 1, (b) DoF 2, and (c) DoF 3

Since the linkage is based on a 3-DoF principal vector linkage, it has three relative DoFs which can be analyzed individually [4]. Figure 3a illustrates the first relative DoF θ_1 where links A_2A_3 and A_3A_0 are immobile while link A_0A_1 solely rotates about A_0 . Then link $P_{43}B_7$ solely rotates about P_{43} while links $P_{12}B_6$ and B_6S solely translate. The linear momentum L_1 of this motion can

be written with respect to reference frame x_1y_1 , which is aligned with A_0A_1 as illustrated, and must equal the linear momentum of the total mass moving with S , which writes:

$$\frac{L_1}{\dot{\theta}_1} = \begin{bmatrix} m_1e_1 + m_2^a l_1 + (m_5 + m_7 + m_8^a)a_1 + m_6(a_2 - p_6) + m_8^b a_2 \\ 0 \end{bmatrix} = \begin{bmatrix} m_{tot} a_1 \\ 0 \end{bmatrix} \quad (2)$$

with total mass $m_{tot} = m_1 + m_2 + m_3 + m_4 + m_5 + m_6 + m_7 + m_8$ and the equivalent masses $m_2^a = m_2(1 - e_2/l_2)$, $m_8^a = m_8(1 - p_8/a_3)$, and $m_8^b = m_8 p_8/a_3$.

Figure 3b illustrates the second DoF θ_2 where link A_0A_3 rotates about P_{42} , link $P_{12}B_6$ rotates about B_6 , link SB_6 is immobile and the other three links solely translate. The linear momentum L_2 of this motion can be written with respect to reference frame x_2y_2 , which is aligned with A_0A_3 as illustrated. Since for this motion the total mass in S is not moving, the linear momentum must equal zero and is written as:

$$\frac{L_2}{\dot{\theta}_2} = \begin{bmatrix} -(m_1 + m_2^a)a_5 + (m_2^b + m_3)(l_4 - a_5) + m_4d_4 - m_5p_5 - (m_6 + m_8^b)h_4 \\ 0 \end{bmatrix} = \begin{bmatrix} 0 \\ 0 \end{bmatrix} \quad (3)$$

with $m_2^b = m_2e_2/l_2$ and $d_4 = l_4 - a_5 - e_4$.

Figure 3c illustrates the third DoF θ_3 where links SB_6 and A_2A_3 solely rotate about B_6 and A_3 , respectively, and all other links are immobile. The linear momentum L_3 of this motion can be written with respect to reference frame x_3y_3 , which is aligned with A_2A_3 as illustrated, and must equal the linear momentum of the total mass moving in S writing:

$$\frac{L_3}{\dot{\theta}_3} = \begin{bmatrix} m_2^b l_3 + m_3e_3 + m_7(a_4 - p_7) + m_8^a a_4 \\ 0 \end{bmatrix} = \begin{bmatrix} m_{tot} a_4 \\ 0 \end{bmatrix} \quad (4)$$

From the linear momentum equations the three force balance conditions are readily obtained as:

$$\begin{aligned} m_1e_1 + m_2^a l_1 + (m_5 + m_7 + m_8^a)a_1 + m_6(a_2 - p_6) + m_8^b a_2 - m_{tot} a_1 &= 0 \\ -(m_1 + m_2^a)a_5 + (m_2^b + m_3)(l_4 - a_5) + m_4d_4 - m_5p_5 - (m_6 + m_8^b)h_4 &= 0 \quad (5) \\ m_2^b l_3 + m_3e_3 + m_7(a_4 - p_7) + m_8^a a_4 - m_{tot} a_4 &= 0 \end{aligned}$$

and after substituting m_{tot} , d_4 , and h_4 they can be rewritten as:

$$(m_1 + m_2 + m_3 + m_4 + m_6 + m_8^b)a_1 - m_1e_1 - m_2^a l_1 - m_6(a_2 - p_6) - m_8^b a_2 = 0 \quad (6)$$

$$\begin{aligned} (m_1 + m_2 + m_3 + m_4 + m_6 + m_8^b)a_5 - (m_2^b + m_3)l_4 - m_4(l_4 - e_4) + m_5p_5 \\ - (m_6 + m_8^b)a_6 = 0 \quad (7) \end{aligned}$$

$$(m_1 + m_2 + m_3 + m_4 + m_5 + m_6 + m_8^b)a_4 - m_2^b l_3 - m_3e_3 + m_7p_7 = 0 \quad (8)$$

These three balance conditions together with the conditions for similarity Eq. (1) give in total six equations. This means that there are six dependent parameters to be calculated with the others given. One option can be to use the

equations to calculate a_1 , a_2 , a_3 , a_4 , a_5 , and a_6 . The sequence of solving the equations then becomes:

$$\begin{aligned}
 I. \quad a_4 &= \frac{m_2^b l_3 + m_3 e_3 - m_7 p_7}{m_1 + m_2 + m_3 + m_4 + m_5 + m_6 + m_8^b} && \text{(from Eq. (8))} \\
 II. \quad a_3 &= \frac{l_2}{l_3} a_4 && \text{(from Eq. (1))} \\
 III. \quad a_1 &= \frac{m_1 e_1 + m_2^a l_1 - m_6 p_6 + (m_6 + m_8^b) \frac{l_1}{l_3} a_4}{m_1 + m_2 + m_3 + m_4} && \text{(from Eq. (6))} \\
 IV. \quad a_2 &= \frac{l_1}{l_3} a_4 + a_1 && \text{(from Eq. (1))} \\
 V. \quad a_5 &= \frac{(m_2^b + m_3) l_4 + m_4 (l_4 - e_4) - m_5 p_5 - (m_6 + m_8^b) \frac{l_4}{l_3} a_4}{m_1 + m_2 + m_3 + m_4} && \text{(from Eq. (7))} \\
 VI. \quad a_6 &= a_5 - \frac{l_4}{l_3} a_4 && \text{(from Eq. (1))}
 \end{aligned} \tag{9}$$

3 Spatial Inherently Balanced Linkage with Two Similar Bennetts

The planar inherently balanced linkage in Fig. 1 can easily be transformed into a spatial inherently balanced linkage. When the two four-bar linkages are made parallelograms with $l_1 = l_3$, $l_2 = l_4$, $a_2 - a_1 = a_4$, and $a_5 - a_6 = a_3$ then the resulting planar linkage becomes as shown in Fig. 4a. With the conditions for similarity Eq. (1) and the balance conditions Eqs. (6–8) the common CoM S is stationary in the fixed pivot for all motion. Then by twisting the revolute pairs of each similar four-bar out of plane according to the Bennett conditions for which the mechanism remains mobile [1], the spatial inherently balanced linkage in Fig. 4b is obtained. Twisting the revolute pairs does not affect the balance and balance conditions, they remain exactly the same with equal values as for the planar version. This is since the principal vectors on which the linkage is based, do not change and are always valid for spatial motion [3]. Only of importance is that the Bennett conditions for the inner and outer four-bar are chosen equal such that the inherently balanced linkage has two similar 4R four-bar Bennett linkages. The parallelogram connecting the two Bennett four-bars remains planar.

Although in this paper all links were assumed mass symmetric, in the out-of-plane direction the links and linkage does not need to be mass symmetric. All links can have a general mass distribution in this direction, comparable to the planar linkage where the out-of-plane mass distribution does not affect the force balance as well. For any out-of-plane mass distribution the common CoM S will be a stationary point on the rotational axis of the fixed joint. In practice this is useful, since especially for producing Bennett linkages with sufficient range of motion without intersecting links, advanced link designs are needed. It is also possible to have all links in this paper have a general CoM, i.e. without mass symmetry in any direction. The balance conditions can be derived with the same shown approach, however it will be more extensive. Then also in general P_{12} and P_{43} will be located off their line through the link joints.

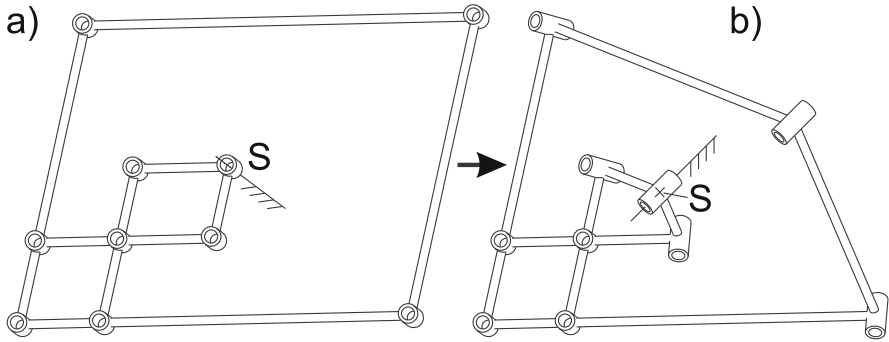


Fig. 4. An inherently balanced double Bennett linkage with common CoM S as fixed joint in (b) can be obtained from the planar version of the linkage where all links are in parallel in (a) by twisting the revolute pairs out of plane. The balance and balance conditions are maintained.

Since twisting the revolute pairs does not affect the force balance, the inherently balanced double Bennett linkage has potential as a reconfigurable and deployable inherently balanced linkage. By actuating the twists the linkage can be altered from planar to spatial, vice versa.

4 Conclusions

In this paper it was shown how a spatial inherently balanced double Bennett linkage could be obtained from a planar inherently balanced linkage of two similar 4R four-bar linkages connected with a parallelogram. Twisting the revolute pairs out of plane according the Bennett conditions does not affect the balance and the balance conditions. The resulting linkage consists of two similar Bennett linkages connected with a planar parallelogram. The balance conditions were derived from the planar linkage by linear momentum equations of each relative degree of freedom individually, showing that this method applies also to inherently balanced linkages that are based on multiple sets of principal vectors.

The approach in this paper can be regarded as an approach to synthesize spatial inherently balanced mechanisms from planar linkage architectures with the advantage to not have to consider complex spatial kinematics. As a bonus, it leads spontaneously to a variety of inherently balanced reconfigurable and deployable spatial linkages, as was shown for the example in this paper.

References

1. Bennett, G.T.: A new mechanism. *Engineering* **76**, 777–778 (1903)
2. Briot, S., Bonev, I.A., Gosselin, C.M., Arakelian, V.: Complete shaking force and shaking moment balancing of planar parallel manipulators with prismatic pairs. *Multi-body Dyn.* **223**(K), 43–52 (2009)

3. Van der Wijk, V.: Methodology for analysis and synthesis of inherently force and moment-balanced mechanisms - theory and applications. Dissertation. University of Twente (2014). Free download: doi:[10.3990/1.9789036536301](https://doi.org/10.3990/1.9789036536301)
4. Van der Wijk, V.: Design and analysis of closed-chain principal vector linkages for dynamic balance with a new method for mass equivalent modeling. *Mech. Mach. Theory* **107**, 283–304 (2017)
5. Van der Wijk, V.: On the grand 4R four-bar based inherently balanced linkage architecture. In: Wenger, P., Flores, P. (eds.) *New Trends in Mechanism and Machine Science*, vol. 43, pp. 473–480. Springer (2017)
6. Van der Wijk, V., Herder, J.L., Demeulenaere, B.: Comparison of various dynamic balancing principles regarding additional mass and additional inertia. *Mechanisms Robot.* **1**(4), 041006 (2009)

3D Revolute Joint with Clearance in Multibody Systems

Narendra Akhadkar¹(✉), Vincent Acary², and Bernard Brogliato²

¹ Schneider Electric, 37 Quai Paul-Louis Merlin, 38000 Grenoble, France
narendra.akhadkar@schneider-electric.com

² INRIA Grenoble Rhône-Alpes and Laboratoire Jean Kuntzman,
University Grenoble-Alpes, 655 avenue de l'Europe, 38334 Saint-Ismier, France
{vincent.acary,bernard.brogliato}@inria.fr

Abstract. The aim of this paper is to understand the influence of radial and axial clearance in the revolute joints on the overall performance of a circuit breaker. A circuit breaker mechanism is made of seven links, seven revolute joints with clearance in both radial and axial direction, four unilateral contacts with friction, and it has forty-two degrees of freedom. The Moreau-Jean nonsmooth contact dynamics (NSCD) numerical method is used to perform the simulations. The numerical results are validated by careful comparisons with experimental data.

Keywords: Joint clearance · Unilateral constraints · Coulomb's friction · Impacts · Circuit breaker

1 Introduction

A miniature circuit breaker is a device that switches and/or protects the lowest common distributed voltage in an electrical system. It is designed to protect conductors and insulation from damage due to overload and short circuit. Usually, the performance of these mechanisms is not as desired, due to the manufacturing tolerances on links, clearances in the joints and the assembly tolerances. The spatial revolute joint with clearance in both axial and radial direction adds five extra degrees of freedom into the system. Compared to planar mechanisms, spatial mechanisms can generate more complicated functions with the same number of links. Most of the previous work is focused on the radial clearance in the planar and spatial revolute joints [8, 10, 11]. However more recently the influence of the axial clearance in the revolute joint has been studied in [15, 17].

Most of the mechanisms in the Schneider Electric company use frictional contacts and the compliant models cannot correctly model the sticking condition. In the nonsmooth contact dynamic (NSCD) approach, the interaction of the colliding bodies is modeled with multiple frictional unilateral constraints [12, 13]. The unilateral constraints are described by set-valued force laws in normal and tangential directions. The normal contact law is based on Signorini's condition while the tangential contact law is based on Coulomb's friction law. Careful

comparisons between numerical results obtained with the NSCD approach, and experimental data are reported in [14, 16], while the use of the NSCD approach for systems with clearances is also advocated in [5, 9]. They demonstrate that the numerical schemes and the model used in this article, though they can be improved, possess very good forecast capabilities.

Our objective is to study the influence of initial conditions and the out-of-plane motion, *i.e.* the polarization effect¹ in the three dimensional case. Another objective is to develop a time efficient virtual test bench using the INRIA open-source simulation software SICONOS². Our aim is to understand the influence of clearance in the revolute joints on the overall behavior of the C-60 miniature circuit breaker where human safety must be guaranteed. To validate the simulation model, experiments are carried-out on the prototype samples and the results are compared with the simulations.

2 Formulation of the Nonsmooth Dynamical Systems

2.1 Normal and Tangential Contact Laws

Let us consider two non overlapping bodies (see Fig. 1), a potential contact point between two bodies is given by the closest points C_A and C_B . A local frame is defined at the potential contact point by $(\mathbf{N}, \mathbf{T}_1, \mathbf{T}_2)$. The gap g_N is defined as the signed distance between the two potential contacting points C_A and C_B . The contact force, denoted by $r = (r_N, r_T)^\top \in \mathbb{R}^3$. Due to the impenetrability assumption one has $g_N \geq 0$. We also neglect adhesive effects so that $r_N \geq 0$. If $r_N > 0$ then we impose $g_N = 0$, and when $g_N > 0$, the normal contact force must

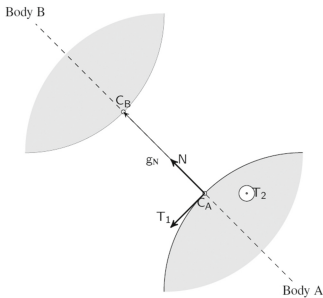


Fig. 1. Contact local frame.

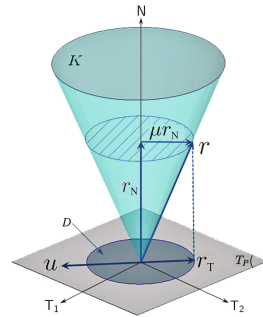


Fig. 2. 3D Coulomb's friction cone, sliding case.

¹ The polarization effect is created by two aspects: the presence of radial clearance in the revolute joint and the forces acting on the parts.

Definition 1. Polarization is the contact position between the two parts under the influence of an external force in an equilibrium stage.

² <http://siconos.gforge.inria.fr/>.

vanish, *i.e.* $r_N = 0$ (no magnetic or distance forces) [1, 3, 6]. These conditions yield a complementarity condition denoted compactly as:

$$0 \leq g_N \perp r_N \geq 0. \quad (1)$$

The normal contact law at the velocity level is expressed as:

$$0 \leq u_N \perp r_N \geq 0, \quad \text{if } g_N = 0. \quad (2)$$

The tangential contact law is the Coulomb friction that constrain the contact force r in the the friction cone (see Fig. 2)

$$r \in K = \{r \in \mathbb{R}^3, \|r_T\| \leq \mu r_N\}. \quad (3)$$

The scalar $\mu \geq 0$ is the coefficient of friction. In case of sliding the tangential force r_T acts in direction opposite to the relative tangential velocity u_T . If the relative tangential velocity u_T is zero then the bodies stick to each other (rolling without slipping). We introduce the modified relative velocity $\hat{u} := u + \mu \|u_T\| \mathbf{N}$, then the Coulomb friction can be equivalently expressed as a second-order cone complementarity condition [4, 7] if $g_N = 0$:

$$K^* \ni \hat{u} \perp r \in K. \quad (4)$$

The cone $K^* = \{v \in \mathbb{R}^3 | r^T v \geq 0, \forall r \in K\}$ is the dual cone of K .

2.2 Newton-Euler Formulation of the Equation of Motion

Let us consider a mechanical system subjected to m constraints, with m_e holonomic bilateral constraints $h^\alpha(q) = 0, \alpha \in \mathcal{E} \subset \mathcal{I}N$, m_i unilateral constraints $g_N^\alpha(q) \geq 0, \alpha \in \mathcal{J} \subset \mathcal{I}N$ and Coulomb friction. The Newton-Euler formulation of such a system is given as:

$$\left\{ \begin{array}{l} \dot{q} = T(q)v, \\ M\dot{v} = F(t, q, v) + H^\top(q)\lambda + G^\top(q)r, \\ H^\alpha(q)v = 0, \\ u^\alpha = G^\alpha(q)v, \quad \hat{u}^\alpha = u^\alpha + \mu^\alpha \|u_T^\alpha\| \mathbf{N}^\alpha \\ r^\alpha = 0, \quad \text{if } g_N^\alpha(q) > 0, \\ K^{\alpha,*} \ni \hat{u}^\alpha \perp r^\alpha \in K^\alpha, \quad \text{if } g_N^\alpha(q) = 0, \\ u_N^{\alpha,+} = -e_r^\alpha u_N^{\alpha,-}, \quad \text{if } g_N^\alpha(q) = 0 \text{ and } u_N^{\alpha,-} \leq 0, \end{array} \right\} \begin{array}{l} \alpha \in \mathcal{E} \\ \alpha \in \mathcal{J} \end{array}$$

where q is the vector of coordinates of the position and the orientation of the body, v is the velocity, the operator $T(q) \in \mathbb{R}^{7 \times 6}$ links the time derivatives of the coordinates to the velocities, M is the total inertia matrix, $F(t, q, v) \in \mathbb{R}^6$ collects all the forces and torques applied to the body. The operators $H \in \mathbb{R}^{m_e \times n}$ and $G \in \mathbb{R}^{3m_i \times n}$ link the local velocity variables in the joints, and at contacts respectively, to the velocity vector of the bodies.

2.3 The Numerical Integration Method

In this paper we use the event-capturing method based on the Moreau-Jean time-stepping scheme [3, 12, 13], where the constraints are solved at the velocity level and thereafter named the NSCD method. It is well-known that velocity level treatment of constraints yields violations of constraints with the drift phenomenon. When we simulate mechanisms with small clearances, this is not tolerable since we have to keep the violation as small as possible with respect to the characteristic length of the clearances. To overcome this limitation of the standard Moreau-Jean time-stepping scheme, we use the combined projection scheme as proposed in [2].

3 The C-60 Miniature Circuit Breaker Mechanism

Miniature circuit breaker construction is simple, however very precise. In fact, a miniature circuit breaker has no replacement parts. It is not designed to be maintained. When a unit goes bad, it is simply replaced. A typical miniature circuit breaker mechanism is depicted in Fig. 3(a).

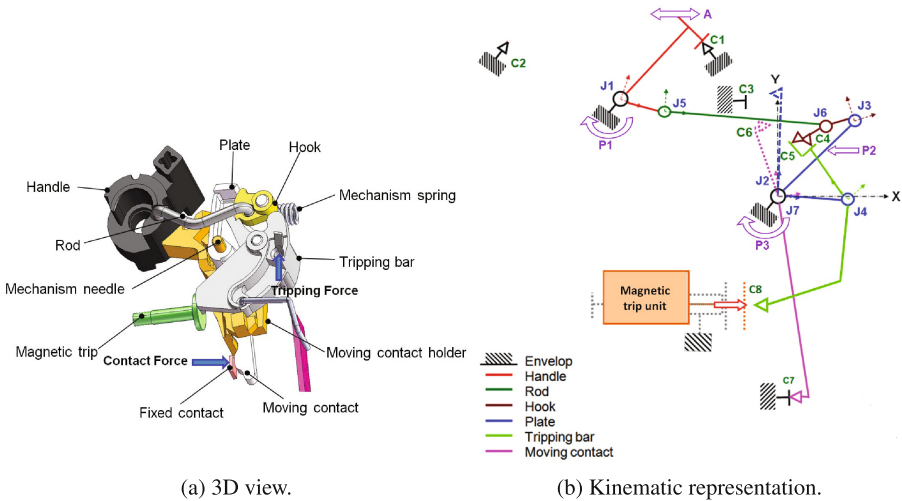


Fig. 3. C-60 circuit breaker mechanism - ON position.

Mechanism working principle: All the mechanism parts are enclosed in-between the case and cover parts. These parts are connected to each other through a revolute joint or frictional contact. In the following section we will see the detailed description of these joints and contacts. In the first step, the primary function of a mechanism is usually formulated in terms of kinematical quantities (link geometry, kinematic constraints, etc). Also the various geometrical relations resulting from the kinematical analysis of the linkage mechanism

are an essential ingredient for the dynamic analysis. The kinematical analysis of a miniature circuit breaker mechanism (hereafter called the C-60 mechanism) is of great importance. The C-60 mechanism consists of seven links, seven revolute joints with clearance in both radial and axial direction and four frictional contacts (see Fig. 3(b)). It has 42 degrees of freedom. The operating mechanism in the ON position is explained as follows:

The close operation leads to ON position of the breaker. In close operation (see Fig. 3(b)), the operating handle (A) is rotated clockwise which closes the contacts C_5 and C_4 through the revolute joints J_1 , J_5 , J_6 , J_3 and J_4 . The frictional contacts C_5 and C_4 have a specific wedge shape profile, which enables the locking between the hook and tripping bar. After the activation of the contacts C_5 and C_4 the motion has been transferred to the moving contact through the plate by revolute joints J_2 and J_7 , which ensure closing of the contact between the moving and the fixed contact. During close operation the handle spring (P_1) and the mechanism springs (P_2 and P_3) get charged, which will be used for the trip operation of the breaker.

3.1 Revolute Joint Between the Case, the Cover and the Handle: J_1

The revolute joint between the case, the cover and the handle is J_1 . The protrusion on the case and cover acts as a journal and the cavity on the handle acts as a bearing. In our modelling approach the ideal revolute joint is replaced by a journal and two circular rings at the extreme ends of the bearing (see Fig. 4) which acts as a spatial revolute joint with clearance. The axial and radial clearances in the revolute joint are modeled by introducing six degrees of freedom between the bearing and the journal. The relative motion between them is restricted by the internal surface of the bearing and the flanges of the journal. The radial clearance can be varied by changing the internal diameter of the bearing. The contact between the flange and the bearing top/bottom surface is a plane-plane contact. In reality, a plane-plane contact is impossible due to the presence of surface roughness and waviness. However the plane-plane contact can be completely described by three contact points. Few limitations of the plane-plane contacts are: more simulation time is required (numerically costly) as the contact detection is done on the entire area, and in return it gives only one contact point

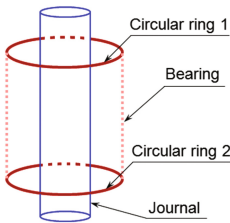


Fig. 4. Revolute joint with clearance J_1 .

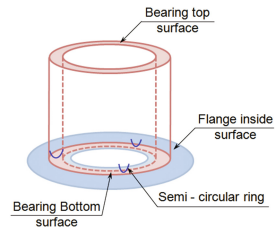


Fig. 5. Modeling of plane-plane contact.

between the plane-plane contact which is practically not correct. The contact between the flange and the bearing face is modeled by considering the plane surface of the flange, while the plane surface of the bearing is replaced by three semi-circular equidistant rings (see Fig. 5).

4 Experimental Validation: Contact Force Versus Displacement

In this section we report comparisons between numerical results obtained with the NSCD method, and experimental data obtained on physical prototypes built by Schneider Electric. The radial clearance in the revolute joints is given as: $J_1 = 0.085$ mm, $J_2 = 0.05$ mm, $J_3/J_4 = 0.06$ mm, $J_5/J_6 = 0.045$ mm and $J_7 = 0.055$ mm. Referring to the arrow in Fig. 3, the comparisons are made by recording force and displacement histories at the moving contact. The test bench consists of the fixture to mount the C-60 breaker and the moving table which comprises a pair of linear motion guide, see Fig. 6. The load cell is mounted on the moving table to measure the force and the bi-axial movement of the moving table is measured by two position sensors. The contact force of the moving contact C_7 (see Fig. 3(b)) is measured with the help of load cell, and is recorded by the computer programme. We have followed a similar methodology for the virtual testing (virtual test bench) of the C-60 product using the simulation.

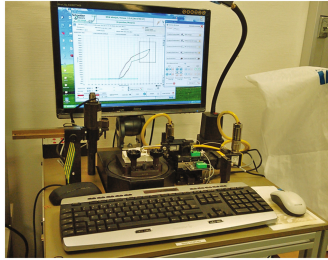


Fig. 6. Experimental test bench for contact/tripping force measurement.

1. In case of experimental test, the effect of polarization of the joints is approximately less by 50% when compared to the total displacement of the moving contact. At the static equilibrium (at the end of forward motion) of the sample-1, the recorded contact force is 15.28 N and the total displacement is 2.0 mm, see Fig. 7(a). The results of the experimental test are compared with the numerical simulation. In case of the numerical test the effect of polarization is similar to that of the experimental test, see Fig. 7(b). However the trajectory of the contact force in both the experiment and numerical tests are not identical, this may be due to the fact that the geometrical variations on the contacting surfaces of the parts are not considered in the case of numerical simulation. In reality the geometrical variations always exist and these

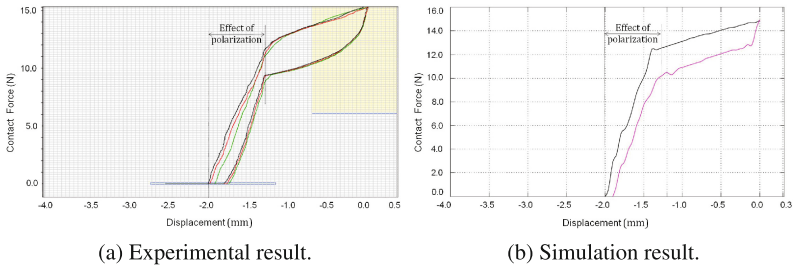


Fig. 7. Sample-1: Contact force versus displacement.

variations may change the polarization of the parts (contact points between the parts). In case of the numerical simulation, the contact force at the static equilibrium is 14.96 N. The percentage relative error in the contact force between the experiment and numerical test is 2.08%.

2. The trajectory of the contact force in case of forward motion is lagging behind the backward motion of the moving contact. This is due to the effects of friction (change in the direction of the frictional forces) in the joints. In case of the numerical simulation, the coefficient of friction between the plastic-plastic materials is considered to be $\mu = 0.3$, and between the steel-plastic materials $\mu = 0.1$. In case of experimental test the real values of the coefficient of friction are not known. This may be one of the reasons behind the slightly different behaviour of the contact force trajectories between the experiment and virtual test.

5 Conclusions

This paper is devoted to the numerical simulation of the C-60 circuit breaker built by Schneider Electric, using the so-called Moreau-Jean NSCD event-capturing numerical scheme. It relies on rigid body assumptions, with set-valued Coulomb's friction, and constant kinematic restitution coefficients. Emphasis is put on the modeling of three dimensional revolute joints with axial and radial clearance. Moreover detailed comparisons with experimental data obtained at the Schneider Electric laboratory, prove the very good prediction capabilities of the NSCD approach, for this type of mechanisms.

References

1. Abadie, M.: Dynamic simulation of rigid bodies: modelling of frictional contact. In: Brogliato, B. (ed.) *Impacts in Mechanical Systems: Analysis and Modelling. Lecture Notes in Physics (LNP)*, vol. 551, pp. 61–144. Springer, New York (2000)
2. Acary, V.: Projected event-capturing time-stepping schemes for nonsmooth mechanical systems with unilateral contact and Coulomb's friction. *Comput. Methods Appl. Mech. Eng.* **256**, 224–250 (2013)

3. Acary, V., Brogliato, B.: Numerical Methods for Nonsmooth Dynamical Systems: Applications in Mechanics and Electronics. Lecture Notes in Applied and Computational Mechanics, vol. 35. Springer, Berlin (2008)
4. Acary, V., Cadoux, F., Lemarchal, C., Malick, J.: A formulation of the linear discrete Coulomb friction problem via convex optimization. *ZAMM J. Appl. Math. Mech. (Zeitschrift für Angewandte Mathematik und Mechanik)* **91**(2), 155–175 (2011)
5. Akhadkar, N., Acary, V., Brogliato, B.: Analysis of collocated feedback controllers for four-bar planar mechanisms with joint clearances. *Multibody Syst. Dyn.* **38**(2), 101–136 (2016)
6. Brogliato, B.: Nonsmooth Mechanics: Models, Dynamics and Control, 3rd edn. Springer International Publishing, Switzerland (2016)
7. De Saxcé, G.: Une généralisation de l'inégalité de Fenchel et ses applications aux lois constitutives. *C. R. Acad. Sci. Ser. II* **314**, 125–129 (1992)
8. Flores, P.: A parametric study on the dynamic response of planar multibody systems with multiple clearance joints. *Nonlinear Dyn.* **61**(4), 633–653 (2010)
9. Flores, P., Leine, R., Glocker, C.: Modeling and analysis of planar rigid multibody systems with translational clearance joints based on the non-smooth dynamics approach. *Multibody Syst. Dyn.* **23**, 165–190 (2010)
10. Gummer, A., Sauer, B.: Influence of contact geometry on local friction energy and stiffness of revolute joints. *J. Tribol.* **134**(2), 021402-1–021402-9 (2012)
11. Haroun, A., Megahed, S.: Simulation and experimentation of multibody mechanical systems with clearance revolute joints. In: *Proceedings of World Academy of Science, Engineering and Technology*, 63. World Academy of Science, Engineering and Technology (2012)
12. Jean, M.: The non-smooth contact dynamics method. *Comput. Methods Appl. Mech. Eng.* **177**(3), 235–257 (1999)
13. Jean, M., Moreau, J.: Dynamics in the presence of unilateral contacts and dry friction: a numerical approach. In: del Piero, G., Maceri, F. (eds.) *Unilateral Problems in Structural Analysis II. CISM Courses and Lectures*, vol. 304, pp. 151–196. Springer, Vienna (1987)
14. Krinner, A., Thümmel, T.: Non-smooth behaviour of a linkage mechanism with revolute clearance joints. In: *New Advances in Mechanisms, Transmissions and Applications*, pp. 233–241. Springer (2014)
15. Orden, J.G.: Analysis of joint clearances in multibody systems. *Multibody Syst. Dyn.* **13**(4), 401–420 (2005)
16. Thümmel, T., Funk, K.: Multibody modelling of linkage mechanisms including friction, clearance and impact. In: *Proceedings of the 10th World Congress on the Theory of Machines and Mechanisms in Oulu*, June 20 to 24, vol. 4, pp. 1387–1392. University Press, Finland (1999)
17. Yan, S., Xiang, W., Zhang, L.: A comprehensive model for 3D revolute joints with clearances in mechanical systems. *Nonlinear Dyn.* **80**(1), 309–328 (2015)

Kinematics and Bifurcation of a Twofold-Symmetric Eight-Bar Linkage

Zhao Tang¹, Dimiter Zlatanov², and Jian Dai^{1,3}(✉)

¹ Key Laboratory of Mechanism Theory and Equipment Design
of Ministry of Education, Tianjin University, Tianjin 300072, China
zhaotang@tju.edu.cn

² PMAR Robotics, University of Genoa, 16145 Genoa, Italy
zlatanov@dim.ec.unige.it

³ Kings College London, University of London, London WC2R 2LS, UK
jian.dai@kcl.ac.uk

Abstract. The paper presents an eight-bar linkage derived from a rotatable kaleidocycle, a hinged ring of eight regular tetrahedra with revolute joint axes along common edges. A simplified derivation of the kinematics closure equation of the mechanism is proposed. The bifurcations of the two-dimensional configuration space of this two-degree-of-freedom linkage is analyzed by screw theory and the different modes of operation are described.

Keywords: Twofold-symmetric linkage · Closure equation · Bifurcation · Singularity · Kaleidocycle

1 Introduction

A kaleidocycle is a ring of an even number of tetrahedra hinged along common edges skew in every body [6, 9]. With eight or more tetrahedra, there is a continuous twisting inward-outward motion of the ring, displaying all the faces when the ring is viewed along its axis [4].

Kaleidocycles have been a known subject in recreational mathematics [2]. They are also of interest to mechanism theory [5, 8]. The equivalent linkage is a $2k$ -bar hinged loop with skew revolute-joint axes in every link. For example, the kaleidocycle composed of six regular tetrahedra can be thought of as a realization of the threefold-symmetric Bricard linkage [1].

In this paper, we study a twofold-symmetric eight-bar linkage derived from the kaleidocycle consisting of eight regular tetrahedra. In Sect. 2, the closure equation of the eight-bar linkage is derived in a new and simplified way. The mobility and bifurcations [10] are analyzed in Sect. 3. The article concludes with Sect. 4.

2 Kinematics

The sketch of the Twofold-symmetric 8-bar linkage is shown in Fig. 1. It is composed of eight equal links connected with eight revolute joints. These joint axes

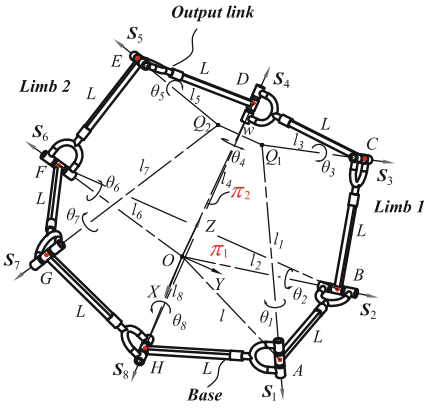


Fig. 1. Twofold-symmetric 8-bar linkage

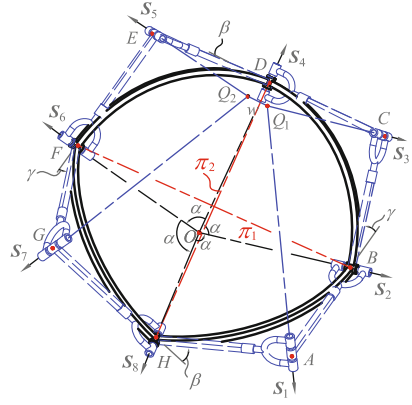


Fig. 2. Equivalent spherical four-bar linkage

are denoted by A, B, \dots, H respectively. The axes of every two adjoining hinges are perpendicular, $A \perp B \perp C \perp \dots \perp H \perp A$. When referring to a “link”, e.g., AB , we will usually mean the common normal line or segment between two adjoining axes.

In the configuration in Fig. 1, the axes B, D, F , and H intersect at point O , while points Q_1 and Q_2 are the intersections of A, C and E, G , respectively.

The distance from O to link i is

$$l_{2i} = l_{2(i+1)} = L \tan \frac{\theta_{2i+1}}{2} \quad (i = 1, 2, 3) \tag{1}$$

Thus,

$$l_2 = l_4 = l_6 = l_8 ; \theta_1 = \theta_3 = \theta_5 = \theta_7 \tag{2}$$

Suppose we now replace each link pair $HA - AB, BC - CD, DE - EF$, and $FG - GH$ by a single rigid body, HB, BD, DF and FH , respectively. (I.e., we fix the value of every second joint angle.) Then, the eight-bar can move as the spherical four-bar linkage shown in Fig. 2. As its four link lengths are identical, measured by the constant angle α , there are two perpendicular planes of symmetry $\pi_1(OBF)$ and $\pi_2(ODH)$. The points Q_1 and Q_2 are reflections in the plane π_2 .

The joints values of the eight-bar in this spherical-four-bar mode can be given as

$$\begin{aligned} \theta_1 = \theta_3 = \theta_5 = \theta_7 &= \pi - \alpha \\ \theta_2 = \theta_6 = \gamma ; \theta_4 = \theta_8 &= \beta \end{aligned} \tag{3}$$

where β and γ are variable (and only one is independent).

For a general spherical four-bar linkage, it can be located on a spherical surface, as shown in Fig. 3, where these links are denoted by the arcs of AB, BC, CD and DA . Axes of their joints are OA, OB, OC and OD , and they

intersect into the center O of the sphere. α_{ij} is the central angle of the arc link and ϕ_i is the angular displacement between two links.

The mathematical mapping between the parameters of geometric link and the angular displacements can be given as [7],

$$c_{12}(c_{34}c_{41} - c_4s_{34}s_{41}) - s_{12}(c_1(c_4c_{41}s_{34} + c_{34}s_{41}) - s_1s_{34}s_4) - c_{23} = 0 \quad (4)$$

where

$$s_{ij} = \sin \alpha_{ij}, \quad c_{ij} = \cos \alpha_{ij}, \quad s_i = \sin \phi_i, \quad c_i = \cos \phi_i$$

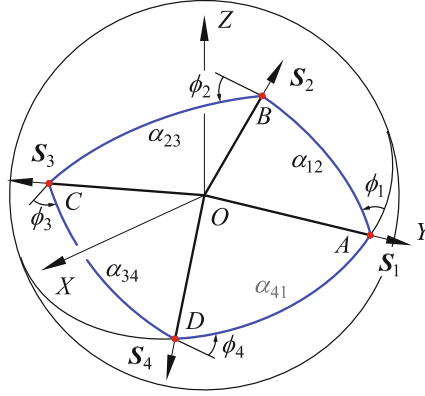


Fig. 3. Mode of spherical four-bar linkage

Because of symmetry, the geometric link parameters and the revolute joints variables of the spherical four-bar linkage in our case satisfy the following conditions:

$$\begin{aligned} \alpha_{41} = \alpha_{12} = \alpha_{23} = \alpha_{34} = \alpha \\ \phi_1 = \phi_3 = \beta; \quad \phi_2 = \phi_4 = \gamma \end{aligned} \quad (5)$$

Substituting Eq. (5) into Eq. (4), the closure equation of the 8-bar linkage can be written as

$$\sin^2 \alpha (\sin \beta \sin \gamma - (\cos \beta + 1)(\cos \gamma + 1) \cos \alpha) = 0 \quad (6)$$

We now note that the initial configuration in Fig. 1 can be for a general value of α . For any given α and β , Eq. (6) determines the value of γ . (Equation (6) is symmetric in β and γ , so we can consider β to be the dependent variable.) We thus obtain a two-dimensional set of configurations, obtained from the initial one by varying α and β (or α and γ).

3 Mobility and Bifurcation

The distance between points Q_1 and Q_2 in Fig. 2 can be derived as

$$w = 2L \sin \frac{\beta}{2} \left(\cot \frac{\beta}{2} - \cot \frac{\gamma}{2} \right) \quad (7)$$

Let $w = 0$, i.e., Q_1 and Q_2 coincide and so the axes of A , C , E , and G intersect in one point. Then,

$$\beta = 0 \text{ or } \beta = \gamma \quad (8)$$

Substituting $\beta = \gamma$ into Eq. (6), the closure equation can be rewritten as

$$\sin^2 \alpha (\sin^2 \gamma - \cos \alpha (1 + \cos \gamma)^2) = 0 \quad (9)$$

Therefore

$$\alpha = 0 \text{ or } \cos \alpha = \tan^2 \frac{\gamma}{2} \quad (10)$$

When Q_1 and Q_2 coincide, the instantaneous mobility of the 8-bar linkage increases. Indeed, since each of the eight hinge axes passes through one of two points, the rank of the screw system spanned by all zero-pitch joint screws is at most five. Therefore the mobility of the loop is at least three, violating the conventional mobility formula for an 8-bar.

3.1 General Configuration

We use a global reference frame $OXYZ$ (fixed in space but not in any of the rigid links) with the symmetry planes π_1 and π_2 , chosen as OYZ and OXZ , respectively. In the figure, the OX and OY axes point down and to the right.

The screw coordinates of H and B , expressed in the global frame, are

$$\begin{aligned} \mathbf{S}_8 &= (m_1, 0, n_1, 0, 0, 0)^T \\ \mathbf{S}_2 &= (0, m_2, n_2, 0, 0, 0)^T \end{aligned} \quad (11)$$

We denote by \mathbf{s}_i a unit vector directed as the axis of the i -joint screw \mathbf{S}_i . As adjoining axes are perpendicular, axis A is normal to axes B and H and so $\mathbf{s}_1 = \mathbf{s}_2 \times \mathbf{s}_8$. From (11), $\mathbf{s}_8 = [m_1, 0, n_1]^T$ and $\mathbf{s}_2 = [0, m_2, n_2]^T$. Hence,

$$\mathbf{S}_1 = (m_2 n_1, m_1 n_2, -m_1 m_2, -kp, kq, kr)^T \quad (12)$$

where

$$p = m_1(m_2^2 + n_2^2 + n_1 n_2), \quad q = m_2(m_1^2 + n_1^2 + n_1 n_2), \quad r = m_1^2 n_2 - m_2^2 n_1$$

$$k = \frac{l}{\sqrt{m_1^2 + m_2^2 + (n_1 + n_2)^2}}$$

and l is the distance from O to axis A .

The coordinates of the eight joint screws can now be written as follows,

$$\begin{aligned}
 \mathbb{S}_{i1} & \begin{cases} \mathbf{S}_1 = (m_2 n_1, m_1 n_2, -m_1 m_2, -kp, kq, kr)^T \\ \mathbf{S}_2 = (0, m_2, n_2, 0, 0, 0)^T \\ \mathbf{S}_3 = (-m_2 n_1, m_1 n_2, -m_1 m_2, -kp, -kq, -kr)^T \\ \mathbf{S}_4 = (-m_1, 0, n_1, 0, 0, 0)^T \end{cases} \\
 \mathbb{S}_{i2} & \begin{cases} \mathbf{S}_5 = (-m_2 n_1, -m_1 n_2, -m_1 m_2, kp, -kq, kr)^T \\ \mathbf{S}_6 = (0, -m_2, n_2, 0, 0, 0)^T \\ \mathbf{S}_7 = (m_2 n_1, -m_1 n_2, -m_1 m_2, kp, kq, -kr)^T \\ \mathbf{S}_8 = (m_1, 0, n_1, 0, 0, 0)^T \end{cases}
 \end{aligned} \tag{13}$$

To analyze the mobility of the linkage we consider it as a parallel mechanism with two leg chains composed of joints, 1 to 4 and 5 to 8, respectively, and we follow the methodology described in [3]. The motion systems of this parallel mechanism are generated by the screws in (13), while the constraint systems are spanned by

$$\begin{aligned}
 \mathbb{S}_{i1}^r & \begin{cases} \mathbf{S}_{11}^r = (0, -\frac{kr}{m_2 n_1}, \frac{kq}{m_2 n_1}, 0, 0, 0)^T \\ \mathbf{S}_{12}^r = (x, y, z, \frac{kl_2 m_2 n_1}{L}, \frac{kl_2 m_1 n_2}{L}, \frac{kl_2 m_1 m_2}{L})^T \end{cases} \\
 \mathbb{S}_{i2}^r & \begin{cases} \mathbf{S}_{21}^r = (0, \frac{kr}{m_2 n_1}, \frac{kq}{m_2 n_1}, 0, 0, 0)^T \\ \mathbf{S}_{22}^r = (x, -y, z, -\frac{kl_2 m_2 n_1}{L}, \frac{kl_2 m_1 n_2}{L}, \frac{kl_2 m_1 m_2}{L})^T \end{cases}
 \end{aligned} \tag{14}$$

where

$$x = -\frac{km_1}{L}, \quad y = -\frac{(k-l_2)m_2}{L}, \quad z = \frac{k(n_1+n_2)-l_2 n_2}{L}, \quad l_2 = \sqrt{l^2 - L^2}$$

and L is the length of link AB .

This shows that $\dim(\mathbb{S}^r) = \text{card}(\mathbb{S}^r) = 4$. So the mobility of the 8-bar linkage calculated from the mobility criterion in [3] is $m = 8 - 6 + 4 - 4 = 2$.

3.2 Singular Configurations

When the distance $|Q_1 Q_2|$ equals to zero ($Q_1 = Q_2$ as shown in Fig. 4), a spanning set of constraint screws of the 8-bar linkage can be derived as

$$\begin{aligned}
 \mathbb{S}_{l_1}^r &= \begin{cases} \mathbf{S}_{11}^r = (0, 0, \frac{kq}{m_2n_1}, 0, 0, 0)^T \\ \mathbf{S}_{12}^r = (x, y, z, \frac{kl_2m_2n_1}{L}, \frac{kl_2m_1n_2}{L}, \frac{kl_2m_1m_2}{L})^T \end{cases} \\
 \mathbb{S}_{l_2}^r &= \begin{cases} \mathbf{S}_{21}^r = (0, 0, \frac{kq}{m_2n_1}, 0, 0, 0)^T \\ \mathbf{S}_{22}^r = (x, -y, z, -\frac{kl_2m_2n_1}{L}, \frac{kl_2m_1n_2}{L}, \frac{kl_2m_1m_2}{L})^T \end{cases}
 \end{aligned} \tag{15}$$

Obviously, $\dim(\mathbb{S}^r) = 3$, $\text{card}(\mathbb{S}^r) = 4$. So in this configuration, the mobility of linkage, calculated as in [3], is $m = 8 - 6 + 4 - 3 = 3$.

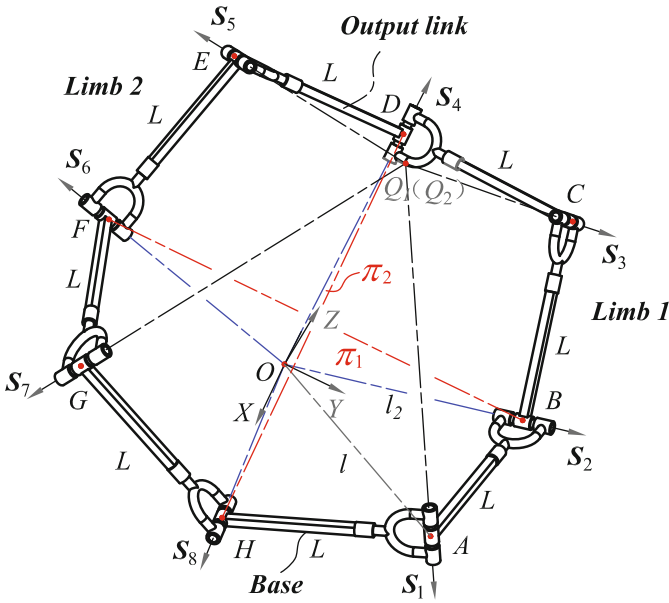


Fig. 4. 8-bar linkage in a singular configuration

3.3 Discussion

Figure 5 illustrates the geometric nature of the bifurcation and the different modes of motion. There are two sheets (two-dimensional regions) of the configuration space where no links or joints coincide. In the first region, exemplified by Fig. 5(a), the axes of the revolute joints A, C, E and G intersect in one point. On the second sheet, Fig. 5(c), B, D, F and H are concurrent instead. On both sheets, the linkage has mobility two and two planes of symmetry. In the singular configuration, Fig. 5(b), the axes of two pairs of revolute joints intersect in one point simultaneously. The mobility of the 8-bar linkage changes to three with four symmetry planes.

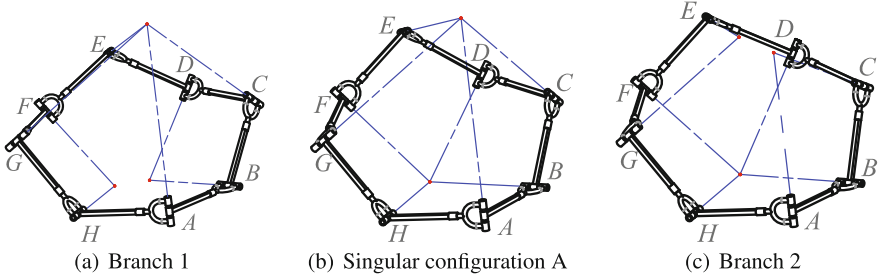


Fig. 5. Geometry of the bifurcation

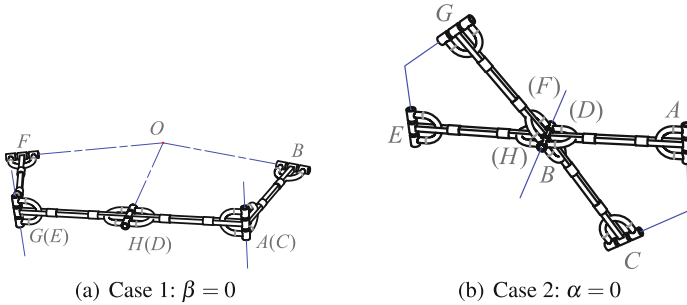


Fig. 6. Two configurations with higher instantaneous mobility

From Eqs. (8) and (10), there are two other special cases: $\beta = 0$ and $\alpha = 0$. In the first, Fig. 6(a), the axes of revolute joints A , H and G are collinear with C , D and E , respectively, while B , D , F and H intersect in one point. In this configuration the mobility of the mechanism is four and the 8-bar linkage enters a 3-DOF region where it operates as a 3R serial chain. In the second case, Fig. 6(b), the axes B , D , F and H coincide. Also here the mechanism can now move as a 3R serial chain, but with coincident hinge axes.

In both cases, a general motion of the 3R serial chain reduces instantaneous mobility to three. While in some special cases, the mobility can stay the same if some condition is met. In Fig. 6(a), all the links should be coplanar and B , $D(H)$, F intersect in one point. In Fig. 6(b), there should be two perpendicular symmetric planes. In these cases, the mobility is always four and there exists a motion to come back to the non-overlapping configuration.

In both cases configurations with higher instantaneous mobility can be obtained when more axes become coincident. And these cases can be reproduced after any cyclic permutation of A, B, \dots, H . These multiple regions have intersections in configurations where even more revolute joints become coincident. The detailed analysis of the topology of the configuration space is rather complex and is omitted here due to lack of space. Moreover, in many of these cases the two-fold symmetry is not maintained. We should note, however, that

although these configurations like the ones in Fig. 6 appear exotic, they constitute “most” of the points in the configuration space, as they form regions with dimensions higher than the “normal” 2-DOF operation modes.

4 Conclusions

This paper presents a two-fold symmetric 8-bar linkage evolved from a kaleidocycle with 8 equilateral tetrahedra. As there are four axes intersecting in one point at all time, the 8-bar linkage is treated as an equivalent spherical four-bar linkage. The closure equation is then obtained easily using methods of spherical four-bar analysis. Screw-system-based analysis identifies the singular configuration and reveals the bifurcation process. As the 8-bar linkage moves from one region of the configuration space to another, the four intersecting axes of revolute joints will switch.

Acknowledgments. The authors wish to acknowledge the financial support received from the Natural Science Foundation of China No. 51535008 and International S&T Cooperation Program of China under No. 2014DFA70710.

References

1. Chen, Y., You, Z., Tarnai, T.: Threefold-symmetric Bricard linkages for deployable structures. *Int. J. Solids Struct.* **42**(8), 2287–2301 (2005)
2. Cundy, H.M., Rollett, A.P.: *Mathematical models*. Tarquin (1981)
3. Dai, J.S., Huang, Z., Lipkin, H.: Mobility of overconstrained parallel mechanisms. *J. Mech. Des.* **128**(1), 220–229 (2006)
4. Fowler, P.W., Guest, S.D.: A symmetry analysis of mechanisms in rotating rings of tetrahedral. In: *Proceedings of the Royal Society of London A: Mathematical, Physical and Engineering Sciences*. The Royal Society, vol. 461, no. 2058, pp. 829–1846 (2005)
5. Gan, W., Pellegrino, S.: Closed-loop deployable structures. In: *Proceeding of the 44th AIAA/ASME/ASCE/AHS/ASC Structures, Structural Dynamics, and Materials Conference*, Norfolk, VA (2003)
6. Glassner, A.: Net results [3D graphics]. *IEEE Comput. Graph. Appl.* **17**(4), 85–89 (1997)
7. He, S.I., Wang, S.E.: Study on input/output equation for spherical 4R mechanism. *Sci-Tech Inf. Dev. Econ.* **2**, 083 (2011)
8. Safsten, C., Fillmore, T., Logan, A., Halverson, D., Howell, L.: Analyzing the stability properties of kaleidocycles. *J. Appl. Mech.* **83**(5), 051001 (2016)
9. Schattschneider, D., Escher, M.C., Walker, W.: *MC Escher kaleidocycles*. Ballantine Books (1977)
10. Zlatanov, D., Bonev, I.A., Gosselin, C.M.: Constraint singularities of parallel mechanisms. In: *ICRA*, pp. 496–502 (2002)

A Novel Kinematic Model of Spatial Four-bar Linkage RSPS for Testing Accuracy of Actual R-Pairs with Ball-bar

Zhi Wang¹, Delun Wang^{1(✉)}, Xiaopeng Li¹, Huimin Dong¹,
and Shudong Yu^{1,2}

¹ School of Mechanical Engineering, Dalian University of Technology,
Dalian 1106024, People's Republic of China
dlunwang@dlut.edu.cn

² Department of Mechanical and Industrial Engineering,
Ryerson University, Toronto, ON, Canada
syu@ryerson.ca

Abstract. A novel kinematic model of spatial four-bar linkage RSPS is firstly presented for accuracy testing of R-pairs. During accuracy testing, the kinematic chain SPS of the ball bar and the R-pair constitute a RSPS mechanism, while the structure parameters of the RSPS mechanism correspond to the mounting parameters of the ball bar. Thus, the mounting position errors of the ball bar are identified by using the kinematic synthesis of the RSPS mechanism, based on the discrete data measured by the ball bar. Furthermore, the relationships between the measured errors and the mounting parameters of the ball bar are analyzed, by using the solutions of the kinematic equations of the RSPS mechanism.

Keywords: Spatial four-bar linkage · Kinematics · Ball bar · Error identification · Accuracy

1 Introduction

The ball bar is a widely used instrument for accuracy testing of machine tools. It was invented by Bryan, and firstly used to measure the errors of the simultaneous motion of two prismatic pairs [1, 2]. Then, a lot of ball bar methods are presented to measure the geometrical errors of the machine tools and robots [3–5]. These methods improved the efficiency of error testing and calibration, especially for multi-axis motions.

For a rotary pair, or R-pair, the accuracy is often represented by radial and axial runouts of the rotor [6, 7]. However, the runouts are influenced by the geometric errors of the measured surface, and related with the mounting positions of the sensors and work-pieces. Some precise artifacts are used as the work-pieces to reduce the influences of geometric errors; these methods are high-precision but time consuming, because it is difficult to mount the work-pieces to a suitable place.

As the ball bar is easy installation and efficient for motion measurement, some ball bar methods are presented to measure the accuracy of R-pairs [8–11]. In these researches, the mounting position errors of the ball bar are eliminated by adjusting

devices, or separated from the measured results by least square circle fitting. The former is time-consuming and the later is based on the assumption of planar motion. In fact, the motions of the ball bar are spatial motions during accuracy testing, and measured results are related with the mounting position of the ball bar. Therefore, how to identify the mounting position errors from the measured data? What are the relationships between the measured data and the mounting positions? These questions are discussed in this paper. A novel method, based on the spatial four-bar linkage RSPS, is firstly presented to identify the mounting errors of the ball bar, and the relationships between the measured errors and the mounting parameters are analyzed by using the geometrical model of the RSPS mechanism.

2 Accuracy Testing of R-Pairs with Ball Bar

A ball bar is composed of two master balls and a precise linear displacement sensor, as shown in Fig. 1. Thus, the result measured by the ball bar is the distance between the centers of the two balls.



Fig. 1. A ball bar with two master balls and one displacement sensor

During accuracy testing of an R-pair, the fixed ball S_A is mounted on a base and the moving ball S_B is mounted on the rotor, as shown in Fig. 2a. In most cases, the displacement sensor is possibly located at the sensitive direction of the rotary errors, such as the axial and radial directions [10]. As the rotor rotates, the ball bar records the distances $s^{(i)}$ between the centers of the two balls at every rotary position. For example, the measured results for one round are shown in Fig. 2b.

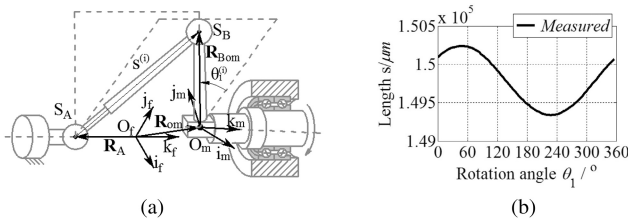


Fig. 2. Accuracy testing of an R-pair with ball bar and the measured data

Generally, the ball S_A is expected to be mounted on the rotational axis of the R-pair, and the measured results are desired to be pure error motions caused by the

R-pair. Unfortunately, the mounting position errors of two balls are inevitable. Sometimes, the mounting position errors are much bigger than the rotary errors of the R-pair, which make the results measured distribute as a trigonometric function, as shown in Fig. 2b. Thus, it is necessary to eliminate the influences of the mounting position errors.

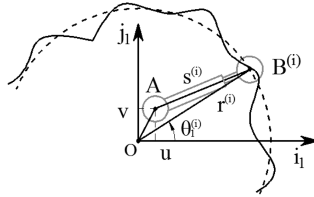


Fig. 3. The least square circle fitting of the measured results

In the existing researches [10], the mounting errors, or the eccentric motions, are often separated by using the least square circle fitting. As shown in Fig. 3, the motion of the ball bar is assumed as a planar motion, and the mounting errors of the ball bar are equivalent to the eccentricity (u, v) of the center point A relative to the rotary axis. Then, the eccentric motions caused by the mounting errors and the rotary error motions of the center point B will be separated. The results are shown in Fig. 4.

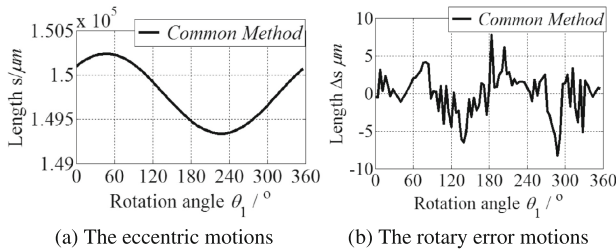


Fig. 4. The eccentric motions and rotary error motions separated by least square fitting

3 Mechanism Model of Ball Bar for Testing R-Pair

The kinematic chain SPS of the ball bar and the R-pair constitute a spatial RSPS mechanism, while the structure parameters of the RSPS mechanism correspond to the mounting parameters of the ball bar. The output motions of the prismatic pair correspond to the motions caused by the mounting positions errors of the ball bar, if the rotary pair rotates without errors. Thus, the mounting positions errors can be identified by kinematic synthesis of the RSPS mechanism.

In order to analyze the motions of the mechanism, a fixed frame $\{C; \mathbf{i}_1, \mathbf{j}_1, \mathbf{k}_1\}$ is employed and fixed to the base of the R-pair. Meanwhile, a moving frame

$\{D; \mathbf{i}_2, \mathbf{j}_2, \mathbf{k}_2\}$ is employed and attached to the moving ball S_B . In the fixed frame, the displacement equation of the RSPS mechanism can be written as

$$\mathbf{R}_{AB} = \mathbf{R}_{CD} + \mathbf{R}_{DB} - \mathbf{R}_{CA} \quad (1)$$

where, \mathbf{R}_{AB} denotes the vector from the center points A to B, whose length $|\mathbf{R}_{AB}| = s$ is the distance measured by the ball bar. The Eq. (1) can be rewritten as

$$s = \sqrt{l_1^2 + l_2^2 + h_1^2 - 2l_2h_1 \cos(\theta_1 - \theta_0)} \quad (2)$$

where, l_1, l_2, h_1 and θ_0 are the structure parameters of the RSPS mechanism, as shown in Fig. 5. The parameters h_1, θ_0 and l_1 locate the position of the center A, and the parameter l_2 determines that of the center B. θ_1 is the rotary angle.

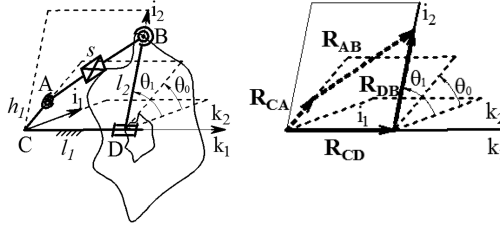


Fig. 5. The spatial RSPS mechanism and its parameters

Currently, the distances measured by the ball bar, denoted by $s^{(i)*}$ ($i = 1, 2, \dots, n$), contain both the motion caused by the mounting errors and the error motion of the R-pair. In order to identify the mounting position errors, a mathematic model of kinematic synthesis of an RSPS mechanism is set up, in which the mounting parameters are equivalent to the structure parameters of RSPS, that is

$$\begin{cases} \Delta_s = \min_{\mathbf{x}} \max_{1 \leq i \leq n} \{ \Delta^{(i)}(\mathbf{x}) \} = \min_{\mathbf{x}} \max_{1 \leq i \leq n} \{ |s^{(i)*} - s^{(i)}| \} \\ s.t. \quad l_1, l_2, h_1 \in (-\infty, +\infty); \quad \theta_0 \in (0, 2\pi) \\ \mathbf{x} = (l_1, l_2, h_1, \theta_0)^T \end{cases} \quad (3)$$

where, Δ_s is the maximum deviation between the distances measured by the ball bar and those calculated by the RSPS mechanism. n is the number of the discrete rotary positions. The output motions $s^{(i)}$ at the rotary position i is

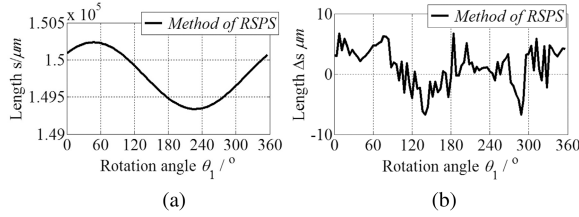
$$s^{(i)} = \sqrt{l_1^2 + l_2^2 + h_1^2 - 2l_2h_1 \cos(\theta_1^{(i)} - \theta_0)} \quad (4)$$

Based on the measured data, a four-bar linkage RSPS with parameters $(l_0, l_1, h_0, \theta_0)$ can be optimally calculated by the Eq. (3), shown in Table 1.

Table 1. The parameters of RSPR corresponding to the ball-bar testing

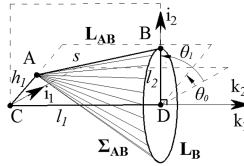
$l_1/\mu\text{m}$	$l_0/\mu\text{m}$	$h_0/\mu\text{m}$	θ_0/rad	$\Delta_s/\mu\text{m}$
63198.6	135798.9	1063.8	2.3114	6.7

The output displacements $s^{(i)}$ of the RSPS mechanism can be calculated by Eq. (4) with the identified parameters, as shown in Fig. 6a; and the remained rotary errors of the center point B in the measuring direction are shown in Fig. 6b.


Fig. 6. The output displacements of RSPS mechanism and the rotary errors

4 RSPS Mechanism and Mounting Errors

In order to discuss the relationships between the mounting parameters of the ball bar and the measured results, the geometrical model of the RSPS mechanism is set up, as shown in Fig. 7. The center-line AB of the ball bar traces a conical surface Σ_{AB} in the fixed frame [11]; the parameters are the same as the RSPS mechanism.


Fig. 7. The geometrical model the RSPS mechanism

For convenience, the Eq. (2) is divided by l_2 to avoid the influences caused by the rotary radius, that is

$$\frac{s}{l_2} = \sqrt{\left(\frac{l_1}{l_2}\right)^2 + \left(\frac{h_1}{l_2}\right)^2} + 1 - 2\frac{h_1}{l_2} \cos(\theta_1 - \theta_0) \quad (5)$$

Based on Eq. (5), the relationships between the mounting parameters and the measured results are discussed as follow.

(1) s/l_2 and l_1/l_2

The parameter l_1/l_2 is inversely proportional to the cone angle of the conical surface, shown in Fig. 7. s/l_2 and l_1/l_2 represent the influences of the mounting direction of the ball bar. The curves in Fig. 8 show that the amplitude of s/l_2 is proportional to the cone angle and the mean value of s/l_2 is inversely proportional to the cone angle.

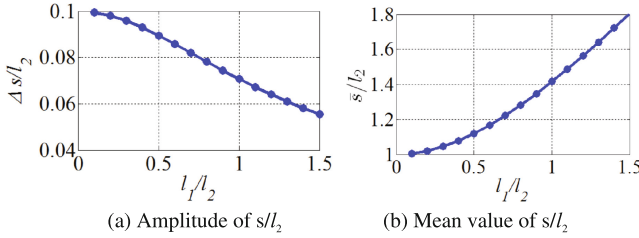


Fig. 8. The relationships between s/l_2 and l_1/l_2

In particular, if the parameter l_1/l_2 is zero, the spatial RSPS mechanism degenerated to be a planar mechanism. In this case, the axial mounting position errors of center points A and B are eliminated; the results measured by the ball bar are radial run-out of the R-pair. The Eq. (2) can be written as

$$s = \sqrt{l_2^2 + h_1^2 - 2l_2h_1 \cos(\theta_1 - \theta_0)} \quad (6)$$

There are three parameters h_1 , l_2 and θ_0 in Eq. (6), corresponding to the radial mounting errors of center points A and B, which are the same as the least square circle fitting discussed in Sect. 2.

(2) s/l_2 and h_1/l_2

The parameter h_1/l_2 is proportional to the eccentricity of the conic node A, shown in Fig. 7. The relationships between s/l_2 and h_1/l_2 represent the influences of the mounting position errors of the ball S_A . The calculated results, shown in Fig. 9, reveal both of the amplitude and mean value of s/l_2 are proportional to the eccentricity of the conic node.

In particular, if the parameter h_1/l_2 is zero, the radial mounting position error of the center point A is eliminated. The Eq. (2) can be written as

$$s = \sqrt{l_1^2 + l_2^2} \quad (7)$$

Two parameters l_1 and l_2 in Eq. (7) correspond to the position of the center point A and the rotary radius of the center points B.

(3) s/l_2 and l_2

The parameter l_2 corresponds to the rotary radius of the center point B, thus, the relationships between s/l_2 and l_2 represent the influences of the mounting position of

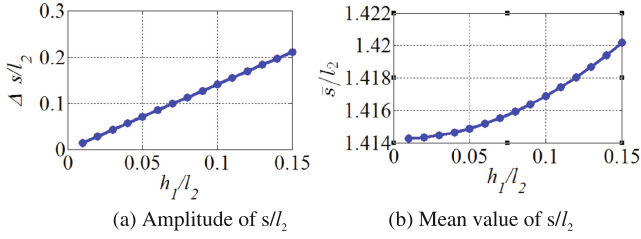


Fig. 9. The relationships between s/l_2 and h_1/l_2

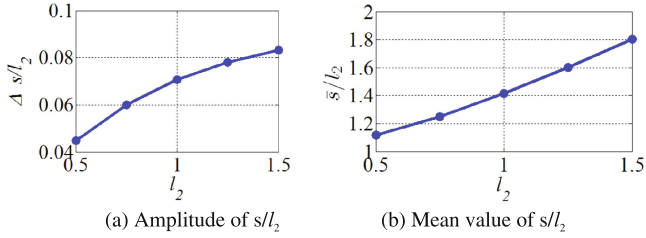


Fig. 10. The relationships between s/l_2 and l_2

the moving ball S_B . The calculated results, shown in Fig. 10, express that the amplitude and mean value of s/l_2 is proportional to the rotary radius.

(4) s/l_2 and θ_0

As known in Eq. (2), the amplitude and mean value of s/l_2 is independent of the parameter θ_0 , but the phase of s/l_2 is. In particularly, if the parameter θ_0 is zero, the Eq. (2) can be written as

$$s = \sqrt{l_1^2 + l_2^2 + h_1^2 - 2l_2h_1 \cos \theta_1} \quad (8)$$

Three parameters l_1 , l_2 and h_1 in Eq. (8) correspond to the axial and radial errors of the center points A and B.

5 Conclusions

- (1) The kinematic model of an RSPS mechanism is presented for accuracy testing of R-pair with ball bar. The structure parameters of the RSPS mechanism correspond to the mounting parameters of the ball bar, and the mounting errors can be identified by kinematic synthesis of an RSPS mechanism.
- (2) The amplitude of s/l_2 is proportional to the cone angle, and the mean value of s/l_2 is inversely proportional to the mounting angle of the ball bar. Both of the amplitude and mean value of s/l_2 are proportional to the eccentricity of the balls S_A and S_B .

Acknowledgments. The authors would gratefully acknowledge the support by the national natural science foundation of China (Grant No. 51275067).

References

1. Bryan, J.: A simple method for testing measuring machines and machine tools Part 1: Principles and applications. *Precis. Eng.* **4**(2), 61–69 (1982)
2. Bryan, J.: A simple method for testing measuring machines and machine tools Part 2: Construction details. *Precis. Eng.* **4**(3), 125–138 (1982)
3. Pakh, H.J., Kim, Y.S., Moon, J.H.: A new technique for volumetric error assessment of CNC machine tools incorporating ball bar measurement and 3D volumetric error model. *Int. J. Mach. Tools Manuf* **37**(11), 1583–1596 (1997)
4. Florussen, G.H.J., Delbressine, F.L.M., et al.: Assessing geometrical errors of multi-axis machines by three-dimensional length measurements. *Measurement* **30**(4), 241–255 (2001)
5. Takeda, Y., Shen, G., Funabashi, H.: A DBB-based kinematic calibration method for inparallel actuated mechanisms using a fourier series. *J. Mech. Design* **126**(5), 1201–1210 (2004)
6. ASME B89.3.4-2010: Axes of Rotation: Methods for Specifying and Testing. American National Standards Institute (2010)
7. ISO 230-7:2006: Test code for machine tools-Part 7: Geometric accuracy of axes of rotation. ISO (2006)
8. Huang, N., Bi, Q., Wang, Y.: Identification of two different geometric error definitions for the rotary axis of the 5-axis machine tools. *Int. J. Mach. Tools Manuf* **91**, 109–114 (2015)
9. Jiang, X., Cripps, R.J.: A method of testing position independent geometric errors in rotary axes of a five-axis machine tool using a double ball bar. *Int. J. Mach. Tools Manuf* **89**, 151–158 (2015)
10. Tsutsumi, M., Tone, S., Kato, N., et al.: Enhancement of geometric accuracy of five-axis machining centers based on identification and compensation of geometric deviations. *Int. J. Mach. Tools Manuf* **68**, 11–20 (2013)
11. Zargarbashi, S.H.H., Mayer, J.R.R.: A model based method for centering double ball bar test results preventing fictitious ovalization effects. *Int. J. Mach. Tools Manuf* **45**(10), 1132–1139 (2005)
12. Wang, D., Wang, W.: *Kinematic Differential Geometry and Saddle Synthesis of Linkages*. Wiley, Singapore (2015)

Model Reduction Methods for Optimal Follow-the-Leader Movements of Binary Actuated, Hyper-redundant Robots

Svenja Tappe^(✉), Dairong Yu, Jens Kotlarski, and Tobias Ortmaier

Institute of Mechatronic Systems, Leibniz Universität Hannover, Hanover, Germany
svenja.tappe@imes.uni-hannover.de

Abstract. A hyper-redundant shaft concept based on unique binary, electromagnetic tilting actuators was proposed for various examination tasks of difficultly accessible areas. Its specific design combines two important aspects required in endoscopic applications: it provides good path following capabilities in combination with high resistance against manipulation forces due to its kinematics and its actuation principle. For endoscope-like exploration, a commonly known follow-the-leader idea is adapted to the binary actuation. It is an efficient and intuitive path planning algorithm promising high path following accuracy. However, classical follow-the-leader approaches are designed for continuously adjustable joints. Hence, their applicability to binary actuated systems is limited. To achieve good path following capabilities optimal switching sequences during forward motion are necessary, resulting in a high computational effort. Therefore, this paper aims to analyze occurring deviations with respect to kinematic relations and proposes based on these results reduced models, i.e. simplified cost functions, for an efficient calculation of optimized switching sequences.

Keywords: Hyper-redundant robot · Binary actuation · Motion planning · Follow-the-leader

1 Introduction

The field of applications for endoscopes has been growing rapidly over the past years, spanning from maintenance of technical systems like turbines to minimally invasive surgery. The systems allow for servicing vastly and lead in this way to a huge saving in related expenses. However, systems have to overcome the discrepancy between flexibility to maneuver in crooked spaces and sufficient stiffness to withstand manipulation forces. In this context, many approaches have been proposed in literature, e.g. [1]. In [8] we proposed a serial chain design of a large number of electromagnetically actuated, one degree of freedom tilting joints. By utilizing electromagnetic actuation, huge holding torques can be provided resulting in a practically rigid system. Furthermore, its hyper-redundancy leads to good adaptation potential with respect to convoluted paths. The kinematics and dynamics model, as well as the analysis of hyper-redundant and binary

actuated systems, have been studied in detailed in [2]. Regarding path-following strategies, several concepts for achieving snake-like locomotion based on mimicking nature have been presented, see e.g. [5, 10]. A follow-the-leader approach for base-fixed robots has been introduced in [11]. In this method, the foremost part of the robot defines a reference path while advancing through its surroundings. The rest of the robot follows the tip and stays as close as possible to the reference path by adjusting the continuous joint angles accordingly, see [3]. Therefore, the follow-the-leader concept is an intuitive way of controlling a robot. It has been adapted to various robot kinematics, see e.g. [4, 6, 7].

Since binary actuated robots have no prospects of continuous interpolation of its joint angles, optimal switching patterns are needed to provide best path-following capabilities. Therefore, [9] introduces motion planning of a binary snake-like robot in two-dimensional space without obstacles based on optimized switch-on times. Constructively, this paper focuses on two main aspects of the follow-the-leader control strategy for binary actuated structures: first, the adaptation of the follow-the-leader motion to spatial manipulators with discrete actuation is introduced and occurring deviations based on kinematic relations are analyzed for the definition of a reduced cost function. Secondly, an efficient tip optimization with decreased parameter space is outlined and compared to existing methods presented in [9].

2 System Concept

The presented model-based approach of analyzing the deviations during follow-the-leader motion of a hyper-redundant binary actuated robot is defined with respect to a unique electromagnetic snake-like robot. Therefore, the system concept, i.e. its kinematic design, is presented briefly in this section.

The employed system is a hyper-redundant snake-like robot, based on a serial chain of a large number of equally built, electromagnetically driven tilting actuators. Each actuator is composed of four half rings made of ferromagnetic material, connected with aluminum joints for magnetic separation. Two individual magnetic circuits are created with pairs of coils arranged on either side of the tilting axis, see Fig. 1(a). By reason of beveled iron cores fixed tilting angles can be achieved, see [12]. With this unique concept, the bistable actuator can reach only two fixed tilting positions on each side. Therefore, it can be denoted as binary. It is not capable of reaching any intermediate positions. For the endoscopic shaft equal tilting actuators are combined to a serial chain. Spatial movements are achieved by twisting the actuators against each other with a fixed twisting angle. The kinematic design and modeling are described in detail in [8]. A picture of the prototypical set-up with ten actuators and the related schematic representation of Denavit Hartenberg (DH) coordinate frames for a generalized model of n actuators is shown in Fig. 1. To achieve endoscope-like exploration, the snake is additionally attached to a prismatic joint, moving the serial chain linearly with adjustable feeding speed.

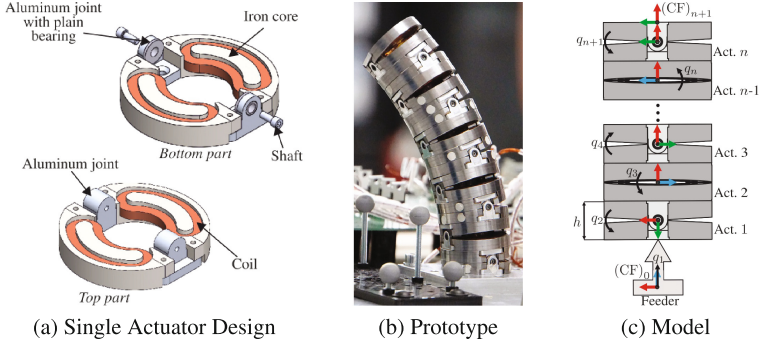


Fig. 1. (a) CAD Model of a single electromagnetic tilting actuator, (b) prototype (without feeding unit) of the hyper-redundant manipulator with $n = 10$ assembled actuators and (c) the related schematic representation of the generalized DH coordinate frames for n actuators with a height of h and a constant twisting angle of $t = 90^\circ$.

3 Tip Optimization Strategy for Follow-the-Leader Motion

A follow-the-leader (FTL) control strategy is used to advance the robot along a reference path. This reference path can either be commanded online based on user inputs during exploration or, desired joint angles can be given beforehand based on fitting the snake to a given reference, see [8]. Regardless of how desired postures are determined, the FTL procedure remains the same. Therefore, the general idea and related considerations can be developed independently. Based on the proposed method in [9], the general FTL idea for spatial systems, its mathematical representation, and the associated optimization strategy is presented in the following sections.

3.1 General Follow-the-Leader Procedure for Spatial Systems

When the robot advances stepwise along a path, the serial chain needs to change from one configuration \mathbf{K}_j to the following \mathbf{K}_{j+1} , see Fig. 2(a). In each step, the serial chain is moved forward by a specific feeding increment Δs and necessary joint angles are determined based on the snake's tip. However, for every transition, some actuators need to perform a tilting movement with respect to the status of its preceding actuators and the applied feeder movement. As binary actuation does not allow for continuous interpolation of the joint angles, a corresponding set of switching sequences $\mathbf{t}_{sw,j}$ need to be identified with the help of an optimization, for ensuring good path-following performance, see Fig. 2(b). In this context $\mathbf{t}_{sw,j}$ describes the individual times of the beginning of the distinctive tilting movements.

In contrast to planar systems (see [9]), one actuator is unable to reach the state of its direct predecessor when applying a constant twist between the actuators in the serial chain, because their tilting axes are rotated and, therefore, point

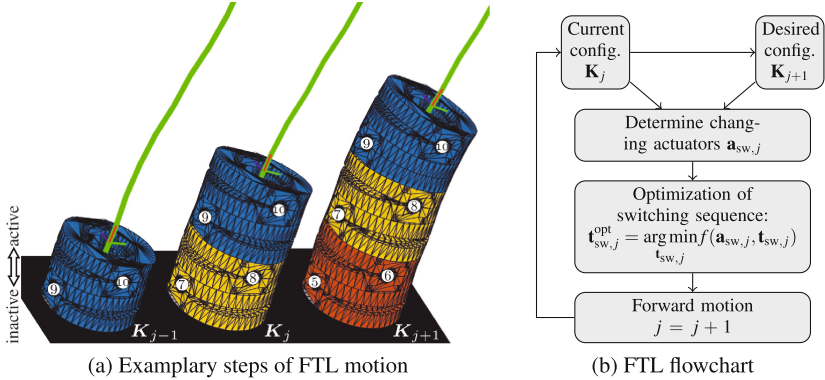


Fig. 2. (a) Exemplary configuration \mathbf{K}_j for the $j^{\text{th}} = 2^{\text{nd}}$ step of the spatial FTL control as well as the previous \mathbf{K}_{j-1} and subsequent \mathbf{K}_{j+1} configuration for a manipulator with $n = 10$ actuators and a twisting angle of $t = 90^\circ$ (colors indicating actuators forming one unit) and (b) flowchart of the general FTL procedure. (Color figure online)

into different directions (see Fig. 1(c)). Taking this into account and considering the symmetric design of the actuators, we propose to regard $k = 180^\circ/t$ actuators as one unit, where t is the constant twisting angle between all actuators (e.g. for $t = 90^\circ$: $k = 2$). Each unit can reach the pose of the corresponding preceding unit when the feeding increment Δs between two configurations correlates to the height of a whole unit. However, due to the continuously twisted actuators, desired joint angles need to be negated when transferring them from one unit to the subsequent. A schematic representation of FTL steps for an actuator chain with $t = 90^\circ$ is shown in Fig. 2(a). Inactive joints, i.e. joints being inside the feeding unit, are mechanically held in a neutral position. For reaching a stable state when leaving the feeding tube, the switch-on times of these actuators are fixed with respect to the feeding speed.

3.2 Mathematical Formulation of a Follow-the-Leader Transition

A general serial chain with a linear feeding device for providing forward motion (joint coordinate q_1 with $q_1 \in [-n \cdot h, 0]$) and n equal actuators (a_1, \dots, a_n , joint coordinates q_2, \dots, q_{n+1}) with a height of h and a tilting angle of $\pm q_{\text{max}}$ are subdivided into u units. Each unit includes k actuators. For the following section the j^{th} step of a general FTL procedure is considered. Without loss of generality, the start configuration \mathbf{K}_j and the end configuration \mathbf{K}_{j+1} for an incremental advancement of $\Delta s = k \cdot h$ can be defined based on the kinematic parameters:

$$\mathbf{K}_j = (q_{1,j}, \mathbf{q}_{1,j}, \dots, \mathbf{q}_{u-1,j}, \mathbf{q}_{u,j})^T, \quad (1)$$

$$\mathbf{K}_{j+1} = (q_{1,j+1}, \mathbf{q}_{1,j+1}, \dots, \mathbf{q}_{u-1,j+1}, \mathbf{q}_{u,j+1})^T \quad (2)$$

$$= (q_{1,j} + \Delta s, -\mathbf{q}_{2,j}, \dots, -\mathbf{q}_{u,j}, \mathbf{q}_{u,j+1})^T, \quad (3)$$

with the vector

$$\mathbf{q}_{p,j} = (q_i, \dots, q_{i+k-1})^T, \text{ with } i = (p-1)k + 2, \quad (4)$$

specifying the joint angles of the p^{th} unit in step j with

$$q_{\{2, \dots, n+1\}} \in \{-q_{\max}, q_{\max}\}. \quad (5)$$

Comparing the two subsequent configurations \mathbf{K}_j and \mathbf{K}_{j+1} , a vector

$$\mathbf{a}_{\text{sw},j} = (a_{x_1}, a_{x_2}, \dots, a_{x_c})^T, \quad x_i \in \{1, \dots, n\}, \quad (6)$$

representing all actuators, needing to change their configuration in the j^{th} step, can be determined, with c being the total number of switching actuators.

Based on the elements of \mathbf{K} position and orientation of each segment can be calculated with the help of homogenous transformation matrices. For minimal deviation of the snake to the reference path, optimal switching sequences $\mathbf{t}_{\text{sw},j}^{\text{opt}}$ have to be derived based on the minimization problem

$$\mathbf{t}_{\text{sw},j}^{\text{opt}} = \arg \min_{\mathbf{t}_{\text{sw},j}} f(\mathbf{a}_{\text{sw},j}, \mathbf{t}_{\text{sw},j}), \quad (7)$$

with the cost function f , e.g. being the maximal occurring deviation of the snake to the reference path as a function of $\mathbf{a}_{\text{sw},j}$ and $\mathbf{t}_{\text{sw},j}$ based on the robots direct kinematic. The elements of $\mathbf{t}_{\text{sw},j}^{\text{opt}}$ represent optimal switch-on times for each of the tilting actuators in $\mathbf{a}_{\text{sw},j}$, describing the instant of time, when the specific actuator needs to start its individual tilting process. Especially for large robotic chains with many actuators, an additional benefit in terms of computation time can be achieved by only considering an appropriate subset of actuators within the cost function of the optimization. For best representation of the original cost function, covering all actuator deviations, different methods exemplary shown in Fig. 3 are developed and evaluated for a serial chain of $n = 60$ actuators based on a detailed analysis of the kinematic design. Best balance of computational effort and representation of occurring errors is generated with an adequate measure combining two main aspects: first, taking always the first actuators from a set of consecutive tilting actuators (marked with red arrows) and the end effector (highlighted in green) into account. They cover the main deviation in most practical cases. To additionally monitor the errors within groups of not changing actuators, further elements are considered with a step width Δ (illustrated in blue). Exemplary evaluation of Δ in Fig. 4 shows, that best representation of the originally occurring errors under consideration of achievable time savings is reached with $\Delta = 5$. Similar results were achieved for all considered reference paths.

3.3 Tip Optimization Strategy

Instead of optimizing switching sequences for all actuators in $\mathbf{a}_{\text{sw},j}$, as proposed in [9], a combined tip optimization strategy is chosen to decrease necessary

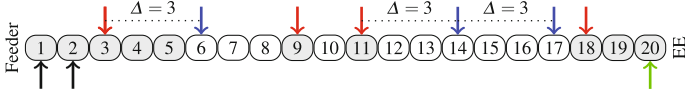


Fig. 3. Example for a reduced number of actuators evaluated in the cost function of the optimization for a serial chain with $n = 20$. Gray boxes indicate switching actuators and arrows mark considered joints within the cost function. (Color figure online)

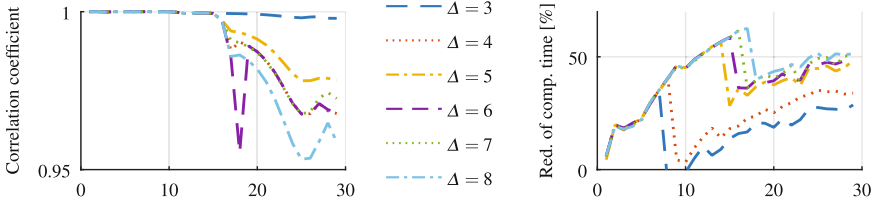


Fig. 4. Results for the achievable accuracy of the reduced cost function for an exemplary reference path compared to the all embracing cost function (left) and achievable savings in computation time (right) for different step width Δ .

computation times, see Fig. 5. The tip optimization strategy aims to optimize only the switch-on time $\mathbf{t}_{\text{sw,red},j}$ of the manipulator tip unit with $\mathbf{a}_{\text{sw,red},j} = (a_{x_{c-u+1}}, \dots, a_{x_c})^T$, while reusing switching sequences $\mathbf{t}_{\text{sw},j-1}^{\text{opt}}$ from the previous transition for the remaining actuators $a_{x_1}, \dots, a_{x_{c-u}}$. The proposed optimized switching sequence is described by

$$\mathbf{t}_{\text{sw},j}^{\text{opt}} = (\mathbf{t}_{\text{sw},j-1}^{\text{opt}T}, \mathbf{t}_{\text{sw,red},j}^{\text{opt}T})^T. \quad (8)$$

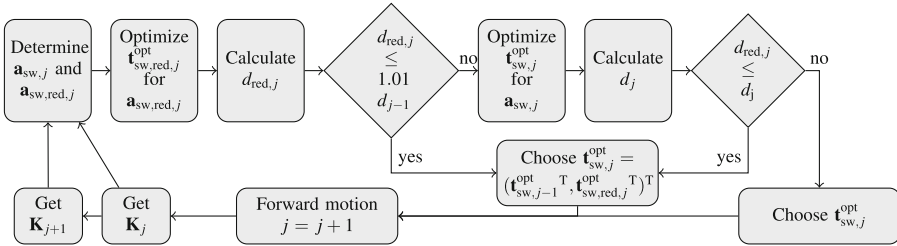


Fig. 5. Flowchart of the tip optimization strategy, reusing optimal switching sequences from previous transitions.

Since the configuration of the tip unit of the snake-like robot has no effect on the deviations of the body, the maximal error of the body joints to the reference path remains unchanged. Under the hypothesis that the time sequence $\mathbf{t}_{\text{sw},j-1}^{\text{opt}}$ from the previous transition $j - 1$ is optimal, the errors to the reference path are minimized, if the maximal deviation $d_{\text{red},j}$ of the tip unit based on the newly obtained time sequence $\mathbf{t}_{\text{sw,red},j}^{\text{opt}}$ is less than the error resulting solely from the body joint d_{j-1} .

However, it cannot be neglected, that the actuators being close to the robot base have a huge impact on the occurring deviations. Minor increase of errors ($\leq 1\%$) might be tolerated, as they are conditioned through the reference path, but it is possible that solely optimizing the tip leads to a significant higher overall error. In this case, a new set of optimized switching sequences $\mathbf{t}_{\text{sw},j}^{\text{opt}}$ for all actuators in $\mathbf{a}_{\text{sw},j}$ is determined and the achievable accuracy d_j is compared to $d_{\text{red},j}$. The sequence leading to best proximity to the reference is used to proceed. By combination of these two steps it can be assured, that remaining errors will not be increased significantly compared to the method from [9].

The results for the achievable path following accuracy and related computation time for the proposed tip optimization strategy compared to the technique proposed in [9] are depicted in Table 1. Results are obtained by pattern search optimization for a serial chain of $n = 60$ actuators with a height of 16 mm and tilting angle of $q_{\text{max}} = 6^\circ$ twisted by $t = 90^\circ$ following the three exemplary considered spatial reference paths shown in Fig. 6. All paths differ in terms of curvature as well as pitch and, therefore, in the number of switching actuators. It is shown, that time savings with a further decrease of remaining errors can be achieved for all considered cases. In 60–70% of the steps time sequences calculated for $\mathbf{a}_{\text{sw},\text{red}}$ are used to proceed, as the reduction of the parameter space by solely optimizing the tip joints lead to better converge and, therefore, less deviation. However, in some cases the optimization for \mathbf{a}_{sw} is performed, but is not bringing further enhancements of accuracy. Therefore, an revised selection criteria might bring a further improvement of time savings and is, hence, part of future work.

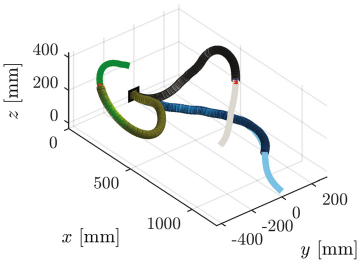


Fig. 6. Exemplary paths used for evaluation of tip-following method.

Table 1. Characteristics of the tip optimization strategy and comparison to the method presented previously.

Characteristics of tip optimization	Path		
	Blue	Gray	Green
Max. error [mm]	40.7	41.4	33.8
Computation time [s]	361.7	175.7	106.4
No. of decisions			
$d_{\text{red},j} \leq 1.01 \cdot d_{j-1}$ [%]	41.4	34.5	44.8
$d_{\text{red},j} \leq d_j$ [%]	20.7	34.5	27.6
$d_{\text{red},j} > d_j$ [%]	37.9	31.0	27.6
Comparison to [9]			
Error improvement	26.1%	10.2%	0.3%
Time saving	44.2%	13.2%	39.5%

4 Conclusion

This paper proposed a follow-the-leader approach for binary actuated spatial snake-like robots, evaluated for a hyper-redundant serial system based on unique electromagnetic tilting actuators. The general procedure, as well as the mathematical formulation of the motion planning algorithm, was introduced. It was outlined, that optimized switching sequences are necessary to obtain good proximity to a reference path to overcome restrictions due to the discrete kinematic set-up. The optimization idea was adapted in a time efficient way, considering solely the manipulator tip joints within the optimization. Only if the maximal overall error is further increased through the selected switching sequences, an optimization regarding all switching actuators is performed to improve the proximity to the path. Results showed, that an increase in accuracy, as well as a significant decrease of computation time, were achieved thanks to the proposed approach. Future work will include the improvement of the selection criteria and the experimental evaluation.

References

1. Burgner-Kahrs, J., Rucker, D.C., Choset, H.: Continuum robots for medical applications: a survey. *IEEE Trans. Rob.* **31**(6), 1261–1280 (2015)
2. Chirikjian, G.S.: Theory and applications of hyper-redundant robotic manipulators. Ph.D. thesis, California Institute of Technology (1992)
3. Choset, H., Henning, W.: A follow-the-leader approach to serpentine robot motion planning. *J. Aerosp. Eng.* **12**(2), 65–73 (1999)
4. Gilbert, H.B., Neimat, J., Webster, R.J.: Concentric tube robots as steerable needles: achieving follow-the-leader deployment. *IEEE Trans. Rob.* **31**(2), 246–258 (2015)
5. Liljebäck, P., Pettersen, K.Y., Stavadahl, Ø., Gravdahl, J.T.: A review on modelling, implementation, and control of snake robots. *Robot. Auton. Syst.* **60**(1), 29–40 (2012)
6. Neumann, M., Burgner-Kahrs, J.: Considerations for follow-the-leader motion of extensible tendon-driven continuum robots. In: 2016 IEEE International Conference on Robotics and Automation (ICRA), pp. 917–923 (2016)
7. Palmer, D., Cobos-Guzman, S., Axinte, D.: Real-time method for tip following navigation of continuum snake arm robots. *Robot. Auton. Syst.* **62**(10), 1478–1485 (2014)
8. Tappe, S., Kotlarski, J., Dörbaum, M., Mertens, A., Ponick, B.: The kinematic synthesis of a spatial, hyper-redundant system based on binary electromagnetic actuators. In: 6th International Conference on Automation, Robotics and Applications (ICARA), pp. 211–216 (2015)
9. Tappe, S., Pohlmann, J., Kotlarski, J., Ortmaier, T.: Towards a follow-the-leader control for a binary actuated hyper-redundant manipulator. In: 2015 IEEE/RSJ International Conference on Intelligent Robots and Systems (IROS), pp. 3195–3201 (2015)
10. Transeth, A.A., Pettersen, K.Y., Liljebäck, P.: A survey on snake robot modeling and locomotion. *Robotica* **27**(07), 999–1015 (2009)

11. William II, R.L., Mayhew IV, J.B.: Obstacle-free control of the hyper-redundant nasa inspection manipulator. In: Fifth National Conference on Applied Mechanics and Robotics, pp. 12–15 (1997)
12. Woehrmann, M., Doerbaum, M., Ponick, B., Mertens, A.: Design of a fully actuated electromagnetic bending actuator for endoscopic applications. In: 9. GMM/ETG Symposium on Innovative Small Drives and Micro-Motor Systems, pp. 1–6 (2013)

Kinematic Design of a Lighting Robotic Arm for Operating Room

J. Sandoval¹(✉), L. Nouaille¹, G. Poisson¹, and Y. Parmantier²

¹ PRISME Laboratory, INSA CVL, University of Orleans, Orléans, France
juan.sandoval-arevalo@univ-orleans.fr

² POLE CAPTEUR, University of Orleans, Orléans, France
yves.parmantier@univ-orleans.fr

Abstract. This paper deals on the design method applied to create a new useful robot for a lighting operating room. We present the specifications for this particular medical application, the proposed kinematic solutions as well as the topological and dimensional syntheses performed to choice the optimal solution. The work presented in this paper was conducted with a closely industrial collaboration, and a patent application of the chosen kinematic solution has been filed.

Keywords: Medical design · Kinematics · Mechanism syntheses

1 Introduction

A lighting for operating room is a poly articulated medical arm. During the surgical operation, the optical axis of the lighting must be focused towards the desired surgical zone. The lighting is pre-positioned by the surgeon (or medical staff) before starting the operation. When the operation begins, the surgeon must not move the lighting arm for aseptic reasons, i.e. he cannot accede to the sterile zone. Therefore, the surgeon must ask to a medical assistant to move the arm, which is much less optimal than in the case of direct manipulation.

The study presented in this paper is developed in the context of the SMILE¹ French regional project, whose goal is to design a lighting robotic arm and control them using a touchless system based on hand gesture recognition [3–6]. The project is composed of two main parts: robotic and imaging parts, respectively. Moreover, only the robotic design study is presented here.

The paper is organized as follows. In Sect. 2 we present the robotic and ergonomic specifications given by the industrial partner project Maquet SAS² to design the mechanism. The different topological solutions developed are presented and compared according to the industrial specifications in Sect. 3. Then, a dimensional synthesis is described in Sect. 4. Conclusions about the proposed approach are presented in the last section.

¹ SMILE: Sterile Manipulation Interface of Lighting Equipment.

² <http://www.maquet.com/fr/>.

2 Specifications

Maquet SAS Company builds manual lighting arms for operating room. For SMILE project, the company defined some specifications for a robot charged of positioning the lighting. Different criteria are specified: kinematic (DoF, workspace), dynamic, environment, aseptic, ergonomic, safety, cost, compatibility with existent system and so on.

For a first step, certain criteria are used to limit the kinematic solutions, e.g. the DoF of the robot for positioning the lighting. Moreover, in this step other specifications are qualitatively analyzed. For defined the specifications, several studies about the positioning of the lighting during surgeries are carrying out, as shown in [9, 11].

2.1 Surgical Scenes and Movement

According to the type of surgery and the needs of the medical staff, it is necessary that the dome of lighting moves towards different positions around the medical scene. Generally three scenes were identified (Fig. 1(a)). In the first scene, the dome is localized behind the surgeon's head, avoiding that the beams of light are pointed towards his eyes. A second scene exists when a vertical projection of the beams of light towards the patient becomes necessary. Finally, in some cases, the dome must turn around a target position, creating a remote center of motion.

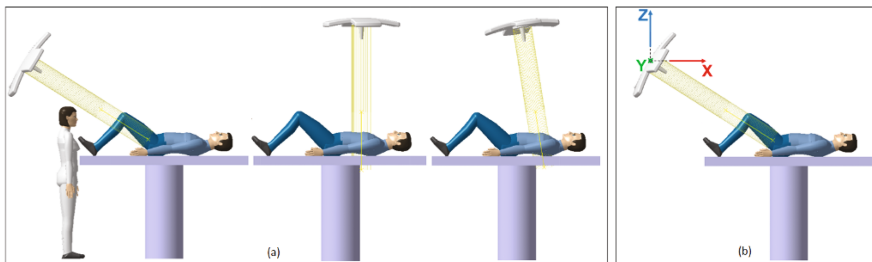


Fig. 1. (a) Operating scenes, (b) 3D movement

Moreover, the lighting dome must be capable to move in the horizontal plane (X, Y); movements in Z-axis are suitable but not mandatory (Fig. 1(b)).

2.2 Medical Gesture

From the observations made by the company, three medical cases of displacement of the dome are specified, denoted by C1, C2 and C3:

C1: the dome moves or turns following a desired surgical trajectory.

C2: the dome turns around a desired surgical position.

The third case (C3) is a combination between C1 and C2.

From precedent experiments conducted by the Maquet SAS Company, C1 represents 8% of medical surgery cases, C2 and C3 correspond to 36% and 56% of medical surgical procedures, respectively. After studying the specifications given by the company, the topological synthesis is carried out to propose kinematic structures adapted to the needs presented above.

3 Topological Synthesis










In this part, we present the topological synthesis of mechanism carried out in the project context. In literature, there are few papers on topological robotics. There are often focused on specific kinematic structures and not linked to a particular application. Tuttle et al. [15] proposed a method of topological synthesis based on finite symmetry of group theory, Mitrouchev [13] used combinatory analysis for topological robotic parallel mechanisms. This method allows to obtain all the possible solutions to the position end-effector and actuators in parallel kinematic chains. Laribi [12] used a method based on a genetic algorithm for the synthesis of plane, spatial and parallel robots. We choose a multi criteria analysis based on a decision matrix to obtain the optimal solution, allowing to include quantitative but also qualitative industrial expert reviews.

3.1 Kinematic Structures

In order to accomplish the overall specifications given by the company, the robot should have at least 4 DoF: 2 DoF for the translation allowing to move the lighting in the horizontal plane and 2 DoF allowing the orientation of the lighting dome. It is important to note that the existent non-robotized arm has only 3 Dof [9].

Based on the specifications presented above, nine kinematic structures have been proposed, as presented in Table 1.

Table 1. Kinematic structures proposed

<i>Solution</i>								
<i>A</i>	<i>B</i>	<i>C</i>	<i>D</i>	<i>E</i>	<i>F</i>	<i>G</i>	<i>H</i>	<i>I</i>
								
4 DoF	4 DoF	3 DoF	3 DoF	3 DoF	3 DoF	4 DoF	5 DoF	4 DoF

Certain of these solutions have only 3 DoF, limiting the robot movements but giving the advantages of lightweight of the overall structure as well as in terms of price.

This step of seeking solutions allows us to propose two structures based on parallel chains. In terms of manufacturing, the parallel robot is more complex than the serial one but it offers a better mechanical balancing, a great accuracy and it guarantees a higher velocity of the manipulated tool [2]. Even if the velocity criterion is not essential for our application, the control of the mechanical balancing is a point of great importance. Nevertheless, the workspace/compactness ratio is often less important than in the case of serial solutions.

3.2 Decision Matrix

After having proposed different kinematic structures, we have compared them to find the optimal/more adapted robot based on the specifications defined by the company. Thus, we defined a decision matrix to classify the kinematic solutions, an example is presented in Table 2 for Solution A (The reference frame is the same used in Fig. 1(b)). This decision matrix is composed of two parts. First, all the solutions are evaluated qualitatively from the criteria defined in the specifications. There are three possibilities of qualification: Yes (if the robot always verify this criterion) or Possible (if the robot comply the criterion under conditions) or not possible (the robot has not level of flexibility). If the last qualification is given, the solution is then penalized for the second part of the decision matrix. Moreover, if a solution obtain “Not possible” for a criterion flexibility “none”, then the solution is automatically annulled.

Table 2. Comparison of proposed solutions – first part

Criterion	Criterion flexibility	Required value	Solution A
Maximum displacement of the center of mass (CoM) of the dome in the (X, Y) plane along X-axis and Y-axis	None	30 cm	Possible
Maximum rotation of the dome around the two directions of the horizontal plane (X, Y)	Possible	$\pm 90^\circ$	Not possible
Maximum rotation of the dome around the vertical axis (Z-axis)	Possible	360°	Possible
Number of links	None	Unlimited	Yes
At least one posture must allow the coincidence between the CoM and the first vertical axis	None	Yes	Possible
The supporting link designed by the company can attach the solution	None	Imperative	Yes
The solution must not disturb the lighting functionalities	None	Imperative	Yes

In the second part, see Table 3, the performance criteria are defined to differentiate the solutions validated in the first part.

Table 3. Comparison of proposed solutions – second part

Criterion	Weight	Quantification	Grade (Solu. A)
Number of DoF lost in case of motor failure	2	≤ 1 (1) / ≥ 1 (0)	1
Possibility to control the vertical translation of the lighting dome	1	Yes (1) / Not (0)	0
Possibility to control the movement of the lighting dome along the horizontal plane while focusing on the target zone	1	Yes (1) / Limited (0.5) / Not (0)	0.5
Similarity with the existent non-robotized system	2	Yes (1) / Not (0)	0
Kinematic complexity (number of links, type of joints, number of actuators) [10]	4	Between 0 and 1	0.27

Table 4. Final ranking of the proposed solutions

	<i>Solution</i>								
	<i>A</i>	<i>B</i>	<i>C</i>	<i>D</i>	<i>E</i>	<i>F</i>	<i>G</i>	<i>H</i>	<i>I</i>
Score	5.39	8.07	7.69	5.25	5.69	7.69	8.12	2.64	3.12
Rank	6	2	3	7	5	3	1	9	8

Each criterion has a weight-coefficient characterizing the priority scale. Each kinematic solution is evaluated by assigning a grade between 0 and 1.

The total score of a solution is defined by adding all the weight-grade products. The ranking of the solutions is presented in Table 4.

From these results, the solution G can be defined as the optimal kinematic solution. Nevertheless, in agreement with Maquet SAS Company, a further analysis will be performed for the parallel solutions H and I, considering their performance in terms of mechanical balancing and accuracy.

3.3 Comparison of Parallel Solutions

We compare the two parallel solutions in four criteria: presence or not of singularity in the workspace (circle with $R = 30$ mm), forces supported by the robot (the light has a mass of around 20 kg), frictions in joints, and workspace/compactness relation. The Solution H is based on a Delta-robot kinematics with 5 DoF [2] whereas the Solution I is based on a 3RRR planar robot with 4 DoF [1, 8].

3.3.1 Singularities

Usually parallel kinematics have more singularity cases than serial solutions [1]. Singularities are positions where the robot cannot be controlled. From the specifications

given above, the workspace can be considered like a disk with 30 mm radius. For the two parallel solutions, singularity positions must be localized outside the disk. By adjusting some geometric parameters, singularities can be moved outside of the workspace in both cases.

3.3.2 Forces

An analysis concerning the forces supported by the robots was carried out. Delta-robot (Solution H) was typically designed for “pick-and-place” tasks [2]. It uses one DoF for a vertical movement carrying the load and two DoF to move in the horizontal plane. Thus, the configuration of the actuators on the Delta-robot allows to support the weight load naturally. On the other hand, the 3RRR robot (Solution I) is a planar robot designed for horizontal displacements [1, 8]. In this case, the actuators are not positioned to move a weight along the horizontal plane or even to support a weight with natural movement of joints. From this point of view, the Solution H looks more adapted for our application.

Finally, some joint frictions are produced when supporting the weight of the lighting dome. Furthermore, these frictions damage passive joints (without actuators). In the case of Solution H, joint movements are naturally generated by the direction of the lighting weight force, transmitting that force to the actuators and generating low passive joint frictions. However, the Solution I is the opposite case, because the weight force is not transmitted to the actuators, producing higher passive joint frictions. A summarized table of this analysis is presented below (Table 5).

Table 5. Comparison of the two parallel kinematics

Model	Singularities	Forces axis	Friction
Solution H	Outside of the workspace	Torques from weight force are transmitted to the actuators	Low passive joint frictions
Solution I	Outside of the workspace	Torques from weight force are not transmitted to the actuators	High passive joint frictions

A last analysis of the parallel solutions was performed comparing the workspace/compactness relation. For the two robots, an adjustment of geometrical parameters was made to obtain the necessary workspace (disk/cylinder of radius 30 mm). CATIA software was used to reproduce all the possible robot movements into the workspace, determining their compactness. The workspace of the Solution H is a cylinder of ratio 30 mm. Figure 2 shows the compactness superposition of the two robots. It is clear that Solution H is more compacted than Solution I.

To conclude, the analysis presented above allows to conclude that Solution H is the more adapted parallel solution to satisfy the specifications of the application.

Nevertheless, in order to reduce the prototype cost and to produce a structure close to the already existent arm, the company decides to develop the serial solution G, whose dimensional phase is presented in the next section.

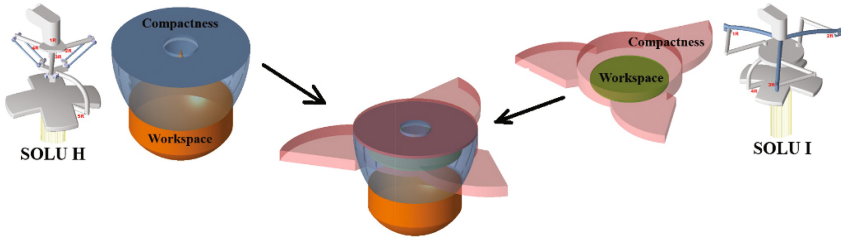


Fig. 2. Comparison of workspace/compactness relation for solution H and I

4 Dimensional Synthesis (Dynamics Analysis)

A dynamic analysis has been performed in Solution G, in order to know the motor characteristics needed in each actuated joint, as well as the torsional and bending forces applied in every link. The goal of this analysis is to find the joint configurations for which the motor torques are maximum. The Newton-Euler algorithm [7] was applied to the Solution G for every possible joint combination. In order to take into account inertial effects, joint velocities and accelerations were considered maximum.

The Solution G presents 4 DoF, two mobility in the horizontal plane (X and Y) and two rotations mobility. Therefore, this solution has 4 revolute joints (q_4, q_5, q_6, q_7), as shown in Fig. 3.

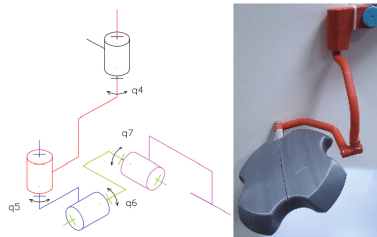


Fig. 3. Solution G – kinematic chain and 3D printed prototype

The dimensions, velocities and accelerations of links used for the dynamic analysis are presented in Table 6. Moreover, a maximum joint speed $\dot{q}_i = \pi/32[rad \cdot s^{-1}]$ and acceleration $\ddot{q}_i = \pi/32[rad \cdot s^{-2}]$ for $i = 4$ to 7 were used.

The Newton-Euler’s algorithm is applied for all the articular combinations according to the robot workspace: $q_4 = 0^\circ, 0^\circ \leq q_5 \leq 31^\circ, -90^\circ \leq q_6 \leq 90^\circ$ and $-90^\circ \leq q_7 \leq 90^\circ$. The obtained results don’t take into account motor weights because they are not chosen yet. Thus, we must apply the algorithm two times, the first one to obtain the characteristics of the motors and choose them, and the second one to include the motor weights. If the results of motor torque and axial forces found in the second step exceed the motor capacities, we must choose another actuator.

Table 6. Details for dynamic analysis

	S4	S5	S6	S7 (Lampe)
Material	Aluminum ($\rho = 2710 \text{ Kg} \cdot \text{m}^{-3}$)			Plastic ($\rho = 1050 \text{ Kg} \cdot \text{m}^{-3}$)
Section	$\varnothing_{ext} = 50 \text{ mm}, \varnothing_{int} = 45 \text{ mm}$			–
Weight	0.926 kg	0.351 kg	1.094 kg	20.16 kg

For the first step of calculation, the results are summarized in Table 7. The second step is omitted in this paper, further details of this analysis will be provided in a next paper.

Table 7. Results obtained in the first step (without motor weights)

	Joint 4	Joint 5	Joint 6	Joint 7
Maximum radial force [N]	1.2356	1.2464	208.33	197.60
Maximum axial force [N]	220.85	211.77	0.82	197.61
Maximum bending moment [Nm]	46.86	85.79	73.73	69.98
Maximum motor torque [Nm]	0.49	0.61	4.44	3.71

5 Conclusions

In this paper, we present the design method applied to create a lighting robotic arm for operating room. This study was carried out in the context of the SMILE regional project in collaboration with Maquet SAS Company. Some kinematic solutions were proposed based on the specifications of the industrial partner. A topological synthesis was then carried out through a decision matrix, combining quantitative and qualitative criteria. A particular analysis was made to the parallel solutions, even if a serial solution was resulted as the optimal in the decision matrix. The chosen solution was then defined in dimensional synthesis, where the maximum torque motors were provided. A patent application [14] for the chosen solution was filed, in order to protect the kinematic design of this robotized lighting arm for operating room. Moreover, a scaled 3D printed prototype was first built and some experiments in operating room using pigs are planned once a motorized real-scale prototype will be produced.

Acknowledgments. This research was supported by the Region Centre Val-de-Loire, France, in the context of the SMILE project.

References

1. Bonev, I.A., Gosselin, C.M.: Singularity loci of planar parallel manipulators with revolute joints. In: Computational Kinematics, Seoul, South Korea, pp. 291–299 (2001)
2. Clavel, R.: Conception d'un robot parallèle rapide à 4 degrés de liberté, Doctoral dissertation, EPFL, Lausanne (1991)
3. Collumeau, J.-F., et al.: Hand-gesture recognition: comparative study of global, semi-local and local approaches. In: 7th International Symposium on Image and Signal Processing and Analysis (ISPA), Zagreb, Croatia, pp. 247–252 (2011)
4. Collumeau, J.-F., et al.: Hand gesture recognition using a dedicated geometric descriptor. In: 3rd International Conference on Image Processing Theory, Tools and Applications (IPTA), Istanbul, Turkey, pp. 287–292 (2012)
5. Collumeau, J.-F., et al.: Fire scene segmentations for forest fire characterization: a comparative study. In: 18th IEEE International Conference on Image Processing, Cardiff, United Kingdom, pp. 2973–2976 (2011)
6. Collumeau, J.-F., et al.: Simulation interface for gesture-based remote control of a surgical lighting arm. In: IEEE International Conference on Systems, Man, and Cybernetics, Cardiff, United Kingdom, pp. 4670–4675 (2013)
7. Craig, J.: Introduction to Robotics: Mechanics and Control, 2nd edn. Addison-Wesley Longman Publishing Co., Inc., Boston (1989)
8. Dash, A.K., et al.: Task-oriented configuration design for reconfigurable parallel manipulator systems. *Int. J. Comput. Integr. Manuf.* **18**(7), 615–634 (2005)
9. Gauvin, A.: Asservissement visuel d'un éclairage opératoire, Doctoral dissertation, Université d'Orléans (2012)
10. Khan, W., et al.: A formulation of complexity-based rules for the preliminary design stage of robotic architectures. In: International Conference on Engineering Design, France (2007)
11. Knulst, A., Mooijweer, R., Jansen, F.W.: Indicating shortcomings in surgical lighting systems. In: Minimally Invasive Therapy & Allied Technologies, pp. 267–275 (2011)
12. Laribi, M.A.: Contribution à la synthèse de mécanismes plans et spatiaux et des robots parallèles par une méthode évolutionnaire, Doctoral dissertation, Poitiers University (2005)
13. Mitrouchev, P., et al.: L'analyse combinatoire pour l'énumération topologique des mécanismes cinématiques en robotique, Congrès Français de Mécanique (2011)
14. Poisson, G., et al.: Suspension de plafond à cinématique améliorée pour porter une pièce d'équipement. In: Institut National de la propriété intellectuelle, France, patent application N BR-27301/FR (2016)
15. Tuttle, E.R., Peterson, E.W., Titus, J.E.: Further applications of group theory to the enumeration and structural analysis of basic kinematic chains. *J. Mech. Transmissions Automat. Des.* *ASME Trans.* **111**, 465–497 (1989)

Elastostatic Modelling of a Wooden Parallel Robot

Lila Kaci^{1,2(✉)}, Clement Boudaud³, Sebastien Briot¹,
and Philippe Martinet^{1,2}

¹ Laboratoire des Sciences du Numérique de Nantes (LS2N),
UMR CNRS 6004, Nantes, France

{Lila.Kaci,Sebastien.Briot,Philippe.Martinet}@ls2n.fr

² École Centrale de Nantes, Nantes, France

³ LIMBHA, Goupe École Supérieure du Bois, Nantes, France
clement.boudaud@ecoledubois.fr

Abstract. Eco-design of industrial robots is a field of research which has been rarely explored in the past. In order to considerably decrease the environmental impact of robot during the design phase, metal or carbon composite parts can be replaced by bio-sourced materials, such as wood. Indeed, wood has interesting mechanical properties, but its performance/dimensions will vary with the atmospheric conditions/external solicitations and with the conditions in which trees have grown. In order to be able to design a stiff industrial robot, robust design approaches must be used. These approaches must be fed with elastostatic models that are able to predict the variability in the robot deformations due to the variability of the wood mechanical properties.

In this paper, we develop an elastostatic model for a wooden parallel robot which is able to cope with the variations of the wood mechanical properties. The prediction of this model in terms of deformations are compared with experimental measurements made on a wooden parallel robot mockup. Results show that there is a good correlation between the measurement displacements and the computed ones.

Keywords: Eco-design · Parallel robot · Elastostatic model · Wood

1 Introduction

The Climate Change Mitigation (CCM) has become a priority in the world, as shown during the COP21. It becomes urgent to decrease the Environmental Impact (EI) of the human activities. Robotics, which takes an increasing place in our everyday life, must also be part of this effort.

A recent study [2] shows that, contrary to what could be imagined, a large percentage (around 50%) of the EI during the entire robot life is due to the use of metallic materials (steel or aluminum, even if they are recycled) for the design of their links. The percentage is even worth if carbon composites are used. The rest of the EI is globally due to the robot energy consumption during use.

A method to reduce EI of robot design, that is rarely used, is to replace the polluting metals and carbon composites with bio-sourced materials (BSM) that have a little (even no) EI [12, 16]. Moreover, BSM have good stiffness performance, and their quantity is only limited by their growing time [10]. In this work, developed in the scope of the French project RobEcolo [3], we are interested in using wood instead of metals to design the robot links.

Using wood in machines is not a new idea. For instance, it is used in chassis of cars [1]. It found also applications in the design of buildings due to its stiffness and low cost [10]. It is also used in Robotics for the design of mock-ups and proof-of-concept prototypes [14, 15]. However, a detailed study of these works shows that wood is never used in critical parts ensuring accuracy. Indeed, the wood performance/dimensions will vary with the atmospheric conditions/external solicitations and with the conditions they have grown [10, 17]; thus, new robot design issues appear: How to be sure that an industrial robot made with wood can be accurate and stiff even if wood properties vary?

A first attempt to introduce wood in industrial robot design was presented in [12]. The results showed that the approach was valid enough to compete with usual materials. However, this study did not deal with the aforementioned issues.

Indeed, the accuracy issue can be treated through proper control approaches: external sensors combined with proper controllers can be used to accurately control the platform pose [4]. Regarding the robot stiffness, we believe that this issue can be handled through robust design approaches [18]. However, these design approaches must be fed with stiffness models which are able to predict the variability of the robot deformations due to the variability in the material properties.

In this vein, the present paper aims at proposing an elastostatic model of a wooden parallel robot being able to predict the deformations and their variability.

2 Mechanical Properties of Wood

Wood is an organic product structure of infinite variation of detail and design. It is on this account that no two types of wood are alike: in reality no two specimens from the same log are identical [11]. Several studies giving the mechanical properties (e.g. Young's modulus, Poisson's ratios) for different pieces of wood can be found in the literature [9, 10]. The properties are defined by repeated tests, that provide mean values and rarely the standard deviation (it is known that the coefficient of variation can reach up to 30% for some characteristics [10]).

We are investigating the wood in the design of industrial parallel robots, hence it is necessary to know the mechanical properties of the wood to define the elastic deformation of the robot due to the loads applied on it. However wood is subject to a scale effect: impact of singularities (e.g. knots, direction of grain) are linked to the size of the pieces of wood. Therefore new tests have to be performed to define the mechanical properties corresponding to the dimension of the robot links. Indeed, values given in [9, 10] are usually obtained for beams of large

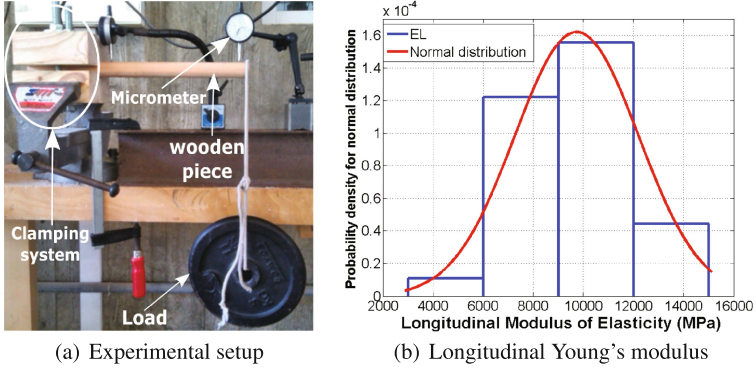


Fig. 1. Experimental setup to define the mechanical properties of Accoya Pine

dimensions unlike the links of our robot which will be much smaller. Moreover, unlike usual material used in robot design, wood is an orthotropic material. The three different directions are longitudinal L , radial R , and tangential T . According to the theory of elasticity, the wood is parameterized by three Young's moduli (E_L , E_R and E_T), six Poisson's ratios (ν_{LR} , ν_{LT} , ν_{RT} , ν_{RL} , ν_{TL} , ν_{TR}) and three moduli of rigidity (G_{LR} , G_{LT} , G_{RT}).

The links of parallel robots have cross-sections with smaller dimensions than the link lengths [13], and can be modeled according to the beam theory (Euler-Bernoulli model). For this reason, in this work only the longitudinal Young's modulus E_L and Poisson's ratio $\nu = \frac{(\nu_{LR} + \nu_{LL})}{2}$ are necessary.

In order to decrease the dimensional variability of wood due to humidity, we decided to design our links with a novel type of acetylated wood [7, 17] named Accoya Pine. This wood is known to have many advantages over raw wood species in terms of durability and dimensional stability. This choice implied that we had to make mechanical tests because no data are provided in literature for this new type of wood. Hence, to define the Young's modulus E_L of Accoya Pine, bending tests were made (testing for the Poisson's ratio is not useful, as it has a relatively small impact on the bending strain [9]). Thirty specimens are used, the dimensions of the specimens are the same as the dimensions of a standard link of the robot we plan to build (length of 30 cm and square section of 3 cm \times 3 cm).

Cantilever tests were performed using loads of 1 kg, 2 kg and 5 kg (Fig. 1(a)) and the measure of the deflection is used to compute E_L (the computation was inspired by the usual EN 408 standard). It is very important to mention that the preconditioning of the specimens was made at a temperature of 20 °C and at a relative humidity of 65%, which for this specific acetylated wood implies a moisture content of 3.1%.

As shown on Fig. 1(b), we obtain a variable Young's modulus which follows a normal distribution with mean value equal to 9732 MPa and a standard deviation of 2462 MPa. This data will be used as input of the model presented in the next section.

3 Estimation of the Robot Elastic Displacement

3.1 Stiffness Modeling of a Five-Bar Mechanism

The planar five-bar mechanism (Fig. 2(a)) is a two degrees-of-freedom (*dof*) parallel robot able to achieve two translations in the plane (x_0Oy_0) . The end-effector is located at point C .

The analytical stiffness model presented in this section is based on matrix structural analysis method. This model was used in [6] in order to calculate the displacement of the end-effector of a parallel robot, under some external loadings.

The five-bar mechanism under study is modelled with four 3D flexible beams, each beam having two nodes at their extremity corresponding of the characteristic points (Fig. 2(b)). Nodes 1 and 8 are clamped onto the ground while some kinematic constraint relations will be imposed to the other nodes in order to parameterize the free rotations of the passive revolute joints.

The stiffness matrix ${}^i\mathbf{K}^i$ associated with the beam i ($i = 1$ to 4 (Fig. 2(b))) and expressed in its local frame \mathcal{R}_i is a 12-dimensional constant square symmetric matrix which depends on the geometrical and mechanical parameters [8].

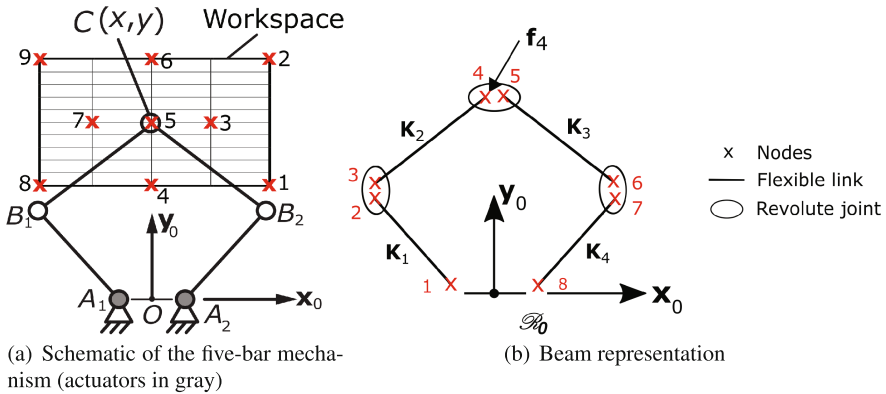


Fig. 2. The five-bar mechanism and its stiffness model

${}^i\mathbf{K}^i$ can be expressed in the base frame of the mechanism \mathcal{R}_0 by using the following relation:

$${}^0\mathbf{K}^i = \mathbf{T}^{-1} {}^i\mathbf{K}^i \mathbf{T} \quad \text{with:} \quad \mathbf{T} = \begin{bmatrix} \mathbf{R} & \mathbf{0}_3 & \mathbf{0}_3 & \mathbf{0}_3 \\ \mathbf{0}_3 & \mathbf{R} & \mathbf{0}_3 & \mathbf{0}_3 \\ \mathbf{0}_3 & \mathbf{0}_3 & \mathbf{R} & \mathbf{0}_3 \\ \mathbf{0}_3 & \mathbf{0}_3 & \mathbf{0}_3 & \mathbf{R} \end{bmatrix} \quad (1)$$

where \mathbf{R} is the rotation matrix from the local frame \mathcal{R}_i to the base frame \mathcal{R}_0 , and $\mathbf{0}_3$ is a (3×3) zero matrix. ${}^0\mathbf{K}^i$ can be decomposed into the four following (6×6) sub-matrices:

$${}^0\mathbf{K}^i = \begin{bmatrix} {}^0\mathbf{K}_{11}^i & {}^0\mathbf{K}_{12}^i \\ {}^0\mathbf{K}_{21}^i & {}^0\mathbf{K}_{22}^i \end{bmatrix} \quad (2)$$

Stiffness assembly [8] is a technique used to define the stiffness matrix of the whole structure. For the five-bar mechanism, all the beam stiffness matrices are assembled in the base frame according to the nodes as follows:

$${}^0\mathbf{K}_t = \begin{bmatrix} {}^0\mathbf{K}_{22}^1 & \mathbf{0}_6 & \mathbf{0}_6 & \mathbf{0}_6 & \mathbf{0}_6 & \mathbf{0}_6 \\ \mathbf{0}_6 & {}^0\mathbf{K}_{11}^2 & {}^0\mathbf{K}_{12}^2 & \mathbf{0}_6 & \mathbf{0}_6 & \mathbf{0}_6 \\ \mathbf{0}_6 & {}^0\mathbf{K}_{21}^2 & {}^0\mathbf{K}_{22}^2 & \mathbf{0}_6 & \mathbf{0}_6 & \mathbf{0}_6 \\ \mathbf{0}_6 & \mathbf{0}_6 & \mathbf{0}_6 & \mathbf{K}_{11}^3 & {}^0\mathbf{K}_{12}^3 & \mathbf{0}_6 \\ \mathbf{0}_6 & \mathbf{0}_6 & \mathbf{0}_6 & {}^0\mathbf{K}_{21}^3 & {}^0\mathbf{K}_{22}^3 & \mathbf{0}_6 \\ \mathbf{0}_6 & \mathbf{0}_6 & \mathbf{0}_6 & \mathbf{0}_6 & \mathbf{0}_6 & {}^0\mathbf{K}_{11}^4 \end{bmatrix}_{(36,36)} \quad (3)$$

The structure of the mechanism is composed of three passive revolute joints, the characteristics of a revolute joint is that all movements of two adjacent nodes are the same except the rotation around joint axis. Those joint properties can be described by using the kinematic relation between two nodal displacements [6].

Assembling all these kinematic relations into a unique expression gives:

$${}^0\mathbf{A}_t \Delta \mathbf{x}_t = \mathbf{0}_{(36,1)} \quad (4)$$

where, in our problem, \mathbf{A}_t is of dimension (15×36) and $\Delta \mathbf{x}_t = [\Delta \mathbf{x}_1^T, \Delta \mathbf{x}_2^T, \dots, \Delta \mathbf{x}_7^T]^T$ is the vector gathering all the nodal displacement $\Delta \mathbf{x}_i$ with $i = 1, 2, \dots, 7$.

In the same way we defined $\Delta \mathbf{x}_t$, the corresponding vector that gathers all the nodal wrenches is given by $\mathbf{f}_t = [\mathbf{f}_1^T, \mathbf{f}_2^T, \dots, \mathbf{f}_7^T]^T$, where \mathbf{f}_j is the wrench applied at node j . Taking into account the constraint expressed in Eq. (4), the displacement of the structure can be obtained using the stiffness relation (relation wrench/displacement) [8]:

$$\mathbf{K}_G \Delta \mathbf{x}_G = \mathbf{f}_G \quad (5)$$

$$\text{where: } \mathbf{K}_G = \begin{bmatrix} {}^0\mathbf{K}_t & \mathbf{A}_t^T \\ \mathbf{A}_t & \mathbf{0}_{15} \end{bmatrix}_{(51,51)}, \quad \Delta \mathbf{x}_G = \begin{bmatrix} \Delta \mathbf{x}_t \\ \boldsymbol{\lambda}_t \end{bmatrix}_{(51,1)}, \quad \text{and} \quad \mathbf{f}_G = \begin{bmatrix} \mathbf{f}_t \\ \mathbf{0}_{15} \end{bmatrix}_{(51,1)} \quad (6)$$

$\boldsymbol{\lambda}_t$ is the Lagrange multipliers vector necessary to take into account the kinematic constraints. The displacement is calculated as follows:

$$\Delta \mathbf{x}_G = \mathbf{K}_G^{-1} \mathbf{f}_G \quad (7)$$

from which the nodal displacement $\Delta \mathbf{x}_t$ can be extracted.

3.2 Predictive Model for the Wooden Robot Deformation

At this step, we have introduced the stiffness model of the five-bar mechanism considering that the Young's modulus and Poisson's ratio are known. However

the experimental results described in Sect. 2 showed how important is the variability of the mechanical properties of the wood. Monte Carlo method [5] can be used to solve any problem having random variables as inputs. The main purpose of this model is to study the influence of the variation of the mechanical properties of the wooden links onto the robot deformation. As robot stiffness depends on its configuration, the study of the displacement in different configurations of the robot is necessary. Hence, we decided to test the robot properties in the workspace which is discretized by the grid shown in Fig. 2(a). For each point of the grid, the method is performed as follows:

1. For each link of the robot, a value of Young's modulus is randomly generated based on the normal distribution identified in Sect. 2.
2. External wrenches are applied on the end-effector. Then the end-effector displacement is obtained through relation (5).
3. The previous two steps are repeated $n = 40000$ times which ensure the stability of the results (identical mean value at $0.1 \mu\text{m}$).
4. Finally, the mean, standard deviation, minimum and maximum values for the 40000 values of the displacements are calculated.
5. The process is then repeated for the other points on the grid.

This method is applied on a case study in the next section. A MATLAB code was written to compute the robot displacement using the modeling procedure presented in Sect. 3.1. The computation of all displacements took around 35 s per robot configuration (for a Pentium 4 2.70 GHz, 16 GB of RAM).

4 Case Study

4.1 Description of Wooden Five-Bar Mechanism Mockup

To validate the model proposed, a wooden five-bar mechanism mockup was developed (Fig. 3). The mockup is composed of four identical links (length of 28 cm and square cross section of $3 \text{ cm} \times 3 \text{ cm}$) made of Accoya Pine wood connected with three passive revolute joints. The distance between the fixed axes on the base is equal to 27 cm.

4.2 Experiments

The experimental measuring setup is made of two micrometers of 0.01 mm resolution as presented in Fig. 3. A force of 10 N acting along \mathbf{x} and \mathbf{y} axis respectively is applied on the end-effector, and the resulting displacements at the end-effector along \mathbf{x} , \mathbf{y} are measured. Tests were carried out for the nine configurations of the robot shown in Fig. 2(a). For a given configuration the experiment is repeated 10 times. Then all the experimental results are compared to the results obtained with a numerical analysis.

The results are summarized in Fig. 4. Concerning the displacements along \mathbf{x} -axis and \mathbf{y} -axis, the graphs show that the maximum and minimum experimental displacements are in the range of deformations predicted by the model.

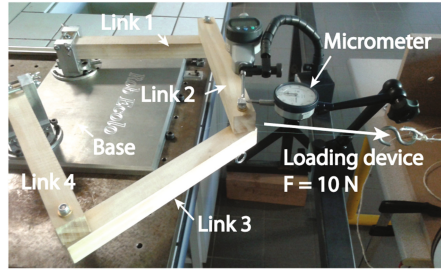


Fig. 3. Experimental setup

Results show that the deflections predicted by the model are in a much wider range than the experimental measurements. This was expected because numerically, 40000 values of rigidity were simulated while, experimentally, only one robot could be produced. Experimental results are globally in between the numerical limits. Nevertheless, few predicted displacements do not match with the measurement. The theoretical and experimental results may differ because of unmodelled phenomena, like:

- The passive joint stiffness was not considered.
- Viscoelasticity characteristics of the wood was not taken into account.

However, from those experiments, we can claim that the theoretical model is satisfactory and the proposed modeling procedure is efficient for predicting a realistic behavior of the wooden parallel robot.

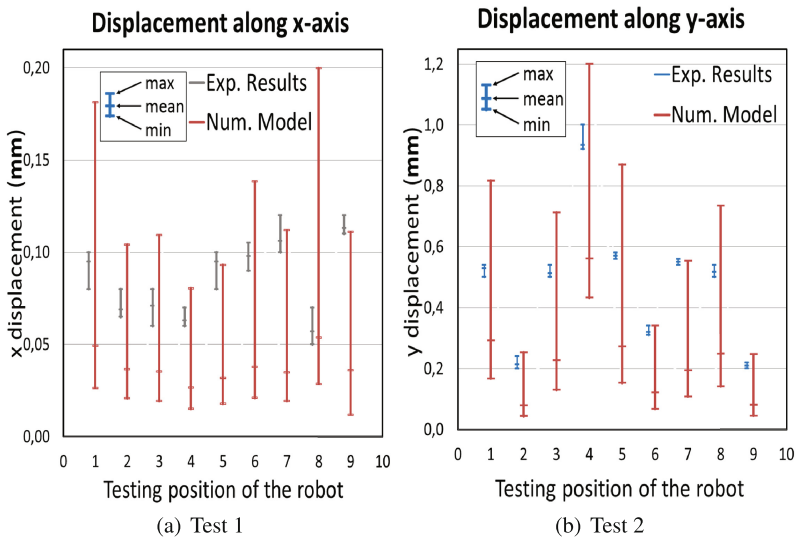


Fig. 4. Measured and simulated displacements

5 Conclusion

Robot eco-design is a field of research in Robotics that should be deeper investigated: this could contribute to the Climate Change Mitigation.

In order to considerably decrease the environmental impact of robot during the design phase, we proposed to replace metal or carbon composite parts by bio-sourced materials, such as wood. Wood has interesting mechanical properties but also drawbacks: its mechanical performance encounters a large variability. In order to be able to design a stiff industrial robot, robust design approaches must be used. These approaches must be fed with elastostatic models that are able to predict the variability in the robot deformations due to the variability of the wood mechanical properties.

In this paper, we developed an elastostatic model for a wooden parallel robot which was able to cope with the variations of the wood mechanical properties. The prediction of this model in terms of deformations were compared with experimental measurements made on a wooden parallel robot mockup. Results have shown that there is a good correlation between the measurement displacements and the computed ones. However, differences occurred between the theoretical and experimental results that may differ because of unmodelled phenomena.

Our future works will concern the refining of the proposed elastic model, the computation of the natural frequencies and the definition of a robust design methodology for wooden industrial robots.

Acknowledgements. This work is supported by the French Région Pays de la Loire in the frame of the project RobEcolo (Convention No. 2015-10773).

References

1. Car manufacturer Morgan. <http://www.morgan3wheeler.co.uk/#technology>
2. Fizians report. http://www.ircyn.ec-nantes.fr/~briot/Project_Review.html
3. Project RobEcolo. <http://robecolo.ircyn.ec-nantes.fr/>
4. Chaumette, F., Hutchinson, S.: Handbook of Robotics. Visual Servoing and Visual Tracking, pp. 563–583. Springer (2008). Chap. 24
5. Cools, R., Nuyens, D.: Monte Carlo and Quasi-Monte Carlo Methods. Springer, Cham (2014)
6. Deblaise, D., Hernot, X., Maurine, P.: A systematic analytical method for PKM stiffness matrix calculation. In: IEEE International Conference on Robotics and Automation, Orlando, Florida, USA (2006)
7. Hill, C.: Wood Modification: Chemical, Thermal and Other Processes. Wiley, Chichester (2006)
8. Imbert, J.: Analyse des structures par éléments finis. Editions Cépaduès (1984). In French
9. Kollmann, F., Côté Jr., W.: Mechanics and rheology of wood. Springer, New York (1968). Chap. 7
10. Kretschmann, D.: Mechanical properties of wood. Forest Products Laboratory, United States Department of Agriculture Forest Service, Madison, Wisconsin (2010). Chap. 5

11. Kretschmann, D.: Stress grades and design properties for lumber, round timber, and ties. Forest Products Laboratory, United States Department of Agriculture Forest Service, Madison, Wisconsin (2010). Chap. 7
12. Laurent, T., Kergueme, J., Arnould, O., Dureisseix, D.: Vers un robot en bois: Première partie 168 (2010). In French
13. Merlet, J.: Parallel Robots, 2nd edn. Springer, Dordrecht (2006)
14. Quigley, M., Asbeck, A., Ng, A.: A low-cost compliant 7-DOF robotic manipulator. In: Proceedings of the 2011 IEEE International Conference on Robotics and Automation, ICRA 2011 (2011)
15. Roennau, A., Kerscher, T., Dillmann, R.: Design and kinematics of a biologically-inspired leg for a six-legged walking machine. In: Proceedings of the 2010 3rd IEEE RAS & EMBS International Conference on Biomedical Robotics and Biomechatronics. The University of Tokyo, Tokyo, Japan (2010)
16. Thakur, V.: Green Composites from Natural Resources. CRC Press, Boca Raton (2013)
17. Wang, C., Piao, C.: From hydrophilicity to hydrophobicity: a critical review. Wood Fiber Sci. **43**(1), 1–16 (2011)
18. Wang, W., Caro, S., Bennis, F., Soto, R., Crawford, B.: Multi-objective robust optimization using a postoptimality sensitivity analysis technique: application to a wind turbine design. J. Mech. Des. **137**(1), 011403-1–011403-11 (2014)

Towards an Autonomous Airborne Robotic Agent

Daniel Soto-Guerrero¹(✉), José Gabriel Ramírez-Torres¹,
and Jean-Pierre Gazeau²

¹ Cinvestav Tamaulipas, Ciudad Victoria, Mexico
{dsoto,grtorres}@tamps.cinvestav.mx

² Institut Pprime, CNRS, Université de Poitiers, Poitiers, France
jean.pierre.gazeau@univ-poitiers.fr

Abstract. Commercially available (UAVs) rely on the Global Positioning System (GPS) to define their flight plan, while assuming an obstacle-free environment. The work presented on this article aims to set the foundation towards an autonomous airborne agent, capable of locating itself by means of computer vision, modeling its environment, planning and executing a three dimensional trajectory. On the first stage of development we solved the localization problem using artificial markers and tested a PID controller to make the vehicle follows a given trajectory (a lemniscate); as results, we show flight data captured during real flights. This development would facilitate the integration of far more complex flight behaviors than GPS only guided flight plans.

1 Introduction

In order to make an autonomous agent out of a UAV, it is required to locate the vehicle with respect to a fixed reference frame, to know its environment and to command it to navigate autonomously. So, given a fully functional UAV with an onboard camera, we aimed to: (a) guarantee a safe operation of the UAV (b) locate it with respect to a fixed reference frame on the ground, using visual feedback and (c) control the vehicle so it can execute flight patterns.

The following sections describe the accomplished intellectual developments, the architecture of the control application, its capabilities and further possible developments.

2 Related Work

A robot consists of a series of highly heterogenous systems that are complex in nature and require an orchestrated integration to function properly, some of those features to name a few are: multi-robot coordination, collision avoidance, human interaction and planning. Therefore, control architectures are proposed to organize by hierarchies the modules providing different functionalities; among one of the most important, the possibility to have a digital representation of the environment on the computer controlling the robot.

The hierarchical architecture of the control application is based on designs already tested in mobile robotics, such as the one proposed by Chen *et al.* [1] (see Fig. 1). The architecture consists of three layers: (a) the Low level control layer allows to directly manage and access all hardware peripherals in real-time. (b) the planner is the process that gives the current status of the robot and its environment, creates a plan for the robot to achieve a certain goal, (c) the sequencer is the intermediate layer between the low level control and the planner that implements a set of *well-tested* [7] behaviors that can be used in sequence to execute the plan created by the planner.

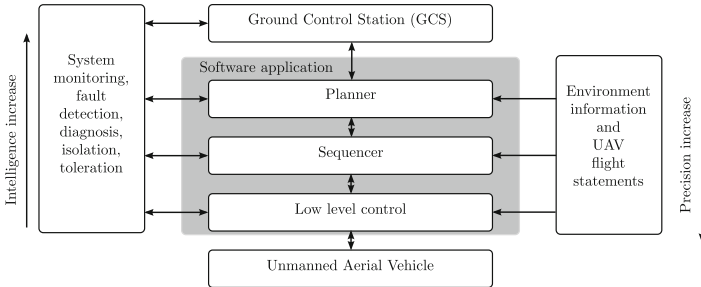


Fig. 1. The three-layer software architecture for an autonomous robot.

Similar architectures to the one shown on Fig. 1 have been used for service robotics, industrial robots interacting with humans [2] and a group of identical robots [5, 10]; their description may differ, but all of their corresponding software architectures can be shaped to a three layer architecture so the objective would remain the same: to provide sensing, planning, supervision and execution capabilities to fulfill a task. As an example, the ability layer on a service robot mentioned by Luna-Gallegos *et al.* [7] can be grouped into the sequencer layer mentioned on this paper as a set of *well-tested* behaviors.

On the field of UAVs, control architectures have been tested following a reactive approach, *i.e.* they act proportionally to an error metric, usually defined by finding and tracking an object with computer vision [11, 12]. On this article, we describe how we plan to develop a three layer architecture for the control of UAVs and the first steps we have taken.

3 Hardware Description

This work was successfully tested with two different vehicles, for which we had to use two different versions of the Low level control layer. The first UAV we tested was the Solo from 3D Robotics, which is compatible with the MAVLink protocol [8] and the second vehicle we tested was the AR-Drone v2. Both platforms are ready-to-fly UAVs and feature an onboard monoscopic camera and a WiFi link.

To connect to the AR-Drone, we used the package created to control it with ROS. The software development was based on the Linux operating system and

the Robotic Operating System (ROS) [9]. For the Solo (see Fig. 2b) we used Gstreamer¹ to receive the video feed and Dronekit (the python library created to interface with UAVs compatible with MAVlink) to gain access to the vehicle. For each vehicle we have a hardware remote control, the pilot has the option to intervene or not in basic maneuvers such as take-off and landing. We gave a bigger priority to pilot commands over autonomous control; in case of unforeseen situations, the pilot can bypass the autonomous control immediately by operating the hardware controller.

The approach we tested was implemented into a three layer architecture on Robotic Operating System (ROS), this simplified its development and looking into the future it will make possible two things: the creation of a swarm of UAVs and its migration onboard the UAV. Increasing the independency of the UAV from the Ground Control Station (GCS).

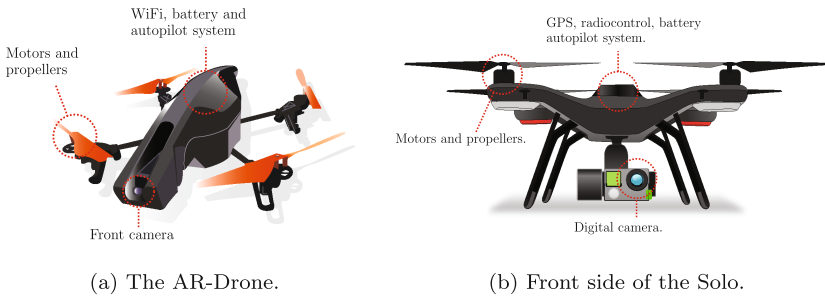


Fig. 2. The two drones tested.

4 Proposed Approach and Methodology

The overall disposal of all components, according to the three layer architecture structure is shown in Fig. 3. The hardware interface to the AR-Drone was the only component fully functional and running on ROS when this development started. From top to bottom we show the Ground Control Station(GCS) and the planner node, the planner remains as future work. The trajectory planner generates the lemniscate trajectory and defines the desired position for the drone $\mathbf{r}_d(t)$. The low level control consists on several nodes, the first one being a hardware interface to the flight controller of the drone and the camera. The current state estimation is accomplished with the computer vision and kalman filter nodes, the current state is then used to define a proper control command in the error estimation and PD controller nodes.

As mentioned before, we aimed to locate the UAV using visual feedback to command it and describe a certain trajectory. The proposed scenario is shown on Fig. 4, the UAV overflies artificial markers fixed on the ground, pointing its

¹ Webpage: <http://gstreamer.freedesktop.org/>.

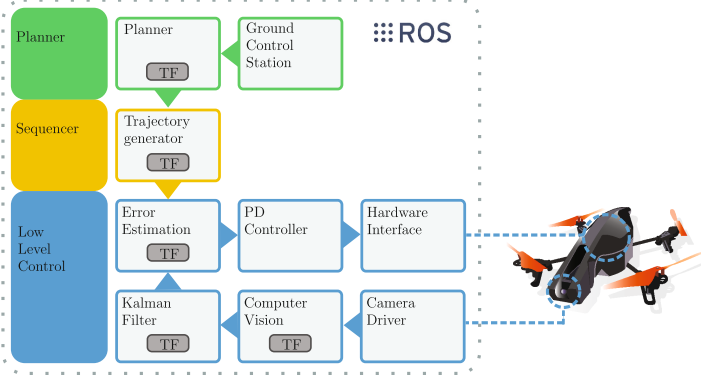


Fig. 3. The three-layer architecture for the UAV

camera downwards, the video feed and navigation data are sent to the Ground Control Station(GCS) for processing. Figure 4 also shows the reference frames attached to the monoscopic camera C , the world reference frame W , the center of gravity of the vehicle B and the NED frame (X: North, Y: East, Z: Down).

Dealing with spatial relationships between reference frames is a very common task in robotics, expressed as homogeneous transformations ${}^W_C\mathbf{T}$ the rigid body transformation from reference frame C to W is denoted by:

$${}^W_C\mathbf{T} = \begin{pmatrix} {}^W_C\mathbf{R} & {}^W_C\mathbf{t} \\ \mathbf{0} & 1 \end{pmatrix}$$

where ${}^W_C\mathbf{R} \in SO(3)$ and ${}^W_C\mathbf{t}$ are the rotation and translation components, respectively. We used the work from Foote [3] to manage all rigid body transformations. Note that by solving ${}^W_C\mathbf{T}$, we can locate B with respect to W . Because the camera is rigidly mounted on the UAV ${}^B_C\mathbf{T}$ is known beforehand and the location of B with respect to W can be computed with ${}^B_W\mathbf{T} = {}^B_C\mathbf{T} {}^W_C\mathbf{T}^{-1}$. To compute ${}^W_C\mathbf{T}$ we used the technique developed by Garrido *et al.* [4]; which consists on segmenting from the images taken by the camera the artificial markers located on the ground, because the size of every marker is known, the pose of the camera is estimated from all the detected corners.

We added a Kalman filter [6] over ${}^B_W\mathbf{T}$ to improve the resilience to errors caused by inaccuracies in inertial measurements, camera parameters, corner detection, image rectification and pose estimation. The state vector for the Kalman filter was defined as $\mathbf{x} = [x, y, z, \psi, \dot{x}, \dot{y}, \dot{z}, \dot{\psi}]$, it defines the position and velocities of the XYZ coordinates and the yaw around the z-axis angle with respect to W . From the inertial sensors onboard the UAV, we receive the horizontal velocity components with respect to the B reference frame, current flight's height and orientation $\mathbf{z}_I = [v_x, v_y, h, \Psi]_{k,B}$ at 200 Hz; the *a priori* estimate of

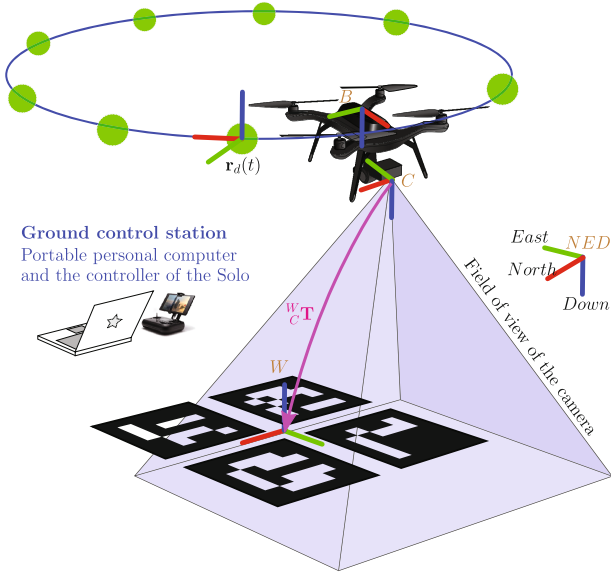


Fig. 4. The use case scenario for the 3DR Solo. For every reference frame, the color convention is: X axis red, Y axis green and Z axis blue. Notice the orientation of B is similar to the NED reference frame. (Color figure online)

the Kalman filter was updated using the inertial measurements with respect to W by rotating Ψ radians around the yaw ψ axis. The state transition model is:

$$\begin{aligned}
 \begin{bmatrix} x \\ y \end{bmatrix}_{k+1} &= \begin{bmatrix} x \\ y \end{bmatrix}_k + \Delta_t \mathbf{R}_z(\psi) \begin{bmatrix} v_x \\ v_y \end{bmatrix}_k & \quad \begin{bmatrix} \dot{x} \\ \dot{y} \end{bmatrix}_{k+1} &= \mathbf{R}_z(\psi) \begin{bmatrix} v_x \\ v_y \end{bmatrix}_k \\
 \dot{z}_{k+1} &= \frac{h_k - z_k}{\Delta_t} & \quad \dot{\psi}_{k+1} &= \frac{\Psi_k - \psi_k}{\Delta_t} \\
 z_{k+1} &= h_k & \quad \psi_{k+1} &= \Psi_k
 \end{aligned}$$

The *a posteriori* step runs at 24 Hz, a slower rate than the *a priori*, using as measurement the pose of the camera $\mathbf{z}_C = [x, y, z, \psi]_k$, estimated by computer vision [4]. After the update process in the Kalman filter, state vector \mathbf{x} defines the latest estimation for the pose of the UAV with respect to W , *i.e.* ${}^B_W\mathbf{T}$.

For now, the trajectory to be described by the vehicle is a lemniscate, defined as a parametric function $\mathbf{r}_d(t)$ that defines the desired position and pose (Euler angles: roll θ_d , pitch ϕ_d and yaw ψ_d , see Fig. 6b):

$$\mathbf{r}_d(t) = \begin{bmatrix} x_d(t) \\ y_d(t) \\ z_d(t) \\ \psi_d(t) \end{bmatrix} = \begin{bmatrix} a \sin(\frac{t}{\epsilon}) \\ b \sin(\frac{2t}{\epsilon}) \\ c \sin(\frac{3t}{\epsilon}) \\ 0 \end{bmatrix} \quad (1)$$

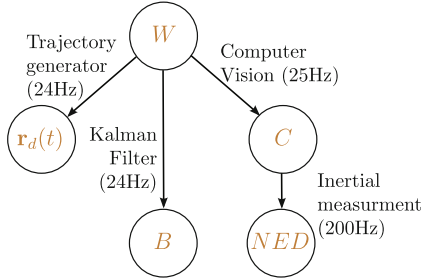


Fig. 5. The graph representing the rigid body transformation between frames.

Figure 5 shows the resultant directed graph using nodes as reference frames and labels on edges as the processes that update the spatial relationship between two reference frames. The direction of every edge represents the origin and target frames of the homogeneous transform. Then, the error measurement is given by:

$${}_{B}^{r_d}\mathbf{T} = \begin{bmatrix} \mathbf{R}_e & \mathbf{t}_e \\ \mathbf{0} & 1 \end{bmatrix} = {}_{W}^{r_d}\mathbf{T} {}_W^B\mathbf{T}^{-1}$$

After decomposing $(\theta, \phi, \psi)_e = \mathbf{R}_e$ on its three Euler angles we can compute a control command using a Proportional-Derivative controller:

$$\mathbf{u} = K_p \begin{bmatrix} \mathbf{r}_d(t) - \mathbf{x} \\ \psi_e \end{bmatrix} + K_d(\dot{\mathbf{r}}_d - \dot{\mathbf{x}})$$

where $\mathbf{x} = [x, y, z, \psi]$ and $\dot{\mathbf{x}} = [\dot{x}, \dot{y}, \dot{z}, \dot{\psi}]$ are estimated by the Kalman filter described before.

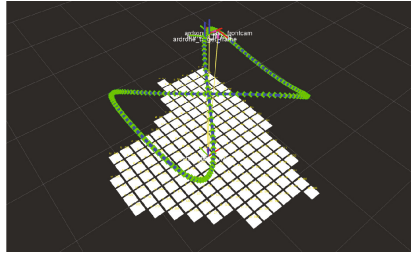
5 Results

The proposed approach was tested with the AR-Drone 2.0 and the 3DR Solo. The AR-Drone was modified, so the front camera pointed downwards and we could get a higher quality image from above the ground level. The Solo had a gimbal installed, as a result, we dynamically had to compute ${}_{C}^B\mathbf{A}$ using the navigational data we received from the UAV. The camera settings for the GoPro are very versatile, for this exercise, we used a *narrow* field of view with a resolution of 1028×720 pixels. The AR-drone was flown indoors at a maximum altitude of 1.4 meters, the Solo flew outdoors and gained altitude to 5 meters above ground level.

The computer vision algorithm was set to track a board of artificial markers with different sizes; for the Solo the board measured 1.4×2.4 m and 2×5 artificial markers, for the AR-Drone we used a board 4×4 m and 20×21 markers (see Fig. 6a). The application here described creates a virtual representation of the world on Rviz, an standard tool on ROS; what is shown on Fig. 6b is a screenshot of Rviz displaying: the location of the vehicle, the trajectory to follow and the detected board.



(a) Artificial markers and the AR-Drone.



(b) The virtual scenario on Rviz.

Fig. 6. The software architecture working, creating a virtual representation of the real world and locating the drone with respect to the center of the ArUco board.

On Fig. 7, we display the results as measured by the computer vision system while executing the lemniscate maneuver in x and y coordinates with respect to W . The r_d plot is the desired trajectory, corresponding to the lemniscate, for completeness, we also display the error plot. The maximum measured error was 30 cm. The parameters for the lemniscate trajectory with the AR-Drone were: $a = 1.0$, $b = 0.8$, $c = 0.2$, $\epsilon = 30.0$, with a height offset of $z = 1.2$.

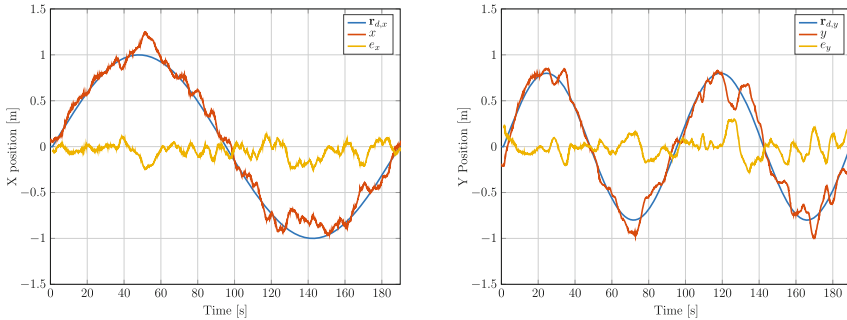


Fig. 7. Navigation data of an actual flight of the vehicle describing the lemniscate trajectory. On both graphs we display the desired trajectory, the estimated position and the error metric.

6 Conclusions and Future Work

We have discussed a three layer architecture intended for the control of UAVs, that successfully guided the vehicle to describe the spline trajectory. Because the framework we used for this development runs on multiple platforms, including ARM on embedded computers, it is plausible to execute it onboard the UAV. Further development on the Sequencer and Planner layers would make the UAV

and autonomous agent and leads the way towards a swarm of UAVs. Additionally, the planner that defined the waypoints will be extended with a path-finding algorithm. This architecture will make possible to integrate far more complex flight plans and do not only rely on GPS for positioning.

This document shows the results from the first step on our development and implementation roadmap. The next step is to execute it onboard the UAV. We are currently looking forward to extending the computer vision system with an visual odometry approach.

References

1. Chen, H., Wang, X.M., Li, Y.: A survey of autonomous control for uav. In: AICI 2009. International Conference on Artificial Intelligence and Computational Intelligence, vol. 2, pp. 267–271, November 2009
2. Dumonteil, G., Manfredi, G., Devy, M., Confetti, A., Sidobre, D.: Reactive planning on a collaborative robot for industrial applications. In: 2015 12th International Conference on Informatics in Control, Automation and Robotics (ICINCO), vol. 02, pp. 450–457, July 2015
3. Foote, T.: Tf: the transform library. In: 2013 IEEE International Conference on Technologies for Practical Robot Applications (TePRA), Open-Source Software workshop, pp. 1–6, April 2013
4. Garrido-Jurado, S., Muñoz Salinas, R., Madrid-Cuevas, F.J., Marín-Jiménez, M.J.: Automatic generation and detection of highly reliable fiducial markers under occlusion. *Pattern Recogn.* **47**(6), 2280–2292 (2014)
5. Goryca, J., Hill, R.C.: Formal synthesis of supervisory control software for multiple robot systems. In: 2013 American Control Conference, pp. 125–131, June 2013
6. Kim, P.: Kalman Filter for Beginners. A-JIN Publishing Company, Seoul (2011)
7. Luna-Gallegos, K.L., Palacios-Hernandez, E.R., Hernandez-Mendez, S., Marin-Hernandez, A.: A proposed software architecture for controlling a service robot. In: 2015 IEEE International Autumn Meeting on Power, Electronics and Computing (ROPEC), pp. 1–6, November 2015
8. Meier, L., Honegger, D., Pollefeys, M.: PX4: a node-based multithreaded open source robotics framework for deeply embedded platforms. In: 2015 IEEE International Conference on Robotics and Automation (ICRA), May 2015
9. Quigley, M., Conley, K., Gerkey, B.P., Faust, J., Foote, T., Leibs, J., Wheeler, R., Ng, A.Y.: Ros: an open-source robot operating system. In: ICRA Workshop on Open Source Software (2009)
10. Schöpfer, M., Schmidt, F., Pardowitz, M., Ritter, H.: Open source real-time control software for the kuka light weight robot. In: 2010 8th World Congress on Intelligent Control and Automation, pp. 444–449, July 2010
11. Vanegas, F., Gonzalez, F.: Uncertainty based online planning for uav target finding in cluttered and gps-denied environments. In: 2016 IEEE Aerospace Conference, pp. 1–9, March 2016
12. Yang, L., Xiao, B., Zhou, Y., He, Y., Zhang, H., Han, J.: A robust real-time vision based gps-denied navigation system of uav. In: 2016 IEEE International Conference on Cyber Technology in Automation, Control, and Intelligent Systems (CYBER), pp. 321–326, June 2016

Autonomous March Control for Humanoid Robot Animation in a Virtual Reality Environment

Víctor H. Andaluz^(✉), Santiago Guamán, and Jorge S. Sánchez

Universidad de las Fuerzas Armadas ESPE, Sangolquí, Ecuador
{vhandaluz1, jsguaman, jssanchez}@espe.edu.ec

Abstract. This article proposes an autonomous control scheme for the march of a humanoid robot applied to virtual reality environments. The control laws proposed for the autonomous displacement of a humanoid robot are based on their kinematic modeling, for which it is considered that the lower extremities of the robot have as reference the midpoint between the separation distance of the right and left leg, the same, what is related to the sacred bone of people. In order to validate the proposed control scheme, a virtual reality simulation environment is implemented, for which it is used as the Unity3D graphics engine.

Keywords: Path control · Tracking control · Virtual environment · Humanoid robot · Kinematic model

1 Introduction

In the last decades, advances in industrial and service robotics have increased, being of great importance the creation of robots that can operate quickly, autonomously and with greater precision [1]. In accordance to the locomotion capability the robots can be moved in various adverse environments, which can be mobile manipulator robots equipped with wheel-based displacement systems, or when the medium arrangement requires, legs, *e.g.*, humanoid robot, spider robot and hexapod robot [1–3].

The humanoid is a robot designed to assimilate the body and movements of a human being and able to perform various functions, *e.g.*, open doors, remind a person to take their medicine, play soccer or dance [3], these are some of the functions that humanoid robots can perform at the moment, these actions can be done through a control scheme or with a programming software [4].

Researchers worldwide have worked on the development of humanoid robots in order to resemble humans and work together [5], therefore a direct and inverse kinematic model has been determined, for the legs of a humanoid robot Bioloid Premium with 12DOF in order to simulate the cycle of the march. The model starts from the selection of main and secondaries coordinates: main for the foot support and secondary for each joint of the links [6], in addition it is tried to develop a robot that allows to give it of mobility and autonomy, able to walk and to raise tiers, this project specifically focuses on the generation of trajectories, starting from an elementary scheme of a kinematic control system [7]. On the other hand, through the kinematic analysis is

intended to present a humanoid robot with basic movement capabilities and with a minimum of actuators to walk, in this case a single motor to generate the movement path of the mechanism. Kinematic synthesis is based on the trajectories described by human movement [8].

This document establishes a control scheme which is composed of a path controller which allows the humanoid robot to have a high degree of autonomy at the moment of following the desired path; while the gait controller determines the step that each leg of the robot must perform, the control scheme is validated using a virtual reality tool, performing bilateral communication between mathematical software and virtual reality software.

2 Virtual Reality Environment

Virtual reality is a tool that can be used for the simulation of control schemes. The 3D modeling of the humanoid robot is done in a tool (CAD). The structure of the humanoid robot presents an imitation of the human being so it has upper and lower limbs, which allow the autonomous march of the robot to be more real. The humanoid robot uses the geometric solid model that contains all the geometry of the surface, detailing the edges and faces of the model, [8] see Fig. 1.

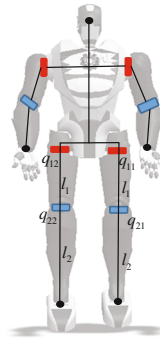


Fig. 1. Humanoid robot developed in solidworks

The process to implement the 3D model of the proposed robot in a virtual reality environment is divided into the following stages: (i) obtaining the 3D model, (ii) adding hierarchies, (iii) generation of the movement, and finally (iv) animation of the humanoid robot for autonomous march control in a virtual reality environment, [8] see Fig. 2.

where, $\dot{\mathbf{h}}_r(t) = [\dot{h}_{xr} \ \dot{h}_{yr} \ \dot{h}_{zr}]^T$ represents the velocities in the working space of the right foot; $\dot{\mathbf{q}}_r(t) = [\dot{q}_{1r} \ \dot{q}_{2r} \ \dot{\psi}]^T$ where, \dot{q}_{1r} and \dot{q}_{2r} are the angular speeds of maneuverability of the right leg; while $\dot{\psi}$ it is the change of orientation regarding the time of the hip with respect to $\{R\}$; and $\mathbf{J}_r(q)$ represents the Jacobian matrix that relates the movement velocities of the joints.

Remark 1. According to the above, to determine the kinematic model of the left leg is obtained with (1) and (2), but with the value of a sign changed. So the kinematic model is,

$$\dot{\mathbf{h}}_l(t) = \mathbf{J}_l(q_l)\dot{\mathbf{q}}_l(t) \tag{3}$$

4 Control Scheme

In this section is present a control scheme composed of a path controller, which allows the robot to follow a desired path; and a march controller that determines the step of each leg of the robot, see Fig. 4.

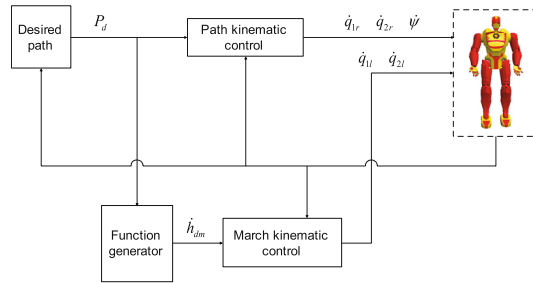


Fig. 4. Control subsystem in parallel in the k instant

Remark 2. In a sampling period k the right leg reaches the desired position through the tracking controller, while with the path controller the left leg performs the gait; at the moment $k + 1$ the controllers are inverted, i.e., the right leg performs the march while the left reaches a desired position of the road.

4.1 Track Tracking Control

As shown in Fig. 5, the way forward is called $P(s)$. The desired position is described with, $P_d = (P_{xd}, P_{yd})$ this point is defined as the closest point to $P(s)$, The unit vector tangent to the path at point P_d is denoted by T ; ψ_d is the orientation of T with respect to the X axis of $\{R\}$; $\tilde{h}_{xp} = P_{xd} - x$ is the position error in the X direction; $\tilde{h}_{yp} = P_{yd} - y$ is the position error in the Y direction; therefore ρ represents the distance between the position of the humanoid robot $h(x, y)$ and the desired point P_d . Where the position error in the direction ρ is $\tilde{\rho} = 0 - \rho = -\rho$, i.e., The desired distance between the

position of the robot $h(x, y)$ and the desired point P_d must be zero; ψ_ρ is the orientation of the error $\tilde{\rho}$ with respect to $\{R\}$.

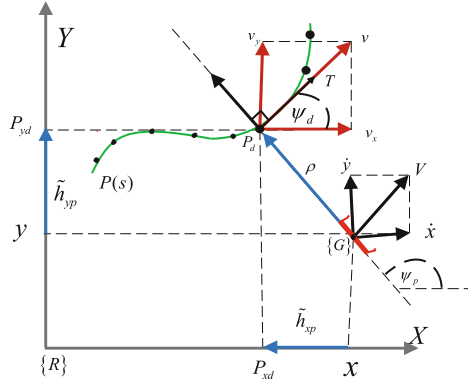


Fig. 5. Orthogonal projection of the point of interest over the trajectory.

To solve the problem of tracking path in the plane $X - Y$ of $\{R\}$ only the direct kinematics of the position in the axis is considered $X - Y$ of the right leg. The kinematic model that is determined for the robot to reach the path is represented by,

$$\begin{cases} h_{xrp} = x + aS_\psi + l_2C_{q_{1r},q_{2r}}C_\psi + l_1C_\psi C_{q_{1r}} \\ h_{yrp} = y - aC_\psi + l_2C_{q_{1r},q_{2r}}S_\psi + l_1C_{q_{1r}}S_\psi \end{cases} \quad (4)$$

Deriving (4), the representation in matrix form is presented by,

$$\dot{\mathbf{h}}_{rp}(t) = \mathbf{J}_{rp}(q_{rp})\dot{\mathbf{q}}_{rp}(t) \quad (5)$$

where $\dot{\mathbf{h}}_{rp}(t) = [\dot{h}_{xrp} \ \dot{h}_{yrp}]^T$ represents the speeds in the plane $X - Y$ of the system $\{R\}$; and \mathbf{J}_{rp} represents the Jacobian matrix that relates the velocities of $\dot{q}_{1rp}(t)$ with respect to the linear speeds in the plane $X - Y$ of $\{R\}$.

The proposed control law to solve the path-tracking problem is based on the inverse kinematics of (5).

$$\mathbf{V}_r(t) = \mathbf{J}_{rp}^\#(\mathbf{V}_{xyd} + \mathbf{K}_p \tanh(\tilde{\mathbf{h}}_p)) \quad (6)$$

where, $\mathbf{J}_{rp}^\#$ is the pseudoinverse Jacobian matrix on the right; $\mathbf{V}_{xyd} = [v \cos(\psi_d) \ v \sin(\psi_d)]^T$ is the desired velocity vector of the path; \mathbf{K}_p is the diagonal matrix of positive gain for the compensation of the error generated; $\tanh(\cdot)$ limits the reference speeds, thus avoiding the saturation of the speed of the robot; $\tilde{\mathbf{h}}_p = [\tilde{h}_{xp} \ \tilde{h}_{yp}]^T$ is the vector of errors defined with, $\tilde{h}_{xp} = P_{xd} - x$, $\tilde{h}_{yp} = P_{yd} - y$; $\mathbf{V}_r(t) = [\dot{q}_{1rp} \ \dot{q}_{2rp} \ \dot{\psi}]^T$ represents the maneuverability vector of the system.

Remark 3. According to the above, for $K + 1$ the law of road control for the left leg is obtained with,

$$\mathbf{V}_l(t) = \mathbf{J}_{lp}^\# (\mathbf{V}_{xyd} + \mathbf{K}_p \tanh(\tilde{\mathbf{h}}_p)) \quad (7)$$

4.2 Control of the March

For control of the march of the humanoid robot, a reference system is determined with respect to $\{L_l\}$, which is located in the center of the thigh of the left leg, see Fig. 3. According to the axis of reference the kinematic model is determined in order to determine a control law based on its kinematics. The kinematic model of the left leg with respect to $\{L_l\}$ this given by,

$$\begin{cases} h_{xrm} = l_1 C_{q_{1lm}} + l_2 C_{q_{2lm}, q_{1lm}} \\ h_{zrm} = l_1 S_{q_{1lm}} + l_2 S_{q_{2lm}, q_{1lm}} \end{cases} \quad (8)$$

where, q_{1lm} and q_{2lm} represent the position of the left leg for the march, l_1 is the length of the thigh and l_2 the length of the leg. The trajectory that is generated is related to the end of the left leg in the position h_{zr} of the kinematic model (3), the parameters of the generated parabola are varied in amplitude and angular frequency according to the desired step. Performing the derivate of (8) the matrix form of the kinematic model is represented by,

$$\dot{\mathbf{h}}_{lm}(t) = \mathbf{J}_{lm}(q_{lm}) \dot{\mathbf{q}}_{lm}(t) \quad (9)$$

where $\dot{\mathbf{h}}_{lm}(t) = [\dot{h}_{xlm} \quad \dot{h}_{zlm}]^T$ represents the velocities in the working space of the left foot with respect to $\{L_l\}$; $\dot{\mathbf{q}}_{lm}(t) = [\dot{q}_{1lm} \quad \dot{q}_{2lm}]^T$ where, \dot{q}_{1lm} and \dot{q}_{2lm} are the angular velocities of maneuverability of the left leg; and \mathbf{J}_{lm} represents the Jacobian matrix of the left leg that relates the joint movement velocities.

The control law proposed according to the kinematic model of the left leg of the humanoid robot is given by,

$$\dot{\mathbf{q}}_{lm}(t) = \mathbf{J}_{lm}^{-1} (\dot{\mathbf{h}}_{dm} + \mathbf{K}_m \tanh(\tilde{\mathbf{h}}_m)) \quad (10)$$

where, \mathbf{J}_{lm}^{-1} is the inverse Jacobian matrix of the left leg; $\dot{\mathbf{h}}_{dm}(t) = [\dot{h}_{xdt} \quad \dot{h}_{zdt}]^T$ is the vector of the desired velocities, i.e., the left leg foot; \mathbf{K}_m is the gain constant for the compensation of the error generated; $\tanh(\cdot)$ limits the reference speeds, thus avoiding the saturation of the speed of the robot; $\tilde{\mathbf{h}}_m(t) = [\tilde{h}_{xm} \quad \tilde{h}_{zm}]$ is the vector of errors defined as $\tilde{h}_{zm} = h_{zd} - h_{zr}$, while to determine the error \tilde{h}_{xm} is considered $\tilde{h}_{xm} = |V|f + |E|g$, where $|V| = \sqrt{(v_x)^2 + (v_y)^2}$, $|E| = \sqrt{(\tilde{h}_{xp})^2 + (\tilde{h}_{yp})^2}$, f y g , are constant of error adjustment.

Remark 4. According to the above, the kinematic model of the right leg respect $\{L_r\}$ of the humanoid robot with (9) is,

$$\dot{\mathbf{h}}_{rm}(t) = \mathbf{J}_{rm}(q_{rm})\dot{\mathbf{q}}_{rm}(t) \tag{11}$$

In addition, the law of march control that is presented for the right leg of the humanoid robot is obtained with (11).

$$\dot{\mathbf{q}}_{rm}(t) = \mathbf{J}_{rm}^{-1}(\dot{\mathbf{h}}_{dm} + \mathbf{K}_m \tanh(\tilde{\mathbf{h}}_m)) \tag{12}$$

Remark 5. From the analysis of the errors of the controllers, previously exposed, they are concluded that they tend asymptotically to zero when $t \rightarrow \infty$, as demonstrated in [9].

5 Results

Figure 6 shows strobe motion in a virtual reality environment, which allows verifying the autonomous functioning of the humanoid robot.



Fig. 6. Stroboscopic movement of the humanoid robot

According to the proposed control scheme, Fig. 7 illustrates the path made by each leg of the humanoid robot and shows the path tracking of the robot when it reaches the desired position.

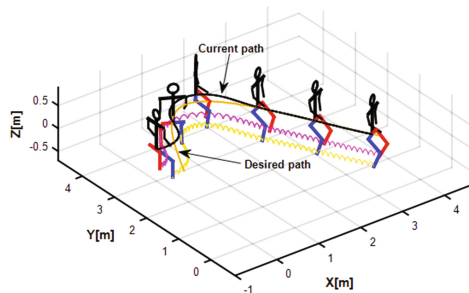


Fig. 7. Path of the step and track of road

Figure 8 (a) shows position and orientation errors of the path controller at the midpoint $\{G\}$, while Fig. 8 (b) illustrates the path controller errors that are generated at the time of the gait step is done.

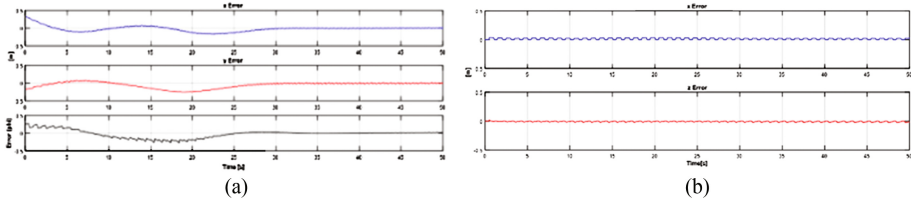


Fig. 8. (a) Errors of the road, (b) errors in the trajectory of the march

6 Conclusions

In this article, a control scheme is presented which includes (i) a control algorithm for the path tracking so that the humanoid robot follows a desired path; and (ii) a trajectory tracking control algorithm which allows the robot to perform the march at the moment it travels to the path. The controllers presented are based on the kinematics of the robot, which fulfill the purpose of generating movement and displacement. In addition, simulations were implemented in a virtual reality environment in order to evaluate the performance of the proposed control scheme, which shows the development of the movement of the lower extremities of the humanoid robot towards the path and the gait that it executes in the instant of movement, through which can be verified that it is possible that the humanoid robot carries out the autonomous march.

References

1. Ramon, J., Camarillo, K., Monsiváis, J., Castillo, G., Pérez, G.I., Pámanes, J.: Kinematic Modeling of a Humanoid Soccer-Player: Applied to BIOLOID Premium Type A Robot, vol. 376, pp. 49–63, Springer (2013)
2. Andaluz, V., Sanchez, D., Bucay, C., Sanchez, C., Morales, V., Rivas, D.: Nonlinear controller of arachnid mechanism based on the jansen, vol. 9979, pp. 328–339. Springer (2016)
3. Barrios, A., Peñin, F., Baleguer, C., Aracil, R.: Fundamentos de Robótica. S.A McGraw-Hill, España (2007)
4. Chevallereau, C., Bessonnet, G., Abba, G., Aoustin, Y.: Bipedal Robots. Wiley ISTE, Great Britain (2009)
5. Paladines, R.: Direct and inverse kinematic model for the legs of the humanoid robot Bioloid Premium. Final career work, Faculty of Engineering in Mechanics and Production Sciences, ESPOL, Guayaquil (2015)

6. Samaniego, F.: Vision algorithms for competitive mini-humanoid platforms with increased capacities. Master thesis, Department of Systems Engineering and Automation, Carlos University III of Madrid, Leganés (2013)
7. Govea, E., Gonzales, G., Rocha, J., Hernández, S., Chávez, A., Castillo, J.: Kinematic design and construction of a humanoid robot with basic walking movements. IEEE, Biennial Congress of Argentina (2014)
8. Andaluz, V., Sánchez, J., Chamba, J., Romero, P., Chicaiza, F., Varela, J., Quevedo, W., Gallardo, C., Cepeda, F.: Unity3D virtual animation of robots with coupled and uncoupled mechanism, vol. 9768, pp. 89–101. Springer (2016)
9. Andaluz, V., Roberti, F., Toibero, J., Carelli, R.: Passivity-based visual feedback control with dynamic compensation of mobile manipulators: Stability and L2-gain performance analysis. *Robot. Autonom. Syst.* **66**, 64–74 (2015)

Control Based on Linear Algebra for Mobile Manipulators

Víctor H. Andaluz^(✉), Edison R. Sásig, William D. Chicaiza,
and Paola M. Velasco

Universidad de las Fuerzas Armadas ESPE, Sangolquí, Ecuador
{vhandaluzl, erssigs, wdchicaizal,
pmvelascol}@espe.edu.ec

Abstract. This paper presents a control algorithm based on linear algebra for trajectory tracking of mobile manipulator robots. The proposed control algorithm considers the kinematics of the robot, which is approximated by the Euler method, the control actions for an optimal operation of the system are obtained solving a system of linear equations. In addition, the stability of the system is analyzed by concepts of linear algebra, where it is shown that the control error tends asymptotically to zero. Simulation results show the good performance of the proposed control system.

Keywords: Mobile manipulator · Model · Controller design · Linear algebra · Numerical methods

1 Introduction

Mobile manipulator is nowadays a widespread term that refers to robots built with a robotic arm mounted on a mobile platform. This kind of system, which is usually characterized by a high degree of redundancy, combines the manipulability of a fixed-base manipulator with the mobility of a wheeled platform. Such systems allow the most usual missions of robotic systems which require both locomotion and manipulation abilities. They are useful in multiple applications in different industrial and productive fields, such as mining, construction, rescue missions or for people assistance [1, 2].

In the literature different control strategies have been proposed. Work [3] solves the trajectory tracking problem by combining neural networks and robust control. The nonlinear mapping characteristic of neural networks and robust control are integrated in an adaptive control algorithm for mobile manipulator robots with non-linearities, perturbations and non-holonomic constraints all at the simulation level. The project carried out in [4] suggests a fuzzy PD controller to adjust the parameters in line depending on the state of the dynamic system. Other advanced control strategies are implemented for example in [5] introduces a constrained predictive control algorithm for a holonomic mobile manipulator robot. Restrictions such as acceleration, velocity, position, and avoiding obstacles are considered.

The control based on linear algebra is a novel technique whose main feature is that there is no need for complex calculations to achieve control signal and simplicity in

performing mathematical operations [6–8]. In addition, the algorithm is easy to understand and implement, allowing direct adaptation to any microcontroller without the use of an external computer [9]. Because it is not a complex algorithm it can run on controllers with low processing capacity [10].

In this work the control based on linear algebra is applied for tasks of tracking of trajectories in mobile manipulator robots. The controller is based on the kinematics of the system formed by a robotic arm mounted on a mobile platform. The structure of the control law consists of a particular solution that meets the raised objective. Additionally, the stability is proved through linear algebra concepts. To validate the proposed control algorithms, experimental results are included and discussed.

This article is organized into 5 Sections. Section 2 presents the robot kinematic model for the mobile manipulator robot. The design of the control algorithm is presented in Sect. 3. The discussion of results is shown in Sect. 4, and finally the conclusions of the paper are presents in Sect. 5.

2 Mobile Manipulator Modeling

In this section, the kinematic model of the mobile manipulator is presented. For this purpose, the mobile manipulator configuration is defined by a vector $\mathbf{q} = [q_1 \ q_2 \ \dots \ q_n]^T = [\mathbf{q}_p^T \ \mathbf{q}_a^T]^T$ of n independent coordinates called generalized coordinates of the mobile manipulator, where \mathbf{q}_a represents the generalized coordinates of the arm, and \mathbf{q}_p the generalized coordinates of the mobile platform. The location of the end-effector of the mobile manipulator is given by the m -dimensional vector of operational coordinates $\mathbf{h} = [h_1 \ h_2 \ \dots \ h_m]^T$ [11].

The kinematic model of a mobile manipulator gives the location of the end-effector as a function of the robotic arm configuration and the platform location [11]. The instantaneous kinematic model of a mobile manipulator gives the derivative of its end-effector location as a function of the derivatives of both the robotic arm configuration and the location of the mobile platform.

$$\dot{\mathbf{h}}(t) = \mathbf{J}(\mathbf{q})\mathbf{v}(t) \quad (1)$$

where $\dot{\mathbf{h}} = [\dot{h}_1 \ \dot{h}_2 \ \dots \ \dot{h}_m]^T$ is the vector of end-effector velocity, $\mathbf{v} = [v_1 \ v_2 \ \dots \ v_{\delta_n}]^T = [v_p^T \ v_a^T]^T$ is the vector of mobile manipulator velocities in which contains the linear and angular velocities of the mobile platform and contains the joint velocities of robotic arm and $\mathbf{J}(\mathbf{q})$ is the Jacobian matrix that defines a linear mapping between the vector of the mobile manipulator velocities $\mathbf{v}(t)$ and the vector of the end-effector velocity [12].

3 Controller Design

In this section, the control law based on linear algebra theory and numerical methods is presented. Furthermore, the stability is proved through linear algebra concepts.

3.1 Kinematic Controller

Through the Euler's approximation of the kinematic model of the mobile manipulator (1), the following kinematic model discrete is obtained

$$\mathbf{h}(k+1) = \mathbf{h}(k) + T_0 \mathbf{J}(\mathbf{q}(k)) \mathbf{v}(k) \quad (2)$$

where, values of \mathbf{h} at the discrete time $t = kT_0$ will be denoted as $\mathbf{h}(k)$, T_0 is the sample time, and $k \in \{0, 1, 2, 3, 4, 5, \dots\}$. Next by the Markov property and to adjusting the performance of the proposed control law [13], the states vector $\mathbf{h}(k+1)$ is replaced by,

$$\mathbf{h}(k+1) = \mathbf{h}_d(k+1) - \mathbf{W}(\mathbf{h}_d(k) - \mathbf{h}(k)) \quad (3)$$

where, \mathbf{W} is a diagonal matrix and its values are obtained in Sect. 3.1, these constants satisfy $0 < \mathbf{diag}(w_{hx}, w_{hy}, w_{hz}) < 1$, allowing to reduce the variations in state variables and \mathbf{h}_d is the desired trajectory.

Then, from (2) and (3), the following system of linear equations is obtained, which allows at each sampling instant to calculate the control actions.

$$\mathbf{J}\mathbf{v} = \mathbf{b} \quad (4)$$

where $\mathbf{v} = [u(k) \quad \omega(k) \quad \dot{q}_1(k) \quad \dot{q}_2(k) \quad \dot{q}_3(k)]^T$ and

$$\mathbf{b} = \frac{1}{T_0} \begin{bmatrix} h_{xd}(k+1) - w_{hx}(e_{hx}(k)) - h_x(k) \\ h_{yd}(k+1) - w_{hy}(e_{hy}(k)) - h_y(k) \\ h_{zd}(k+1) - w_{hz}(e_{hz}(k)) - h_z(k) \end{bmatrix}$$

From (4), which is a set of three equations with five unknown variables, its solution by least squares is obtained by solving the normal equations.

$$\mathbf{v}_{ref} = \mathbf{J}^T (\mathbf{J}\mathbf{J}^T)^{-1} \frac{1}{T_0} \begin{bmatrix} h_{xd}(k+1) - w_{hx}(e_{hx}(k)) - h_x(k) \\ h_{yd}(k+1) - w_{hy}(e_{hy}(k)) - h_y(k) \\ h_{zd}(k+1) - w_{hz}(e_{hz}(k)) - h_z(k) \end{bmatrix} \quad (5)$$

4 Simulation Results

In order to assess and discuss the performance of the controller based on linear algebra. It's developed a simulation platform for mobile manipulator on Matlab[©] platform. This is an online simulator, which allows users to view three-dimensional environment navigation of a mobile manipulator.

To check the performance of the control system presents in (5). Two tests are implemented: the first desired trajectory for the end-effector of the mobile manipulator is described by $\mathbf{h}_d = [h_{xd} \ h_{yd} \ h_{zd}]^T$, where $h_{xd} = 0.1t$, $h_{yd} = 0.3 \sin(0.3t)$ and $h_{zd} = 0.5$, the mobile platform starts at $\mathbf{q}_p = [0 \text{ m} \ -0.2 \text{ m} \ 0 \text{ rad}]^T$; the robotic arm at $\mathbf{q}_a = [0 \text{ rad} \ \frac{\pi}{4} \text{ rad} \ -\frac{\pi}{2} \text{ rad}]^T$, Figs. 1 to 4, represent the experimental results.

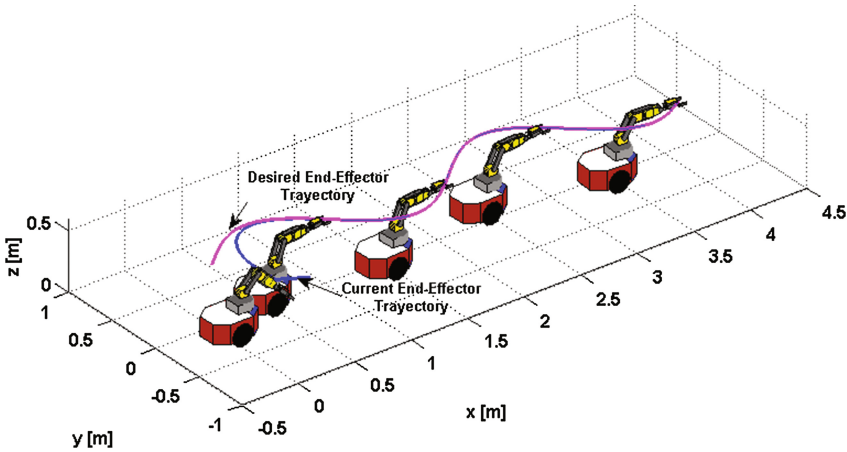


Fig. 1. Stroboscopic movement of the mobile manipulator in the trajectory tracking experiment

Figure 1, shows the desired trajectory and the current trajectory of the end-effector. It can be seen that the proposed controller presents a good performance. Figure 2, shows the evolution of the tracking errors, which remain close to zero, while Figs. 3 and 4 show the control actions.

The second desired trajectory is described by $\mathbf{h}_d = [h_{xd} \ h_{yd} \ h_{zd}]^T$, where $h_{xd} = 0.7 + \sin(0.4t)$, $h_{yd} = \sin(0.2t)$ and $h_{zd} = 0.37 + 0.1 \sin(0.2t)$. In this experiment, the mobile platform starts at $\mathbf{q}_p = [0.8 \text{ m} \ -0.1 \text{ m} \ \pi \text{ rad}]^T$; the robotic arm at $\mathbf{q}_a = [0 \text{ rad} \ \frac{\pi}{2} \text{ rad} \ -\frac{\pi}{2} \text{ rad}]^T$, The following figures illustrate the simulation results.

Figure 5, shows the desired trajectory and the current trajectory of the end-effector. It can be seen that the proposed controller presents a good performance. Figure 6, shows the evolution of the tracking errors, which remain close to zero, while Figs. 7 and 8 show the control actions.

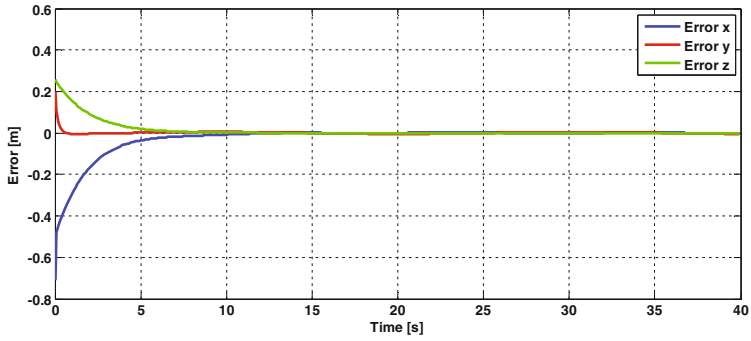


Fig. 2. Control errors of the mobile manipulator

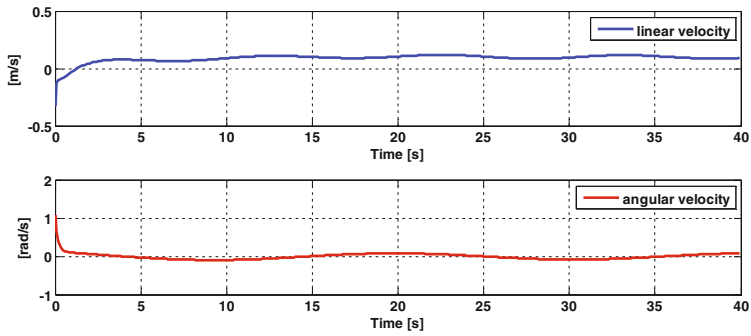


Fig. 3. Velocity commands to the mobile platform

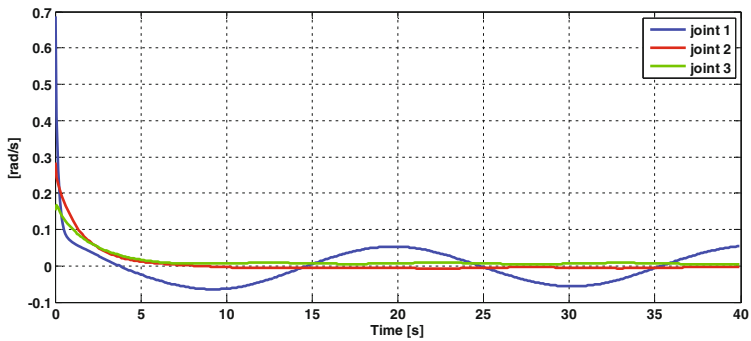


Fig. 4. Joint velocity commands to the robotic arm

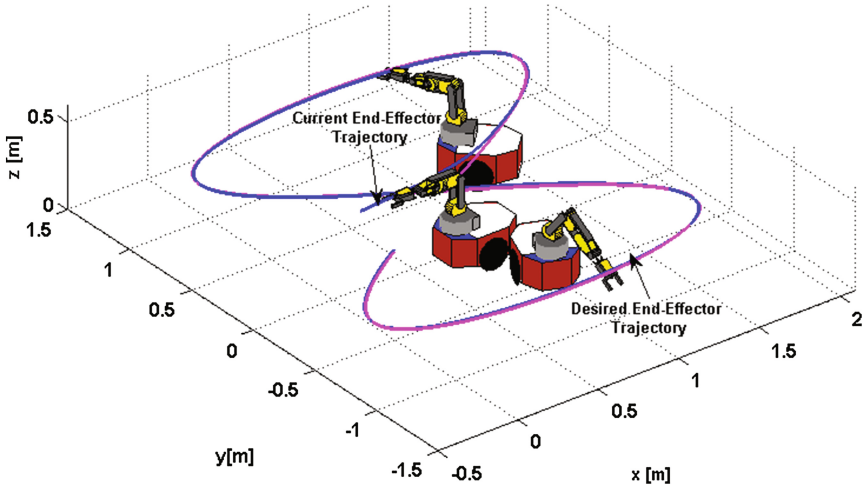


Fig. 5. Stroboscopic movement of the mobile manipulator in the trajectory tracking experiment

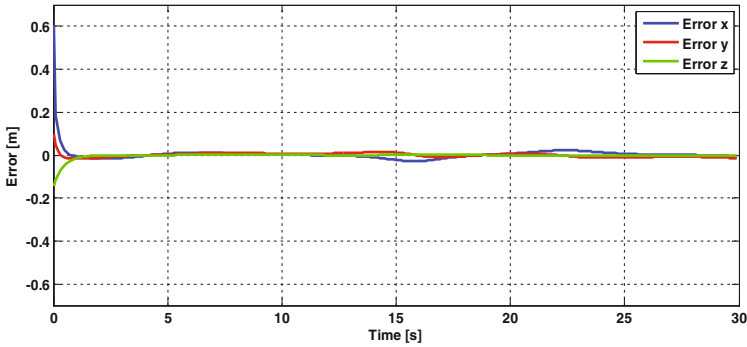


Fig. 6. Control errors of the mobile manipulator

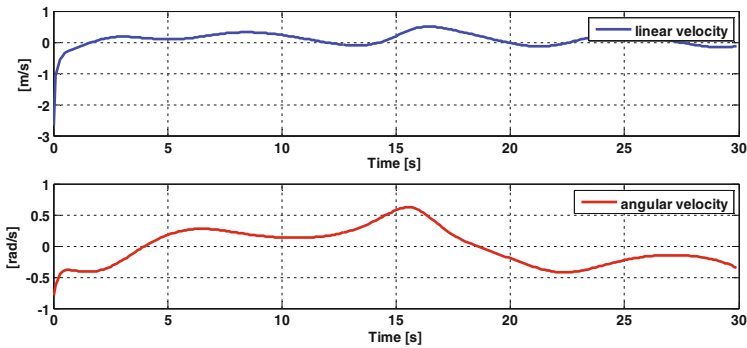


Fig. 7. Velocity commands to the mobile platform

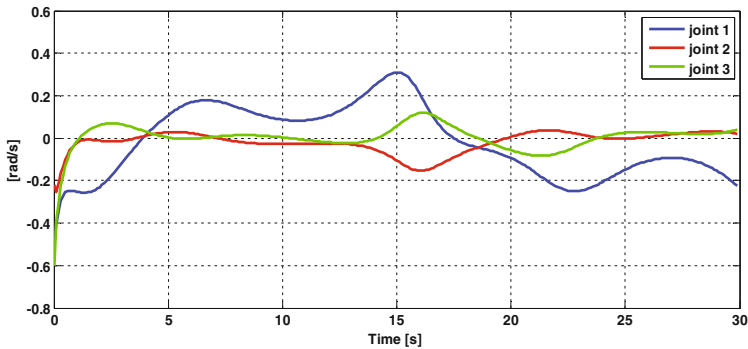


Fig. 8. Joint velocity commands to the robotic arm

5 Conclusions

In this work it was proposed a control algorithm based on concepts of linear algebra and numerical methods for trajectory tasks of mobile manipulators robots. The structure of the control algorithm consists of a particular solution that meets the stated objective. The stability and performance of the proposed control algorithm was demonstrated analytically through concepts of linear algebra. The simulation results obtained show the good performance of the proposed control algorithm.

Acknowledgments. The authors would like to thanks to the Consorcio Ecuatoriano para el Desarrollo de Internet Avanzado -CEDIA-, and the Universidad de las Fuerzas Armadas ESPE for financing the project “Tele-Operación Bilateral Cooperativo de Múltiples Manipuladores Móviles – CEPRAIX-2015-05”.

References

1. Padois, V., Fourquet, J.-Y., Chiron, P.: Kinematic and dynamic model-based control of wheeled mobile manipulators: a unified framework for reactive approaches. *Robotica* **5**, 157–173 (2007). Cambridge University Press
2. Rosales, A., Scaglia, G., Mut, V., Sciascio, F.D.: Navegación de Robots Móviles en entornos no Estructurados utilizando Álgebra Lineal. *Revista Iberoamericana de Automática e Informática Industrial RIAI* **6**, 79–88 (2009)
3. Naijian, C., Hao, Y., Xiangdong, H., Changsheng, A., Chenglong, T., Xiangkui, L.: Adaptive robust control of the mobile manipulator based on neural network. In: IEEE Conference Publications: 2016 IEEE 11th Conference on Industrial Electronics and Applications (ICIEA), pp. 2425–2430 (2016)
4. Karray, A., Feki, M.: Tracking control of a mobile manipulator with fuzzy PD controller. In: IEEE Conference Publications: 2015 World Congress on Information Technology and Computer Applications (WCITCA), pp. 1–5 (2015)

5. Avanzini, G.B., Zanchettin, A.M., Rocco, P.: Constraint-based model predictive control for holonomic mobile manipulators. In: IEEE Conference Publications: 2015 IEEE/RSJ Conferencia Internacional de Robótica Inteligente y Sistemas (IROS), pp. 1473–1479 (2015)
6. Scaglia, G., Rosales, A., Quintero, L., Mut, V., Agarwal, R.: A linear-interpolation-based controller design for trajectory tracking of mobile robots. *Control Eng. Pract.* **18**(3), 318–329 (2010). ELSEVIER
7. Rómoli, S., Serrano, M.E., Ortiz, O.A., Vega, J.R.: Tracking control of concentration profiles in a fed-batch bioreactor using alinear algebra methodology. *ISA Trans.* **57**, 162–171 (2015). Elsevier Ltd
8. Gandolfo, D., Rosales, C., Patiño, D., Scaglia, G., Jordan, M.: Trajectory tracking control of a pvtol aircraft based on linear algebra theory. *Asian J. Control* **16**, 1849–1858 (2014)
9. Rosales, A., Scaglia, G., Mut, V., Sciascio, F.D.: Trajectory tracking of mobile robots in dynamic environments—a linear algebra approach. *Robotica* **27**(7), 981–997 (2009). Cambridge University
10. Špinka, O., Hanz’lek, Z.: Energy-aware navigation and guidance algorithms for unmanned aerial vehicles. In: IEEE Conference Publications: 2011 IEEE 17th International Conference on Embedded and Real-Time Computing Systems and Applications, vol. 2, pp. 83–88 (2011)
11. Bayle, B., Fourquet, J.-Y., Renaud, M.: Kinematic modelling of wheeled mobile manipulators. In: IEEE: International Conference on Robotics & Automation, vol. 1, pp. 69–74 (2003)
12. Andaluz, V., Roberti, F., Toibero, J.M., Carelli, R.: Adaptive unified motion control of mobile manipulators. *Control Eng. Pract.* **20**, 1337–1352 (2012). ELSERVIER
13. Romoli, S., Scaglia, G., Serrano, M.E., Godoy, S., Ortiz, O.A., Vega, J.R.: Control of a fed-batch fermenter based on a linear algebra strategy. *IEEE J. Mag.* **12**, 1206–1213 (2014)

Modeling and Kinematic Nonlinear Control of Aerial Mobile Manipulators

Jessica S. Ortiz¹(✉), Alex P. Erazo², Christian P. Carvajal¹,
José A. Pérez¹, Luis E. Proaño¹, Franklin M. Silva M.¹,
and Víctor H. Andaluz¹

¹ Universidad de las Fuerzas Armadas ESPE, Sangolquí, Ecuador
{jsortiz4, fmsilva, vhandaluz1}@espe.edu.ec,
chriss2592@hotmail.com, joansll@hotmail.com,
luis.e.proa@gmail.com

² Escuela Superior Politécnica de Chimborazo, Riobamba, Ecuador

Abstract. This work proposes a kinematic modeling and a kinematic nonlinear controller for an autonomous aerial mobile manipulator robot that generates saturated reference velocity commands for trajectory tracking problem. In the kinematic modeling is considered through of a quadcopter-inner-loop system to independently track four velocity commands: forward, lateral, up/downward, and heading rate; and arm-inner-loop system to independently track angular velocity commands. Stability and robustness of the complete control system are proved through the Lyapunov method. Finally, simulation results are presented and discussed, which validate the proposed controller.

Keywords: Aerial mobile manipulators · Kinematic modeling · Nonlinear controller · Lyapunov

1 Introduction

The area of Robotics has evolved presenting new technologies that allow to improve the intelligence and mobility of robots. Mobile manipulators have been one of the main topics of academic research in recent years and allowing more sophisticated tasks, especially for unmanned aerial vehicles (UAVs), the mobility of these is not limited to displacement on flat surfaces. Expanding tasks such as: (i) construction of high platforms [1]; (ii) cargo transport to unaffordable areas [2]; (iii) aplicaciones en lineas de alta tension [3]; (iv) tasks that are dangerous or monotonous to humans, among others [4, 5].

For the mobility of the robots, platforms have been developed that can work in environments: terrestrial, aquatic and air, for this are used wheels/legs, propellers and propellers [6–8]. The combination of mobile platforms with robotic arms are denominated as mobile manipulators, these allow to increase the workspace and applications in the domestic, commercial, military area, among others [9–12]. There are several ways of performing the study and control of these systems, (i) one of them is to do it separately, *i.e.*, the kinetic model is made of the mobile platform as the manipulator, also the control is made to each of these parts. The point of interest of the kinematic analysis of the mobile platform is done with respect to the center of mass and the point

of interest of the kinetic analysis of the manipulator is done with respect to the operating end; (ii) the kinematic study is done together, *i.e.*, kinematic modeling and control is done from the system together, for the modeling and control of this system is done with respect to the end effector of the mobile manipulator.

This paper presents a non-linear control strategy for resolving the trajectory tracking problem of a aerial mobile manipulator. Which is constituted by an quadcopter mounting a robotic arm of 3 degrees of freedom mounted on back of base. For the design of the controller, the kinematic model of the aerial mobile manipulator is used which has as input the velocity and orientation, this controller is designed based on seven velocities commands of the aerial mobile manipulator, four corresponding to the aerial platform: forward, lateral, up/downward and orientation, the last three are those who command the manipulator robot. It is also pointed out that the workspace has a single reference that is located in the operative end of the aerial mobile manipulator $\langle R(x y z) \rangle$. The stability of the controller is analyzed by the Lyapunov's method and to validate the proposed control algorithm, experimental processes are presented and discussed in this paper.

2 Aerial Mobile Manipulators Model

The mobile manipulator configuration is defined by a vector \mathbf{q} of n independent coordinates, called generalized coordinates of the aerial mobile manipulator, where $\mathbf{q} = [q_1 \ q_2 \ \dots \ q_n]^T = [\mathbf{q}_h^T \ \mathbf{q}_a^T]^T$ where \mathbf{q}_a represents the generalized coordinates of the *robotic arm*, and \mathbf{q}_h the generalized coordinates of the *aerial mobile platform*. We notice that $n = n_h + n_a$, where n_h and n_a are respectively the dimensions of the generalized spaces associated to the aerial mobile and to the robotic arm. The configuration $\mathbf{q}\psi$ is an element of the aerial mobile manipulator *configuration space*; denoted by \mathcal{N} . The location of the end-effector of the aerial mobile manipulator is given by the m -dimensional vector $\mathbf{h} = [h_1 \ h_2 \ \dots \ h_m]^T$, where \mathbf{h} define the position and the orientation, respectively, of the end-effector of the aerial mobile manipulator in \mathcal{R} . Its m coordinates are the *operational coordinates of the aerial mobile manipulator*. The set of all locations constitutes the *aerial mobile manipulator operational space*, denoted by \mathcal{M} .

The location of the aerial mobile manipulator end-effector can be defined in different ways according to the task, *i.e.*, it can be considered only the position of the end-effector or both its position and its orientation.

2.1 Aerial Mobile Manipulator Kinematic Modeling

The *kinematic model of an aerial mobile manipulator* gives the location of the end-effector \mathbf{h} as a function of the robotic arm configuration and the aerial mobile location (or its operational coordinates as functions of the robotic arm's generalized coordinates and the mobile aerial's operational coordinates).

$$\begin{cases} \{ : \mathcal{N}_a \times \mathcal{M}_h \rightarrow \mathcal{M} \\ (\mathbf{q}_h, \mathbf{q}_a) \mapsto \mathbf{h} = f(\mathbf{q}_h, \mathbf{q}_a) \end{cases}$$

where, \mathcal{N}_a is the *configuration space* of the robotic arm, \mathcal{M}_h is the *operational space of the aerial mobile*.

The *instantaneous kinematic model of an aerial mobile manipulator* gives the derivative of its end-effector location as a function of the derivatives of both the robotic arm configuration and the location of the aerial mobile platform,

$$\dot{\mathbf{h}} = \frac{\partial f}{\partial \mathbf{q}}(\mathbf{q}_p, \mathbf{q}_a) \mathbf{v}$$

where, $\dot{\mathbf{h}} = [\dot{h}_1 \ \dot{h}_2 \ \dots \ \dot{h}_m]^T$ is the vector of the end-effector velocity, $\mathbf{v} = [v_1 \ v_2 \ \dots \ v_{\delta_n}]^T = [\mathbf{v}_h^T \ \mathbf{v}_a^T]^T$ is the control vector of mobility of the aerial mobile manipulator. Its dimension is $\delta_n = \delta_{nh} + \delta_{na}$, where δ_{nh} and δ_{na} are respectively the dimensions of the control vector of mobility associated to the aerial mobile platform and the robotic arm, respectively.

Now, after replacing $\mathbf{J}(\mathbf{q}) = \frac{\partial f}{\partial \mathbf{q}}(\mathbf{q}_h, \mathbf{q}_a)$ in the above equation, we obtain

$$\dot{\mathbf{h}}(t) = \mathbf{J}(\mathbf{q})\mathbf{v}(t) \quad (1)$$

where, $\mathbf{J}(\mathbf{q})$ is the Jacobian matrix that defines a linear mapping between the vector of the aerial mobile manipulator velocities $\mathbf{v}(t)$ and the vector of the end-effector velocity $\dot{\mathbf{h}}(t)$. The Jacobian matrix is, in general, a function of the configuration $\mathbf{q}(t)$.

2.2 Case Study: Quadcopter and Robotic Arm

The kinematic model of the aerial mobile manipulator is composed by a set of seven velocities represented at the spatial frame $\langle H \rangle$. The displacement of the aerial mobile manipulator is guided by the three linear velocities u_l , u_m and u_n defined in a rotating right-handed spatial frame $\langle H \rangle$, and the angular velocity ω , as shown in Fig. 1.

Each linear velocity is directed as one of the axes of the frame $\langle H \rangle$ attached to the center of gravity of the quadcopter: u_l points to the frontal direction; u_m points to the left-lateral direction, and u_n points up. The angular velocity ω rotates the referential system $\langle H \rangle$ counterclockwise, around the axis H_z (considering the top view). While the maneuverability of the robotic arm is defined by three angular velocities with respect to the reference system $\langle H \rangle$, *i.e.*, \dot{q}_1 rotates with respect to the axis n , and \dot{q}_2 , \dot{q}_3 rotate with respect to the axis m of the reference system $\langle H \rangle$. In other words, the Cartesian motion of the aerial mobile manipulator at the inertial frame $\langle \mathcal{R} \rangle$ is defined as,

$$\begin{cases} \dot{h}_x = u_l C_\psi - u_m S_\psi + l_2 S_{q_2} C_{\psi q_1} \dot{q}_2 + l_2 C_{q_2} S_{\psi q_1} (\dot{\psi} + \dot{q}_1) + l_3 S_{q_2 q_3} C_{\psi q_1} (\dot{q}_2 + \dot{q}_3) + l_3 C_{q_2 q_3} S_{\psi q_1} (\dot{\psi} + \dot{q}_1) \\ \dot{h}_y = u_l S_\psi - u_m C_\psi + l_2 S_{q_2} S_{\psi q_2} \dot{q}_2 - l_2 C_{q_2} C_{\psi q_1} (\dot{\psi} + \dot{q}_1) + l_3 S_{q_2 q_3} S_{\psi q_1} (\dot{q}_2 + \dot{q}_3) - l_3 C_{q_2 q_3} C_{\psi q_1} (\dot{\psi} + \dot{q}_1) \\ \dot{h}_z = u_n - l_1 - l_2 S_{q_2} - l_3 S_{q_2 q_3} \end{cases} \quad (2)$$

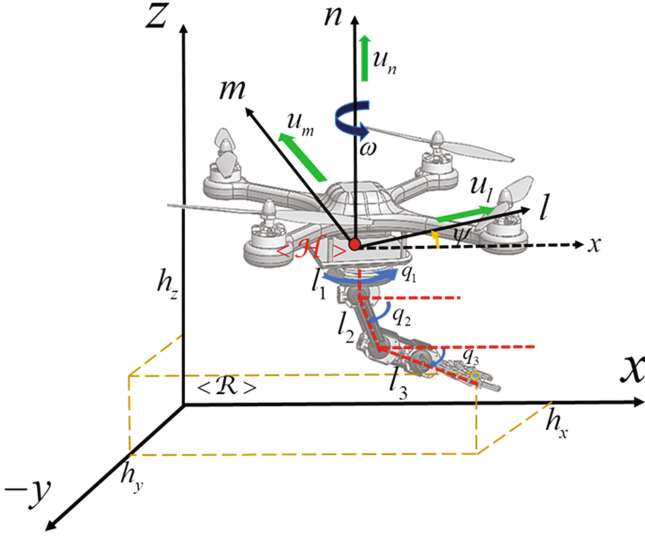


Fig. 1. Schematic of the aerial mobile manipulator.

where h_x, h_y, h_z and ψ are all measured with respect to the inertial frame $\langle \mathcal{R} \rangle$; $C_\alpha = \cos(\alpha)$; $C_{\alpha\beta} = \cos(\alpha + \beta)$; $S_\alpha = \sin(\alpha)$ and $S_{\alpha\beta} = \sin(\alpha + \beta)$. The point of interest (whose position is being controlled) is the end/effector of the aerial mobile manipulator. Also the equation system (2) can be written in compact form as $\dot{\mathbf{h}} = f(\mathbf{h}, \mathbf{q})\mathbf{u}$, i.e.,

$$\dot{\mathbf{h}}(t) = \mathbf{J}(\mathbf{q}, \psi)\mathbf{v}(t) \tag{3}$$

where, $\mathbf{J}(\mathbf{q}, \psi) \in \mathbb{R}^{m \times n}$ with $m = 3$ and $n = 7$ represents the Jacobian matrix that defines a linear mapping between the velocity vector of the aerial mobile manipulator $\mathbf{v} \in \mathbb{R}^n$ where $\mathbf{v} = [u_l \ u_m \ u_n \ \psi \ \dot{q}_1 \ \dot{q}_2 \ \dot{q}_3]^T$ and the velocity vector of the operative end $\dot{\mathbf{h}} \in \mathbb{R}^m$ where $\dot{\mathbf{h}} = [\dot{h}_x \ \dot{h}_y \ \dot{h}_z]^T$.

3 Controller Design and Stability Analysis

As represented in Fig. 2, the trajectory is given time-varying trajectory $\mathbf{h}_d(t)$ and its successive derivatives $\dot{\mathbf{h}}_d(t)$ which respectively describe the desired velocity of the robot. That's, the desired trajectory for the end-effector of the aerial mobile manipulator is defined by a vector $\mathbf{h}_d(t) = [h_{xd} \ h_{yd} \ h_{zd}]^T$ in $\langle \mathcal{R}(\mathcal{X}, \mathcal{Y}, \mathcal{Z}) \rangle$. The desired trajectory doesn't depend on the instantaneous position of the end-effector of the aerial mobile manipulator, but it's defined only by the time varying trajectory profile alone.

The controller proposed to solve the trajectory tracking problem of the aerial mobile manipulator, the proposed kinematic controller is based on the kinematic model of the aerial mobile manipulator (3). Hence following control law is proposed,

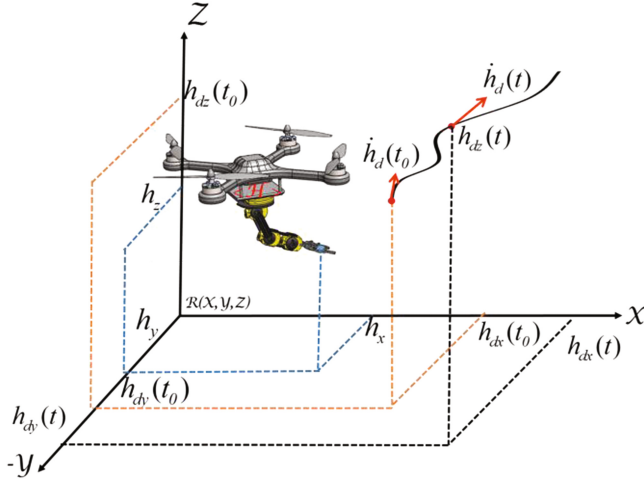


Fig. 2. Problem of control of the trajectory tracking.

$$\mathbf{v} = \mathbf{J}^\# (\dot{\mathbf{h}}_d + \mathbf{L}_K \tanh(\mathbf{L}_K^{-1} \mathbf{K} \tilde{\mathbf{h}})) \quad (4)$$

where $\dot{\mathbf{h}}_d$ is the velocity of the aerial mobile manipulator for the controller; $\mathbf{J}^\#$ is the matrix of pseudoinverse kinematics for the aerial mobile manipulator where $\mathbf{J}^\# = \mathbf{W}^{-1} \mathbf{J}^T (\mathbf{J} \mathbf{W}^{-1} \mathbf{J}^T)^{-1}$ with \mathbf{W} being a definite positive matrix that weighs the control actions of the system; while that $l_x > 0$, $k_x > 0$, $l_y > 0$, $k_y > 0$, $l_z > 0$ and $k_z > 0$ are gain constants of the controller that weigh the control error respect to the inertial frame $\langle \mathcal{R} \rangle$; and the $\tanh(\cdot)$ represents the function saturation of maneuverability velocities in the aerial mobile manipulator.

The other hand, the behaviour of the control error of the end-effector $\mathbf{h}(t)$ is now analyzed assuming perfect velocity tracking. By substituting (4) in (3) it is obtained the close loop equation,

$$\dot{\mathbf{h}}_d + \mathbf{L} \tanh(\tilde{\mathbf{h}}) = \mathbf{0} \quad (5)$$

For the stability analysis the following Lyapunov candidate function is considered

$$V(\tilde{\mathbf{h}}) = \frac{1}{2} \tilde{\mathbf{h}}^T \tilde{\mathbf{h}}. \quad (6)$$

Its time derivative on the trajectories of the system is, $\dot{V}(\tilde{\mathbf{h}}) = -\tilde{\mathbf{h}}^T \mathbf{L}_K \tanh(\mathbf{L}_K^{-1} \mathbf{K} \tilde{\mathbf{h}})$. A sufficient condition for $\dot{V}(\tilde{\mathbf{h}}) < 0$ to be negative definite is,

$$\tilde{\mathbf{h}}^T \mathbf{L}_K \tanh(\mathbf{L}_K^{-1} \mathbf{K} \tilde{\mathbf{h}}) > 0 \tag{7}$$

Hence, according to (4) and recalling that \mathbf{K} is diagonal positive definite, the control error vector $\lim_{t \rightarrow 0} \tilde{\mathbf{h}}(t) = 0$ asymptotically.

4 Results and Discussions

This section presents the simulation results of the waypoint tracking flight task in the 3D space using the kinematic nonlinear controller designed in the previous section. The goal of the simulations is to test the stability and performance of the proposed controller. Figure 3 represents the block diagram of the simulation system. The quadcopter model considers not-ideal dynamics, such as flapping, drag, and actuator dynamics, and it describes accurately the system’s dynamics both for hovering and for low speed translational flights.

In order to assess and discuss the performance of the proposed controller, it was developed a simulation platform for aerial mobile manipulators with Matlab interface, see the Fig. 4. This is an online simulator, which allows users to view three-dimensional environment navigation of the robot.

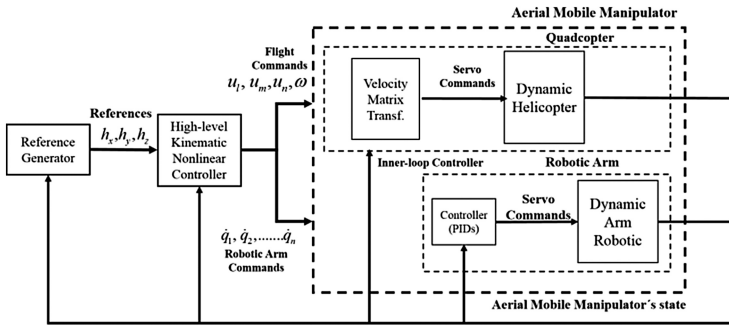


Fig. 3. Block diagram of the simulation system.

For the simulation presented below the trajectory tracking to be followed is a saddle described by, $h_{xd} = 0.07t$; $h_{yd} = 0.2 + 0.7 \sin(0.2t)$ and $h_{zd} = 3 + 0.2 \sin(0.4t)$. The desired velocity of the end-effector of the aerial mobile manipulator will depend of the desired trajectory. Figure 5 shows the stroboscopic movement on the $\mathcal{X} - \mathcal{Y} - \mathcal{Z}$ respect to the inertial frame $\langle \mathcal{R} \rangle$. It can be seen that the proposed controller works correctly. The position error $\tilde{h}_x, \tilde{h}_y, \tilde{h}_z$ of the aerial mobile manipulator is illustrated in Fig. 6, where it can be seen the error $\tilde{\mathbf{h}}(t) \rightarrow \mathbf{0}$ asymptotically (Figs. 7 and 8).

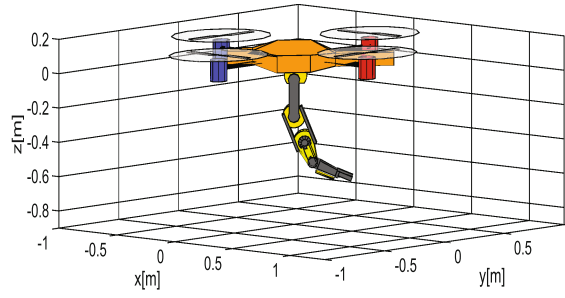


Fig. 4. Aerial mobile manipulator robot used by simulation platform developed

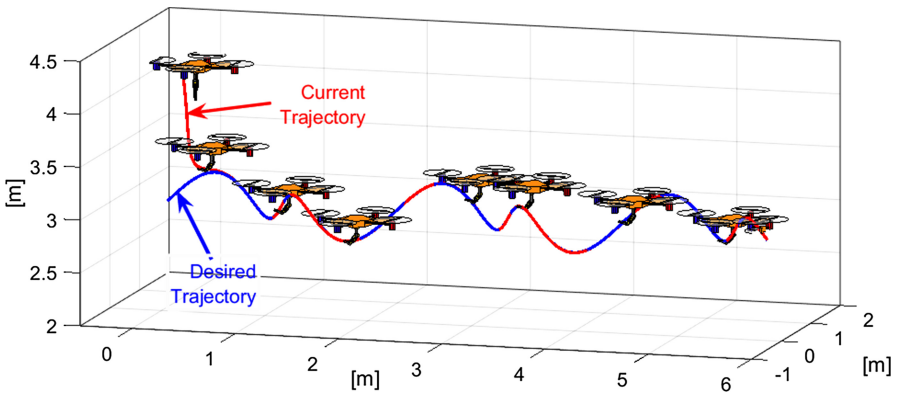


Fig. 5. Stroboscopic movement of the aerial mobile manipulator in the trajectory tracking problem.

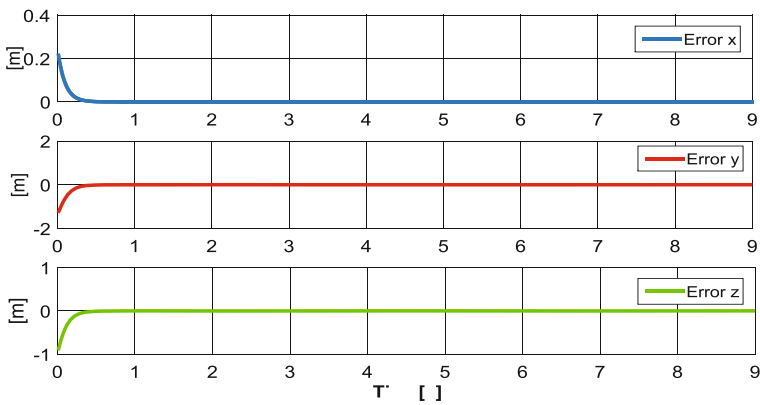


Fig. 6. Control errors of the end-effector of the aerial mobile manipulator.

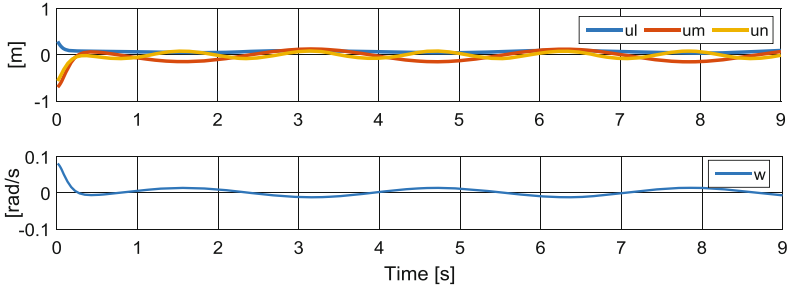


Fig. 7. Commands of Drone reference velocities by controller.

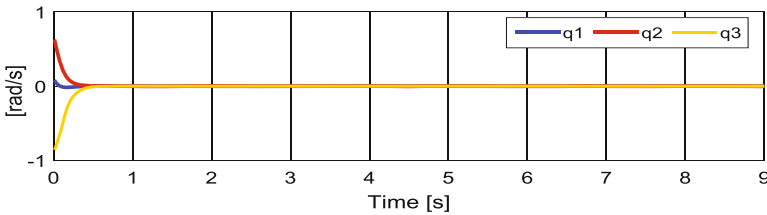


Fig. 8. Commands of Arm reference velocities by controller.

5 Conclusions

A kinematic controller -responsible to accomplish the task of trajectory tracking- is here proposed to solve the 3D trajectory tracking problem for a miniature aerial mobile manipulator. The main advantage of the control laws here proposed lies in their simplicity and easiness of implementation, when compared to other yet available in the literature. In addition, the system stability has been analytically proven. The simulation’s results have proven the controller’s ability to globally and asymptotically drive the controlled state variables to zero and simultaneously prevent any saturation in the flight commands. As future work, the implementation of such control system onboard a real aerial mobile manipulator will be tested, whose results are expected to confirm the effectiveness of the proposed control system.

References

1. Marquez, F., Maza, I., Ollero, A.: Comparacion de planificadores de caminos basados en muestro para un robot aereo equipado con brazo manipulador. Comité Español de Automática de la CEA-IFAC (2015)
2. Cano, R., Pérez, C., Pruaño, F., Ollero, A., Heredia, G.: Diseño Mecánico de un Manipulador Aéreo Ligero de 6 GDL para la Construcción de Estructuras de Barras. ARCAS (ICT-2011– 287617) del séptimo Programa Marco de la Comisión Europea y el proyecto CLEAR (DPI2011-28937-C02-01) (2013)

3. Kim, S., Choi, S., Kim, H.J.: Aerial manipulation using a quadrotor with a two dof robotic arm. In: IEEE/RSJ International Conference on Intelligent Robots and Systems, Tokyo, Japan, pp. 4990–4995 (2013)
4. Alisher, K., Alexander, K., Alexandr, B.: Control of the mobile robots with ROS in robotics courses. In: 25th DAAAM International Symposium on Intelligent Manufacturing and Automation (2014)
5. Andaluz, G., Andaluz, V., Terán, H., Arteaga, O., Chicaiza, F., Varela, J.: Modeling dynamic of the human-wheelchair system applied to NMPC. In: Intelligent Robotics and Applications, pp. 179–190 (2016)
6. Díaz, C., Roa-Guerrero, E.: Development of mobile robotics platform for identification of land mines antipersonal in different areas of Colombia. IEEE (2015)
7. Yannick Morel, Y., Porez, M., Ijspeert, A.: Estimation of relative position and coordination of mobile underwater robotic platforms through electric sensing. IEEE (2012)
8. Guilherme, V., Raffo, G., Ortega, M., Rubio, F.: Backstepping/nonlinear H^∞ control for path tracking of a quadrotor unmanned aerial vehicle. IEEE (2008)
9. Brandao, A., Andaluz, V., Sarcinelli-Filho, M., Carelli, R.: 3-D path-following with a miniature helicopter using a high-level nonlinear underactuated controller. IEEE (2011)
10. Andaluz, V., Carreli, R., Salinas, L., Roberti, F., Toibero, J.: Visual control with adaptive dynamical compensation for 3D target tracking by mobile manipulators. *Mechatronics* **22**(4), 491–502 (2012)
11. Boudjit, K., Larbes, C.: Detection and target tracking with a quadrotor using fuzzy logic. IEEE (2016)
12. From, P.J., Gravidahl, J.T., Pettersen, K.Y.: *Vehicle-Manipulator Systems*. Springer, London (2014)

Path Planning Based on Visual Feedback Between Terrestrial and Aerial Robots Cooperation

Jessica S. Ortiz^(✉), Cristhian F. Zapata, Alex D. Vega,
and Víctor H. Andaluz

Universidad de Las Fuerzas Armadas ESPE, Sangolquí, Ecuador
{jsortiz4, cfzapata2, advegal, vhandaluz1}@espe.edu.ec

Abstract. This paper presents an algorithm for path planning in which the evasion of fixed and mobile obstacles is considered in order to be followed by an unmanned land vehicle; path planning is based on visual feedback through an unmanned aerial vehicle. In addition, a path planning algorithm is proposed for the ground vehicle in which a non-constant velocity is considered that is a function of the control error, of the curvature of the road to be followed. The stability of the control algorithm is tested through the Lyapunov method. Finally the experimental results are presented and discussed in which the proposal is validated.

Keywords: Path planning · Robots cooperation · UGV · UAV

1 Introduction

Path Planning determines the path that an autonomous mobile robot must follow for moving from one place to another. For Therefore it is necessary to create a map of the environment where the fixed and moving obstacles coordinates are defined to be evaded by the robot [1–5]. Path Planning has a wide range of application fields, *e.g.*, network routing, videogames, gene sequencing, and others [2, 3].

There are several ideas to execute path planning, one is proposed by mapping the environment by means of sensory devices in order to avoid collision with fixed and movable obstacles [4]. Some of the most common algorithms are: (i) *artificial potential fields* that are implemented with proximity sensors; (ii) *probabilistic maps*, which distribute a set of points (nodes) randomly in the collision-free configuration space by joining each point and thus reaching the desired goal; (iii) *RRT algorithm* which operates by constructing a T spanning tree composed of nodes and links that increase gradually and randomly from a point of origin until reaching the finish point [6]; (iv) *Fuzzy logic methods*, these are a convenient tool for handling uncertain data in automatic decision-making systems in static and dynamic environments [16]; and (v) *FNN algorithm* is built with robustness, controllability, experience in fuzzy control and Neural Network, the traditional neural provides diffuse input signals and structure weights, whose learning algorithm is always the neural network learning algorithm [17].

The techniques for constructing the Path Planning map are made through laser and vision sensors. Vision sensors focus on the use of cameras e.g. a webcam that collect data and information from the environment for navigation purposes which allows determining the path that the unmanned ground vehicles (UGV) will follow. The vision system is able to detect fixed and moving obstacles and provide position information from the environment image [7–9, 15]. Laser devices attached to mobile robots make navigation easier. One advantage of laser sensors is that they provide exact measurements (length, depth) of the environment where it works [10].

With the development of unmanned aerial vehicles, (UAV), heterogeneous systems of robots composed of an UAV and a UGV allow several applications which facilitate the activities to the human being, for which they are important in different fields as the exploration, surveillance and navigation. Each robot has specific tasks over an objective sharing information to perform the implementation of cooperation tasks [11–13].

That said, the present work proposes the cooperative control between an UAV and an UGV. The control scheme is made up of 4 layers each working as an independent module, (i) *Layer I* is made up by an offline planning that has the responsibility of setting up the initial coordinates of the robot and a task planning responsible for setting up the coordinates of the target point that the robot must reach; (ii) *Layer II* is in charge of obtaining the images of the workspace by means of a camera attached to the bottom of the UAV, this emulates the eyes of the terrestrial robot. Objects are identified owing to image processing; this is fulfilled thanks to previously defined features. Path Planning is created by a heuristic algorithm, this is generated by aleatory paths that set a path in order to reach a desired goal in the shortest time; (iii) *Layer III* is in charge of generating the control signals to the system, so that the UGV fulfills the task defined in the planning layer; and finally (iv) *Layer IV* represents the environment where all fixed and moving objects are found.

2 Robot's Cooperation

The heterogeneous cooperation that exists between the UGV and the UAV allows execute of cooperative way the translation task in big workspace. A fundamentally task has purpose to arrive an finish point from a start point without colliding with fixed and/or moving objects that are located in the workspace, in this context the UAV is in charge of obtaining the images of the environment and processing them in order to generate a path planning, which will be followed by the UGV in order to execute the planned task [13].

As represented in Fig. 1, the path to be followed is denoted as \mathcal{P} . The actual desired location $\mathbf{P}_d = [P_{xd} \ P_{yd}]^T$ is defined as the closest point on \mathcal{P} to the UGV, with a desired orientation ψ_d . In Fig. 1, ρ represents the distance between the UGV position \mathbf{h} and \mathbf{P}_d , and $\tilde{\psi}$ is the error orientation between ψ_d and ψ .

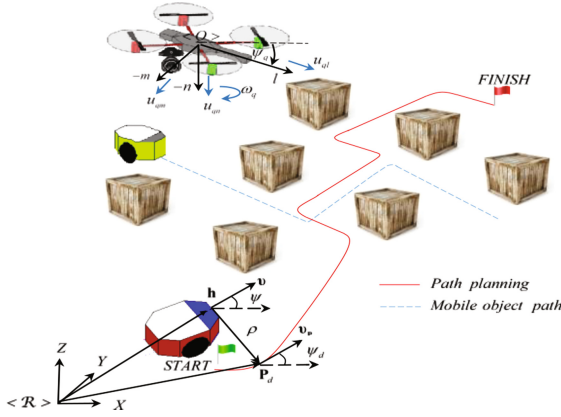


Fig. 1. Path following problem for a mobile robot

Given a path \mathcal{P} in the operational space of the UGV and the desired velocity module v for the robot, the path following problem for the UGV consists in finding a feedback control law $\mathbf{v}_{\text{ref}}(t) = (s, v, \rho, \tilde{\psi})$, such that

$$\lim_{t \rightarrow \infty} \rho(t) = 0 \text{ and } \lim_{t \rightarrow \infty} \tilde{\psi}(t) = 0 \tag{1}$$

The error vector of position and orientation between the UGV and the point \mathbf{P}_d can be represented as, $\tilde{\mathbf{h}} = \mathbf{P}_d - \mathbf{h}$ and $\tilde{\psi} = \psi_d - \psi$. Therefore, if $\lim_{t \rightarrow \infty} \tilde{\mathbf{h}}(t) = \mathbf{0}$ then $\lim_{t \rightarrow \infty} \rho(t) = 0$ and $\lim_{t \rightarrow \infty} \tilde{\psi}(t) = 0$, as it will be explained in the following sections.

Hence, the desired position and desired velocity of the UGV on the path \mathcal{P} , are defined as $\mathbf{h}_d(s, h) = \mathbf{P}_d(s, h)$ and $\mathbf{v}_{hd}(s, h) = \mathbf{v}_p(s, h)$. Where \mathbf{v}_p is the desired velocity of the UGV at location \mathbf{P}_d . Note that the component of \mathbf{v}_p has to be tangent to the trajectory due to kinematics compatibility [14].

2.1 Mobile Platform Modeling

This work is based in *Unicycle-like mobile platform*. A *Unicycle-UGV* is a driving robot that can rotate freely around its axis. The term unicycle is often used in robotics to mean a generalized cart or car moving in a two-dimensional world; these are also often called *unicycle-like* or *unicycle-type* vehicles [15].

The unicycle-like mobile platform position is defined by a point located in front of the wheels axis center; hence the *configuration instantaneous kinematic model* of the holonomic mobile platform is defined as,

$$\begin{cases} \dot{x} = u \cos \psi - a \omega \sin \psi \\ \dot{y} = u \sin \psi + a \omega \cos \psi \\ \dot{\psi} = \omega \end{cases} \quad (2)$$

where the *control (of manoeuvrability) of the UGV* is defined by $\mathbf{v}_p = [u \ \omega]^T$ in which u and w represent respectively the linear and angular velocities of the UGV. Also the equation system (2) can be written in compact form as

$$\begin{aligned} \dot{\mathbf{h}}_p &= \mathbf{J}_p(\psi) \mathbf{v}_p \\ \dot{\psi} &= \omega \end{aligned} \quad (3)$$

2.2 UAV Modeling

On the other hand, the kinematic model of the UAV is composed by a set of four velocities represented at the spatial frame $\langle Q \rangle$. The displacement of the UAV is guided by the three linear velocities u_{ql} , u_{qm} and u_{qn} defined in a rotating right-handed spatial frame $\langle Q \rangle$, and the angular velocity ω_q , as shown in Fig. 1.

Each linear velocity is directed as one of the axes of the frame $\langle Q \rangle$ attached to the center of gravity of the UAV: u_{ql} points to the frontal direction; u_{qm} points to the left-lateral direction, and u_{qn} points up. The angular velocity ω_q rotates the referential system $\langle Q \rangle$ counterclockwise, around the axis Z_q (considering the top view). In other words, the Cartesian motion of the UAV at the inertial frame $\langle \mathcal{R} \rangle$ is defined as,

$$\begin{bmatrix} \dot{x}_q \\ \dot{y}_q \\ \dot{z}_q \\ \dot{\psi}_q \end{bmatrix} = \begin{bmatrix} \cos \psi_q & -\sin \psi_q & 0 & 0 \\ \sin \psi_q & \cos \psi_q & 0 & 0 \\ 0 & 0 & 1 & 0 \\ 0 & 0 & 0 & 1 \end{bmatrix} \begin{bmatrix} u_{ql} \\ u_{qm} \\ u_{qn} \\ \omega_q \end{bmatrix}$$

$$\dot{\mathbf{h}}_q = \mathbf{J}(\psi_q) \mathbf{u}_q \quad (4)$$

where $\dot{\mathbf{h}}_q \in \mathfrak{R}^n$ with $n = 4$ represents the vector of axis velocities of the $\langle \mathcal{R}, \mathcal{X}, \mathcal{Y}, \mathcal{Z} \rangle$ system and the angular velocity around the axis \mathcal{Z} ; $\mathbf{J}(\psi_q) \in \mathfrak{R}^{n \times n}$ is a singular matrix; and the control of maneuverability of the UAV is defined $\mathbf{u}_q \in \mathfrak{R}^n$.

2.3 UGV's Controller Design

The problem of control is to find the control vector of maneuverability of the UGV ($\mathbf{v}_c(t) | t \in [t_0, t_f]$) to achieve the desired operational motion. Thus, the proposed kinematic controller is based on the kinematic model of the unicycle-like UGV (3), *i.e.*, $\dot{\mathbf{h}} = f(\mathbf{h})\mathbf{v}$. Hence the following control law is proposed,

$$\mathbf{v}_c = \mathbf{J}^{-1}(\mathbf{v}_p + \mathbf{L} \tanh(\mathbf{L}^{-1} \mathbf{K} \tilde{\mathbf{h}})) \quad (5)$$

where $\tilde{\mathbf{h}} = [\tilde{h}_x \ \tilde{h}_y]^T$ represents the position error of the robot defined as $\tilde{h}_x = P_{xd} - x$ and $\tilde{h}_y = P_{yd} - y$; $\mathbf{v}_p = [v \cos \psi_d \ v \sin \psi_d]^T$ is the desired velocity vector on the path; \mathbf{L} and \mathbf{K} are definite positive diagonal matrices that weigh the control error. In order to include an analytical saturation of velocities in the UGV, the $\tanh(\cdot)$ function, which limits the error $\tilde{\mathbf{h}}$, is proposed. The expression $\tanh(\mathbf{L}^{-1} \mathbf{K} \tilde{\mathbf{h}})$ denote a component by component operation.

Remark 1. The control algorithm presented in Subject. 2.3 is applicable for the autonomous kinematic control of the UAV. The control law structure (5) will be the same considering the kinetic model (4) presented in Sect. 2.1. *i.e.*, it must be considered that the workspace of the UAV will be in the three axes of the reference system $\langle \mathcal{R}, \mathcal{X}, \mathcal{Y}, \mathcal{Z} \rangle$. The path to be followed by the UAV is determined in Layer I according to the task to be executed.

3 Image Processing

For image processing, the acquisition of images is performed by means of a vision camera installed in the lower part of the UAV, parallel to the $\mathcal{X} - \mathcal{Y}$ plane of the reference system \mathcal{R} . The images are processed in order to identify the fixed and mobile objects that exists in the workspace, recognizing the environment and position of the elements so that the UGV can move from a start point to a finish point without colliding with the objects that are in the environment. The implemented image processing is described in Fig. 2 so much for to identify fixed and moving objects, each block performs a specific function at the time of image processing.

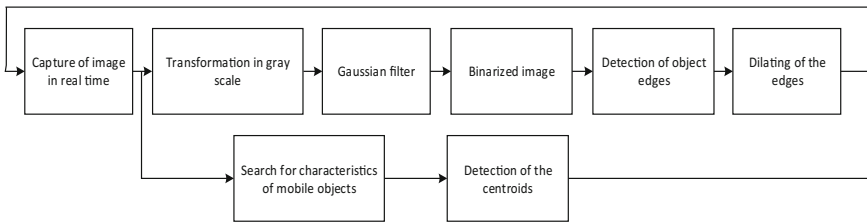


Fig. 2. Block diagram for identification and treatment of fixed and mobile objects.

According to Fig. 2 captured from the workspace image for fixed objects the grayscale transformation is performed, a Gaussian filter is used in order to eliminate noise in the image. Also, binarization of the image plane is performed in order to differentiate objects from the UGV workspace, once this is done, the edges of the objects are detected, see Fig. 3(a), then the image dilates for the purpose of that UGV don't collide with them, Fig. 3(b).

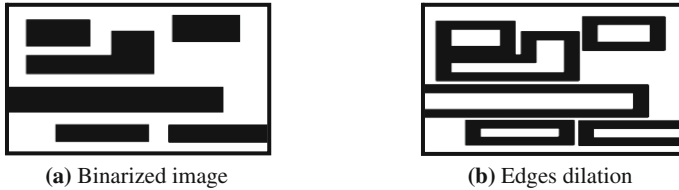


Fig. 3. Dilation process of objects

Mobile objects are defined by an established color, the same to be searched within the matrices of R, G, B of the image allowing to find objects, Finally the centroids of the objects are found in order to make a distance comparison with the path generated by the Path Planning and prevent the UGV from colliding.

4 Path Planning

Figure 4 shows the flowchart for generating the route planning to be followed by the UGV. To trace a path between the start point and the finish point, is verified there is not exist any obstacles. If not, a new aleatory path is generated from a start point to the finish point along the workspace, -procedure image-until there is exist a line of sight between the two points. The path generated must not intersect with any fixed or mobile obstacle.

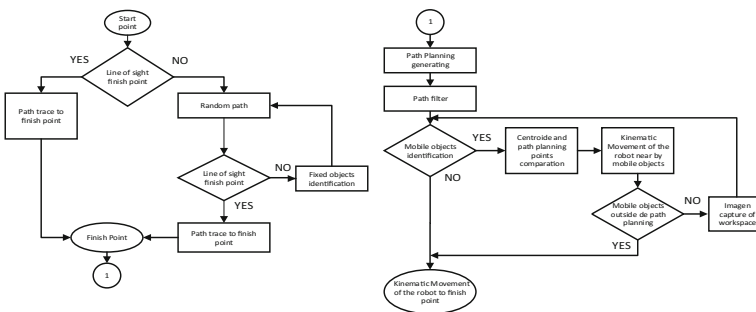
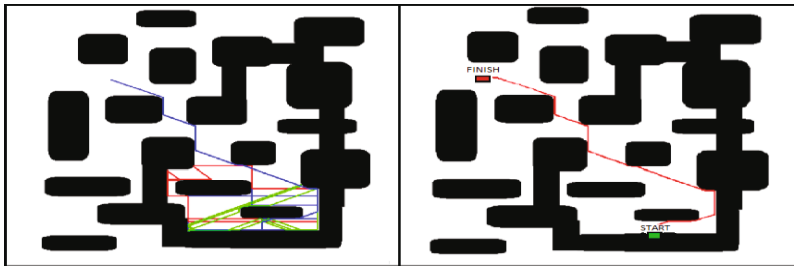


Fig. 4. Flow diagram of the path planning algorithm

The aleatory path is constructed as follows: A point is thrown in the image plane of the workspace, if this is in a pixel of value 1 that point is valid, otherwise it is discriminated against looks for a new point until it is in a valid position. With the valid point found, a line with the same direction and course is sent from the start point to the generated point. The new point takes the faculty of being the start point, and the whole process is carried out indefinitely to construct a random trajectory always with reference to the finish point.

Figure 5 shows the Path Planning constructed from a start point to a finish point. If there are moving objects in the outskirts of the route generated by the Path Planning, the UGV moves to a point close to the position of the moving object; in the following periods of sampling new images of the workspace are acquired that allow to verify that the obstacle is not over the wanted path and thus to be able to move to the UGV. If there are more mobile objects, this process is carried out indefinitely until reaching the end point.

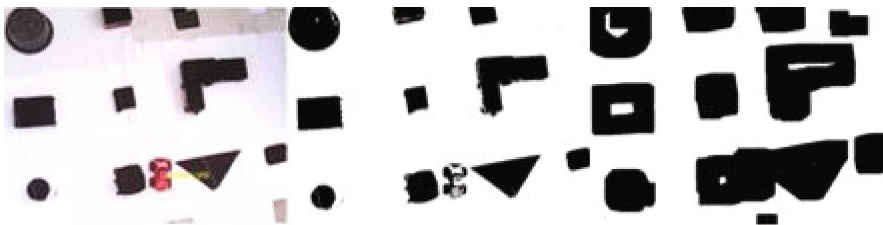


(a) Lines of various colors are aleatory paths
 (b) Red line, final path from a start point to a finish point

Fig. 5. Path planning

5 Experimental Results

This section presents the simulation results of the proposed algorithm for path planning that will be followed by the UGV without colliding with fixed and mobile obstacles. The objective of the simulation is to test the path planning, stability and performance of the proposed controllers. For the communication a TCP/IP protocol is used, the master system is the PC and the slave system is the UAV, the camera installed in the UAV will send the information of the workspace, this data will be processed by the master station in order to generate a path that will be followed by UGV from a start point to a finish point. The first image in Fig. 6(a) shows the workspace captured by the camera installed on the bottom of the UAV. In Fig. 6(b) presents the binarization of the workspace. The Fig. 6(c) shows the dilation result of the objects. In Fig. 7 it shows the Path Planning generated from a start point to a finish point. Figure 8 shows the improved Path Planning that will be followed by the UGV.



(a) Real image
 (b) Binarization
 (c) Dilation

Fig. 6. Workspace image processing



The Fig. 9(a) indicates the identification of the mobile object this is in the vicinity of the generated Path Planning, where by the UGV will be moved to a point close to the position of the object as shown in Fig. 9(b). New images are acquired to check that the moving obstacle is not over the desired path and thus to move the UGV to the finish point, see Fig. 9(c).

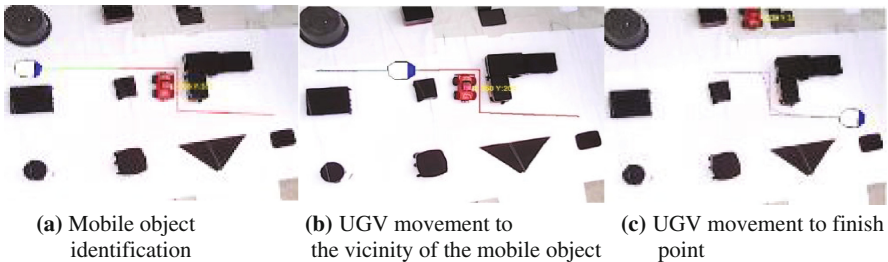


Fig. 9. Path planning process

Finally, in Fig. 10 shows the evolution of the velocity of the UGV, it is diminished in the presence of large control errors.

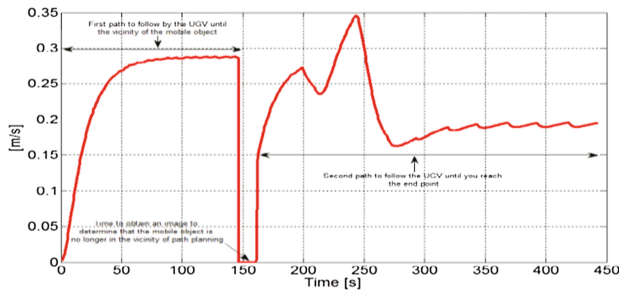


Fig. 10. UGV velocity

6 Conclusions

In this paper a multilayer scheme was presented in order to solve the problem of heterogeneous cooperation between UAV and UGV for displacement tasks in relatively large work spaces. It was proposed a path planning algorithm based on visual feedback with the objective of determining the path to be followed by the UGV avoiding the collision of fixed and mobile obstacles, finally was proposed a control algorithm for the tracking of roads in which it is considered a velocity not constant the same that can depend on the curvature of the road, error or other factors of control.

References

1. Memon, K., Memon, S., Memon, B., Memon, A., Zaigham, A.: Real time implementation of path planning algorithm with obstacle avoidance for autonomous vehicle. In: IEEE-INDIACom, pp. 2048–2053 (2016)
2. Koenig, S., Likhachev, M.: Fast replanning for navigation in unknown terrain. *IEEE Trans. Rob.* **21**, 354–363 (2005)
3. Peng, X., Lin, H., Dai, J.: Path planning and obstacle avoidance for vision guided quadrotor UAV navigation. In: 2016 12th IEEE International Conference on Control and Automation (ICCA), pp. 984–989 (2016)
4. Guo, Y., He, Y., Wen, F., Yuan, K.: Pedestrian localization in distributed vision system for mobile robot global path planning. In: 2016 IEEE International Conference on Mechatronics and Automation, pp. 1024–1029, (2016)
5. Ibrahimovic, B., Velagić, J.: Modified robust panel method for mobile robot path planning in partially unknown static and dynamic environments. In: 2016 3rd Conference on Control and Fault-Tolerant Systems (SysTol), pp 51–58 (2016)
6. Brandt, D.: Comparison of A* and RRT-connect motion planning techniques for self-reconfiguration planning. In: 2006 IEEE/RSJ, pp. 892–897 (2006)
7. Rashidan, M., Mustafah, Y., Hamid, S., Shawgi, Y., Rashid, N.: Vision aided path planning for mobile robot. In: 2014 International Conference on Computer and Communication Engineering. IEEE Conference Publications, pp. 5–8 (2016)
8. Byrne, J., Cosgrove, M., Mehra, R.: Stereo based obstacle detection for an unmanned air vehicle. In: Proceedings 2006 IEEE-ICRA, pp. 2830–2835 (2006)
9. Mezouar, Y., Chaumette, F.: Path planning for robust image-based control. *IEEE Trans. Robot. Autom.* **18**, 534–549 (2002)
10. Baltzakis, H., Argyros, A., Trahanias, P.: Fusion of laser and visual data for robot motion planning and collision avoidance. *Mach. Vis. Appl.* **15**, 92–100 (2003). Springer
11. Cai, Y., Sekiyama, K.: Subgraph matching route navigation by UAV and ground robot cooperation. In: IEEE- CEC Congress Evolutionary Computation, pp. 4881–4886 (2016)
12. Kim, J., Sukkarieh, S.: Autonomous airborne navigation in unknown terrain environments. *IEEE Trans. Aeronaut. Electron. Syst.* **40**(3), 1031–1045 (2004)
13. Duan, H., Liu, S.: Unmanned air/ground vehicles heterogeneous cooperative techniques. *Sci. China Technol. Sci.* **53**(5), 1349–1355 (2010). Springer
14. Andaluz, V., Canseco, P., Varela, V., Ortiz, J., Pérez, M., Morales, V., Robertí, F., Carelli, R.: Modeling and control of a wheelchair considering center of mass lateral displacements. In: 8th International Conference on Intelligent Robotics and Applications, ICIRA 2015, pp 254–270. Springer (2015)

15. Andaluz, V., Roberti, F., Toibero, J., Carelli, R., Wagner, B.: Adaptive dynamic path following control of an unicycle-like mobile robot. In: 4th International Conference on Intelligent Robotics and Applications, ICIRA 2011, pp 563–574. Springer, Germany (2011)
16. Sandeep, B.S., Supriya P.: Analysis of fuzzy rules for robot path planning. In: 2016 International Conference on Advances in Computing, Communications and Informatics (ICACCI), pp. 309–314. IEEE Conference Publications (2016)
17. Huan, Z., Zhiguo, S., Xiancui, W.: A rapid path planning adaptive optimization algorithm based on fuzzy neuronal network for multi-robot systems. In: International Conference on Cyberspace Technology (CCT 2013), pp. 32–38 (2013)

Biomechanics

Dynamic Analysis and Control of a Hybrid Serial/Cable Driven Robot for Lower-Limb Rehabilitation

Mourad Ismail¹(✉), Samir Lahouar², and Lotfi Romdhane^{1,3}

¹ Mechanical Laboratory of Sousse (LMS),
National Engineering School of Sousse,
University of Sousse, 4000 Sousse, Tunisia

mourad.smail@gmail.com, lotfi.romdhane@gmail.com

² Laboratoire de Génie Mécanique (LGM), National Engineering School
of Monastir, University of Monastir, 5019 Monastir, Tunisia
samirlahouar@gmail.com

³ Mechanical Engineering Department, American University of Sharjah,
PO Box 26666, Sharjah, United Arab Emirates

Abstract. In this work, we propose the use of a hybrid serial/cable driven robot for lower limb rehabilitation of disabled patients. The robot consists of an exoskeleton actuated via cables. A strategies to calculate and keep the values of the tensions in the cables positive during the motion is investigated. We show that the Null Space method yields good results and is less demanding in computational time; hence it is a good choice for real-time implementations. The human walking were simulated to show the effectiveness of the proposed method. The simulation results show that the values of the tensions in the cables can be maintained positive during the motion. The presented work shows that this hybrid parallel-serial cable robot could be used for rehabilitation of the lower limb.

Keywords: Rehabilitation robot · Hybrid serial/Cable robot · Positive tensioning · Dynamic modeling · Stiffness

1 Introduction

Robotic Rehabilitation is getting more and more popular during the last few years [1]. This increase is mainly due to its relative effectiveness, in general [2–4], and in medical applications [5], in particular. Rehabilitation is used to recover from any movement disorder and mainly as a movement therapy for stroke and spinal cord injury. According to [6, 7] strokes are the second cause of disability, 15 million people worldwide suffer a stroke every year. Almost, six million died and another five million are left permanently disabled. Rehabilitation can be the best and maybe the only way to regain movement for these patients.

Robotic rehabilitation can be seen as a robot-assisted medical rehabilitation, where the robot is not meant to replace the handicapped member, but rather assist the patient to boost his autonomy. [8].

The emergence of robotic therapy as treatment for both upper and lower extremities has revealed a numerous challenges like modeling [9] of both the exoskeleton and the limb, dynamic identification [7, 10], controller design [11, 12] and adaptive control [7], sensing and measurement [13]. Two different devices have been studied in the literature. The first one is an exoskeleton, where the extremity of the patient is actively driven by the robot. This type of devices is mainly used for patients that cannot recover their autonomy. The second device is robotic rehabilitation, where the patient is trained by the robot, in order to improve the strength of his extremity. The final objective is to have the patient recover his autonomy after a certain number of training sessions.

Actuation is also a challenging problem. Rather than using electric motors, in [14] the authors suggested the use of a pneumatically actuated prosthesis which helps to reduce the cost and provides a higher power-to-weight ratio. In this work, we consider solving the problem of lower limbs rehabilitation by the means of a hybrid serial/cable robot, which benefits from both the stiffness of serial manipulators and the higher power-to-weight ratio of cable robots, making it a good candidate for rehabilitation applications. As joints are not directly actuated, the use of cables reduces greatly the cost and the complexity of the mechanical construction. On the other hand, the unidirectional nature of the force that can be applied by cables suggests the use of a specific control scheme to keep a positive tension in the cables. The problem becomes more challenging when a given dynamic response of the exoskeleton is needed.

The used robot [15, 16] consists of an exoskeleton actuated via cables. First, we start by studying the control problem of a special case where cables are attached to the feet, then we generalize the study to all possible attachment points between the fixed frame and the mechanical passive serial support.

2 Modeling

The exoskeleton proposed in this work can be thought of as a hybrid serial/cable robot (See Fig. 1). Because a total control over the lower limbs is needed, a planar, fully constrained and fully actuated robot is used. It has three degrees of freedom, and it moves in a vertical plane. The robot includes a serial support composed of three links and three passive joints. The actuation is provided by the mean of 4 cables attached to the exoskeleton and windings around four pulleys which are actuated using four motors. The three links undergo the effects of gravity, which are the only external forces applied to the system, along with the four torques of the actuators. The geometric parameters of the system are defined in Fig. 1.

Hybrid serial/cable robot is a combination of a serial passive arm actuated via cables. A full study of the kinematics of the cable robot can be found in [15].

The upper body weight is considered to be completely compensated by the force applied by the spring since the patient legs are tightly attached to the exoskeleton which is fixed in the center O of the reference frame R_0 .

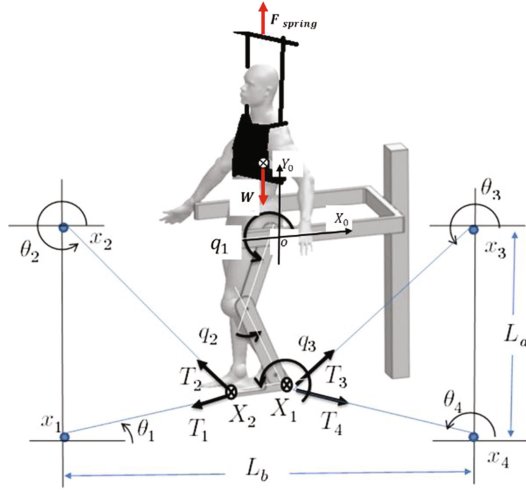


Fig. 1. Hybrid parallel/serial rehabilitation robot

One can express the dynamics of the system according the Lagrange formulation:

$$\frac{d}{dt} \left(\frac{dL}{d\dot{\mathbf{q}}} \right) - \frac{dL}{d\mathbf{q}} = \boldsymbol{\tau} - \mathbf{C}\dot{\mathbf{q}} \quad (1)$$

$$\mathbf{M}(\mathbf{q})\ddot{\mathbf{q}} + \mathbf{n}(\mathbf{q}, \dot{\mathbf{q}}) + \mathbf{p}(\mathbf{q}) = \boldsymbol{\tau} - \mathbf{C}\dot{\mathbf{q}} \quad (2)$$

$\boldsymbol{\tau} = [\tau_1 \tau_2 \tau_2]^T$, Where $\boldsymbol{\tau}$ the generalized torque applied to the robot joint. c_i is the viscos friction of the exoskeleton joints q_i .

The 3×3 matrix $\mathbf{M}(\mathbf{q})$ is the mass matrix, the 3×1 vector $\mathbf{n}(\mathbf{q}, \dot{\mathbf{q}})$ is the centrifugal and Coriolis forces vector and the 3×1 vector $\mathbf{p}(\mathbf{q})$ is the gravity force vector.

The tension exerted by cables 1 and 2 is $\mathbf{T}_{12} = [T_1 \ T_2]^T$ in the same way $\mathbf{T}_{34} = [T_3 \ T_4]^T$ is the tension of cable 3 and 4. Hence, the relationship between joint torques and cable tensions can be expressed as:

$$\mathbf{J}_2(\mathbf{q})^T \mathbf{S}(\theta_1, \theta_2) \mathbf{T}_{12} + \mathbf{J}_1(\mathbf{q})^T \mathbf{S}(\theta_3, \theta_4) \mathbf{T}_{34} = \boldsymbol{\tau} \quad (3)$$

$$\text{Where } \mathbf{S}(\theta_{ij}) = - \begin{bmatrix} \cos(\theta_i) & \cos(\theta_j) \\ \sin(\theta_i) & \sin(\theta_j) \end{bmatrix}.$$

The dynamics of the pulleys and the actuators cannot be neglected, however, and the following expression represents their dynamics, where j is moment of inertia and c the Coulomb friction:

$$\boldsymbol{\tau}_m - \mathbf{I}_m \ddot{\boldsymbol{\beta}} - \mathbf{C}_m \dot{\boldsymbol{\beta}} = \mathbf{r} \mathbf{T} \quad (4)$$

Where $\mathbf{T} = [\mathbf{T}_1 \quad \mathbf{T}_2 \quad \mathbf{T}_3 \quad \mathbf{T}_4]^T$ and τ_m is the motor torque.

Let β_i be the pulley's angular position, one can express the system dynamics as

$$\mathbf{M}(\mathbf{q})(\ddot{\mathbf{q}}) + \mathbf{n}(\mathbf{q}, \dot{\mathbf{q}}) + \mathbf{p}(\mathbf{q}) = \mathbf{J}(\mathbf{q})^T \mathbf{S}(\theta) \frac{(\tau_m - I_m \ddot{\beta} - C_m \dot{\beta})}{r} - \mathbf{C} \dot{\mathbf{q}} \quad (5)$$

For more convenience we define $\mathbf{M}^*(\mathbf{q}, \theta) = r\mathbf{S}^{-1}(\theta)\mathbf{J}(\mathbf{q})^{+T}\mathbf{M}(\mathbf{q})$ and $\mathbf{n}^*(\mathbf{q}, \dot{\mathbf{q}}, \theta, \dot{\beta}, \ddot{\beta}) = r\mathbf{S}^{-1}(\theta)\mathbf{J}(\mathbf{q})^{+T}(\mathbf{n}(\mathbf{q}, \dot{\mathbf{q}}) + \mathbf{p}(\mathbf{q}) + \mathbf{C} \dot{\mathbf{q}}) - I_m \ddot{\beta} - C_m \dot{\beta}$

We get:

$$\mathbf{M}^*(\mathbf{q}, \theta)\ddot{\mathbf{q}} + \mathbf{n}^*(\mathbf{q}, \dot{\mathbf{q}}, \theta, \dot{\beta}, \ddot{\beta}) = \tau_m \quad (6)$$

Finally we simulate the robot according to Eq. (6).

The actuator friction and inertia are taken into account according to Eq. (4). The simulation relies on the dynamics of the exoskeleton, which is defined by the mass matrix \mathbf{M}^* and the force vector \mathbf{n}^* . The solution is obtained using the ordinary differential equation numerical solver ode23t in MATLAB.

3 Task Space Control and Positive Cable Tensioning

The control strategy needs to track the positions of both \mathbf{X}_1 and \mathbf{X}_2 simultaneously in the task space [17] and also be able to keep positive and bounded tensions. To track $\mathbf{X} = \begin{bmatrix} \mathbf{X}_1 \\ \mathbf{X}_2 \end{bmatrix}$. We use the inverse dynamics to get the desired motors torque.

$$\tau_m = \mathbf{M}^*(\mathbf{q}, \theta)\mathbf{J}^+(\ddot{\mathbf{X}} - \mathbf{J}\dot{\mathbf{q}}) + \mathbf{n}^*(\mathbf{q}, \dot{\mathbf{q}}, \theta, \dot{\beta}, \ddot{\beta}) \quad (7)$$

Where $\ddot{\mathbf{q}} = \mathbf{J}^+(\ddot{\mathbf{X}} - \dot{\mathbf{J}}\dot{\mathbf{q}})$.

Through a PID controller Fig. 2, the desired torques for a given motion can be calculated as follows:

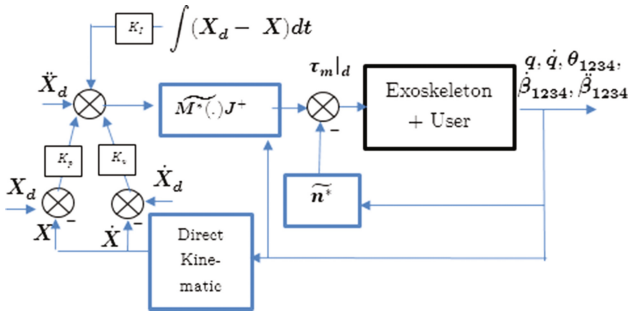


Fig. 2. Proposed controller scheme

$$\tau_{m|d} = \mathbf{M}^*(\tilde{\mathbf{q}}, \theta) \mathbf{J}^+ \left(\tilde{\mathbf{X}}_d + \mathbf{K}_v \delta \dot{\mathbf{X}} + \mathbf{K}_p \delta \mathbf{X} + \mathbf{K}_I / \delta \mathbf{X} - \dot{\mathbf{J}} \dot{\mathbf{q}} \right) + \mathbf{n}^* \left(\mathbf{q}, \tilde{\mathbf{q}}, \theta, \dot{\beta}, \ddot{\beta} \right) \quad (8)$$

Where $\mathbf{M}^*(\tilde{\mathbf{q}}, \theta)$ and $\mathbf{n}^*(\mathbf{q}, \tilde{\mathbf{q}}, \theta, \dot{\beta}, \ddot{\beta})$ are estimation of \mathbf{M}^* and \mathbf{n}^* and $\tau_{m|d} = [\tau_{m1} \ \tau_{m2} \ \tau_{m3} \ \tau_{m4}]^T$ the desired torques to control \mathbf{X}_2 by the mean of motor 1 and 2 through cable 1 and cable 2 respectively \mathbf{X}_1 by the mean of motor 3 and 4 through cable 3 and cable 4. To track \mathbf{X}_1 and \mathbf{X}_2 simultaneously, the desired torque applied to the joints is:

$$\tau_d = \mathbf{M}(\mathbf{q}) \left\{ \mathbf{J}^+ \left(\tilde{\mathbf{X}}_d + \mathbf{K}_v \delta \dot{\mathbf{X}} + \mathbf{K}_p \delta \mathbf{X} + \mathbf{K}_I / \delta \mathbf{X} - \dot{\mathbf{J}} \dot{\mathbf{q}} \right) \right\} + \mathbf{n}(\mathbf{q}, \dot{\mathbf{q}}) + \mathbf{p}(\mathbf{q}) + \mathbf{C} \dot{\mathbf{q}} \quad (9)$$

The minimum cable tension is given by:

$$\hat{\mathbf{T}} = \dot{\mathbf{S}}^+(\theta) \mathbf{J}(\mathbf{q})^+ \tau_d \quad (10)$$

To optimize the cable tension, we could add $\mathbf{N}(\mathbf{J}(\mathbf{q})^T \dot{\mathbf{S}}(\theta)) \mathbf{k}$ so that $\hat{\mathbf{T}} + \mathbf{N}(\mathbf{J}(\mathbf{q})^T \dot{\mathbf{S}}(\theta)) \mathbf{k}$ becomes positive (Fig. 3). Where \mathbf{k} is a positive vector. And finally:

$$\tau_m = \mathbf{r} \hat{\mathbf{T}} - (\mathbf{I}_m \dot{\beta} + \mathbf{C}_m \ddot{\beta}) \quad (11)$$

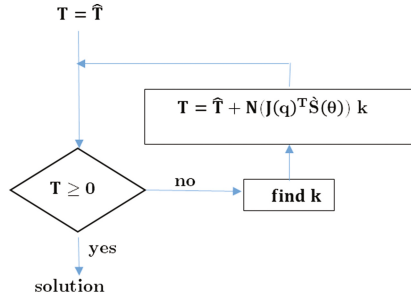


Fig. 3. Real time approach to find k

4 Simulations Results

There is an infinite number of variations to where one could attach the cables both in the exoskeleton and the fixed frame. In fact, some cable attachment point configurations will yield a better dynamic response and more importantly, will keep positive and

bounded cable tensions. To avoid going through elaborated optimization strategies, we simply selected one configuration, based on some trial and error tests. This configuration is illustrated in Fig. 4.

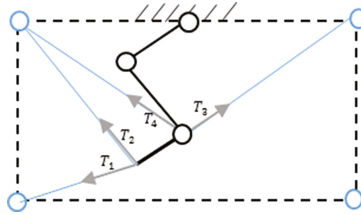


Fig. 4. Cable attachment configuration chosen for the simulations.

The two phases of a typical human walk on a treadmill are presented in Fig. 5a and b. In the first phase the path describing the heel and the toe movement is defined by a set of discrete points.

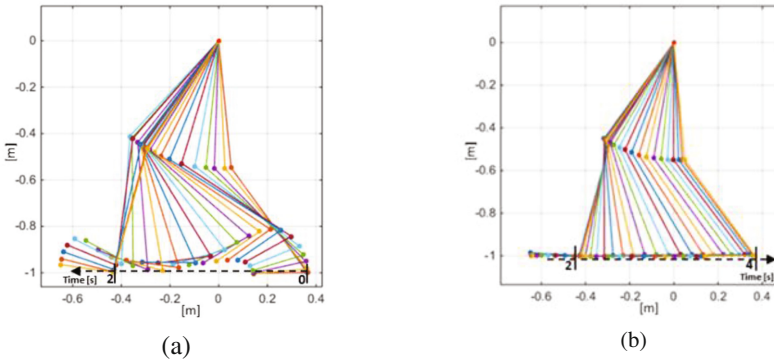


Fig. 5. human walk (a) first phase; (b) second phase.

The second phase uses two points, the initial and final pose of the heel and toe. The trajectory is a straight line and described by a quintic polynomial profile.

Figure 6 shows the tensions in the four cables and along the whole trajectory. We control the stiffness of the robot by varying the internal forces, which depend on in the value of γ a scalar describing the stiffness of the system.

As γ increases, tensions increase in average, except for cable 4 Fig. 6 which decreases in our case from 40 N to less than 5 N.

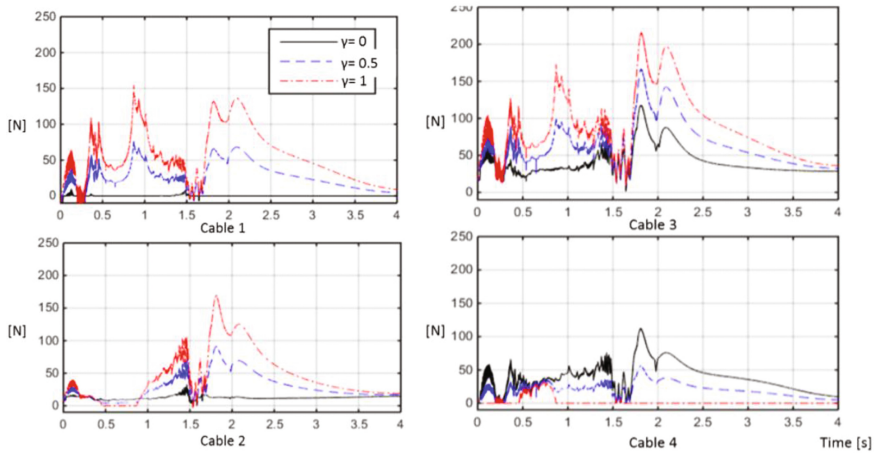


Fig. 6. Cable tensions

5 Conclusion

In this work, we demonstrated the effectiveness of using a hybrid cable-driven robot with a serial passive exoskeleton for lower limbs rehabilitation. Two control strategies, i.e., the linear programming method and the null space method, were investigated and compared. The null space method was shown to be more effective for real-time control. Two different trajectories, simulating the human walking were analyzed. The tensions in the cables were calculated and the simulations showed that it is possible to keep positive tensions in the cables, at all times. The presented work showed that this hybrid parallel-serial cable robot could be used for rehabilitation of the lower limb.

References

1. Kwee, H.H.: The spartacus telethesis: soft touch. In: Proceedings of the First International Conference on Telemanipulators for the Physically Handicapped, Rocquencourt, France (1978)
2. Foulds, R. (ed.): Interactive Robotic Aids - One Option for Independent Living: An International Perspective, vol. 37. World Rehabilitation Fund, New York (1986). Monograph
3. Egginton, R., S.J.: Proceedings of the First International Workshop on Robotic Applications in Medical and Health Care. National Research Council of Canada, Ottawa (1988)
4. Gilbert, M.: International Conference on Rehabilitation Robotics. duPont Institute, Wilmington, Delaware (1990)
5. Krebs, H.I., et al.: A paradigm shift for rehabilitation robotics. *IEEE Eng. Med. Biol. Mag.* **27**(4), 61–70 (2008)
6. Mukherjee, D., Patil, C.G.: Epidemiology and the global burden of stroke. *World Neurosurg.* **76**(6), S85–S90 (2011)

7. Mackay, J., et al.: The Atlas of Heart Disease and Stroke. World Health Organization (2004)
8. Rocon, E., Pons, J.L.: Exoskeletons in Rehabilitation Robotics. Springer, Heidelberg (2011). p. 137
9. Woo, H.S., Kwon, O.: Combined kinematic analysis of a hybrid 7-DOF rehabilitation robot. In: 2012 Proceedings of the 12th International Conference on Control, Automation and Systems (ICCAS) (2012)
10. Guo, X., Yan, Y.: Application of dynamics parameter identification of limb for rehabilitation robot. In: 2010 Proceedings of the 3rd International Conference on Biomedical Engineering and Informatics (2010)
11. Ozkul, F., Barkana, D.E.: Design of an admittance control with inner robust position control for a robot-assisted rehabilitation system RehabRoby. In: 2011 IEEE/ASME International Conference on Advanced Intelligent Mechatronics (AIM) (2011)
12. Wang, H., et al.: Realization of human-computer interaction of lower limbs rehabilitation robot based on sEMG. In: 2014 IEEE Proceedings of the 4th Annual International Conference on Cyber Technology in Automation, Control, and Intelligent Systems (CYBER) (2014)
13. Zhang, F., et al.: Research on sensing and measuring system for a hand rehabilitation robot. In: 2013 IEEE International Conference on Robotics and Biomimetics (ROBIO) (2013)
14. Zheng, H., Shen, X.: Design and control of a pneumatically actuated transtibial prosthesis. *J. Bionic Eng.* **12**(2), 217–226 (2015)
15. Ismail, M., Lahouar, S., Romdhane, L.: Collision-free and dynamically feasible trajectory of a hybrid cable–serial robot with two passive links. *Robot. Auton. Syst.* **80**, 24–33 (2016)
16. Lahouar, S., et al.: Collision free path-planning for cable-driven parallel robots. *Robot. Auton. Syst.* **57**(11), 1083–1093 (2009)
17. Hsu, P., Hauser, J., Sastry, S.: Dynamic control of redundant manipulators. In: 1988 Proceedings of the IEEE International Conference on Robotics and Automation (1988)

Kinematic Analysis of Active Ankle Using Computational Algebraic Geometry

Shivesh Kumar^{1(✉)}, Abhilash Nayak³, Bertold Bongardt¹, Andreas Mueller⁴,
and Frank Kirchner^{1,2}

¹ Robotics Innovation Center, German Research Center for Artificial Intelligence
(DFKI GmbH), 28359 Bremen, Germany

{shivesh.kumar,bertold.bongardt,frank.kirchner}@dfki.de

² Fachbereich Mathematik und Informatik, Arbeitsgruppe Robotik,
Universität Bremen, 28359 Bremen, Germany

³ IRCCyN, Ecole Centrale de Nantes, 44321 Nantes, France
Abhilash.Nayak@irccyn.ec-nantes.fr

⁴ Institute of Robotics, Johannes Kepler University Linz, 4040 Linz, Austria
a.mueller@jku.at

Abstract. ACTIVE ANKLE is a novel 3 DoF parallel mechanism which works in an almost spherical manner. Its geometry provides various advantages like good stress distribution, low link diversity and robust construction. Determining all the solutions to the direct kinematics problem is an important and challenging step in kinematic analysis of any newly invented parallel manipulator due to the coupled nature of the constraint equations. In this paper, we make use of powerful methods in computational algebraic geometry to provide a rational univariate representation of direct kinematics solution in the form of a 40° univariate polynomial. In the presented analysis, up to 16 real solutions of the direct kinematics problem for this mechanism have been obtained. In addition, the results of its torsional motion analysis are presented and singularities of the mechanism are highlighted during this motion. Also, the assembly modes where this mechanism behaves as an almost-spherical device are identified, which is the main contribution of the paper.

Keywords: Parallel manipulator · Kinematic analysis · Direct kinematics · Algebraic geometry

1 Introduction

A novel, almost-spherical parallel manipulator (ASPM) ACTIVE ANKLE (Fig. 1) and its comparison with similar mechanisms like AGILE EYE has recently been introduced in [5, 6]. Due to its unique, simple and compact $3[R2[SS]]$ design (topological equivalent of DELTA robot), the constraint of moving the end-effector about an exact center (of rotation) in case of spherical parallel manipulators (SPM) is relaxed to almost spherical motions that includes a shift of the end effector about a tolerated, very small domain. Due to the presence of a closed

loop in each leg, the mechanism offers high stiffness and orientation accuracy. The mechanism features a low link diversity and its simple, robust and modular design makes it highly suitable for many applications. While the primary application of the ACTIVE ANKLE is an active ankle joint in an exoskeleton or a humanoid, it could also be integrated as a submechanism into a regional manipulator for obtaining precise six DOF motions if the constrained translations of the ASPM are compensated by the previous joints of the overall device.

Solving the direct kinematics of any newly invented parallel manipulator is usually challenging. Since the last few decades, increasingly sophisticated computational tools are being developed for numerical algebraic geometry that can assist derivation and solution of polynomial systems which describe the mechanism geometry [1, 2]. This paper aims to provide the solution to direct kinematics problem (DKP) of the ACTIVE ANKLE mechanism using powerful tools from computational algebraic geometry. The motivation stems from the desire to identify those DKP solutions, i.e. the assembly modes, that have the lowest deviation from a perfect spherical motion. In particular, we are interested in exploring the upper bounds on the number of solutions of its DKP and identifying assembly modes where the mechanism behaves in an *almost-spherical* manner. The torsional motion of this mechanism corresponds to adduction-abduction movements when employed as an ankle joint (see [6] for foot interface unit) and hence analysis of this movement is of practical interest.

The paper is organized as follows: Sect. 2 presents the manipulator's architecture and constraint equations. Section 3 presents the solution to the direct kinematics problem by first deriving an upper bound on the total number of solutions and later exploring the number of real solutions by discretizing the configuration space. Section 4 presents the torsional motion analysis of this mechanism and highlights some of the singularities. Section 5 concludes the paper by summarizing new insights into the mechanism's geometry.



Fig. 1. ACTIVE ANKLE prototype

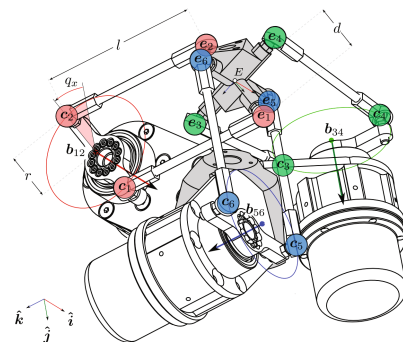


Fig. 2. ASPM architecture

2 Architecture and Constraint Equations

The mechanism ACTIVE ANKLE shown in Fig. 2 comprises of three legs each of which consist of a revolute joint and a spatial quadrilateral linkage with four spherical joints. The motors actuate the three revolute joints whose axes are aligned along the vectors $\hat{\mathbf{i}}$, $\hat{\mathbf{j}}$ and $\hat{\mathbf{k}}$. The fixed global coordinate frame G is chosen such that it is coincident with moving end effector coordinate frame E when the mechanism is in its zero configuration. The position vectors of the spherical joint centers are \mathbf{c}_i (on the crank) and \mathbf{e}_i (on the end-effector), $i = 1, 2, \dots, 6$. The vector $\mathbf{e} = (e_x, e_y, e_z)^T$ indicates the position of the moving coordinate frame E . The connecting rod length, l , crank radius, r and half-length of end effector segment d ($= \|\mathbf{e} - \mathbf{e}_i\|$) constitute the design parameters. For input joint variables q_x, q_y and q_z , the homogeneous coordinates of \mathbf{c}_i in the ground frame G and \mathbf{e}_i in the end-effector frame E are written as follows:

$$\begin{aligned}
 \mathbf{c}_1^G &= [1, 0, r \cos(q_x), l + r \sin(q_x)]^T & \mathbf{e}_1^E &= [1, 0, d, 0]^T \\
 \mathbf{c}_2^G &= [1, 0, -r \cos(q_x), l - r \sin(q_x)]^T & \mathbf{e}_2^E &= [1, 0, -d, 0]^T \\
 \mathbf{c}_3^G &= [1, l + r \sin(q_y), 0, r \cos(q_y)]^T & \mathbf{e}_3^E &= [1, 0, 0, d]^T \\
 \mathbf{c}_4^G &= [1, l - r \sin(q_y), 0, -r \cos(q_y)]^T & \mathbf{e}_4^E &= [1, 0, 0, -d]^T \\
 \mathbf{c}_5^G &= [1, r \cos(q_z), l + r \sin(q_z), 0]^T & \mathbf{e}_5^E &= [1, d, 0, 0]^T \\
 \mathbf{c}_6^G &= [1, -r \cos(q_z), l - r \sin(q_z), 0]^T & \mathbf{e}_6^E &= [1, -d, 0, 0]^T
 \end{aligned} \tag{1}$$

To express \mathbf{e}_i in the global frame, a coordinate transformation is used as follows:

$$\mathbf{e}_i^G = \mathbf{M} \mathbf{e}_i^E \tag{2}$$

where, \mathbf{M} is the transformation matrix algebraically described by unit quaternions and position coordinates. With this choice, we obtain a formulation in terms of 7 parameters which further eases the Gröbner basis computation.

$$\mathbf{M} = \begin{bmatrix} 1 & 0 & 0 & 0 \\ e_x & x_0^2 + x_1^2 - x_2^2 - x_3^2 & -2x_0x_3 + 2x_1x_2 & 2x_0x_2 + 2x_1x_3 \\ e_y & 2x_0x_3 + 2x_1x_2 & x_0^2 - x_1^2 + x_2^2 - x_3^2 & -2x_0x_1 + 2x_3x_2 \\ e_z & -2x_0x_2 + 2x_1x_3 & 2x_0x_1 + 2x_3x_2 & x_0^2 - x_1^2 - x_2^2 + x_3^2 \end{bmatrix} \tag{3}$$

where, e_x, e_y and e_z represent the position of the end effector center in the global frame. The parameters x_i ($i = 0, \dots, 3$) are the orientation quaternions satisfying:

$$g_1 := x_0^2 + x_1^2 + x_2^2 + x_3^2 - 1 = 0 \tag{4}$$

The distance between \mathbf{c}_i and \mathbf{e}_i is fixed and equal to rod length l (see Fig. 2). Thus, we can set up six constraint equations for this mechanism:

$$\|\mathbf{e}_i - \mathbf{c}_i\|^2 = l^2 \quad i = 1, \dots, 6 \tag{5}$$

The six constraint equations after simplifications along with orientation quaternion normalization equation ($g_1 = 0$) form an ideal $\mathfrak{J} = \langle g_1, g_2, g_3, g_4, g_5, g_6, g_7 \rangle$, where:

$$g_2 := (-4e_z r + 4lr) \sin q_x - 4r \cos q_x e_y - 8e_x d(x_0 x_3 - x_1 x_2) + 4e_y d(x_0^2 - x_1^2 + x_2^2 - x_3^2) + 8e_z d(x_0 x_1 + x_2 x_3) - 8dl(x_0 x_1 + x_2 x_3) = 0 \quad (6)$$

$$g_3 := (-4e_y r + 4lr) \sin(q_z) - 4r \cos(q_z) e_x - 8e_z d(x_0 x_2 - x_1 x_3) + 4e_x d(x_0^2 + x_1^2 - x_2^2 - x_3^2) + 8e_y d(x_0 x_3 + x_1 x_2) - 8dl(x_0 x_3 + x_1 x_2) = 0 \quad (7)$$

$$g_4 := (-4e_x r + 4lr) \sin(q_y) - 4r \cos(q_y) e_z - 8e_y d(x_0 x_1 - x_2 x_3) + 4e_z d(x_0^2 - x_1^2 - x_2^2 + x_3^2) + 8e_x d(x_0 x_2 + x_1 x_3) - 8dl(x_0 x_2 - x_1 x_3) = 0 \quad (8)$$

$$g_5 := (-8drx_0 x_1 - 8drx_2 x_3) \sin(q_x) + 2e_x^2 + 2e_y^2 + 2e_z^2 - 4e_z l + 2d^2 + 2r^2 + (-4drx_0^2 + 4drx_1^2 - 4drx_2^2 + 4drx_3^2) \cos(q_x) = 0 \quad (9)$$

$$g_6 := (-8drx_0 x_3 - 8drx_1 x_2) \sin(q_z) + 2e_x^2 + 2e_y^2 + 2e_z^2 - 4e_y l + 2d^2 + 2r^2 + (-4drx_0^2 - 4drx_1^2 + 4drx_2^2 + 4drx_3^2) \cos(q_z) = 0 \quad (10)$$

$$g_7 := (-8drx_0 x_2 - 8drx_1 x_3) \sin(q_y) + 2e_x^2 + 2e_y^2 + 2e_z^2 - 4e_x l + 2d^2 + 2r^2 + (-4drx_0^2 + 4drx_1^2 + 4drx_2^2 - 4drx_3^2) \cos(q_y) = 0 \quad (11)$$

3 Solving Direct Kinematics

The sine and cosine in Eqs. (6) to (11) are replaced with the tangent half-angle expressions: $\sin(q_i) = \frac{2t_i}{1+t_i^2}$, $\cos(q_i) = \frac{1-t_i^2}{1+t_i^2}$ where, $t_i = \tan(\frac{q_i}{2})$, $i = x, y, z$. To this end, t_x, t_y and t_z are the inputs and $x_0, x_1, x_2, x_3, e_x, e_y$ and e_z are the outputs to be solved for in the seven equations $g_i = 0$, $i = 1..7$. The design parameters are substituted as $l = 10$ cm, $d = r = 3.5$ cm.

3.1 Rational Univariate Representation of DKP Solution

A Gröbner basis of the ideal $\mathfrak{J} = \langle g_1, g_2, g_3, g_4, g_5, g_6, g_7 \rangle$ is calculated over the field $\mathbb{K}[x_0, x_1, x_2, x_3, e_x, e_y, e_z]$. It was possible to compute the Gröbner basis only after substituting certain values to the inputs q_x, q_y and q_z and to the design parameters. For the lexicographic ordering $x_0 <_{lex} \{e_j, x_i\}$ and $x_i <_{lex} \{e_j, x_0\}$ ($i = 1, 2, 3; j = x, y, z$), the univariate polynomial in x_0 and x_i turned out to be of degree 28 and 75, respectively which should be halved to find unique solutions due to Eq. (4). For $e_j <_{lex} x_i$ ($i = 0, 1, 2, 3; j = x, y, z$), the polynomial in e_j was of degree 40. Hence, a bound on the maximum number of solutions can be found as $\max\{28/2, 75/2, 40\}$. Thus, the ACTIVE ANKLE can have a maximum of 40 direct kinematic solutions.

3.2 Finding Real Solutions

For $t_x = t_y = t_z = \tan(\frac{30^\circ}{2})$, the **RootFinding[Isolate]** function of Maple is used to find out all the real solutions for the set of constraint equations. The algorithm behind this function finds out the rational univariate representation of the set of polynomials and isolates the real roots of these univariate polynomials based on Descartes' rule of sign and the bisection strategy in a unified framework [4].

A total of 32 direct kinematic solutions are obtained for $q_x = q_y = q_z = 30^\circ$. Due to Eq. (4), this number is to be halved to discard repeated roots. Thus, there are 16 unique assembly modes for the given input. For each assembly mode, the end effector position (e_x, e_y, e_z) and the axis-angle representation (a_x, a_y, a_z, θ) are expressed as follows: $a_x = \frac{x_1}{\sqrt{1-x_0^2}}$, $a_y = \frac{x_2}{\sqrt{1-x_0^2}}$, $a_z = \frac{x_3}{\sqrt{1-x_0^2}}$, $\theta = 2 \cos^{-1}(x_0)$. The configuration of these assembly modes is listed in Table 1.

Table 1. Overview of 16 solutions for the DKP with $q_x = q_y = q_z = 30^\circ$.

No	e_x (cm)	e_y (cm)	e_z (cm)	a_x	a_y	a_z	θ (deg)
1	1.69	1.69	1.69	-0.57	-0.57	-0.57	159.1°
2	4.93	4.93	4.93	-0.57	-0.57	-0.57	148.7°
3	0.06	0.06	0.06	-0.57	-0.57	-0.57	44.3°
4	6.6	6.6	6.6	-0.57	-0.57	-0.57	23.6°
5	0.69	2.12	2.59	-0.28	0.12	-0.94	139.4°
6	2.12	2.59	0.69	0.12	-0.94	-0.28	139.4°
7	2.6	0.69	2.12	0.94	0.28	-0.12	139.4°
8	1.82	3.47	3.78	-0.16	0.32	-0.93	157°
9	3.78	1.82	3.47	0.93	0.16	-0.32	157°
10	3.47	3.78	1.82	0.32	-0.93	-0.16	157°
11	0.63	0.89	1.43	-0.57	0.22	-0.78	107.3°
12	0.89	1.43	0.63	0.22	-0.78	-0.57	107.3°
13	1.43	0.63	0.89	0.78	0.57	-0.22	107.3°
14	5.16	5.88	5.37	0.52	0.06	-0.84	86.1°
15	5.88	5.37	5.16	-0.06	0.84	-0.52	86.1°
16	5.37	5.16	5.88	0.84	-0.52	-0.06	86.1°

Among them, No. 3 and 4 are shown in Figs. 3 and 4. The points corresponding to the position vector \mathbf{c}_i can move on the circumference of those circles drawn. The points \mathbf{e}_i form a spatial cross, the center of which represents the end effector point (shown as black sphere). No. 1 – 4 show the assembly modes where $e_x = e_y = e_z$ and $a_x = a_y = a_z$. Since, $q_x = q_y = q_z$, the other twelve assembly modes are observed in triplets with the same axis angle θ and permuted values of (e_x, e_y, e_z) and (a_x, a_y, a_z) . Four such triplets are observed in solutions 5 to 7, 8 to 10, 11 to 13 and 14 to 16 in Table 1. This pattern may not be visible when

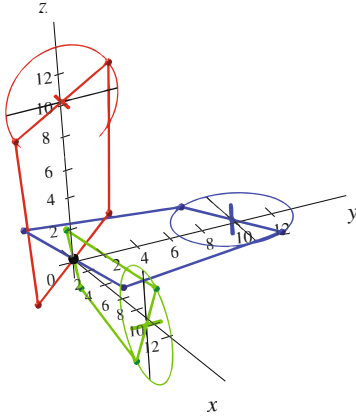


Fig. 3. Assembly Mode 3 (refer Table 1)

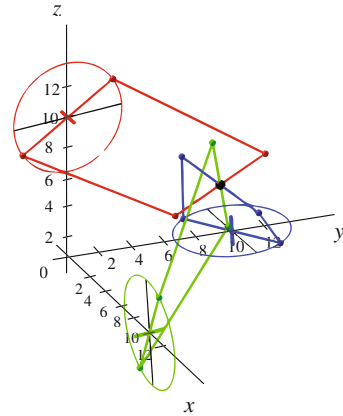


Fig. 4. Assembly Mode 4 (refer Table 1)

$t_i \neq t_j \forall i, j = x, y, z$. In addition, this method is used to record the percentage of number of real solutions to DKP by varying q_x, q_y and q_z from -180° to 180° in finite increments [3]. For convenience, the configuration space is partitioned into 1331 permutations of input angles and the results are shown in Table 2. It may be noted that the number of real solutions for any configuration can only be an even number due to an even upper bound on the total number of solutions.

Table 2. Overview of the solvability of the DKP for $q = (q_x, q_y, q_z)^T \in \mathcal{S}^3$ with discretization $\mathcal{S} = [-180^\circ, 180^\circ]$ in 11 steps ($|\mathcal{S}| = 11$ and $|\mathcal{S}^3| = 1331$).

Real solutions	0	2	4	6	8	10	12	14	16	Σ
Complex solutions	40	38	36	34	32	30	28	26	24	
Number of poses	204	282	237	222	287	83	12	0	4	1331
Fraction of poses	15.33	21.19	17.80	16.68	21.56	6.24	0.90	0	0.30	100%

4 Torsional Motion Analysis

The torsional motion of this manipulator is of practical interest because it corresponds to the adduction-abduction movement when employed as an ankle joint. The torsional motion can be characterized by substituting $e_x = e_y = e_z = e$ and $t_x = t_y = t_z = t$ in seven constraint equations. The Gröbner basis for the ideal \mathcal{J} , now defined over a reduced field $\mathbb{K}[x_0, x_1, x_2, x_3, e]$, is calculated with pure lexicographic order $e <_{lex} x_3 <_{lex} x_2 <_{lex} x_1 <_{lex} x_0$ using Maple software.

This yields a Gröbner basis consisting of five polynomials, out of which the first one is an input (t) – output (e) agnostic description of the mechanism.

$$\begin{aligned}
G_1 := & (9t^8 + 36t^6 + 54t^4 + 36t^2 + 9)e^4 + (-1347t^8 - 441t^7 - 4359t^6 - 1029t^5 \\
& - 5877t^4 - 735t^3 - 4065t^2 - 147t - 1200)e^3 + (74251t^8 + 14700t^7 \\
& + 142899t^6 + 44296t^5 + 139207t^4 + 54096t^3 + 98701t^2 + 24500t + 47350)e^2 \\
& + (-1710100t^8 + 980000t^7 + 220500t^6 + 19600t^5 + 1239700t^4 - 19600t^3 \\
& + 739900t^2 - 980000t - 490000)e + 12005000t^8 - 24010000t^7 - 12005000t^6 \\
& + 48020000t^5 - 12005000t^4 - 24010000t^3 + 12005000t^2 = 0
\end{aligned} \tag{12}$$

It shows that a maximum of four assembly modes and a maximum of eight working modes (solutions to the inverse kinematics problem) are possible on the subvariety defined by $e_x = e_y = e_z$. The implicit plot of Eq. (12) after substituting $t = \tan(q/2)$ is shown in Fig. 5 for $e = 0, \dots, 7$ cm and $q = q_x = q_y = q_z = -180^\circ, \dots, 180^\circ$. For a value of $q = q_x = q_y = q_z = 30^\circ$, four values of e observed in this figure match with the values noted in Table 1. From Fig. 5, one could also note that the assembly modes shown in Figs. 3 and 4 were actually the *almost-spherical* assembly modes for this mechanism because in these assembly modes the change in end effector's position is minimal.

The second equation of Gröbner's basis in e , t and x_0 is found out to be:

$$\begin{aligned}
G_2 := & (9t^4 + 18t^2 + 9)e^2 + (-600t^4 - 294t^3 - 906t^2 - 600)e \\
& + (9800t^4 - 9800)x_0^2 + 4900t^4 - 14700t^2 + 9800 = 0
\end{aligned} \tag{13}$$

Eliminating e from Eqs. (12) and (13) and substituting $t = \tan(q/2)$ and $x_0 = \cos(\theta/2)$ results in an implicit equation in terms of the axis angle θ (representing the rotational workspace) and the actuated variable q . Figure 6 shows the implicit plot of q vs. θ for $\theta = -180^\circ, \dots, 180^\circ$ and $q = q_x = q_y = q_z = -180^\circ, \dots, 180^\circ$.

A Jacobian matrix \mathbf{J} of dimension 5×5 is calculated by partially differentiating the constraint polynomials with respect to the variables of the considered field. When the determinant of this Jacobian vanishes, the mechanism reaches a singularity. Considering the Gröbner basis equations and $\det(\mathbf{J}) = 0$, other variables are eliminated to obtain the Eq. (14) only in terms of $t_x = t_y = t_z = t = \tan(q/2)$.

$$\begin{aligned}
\det(\mathbf{J}) := & (t - 1)(t + 1)(t^2 + 1)(2601t^{12} - 408t^{11} - 55370t^{10} + 54732t^9 \\
& + 240101t^8 - 491700t^7 + 771464t^6 - 925624t^5 + 751804t^4 \\
& - 497200t^3 + 259600t^2 - 80000t + 10000) = 0
\end{aligned} \tag{14}$$

Solving for t and hence q results in six unique solutions which are noticeable as cusps in Figs. 5 and 6. For instance, $q = 90^\circ$ is one of the singularities when e reaches a value of 6.6 cm. Since, other values of e are indeed possible for an input angle of 90° , it is important to mention the magnitude of the pair $\{e, q\}$ or $\{\theta, q\}$ while representing these singularities.

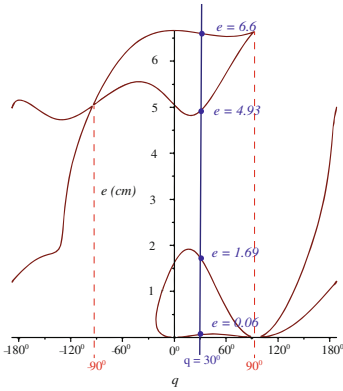


Fig. 5. Implicit plot between q and e

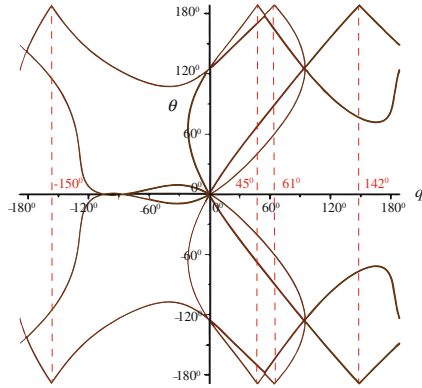


Fig. 6. Implicit plot between q and θ

5 Conclusion

This paper presents some global insights into the geometry of the ACTIVE ANKLE mechanism through its direct kinematics analysis using tools from computational algebraic geometry. It is established that the upper bound to the number of unique solutions to direct kinematics problem is 40 which supports our observation that once the actuator angles are fixed in the three legs, ACTIVE ANKLE behaves as a special instance of 6–6 STEWART platform. In practice, a maximum of 16 real solutions of the direct kinematics problem were found. In addition, the results of the torsional motion analysis which is of practical interest is presented and some singularities of the mechanism are highlighted. Moreover, the assembly modes where the mechanism behaves as an *almost-spherical* device are identified.

Acknowledgements. The work presented in this paper was performed within the project Recupera-Reha, funded by the German Aerospace Center (DLR) with federal funds from the Federal Ministry of Education and Research (BMBF) (Grant 01-IM-14006A). The fourth author acknowledges that this work has been partially supported by the Austrian COMET-K2 program of the Linz Center of Mechatronics (LCM).

References

1. Husty, M.L., Pfurner, M., Schröcker, H.P., Brunthaler, K.: Algebraic methods in mechanism analysis and synthesis. *Robotica* **25**(6), 661–675 (2007)
2. McCarthy, J.M. (ed.): 21st Century Kinematics. Springer, London (2013)
3. Merlet, J.: Direct kinematics. In: *Parallel Robots*, pp. 105–152. Springer, Dordrecht (2006)
4. Rouillier, F.: Efficient isolation of polynomial's real roots. *J. Comput. Appl. Math.* **162**(1), 33–50 (2004)

5. Simnofske, M.: Ausrichtungsvorrichtung zum Ausrichten einer Plattform in drei rotatorischen Freiheiten. Patent application, DE102013018034A1 (2015)
6. Simnofske, M., Kumar, S., Bongardt, B., Kirchner, F.: Active ankle - an almost-spherical parallel mechanism. In: 47th International Symposium on Robotics (ISR), June 21–22, Munich, Germany. VDE Verlag (2016)

Optimization of a Redundant Serial Spherical Mechanism for Robotic Minimally Invasive Surgery

Carl A. Nelson¹(✉), Med Amine Laribi², and Said Zeghloul²

¹ Department of Mechanical and Materials Engineering,
University of Nebraska-Lincoln, Lincoln, NE 68588-0526, USA
cnelson5@unl.edu

² Department of GMSC, Pprime Institute,
CNRS - University of Poitiers - ENSMA - UPR 3346, Poitiers, France
{med.amine.laribi, said.zeghloul}@univ-poitiers.fr

Abstract. Serial spherical linkages have been used in the design of a number of robots for minimally invasive surgery, in order to mechanically constrain the surgical instrument with respect to the incision. However, the typical serial spherical mechanism suffers from conflicting design objectives, resulting in an unsuitable compromise between avoiding collision with the patient and producing good kinematic and workspace characteristics. In this paper we propose a redundant serial spherical linkage to achieve this purpose and present a multi-objective optimization for achieving the aforementioned design goals. The sensitivity of the solution to uncertainties in the design parameters is investigated.

Keywords: Serial spherical mechanism · Redundant linkage · Surgical robot · Minimally invasive surgery

1 Introduction

In minimally invasive surgery, the instruments are inserted through small incisions, which thereafter serve as kinematic constraints allowing four degrees of freedom (DOF) per instrument (three rotations centered at the incision point, often referred to as the remote center of motion [3], and one translation through the incision) [18]. Various spherical mechanisms have been proposed in the surgical robotics literature for mechanically constraining the instruments to avoid motions that would cause trauma to the tissue at the incision location [1, 5, 6, 11, 14, 15]. Among these are serial spherical linkages, either actuated at each joint [2, 16] or powered by actuators on a fixed base with motion transmitted through gearing [17, 18], cables [7], or other means.

The typical serial spherical mechanism has three intersecting rotation axes fixed in two links, providing the three rotational DOF mentioned previously. The lengths of the two links must be chosen carefully in order to provide adequate workspace (usually considered as a cone whose apex half-angle is at least 30° [12]) without interference (collision) between the robot and the patient. However, these two primary design objectives are in opposition, as the larger links required to increase workspace also increase the impingement of the robot in the space occupied by the patient.

In this paper, we propose solving this problem by introducing an additional (redundant) link. We present a multi-objective optimization considering the workspace requirements, the kinematic performance, and the collision constraint.

2 Methods

The proposed robot architecture is a classic serial spherical linkage (two links and three joints with intersecting axes) with a redundant link (and joint) added, as shown in Fig. 1. Singularities (well know for this type of robot) are avoided by restricting the motion of each joint to avoid alignment of adjacent links. We similarly avoid internal collisions within the robot itself. Thus the robot remains in a single operating mode throughout its used workspace. The problem consists of finding the optimal link parameters, expressed as angles α_i , which satisfy the objectives and constraints mentioned previously.

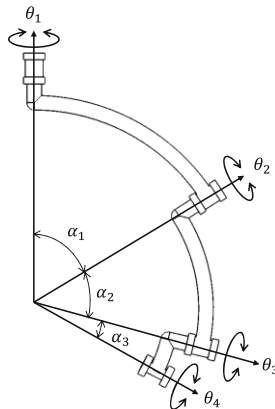


Fig. 1. Redundant serial spherical arm

The task-based synthesis and optimization of medical robots is a rich topic area in the literature [3, 4, 8]. Building from classical performance indices in robotics, specialized indices have been proposed to account for workspace requirements in this type of robot [9, 17]. However, it is less common to see optimization approaches in medical robotics which account for the avoidance of collisions between the robot and the patient.

We adopt a multi-objective optimization approach considering workspace, kinematic performance, and robot compactness as criteria. For the workspace criterion, we recognize that the actual workspace will not be exactly equal to the conical section of a spherical surface described previously, so we base the optimization on a conservative measure of such an idealized workspace inscribed within the actual workspace. The actual workspace is directly calculated by forward kinematics, discretizing the joint space within the limited range of motion previously mentioned. Collision avoidance is

directly accounted for within the optimization subroutine by throwing out any workspace points at which any part of the robot penetrates a planar boundary passing through the surgical incision and orthogonal to the neutral axis of the surgical trocar. Such cases are shown in Fig. 2. For the kinematic performance criterion, we use the improved indices proposed by Olds [10], which give worst-case measures of position error (max) and velocity (min) in the two-dimensional workspace. Compactness is measured as the sum of the link angles α_i .

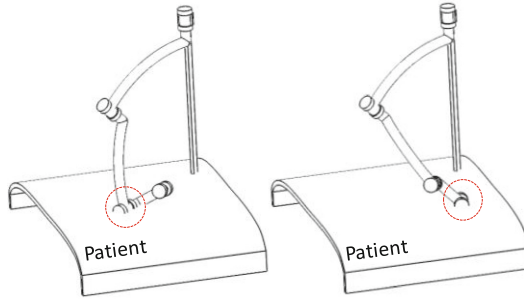


Fig. 2. Robot/patient collision cases (circle indicates area of collision)

As inputs, we use the three joint angles $(\theta_{1,2,3})$, and as outputs the pan (left-to-right) and tilt (down-to-up) angles intuitive to surgeons in the context of laparoscopic camera orientation. The joint angle θ_4 is not used as an input since it is for instrument self-rotation and does not affect tool position. Based on a neutral position with all robot links aligned and extended in the positive tilt direction,

$$p = \alpha_1 \sin \theta_1 + \alpha_2 \sin(\theta_1 + \theta_2) + \alpha_3 \sin(\theta_1 + \theta_2 + \theta_3) \quad (1)$$

$$t = \alpha_1 \cos \theta_1 + \alpha_2 \cos(\theta_1 + \theta_2) + \alpha_3 \cos(\theta_1 + \theta_2 + \theta_3) \quad (2)$$

where p is the pan angle and t is the tilt angle, and the Jacobian is

$$\mathbf{J} = \begin{bmatrix} J_{11} & J_{12} & J_{13} \\ J_{21} & J_{22} & J_{23} \end{bmatrix} \quad (3)$$

$$J_{11} = \alpha_1 \cos \theta_1 + \alpha_2 \cos(\theta_1 + \theta_2) + \alpha_3 \cos(\theta_1 + \theta_2 + \theta_3)$$

$$J_{12} = \alpha_2 \cos(\theta_1 + \theta_2) + \alpha_3 \cos(\theta_1 + \theta_2 + \theta_3)$$

$$J_{13} = \alpha_3 \cos(\theta_1 + \theta_2 + \theta_3)$$

$$J_{21} = -\alpha_1 \sin \theta_1 - \alpha_2 \sin(\theta_1 + \theta_2) - \alpha_3 \sin(\theta_1 + \theta_2 + \theta_3)$$

$$J_{22} = -\alpha_2 \sin(\theta_1 + \theta_2) - \alpha_3 \sin(\theta_1 + \theta_2 + \theta_3)$$

$$J_{23} = -\alpha_3 \sin(\theta_1 + \theta_2 + \theta_3)$$

Because the robot is redundant, the Jacobian matrix is not square. Therefore, we adapt the indices [10] to include the pseudoinverse:

$$\mu_{\min} = \frac{1}{\max \|\mathbf{J}^*_{*i}\|_2} \quad (4)$$

$$\mu_{\max} = \max \frac{\|\mathbf{J}\dot{\boldsymbol{\theta}}\|_2}{\|\dot{\boldsymbol{\theta}}\|_\infty} \quad (5)$$

with the pseudoinverse of the Jacobian expressed as

$$\mathbf{J}^* = \mathbf{J}^T (\mathbf{J}\mathbf{J}^T)^{-1} \quad (6)$$

and \mathbf{J}^*_i indicating the i^{th} row of \mathbf{J}^* . Here μ_{\min} represents the worst-case velocity, and μ_{\max} represents the worst-case position error. As suggested in [10], we allow the velocity vector to take on its various possible extreme values in the calculation of μ_{\max} :

$$\dot{\boldsymbol{\theta}} = \left\{ \begin{array}{c} 1 \\ 1 \\ 1 \end{array} \right\}, \left\{ \begin{array}{c} 1 \\ -1 \\ 1 \end{array} \right\}, \left\{ \begin{array}{c} 1 \\ 1 \\ -1 \end{array} \right\}, \left\{ \begin{array}{c} 1 \\ -1 \\ -1 \end{array} \right\} \quad (7)$$

The kinematic performance is expressed as the worst of these two metrics (μ_{\min} and μ_{\max}) at each point in the workspace and averaged across the entire feasible workspace (as sampled in the joint space).

The *fgoalattain()* function in MATLAB was used to carry out the optimization. This function is an implementation of the sequential quadratic programming (SQP) method and allows multiple objectives to be weighted within a single objective function. In contrast to the Pareto approach, in which no criterion is allowed to get worse from one iteration to the next, the *fgoalattain()* function provides better convergence by allowing the search direction to experience “tradeoffs” between the individual criteria in order to optimize the global criterion.

The redundant serial arm was optimized using allowable ranges of the link parameters $\boldsymbol{\alpha}$ and joint variables $\boldsymbol{\theta}$ as indicated in Table 1, and weights of 0 on workspace and collision avoidance, 0.3 on kinematic performance, and 0.5 on compactness (where 0 indicates a hard constraint and 1 represents an unenforced objective). These weights were chosen to enforce the need for safety and adequate workspace without completely neglecting the other desirable characteristics.

Table 1. Parameter values used in optimization

Parameter	Lower bound (°)	Upper bound (°)
$\alpha_{1,2,3}$	9	120
θ_1	-85	85
θ_2	5	175
θ_3	-175	-5

3 Results and Discussion

The serial arm parameters obtained through optimization were $S: \{\alpha_1 = 46.7^\circ, \alpha_2 = 44^\circ, \alpha_3 = 18.9^\circ\}$. The resulting robot is shown in Fig. 3. The workspace and collision avoidance criteria are fully satisfied, and the kinematic performance of the robot can be seen in Fig. 4. As allowed by the *fgoalattain()* function, neither the performance nor the compactness criteria were fully satisfied; this is to be expected, as the robot is not expected to be perfectly small nor fully isotropic throughout the workspace.

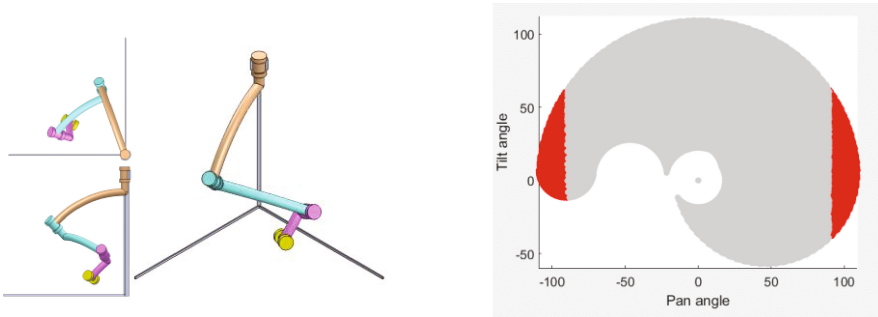


Fig. 3. The obtained redundant serial spherical mechanism: (left) computer rendering; (right) pan-tilt workspace – red area is excluded based on collision (Color figure online)

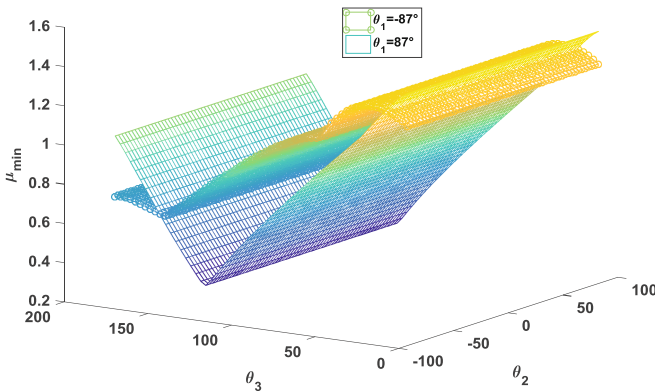


Fig. 4. Performance of optimized manipulator: the distribution of μ_{\min} in joint space for $\theta_1 = \pm 87^\circ$.

The obtained result indicates that the algorithm performs in a stable manner and provides consistent results. Next, the variability of the optimized redundant serial spherical linkage performance generated by the design parameters will be estimated. Thus, the case of optimal solution S , given at the beginning of this section, will be studied.

Each uncertain design parameter is represented by a statistical distribution. For a normal distribution this requires a mean value and a standard deviation. A Monte Carlo simulation [13] is performed for every design parameter where each evaluation consists of a specified number of runs as shown in Fig. 5.

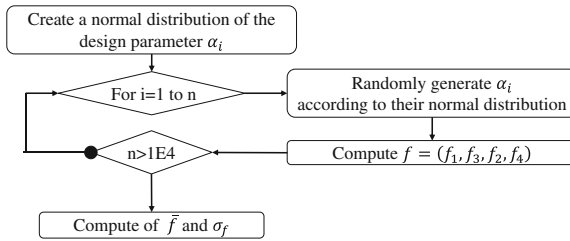


Fig. 5. Monte Carlo simulation flowchart

For each Monte Carlo simulation, all the deterministic design variables, α_i , are fixed at their nominal values and the uncertain design variables, $\tilde{\alpha}_i$, are selected randomly from their statistical distributions assumed to vary within $\pm 5\%$ of the specified nominal values. With the Monte Carlo simulation, we perform $n = 10^4$ simulations to determine the mean value $\bar{f} = \{\bar{f}_1, \bar{f}_2, \bar{f}_3, \bar{f}_4\}$ as well as the respective standard deviations $\sigma_f = \{\sigma_{f_1}, \sigma_{f_2}, \sigma_{f_3}, \sigma_{f_4}\}$. The evolution of each performance is presented in Fig. 6. The sensitivity study result of the optimal solution S is shown in Table 2.

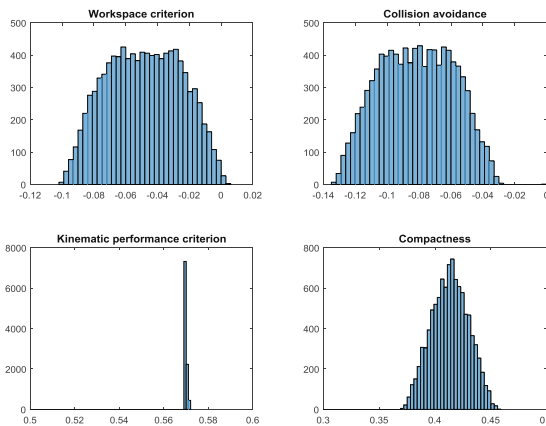


Fig. 6. Effect of the design parameters’ uncertainty on the objective functions

We observe through these data the high sensitivity of the structure on the first two criteria, respectively workspace and collision avoidance. The variation around the optimal values of the design parameters leads to a large violation of the performance criteria in relation with the workspace and collision avoidance. This first observation justifies the choice of the very strict condition on the respective weights at the definition of the optimization problem.

Table 2. Sensitivity of the optimal solution.

Objective function	Mean value \bar{f}_i	Standard deviation σ_{f_i}	Sensitivity s_i
Workspace: f_1	0.0483	0.0232	144.28%
Collision: f_2	0.0815	0.0232	85%
Kinematic performance: f_3	0.5697	0.0057	3%
Compactness: f_4	0.4133	0.0169	12%

In contrast, the last two criteria, respectively kinematic performance and compactness, are less sensitive to the disturbance of the design parameters. The calculated sensitivity is of about 15%.

Consequently, by considering the uncertainties of the design parameters the workspace and collision avoidance given by the optimal solution S are no longer guaranteed. These two performances should be defined as constraints and not as criteria. Therefore, the optimal solutions, obtained by the multi-objective optimization presented previously, are not robust due to the design parameter uncertainties. This problem merits further work.

4 Conclusions

In this work a redundant serial spherical linkage has been presented to cope with the problems of the classic serial spherical mechanism for medical robots. Four design objectives have been presented and adapted to the proposed redundant mechanism: workspace, kinematic performance, avoiding collision and compactness. A multi-objective optimization problem is formulated in this aim and solved using the *fgoalattain()* function. The obtained optimal solution perfectly satisfies the workspace criterion as well as the collision avoidance requirement. However, neither the performance nor the compactness criteria were fully satisfied and this is due to the tradeoffs allowed by the optimization method. This type of result facilitates the designer's choice of a suitable solution by generating a specific solution without going through a Pareto front. A sensitivity study is performed based on the Monte Carlo method which shows that the deterministic optimal solutions can be strongly affected by the uncertainties in the design parameters. A robust multi-objective optimization will be addressed in future work to cope with this sensitivity problem.

Acknowledgments. This work is sponsored by the French government research program Investissements d'avenir through the Robotex Equipment of Excellence (ANR-10-EQPX-44) and by a faculty development fellowship from the University of Nebraska-Lincoln.

References

1. Berkelman, P., Boidard, E., Cinquin, E., Troccaz, J.: LER: the light endoscope robot. In: Proceedings IEEE/RSJ International Conference on Intelligent Robots and Systems (IROS), pp. 2835–2840, Las Vegas, NV, USA (2003)
2. Courreges, F., Smith-Guerin, N., Poisson, G., Vieyres, P., Gourdon, A., Szpieg, M., Merigeaux, O.: Real-time exhibition of a simulated space tele-echography using an ultra-light robot. In: Proceedings ISAIRAS, Canada (2001)
3. Eldridge, B., Gruben, K., LaRose, D., Funda, J., Gomory, S., Karidis, J., McVicker, G., Taylor, R., Anderson, J.: A remote center of motion robotic arm for computer assisted surgery. *Robotica* **14**(1), 103–109 (1996)
4. Essomba, T., Nouaille, L., Laribi, M.A., Nelson, C.A., Zeghloul, S., Poisson, G.: Spherical wrist dimensional synthesis adapted for tool-guidance medical robots. *Mech. Ind.* **15**(3), 217–223 (2014)
5. Kang, H., Wen, J.T.: EndoBot: a robotic assistant in minimally invasive surgeries. In: Proceedings of the IEEE International Conference on Robotics and Automation, Seoul, South Korea, pp. 2031–2036 (2001)
6. Laribi, M.A., Rivière, T., Arsicault, M., Zeghloul, S.: A design of slave surgical robot based on motion capture. In: Proceedings 2012 IEEE International Conference on Robotics and Biomimetics (ROBIO2012), 11–14 December, Guangzhou, China, pp. 600–605 (2012)
7. Nelson, C.A., Zhang, X.: Equivalent mechanisms techniques for redesign of a spherical surgical tool manipulator. In: ASME IDETC 2010, Montréal, Québec, Canada, 15–18 August, ASME Paper No. DETC2010-28367 (2010)
8. Nouaille, L., Laribi, M.A., Nelson, C.A., Essomba, T., Poisson, G., Zeghloul, S.: Design process for robotic medical tool-guidance manipulators. *Proc. IMechE Part C: J Mech. Eng. Sci.* **230**(2), 259–275 (2016)
9. Nouaille, L., Poisson, G., Zhang, X., Nelson, C.A.: Method of dimensional optimization of spherical robots for medical applications using specialized indices. *Adv. Robot.* **28**(3), 173–186 (2014)
10. Olds, K.: Global indices for kinematic and force transmission performance in parallel robots. *IEEE Trans. Robot.* **31**(2), 494–500 (2015)
11. Rininsland, H.: ARTEMIS. A telemanipulator for cardiac surgery. *Eur. J. Cardio-thorac. Surg.* **16**(2), 106–111 (1999)
12. Rosen, J., Brown, J.D., Chang, L., Barreca, M., Sinanan, M., Hannaford, B.: The BlueDRAGON – a system for measuring the kinematics and the dynamics of minimally invasive surgical tools in-vivo. In: Proceedings IEEE International Conference on Robotics and Automation, Washington, DC, pp. 1876–1881 (2002)
13. Schinozuka, M.: Monte Carlo solution of structural dynamics. *Comput. Struct.* **2**, 855–874 (1972)
14. Tanev, T.K., Cammarata, A., Marano, D., Sinatra, R.: Elastostatic model of a new hybrid minimally invasive surgery robot. In: Proceedings 14th IFToMM World Congress, Taipei, Taiwan, 25–30 October 2015
15. Vaida, C., Gherman, B., Pisla, D., Plitea, N.: A spherical robot arm for instruments positioning in minimally invasive medical applications. In: Proceedings 2nd IFToMM Asian Conference on Mechanism and Machine Science, Tokyo, Japan, 7–10 November (2012)

16. Zemiti, N., Ortmaier, T., Vitrani, M.A., Morel, G.: A force controlled laparoscopic surgical robot without distal force sensing. In: Proceedings 9th International Symposium on Experimental Robotics, ISER 2004, Singapore (2004)
17. Zhang, X., Nelson, C.A.: Multiple-criteria kinematic optimization for the design of spherical serial mechanisms using genetic algorithms. *J. Mech. Des.* **133**(1), 011005 (2011)
18. Zhang, X., Nelson, C.A.: Kinematic analysis and optimization of a novel robot for surgical tool manipulation. *J. Med. Devices* **2**(2), 021003 (2008)

Kinematic Analysis for a Prostate Biopsy Parallel Robot Using Study Parameters

Iosif Birlescu¹, Paul Tucan¹, Bogdan Gherman¹, Calin Vaida¹,
Nicolae Crisan², Corina Radu², Nicolae Plitea¹, and Doina Pisla¹(✉)

¹ CESTER, Technical University of Cluj-Napoca,
Memorandumului 28, Cluj-Napoca 400114, Romania
doina.pisla@mep.utcluj.ro

² Iuliu Hatieganu University of Medicine and Pharmacy,
Cluj-Napoca, Romania
nicolae.crisan@umfcluj.ro

Abstract. The paper presents the forward kinematics computation for a parallel robotic system designed for prostate biopsy using Study parameters. The manipulator is analyzed on its smaller kinematic chains to facilitate the computation, in a way that no information is lost from the robotic system functionality. Kinematic solutions examples are presented based on numerical values given for the robot geometric parameters and active joint position.

Keywords: Parallel robot · Study parameters · Forward kinematics

1 Introduction

Computations regarding the kinematics and singularities of robotic structures are of great interest since they provide valuable information about the manipulator functionality. This information has the capability to reduce the risk factor of using a robotic structure in various procedures, which is especially important in medical applications where the patient and medical staff safety is a priority [1]. Image guided prostate biopsy is one procedure where the benefit of using a robotic system outweighs the risk [1, 2]. One particular way to access the prostate tissue is transperineally, guided by a transectal ultrasound (TRUS) probe inserted into the patients' rectum, where the advantages are that the entire prostate volume can be sampled, and lesser infection risk [3–5].

The focus of this paper is the computation of the forward kinematics of the BIO – PROS 3 robotic system, using Study parameters. BIO – PROS 3 robotic system kinematics and singularities were studied in previous work, using a classical method where the kinematics are derived from the robot geometric model, and the singularities are studied from the vanishing points of the determinants of the Jacobi matrices A and B [4]. It has been pointed out in [6] that the singularity analysis using the Study parameters method may provide more singular configurations than the analysis of the Jacobi matrices. Study parameters method for solving the forward kinematics, parameterize the Euclidean displacement using quaternions, and computes a set of 8 parameters as shown in [7–9]. Computations based on the method were done to

describe mechanisms such as: the Stewart-Gough platform [7], 3-RPS manipulator [8], and a medical robot (PARA-BRACHYROB) for brachytherapy [6].

The complexity of the BIO-PROS 3 robot did not allow the kinematic computation of the whole mechanism using the Study parameters. As an alternative, a geometric parameter was introduced, in a way that the kinematic results were not affected, but Maple managed the computation.

The following sections of this paper are structure as follows. Section 2 presents the BIO – PROS 3 robotic system, and the forward kinematics computation using Study parameters, and illustrates examples based on numerical values (for active joints and structural parameters). Section 3 presents the conclusions and proposed further research.

2 BIO-PROS 3 Parallel Robot

BIO-PROS 3 is a robotic system (Fig. 1) from the parallel robots family [10] designed for transperineal prostate biopsy, which contains two independent modules, one for biopsy gun guidance (Fig. 2a), and one for transrectal ultrasound (TRUS) probe guidance (Fig. 2b) [4]. For transperineal prostate biopsy the insertion of both TRUS probe and biopsy needle follow a linear path ($\pm 10^\circ$ needle angulation is preferred relative to TRUS probe insertion axis [2]). The positioning and insertion of the TRUS probe is achieved by the module active joints, while for the biopsy gun, the position is obtained by the module active joints and the needle insertion is realized with a redundant DOF from an insertion instrument (such as [5]) to increase precision.

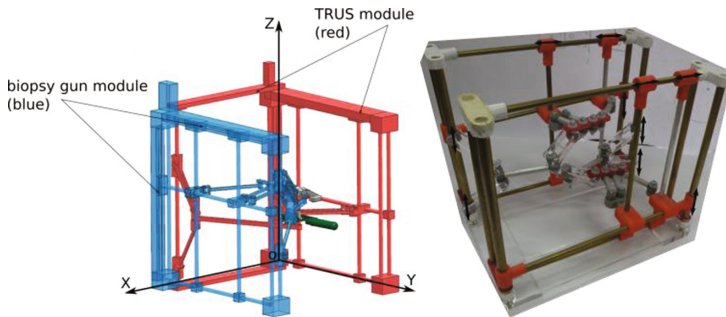


Fig. 1. BIO-PROS 1 parallel robot CAD representation [4] on left; 3D printed model on right.

2.1 Robotic System Description

Each module has 5 active joints, q_i for the TRUS probe guiding module, and q'_i for the biopsy gun guiding module, which leads in turn to 5 DOF manipulators. By defining a fixed coordinate frame OXYZ placed in the robotic systems base (see Fig. 2), a moving frame O'X'Y'Z' is introduced (placed on the manipulators end effector). The two modules are similar in functionality and architecture, the difference being that the

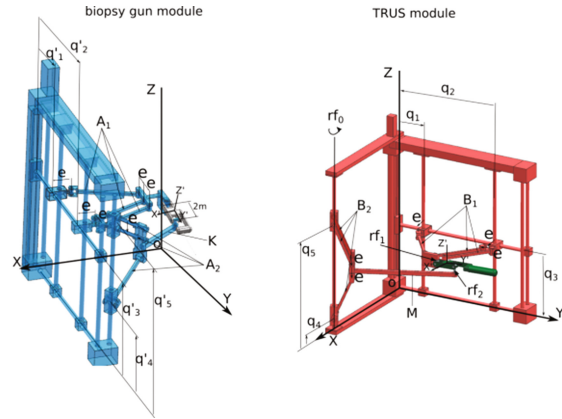


Fig. 2. BIO-PROS 3; biopsy gun module on left; TRUS module on right.

kinematic chain actuated by q_{4-5} (of the TRUS guidance module) lies on a plane orthogonal to the plane in which q_{1-3} are constrained, in opposition to the biopsy gun guiding module, where the kinematic chain actuated by q'_{4-5} lies in the same plane with the active joints q'_{1-3} . For the TRUS guidance module, the end effector represents (mechanically speaking) a link between two cardan joints (rf_1 and rf_2 on Fig. 2), and its motion is obtained from the motion of a platform with constant orientation linked with rf_1 , working in Cartesian coordinates (actuated by q_{1-3}), combined with the motion of a kinematic chain (linked in rf_2 and actuated by q_{4-5}) that works in cylindrical coordinates and has a free rotation rf_0 around an axis defined by the translation axis of both active joints q_{4-5} (see Fig. 3).

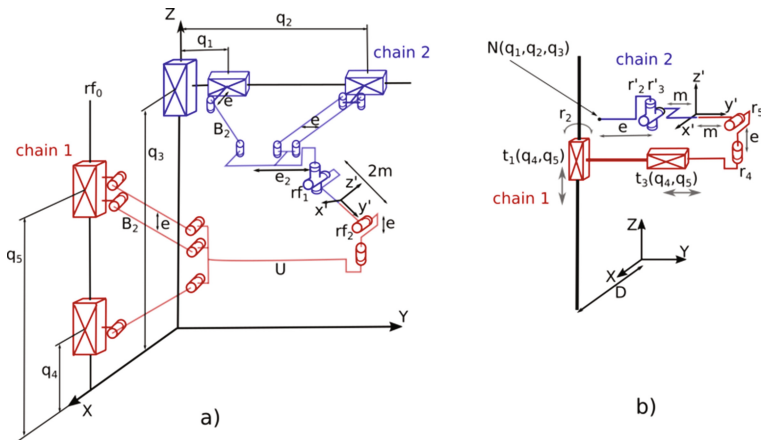


Fig. 3. Kinematic representation of BIO-PROS 3.

2.2 Forward Kinematics

Study parameters are used to compute the forward kinematics of the robotic system, since the Study method is free of parameterization singularities [6]. Two distinct kinematic chains are defined (chain 1 and chain 2) that intersect in the mobile coordinate frame $O'X'Y'Z'$ (for each module) as shown in Fig. 3. The kinematic chain 1 has at its basis a type R-2PRR mechanism with 3 DOF (one being a free rotation), and the kinematic chain 2 is type P-2PRR with 3 translational DOF.

A computation of the kinematics regarding the whole mechanism (as sketched in Fig. 3a) was not possible in Maple using an Intel i7 3.6 GHz with 16 GB of RAM computer configuration. For this reason, the computation was performed on separated kinematic chains as described further in this section. Figure 3b illustrates the simplest way to sketch the kinematics of the manipulator by taking into account how each joint influences the mobile coordinate frame position and orientation. Since a point $N(x, y, z) = f(q_1, q_2, q_3)$ (fixed on the platform with constant orientation) is introduced as a way to facilitate the computation, Fig. 3b illustrates the kinematics of both TRUS and biopsy gun modules. Were D represents a displacement on X and Y axes for the needle module, and a displacement on X for the TRUS module. Hereafter the paper is focused on describing the TRUS module since the computation is identical for both modules.

To find the Study parameters of a moving frame $O'X'Y'Z'$ relative to the fixed frame OXYZ, the Denavit–Hartenberg (DH) parameters are written for each joint/link, and the matrices are multiplied to obtain the constraint conditions:

$$\begin{aligned}
 C_1 &= Td \cdot T_1 \cdot R_2 \cdot T_3 \cdot R_4 \cdot Te \cdot R_5 \cdot M \\
 C_2 &= N \cdot Te' \cdot R_2' \cdot R_3' \cdot M'
 \end{aligned}
 \tag{1}$$

Table 1 contains the parameters for each DH matrix transformation, where r_i (and r'_i) represent free rotation parameters derived from the R_i (and R'_i) using the half angle formulae.

Table 1. Parameters for the DH transformation matrices

$CI/C2$	Parameter	Description	Type
Td/N	$dx/Xn, Yn Zn$	Displacement on X/XYZ	Geometric parameter/active translation
T_1	t_1	Displacement on Z	Active translation
R_2/R'_2	r_2/r'_2	Rotation around Z	Free rotation
T_3/Te'	t_3/e_2	Displacement on Y	Active translation/geometric parameter
R_4	r_4	Rotation around Z	Free rotation
Te	e	Displacement on Z	Geometric parameter
R_5/R'_3	r_5/r'_3	Rotation around X	Free rotation
M/M'	m	Displacement on Y	Geometric parameter

From C_1 and C_2 the Study parameters are computed (as described in [7]) yielding Eqs. (2) and (3). Regarding Study parameters as algebraic varieties, two polynomial ideals are generated, I for Eq. (2) and I' for Eq. (3). Maple software was not able to generate a Gröbner basis for I (on the computer previously mentioned), therefore the linear implicitization algorithm (also used in [9]) was used before computing a Gröbner basis G .

$$\begin{bmatrix} x_0 \\ x_1 \\ x_2 \\ x_3 \\ y_0 \\ y_1 \\ y_2 \\ y_3 \end{bmatrix} = \begin{bmatrix} 2 \cdot r_2 - 2 \\ 2(r_2 \cdot r_4 - 1)r_5 \\ -2(r_4 + r_2)r_5 \\ -2(r_4 + r_2) \\ r_2(r_5 \cdot dx \cdot r_4 - t_1 - e + m \cdot r_5 + t_3 \cdot r_5) + r_4(-t_1 - e + m \cdot r_5 - r_5 \cdot t_3) - dx \cdot r_5 \\ r_2(dx \cdot r_4 - t_1 \cdot r_5 + m - e \cdot r_5 - t_3) + r_4(-e \cdot r_5 + t_3 + m - r_5 \cdot t_1) + dx \\ r_2(e \cdot r_5 \cdot r_4 + t_3 \cdot r_4 + m \cdot r_4 - r_5 \cdot r_4 \cdot t_1 - dx) - dx \cdot r_4 + r_5 \cdot t_1 - m + e \cdot r_5 + t_3 \\ r_2(-t_1 \cdot r_4 - e \cdot r_4 + m \cdot r_4 \cdot r_5 - r_5 \cdot t_3 \cdot r_4 + r_5 \cdot dx) + r_5 \cdot r_4 \cdot dx + e - r_5 \cdot m + t_1 - t_3 \cdot r_5 \end{bmatrix} \quad (2)$$

$$\begin{bmatrix} x'_0 \\ x'_1 \\ x'_2 \\ x'_3 \\ y'_0 \\ y'_1 \\ y'_2 \\ y'_3 \end{bmatrix} = \begin{bmatrix} 2 \\ 2r'_3 \\ 2r'_2 \cdot r'_3 \\ 3r'_2 \\ r'_3 \cdot r'_2 \cdot Yn + m \cdot r'_3 \cdot r'_2 + r'_2 \cdot r'_3 \cdot e_2 + Xn \cdot r'_3 + r'_2 \cdot Zn \\ r'_2 \cdot r'_3 \cdot Zn - e_2 \cdot r'_2 - Yn \cdot r'_2 + m \cdot r'_2 - Xn \\ -r'_3 \cdot Zn + r'_2 \cdot Xn - e_2 - Yn - m \\ -r'_2 \cdot r'_3 \cdot Xn + Yn \cdot r'_3 + r'_2 \cdot r'_3 - r'_3 \cdot m - Zn \end{bmatrix} \quad (3)$$

In the case of I' Maple returned a Gröbner basis (denoted G'). The mentioned Gröbner bases contain polynomials with Study parameters as variables. Solutions for the forward kinematic problem must be solutions both G and G' . Maple was able to compute a basis G^* with the information from both G and G' after providing numerical values for some geometric parameters (in this example $e = 10$, $e_2 = 10$, $dx = 350$, $m = 50$). The basis G^* has a univariate polynomial (in x_3) of degree 8. By inputting numerical values for the active joints in G^* and solving for x_i, y_i , numerical values for Study parameters are obtained. For a numerical example the following values were used: $\{t_1 = 100, t_3 = 300, Xn = 300, Yn = 250, Zn = 120\}$; all the dimensions are expressed in mm. The computation yields 8 solutions but only 4 are of interest (the other 4 the first 4 multiplied by -1). The numerical values obtained are included in Table 2, and a kinematic representation of two solutions is illustrated in Fig. 4. The other two solutions represent the same displacement but with different orientation (a rotation around Z' axis combined with a rotation around X' axis by a value of π).

Table 2. Numeric solutions for Study parameters

x_0	x_1	x_2	x_3	y_0	y_1	y_2	y_3
-0.035	0.705	-0.706	0.035	-0.151	-4.080	-3.155	18.222
0.028	-0.559	-0.827	0.414	-20.968	-5.819	3.545	6.361
-0.827	0.041	-0.028	0.559	3.545	6.361	20.968	5.819
0.706	-0.035	-0.035	0.705	3.155	-18.222	-0.151	-4.080

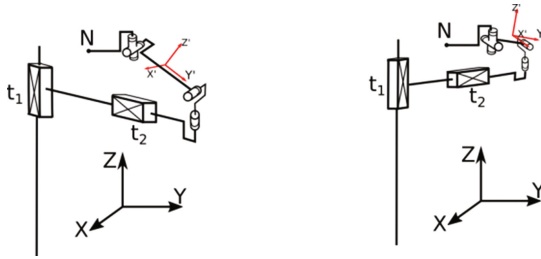


Fig. 4. Solutions for the forward kinematic problem.

Since a generalization was used to compute the forward kinematics (using the simplest kinematic representation illustrated in Fig. 3b), the forward kinematics for the $2\underline{P}RR$ mechanism is also computed using Study parameters. Following the kinematic representation from Fig. 5, the Study parameters were computed (after multiplying the matrices according to DH parameters) for three kinematic paths (illustrated as a, b, c in Fig. 5) yielding the Study parameters denoted $x_i^{a,b,c} : y_i^{a,b,c}$ (Eqs. 4-7).

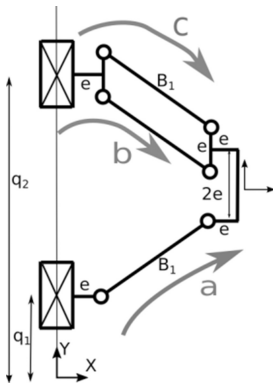


Fig. 5. Kinematic sketch for the $2\underline{P}RR$ mechanism

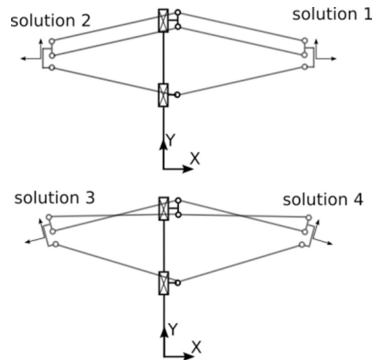


Fig. 6. Kinematic solutions for the $2\underline{P}RR$ mechanism

After computing three Gröbner bases (one for each ideal generated by Study parameters $x_i^{a,b,c} : y_i^{a,b,c}$) Maple Software was able to compute a base that contain the information from all three previous bases. Six distinct solutions, four of them being real (the remaining 2 complex solutions are not of interest) were returned after the following numerical values were input in the computation: $\{q_1 = 100, q_2 = 200, q_3 = 100, B_1 = 150, e = 10\}$. Table 3 displays the numerical values for the solutions, and Fig. 6 illustrates a sketch of these solutions (with only solution 1 being of interest due to the robot functionality).

Table 3. Numeric solutions for Study parameters for the 2PRR mechanism

x_0	x_1	x_2	x_3	y_0	y_1	y_2	y_3
1	0	0	0	0	-82.284	-75	-100
1	0	0	0	0	62.284	-75	-100
0.510	0	0	-0.859	-85.970	85.161	26.351	-51.079
0.510	0	0	0.859	85.970	-95.376	26.351	-51.079

$$\begin{bmatrix} x_0^{a,b,c} \\ x_1^{a,b,c} \\ x_2^{a,b,c} \\ x_3^{a,b,c} \\ y_0^{a,b,c} \\ y_1^{a,b,c} \\ y_2^{a,b,c} \\ y_3^{a,b,c} \end{bmatrix} = \begin{bmatrix} 2 \cdot r_4 \cdot r_5 - 2 \\ 0 \\ 0 \\ 2 \cdot t_4 - 2 \cdot t_5 \\ -(r_5 + r_4)q_3 \\ y_1^{a,b,c} \\ y_2^{a,b,c} \\ -(r_4 \cdot r_5 - 1)q_3 \end{bmatrix} \quad (4)$$

$$\begin{aligned} y_1^a &= (B_1 r_5 - 2e r_5 - e + q_1) r_4 - e r_5 + q_1 r_5 + 2e + B_1 \\ y_2^a &= (-q_1 r_5 - e r_5 + B_1) r_4 + q_1 + e - r_5 B_1 \end{aligned} \quad (5)$$

$$\begin{aligned} y_1^b &= (B_1 r_5 - 2e r_5 - e + q_2) r_4 - e r_5 + q_2 r_5 + 2e + B_1 \\ y_2^b &= (-q_2 r_5 + e r_5 + B_1) r_4 + q_2 - e - r_5 B_1 \end{aligned} \quad (6)$$

$$\begin{aligned} y_1^c &= (B_1 r_5 - 2e r_5 - 3e + q_2) r_4 - 3e r_5 + q_2 r_5 + 2e + B_1 \\ y_2^c &= (-q_2 r_5 + e r_5 + B_1) r_4 + q_2 - e - r_5 B_1 \end{aligned} \quad (7)$$

3 Conclusions

The forward kinematics computation presented in this paper was conducted using Study parameters. Due to computing limitations the manipulator kinematic chains were treated independently but no global information of the manipulator functionality was lost. A detailed (mathematically speaking) representation of kinematic solutions was presented, with two possible (mechanically speaking) solutions for the manipulator, and one possible solution for the 2PRR mechanism. Based on the results of this paper, future research is planned to achieve a complete singularity analysis using Study parameters. Furthermore, the inverse kinematics analysis is planned, in order to practically validate the robotic system for its particular task (transperineal prostate biopsy under TRUS guidance).

Acknowledgments. This paper was realized within the Partnership Programme in priority domains - PN-II, which runs with the financial support of MEN-UEFISCDI through Project no. 247/2014, code PN-II-PT-PCCA-2013-4-0647 – ROBOCORE and also the Project no 59/2015, code PN-II-RU-TE-2014-4-0992 – ACCURATE.

References

1. Tarun, K.P., et al.: AAPM and GEC-ESTRO guidelines for image-guided robotic brachytherapy: report of Task Group 192. *Am. Assoc. Phys. Med.* (2014)
2. Stoianovici, D., et al.: MRI stealth robot for prostate interventions. *Minim. Invasive Ther. Allied Technol.* **16**(4), 241248 (2007)
3. Chang, D., Challacombe, B., Lawrentschuk, N.: Transperineal biopsy of the prostate-is this the future? *Nat. Rev. Urol.* **10**(12), 690–702 (2013)
4. Gherman, B., Plitea, N., Pisla, D.: An innovative parallel robotic system for transperineal prostate biopsy. In: Wenger, P., Flores, P. (eds.) *New Trends in Mechanism and Machine Science. MMS*, vol. 43, pp. 421–429. Springer, Cham (2017). doi:[10.1007/978-3-319-44156-6_43](https://doi.org/10.1007/978-3-319-44156-6_43)
5. Vaida, C., et al.: Design of a needle insertion module for robotic assisted transperineal prostate biopsy. In: *MESROB 2016 - 5th International Workshop on Medical and Service Robots*, Graz Austria, July 2016
6. Vaida, C., Pisla, D., Schadlbauer, J., Husty, M., Plitea, N.: Kinematic analysis of an innovative medical parallel robot using study parameters. In: Wenger, P., Chevallereau, C., Pisla, D., Bleuler, H., Rodić, A. (eds.) *New Trends in Medical and Service Robots. MMS*, vol. 39, pp. 85–99. Springer, Cham (2016). doi:[10.1007/978-3-319-30674-2_7](https://doi.org/10.1007/978-3-319-30674-2_7)
7. Husty, M., Pfurner, M., Schroecker, H.P., Brunthaler, K.: Algebraic methods in mechanism analysis and synthesis. *Robotica* **25**(6), 661–675 (2007)
8. Husty, M., Schroecker, H.P.: Algebraic geometry and kinematics. *Nonlinear Comput. Geometry* **151**, 85–107 (2009)
9. Schadlbauer, J., Walter, D.R., Husty, M.: The 3-RPS parallel manipulator from an algebraic viewpoint. *Mech. Mach. Theory* **75**, 161–176 (2014)
10. Plitea, N., Pisla, D., Vaida, C., Gherman, B., Tucan, P., Covaciu, F.: Family of innovative parallel robots for transperineal prostate biopsy, Patent pending: A/00191/13.03.2015 (2015)

Optimum Walking of the Bioloid Humanoid Robot on a Rectilinear Path

Gabriela Reyes¹, Jose Alfonso Pamanes^{1(✉)}, Jesus Edurado Fierro¹,
and Victor Nunez²

¹ Division of Postgraduate Studies and Research, Institute of Technology
of La Laguna (ITLag)/National Institute of Technology,
Blvd. Revolucion y Cuauhtemoc, C.P 27000 Torreon, Coahuila, Mexico
japamanesg@correo.itlalaguna.edu.mx

² Polytechnic University of Sinaloa (UPSIN),
C.P. 82199 Mazatlan, Sinaloa, Mexico
jnunez@upsin.edu.mx

Abstract. A method is presented in this paper to determine optimal values of the parameters for the gait of a humanoid robot. These parameters are relevant for a stable walking of the robot when this one follows a rectilinear path. By applying such optimal parameters the set of zero moment points of the support foot, corresponding to a step in the walking, is located as close as possible to the center of the footprint of the support foot. The computation of the optimal parameters is accomplished by minimization of a nonlinear objective function that describe the distance from the center of the footprint to a typical remote zero moment point (ZMP) estimated from a sample of such points generated during a step. A study case is presented to illustrate the efficacy of the proposed method. This one provide some advantages compared with other approaches in the literature.

Keywords: Bioloid robot · Biped robots · Optimum walking · Humanoid walking

1 Introduction

High instability during the walking is characteristic in humanoid biped robots. Relatively slow perturbations may cause that the robot falls during the walking. Thus, great challenges exists in designing, motion planning and control of humanoids in order to reduce the instability as much as possible. The main goal of studies developed on biped locomotion is to get a stable walking. The criterion of stability of biped robots applied in most of research works is based on the notion of the Zero Moment Point (ZMP), proposed by Vukobratovic [1]. Indeed, Shi et al. [2], for instance, proposed to minimize the deviation between the center of the stable region and the ZMP by defining the optimal trajectory of the hip of a biped. The authors studied a 12 degree of freedom (DOF) robot and they specified the pelvis motion by using sinusoidal functions. These kind of functions, however, produces impact forces during the landing of the free foot. In other work [3] the maximization of the stability margin of a biped was proposed by using optimal values of two parameters. The gait of the robot is based on third order

spline functions. In this case the impact forces aren't neither avoided. Other authors [4], based on a human walking, specify an *ideal* trajectory of the ZMP and then the pelvis motion of the robot is determined such that the real trajectory of the ZMP is near to the ideal one.

In more recent works, others criteria were applied in synthesizing walking patterns. To reduce the instability, in [5] the motion planning was oriented to compensate the yaw moment of the robot during the walking. On the other hand, a method was proposed in [6] to generate walking patterns that require the lowest friction forces.

In the present paper an approach is introduced to establish the optimal values of walking parameters that maximize the stability margin of the robot during the simple support phase of the walking. The proposed method is applied to the Bioloid humanoid robot with 12 DOF in legs. The gait of the humanoid is based on the cycloidal functions proposed in [7].

The next section describes the main features of the gait applied for the robot. The formulation of the optimization problem and the process to solve it are presented in third section. Then, this method is applied for walking optimization of the Bioloid robot for a rectilinear path. Finally the conclusion of the work is presented.

2 Specification of a Walking

In the walking pattern of a biped robot, the desired poses for both the pelvis and the oscillating (or *free*) foot are specified with respect to a world's frame ($x_W-y_W-z_W$) as time functions. The points for position specification of these bodies are O_p (*pelvis*) and O_f (*free foot*), showed in Fig. 1. The positions are given in Cartesian coordinates. For orientation with respect to the world's frame, the Bryant angles λ , μ and ν are applied to frames $x_p-y_p-z_p$ and $x_f-y_f-z_f$ attached to the pelvis and the free foot, respectively. Both frames and the world's frame are shown in Fig. 1. The Bryant angles correspond to successive rotations applied in the order $x-y-z$ to a frame whose orientation initially matches the world's frame in order to obtain the desired orientations. The equations that define all the coordinates as time functions are those proposed in [7]. Some of the main walking parameters are appreciated in Fig. 2.

The cycle of a step is composed by two phases: single support phase (SSP) and double support phase (DSP). The first one is achieved during a period T_S , when only one foot is in contact with the floor while the other foot is moving forwards. DSP is accomplished in a period T_D and starts when the moving foot lands and both feet keep the contact with the floor. DSP finishes when the rear foot leaves the floor to start the next step. In SSP both the hip and the free foot move. In DSP only the hip moves. Each step period is $T = T_S + T_D$. The SSP is the most instable one during the walking and requires of a suitable motion planning.

The walking process is achieved in 3 stages: stage 1 or *starting* (completed in one step), stage 2 or *cruising* (completed in n_p steps) and stage 3 or *stopping* (completed in one step). In stage 1, the pelvis accelerates on direction x_W from zero velocity by using a starting semi-cycloidal motion until cruising speed (V_{max}). This stage occurs in the period T_1 of the first step. The x coordinates of position for both feet when the walking begins ($t=0$) are zero. The period of each step in cruising stage is T_2 with the pelvis

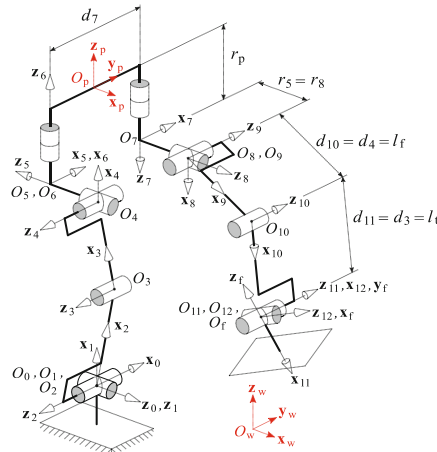


Fig. 1. Kinematic scheme of legs of the Bioloid humanoid

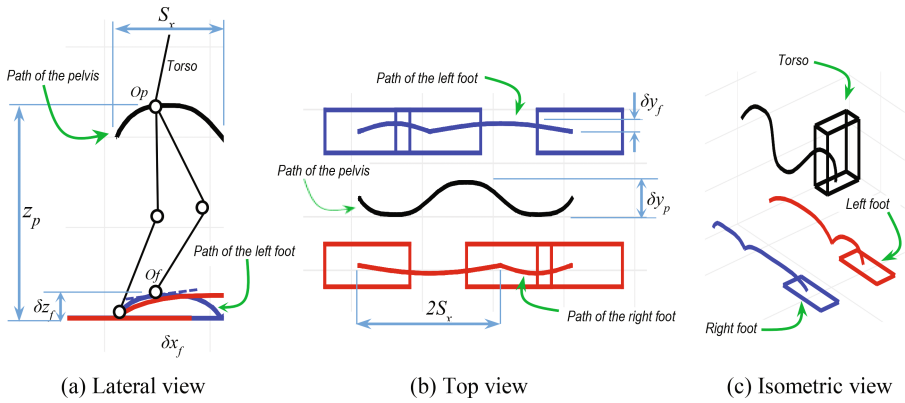


Fig. 2. Paths and main parameters for motion of pelvis and feet

moving in direction x_w with speed V_{max} . In stage 3 the speed of the pelvis decreases by using a stopping semi-cycloidal motion, from V_{max} to zero, in the time T_3 of the last step. A step at each stage has one single support phase (SSP) and one double support phase (DSP). In rectilinear walking in direction x_w , both feet finish their motion having the same x coordinate. The total time is $T_T = T_1 + n_p T_2 + T_3$ for the walking. The main parameters of the walking equations are shown in Fig. 2.

3 Optimization Problem

The geometry of a path of the ZMP that is generated on a footprint during the walking of a humanoid robot is determined by the dynamics of the robot’s motion. The features of such a motion depends on the parameters of equations that define the walking. Thus, the coordinates of the ZMP are implicit functions of the parameters of the walking pattern. Consequently, the optimal values of such parameters must be computed for the best behavior of the ZMP.

The criterion used in this work for optimization of walking consists in the location of the set of ZMP associated to a step in SSP as close as possible to the center of the sole of the support foot. The following procedure is proposed to solve this problem.

For an arbitrary set of walking parameters, the coordinates corresponding to a sample of n_{pm} zero moment points P_i are taken ($i = 1, 2, \dots, n_{pm}$), which correspond to a single step in SSP during the walking. Such coordinates are obtained in a simulation process by using the *Webots*© software. Then, the distances d_i are computed between each one of the P_i of the sample and the centroid C_0 of the sole of the support foot. The zero moment points of the set and C_0 are schematized for the sole of the humanoid in Fig. 3, and a distance d_i is also indicated. We compute the mean \bar{d} and the standard deviation d_σ of the set of distances and replace them in the following objective function:

$$f = \bar{d} + d_\sigma \tag{1}$$

where

$$\bar{d} = \frac{1}{n_{pm}} \sum_{i=1}^{n_{pm}} d_i \tag{2}$$

$$d_\sigma = \sqrt{\frac{1}{n_{pm}} \sum_{i=1}^{n_{pm}} (d_i - \bar{d})^2} \tag{3}$$

It can be observed that f represents a typical large distance of the set of distances d_i . Therefore, a set of distances as close as possible to the centroid C_0 corresponds to the minimum value of f . Such a set can be obtained by using optimal values of some significant parameters of the walking pattern. When f is minimized, then the stability margin of the robot will be maximized.

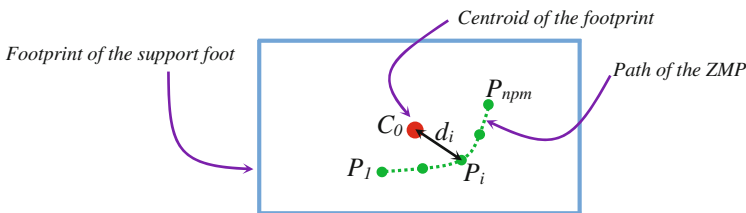


Fig. 3. Sample of zero moment points P_i for a step of a walking.

Because of f is not an explicit function of parameters of the walking pattern, the optimal values of such parameters cannot be computed in a conventional way. Thus, we use a regression model to obtain an approximative function f^* whose independent variables are the parameters of the walking pattern. In a first assessment of our approach we use only two parameters of walking as optimization variables, and propose the following quadratic function as a regression model:

$$f^* = b_0 + (w_1 - b_1)^2 + (w_2 - b_2)^2 \quad (4)$$

The coefficients b_0, b_1, b_2 are the parameters of the function (4), and w_1, w_2 are the independent variables of walking. Thus, the values of the coefficients b_0, b_1 and b_2 must be determined in such a way that f^* approaches to f as much as possible for a sample of sets of the independent variables. Such values of coefficients will be optimal.

To compute the optimal values of coefficients of function (4), the method starts with an arbitrary set of values of b_0, b_1 and b_2 . Then the function f^* is evaluated by Eq. (4) for six different sets of values of parameters w_1 and w_2 chosen by the user. The greater the number of sets is, the better optimal coefficients we obtain. In this work we chose six sets of values of w_1 and w_2 and suitable results were obtained.

On the other hand, for the same sets of variables w_1 and w_2 used in evaluation of the approximative function f^* , we additionally evaluate the exact function f of Eq. (1). The specific values of f evaluated for the set of variables w_1 and w_2 will be termed f_w . Clearly, for each set of w_1 and w_2 , there will exist an error of f^* with respect to f_w , which is defined as

$$e = |f^* - f_w| \quad (5)$$

When this error is evaluated for the six sets of values of w_1 and w_2 , we have six errors that must be globally minimized in the process of optimization of coefficients b_0, b_1 and b_2 . For this optimization we propose the following objective function:

$$f_e = \bar{e} + e_\sigma \quad (6)$$

where \bar{e} is the mean error, and e_σ the standard deviation, of the set of errors evaluated by Eq. (5).

To evaluate the functions f_w that are employed in Eq. (5) during the process of minimization of (6), numeric experiments must be achieved by using the sets of variables w_1 and w_2 . Such experiments consist in simulations of walking of the robot by using the current values of w_1 and w_2 and the other walking parameters that are constant. In Table 1 the values given for these parameters are displayed. The values of those parameters not included in this Table are zero.

On the other hand, the two walking parameters that will be considered as independent variables w_1 and w_2 must be chosen for computation of b_0, b_1 and b_2 . In previous experimental studies on the walking of the Bioloid robot [8] it was observed that the balancing of the robot was more sensitive to changes in values of the lateral displacements δy_p of the pelvis. Consequently, in this work we use the displacements

Table 1. Parameters specified for the numerical experiments

Parameter	Units	Value
n_p	steps	6
T_{SS}	sec	1
T_{DS}	sec	1
z_{pini}	m	0.125
δx_p	m	0.030
δz_p	m	0.005
δx_f	m	0,030
δy_f	m	0.010
δz_f	m	0.015
μ_p in	deg	15

Table 2. Sets of independent variables considered for the numerical experiments

Experiment	δy_{ps} (m)	δy_{pd}	f(m)
1	0.010	0.025	0.0241
2	0.010	0.030	0.0238
3	0.012	0.026	0.0208
4	0.013	0.028	0.0202
5	0.015	0.025	0.0229
6	0.015	0.030	0.0209

δy_{ps} and δy_{pd} of point Op of the pelvis in direction y_w , associated to the single support phase and double support phase, respectively. Thus, we define:

$$w_1 \equiv \delta y_{ps} \tag{7}$$

$$w_2 \equiv \delta y_{pd} \tag{8}$$

The meaning of these independent variables in the motion of the biped can be appreciated in Fig. 4. The six sets of δy_{ps} and δy_{pd} considered are given in Table 2.

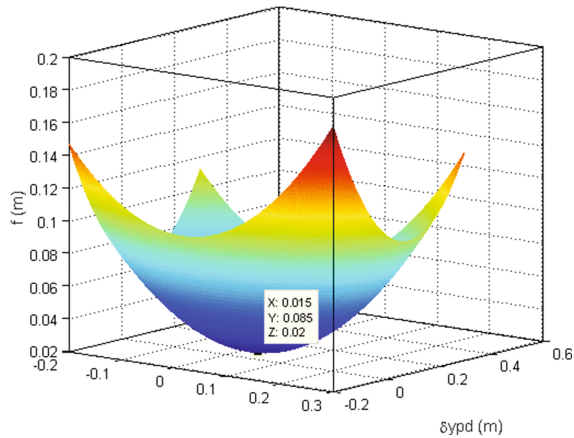
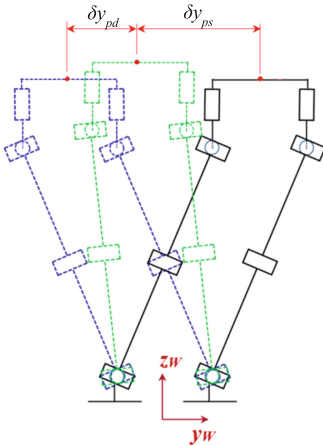


Fig. 4. Independent variables of functions (1) and (4)

Fig. 5. Plot of function (4) with optimal values of b_0 , b_1 and b_2

Thus, minimizing function (6) by using the function *fmincon* of *Matlab*© for these sets of parameters we obtain $b_0 = 0.020$, $b_1 = 0.015$ and $b_2 = 0.085$. The function *fmincon* is based on the *Interior Point* algorithm [9]. Such a function minimize constrained non-linear functions.

The plot of function (4) with the obtained values of b_0 , b_1 , b_2 is shown in Fig. 5. The optimal values of w_1 and w_2 are gotten by using the partial derivatives of (4) with respect to w_1 and w_2 . Making equal to zero such derivatives we obtain:

$$w_{1Opt} = b_1 = 0.015m$$

$$w_{2Opt} = b_2 = 0.085m$$

Therefore, we have $\delta y_{psOpt} = 0.015m$ and $\delta y_{pdOpt} = 0.085m$ as the values of the independent variables which minimize the objective function. Finally we achieve a simulation by using these values for displacements of the pelvis, in single and double support phases, in order to obtain the optimum path of the ZMP on the footprint of the support foot during the walking. The obtained optimum paths are shown in Fig. 6 for 6 steps of walking, and a sample of postures of the robot during the walking is presented in Fig. 7.

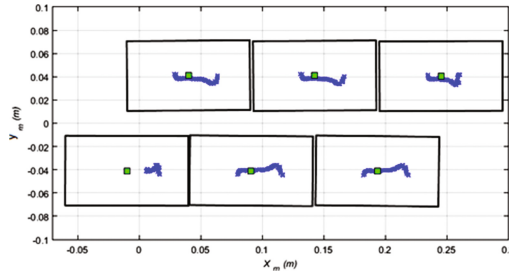


Fig. 6. Paths of the ZMP obtained by using optimal parameters of walking

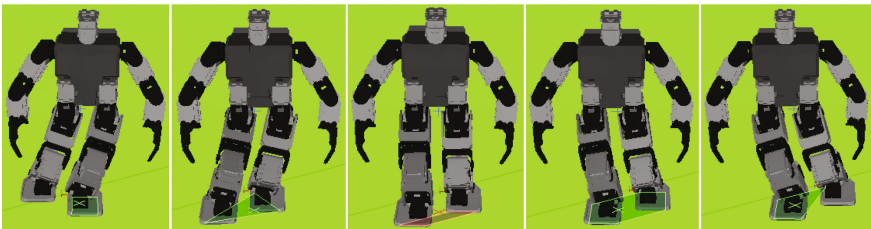


Fig. 7. Simulation of one step for the optimum walking in Webots©

4 Conclusion

A method was proposed in this paper to obtain the values of parameters that optimize the gait of the Bioloid humanoid robot during a rectilinear walking. The set of zero moment points of the support foot, corresponding to a step in the walking, is located as close as possible to the center of the footprint of the support foot. Consequently, the stability margin of the robot is maximized during the walking.

The considered walking pattern is based on cycloidal motions of the pelvis and free foot, as proposed in [7]. The equations of this pattern are explicitly expressed in function of geometric parameters such as the lateral and vertical displacements of the pelvis, size of the steps, amount of rotations of the torso and the free foot, etc. This feature of the walking pattern allows to identify the relevant parameters for optimization of the gait. The study case presented in the paper shows the efficacy of the proposed method. Indeed, by applying the obtained optimal parameters the greatest stability margin is obtained compared with those corresponding to sets of parameters in Table 2.

In future work, an experimental validation of the results in this study will be accomplished. Besides, curvilinear paths and more parameters will be considered for optimization. In following curvilinear paths, and taking into account centrifugal forces, different optimal parameters will be required for lateral displacements of the pelvis in motions from the right to the left than those required from the left to the right, as previously observed in a preliminar study [10].

Acknowledgments. This work was supported by the CONACyT (National Council of Research and Technology) and the DGTN (General Direction of the National Institute of Technology) of the Ministry of Public Education of Mexico.

References

1. Vukobratović, M., Jurčić, D.: Contribution to the synthesis of biped gait. *IEEE Trans. Bio-Med. Eng.* **16**(1) (1969)
2. Shih, C., Zhu, Y., Gruver, W.: Optimization of the biped robot trajectory. In: *Proceedings of the 1991 IEEE International Conference on Robotics and Automation*, pp. 899–903 (1991)
3. Huang, Q., Yokoi, K., Kajita, S., Kaneko, K., Arai, H., Koyachi, N., Tanie, K.: Planning walking patterns for a biped robot. *IEEE Trans. Robot. Autom.* **17**(3), 280–289 (2001)
4. Shi, J., Li, Y., Chung, S., Lee, T., Gruver, W.: Trajectory synthesis and physical admissibility for a biped robot during the single support phase. In: *Proceeding of the IEEE International Conference on Robotics and Automation*, pp. 1646–1652 (1990)
5. Hirabayashi, T., Ugurlu, B., Kawamura, A., Zhu, C.: Yaw moment compensation of biped fastwalking using 3D inverted pendulum. In: *10th IEEE International Workshop on Advanced Motion Control Proceeding of the AMC 2008*, pp. 296–300 (2008)
6. Khadiv, M., Moosavian, S.A.A., Yousefi-Koma, A., Sadedel, M., Mansouri, S.: *Optimal gait planning for humanoids with 3D structure walking on slippery surfaces*. *Robotica*, pp. 1–19. Cambridge University Press (2015)

7. Arias, L., Olvera L., Pamanes, J.A., Nunez, J.V.; Patrón de marcha 3D de tipo cicloidal para humanoides y su aplicación al robot Bioloid. *Revista Iberoamericana de Ingeniería Mecánica (RIBIM)*, pp. 03–22 (2014)
8. Nunez, V., Olvera, L., Pamanes, J.A.: Simulation and experimentation of walking of the bioloid humanoid robot. In: *Proceeding of the 13th IFToMM World Congress on Theory of Machines and Mechanisms*, Guanajuato, México, pp. 1644–1650 (2011)
9. Byrd, R.H., Gilbert, J.C., Nocedal, J.: A trust region method based on interior point techniques for nonlinear programming. *Math. Program.* **89**(1), 149–185 (2000)
10. Reyes, G., Pamanes, J.A., Nunez, V.: Análisis de la Marcha del Robot Humanoide Bioloid en una Ruta Circular con Parámetros Óptimos. *Memorias del XIII Congreso Mexicano de Robotica (COMRob 2011) de la AMRob*. Artículo A25, Matehuala, Mexico (2011)

A New Experimental Set-up for Training Multi-parameter Gaits

Sami Bennour^{1,2}(✉), Houssein Lamine², Baptiste Ulrich¹,
Thomas Legrand¹, Brigitte Jolles^{1,3}, Julien Favre¹,
and Lotfi Romdhane^{2,4}

¹ Swiss BioMotion Lab, Department of Musculoskeletal Medicine,
Centre Hospitalier Universitaire Vaudois and University
of Lausanne, Lausanne, Switzerland
sami.bennour@gmail.com

² Mechanical Laboratory of Sousse, National Engineering School of Sousse,
University of Sousse, Sousse 4000, Tunisia

³ Institute of Microengineering, Ecole Polytechnique Fédérale de Lausanne,
Lausanne, Switzerland

⁴ Mechanical Engineering Department, American University of Sharjah,
PO Box 26666, Sharjah, United Arab Emirates

Abstract. The purpose of this work is to estimate changes in the knee flexion angle in response to modifications in the human walking. We developed an experimental application divided into two parts: the first one serves to supply visual instructions projected on the ground to be followed by a patient during walking trials and the second measures certain biomechanical parameters. A number of healthy subjects are recruited for walking trials. Our first objective was to ask a subject to follow a number of visual instructions during modified walking trials and then check if he properly followed the instructions. The set of the instructions drawn on the ground represent certain spatial parameters. Every candidate follows in real time a specific walking pattern based on his recorded natural walking in the way that gait parameters, i.e., step width, stride length and foot progression angle, are varied. Thereby, effects of these variations on the knee flexion angle are identified.

Keywords: Knee flexion angle · Stride length · Step width · Foot progression angle · Video projection

1 Introduction

The gait analysis evaluates pathologies and helps clinicians to establish effective rehabilitation programs. Secondly, it allows to quantify objectively the effectiveness of rehabilitation or treatment protocols. Changes in gait parameters were studied in several pathologies [1–5]. Step width, stride length and foot progression angle are among the most important spatial parameters of walking. These fundamental parameters allow to: have a global representation of walking, measure the performance of an individual and quantify the effectiveness of a treatment [6–10].

All changes in the spatial parameters can be seen as coping mechanisms to reduce patients' pain during pathological walking [11]. These variations are the result of the adaptation of the lower limbs' kinematics.

Again, changing the spatial parameters is considered among the important techniques for walking rehabilitation. In the literature, only few systems were developed for modification of gait parameters in real-time walking with visual and tactile feedback [12–14]. The disadvantage of these systems is that they don't provide real-time instruction. So far, the commercial-available systems project spatial parameters on treadmills, but not on the ground [15].

Altogether, this suggests that we need a multi-sensorial feedback system for gait training capable of projecting the instructions (modifications of spatial parameters) on the ground during walking analysis in real time with multi-sensorial feedback.

Regarding the analysis process, the majority of researches has investigated the effect of walking speed on the kinematics of the lower limbs. In contrast, we study the effects of spatial parameters. However, there is a paucity of studies that assess the relationship between lower limb kinematics and spatial parameters when walking. This information is required to build rehabilitation protocol.

Therefore, the first objective of this study was to develop a multi-sensorial feedback system in order to modify the spatial parameters of walking (stride length, step width and foot progression angle) through the combination of: a motion capture system, a protocol management unit and a ground projection device. This study aims at assessing the potential of these new techniques by quantifying the errors at which healthy subjects can follow gait modification instructions projected on the floor (i.e., the errors between target and subject footsteps). Finally, this research points the effect of variations in spatial gait parameters on sagittal-plane angles of the lower limbs.

2 Experimental Setup

Our experimental system consists of two parts synchronized with each other in real time and managed by a central processing unit. Motion tracking of human walking is ensured by a VICON system. The measures will be sent to the processing unit to calculate certain biomechanical parameters. The second part of processing is the definition of a protocol that applies modifications with reference to data of recorded normal gait. A system introduced by a two video projectors, is used to project visual instructions, provided by the processing unit on the floor where the patient is asked to follow them during tests of guided walking (Fig. 1).

During experimental tests, the VICON system (16 infrared cameras) is used to measure and record the trajectories of 26 markers placed on the body of the candidate. Then using an inverse kinematic model we calculate the angle of knee. To perform a guided walking, the projection system provides visual cues to the candidate. These indications represent the spatial parameters that the subject is asked to follow during a walk test. For our purposes we are interested in the following gait parameters: step width (L_{SW}^{set}), stride length (L_{SL}^{set}), and foot progression angle (θ_{FPA}^{set}) (Fig. 2).

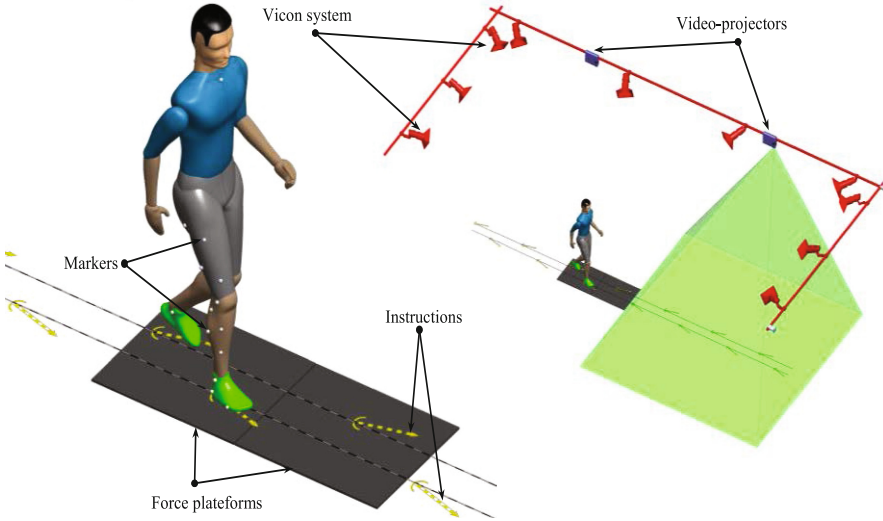


Fig. 1. Illustration of the augmented-reality gait retraining system

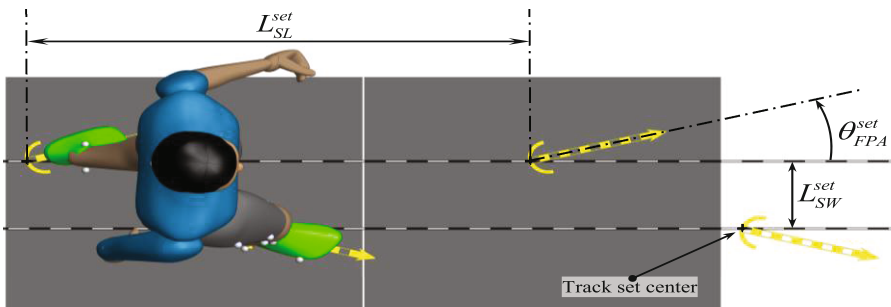


Fig. 2. Illustration of the step width (L_{SW}^{set}), stride length (L_{SL}^{set}) and foot angle (θ_{FPA}^{set}) variables.

2.1 Recruited Subjects

Ten healthy subjects participated in this study after providing informed consent (6 male; 25.2 ± 6 years old; 21.61 ± 1.85 kg/m²).

2.2 Baseline Gaits

For every candidate, a specific model with 26 markers was developed: 1 on the upper manubrium point, 1 on the first thoracic vertebra calcaneus, 4 on the pond, 4 on thigh, 2 on the knee, 4 on the shank, 2 on both malleolus, 1 on heel, 1 on metatarsal and 6 on the left lower limb. Markers placed on the knee and on the internal malleolus of the ankle are used for calibration. The others are used during motion tracking.

Static tests were made for the calibrations which aim to identify the reference positions for every markers and the anatomical centers of the articulations.

The subjects achieve five trials of natural walking with their own speeds on two instrumented platforms of strengths. Trajectories of markers were recorded with the 16 cameras of the Vicon system. Then, the processing unit computes in real time the knee flexion angle.

2.3 Protocol of Gait Training

In addition to 5 tests of normal walking, a protocol was defines where 3 spatial parameters are varied (step width, stride length and foot progression angle). The subject performs the trials of the modified walking by referring to its natural one.

Twenty-seven gait trials were collected for each participant. They consisted of all combinations of modifications ($27 = 3 * 3 * 3$) in step width (decreased, normal, and increased), stride length (decreased, normal, and increased), and foot progression angle (decreased, normal, and increased). During the trials, a subject is asked to keep its natural walking speed. The visual instructions are shown on the ground, along the zone of test, with arrows indicating the target movement for every test.

To control the quality of the walking realized by the candidate, our system shows the real tracks as feedback information. The errors of the parameters is calculated by comparing desired and real tracks (Fig. 3).

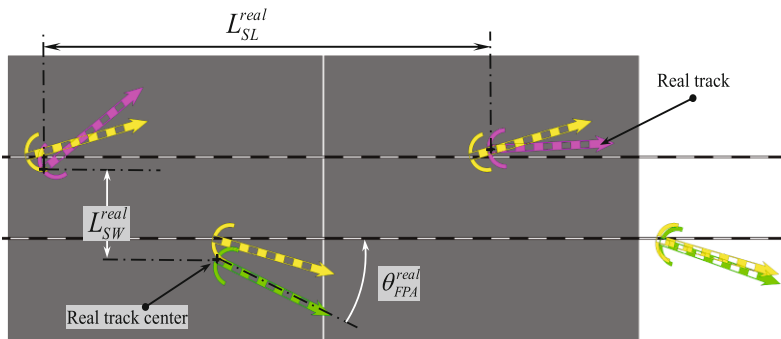


Fig. 3. Illustration of the real step width (L_{SW}^{real}); stride length (L_{SL}^{real}) and foot angle (θ_{FPA}^{real}) variables.

Analysis of results was carried out relying on four descriptive kinematic features of the knee flexion angle (Table 1 and Fig. 4).

The first part of the statistical analysis consisted of characterizing the modifications in step width, stride length and foot progression angle performed by the subjects. This analysis is a three-way repeated ANOVA test on the 270 data points (27 repeats for 10 participants), for each gait variable we determine if the instructions to modify step width, stride length and progression angle were significant factors for the variations

Table 1. Description of gait kinematic features.

	Joint	Kinematic feature	Description
1	Knee	KFA1	Maximum knee extension around heel-strike
2		KFA2	Maximum knee flexion during midstance
3		KFA3	Maximum knee extension during terminal stance
4		KFA4	Maximum knee flexion during swing

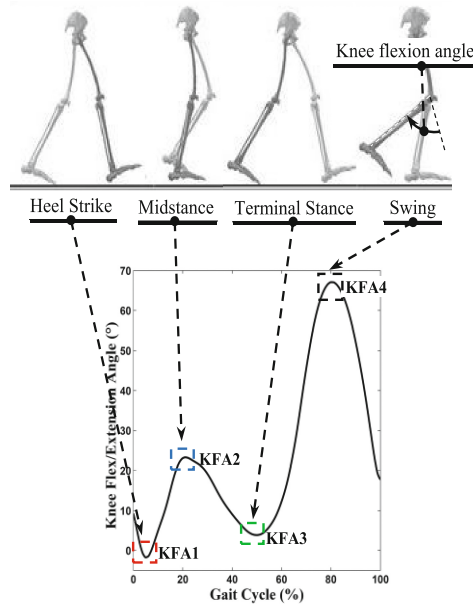


Fig. 4. Knee flexion angle throughout the gait cycle.

observed in each gait variable. The significance level for this analysis was set a priori to $\alpha = 0.05$. Next, post-hoc analysis was done for each significant factor and consisted of paired t-tests to compare the gait variables (step width, stride length and foot progression angle) among levels of modifications (decreased, normal, and increased). To account for multiple comparisons a Bonferroni-corrected $\alpha = 0.005$ and $\alpha = 0.001$ was used for post-hoc analysis. The second part of the analysis aimed to determine if the 4 descriptive kinematic features of knee flexion angle (KFA1, KFA2, KFA3 and KFA4) varied relative to the instructions to modify gait. This analysis was done using similar three-way repeated ANOVA tests and post-hoc t-tests as described above.

3 Results

When asked to walk normally, participants walked with a step width of 0.09 ± 0.02 m, stride length of 1.58 ± 0.15 m (mean \pm standard deviation), and progression angle of $2.6 \pm 3.7^\circ$. During all tests of training walks, subjects attained to follow instructions with errors 0.00 ± 0.01 m of step width, 0.00 ± 0.01 m, stride length, $0.1 \pm 2.2^\circ$, and foot progression angle.

Participants successfully followed the instructions to modify gait, as they significantly decreased and increased their step width (mean changes of -0.09 ± 0.02 m narrower and 0.16 ± 0.03 m wider), stride length (mean changes of -0.14 ± 0.02 m shorter and 0.15 ± 0.02 m longer) and progression angle (mean changes of $-10.1 \pm 3.9^\circ$ toe-in and $9.5 \pm 2.9^\circ$ toe-out) when they were instructed to do so (main diagonal of plots in Fig. 5). For the three instructions to modify gait, it was noted that they haven't an effect to induce cross-talk (plots out of the main diagonal in Fig. 5), except for instructions to modify progression angle which they have an effect on step width.

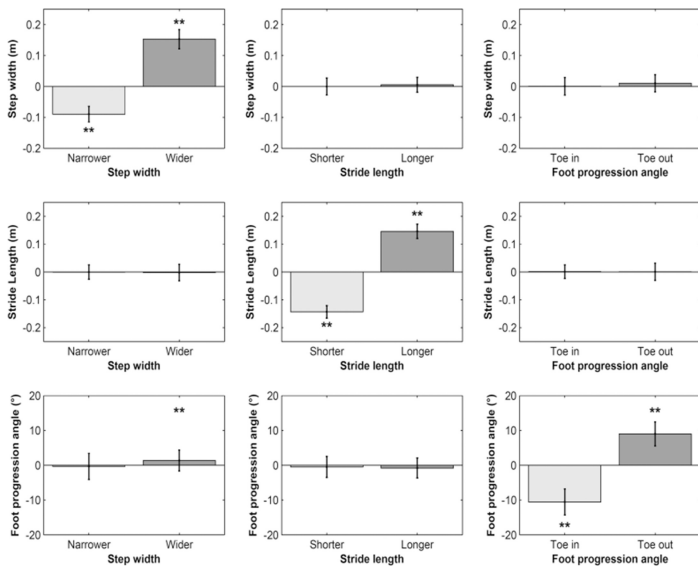


Fig. 5. Mean \pm standard deviation of the step width (1st row), stride length (2nd row), and foot progression angle (3rd row) variables divided according to the levels of the instructions of modify gait (1st column: step width, 2nd column: stride length, and 3rd column: foot progression angle). Each of the 9 graphs is based on 270 data points (27 trials from 10 subjects) either divided into three levels. The symbols (** and *) at the top of the bars correspond to the post-hoc analysis of the three-way repeated ANOVA, indicating significant differences between levels ($p < 0.001$ for (**)) and $p < 0.005$ for (*).

Analyzing the first peak of knee flexion angle (KFA1) relative to the instructions to modify gait using repeated three-way ANOVA showed that only the stride length had a significant effect on this variable ($p = 0.002$). As reported in Figs. 6 and 7, shorter

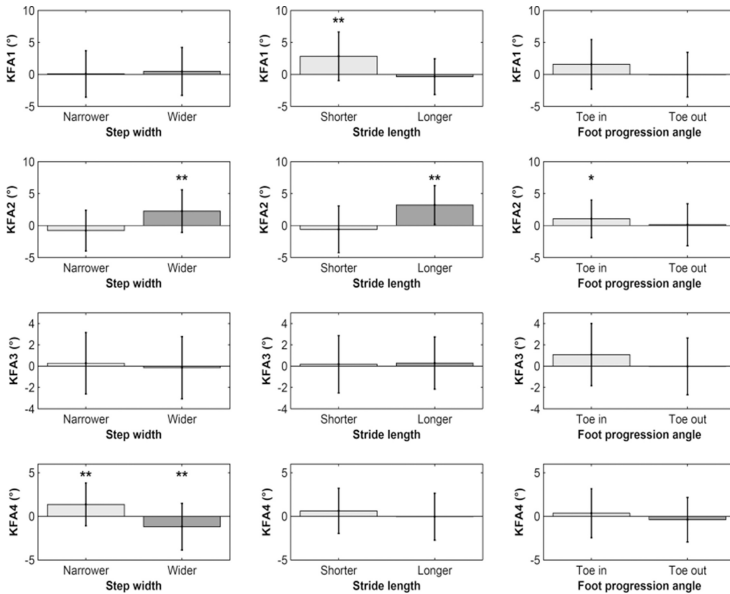


Fig. 6. Mean \pm standard deviation of the first KFA peak (1st row), second KFA peak (2nd row), third KFA peak (3rd row), and fourth KFA peak (4th row) variables divided according to the levels of the instructions of modify gait (1st column: step width, 2nd column: stride length, and 3rd column: foot progression angle). Each of the 12 graphs is based on 270 data points (27 trials from 10 subjects) either divided into three levels. The symbols (** and *) at the top of the bars correspond to the post-hoc analysis of the three-way repeated ANOVA, indicating significant differences between levels ($p < 0.001$ for (**)) and $p < 0.005$ for (*).

stride length increased the KFA1 by $2.8 \pm 3.8^\circ$ and longer stride length decreased the KFA1 by $-0.4 \pm 2.8^\circ$ compared to normal stride length.

The ANOVA for the second peak of knee flexion angle (KFA2) indicated that step width ($p = 0.001$), stride length ($p < 0.001$), and progression angle ($p = 0.021$) had an effect on this gait variable. Specifically, narrower step width and shorter stride length decreased the KFA2 by $-0.8 \pm 3.2^\circ$ and $-0.6 \pm 3.7^\circ$ compared to walking with normal step width, normal stride length, and normal progression angle, respectively (Figs. 6 and 7). Wider step width, longer stride length, toeing-in and toeing-out increased the KFA2 by $2.3 \pm 3.3^\circ$, $3.2 \pm 3^\circ$, $1 \pm 3.3^\circ$ and $0.1 \pm 3.3^\circ$ compared to normal step width, normal stride length and normal progression angle.

The ANOVA for the third peak of knee flexion angle (KFA3) indicated that neither instructions to modify gait had an effect on this gait variable.

The repeated three-way ANOVA for the fourth peak of knee flexion angle (KFA4) showed that only step width ($p = 0.003$) had an effect on this variable. The analysis also indicated a significant interaction term between step width and stride length ($p = 0.047$). Narrower step width increased the peak by $1.4 \pm 2.5^\circ$ and wider step decreased the peak by $-1.2 \pm 2.7^\circ$ compared to walking at normal step width (Figs. 6 and 7).

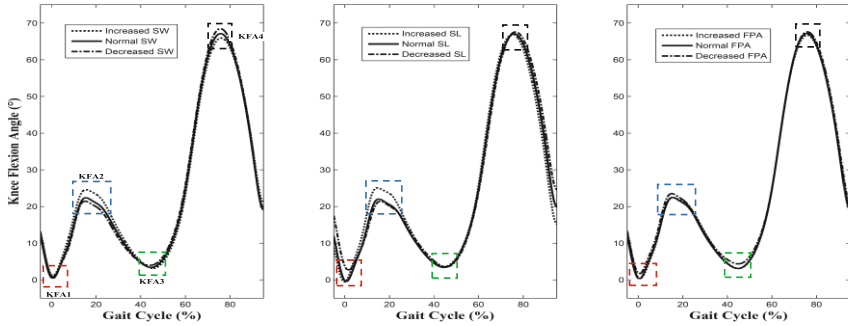


Fig. 7. Comparison graph of knee flexion angle for the normal walking condition (solid line) and for the combination of modifications: decreased step width, decreased stride length and decreased foot progression angle (dashed line), and increased step width, increased stride length and increased foot progression angle (dotted line).

4 Discussion

In this study we have developed a multi-sensorial feedback system to modify the spatial parameters of walking. A set of gait parameters, i.e., step width, stride length and foot progression angle were measured and modified individually for each subject. The visual instructions of gait parameters are provided such that subjects are asked to follow them during the walking tests. Much appreciation was noticed by the subjects during the experimental trials due to the availability of visual cues.

This study showed that errors between the values of visual cues and the real measurements are minimal when all subjects reached to follow faithfully the indications projected on the floor.

For the three instructions to modify gait, the system allowed a minimal cross-talk. Only the instructions to modify progression angle had an effect on step width.

This study highlighted the interaction of a general combination of gait changes (step width, stride length and angle progression) associated with changes in the 4 descriptive kinematic features of knee flexion angle (KFA1, KFA2, KFA3 and KFA4). These interactions are particularly important because, as shown in this study, some kinematic walk variables are difficult to change, without causing unintended side changes in other kinematic gait variables. The results showed that only KFA2 has relationship with variations of the three parameters (step width, stride length and foot progression angle) (Fig. 7 and Table 2). KFA1 and KFA4 have relationships with one parameter (step width for KFA1 and stride length for KFA4). Contrariwise, the variations of three parameters have no effect on KFA3. Again, this study showed that stride length is the most influential parameter on the kinematic parameters, in second round comes the step width and in last place comes the foot progression angle.

Moreover, in this study it was found that the increase or decrease of a parameter (step width, stride length and progression angle) had a single effect. We noticed toeing-in and-out Increased the KFA2.

Table 2. Summary of significant changes in knee flexion angle relative to instructions to increase or decrease footprint parameters.

Kinematic feature	Step width		Stride length		Foot progression angle	
	narrower	wider	shorter	longer	Toe in	Toe out
KFA1	-	-	↑	↓	-	-
KFA2	↓	↑	↓	↑	↑	↑
KFA3	-	-	-	-	-	-
KFA4	↑	↓	-	-	-	-
Level:	increased		decreased			

5 Conclusion

The present study also brought new insight by testing changes of kinematic gait parameters (step width, stride length and foot progression angle), parameters not often taken into account in studies of the modification of walking to reduce the knee moment adduction [14, 16–19].

A limitation in this study was that the tests were carried out on healthy young subjects. It is not clear whether the visual instructions (step width, stride length and angle progression) will be respected during tests performed by older subjects or subjects with articular or neuronal pathologies, because these people have limitations of visual sensations, proprioception, stability and learning abilities.

In the future, the system can be extended to include other gait parameters and to autoadapt the instructions in order to bring the patient to predefined walking patterns. Future research could focus on patients with various conditions: OA [18, 19], amputation [20], ACL [21] or older subjects.

Acknowledgments. This study was partially funded by the Swiss government excellence scholarship for foreign scholar program (grant #2015.0742).

Author Contributions: Messrs. Favre, Bennour, Ulrich and Legrand each participated in conceptualization of the research study, acquisition, analysis, and interpretation of the data, and drafting of the manuscript. Dr. Jolles participated in analysis of the data and drafting of the manuscript. Messrs. Lamine and Romdhane participated in interpretation of the data and drafting of the manuscript.

References

1. Turnbull, G.I., Charteris, J., Wall, J.C.: A comparison of the range of walking speeds between normal and hemiplegic subjects. *Scand. J. Rehabil. Med.* **27**, 175–182 (1995)
2. Nelson, A.J., Zwick, D., Brody, S., Doran, C., Pulver, L., Rooz, G., et al.: The validity of the GaitRite and the Functional Ambulation Performance scoring system in the analysis of Parkinson gait. *NeuroRehabilitation* **17**, 255–262 (2002)

3. Camicioli, R., Licsis, L.: Motor impairment predicts falls in specialized Alzheimer care units. *Alzheimer Dis. Assoc. Disord.* **18**, 214–218 (2004)
4. Toole, T., Maitland, C.G., Warren, E., Hubmann, M.F., Panton, L.: The effects of loading and unloading treadmill walking on balance, gait, fall risk, and daily function in Parkinsonism. *NeuroRehabilitation* **4**, 307–322 (2005)
5. Lin, P.Y., Yang, Y.R., Cheng, S.J., Wang, R.Y.: The relation between ankle impairments and gait velocity and symmetry in people with stroke. *Arch. Phys. Med. Rehabil.* **87**, 562–568 (2006)
6. McDonough, A.L., Batavia, M., Chen, F.C., Kwon, S., Ziai, J.: The validity and reliability of the GAITRite system's measurements: A preliminary evaluation. *Arch. Phys. Med. Rehabil.* **82**, 419–425 (2001)
7. Webster, K.E., Wittwer, J.E., Feller, J.A.: Validity of the GAITRite walkway system for the measurement of averaged and individual step parameters of gait. *Gait Posture* **22**, 317–321 (2005)
8. Bilney, B., Morris, M., Webster, K.: Concurrent related validity of the GAITRite® walkway system for quantification of the spatial and temporal parameters of gait. *Gait Posture* **17**, 68–74 (2003)
9. Menz, H.B., Latt, M.D., Tiedemann, A., Mun, S.K.M., Lord, S.R.: Reliability of the GAITRite® walkway system for the quantification of temporo-spatial parameters of gait in young and older people. *Gait Posture* **20**, 20–25 (2004)
10. Thorpe, D.E., Dusing, S.C., Moore, C.G.: Repeatability of temporo-spatial gait measures in children using the GAITRite electronic walkway. *Arch. Phys. Med. Rehabil.* **86**, 2342–2346 (2005)
11. Hulet, C., Hurwitz, D.E., Andriacchi, T.P., Galante, J.O., Vielpeau, C.: Functional gait adaptations in patients with painful hip. *Rev. Chir. Orthop. Reparatrice Appar. Mot.* **86**, 581–589 (2000)
12. Barrios, J.A., Crossley, K.M., Davis, I.S.: Gait retraining to reduce the knee adduction moment through real-time visual feedback of dynamic knee alignment. *J. Biomech.* **43**, 2208–2213 (2010)
13. Hunt, M.A., Simic, M., Hinman, R.S., Bennell, K.L., Wrigley, T.V.: Feasibility of a gait retraining strategy for reducing knee joint loading: increased trunk lean guided by real-time biofeedback. *J. Biomech.* **44**, 943–947 (2011)
14. Shull, P.B., Lurie, K.L., Cutkosky, M.R., Besier, T.F.: Training multi-parameter gaits to reduce the knee adduction moment with data-driven models and haptic feedback. *J. Biomech.* **44**, 1605–1609 (2011)
15. Heeren, A., van Ooijen, M., Geurts, A.C., Day, B.L., Janssen, T.W., Beek, P.J., Roerdink, M., Weerdesteyn, V.: Step by step: a proof of concept study of C-Mill gait adaptability training in the chronic phase after stroke. *J. Rehabil. Med.* **45**(7), 616–622 (2013)
16. Lynn, S.K., Kajaks, T., Costigan, P.A.: The effect of internal and external foot rotation on the adduction moment and lateral-medial shear force at the knee during gait. *J. Sci. Med. Sport* **11**, 444–451 (2008)
17. Anthony, G.S., Benjamin, J.F., Kay, M.C., Rana, S.H., Marcus, G.P.: The effect of gait modification on the external knee adduction moment is reference frame dependent. *Clin. Biomech.* **23**, 601–608 (2008)
18. Russell, E.M., Braun, B., Hamill, J.: Does stride length influence metabolic cost and biomechanical risk factors for knee osteoarthritis in obese women? *Clin. Biomech.* **25**, 438–443 (2010)
19. Favre, J., Erhart-Hledik, J.C., Chehab, E.F., Andriacchi, T.P.: A general scheme to reduce the knee adduction moment by modifying a combination of gait variables. *J. Orthop. Res.* **34** (9), 1547–1556 (2016)

20. Yang, L., Dyer, P.S., Carson, R.J., Webster, J.B., Bo Foreman, K., Bamberg, S.J.: Utilization of a lower extremity ambulatory feedback system to reduce gait asymmetry in transtibial amputation gait. *Gait Posture* **36**, 631–634 (2012)
21. Dowling, A.V., Favre, J., Andriacchi, T.P.: Inertial sensor-based feedback can reduce key risk metrics for anterior cruciate ligament injury during jump landings. *Am. J. Sports Med.* **40**, 1075–1083 (2012)

Cable Robots

Comprehensive Dynamic Study of an Unloaded Walking Within a Cable-Based Gait Trainer

Houssein Lamine¹(✉), Sami Bennour¹, and Lotfi Romdhane^{1,2}

¹ Mechanical Laboratory of Sousse (LMS), National Engineering School of Sousse, University of Sousse, 4000 Sousse, Tunisia
houssein.lamine@gmail.com, sami.bennour@gmail.com,
lotfi.romdhane@gmail.com

² Mechanical Engineering Department, American University of Sharjah, PO Box 26666, Sharjah, United Arab Emirates

Abstract. In this paper, we investigate an inverse dynamic study of an upright unloaded walking. This motion is produced through a gait training machine that emulates the overground walking through: a body weight support device and a cable driven legs trainer. The input motion is the kinematics of a normal gait and the output information is the required actuation wrench to drive the lower limb during gait simulation. The dynamic study is carried out using two methods: Newton-Euler approach and Matlab SimMechanics model. The effect of gait simulation parameters on the behaviour of the actuation wrench is discussed. These results are very useful in estimating optimal gait training parameters and also to design the gait trainer.

Keywords: Gait training · Partial unloaded walking · Newton-Euler · Matlab SimMechanics

1 Introduction

Human gait simulation has been widely investigated in various applications: design of humanoid robot, identification of gait anomalies, therapy designing for impaired subjects, enhance performance of able-bodies, design of orthoses and prosthetics [1–3] ...

In our case, we are interested to the design of a gait training machine called the Cable Driven Legs Trainer (CDLT). Such devices are used to rehabilitate subjects having a gait disorders. Gait rehabilitation consists in the simulation of walking motion within robotized machines. Intense and task-specific practice of the gait stepping motion allows to recover independent over-ground walking [4].

Our first objective is to conduct an inverse dynamic simulation of a gait within the CDLT. The input motion is the kinematics of a normal gait and the target output information is the required wrench to move the lower limb during a gait cycle. This dynamic study is achieved using two methods: Newton-Euler approach [5] and Matlab SimMechanics model. Afterwards, the second purpose is to study the effect of some gait simulation parameters on the actuation wrench, every parameter is varied in turn and its effect is discussed. Further, two simulation scenarios are presented: on ground and off-ground walking.

The paper is organized as follows. In Sect. 2, a dynamic modeling of the human body is presented. Then, free-body diagram and dynamic equations are given in Sect. 3. A dynamic simulation using MATLAB Simmechanics is investigated in Sect. 4. In the last Sect. 5, the results of a case study using the two simulation approaches are shown. Further, the effect of gait simulation parameters on the actuation wrench is discussed.

2 Dynamic Modeling

The CDLT is a cable robot-based gait training machine shown in Fig. 1. It includes: (i) a Body Weight Support Device (BWSD) to suspend the patient in vertical posture while applying a certain amount of unloading, (ii) a Cable Driven Legs Manipulator (CDLM) to move the lower limb in the sagittal plane through the leg’s orthosis, which is controlled by four cables and (iii) a Treadmill to emulate the forward movement of walking.

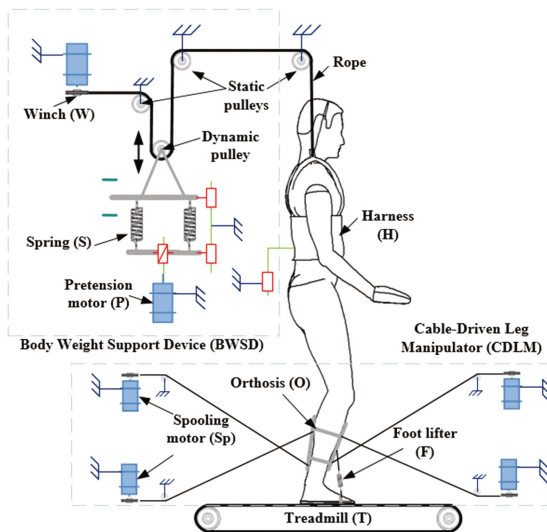


Fig. 1. Diagram of the Cable Driven Legs Trainer (CDLT)

As depicted in Fig. 2(a), the body is represented by a planar four-link mechanism: the upper body (known also as HAT segment [6]), the thigh, the leg and the foot. The linkage between the trunk and the fixed frame is modeled as a prismatic joint. For the hip, knee and ankle, they are modeled as revolute joints.

Based on anthropometric specifications [7], length and inertia specifications of each segment are written in function of the mass m and/or the height h of the body (see Fig. 2).

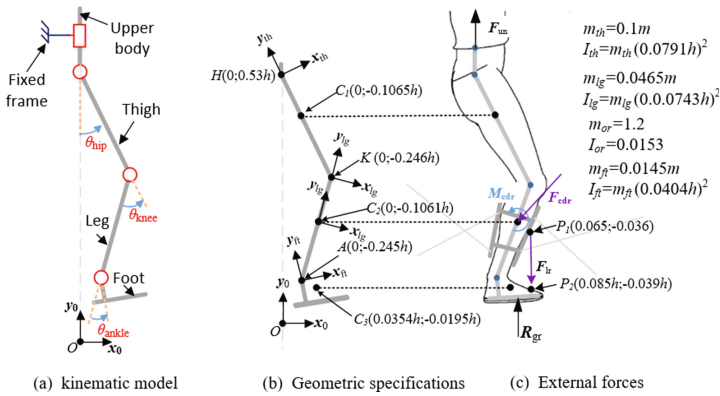


Fig. 2. Dynamic modeling of the human body (SI unit)

It is substantial to mention that the following assumptions were made: (i) All the joints are considered passive, (ii) No relative motion between the orthosis and the leg and (iii) Lower limb kinematics are the same as during normal walking. Hereafter, the main external loads acting on the human body are (Fig. 2(c)): F_{un} , the unloading force produced by the BWS, R_{gr} , the ground reaction force applied at the sole of the foot, F_{lr} , the footlifter force acting between the leg’s orthosis and the foot which can be neglected and, F_{cdr} and M_{cdr} , the resultant force and moment, which are the actuation unknowns of the inverse dynamic simulation.

3 Newton-Euler Approach

One shall note that the equilibrium equations are written in relation to the CoM of each segment, thus moments of the weight forces are zero. Furthermore, the transmitted torque from one segment to another is regarded as zero since the joints are assumed to be passive.

The free-body diagram of the human body is shown in Fig. 3. It depicts all exerting forces on the upper body, the thigh, the leg and the foot.

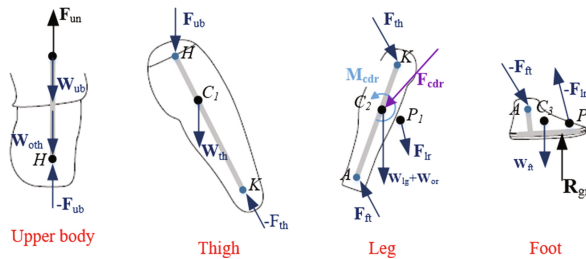


Fig. 3. Free-body diagrams of body segments

The upper body is assumed to be translating along the vertical direction and it is subjected to: the unloading force \mathbf{F}_{un} , the upper body weight \mathbf{W}_{ub} , the thigh force \mathbf{F}_{th} and the thigh weight of the opposite lower limb:

$$\mathbf{F}_{un} - (1/\alpha) \cdot \mathbf{F}_{ub} + \mathbf{W}_{ub} + \mathbf{W}_{oth} = (m_{ub} + m_{th}) \cdot \mathbf{a}_{ub} \quad (1)$$

Note, we consider that the opposite leg and foot are balanced by the opposite orthosis. In addition, the unloading force is computed based on: body mass m , spring constant K , the gravity intensity g , the amount of unloading BWS and the vertical motion y_0 :

$$\mathbf{F}_{uny} = (k/2) \cdot (y_0 + \Delta y/2) \text{ such that } y_0 = (BWS \cdot g \cdot m)/(k/2) \quad (2)$$

Further, α is a coefficient that defines the participation of one limb to support the body weight (Fig. 4): α is equal to 1 during single limb stance and zero during swing time. Throughout double support phases, it varies from 0 to 1 based on the ratio between left and right vertical reaction of the feet: $\alpha = (NRv_{right} + NRv_{left})/NRv_{right}$.

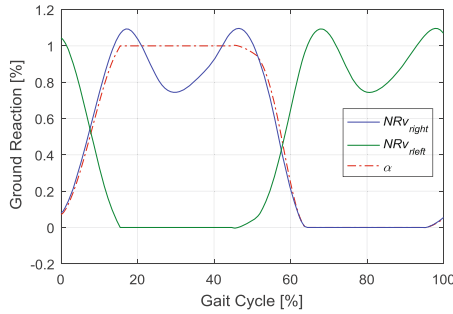


Fig. 4. Curve of α coefficient.

Forces applied on the thigh are: the upper body force \mathbf{F}_{ub} , the thigh weight \mathbf{W}_{th} , and the force of the leg $-\mathbf{F}_{th}$:

$$\begin{aligned} \mathbf{F}_{ub} - \mathbf{F}_{th} + \mathbf{W}_{th} &= m_{th} \cdot \mathbf{a}_{th} \\ \mathbf{M}_{ub} - \mathbf{M}_{th} &= I_{th} \cdot \dot{\omega}_{th} \end{aligned} \quad (3)$$

For the foot segment, exerting forces are: the ground reaction force \mathbf{R}_{gr} , the foot weight \mathbf{W}_{ft} , the thigh force $-\mathbf{F}_{ft}$ and the foot-lifter force \mathbf{F}_{lr} .

$$\begin{aligned} -\mathbf{F}_{ft} - \mathbf{F}_{lr} + \mathbf{R}_{gr} + \mathbf{W}_{ft} &= m_{ft} \cdot \mathbf{a}_{ft} \\ -\mathbf{M}_{ft} - \mathbf{M}_{lr} + \mathbf{M}_{gr} &= I_{ft} \cdot \dot{\omega}_{ft} \end{aligned} \quad (4)$$

The ground reaction is calculated based on the normalized ground reaction (see Fig. 5(b)):

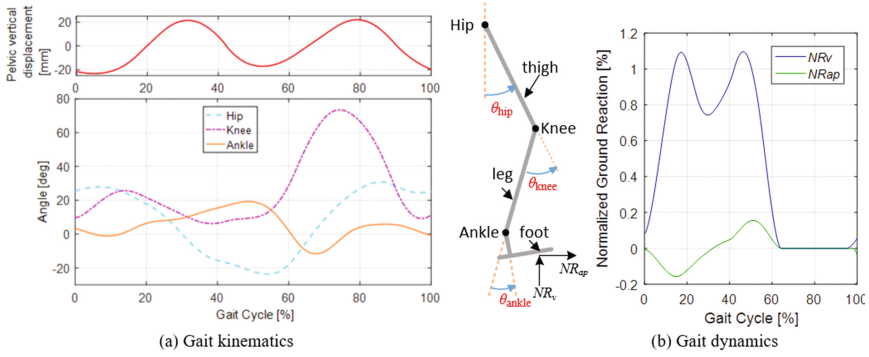


Fig. 5. Gait kinematics and dynamics

$$\mathbf{R}_{gr} = \mathbf{W}_n \cdot \mathbf{NR}_{gr} \text{ such that } \mathbf{W}_n = m \cdot g - F_{uny} \text{ and } \mathbf{NR}_{gr} = (\mathbf{NR}_v \quad \mathbf{NR}_{ap})^T \quad (5)$$

Considering the leg segment, its equilibrium is marked by the term of the actuation wrench \mathbf{F}_{cdr} and \mathbf{M}_{cdr} :

$$\begin{aligned} \mathbf{F}_{th} + \mathbf{F}_{ft} + \mathbf{W}_{lg} + \mathbf{W}_{or} + \mathbf{F}_{lr} + \mathbf{F}_{cdr} &= (m_{lg} + m_{or}) \cdot \mathbf{a}_{lg} \\ \mathbf{M}_{th} + \mathbf{M}_{ft} + \mathbf{M}_{lr} + \mathbf{M}_{cdr} &= (\mathbf{I}_{lg} + \mathbf{I}_{or}) \cdot \dot{\boldsymbol{\omega}}_{lg} \end{aligned} \quad (6)$$

The investigated Newton-Euler equations are solved recursively as follows: the upper body, the thigh, the foot and finally the leg in order to get the actuation wrench.

One shall note that linear and angular accelerations are obtained by numerical derivation of the pose equations of body segments using the kinematics of a normal gait (see Fig. 5(a)).

4 Matlab SimMechanics Model

In this section, we present the manner through which the inverse dynamic problem is conducted employing MATLAB SimMechanics Software.

The first step in model development is the creation of body parts and the definition of joints. The developed SimMechanics model is shown in Fig. 6. As well as the kinematic model of Fig. 2: the “Upper body” has a prismatic joint with the fixed frame “Base” and the body segments (“Upper Body”, “Thigh”, “Leg + Orthosis” and “Foot”) are articulated with 3 revolute joint blocks: “Hip joint”, “Knee joint” and “Ankle joint”. Moreover, geometric and inertia specifications are, carefully, written into body blocks.

Next, the external forces are applied according to the formulation investigated in Sect. 3. The unloading force “ F_{un} ” is computed in the block “BWS” in relation to a desired unloading “BWS” using Eq. (2). Knowing the position of placement points P_1 and P_2 , The footlifter force “ F_{lr} ” is computed based on moment equilibrium of the foot weight about the ankle joint. The ground reaction force “ R_{gr} ” is computed using Eq. (5) and it is applied on the foot segment. Lastly, by inputting the curve of α

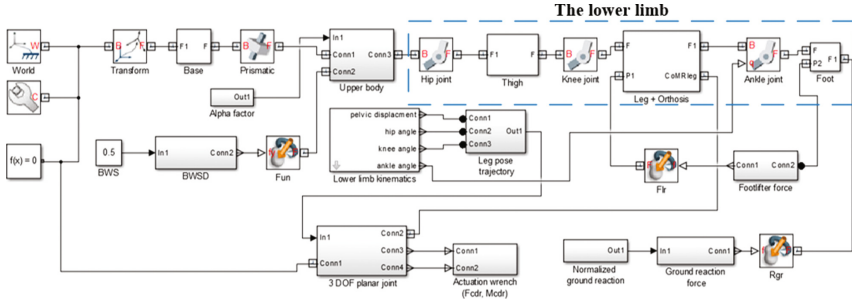


Fig. 6. Matlab SimMechanics model

coefficient (Fig. 4), the action of the upper body force on the thigh is computed inside the block “Upper body”.

Lastly, in order to obtain the actuation wrench, the used method is to actuate the lower limb through an active joint “3 DOF planar joint” placed at the leg center of mass, for the other joints, they are kept passive. This custom joint has two linear and one rotational DOFs taking place in the sagittal plane. The data of the block “Lower limb kinematics” are fed to the block “leg pose trajectory”, in which the leg trajectory is computed using the gait kinematics (Fig. 5(a)) and then sent to the leg segment for actuation.

By running the simulation, the actuation wrench (\mathbf{F}_{cdr} , \mathbf{M}_{cdr}) is computed inside the “3 DOF planar joint” block and this information is collected from the block “Actuation wrench (Fcdr, Mcdr)”.

5 Results and Discussion

For illustration, we consider the example of a body having a mass $m = 100$ kg and a tall $h = 1.7$ m. Based on anthropometric specifications presented in Fig. 2, all the geometric and inertia data were obtained. Furthermore, the amount of unloading is $BWS = 50\%$ and the gait cycle time is $tc = 1.5$ s. Figure 7 visualizes the curves of the actuation wrench using the two solving approaches, i.e., Newton-Euler equations (N-E) and SimMechanics model (SM). Results of both approaches are consistent, only few differences can be observed.

In the sequel, the effect of varying the gait training parameters (tc , m , h , BWS) will be discussed. Figure 8 shows the curves of actuation wrench while the training parameters are varied: time of gait cycle ($tc = 1.0$ s, 1.5 s and 2.0 s), body mass ($m = 80$ kg, 100 kg and 120 kg), body height ($h = 1.5$ m, 1.7 m and 1.9 m) and unloading percentage ($BWS = 30\%$, 50% and 70%). Note, each parameter is varied each time, and the others are kept for the following values ($tc = 1.5$ s, $m = 100$ kg, $h = 1.7$ m, $BWS = 50\%$).

Observing the effect tc , the actuation wrench components increases as well as the walking speed, note that gait cycle time is scaled to 100% since the duration is in relation to the tc . Also the same remark can be concluded for the raise of the body

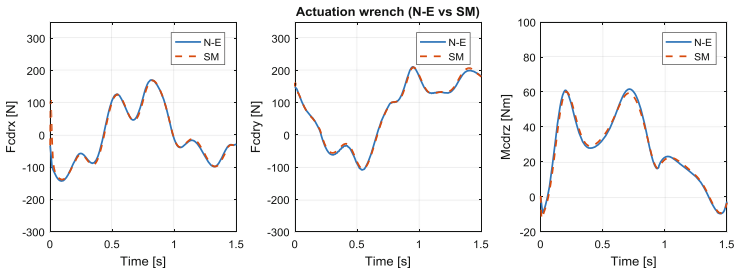


Fig. 7. Curves of the actuation wrench during on-ground walking using Newton-Euler and SimMechanics

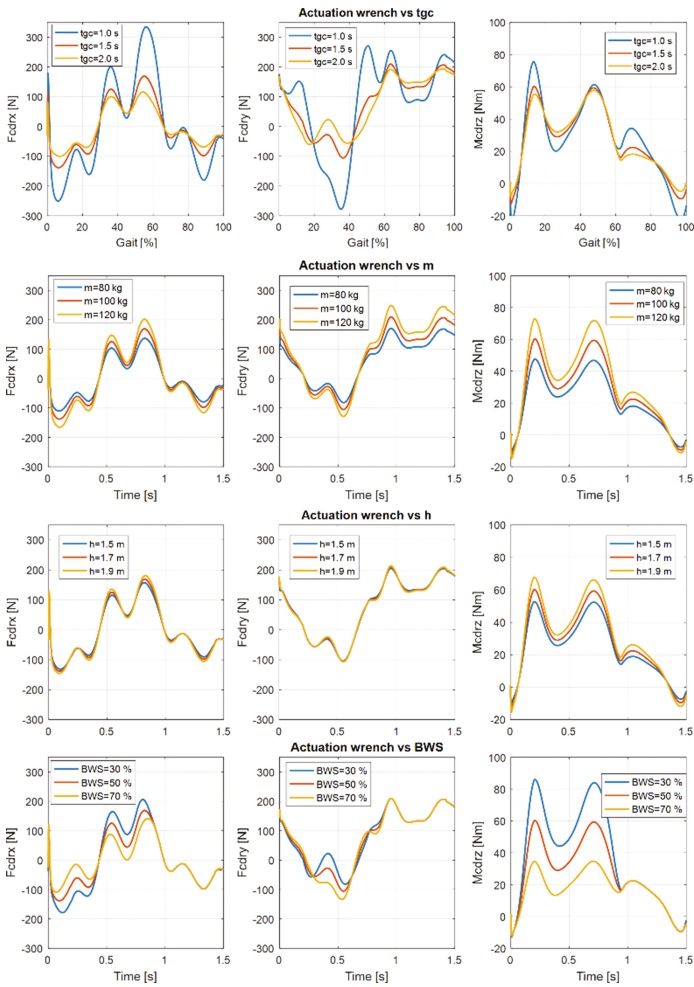


Fig. 8. Curves of actuation wrench in response to variation of gait training parameters

mass m . the latter observations confirms that mass and acceleration are determinant factors in dynamics. Considering the impact of changes in the body tall h , F_{cdrx} increases slightly and F_{cdry} is practically invariant, only M_{cdrz} varies little remarkably in response to height augmentation. Now examining the effect of the weight unloading BWS , F_{cdry} is almost remaining unchanged, in contrast, F_{cdrx} rises notably and M_{cdrz} increases greatly. For the last case, one can observe that the wrench is exactly the same during the swing phase ($t > 0.9$ s) since the current lower limb is above the ground, thus there is no unloading.

Moreover, it is worth mentioning that for gait training, two scenarios are involved: the off-ground and the on-ground walking. The first happens at the beginning of a training session when some cycles of an off-ground walking are achieved for familiarization. Afterward, the on-ground walking occurs.

One may remark that over the swing phase ($t > 0.9$ s), the on-ground and off-ground curves have almost the same behavior since in both simulations the limb is above the ground. The pelvic motion, which is only active for the on-ground case, induces a small difference between the two curves. When comparing both actuation moments M_{cdrz} , it is clear that the required torque is higher for the on-ground walking due to the need to resist the effect of the ground reaction. Conversely, F_{cdrx} isn't sensitive to the ground reaction. In addition, for the off-ground case, the F_{cdry} component is always positive, an upward force is required to maintain the leg in the air. Therefore, this force is more influenced by the off-ground walking (Fig. 9).

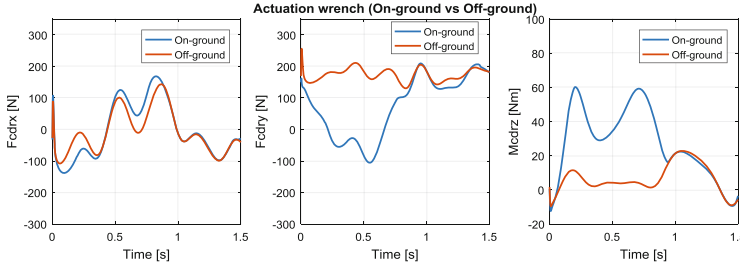


Fig. 9. Curves of actuation wrench for on-ground and off-ground walking

The obtained results are very helpful for clinicians in estimating the optimal gait training parameters. Some effects may be estimated, for example the effect of the BWS amount or the gait speed on muscular activity [8], or also their effects on patient with Knee Osteoarthritis [9]. In addition, results will be used in the design of the CDLT.

6 Conclusions

A dynamic analysis of an unloaded walking within the CDLT was investigated and described. The target information was the wrench required to drive the lower limb. Two approaches were implemented to solve the dynamic problem: Newton-Euler and

SimMechanics model. The gait simulation parameters: walk speed, body weight, patient tall and unloading amount are varied in order to observe their influence on the curves of the actuation wrench. Furthermore, the effect of the on-ground and off-ground walking are also presented.

Ongoing works are carried out to the development of musculoskeletal models, which allows to estimate activity or contribution of muscles. In addition, development of foot–ground contact model is very essential for a precise prediction of intersegmental forces.

References

1. Teachasrisaksakul, K., Zhang, Z., Yang, G.-Z., Lo, B.: Imitation of dynamic walking with BSN for humanoid robot. *IEEE J. Biomed. Heal. Inform.* **19**(3), 794–802 (2015)
2. Rajagopal, A., Dembia, C.L., DeMers, M.S., Delp, D.D., Hicks, J.L., Delp, S.L.: Full-body musculoskeletal model for muscle-driven simulation of human gait. *IEEE Trans. Biomed. Eng.* **63**(10), 2068–2079 (2016)
3. Shourijeh, M.S., McPhee, J.: Foot–ground contact modeling within human gait simulations: from Kelvin-Voigt to hyper-volumetric models. *Multibody Syst. Dyn.* **35**(4), 393–407 (2015)
4. Benito-Penalva, J., Edwards, D.J., Opisso, E., Cortes, M., Lopez-Blazquez, R., Murillo, N., Costa, U., Tormos, J.M., Vidal-Samsó, J., Valls-Solé, J., et al.: Gait training in human spinal cord injury using electromechanical systems: effect of device type and patient characteristics. *Arch. Phys. Med. Rehabil.* **93**(3), 404–412 (2012)
5. Tözeren, A.: *Human Body Dynamics: Classical Mechanics and Human Movement*. Springer Science & Business Media, New York (2000)
6. Zajac, F.E., Neptune, R.R., Kautz, S.A.: Biomechanics and muscle coordination of human walking: part i: introduction to concepts, power transfer, dynamics and simulations. *Gait Posture* **16**(3), 215–232 (2002)
7. Winter, D.A.: *Biomechanics and Motor Control of Human Movement*. Wiley, Hoboken (2009)
8. Van Kammen, K., Boonstra, A., Reinders-Messelink, H., den Otter, R.: The combined effects of body weight support and gait speed on gait related muscle activity: a comparison between walking in the Lokomat exoskeleton and regular treadmill walking. *PLoS ONE* **9**(9), e107323 (2014)
9. Watanabe, S., Someya, F.: Effect of body weight-supported walking on exercise capacity and walking speed in patients with knee osteoarthritis: a randomized controlled trial. *J. Japanese Phys. Ther. Assoc.* **16**(1), 28–35 (2013)

A Cable-Driven Robot for Upper Limb Rehabilitation Inspired by the Mirror Therapy

Lukas Tappeiner¹, Erika Ottaviano², and Manfred L. Husty¹(✉)

¹ Unit Geometry and CAD, University of Innsbruck,
Technikerstraße 13, 6020 Innsbruck, Austria

Lukas.Tappeiner@student.uibk.ac.at, manfred.husty@uibk.ac.at

² Department of Civil and Mechanical Engineering,
University of Cassino and Southern Lazio, Cassino, Italy
ottaviano@unicas.it

Abstract. The paper presents the development of a mechatronic system composed by a cable-driven robot and a vision system to be used for upper limb rehabilitation. It is inspired by the mirror therapy that is a valuable method for enhancing motor recovery in post stroke hemiparesis making use of the mirror-illusion created by the movement of a sound limb that is perceived as the paretic limb. In particular, a software has been developed and it is able to acquire images of a target, i.e. the hand of an individual, and after image processing, reproduces the target movement by a cable-driven manipulator. More specifically, the end-effector of the manipulator can be fixed to the paralyzed hand of the individual. The development of a planar 4-2 cable-driven parallel robot by low-cost mechanical design and easy control can be effective for the home-care of individuals for continuous training and recovering. First experimental tests are provided to show the feasibility of the system.

Keywords: Cable-driven parallel robot · Rehabilitation · Mechatronics

1 Introduction

Stroke is the leading cause of disability among adults in developed countries and leaves a significant number of individuals with motor, cognitive, or language deficits. The paralysis of the upper limb is the most frequent consequence of brain injury, and very often the rehabilitation procedures deal with repetitive passive movements, with the aim to restore if possible the damaged functions, or alternatively to teach how to handle differently those functions.

Although for long time it was assumed that after a brain injury, a patient has 3 to 6 months for maximizing the effects of recovery, recent studies show that a long-term stroke rehabilitation has very positive benefits to individuals in the chronic stage of stroke [15]. Intensive stroke rehabilitation is associated with enhanced and faster improvements, in particular, the intensity of exercise therapy has great effect on daily-life, gait, and dexterity in patients with stroke [9]. In addition daily practice sessions can significantly improve complex motor tasks [6, 7].

Modern rehabilitation therapy is in the most cases supported by technical systems. The Mirror Therapy (MT) induces a visual illusion that appears to mimic the movement of the paretic part [4, 13] in which the perception, more than being a simple feedback mechanism, enhance motor recovery of the impaired part [1, 2].

In recent years, Robotics has been applied to rehabilitation [11] and assistive tasks, as in [8, 12]. In the end-effector devices, the hand or the whole human forearm is fixed on an end-effector of a robot, either made of rigid links as in [5], or operated by cables [11]. The exoskeletal devices encloses the shoulder, the elbow and the hand and allows a better guidance of all articulations of the upper limb [10]. Another classification deals with the use of both upper limbs (bimanual) or the use of the affected part only (unilateral). In this paper we present the design and operation of a cable-driven robot, which has been inspired by the MT, for long-term stroke rehabilitation to be performed daily at home having bimanual characteristics. In particular, the motion of the unaffected upper limb is followed by a camera and reproduced by a cable robot that drives the affected upper limb. The paper is organized as follows: in Sect. 2, the design of a cable-driven robot is described with the motion capture system, Sect. 3 reports experimental set-up and tests, finally conclusions are outlined.

2 The Design of a Cable-Driven Robot RehaBot

The system proposed is a cable driven robot that acts in a plane, so that it can be used for a planar mirror therapy. The robot Fig. 1 consists of a frame, which is of rectangular shape, four stepper motors connected to the rectangular end effector board via four cables. The motion of the non-paralyzed limb should be transferred to the paralyzed limb. Therefore, the robot guides the paralyzed arm on a trajectory, which is the mirrored trajectory of the non-paralyzed limb. A motion capturing system is used to observe the motion of the non-paralyzed arm. This robot can be classified as a proximal, bimanual end-effector robot.

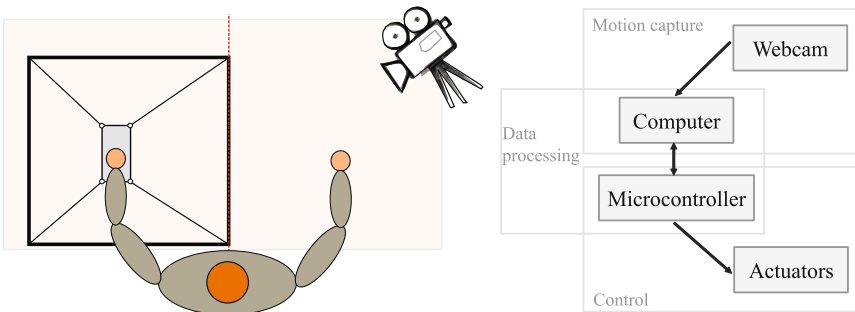


Fig. 1. Basic principle of the cable-driven robot for rehabilitation tasks: (a) lay-out; (b) scheme.

2.1 A Model for the Cable-Driven Robot

Let us consider a cable-driven manipulator with m cables and n DOFs in Fig. 2, and denote with $OXYZ$ a global reference frame attached to the fixed base, and a reference frame is attached to the moving platform at point K .

A commonly used model for the kinematic analysis is based on the assumption of mass less inextensible cables, with the hypothesis that they are always in tension and can thus be treated as line segments representing bilateral constraints.

Inverse kinematics consists in computing the vector connecting each cable attachment point \mathbf{A}_i , to the ending point of the cable attached to the mobile platform \mathbf{B}_i . Vectors \mathbf{B}_i are given in the K reference frame and \mathbf{A}_i are given in the O coordinate frame. ${}^O\mathbf{R}_K$ is the rotation matrix between the two frames.

The vectors representing the cable lengths can be evaluated in the form

$${}^O\mathbf{l}_i = {}^O\mathbf{A}_i - ({}^O\mathbf{R}_K {}^K\mathbf{B}_i + {}^O\mathbf{r}) \tag{1}$$

The Jacobian matrix associated to the Inverse Kinematics can be written as

$$\mathbf{J} = \begin{pmatrix} \hat{\mathbf{l}}_1^T & -(\hat{\mathbf{l}}_1^T \times \mathbf{R}_K {}^K\mathbf{B}_1)^T \\ \hat{\mathbf{l}}_2^T & -(\hat{\mathbf{l}}_2^T \times \mathbf{R}_K {}^K\mathbf{B}_2)^T \\ \vdots & \vdots \\ \hat{\mathbf{l}}_m^T & -(\hat{\mathbf{l}}_m^T \times \mathbf{R}_K {}^K\mathbf{B}_m)^T \end{pmatrix} \tag{2}$$

$\hat{\mathbf{l}}_i^T$ being the transpose of the unity vector in cable directions.

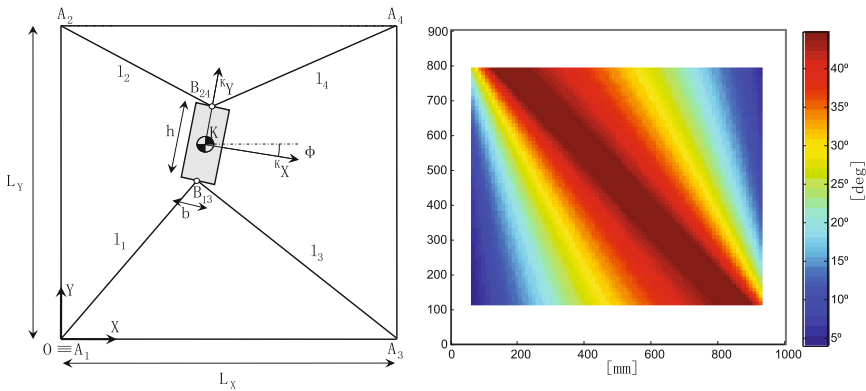


Fig. 2. A scheme for the kinetostatic analysis and workspace of the 4-2 planar cable-driven robot.

The Jacobian is a linear mapping between the rotation and translation velocity of the end effector and the joint velocities, The transpose of \mathbf{J} in Eq. 2 maps the cable forces \mathbf{t} to the external forces \mathbf{F} and torques \mathbf{M} and it is used to check the cables forces distribution, and the static equilibrium for each pose, i.e. all tensions must be strictly positive [3]. The resulting robot work-space is shown in Fig. 2 (right).

$$\mathbf{J}^T = \begin{pmatrix} t_1 \\ t_2 \\ \vdots \\ t_m \end{pmatrix} = \begin{pmatrix} \mathbf{F} \\ \mathbf{M} \end{pmatrix} \quad (3)$$

2.2 Motion Capture System

The motion capture system is based on a single camera and an optical marker. The camera stream is analyzed to find the optical marker. The result is filtered by Kalman, which has been implemented for this application. Then, the motion is computed by solving a back-projection problem using homography, which is fundamental for the motion capturing system of the robot [14]. It is a planar cable-driven robot, and for the motion capturing, a single camera is used. Therefore, the constraints of the homography are satisfied without the knowledge of the intrinsic and the extrinsic parameters. Detailed description is reported in [14].

2.3 Control and programming

Basic idea for the development of the control strategy is inspired by the principles of the mirror therapy, in particular using the master-slave principle. The trajectory is given by tracking a marker fixed on the unaffected body part (the hand) that acts as target. Then the end-effector of the cable-robot corresponds to the slave with the task of following the mirrored configuration of the master, as shown in Fig. 3. When the master moves, then the slave forces the paralyzed hand fixed to it to follow the mirrored trajectory. Therefore, knowing the pose of the marker fixed to the non-paralyzed hand from the motion capturing system, through the actuation and control of the system, the end-effector is driven on the mirrored trajectory. The blue marker is the master with vector \mathbf{r}_m . A “virtual end-effector” is

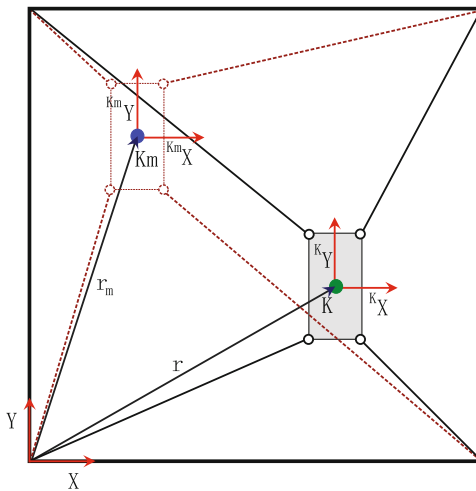


Fig. 3. Principle of control

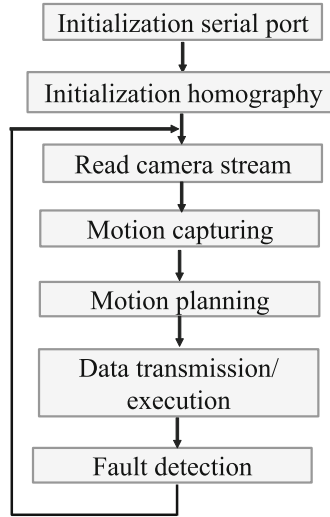


Fig. 4. A scheme of the operations of the rehabilitation cable-robot.

considered to evaluate cable lengths l_{mi} indicated by dashed lines in the Fig. 3. The cable lengths of the slave are in an actual pose l_{si} . Knowing the real lengths of the cables of the end-effector, we know the lengths, which the end effector has in the position of the master. Therefore, the information is used to drive the motors to the target position, i.e. the mirrored position of the master.

The control of the system is performed using a master-slave principle. The position of the hand is tracked. This defines the position, which the end effector has to reach. Moving the hand causes an offset between the end effector and the master. This offset is used to calculate the steps that each stepper motor has to drive. A scheme of the rehabilitation robot operations is given in Fig. 4. Figure 5 shows a scheme for the robot connections. It has to be mentioned that the motion

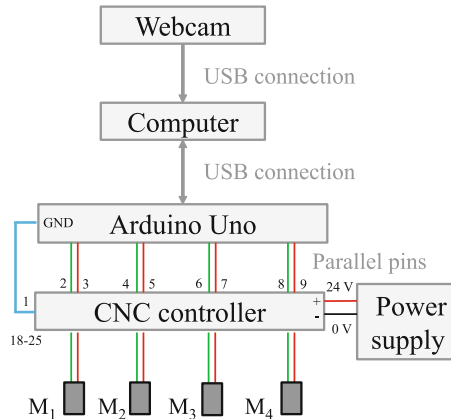


Fig. 5. A scheme of connections for the rehabilitation cable-robot.

of the non-paralyzed hand should not interfere with the robot frame during the rehabilitation task. Therefore, the rehabilitation robot will be designed according to Fig. 1 to avoid collisions, interference, and cables wrapping. In this paper we have used an available prototype, as it will be shown in Sect. 3.

3 Experimental Tests

Experimental tests were carried out with an available laboratory prototype as shown in Fig. 6. In particular, given trajectories were reproduced i.e. a circle

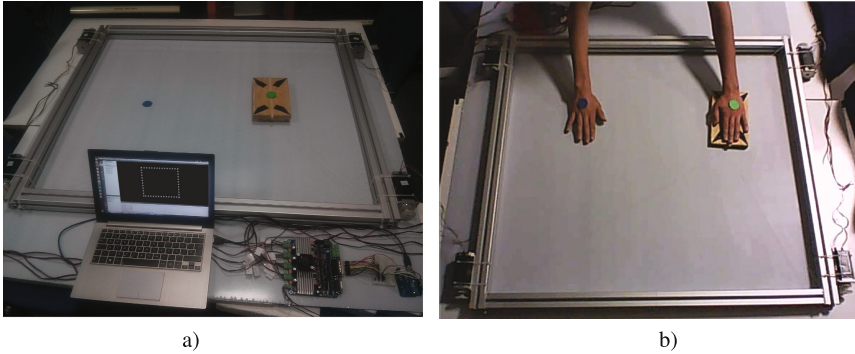


Fig. 6. Experimental tests: (a) laboratory set-up; (b) mirrored trajectory

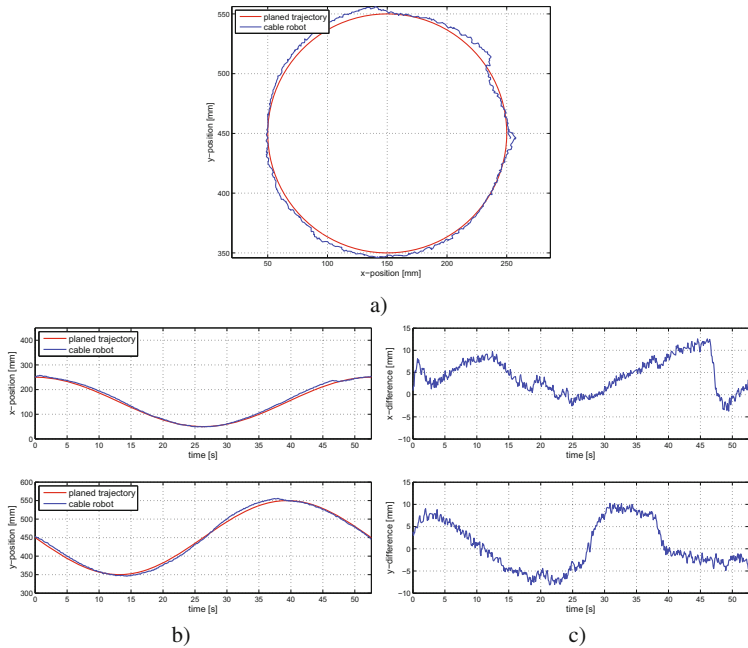


Fig. 7. Experimental tests: (a) master (red) slave (blue) trajectories; (b) x and y components; (c) differences between master and slave. (Color figure online)

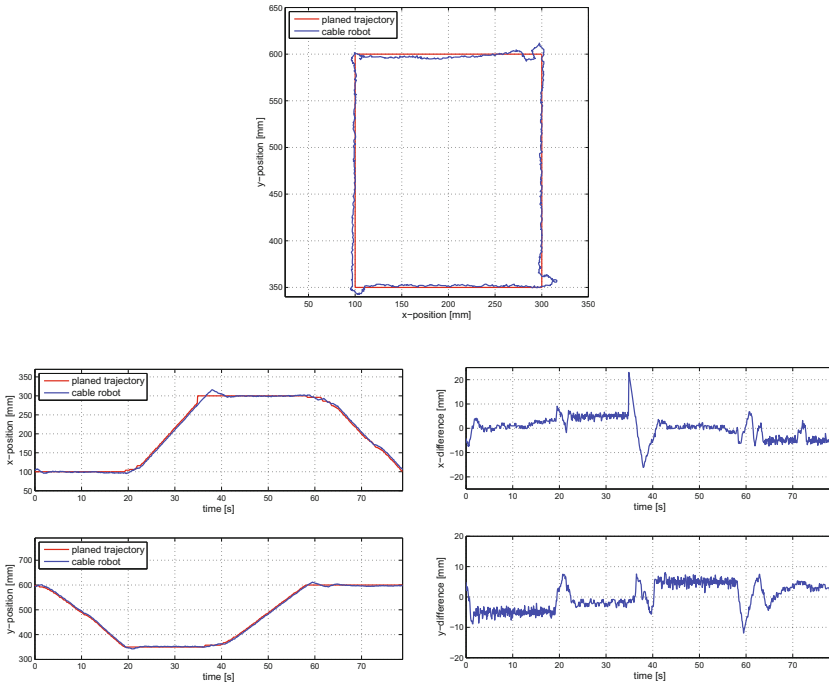


Fig. 8. Experimental tests: (a) master (red) slave (blue) trajectories; (b) x and y components; (c) differences between master and slave. (Color figure online)

and a square, as shown in Figs. 7 and 8. Nevertheless, a set of experiments have been performed also with natural trajectories and that the associated motion was followed precisely. In particular, during the experiments, the trajectories of the master in red, and the slave in blue, were recorded for further analysis.

Data processing allows evaluating differences in trajectories giving a measure of the repeated exercises for continuous training and verification of recovery.

4 Conclusions

In this paper, we presented the mechatronic design and implementation of a rehabilitation system based on a cable-driven manipulator inspired by the mirror therapy. Experimental tests showed encouraging performance of the system developed for the home-care and continuous training during the upper limb rehabilitation.

Acknowledgements. The first author spent a period of study at the University of Cassino and Southern Lazio within the ERASMUS + program 2015–2016 for developing a Laboratory training and his Master Thesis.

References

1. Arya, K.: Underlying neural mechanisms of mirror therapy: implications for motor rehabilitation in stroke. *Neurol. India* **64**, 38–44 (2016)
2. Arya, K., Pandian, S., Kumar, D., Puri, V.: Task-based mirror therapy augmenting motor recovery in poststroke hemiparesis: a randomized controlled trial. *Jnl. Stroke Cerebrovasc Dis.* **24**(8), 1738–1748 (2015)
3. Bruckmann, T., Mikelsons, L., Brandt, T., Hiller, M., Wire, S.D., Robots Part, I., Kine-matics, A.: Wire Robots Part I Kinematics, Analysis & Design, Parallel Manipulators, New Development, pp. 109–132. InTech, Vienna (2008)
4. Grünert-Plüss, N., Hufschmid, U., Santschi, L., Grünert, J.: Mirror therapy in hand rehabilitation: a review of the literature, the St. Gallen protocol for mirror therapy and evaluation of a case series of 52 patients. *The British. J. Hand Ther.* **13**(1), 4–11 (2008)
5. Hogan, N., Krebs, H.I., Charnnarong, J., Srikrishna, P., Sharon, A.: MIT-MANUS: a workstation for manual therapy and training I. In: *Proceedings IEEE International Workshop on Robot and Human Communication*, pp. 161–165 (1992)
6. Karni, A., Meyer, G., Jezard, P., Adams, M., Turner, R., Ungerleider, L.: Functional MRI evidence for adult motor cortex plasticity during motor skill learning. *Nature* **377**(6545), 155–8 (1995)
7. Krakauer, J.: Motor learning: its relevance to stroke recovery and neurorehabilitation. *Curr. Opin. Neurol.* **19**(1), 84–90 (2006)
8. Krishnan, R., Pugazhenthii, S.: Mobility assistive devices and self-transfer robotic systems for elderly, a review. *Intel. Serv. Robot.* **7**(37) (2014). doi:[10.1007/s11370-013-0142-6](https://doi.org/10.1007/s11370-013-0142-6)
9. Kwakkel, G., van Peppen, R., Wagenaar, R., Wood, D., Richards, C., Ashburn, A., Miller, K., Lincoln, N., Partridge, C., Wellwood, I., Langhorne, P.: Effects of augmented exercise therapy time after stroke: a meta-analysis. *Stroke* **35**(11), 2529–2539 (2004)
10. Mao, Y., Agrawal, S.K.: Design of a cable-driven arm exoskeleton (carex) for neural rehabilitation. *IEEE Trans. Robot.* **28**(4), 922–931 (2012)
11. Mayhew, D., Bachrach, B., Rymer, W.Z., Beer, R.F.: Development of the macarm - a novel cable robot for upper limb neurorehabilitation. In: *9th International Conference on Rehabilitation Robotics*, 2005, pp. 299–302 (2005)
12. Rea, P., Ottaviano, E., Castelli, G.: A procedure for the design of novel assisting devices for the sit-to-stand. *J. Bionic Eng.* **10**(4), 488–496 (2013)
13. Rothgangel, A., Braun, S.M., Beurskens, A., Seitz, R., Wade, D.T.: The clinical aspects of mirror therapy in rehabilitation: a systematic review of the literature. *Int. J. Rehabil. Res.* **34**, 1–13 (2011)
14. Tappeiner, L.: A simple cable driven robot for stroke rehabilitation. Master thesis, University of Innsbruck (2017)
15. Teasell, R., Mehta, S., Pereira, S., McIntyre, A., Janzen, S., Allen, L., Lobo, L., Viana, R.: Time to rethink long-term rehabilitation management of stroke patients. *Top Stroke Rehabil.* **19**(6), 457–462 (2012)

Computing Cross-Sections of the Workspace of Cable-Driven Parallel Robots with 6 Sagging Cables

Jean-Pierre Merlet^(✉)

HEPHAISTOS Project, Université Côte d'Azur, Inria, Nice Cedex, France
Jean-Pierre.Merlet@inria.fr

Abstract. Finding the workspace of cable driven parallel robots (CDPR) with sagging cables (i.e. elastic and deformable cables) is a problem that has never been fully addressed in the literature as this is a complex issue: the inverse kinematics may have multiple solutions and the equations that describe the problem are non-linear and non algebraic. We address here the problem of determining an approximation of the border of horizontal cross-sections of the workspace for CDPR with 6 cables. We present an algorithm that give an outline of this border but also rises several theoretical issues. We then propose another algorithm that allow to determine a polygonal approximation of the workspace border induced by a specific constraint. All these algorithms are illustrated on a very large CDPR.

Keywords: Cable-driven parallel robots · Kinematics · Workspace

1 Introduction

Since a few year there has been a significant renewal in the interest for cable-driven parallel robots (CDPR) who use coiling cables as actuators instead of rigid linear actuators. Beside the classical advantages inherent to a parallel structure (improved accuracy, excellent load/weight ratio) CDPR have the huge advantage to possibly provide a very large workspace with excellent lifting capacity: our MARIONET-CRANE robot with a lifting capacity of 2.5 tons has been deployed outdoor over a $75\text{ m} \times 35\text{ m} \times 25\text{ m}$ workspace. But having such large workspace requires having very large cable lengths so that the elasticity and own mass of the cables affect the performances of the platform (positioning accuracy, stiffness, ...). The purpose of this paper is first to identify the factors that may limit the robot workspace and then to propose an algorithm for computing the border of horizontal cross-section of this workspace, assuming a given altitude and orientation of the platform. Workspace calculation for parallel robots with rigid legs is a well-addressed subject [7, 15] but the unilateral action of the cables, that can only pull but cannot push, introduces new workspace limiting factors. Numerous works have addressed the problem of workspace calculation of CDPR [1–6, 8, 10, 12, 17, 20, 22] but most of them assume non deformable and non elastic

cables. Discretisation-based method has been proposed for elastic cables [11] and for a simplified sagging cable model [18]. But this approach requires to assume that the inverse kinematics problem has a single solution, which is not true for a complete sagging cable model [14]. In this paper we will propose a preliminary algorithm for computing cross-sections of the CDPR workspace using a realistic cable model, assuming that the orientation and altitude of the platform is fixed and that the robot has 6 cables.

2 Notations

We will assume that the output of the coiling system for cable i is a single point A_i , while the cable is connected at point B_i on the platform. We define a reference frame \mathcal{R} with an arbitrary origin O whose z axis is the local vertical and a frame attached to the platform (the *mobile frame*) with G , the center of mass of the platform, as origin and arbitrary x, y, z axis. We then consider the vertical plane that includes the i -th cable and we define another frame \mathcal{R}_c^i for the i -th cable with origin at A_i , the same z axis than \mathcal{R} and a y axis that is perpendicular to the plane. The length at rest of the i -th cable will be denoted L_0^i .

3 Cable Model

In this paper we will use the Irvine sagging cable model that is valid for elastic and deformable cable with mass [9]. Experimental works have shown a very good agreement between this model and the behavior of cables classically used for CDPR [19]. This model is established in the \mathcal{R}_c^i frame in which the coordinates of A_i are $(0, 0, 0)$ while the coordinates of point B_i are $(x_b \geq 0, 0, z_b)$. In this frame vertical and horizontal forces F_z, F_x are exerted on the cable at point B_i .

The coordinate x, z of a point on this cable at the curvilinear coordinate s (in the range $[0, L_0]$) is given by [9]:

$$\begin{aligned} x &= \frac{F_x s}{EA_0} + \frac{F_x}{\mu g} (\sinh^{-1}(\frac{F_z + \mu g(s - L_0)}{F_x}) - \sinh^{-1}(\frac{-\mu g L_0 + F_z}{F_x})) \\ z &= \frac{F_z s + \mu g(1/2 s^2 - L_0 s)}{EA_0} + \frac{\sqrt{F_x^2 + (F_z + \mu g(s - L_0))^2} - \sqrt{F_x^2 + (-\mu g L_0 + F_z)^2}}{\mu g} \end{aligned} \quad (1)$$

where E is the Young modulus of the cable material, μ its linear density, A_0 the surface of the cable cross-section and $F_x > 0$. The coordinates of B are obtained for $s = L_0$ and are related to the forces F_x, F_z by:

$$x_b = F_x \left(\frac{L_0}{EA_0} + \frac{\sinh^{-1}(F_z) - \sinh^{-1}(F_z - \frac{\mu g L_0}{F_x})}{\mu g} \right) \quad (2)$$

$$z_b = \frac{\sqrt{F_x^2 + F_z^2} - \sqrt{F_x^2 + (F_z - \mu g L_0)^2}}{\mu g} + \frac{F_z L_0}{EA_0} - \frac{\mu g L_0^2}{2EA_0} \quad (3)$$

4 Workspace Limitations

4.1 Cable Tension Limit and Cable Sagging

An evident reason that may limit the workspace is the maximal allowed tension in the cable. The maximal tension τ_A in a cable is obtained at point A and should be lower than the maximal allowed tension for the cable τ_{lim} i.e. $\tau_A = \sqrt{F_x^2 + (F_z + \mu g L_0)^2} \leq \tau_{lim}$.

A less obvious reason that may limit the workspace of a CDPR is that the sagging of some cable(s) may lead to have the cable on the ground. Deriving the cable model equation shows that z is extremal for $s_0 = L_0 + F_z/(\mu g)$. If s_0 lie in the range $[0, L_0]$ then the cable is sagging and its minimal altitude z_m is obtained by substituting s by s_0 in Eq. (1). If z_g is the ground altitude, then we should have $z_g \leq z_o$. If $s_0 \notin [0, L_0]$, then the lowest point of the cable is B and we will assume that this point cannot reach the ground.

4.2 Inverse Kinematics and Singularity

A necessary condition for a pose to belong to the workspace of a CDPR is that the inverse kinematics (IK) for this pose has at least one solution in the L_0 's. We thus consider the IK of a CDPR with n cables. Being given a pose of the platform (2, 3) provide $2n$ equation while having $3n$ unknowns (the F_x, F_z, L_0 for each cable). Additional equations are obtained by considering the mechanical equilibrium of the CDPR. Let \mathbf{f}_i be the force exerted by the cable at point B_i by the i -th cable. We have already seen that the components of \mathbf{f}_i in the reference frame \mathcal{R}_c^i are $(F_x^i, 0, F_z^i)$. For a given location of B_i it is easy to calculate a rotation matrix \mathbf{R}_i corresponding to a rotation around the z axis so that the components of \mathbf{f}_i in \mathcal{R} are obtained by $\mathbf{R}_i(F_x^i, 0, F_z^i)^T$. The mechanical equilibrium equations may thus be written as:

$$\sum_{j=1}^{j=n} \mathbf{f}_j = mg \quad \sum_{j=1}^{j=n} \mathbf{GB}_i \times \mathbf{f}_j = 0 \quad (4)$$

where m is the platform mass. These equations provide 6 additional constraints without increasing the number of unknowns. Hence we end up with $2n + 6$ for $3n$ unknowns. As we assume a CDPR with $n = 6$ cables the IK amounts to solve a square system of 18 equations in 18 unknowns, a problem that has been addressed in [14]. It has been shown that the system may have from 0 to multiple solutions. Hence a pose may not belong to the workspace simply because it has no IK solution or because the IK equations are singular. We will not make any distinction between a singular pose or a pose that has no IK solution as both forbid a pose to be part of the workspace. We will denote by *outside conditions* all limiting conditions that always include singularity and no IK solution while the other limiting conditions presented in Sect. 4.1 may or may not be taken into account.

5 Workspace Calculation

As determining the workspace of CDPR is a complex issue we will simplify the problem by determining only 2D horizontal cross-sections of this workspace, assuming that both the altitude and the platform orientation are fixed.

A possible strategy to determine such a cross-section has been proposed in [13]. This strategy first relies on the solving of the IK at a given pose \mathbf{X}_0 , assuming that we are able to find a pose at which the IK has at least one solution. Then for a given IK solution S_j at \mathbf{X}_0 it has been shown that it is possible to determine an ϵ such that for all pose \mathbf{X} such that $\|\mathbf{X} - \mathbf{X}_0\|_\infty \leq \epsilon$ there is a single solution S of the IK such that $\|S - S_j\|_\infty \leq \epsilon$. Furthermore it was also shown that the solution for a particular \mathbf{X} can be safely calculated with the Newton-Raphson scheme, using S_j as initial guess. With this result we can calculate a square surrounding \mathbf{X}_0 that is part of the workspace. The process is then repeated recursively starting from the corners of the square, while a pose is rejected if the ϵ for this pose is lower than a fixed threshold. We thus get an approximation of the workspace as a list of boxes that are guaranteed to be part of the workspace. Although this procedure is safe, trials have shown that the maximal value of ϵ was very small, leading to a very large computation time for CDPR with large workspace.

5.1 Approximate Border Calculation

We now describe another approach, called the *approximate border calculation*, which focus on determining only the border of the workspace.

First let us define a pose as *out* if at least one of the outside condition is satisfied. Conversely a pose will be denoted *in* if none of these conditions are fulfilled. We now define the α set of a pose \mathbf{X} (called the *heart* of the α set) with coordinates (x, y) as the set of 8 poses whose coordinates (x_u, y_u) are defined as $x_u = x + k_1\alpha, y_u = y + k_2\alpha$ with $k_1, k_2 \in [-1, 0, 1]$ excluding the case where $k_1 = k_2 = 0$. A pose \mathbf{X} and its α set are part of the approximate border if:

- at least one pose of its α set or the pose itself is in
- at least one pose of its α set or the pose itself is out

If these conditions are fulfilled, then the pose \mathbf{X} will be called an α part of the border to indicate that \mathbf{X} and its α set are part of the approximate border. Our objective is now to compute poses that are part of the approximate border. For that purpose we assume that α is chosen small enough so that the Newton-Raphson (NR) scheme used with as initial guess one the IK solution for \mathbf{X} may be used to determine if

- the IK has no solution or is singular (NR does not converge)
- the pose is in or out if the NR converges

Under these conditions we may determine if a pose \mathbf{X} and its α set are part of the approximate border, provided that we have an IK solution for this pose. Note that we associate to each pose of the α set an IK solution except that for the singular one we attach the IK solution of one of the in pose of the α set.

5.2 Propagation

Assume that we have determined a \mathbf{X} and its α set that are part of the approximate border (AB). Our objective is now to find other poses that belong to the AB. For that purpose we will consider each pose \mathbf{X}_i of the α set of \mathbf{X} and check if \mathbf{X}_i is an α part of the border. Note that we have already checked the in or out status of some of the poses of the α set of \mathbf{X}_i but this set includes new poses, the status of which has to be determined. As soon as a new α part of the border is discovered this process is repeated. In this way we *propagate* the approximate border. All poses that are an α part of the border are stored, together with their IK solution and in/out status. The propagation algorithm also maintain a list \mathcal{L} of poses that have to be processed for completing the propagation. This propagation stops when this list is empty.

5.3 Initialization

As mentioned in the previous section it is necessary to determine at least one pose that is inside the workspace and has at least one pose in its α set that is out. For that purpose we will assume that we have been able to determine one pose \mathbf{X}_{in} of coordinates (x_{in}, y_{in}) that has at least one IK solution, possibly using the algorithm proposed in [14]. We then consider the pose of coordinates $(x_{in} + k\alpha, y_{in})$ where k is an integer. We start with $k = 0$ and increment k by 1 until the pose is out (the NR scheme is used with the IK solution obtained for $k - 1$ as initial guess of the solution for k). With this approach we will find k_1 such that the pose of coordinates $(x_{in} + (k_1 - 1)\alpha, y_{in})$ is in and $(x_{in} + k_1\alpha, y_{in})$ is out: we have hence obtained a starting point for the propagation. Note that k_1 may depend on the choice of the IK solution for \mathbf{X}_{in} . Other starting poses for the propagation may be obtained similarly by considering the poses $(x_{in} - k\alpha, y_{in})$, $(x_{in}, y_{in} + k\alpha)$, $(x_{in}, y_{in} - k\alpha)$. All these poses are stored in the list \mathcal{L} of the propagation algorithm.

After having obtained these starting poses we run the propagation algorithm for computing the approximate border. This algorithm may raise some theoretical issues but before mentioning them we will consider an example.

6 Examples

We consider as example our large scale robot MARIONET-CRANE [16]. This robot is a suspended CDPR (i.e. there is no cable pulling the platform downward) with 6 cables, whose A_i, B_i coordinates are given in Table 1. The cables characteristics are $E = 100^9 \text{N/m}^2$, $\mu = 0.079 \text{kg/m}$ and their diameter is 4 mm. The maximal tension in the cables is 13734 N. We start by assuming that the platform mass is 100 kg. We assume that the center of mass of the platform is at a height of 200 cm and that the platform orientation is such that the mobile frame axis coincide with the reference frame axis. Our previous work have shown that the pose

Table 1. Coordinates of the A_i and B_i points on the base and on the platform (in cm, by rows)

x	y	z	x	y	z	x	y	z	x	y	z
-325.9	-47.5	882.6	942.1	-348.2	1155.5	-10	-93	-3	10	-93	-3
953.8	379.7	1153.3	557.0	2041.4	870.4	27	50	-7	27	50	-7
-250.5	1681.0	864.9	-334.2	942.1	878.8	-27	50	-7	-27	50	-7

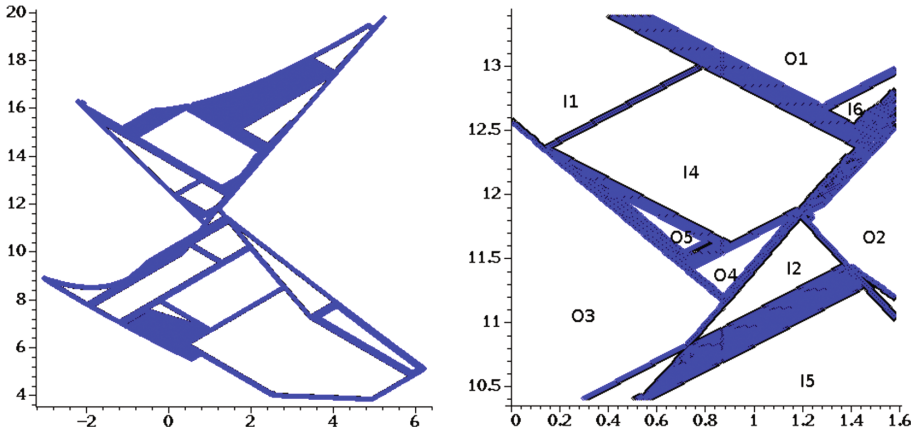


Fig. 1. Approximate border for $m = 100$ and a detailed view (Color figure online)

with coordinates (300,800) has a single IK solution and we use it as the initialization point. First we assume that the only outside condition is the singularity for the NR scheme. Figure 1 shows the approximate border in that case.

It can be seen that an outside border has been determined but there are several regions within the inside of the workspace. A detailed view is presented in Fig. 1 for $x \in [0, 1.58](m)$, $y \in [10.4, 13.4](m)$. It can be seen that the inside regions are of two different types: either in (for which the point on the border are in, in black on the figure), labeled I on the drawing, or out (the pose on the border are singular, in blue), labeled O. However there may be singular poses that are included in the in region. For the poses on the border the maximal tensions are 237762, 94687, 588078, 643676, 481622 and 468928 N while the maximal L_0 are 129613, 221416, 1517647, 236185, 445492 and 1210157 m.

If we assume now that the cable tensions cannot exceed 13734 N we get the workspace presented in Fig. 2. It may be seen that the approximate workspace is reduced because of the tension constraint (pose that do not respect this constraint are in black in the drawing). In that case the maximal L_0 are 5959, 6331, 11817, 11613, 11815 and 11813 m. Although these values are much less than in the previous case, it may be seen that they are still very high and well over reasonable values.

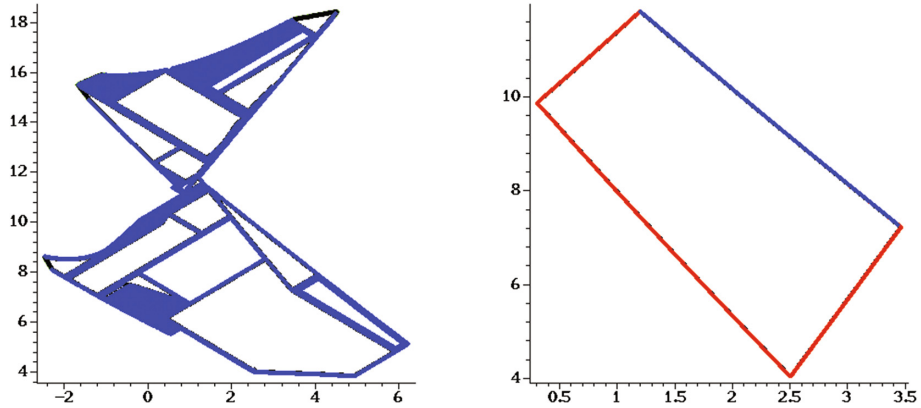


Fig. 2. On the left approximate border for $m = 100$ and $\tau \leq 13734$ N and on the right approximate border for $m = 100$ and 0 as minimal height for the cables (Color figure online)

If we impose now that the minimal height of the cable cannot be lower than 0 we get the workspace presented in Fig. 2 where 3 of the 4 border components are obtained because of this constraint (in red in the drawing) while one element is due to singularity (in blue). In that case the maximal tension in the cable are 592, 470, 377, 705, 669 and 493 N while the maximal L_0 are 13.96, 19.09, 19.25, 20.31, 17.90 and 13.59 m.

7 Conclusions

In this paper we have shown that the exact determination of the border of the workspace of CDPR with sagging cables is a complex issue even if only workspace cross-sections are to be determined. We have proposed preliminary algorithms that give insights on the workspace but also raise several theoretical issues that need to be furthermore considered. Other extension will be to consider cable interference and the possibility of having more (or less) than 6 cables.

References

1. Barrette, G., Gosselin, C.: Determination of dynamic workspace of cable-driven planar parallel mechanisms. *ASME J. Mech. Des.* **127**(2), 242–248 (2005)
2. Berti, A., Merlet, J.P., Carricato, M.: Workspace analysis of redundant cable-suspended parallel robots. In: 2nd International Conference on Cable-Driven Parallel Robots (CableCon), pp. 41–54, Duisburg, 24–27 August 2014
3. Diao, X., Ma, O.: Workspace determination of general 6 d.o.f. cable manipulators. *Adv. Robot.* **22**(2–3), 261–278 (2008)
4. Fattah, A., Agrawal, S.: On the design of cable-suspended planar parallel robots. *ASME J. Mech. Des.* **127**(5), 1021–1028 (2005)

5. Ferraresi, C., Paoloni, M.F.P.: A new methodology for the determination of the workspace of six-DOF redundant parallel structures actuated by nine wires. *break Robotica* **25**(1), 113–120 (2007)
6. Gagliardini, L., Gouttefarde, M., Caro, S.: Determination of a dynamic feasible workspace for cable-driven parallel robot. In: ARK, Grasse, 27–30 June 2016
7. Gosselin, C.: Determination of the workspace of 6-DOF parallel manipulators. *ASME J. Mech. Des.* **112**(3), 331–336 (1990)
8. Gouttefarde, M., Daney, D., Merlet, J.P.: Interval-analysis based determination of the wrench-feasible workspace of parallel cable-driven robots. *IEEE Trans. Robot.* **27**(1), 1–13 (2011)
9. Irvine, H.M.: *Cable Structures*. MIT Press, Cambridge (1981)
10. Jeong, J., Kim, S., Kwak, Y.: Kinematics and workspace analysis of a parallel wire mechanism for measuring a robot pose. *Mech. Mach. Theory* **34**(6), 825–841 (1999)
11. Korayem, M., Bamdad, M., Saadat, M.: Workspace analysis of cable-suspended robots with elastic cable. In: *IEEE International Conference on Robotics and Biomimetics, ROBIO 2007*, pp. 1942–1947 (2007)
12. Lim, W., et al.: A generic force closure algorithm for cable-driven parallel manipulators. *Mech. Mach. Theory* **46**(9), 1265–1275 (2011)
13. Merlet, J.P.: On the workspace of suspended cable-driven parallel robots. In: *IEEE International Conference on Robotics and Automation, Stockholm*, 16–20 May 2016
14. Merlet, J.P.: A new generic approach for the inverse kinematics of cable-driven parallel robot with 6 deformable cables. In: ARK, Grasse, 27–30 June 2016
15. Merlet, J.P.: Determination of 6D workspaces of gough-type parallel manipulator and comparison between different geometries. *Int. J. Robot. Res.* **18**(9), 902–916 (1999)
16. Merlet, J.P., Daney, D.: A portable, modular parallel wire crane for rescue operations. In: *IEEE International Conference on Robotics and Automation*, pp. 2834–2839, Anchorage, 3–8 May 2010
17. Pusey, J., et al.: Design and workspace analysis of a 6–6 cable-suspended parallel robot. *Mech. Mach. Theory* **139**(7), 761–778 (2004)
18. Riehl, N., et al.: On the static workspace of large dimension cable-suspended robots with non negligible cable mass. In: *34th Annual Mechanisms and Robotics Conference, Montréal*, 15–18 August 2010
19. Riehl, N., et al.: On the determination of cable characteristics for large dimension cable-driven parallel mechanisms. In: *IEEE International Conference on Robotics and Automation*, pp. 4709–4714, Anchorage, 3–8 May 2010
20. Stump, E., Kumar, V.: Workspaces of cable-actuated parallel manipulators. *ASME J. Mech. Des.* **128**(1), 159–167 (2006)
21. Tapia, R.: The Kantorovitch theorem for Newton’s method. *Am. Mathe. Mon.* **78**(1.ea), 389–392 (1971)
22. Verhoeven, R.: Analysis of the workspace of tendon-based Stewart platforms. Ph.D. thesis, University of Duisburg-Essen, Duisburg (2004)

Efficient Computation of the Workspace Boundary, Its Properties and Derivatives for Cable-Driven Parallel Robots

Andreas Pott^(✉)

Institute for Control Engineering and Manufacturing Units,
University of Stuttgart, Stuttgart, Germany
andreas.pott@isw.uni-stuttgart.de

Abstract. The workspace is an important property in the design of every cable-driven parallel robot. As the workspace is a complicated geometric object, it is difficult to describe changes in shape and size of the workspace when varying the design parameters of the robot. In this paper, we present an efficient method called *differential workspace hull* to describe and compute the workspace properties. The method is based on a triangulation of the surface of the robot's workspace. Furthermore, we establish an algorithm that allows to compute the influence of small changes in the design parameters on the workspace shape. A numerical example underlines the computational efficiency and accuracy of the presented method.

Keywords: Cable-driven parallel robots · Workspace boundary · Differential · Parameter design

1 Introduction

The workspace \mathcal{W} of a robot is the set of all poses that may be generated by this robot. For analysis and application planning, the workspace is one of its main characteristics. As the general workspace is a six dimensional volumetric object, its characterization is difficult. Merlet [5] introduces a couple of concepts to formulate meaningful descriptions such as the *constant orientation workspace* \mathcal{W}_{CO} or the *total orientation workspace* \mathcal{W}_{TO} . These workspaces are three-dimensional subsets of the general workspace and can be represented as geometric objects e.g. in CAD software and stored using conventional file formats.

The determination of the workspace for cable-driven parallel robots attracted some attention. The key workspace criterion for a cable robot is its ability to control the mobile platform with positive tension in the cables which is called *wrench-feasibility* [3, 13] and to exert wrenches with the end-effector [1]. Other restrictions include the consideration of limited capabilities of the actuators in terms of velocities and accelerations as well as the avoidance of cable-cable collisions [7] and singularities.

Different methods were proposed to compute the workspace of cable robots. Interval analysis allows to make volumetric computation of the workspace. Bruckmann [2] developed an interval test for wrench-feasibility allowing for a guaranteed and continuous workspace computation. Gouttefarde [4] uses interval analysis to determine the wrench-feasible workspace. The interval algorithms are rigorous in numerical evaluation but insensitive to small changes in its input parameters.

As a way of pragmatic representation of the workspace, one can consider only the surface or boundary of \mathcal{W}_{CO} and \mathcal{W}_{TO} . Thus, its geometric representation is a surface in space and a convenient representation is triangulation [8]. An analytical formula for the determination of the boundary of the workspace is presented by Verhoeven [12] and it is found to be a system of univariate polynomial inequations. Unfortunately, the general expression is so complex that it seems out of reach to deal with these equations even when using advanced computer algebra systems. However, it provides insight into the structure of the wrench-closure workspace boundary that consists of pieces of polynomial surfaces with degree n where n is the degree-of-freedom of the robot. Recently, this structure is exploited in a symbolic-numeric scheme to identify its components [11] and Merlet presented a similar approach for the wrench-feasible workspace of suspended robots [6]. Both results motivate this work to employ an approximation through triangles.

2 Numeric Determination of the Workspace Boundary

In this paper, we recall a method to compute the boundary of the workspace based on triangulation [8]. It is assumed that a compact region of the workspace is sought where disconnected other regions are neglected. This assumption is justified for the design of cable robots where one usually seeks robots with a compact and connected workspace. The computation of the workspace boundary aims at speed and precision rather than rigorous results or insight into the mathematical structure of the workspace.

In the following, we assume that a quality index is used in terms of a function $g(\mathbf{r}, \mathbf{R})$. The function g yields a positive value if the pose described by the position vector \mathbf{r} and the orientation matrix \mathbf{R} of the mobile platform belongs to the workspace. For cable robots, such functions can be implemented by testing if the pose is *wrench-feasible* e.g. by computing a force distribution [9, 10]. If the workspace test yields a Boolean result, true is associated with a value of 1 and false is interpreted as -1 .

The workspace for a given orientation of the cable robot is represented by a triangulation of its boundary. The idea for the determination of the workspace is to start with a unity sphere around the estimated center \mathbf{m} and to successively extend this sphere in radial direction. Clearly, this assumption may lead to an underestimation of the workspace and the estimation depends on the chosen value of \mathbf{m} . The surface of the sphere is approximated by triangles which are created from n_s iterative subdivisions of the faces of an octahedron [8] (Fig. 1).

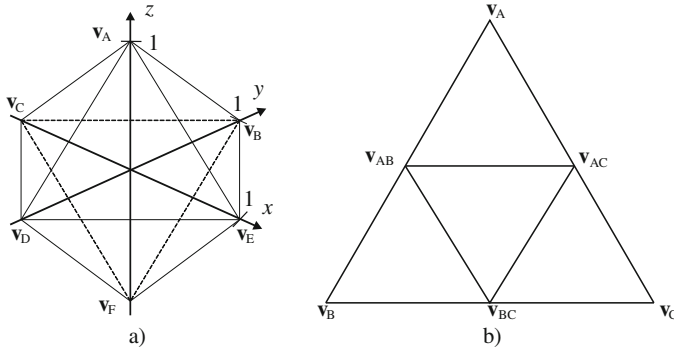


Fig. 1. (a) Unit octahedron (b) subdivision step for triangles

By making iterative subdivisions from the triangular faces of this octahedron, two sets are derived. Firstly, the set of the vertices $\mathcal{V} = \{\mathbf{v}_1, \dots, \mathbf{v}_{n_V}\}$ of the triangular mesh, and the set of triangles $\mathcal{L} = \{F_1, \dots, F_{n_T}\}$ with triples of vertices indicating which triples form a triangle of the mesh. Each triangle has the form $F_i = (\mathbf{v}_{3i+1}, \mathbf{v}_{3i+2}, \mathbf{v}_{3i+3})$. Thus, we have a set \mathcal{L} containing $n_T = 2^{2n_S+3}$ triangles.

In the second step, the vertices of the triangles are projected onto the boundary of the workspace. Starting from the estimated center \mathbf{m} of the workspace, the line

$$L_i : \mathbf{v}_i^{(h)} = \mathbf{m} + \lambda_i \mathbf{v}_i \quad \lambda_i \in [0 \dots r_{\text{Max}}] \quad (1)$$

is searched for the boundary of the workspace, which is defined by a given maximum search range r_{Max} . For each position \mathbf{r} generated by the iterations of the line search, we can compute an arbitrary workspace criterion such as wrench-closure, wrench-feasibility, reachability, intersection, or feasible deflection using the function $g(\mathbf{r}, \mathbf{R})$. The numerical results presented in this contribution are computed with a *regula falsi* method as it is simple and efficient for Boolean criteria. If the workspace criterion evaluates to a continuous function, methods such as Newton iteration can speed up the computation of the roots of the function. If multiple roots are found, the smallest λ_i is a conservative value for the boundary. Also rigorous search methods such as interval analysis can be used to find the first root of the workspace criterion. Furthermore, sampling or interval evaluation of a set of orientations $\mathcal{R} \subset \text{SO}_3$ allows to generalize the method to compute the total orientation workspace (see Sect. 2.1).

Finally, one ends up with the vertex $\mathbf{v}_i^{(h)} = \mathbf{m} + \lambda_i \mathbf{v}_i$ approximating the hull of the workspace with an accuracy ε_L . The corresponding triangles are rendered into a new set $\mathcal{L}^{(h)}$. Such data can be easily stored in a file such as stereo-lithography data file format (STL) or virtual reality modeling language (VRML) according to ISO 14772 which can be loaded and visualized with most CAD tools.

The rationale behind this generation of the triangular grid is to separate the structure of the grid from the actual geometry. Having generated the directions

\mathbf{v}_i for the line search, one can store the direction and the length λ_i of these vertices in separated data structure. The direction vectors \mathbf{v}_i can be pre-computed as a grid of a given resolution (i.e. iteration depth n_{ts}). Thus, if the robot undergoes small changes in its geometry, one can re-compute the length of its vertices λ_i and perform a one-to-one comparison to the values of the original robot.

2.1 Boundary Computation for Different Types of Workspace

Having defined the data model and search strategy, one can compute the different types of the workspace. The strategy described above is straightforward to use for computing the constant orientation workspace \mathcal{W}_{CO} simply by setting one specific orientation \mathbf{R} for the platform. If one is interested in the maximum workspace \mathcal{W}_{Max} , one has to modify the evaluation of the function $g(\mathbf{r}, \mathbf{R})$. A position is said to belong to the maximum workspace \mathcal{W}_{Max} , if any one orientation in a set $\mathcal{R} = SE_3$ belongs to the workspace. Thus, in the performance criterion, the function $g(\mathbf{r}, \mathbf{R})$ tests a discrete grid or an interval range of orientations to be checked after the other, until an orientation is found that belongs to the workspace or until all are found to be invalid. In this case, the $g(\mathbf{r})$ is treated to be valid. This can be understood as a Boolean disjunction (logical: or) between the evaluation of all $g(\mathbf{r}, \mathbf{R}), \mathbf{R} \in SE_3$. If no orientation was found to be valid, then the pose and thus $g(\mathbf{r})$ is invalid.

Computing valid positions for the total orientation workspace \mathcal{W}_{TO} is done respectively but instead of searching for at least one entry in a subset $\mathcal{R} \subset SO_3$ where the workspace test is valid, one cancels the test if one element fails. In this case, $g(\mathbf{r})$ evaluates to invalid for that position. In contrast, successfully completing the full list \mathcal{R} evaluates to valid. This is equivalent to the Boolean conjunction (logical: and) of all single tests $g(\mathbf{r}, \mathbf{R}), \mathbf{R} \in \mathcal{R}$.

2.2 Computing Properties of the Workspace from the Boundary

The triangulated boundary allows for geometric characterizations of the workspace. It is straightforward to calculate the surface $S(\mathcal{W})$, the volume $V(\mathcal{W})$, and the center of gravity $\mathbf{c}(\mathcal{W})$ of the workspace from the vertices as follows

$$S(\mathcal{W}) = \frac{1}{2} \sum_{\mathcal{L}} \|(\mathbf{v}_A - \mathbf{v}_B) \times (\mathbf{v}_A - \mathbf{v}_C)\|_2 \quad (2)$$

$$V(\mathcal{W}) = \frac{1}{6} \sum_{\mathcal{L}} ((\mathbf{v}_A - \mathbf{m}) \times (\mathbf{v}_B - \mathbf{m})) \cdot (\mathbf{v}_C - \mathbf{m}) \quad (3)$$

$$\mathbf{c}(\mathcal{W}) = \frac{1}{4V(\mathcal{W})} \sum_{\mathcal{L}} (\mathbf{v}_A + \mathbf{v}_B + \mathbf{v}_C + \mathbf{m}). \quad (4)$$

For the volume, one can find a convenient shortcut if one substitutes $\mathbf{v}_i - \mathbf{m} = \lambda_i \mathbf{u}_i$ in the parametric form with the direction \mathbf{u}_i and its length from the line search λ_i . Then, the equation for the volume becomes

$$V(\mathcal{W}) = \frac{1}{6} \sum_{\mathcal{L}} \lambda_A \lambda_B \lambda_C (\mathbf{u}_A \times \mathbf{u}_B) \cdot \mathbf{u}_C, \quad (5)$$

where the scalar value of the product $(\mathbf{u}_A \times \mathbf{u}_B) \cdot \mathbf{u}_C$ is equal for all triangles and depends only on the number of subdivisions n_s done. This simplification holds true if a regular solid such as the octahedron is used to generate the grid. Thus, one finds the simple form

$$V(\mathcal{W}) = \frac{(\mathbf{u}_A \times \mathbf{u}_B) \cdot \mathbf{u}_C}{6} \sum^{\mathcal{L}} \lambda_A \lambda_B \lambda_C, \quad (6)$$

with the constant factor $V_i^{(n_s)} = (\mathbf{u}_A \times \mathbf{u}_B) \cdot \mathbf{u}_C$.

The accurate determination of these numbers is useful for designing of cable robots, especially if one wants to take derivatives of these indices. For computing derivatives (see Sect. 2.3), one can seldom compute the expressions in closed-form. If one has to rely on numerical approximation through finite differences, the computation for neighboring values should be as accurate as possible. Therefore, one has to balance the accuracy used in the line search with the step width of the finite difference such that the results are meaningful.

2.3 Differential Hull

When analyzing the workspace of a cable robot, an interesting aspect is how the workspace depends on the geometrical and technical parameters or more generally speaking how it depends on the assumptions made and the algorithm settings. In general, the computed workspace will be changed if the parameters are differentially altered. Therefore, doing a sensitivity analysis on the parameters influencing the result of the workspace computation is revealing and can be done efficiently based on the workspace hull model proposed above. Mathematically speaking, one may ask for the derivations of the workspace caused by infinite changes of the describing parameters such as the positions of the winches \mathbf{a}_i , the geometry of the platform \mathbf{b}_i or the feasible forces in the cables $f_{\text{Min}}, f_{\text{Max}}$ (see also Table 1). One may also ask for the sensitivity of the constant orientation workspace \mathcal{W}_{CO} for changes in the orientation \mathbf{R}_0 . Since the workspace is a continuous set, the changes in shape and size mainly happen on its boundary. Here, the possibility is neglected that the parameter change generates a hole in the workspace which would change the workspace's topological structures. Therefore, the change in the parameters will only influence the hull of the workspace. As we have already seen when computing the workspace, it is difficult to find a closed-form solution of the workspace, hence, for computation we cannot compute the derivations symbolically. Clearly, numerical approximation using finite differences is a possible way. If we compute the workspace using discretization or interval techniques, the solution is insensitive in terms of small changes in the parameters unless one uses very small thresholds for the discretization. This problem applies both for simple discretization as well as for interval analysis. In contrast, the approximation of the workspace boundary through the hull algorithm separates the granularity of the used grid from the accuracy in the computation. Once the number of triangles is chosen, the points on the hull can be efficiently computed with high accuracy yielding sensitivity to parameter changes.

Table 1. Overview of the parameters to be studied with the differential hull.

Geometry	Technology	Algorithm setting
Proximal anchor points \mathbf{a}_i	Cable force limits $f_{\text{Min}}, f_{\text{Max}}$	Settings of the force distribution algorithm (e.g. max. iterations)
Distal anchor points \mathbf{b}_i	Cable length limits $l_{\text{Min}}, l_{\text{Max}}$	
Pulley radius r_{R}	Applied wrench \mathbf{w}_{P}	Platform orientation \mathbf{R} (for constant orientation workspace)
	Maximum cable velocity \dot{l}_{Max}	
	Maximum cable acceleration \ddot{l}_{Max}	

If we now consider small changes in the geometry of the robot, we can accurately track the change in the workspace boundary with moderate computational burdens. To better understand the approach, it is important to note that the steps for determining the search directions \mathbf{v}_i for the hull determination can be completed before computing the values for λ_i for each vertex. Therefore, one changes the robot model by an increment Δp and compute the resulting value for λ'_i . A suitable approximation is

$$\delta_p \approx \frac{\lambda'_i - \lambda_i}{\Delta p}. \quad (7)$$

The concept of the differential workspace can be extended to compute the influence of the parameters on the shape of the workspace, i.e. to compute the derivatives of the vertices of the workspace or on the derive of the properties surface $S(\mathcal{W})$, volume $V(\mathcal{W})$, center of gravity $c(\mathcal{W})$ of the workspace, i.e. through finite differences, one computes the derivation or sensitivity

$$\frac{\partial S(\mathcal{W})}{\partial p}, \quad (8)$$

where p is any numerical parameter of the geometry of the robot, the robot's technical parameters, or an algorithm parameter. An overview of parameters applicable for the sensitivity analysis is given in Table 1.

3 Results

In this section, an example of the differential hull approach is presented. The case study is based on the IPAnema 1 robot and the differential hull is computed for the partial derivations of the workspace hull for changes in the x -component of the first proximal anchor point \mathbf{a}_1 . Using the differential hull, the change in the shape and size of the workspace is determined. Therefore, the algorithm computes a finite difference approximation for the differential

$$\delta_{a_{1x}} = \frac{\partial \mathcal{W}(a_{1x})}{\partial a_{1x}}, \quad (9)$$

where the differences in the vertex \mathbf{v}_i are actually expressed as differences $d\lambda_i$ in the length of vertex \mathbf{v}_i . The results are visualized in Fig. 2. Red lines in the diagrams indicate regions with positive values of the derivatives $d\mathbf{v}_i$ and thus a growth in the workspace. In contrast, blue lines represent negative derivatives which correlate with a local decrease in workspace volume. In Fig. 2b, the same results are shown in order to highlight the region with negative derivatives that are occluded by the hull in the left plot since the negative derivatives are pointing inwards from the surface of the workspace. To compute the hull, the threshold for the line search is $\varepsilon = 10^{-6}$ and the finite difference in \mathbf{a}_{1X} was $\Delta\mathbf{a}_{1X} = 10^{-3}$. The absolute values of the finite differences range between -0.001418 and 0.001277 which indicates at maximum a one-to-one relation between the changes in the geometry and the changes in the workspace.

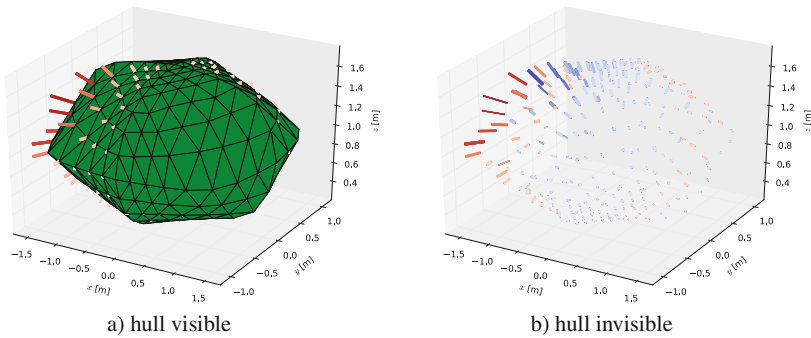


Fig. 2. Differential hull of the constant orientation workspace \mathcal{W}_{CO} of the IPANema 1 robot computed with closed-form method for a finite difference in the x -component of the first proximal anchor point \mathbf{a}_{1X} . The magnitude of the differences is amplified to make the effect of the change visible. (a) The plot shows the hull with the normal lines indicating magnitude and sign of the finite difference. (b) The same analysis but with an invisible hull. (Color figure online)

The computation of the differential hull is very fast; the determination of the case study took around 30 ms on a Core i5-3320M with 2.6 GHz. Therefore, all partial derivatives of the workspace volume, surface, and bounding box can be determined in less than one second making the evaluation of these differences an interesting tool for the design of cable robots.

4 Conclusions

In this paper, we proposed a scheme to compute triangulations of the constant orientation workspace as well as of the total orientation workspace for cable-driven parallel robots. The presented form for this triangulation allows to determine properties such as volume and surface both in a fast and accurate way. As changes in length of the vertices are sensitive to small changes in the geometry of the robots, it is proposed to numerically estimate the derivatives of the

workspace geometry with respect to changes in the geometry parameters. This presents a useful tool in the design procedure of cable robots as one can establish relations between geometry and robot properties to perform targeted manipulation of the geometry, e.g. to determine geometric parameters that lead to a local growth of the workspace.

Acknowledgements. The author would like to thank the German Research Foundation (DFG) for financial support of the project within the Cluster of Excellence in Simulation Technology (EXC 310/1) at the University of Stuttgart.

References

1. Bouchard, S., Moore, B., Gosselin, C.: On the ability of a cable-driven robot to generate a prescribed set of wrenches. *J. Mech. Robot.* **2**(1), 1–10 (2010). doi:[10.1115/1.4000558](https://doi.org/10.1115/1.4000558). <http://www.scopus.com/inward/record.url?eid=2-s2.0-78651563640&partnerID=40&md5=c38295e45251f9867a7ab0ec3793dd42>
2. Bruckmann, T., Mikelsons, L., Schramm, D., Hiller, M.: Continuous workspace analysis for parallel cable-driven Stewart-Gough platforms. *PAMM* **7**(1), 4010,025–4010,026 (2007). doi:[10.1002/pamm.200700774](https://doi.org/10.1002/pamm.200700774)
3. Ebert-Uphoff, I., Voglewede, P.A.: On the connections between cable-driven parallel manipulators and grasping. In: *IEEE International Conference on Robotics and Automation*, pp. 4521–4526, New Orleans (2004)
4. Gouttefarde, M., Daney, D., Merlet, J.P.: Interval-analysis-based determination of the wrench-feasible workspace of parallel cable-driven robots. *IEEE Trans. Robot.* **27**(1), 1–13 (2011). doi:[10.1109/TRO.2010.2090064](https://doi.org/10.1109/TRO.2010.2090064). <http://ieeexplore.ieee.org/stamp/stamp.jsp?arnumber=5657268>
5. Merlet, J.P.: *Parallel Robots*, 2nd edn. Springer, Dordrecht (2006)
6. Merlet, J.P.: On the workspace of suspended cable-driven parallel robots. In: *IEEE International Conference on Robotics and Automation*, pp. 841–846, Stockholm, Sweden (2016)
7. Perreault, S., Cardou, P., Gosselin, C., Otis, M.J.D.: Geometric determination of the interference-free constant-orientation workspace of parallel cable-driven mechanisms. *ASME J. Mech. Robot.* **2**(3) (2010). doi:[10.1115/1.4001780](https://doi.org/10.1115/1.4001780)
8. Pott, A.: forward kinematics and workspace determination of a wire robot for industrial applications. In: *Advances in Robot Kinematics (ARK)*, pp. 451–458. Springer (2008)
9. Pott, A.: An improved force distribution algorithm for over-constrained cable-driven parallel robots. In: *Computational Kinematics*, pp. 139–146. Springer (2013)
10. Pott, A., Bruckmann, T., Mikelsons, L.: Closed-form force distribution for parallel wire robots. In: *Computational Kinematics*, pp. 25–34. Springer, Heidelberg, Berlin (2009)
11. Pott, A., Kraus, W.: Determination of the wrench-closure translational workspace in closed-form for cable-driven parallel robots. In: *IEEE International Conference on Robotics and Automation*, pp. 882–888, Stockholm, Sweden (2016)
12. Verhoeven, R.: Analysis of the workspace of tendon-based stewart platforms. Ph.D. thesis, University of Duisburg-Essen, Duisburg, Germany (2004)
13. Verhoeven, R., Hiller, M.: Estimating the controllable workspace of tendon-based stewart platforms. In: *Advances in Robot Kinematics (ARK)*, pp. 277–284, Portorož, Slovenia (2000)

Application of the Rigid Finite Element Method to the Simulation of Cable-Driven Parallel Robots

Philipp Tempel¹(✉), Andreas Schmidt², Bernard Haasdonk²,
and Andreas Pott¹

¹ Institute for Control Engineering of Machine Tools
and Manufacturing Units (ISW), University of Stuttgart,
Seidenstr. 36, 70174 Stuttgart, Germany

{philipp.tempel, andreas.pott}@isw.uni-stuttgart.de

² Institute for Applied Analysis and Numerical Simulation (IANS),
University of Stuttgart, Pfaffenwaldring 57, 70569 Stuttgart, Germany
{andreas.schmidt, bernard.haasdonk}@mathematik.uni-stuttgart.de

Abstract. Kinematics and dynamics of cable-driven parallel robots are affected by the cables used as force and motion transmitting elements. Flexural rigidity of these cables is of major interest to better understand dynamics of these systems and to improve their accuracy. The approach for modeling spatial cable dynamics, as presented in this paper, is based on the modified rigid-finite element method using rigid bodies and spring-damper elements. With this, a simulation of a planar 3 degrees of freedom cable-driven parallel robot is constructed as a multi-body dynamics model. Under consideration of holonomic constraints and Baumgarte stabilization, a simulation framework for the simulation of cable-driven parallel robots including dynamics of the cables is developed and presented.

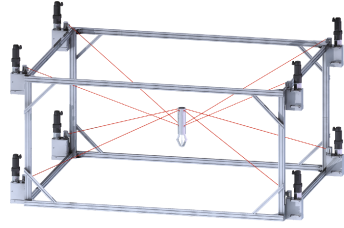
Keywords: Parallel kinematics · Multi-body dynamics · Flexible joints · Holonomic systems · Model order reduction

1 Introduction

Cable-driven mechanisms have been known for thousands of years starting in ancient Egypt and reaching all the way till modern centuries. Such systems, like mooring, supporting, or lifting devices in offshore engineering, cable-suspension bridges, or cranes are very likely known to the reader. Another field of application comes from replacing rigid links usually found in Gough-Stewart platforms (see Fig. 1a) with cables, yielding a cable-driven parallel robots (shortened cable robot, see Fig. 1b). This enables such systems to outperform their rigid-link counterparts by magnitudes when it comes to dynamics, workspace, or payload. On the downside, these benefits come at a cost stemming from the use of flexible links as force and motion transmitting elements as these introduce unilateral



(a) CAD rendering of a Gough-Stewart platform, a general hexapod with 6 degrees of freedom and 6 actuators.



(b) Representation of a general cable robot with 6 degrees of freedom and 8 actuators (cables).

Fig. 1. Comparative display of a general Gough-Stewart platform (a) and a cable robot (b).

constraints into the system: cables can only exert tensile forces i.e., can only pull. Additionally, their resistance to transversal forces i.e., perpendicular to the cable's neutral axis, is negligible. This effect is very prominent when jerky motions or sharp changes in the direction of motion along a trajectory occur.

Industrial application of the cable robot technology was first studied by Albus et al. for the NIST RoboCrane [2]. To foster research, cables were assumed ideal i.e., to be forming a straight line between two points without any longitudinal flexibility or inherent dynamics. However, mechanical properties of cables differ from rigid links thus modeling of cables was further extended. Besides considering cable longitudinal flexibility by means of linear [10] or non-linear models [5, 8], the dynamics were researched in only very limited extend. In [7], the authors employed XDE to simulate cable robots with discretized cables allowing for coiling, yet the Reissner beam for cable modeling with a resolution of 0.02 m makes for very slow simulation and induced oscillations. The cable robot analysis and simulation framework CASPR [6] provides tools for designing cable robots, yet simulation also allows for only state of the art cable models. A multi-body approach for large-span suspended cable robots was introduced in [3], neglecting extensibility of the cables as well as bending stiffness, yet the authors explicitly consider winding of the cables.

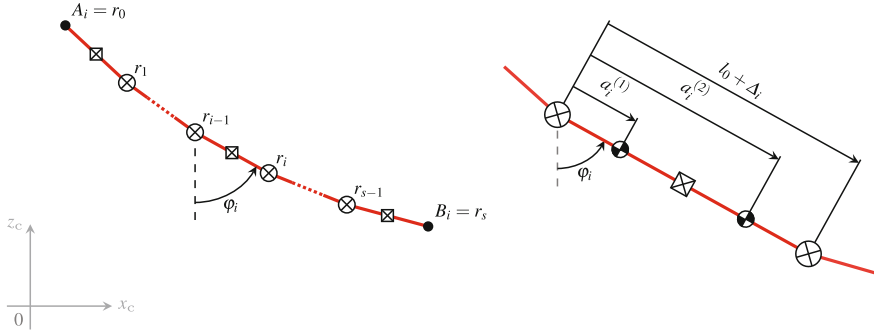
In this contribution, the well-established finite element discretization method for cables based on the modified rigid finite element method derived by [1], accounting for both bending and longitudinal flexibility, is applied to simulation of cable robots. The model is extended such that it allows for attaching multiple cables to arbitrary points on a rigid body that is assumed to represent the mobile platform of cable robots. To account for expensive evaluation of the extended system dynamics, model order reduction techniques are further employed reducing the computational complexity and enabling efficient simulation of the system.

The structure of this paper is as follows: in Sect. 2, the model of a single cable is derived as well as the synthesis for a multi-cable setup including the cable robot mobile platform is shown. Analysis of the model is performed and numerical results are given, including application of model order reduction techniques since calculation of the equation dynamics is time-consuming. After a

discussion of the combined model in Sect. 3 highlighting its applicability to simulation of cable robots, a conclusion is drawn in Sect. 4 also pointing out further steps to improving the model.

2 Model Synthesis and Analysis

In this section, we derive the dynamics of the system used for simulation of a cable robot. The model is based on the modified rigid finite element approach presented by Adamiec–Wójcik et al. [1]. Since our coordinate system and notation differ and due to the importance of several components to the work presented here, we will briefly reproduce the derivation.



(a) Division of the cable into s segments interconnected with radial spring and damper elements inbetween.

(b) Segment of the cable modeled as rigid finite element (rfe) in a deformed state.

Fig. 2. Planar cable model used with division of the cable (a) into s segments composed of two rfes adjoined through linear sde shown in (b).

2.1 Cable Dynamics

We assume a planar cable model as shown in Fig. 2 comprised of stretching and bending stiffness. The cable is fixed at A_i and split into s rigid finite elements (rfes) with generalized coordinates strain Δ_i and angle φ_i in $\mathbf{q}_i = [\Delta_i, \varphi_i]^T$. Each segment, denoted with ⁽¹⁾ and ⁽²⁾, is composed of two rigid bodies of mass m_i and moment of inertia J_i connected via a linear spring-damper element (sde). The full system state is

$$\mathbf{q} = [\Delta_1, \varphi_1, \Delta_2, \varphi_2, \dots, \Delta_s, \varphi_s]^T = [\mathbf{q}_1^T, \mathbf{q}_2^T, \dots, \mathbf{q}_s^T]^T. \quad (1)$$

The coordinate of each rfe segment can be readily derived to read

$$\mathbf{r}_i = \mathbf{r}_0 + \sum_{k=1}^i (l_0 + \Delta_k) \begin{bmatrix} \sin \varphi_k \\ -\cos \varphi_k \end{bmatrix}, \quad i = 1, \dots, s, \quad (2)$$

where $l_0 = L/s$ is the unstrained length of each segment. Furthermore, the position of the distal point of the cable is to be given by $\mathbf{r}_{\text{end}}(t)$, which translates to the holonomic constraint $\Phi(t) \equiv 0$ with

$$0 \equiv \boldsymbol{\Phi}(t) = \mathbf{r}_s(t) - \mathbf{r}_{\text{end}}(t) \quad t \geq 0. \quad (3)$$

The governing system dynamics are established through Lagrangian mechanics

$$\frac{d}{dt} \frac{\partial \mathcal{L}}{\partial \dot{q}_i} - \frac{\partial \mathcal{L}}{\partial q_i} + \sum_{j=1}^c \lambda_j \frac{\partial \boldsymbol{\Phi}_j}{\partial q_i} = \frac{\partial P}{\partial \dot{q}_i} + \sum_{j=1}^s \mathbf{F}_j \cdot \frac{\partial \mathbf{r}_j}{\partial q_i}, \quad i = 1, \dots, 2s \quad (4)$$

in which $\mathcal{L} = \sum_{i=1}^s T_i - U_i$ is the Lagrangian, $\boldsymbol{\Phi}_j$ is the j th component of the geometric constraints vector from Eq. (3) (in planar case $c \equiv 2$) and λ_j are Lagrange multipliers. Additional external forces $\mathbf{F}_j = [F_{j,x}, F_{j,z}]^\top$ at the massless side \mathbf{r}_j (cf. Eq. (2)) are also considered. Kinetic energies T_i , potential energies U_i , and dissipative energies P_i of the i th segment are

$$T_i = \frac{m_i}{2} \left(\|\dot{\mathbf{r}}_i^{(1)}\|^2 + \|\dot{\mathbf{r}}_i^{(2)}\|^2 \right) + \frac{1}{2} \left(J_i^{(1)} + J_i^{(2)} \right) \dot{\varphi}_i^2, \quad (5a)$$

$$U_i = \frac{c_L}{2} \Delta_i^2 + \frac{c_R}{2} (\varphi_i - \varphi_{i-1})^2 + m_i g \left(\mathbf{r}_{i,z}^{(1)} + \mathbf{r}_{i,z}^{(2)} \right), \quad (5b)$$

$$P_i = \frac{d_L}{2} \dot{\Delta}_i^2 + \frac{d_R}{2} (\dot{\varphi}_i - \dot{\varphi}_{i-1})^2, \quad (5c)$$

considering spring and damper elements with respective linear and angular spring coefficients c_L , c_R , and linear and angular damper coefficients d_L and d_R , respectively.

The system dynamics can be described through the index-3 differential algebraic equation system

$$\mathbf{M}(t, \mathbf{q}, \dot{\mathbf{q}}) \cdot \ddot{\mathbf{q}} = \mathbf{f}(t, \mathbf{q}, \dot{\mathbf{q}}) + \mathbf{B}(t, \mathbf{q}, \dot{\mathbf{q}}) \cdot \mathbf{F}(t) - \boldsymbol{\Phi}_q(t, \mathbf{q})^\top \cdot \boldsymbol{\lambda}, \quad 0 = \boldsymbol{\Phi}(t, \mathbf{q}). \quad (6)$$

Stable numerical simulations without induced drift requires index reduction to receive an index-1 system, which is achieved by applying Baumgarte stabilization technique (compare [4]):

$$\begin{bmatrix} \mathbf{M} & \boldsymbol{\Phi}_q^\top \\ \boldsymbol{\Phi}_q & 0 \end{bmatrix} \begin{bmatrix} \ddot{\mathbf{q}} \\ \boldsymbol{\lambda} \end{bmatrix} = \begin{bmatrix} \mathbf{f} + \mathbf{B} \cdot \mathbf{F} \\ \gamma - 2\alpha \dot{\boldsymbol{\Phi}} - \beta^2 \boldsymbol{\Phi} \end{bmatrix}, \quad \gamma \equiv -(\boldsymbol{\Phi}_q \dot{\mathbf{q}})_q \dot{\mathbf{q}} - 2\boldsymbol{\Phi}_{qt} \dot{\mathbf{q}} - \ddot{\boldsymbol{\Phi}} \quad (7)$$

2.2 Multi-cable Dynamics with Platform

We extend the model derived in Sect. 2.1 such that it is applicable to simulation of cable robots consisting of a platform and m cables. To begin with, we assume the platform to be of rectangular shape with width and height w and h , respectively, mass m_p , and moment of inertia J_p . The platform can be described by the generalized coordinates $\mathbf{q}_p = [x_p, z_p, \Theta_p]^\top$ with Cartesian position $\mathbf{r}_p = [x_p, z_p]^\top$ and angle of rotation Θ_p . Further stating the cables are attached to the platform at the cable attachment points \mathbf{b}_i w.r.t. the platform's coordinate system, the holonomic constraints according to Eq. (3) for the distal point of the i th cable $\mathbf{r}_{i,\text{end}}(t)$ and the cable attachment point on the platform $\mathbf{r}_{b_i}(t)$ yield

$$\mathbf{r}_{\text{end}}^{(i)}(t) = \mathbf{r}_p(t) + \mathbf{R}\mathbf{b}_i, \quad \mathbf{r}_{b_i}(t) = \mathbf{r}_s^{(i)}(t). \quad (8)$$

where $\mathbf{R} = \mathbf{R}(\Theta_p)$ is the rotation matrix for the current platform rotation. The dynamics of the platform can be easily derived from Lagrangian mechanics under consideration of holonomic constraints similar to Eqs. (4) and (7), respectively.

2.3 Model Order Reduction

The nonlinear DAE system Eq. (7) contains functions that are costly to evaluate. This is due to the complex trigonometric couplings and interactions within all nodes in the system. The overall computational demands might thus be too high to allow for efficient simulations. Model order reduction (MOR) techniques can help to overcome the above mentioned limitations by replacing the computationally expensive model with cheap yet accurate surrogates. For this purpose we employ the so-called trajectory-piecewise-linear approach (TPWL-approach), which was first introduced in [9]. By using this technique, the complex non-linear functions are replaced by a weighted linear combination of linearizations around several well-chosen points in the state space: We hence choose a set of linearization points $\{\bar{t}_i, \bar{\mathbf{q}}_i\}_{i \in I}$ for a preferably small set $I = \{1, \dots, N_I\}$, and replace the non-linear functions by linearizations of the following form:

$$\mathbf{f}(t, \mathbf{q}, \dot{\mathbf{q}}) \approx \sum_{i \in I} \omega_i(\mathbf{q}) (\mathbf{f}(\bar{t}_i, \bar{\mathbf{q}}_i, \bar{\dot{\mathbf{q}}}_i) + D\mathbf{f}(\bar{t}_i, \bar{\mathbf{q}}_i, \bar{\dot{\mathbf{q}}}_i)(\mathbf{q} - \bar{\mathbf{q}}_i)). \quad (9)$$

The weightings $\omega_i(\mathbf{q})$ are chosen in such a way that $\sum_{i \in I} \omega_i(\mathbf{q}) = 1$ and are calculated in order to switch and interpolate between the linearized models, depending on where in the state space the simulation currently is located. More sophisticated techniques and dimension reduction via projection can furthermore yield significant speedups as discussed in [9]. In our case, we apply the TPWL approach to the equations for \mathbf{f} only, and keep the nonlinear holonomic constraint equations to guarantee that the cables are correctly linked.

3 Discussion

For numerical simulation, we choose two cables with length $L_0 = 3$ m and a platform of size $1 \text{ m} \times 0.3 \text{ m}$. The cables are suspended at $\mathbf{r}_0^{(1)} = [0, 0]^\top$ and $\mathbf{r}_0^{(2)} = [1, -0.25]^\top$ and are attached at $\mathbf{b}_1 = [-0.5, 0.15]^\top$ m and $\mathbf{b}_2 = [0.5, 0.15]^\top$ m, respectively. We choose $s = 20$ segments for the discretization of either cable, resulting in a DAE system of dimension 170, including the algebraic equations and Lagrange multipliers. All functions in the DAE formulation from Eq. (6) are derived analytically by utilizing the symbolic calculation techniques of MAPLE, and are then exported to optimized MATLAB functions. The resulting DAE system is solved by using MATLAB's builtin `ode15s` solver with default accuracy.

As a test case, we simulate the system for $T = 15$ s, where we apply a time-dependent force on the center of the platform as depicted in Fig. 3. With this setup we aim to investigate the transition of the cables from tensed to non-tensed and back to tensed state. For such, the external force on the platform is applied in

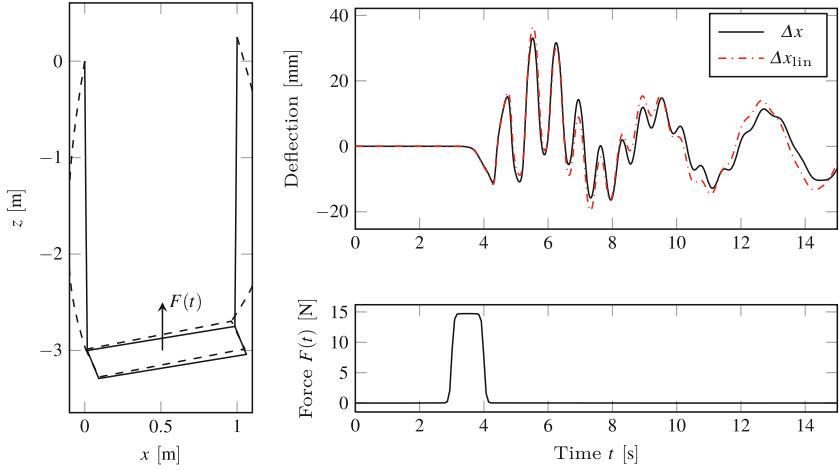


Fig. 3. The simulation setting for our experiments (left). The solid line shows the system at $t = 0$ s, the dashed line at $t = 4.3$ s. The right plots show the x -deflection of the platform (top) for the full (Δx) and linearized (Δx_{lin}) simulations, as well as the applied external force (bottom).

the positive z -direction i.e., negative direction of gravity to make the cables slack. During increasing force, the platform is being pushed up and the cables go slack. With the external force decreasing, the cables get tensed again yet apply different forces onto the platform. Comparing this behavior with the standard cable model of straight lines, the platform's bouncing motion looks more realistically since the flexural rigidity of the cables is not explicitly considered.

The simulation was run with the full non-linear model and took 39.1 s. By using the proposed TPWL-approach for \mathbf{f} only, where we choose the initial configuration and the true solution at times $t \in \{4.2 \text{ s}, 5 \text{ s}, 5.5 \text{ s}\}$ as linearization points, we can simulate the system in 20 s and thus gain almost 53% speedup while making a relative error of only 4.1%, measured in the space-time norm $\|\mathbf{q}\| := \left(\int_0^T \|\mathbf{q}(t)\|^2 dt \right)^{1/2}$. Automatic techniques for the choice of the linearization points and projection-based MOR techniques yield more accurate and efficient results.

4 Conclusions

A cable model based on the modified rigid finite element method, as presented in this paper, shows reasonable results for the motion of the cables and the platform. Using the approach given in this work, cables can be attached to a rigid body representing the mobile platform. Due to the time-consuming evaluation of the system dynamics, advanced mathematical techniques are employed to accelerate the calculations. A combination of the proposed linearization ansatz and a projection-based technique will lead to even larger speed-ups.

Currently, the dynamics of the platform can only be simulated very limitedly, despite the model allowing for additional dynamics of the platform to simulate cable robots with up to 6 degrees of freedom and additional cables. To further improve numerical results, the mechanical properties of the cable need to be more closely obtained. As is known by related contributions, elasticity of the used fiber cables is non-linear thus applying Hooke's law for tension may not be accurate enough. Additionally, initial investigations make assuming a progressive bending stiffness of the cable with very small resistance more accurate. With the modularity of the model, all of these approaches can easily be integrated in the presented simulation framework and thus will be investigated in future work.

Acknowledgements. The authors would like to thank the German Research Foundation (DFG) for financial support of the project within the Cluster of Excellence in Simulation Technology (EXC 310/2) at the University of Stuttgart.

References

1. Adamiec-Wójcik, I., Awrejcewicz, J., Brzozowska, L., Drg, L.: Modelling of ropes with consideration of large deformations and friction by means of the rigid finite element method. In: Awrejcewicz, J. (ed.) *Applied Non-Linear Dynamical Systems*. Springer Proceedings in Mathematics & Statistics, vol. 93, pp. 115–137. Springer International Publishing, Cham (2014). doi:[10.1007/978-3-319-08266-0_9](https://doi.org/10.1007/978-3-319-08266-0_9)
2. Albus, J.S., Bostelman, R.V., Dagalakis, N.G.: The NIST RoboCrane. *J. Res. Nat. Inst. Stand. Technol.* **97**, 373–385 (1992)
3. Collard, J.F., Lamaury, J., Gouttefarde, M.: Dynamics modelling of large suspended parallel cable-driven robots. In: 2011 ECCOMAS Thematic Conference on Multibody Dynamics, pp. 1–13 (2011)
4. Flores, P., Pereira, R., Machado, M., Seabra, E.: Investigation on the Baumgarte stabilization method for dynamic analysis of constrained multibody systems. In: Ceccarelli, M. (ed.) *Proceedings of EUCOMES 2008*, pp. 305–312. Springer, Dordrecht (2008). doi:[10.1007/978-1-4020-8915-2_37](https://doi.org/10.1007/978-1-4020-8915-2_37)
5. Kozak, K., Zhou, Q., Wang, J.: Static analysis of cable-driven manipulators with non-negligible cable mass. In: *IEEE Conference on Robotics, Automation and Mechatronics*, vol. 2, pp. 886–891 (2004). doi:[10.1109/RAMECH.2004.1438035](https://doi.org/10.1109/RAMECH.2004.1438035)
6. Lau, D., Eden, J., Tan, Y., Oetomo, D.: CASPR: a comprehensive cable-robot analysis and simulation platform for the research of cable-driven parallel robots. In: 2016 IEEE/RSJ International Conference on Intelligent Robots and Systems (IROS), pp. 3004–3011 (2016). doi:[10.1109/IROS.2016.7759465](https://doi.org/10.1109/IROS.2016.7759465)
7. Michelin, M., Baradat, C., Nguyen, D.Q., Gouttefarde, M.: Simulation and control with XDE and Matlab/Simulink of a cable-driven parallel robot (CoGiRo). In: Pott, A., Bruckmann, T. (eds.) *Cable-Driven Parallel Robots. Mechanisms and Machine Science*, vol. 32, pp. 71–83. Springer International Publishing, Cham (2015). doi:[10.1007/978-3-319-09489-2_6](https://doi.org/10.1007/978-3-319-09489-2_6)
8. Miermeister, P., Kraus, W., Lan, T., Pott, A.: An elastic cable model for cable-driven parallel robots including hysteresis effects. In: Pott, A., Bruckmann, T. (eds.) *Cable-Driven Parallel Robots. Mechanisms and Machine Science*, vol. 32, pp. 17–28. Springer International Publishing, Cham (2015). doi:[10.1007/978-3-319-09489-2_2](https://doi.org/10.1007/978-3-319-09489-2_2)

9. Rewieński, M., White, J.: A trajectory piecewise-linear approach to model order reduction and fast simulation of nonlinear circuits and micromachined devices. In: Proceedings of the 2001 IEEE/ACM International Conference on Computer-Aided Design, pp. 252–257. IEEE Press (2001)
10. Verhoeven, R.: Analysis of the workspace of tendon-based Stewart platforms. Ph.D. Thesis. Universität Duisburg-Essen, Duisburg, Germany (2004)

Cams/Gear

Evaluating the Knot Vector to Synthesize the Cam Motion Using NURBS

T.T.N. Nguyen^(✉), S. Kurtenbach, M. Hüsing, and B. Corves

Department of Mechanism Theory and Dynamics of Machines,
RWTH Aachen University, Aachen, Germany
{Nguyen-Thi,kurtenbach,huesing,corves}@igm.rwth-aachen.de

Abstract. A Non Uniform Rational B-Spline (NURBS) is used for synthesizing the motion curve of cam mechanisms because it is flexible and satisfies arbitrary boundary conditions from the working requirement of machinery systems. For using NURBS curve as motion curves of cam mechanisms, selecting the knot vector is very important. This work presents the effect of the knot vector on the displacement, velocity, acceleration, and jerk curves. The linear system of equations for solving the cam motion is also presented. A general computation of the knot vector of NURBS for synthesizing the motion curve is presented. Several examples illustrate this research.

Keywords: Parameterization method · Knot vector · NURBS · Cam motion synthesis

1 Introduction

The synthesis of motion curves for cam mechanisms depends on working requirements and application situations of machinery systems. The boundary conditions of the displacement function are not only displacement constraints but also the velocity, acceleration, and jerk constraints. Frequently, designers must refine the displacement functions, where their derivatives can reduce the maximum values of acceleration and jerk.

There are several standard functions such as harmonic, cycloidal, trapezoidal, and polynomial [1–3]. The disadvantage of these functions is limited by a number of boundary conditions. For motion curves, polynomial functions are commonly used in cam design. However, displacement curves can be oscillating with the high order of polynomial if the number of boundary conditions becomes large. Therefore, acceleration and jerk curves can occur peak values.

In several recent decades, spline functions, B-spline and NURBS curves, have been used to synthesize motion curves of cam mechanisms [8–13]. The main advantage of using these curves for displacement functions is unlimited boundary conditions from working requirements. Moreover, these curves and their derivatives can be controlled by several parameters such as the knot vector, control points, and weights. The knot vector is one of the important parameters

since it is directly connected with the shape of these curves. The uniform spacing method is commonly used for calculating the knot vector as shown in [8–11]. This method is very comfortable to calculate the knot vector. Other researches used the knot vector that is specified in the increasing direction of the independent cam rotation [12, 13].

Until now, the knot vector is still interesting to calculate the shape of curves. In this paper, we present the effect of the knot vector on the kinematics of the cam motion. Several methods for computing the knot vector are used for NURBS curve. Here, the study cases with a large number of boundary conditions of the displacement, velocity, acceleration, and jerk are considered to synthesize of the motion curve of cam mechanisms.

The organization of this paper is as follows. Section 2 shows the description of NURBS and briefly presents a general synthesis of motion curves with NURBS. The linear system of equations is established. The computation of the knot vector for synthesizing motion curves is present in Sect. 3. Section 4 shows the effect of knot vector to motion curves by two examples. Conclusion is presented in Sect. 5.

2 Description of NURBS Curve for Cam Motion

2.1 NURBS Curve Formulation

A detailed introduction to Non-Uniform Rational B-Spline (NURBS) curve can be found in [4]. A NURBS curve of degree, p , is defined by $n + 1$ control points P_i , $i = 0, \dots, n$ and the knot vector \mathbf{U} . A NURBS curve is expressed as

$$C(u) = \frac{\sum_{i=0}^n N_{i,p}(u) w_i P_i}{\sum_{j=0}^n N_{j,p}(u) w_j}, \quad u \in [a, b]. \tag{1}$$

Here, w_i are weights and they are positive. $N_{i,p}$ are the B-spline basis functions that are defined over the knot vector \mathbf{U}

$$\mathbf{U} = \{u_0, u_1, u_2, \dots, u_m\}, \tag{2}$$

with $m = n + p + 1$. The knot vector is a nondecreasing sequence of real number, and u_i are called knots. The knot vector is also expressed as

$$\mathbf{U} = \{\underbrace{a, \dots, a}_{p+1}, u_{p+1}, \dots, u_{m-p-1}, \underbrace{b, \dots, b}_{p+1}\}. \tag{3}$$

From Eq. (1), the basis functions $N_{i,p}$ are calculated by using the knot vector as

$$N_{i,0}(u) = \begin{cases} 1 & \text{for } u_i \leq u < u_{i+1} \\ 0 & \text{otherwise} \end{cases} \tag{4}$$

$$N_{i,p}(u) = \frac{u - u_i}{u_{i+p} - u_i} N_{i,p-1}(u) + \frac{u_{i+p+1} - u}{u_{i+p+1} - u_{i+1}} N_{i+1,p-1}(u).$$

Setting

$$R_{i,p}(u) = \frac{N_{i,p}(u) w_i}{\sum_{j=0}^n N_{j,p}(u) w_j}, \tag{5}$$

they are called the rational basis functions. Thus, the Eq. (1) can be written as

$$C(u) = \sum_{i=0}^n R_{i,p}(u) P_i. \tag{6}$$

Furthermore, the k^{th} derivative of NURBS curve can be computed as

$$C^k(u) = \sum_{i=0}^n R_{i,p}^k(u) P_i. \tag{7}$$

2.2 Cam Motion Using NURBS Curve

The derivative of NURBS curve with degree p is continuous up to $(p-1)$. Therefore, in this paper, the NURBS curve with degree $p = 5$ is used for synthesizing the motion curves because its derivative is continuous up to jerk function.

With the cam motion using NURBS curve, we denote u as the angle of cam shaft. The given boundary conditions of the displacement, velocity, acceleration, and jerk are respectively $C(u_j)$, $C^1(u_k)$, $C^2(u_l)$, and $C^3(u_h)$ at u_j , u_k , u_l , and u_h . For the number of boundary conditions, $n + 1 = d + e + f + g$, the linear system of equations can be written as

$$\mathbf{C} = \mathbf{R} \mathbf{P}, \tag{8}$$

where the matrix \mathbf{C} with size $(n + 1) \times 1$ can be expressed by

$$\mathbf{C} = [C(u_j) \quad C^1(u_k) \quad C^2(u_l) \quad C^3(u_h)]^T, \tag{9}$$

for $j = 1, \dots, d$, $k = 1, \dots, e$, $l = 1, \dots, f$, and $h = 1, \dots, g$.

Here, the matrix \mathbf{R} with size $(n + 1) \times (n + 1)$, presents the values of rational basis functions, the first derivative, the second derivative, and the third derivative at u_j , u_k , u_l , and u_h respectively. \mathbf{R} can be written as

$$\mathbf{R} = [R_{i,p}(u_j) \quad R_{i,p}^1(u_k) \quad R_{i,p}^2(u_l) \quad R_{i,p}^3(u_h)]^T, \quad \text{for } i = 0, \dots, n. \tag{10}$$

From Eq. (8), \mathbf{P} can be presented by

$$\mathbf{P} = [P_0, P_1, \dots, P_n]^T. \tag{11}$$

As mentioned above, P_i are control points.

Solving the linear system of equations as shown in Eq. (8), we obtain the control points. It means that the motion curve of cam mechanisms is established.

3 Computation of the Knot Vector for Synthesizing Cam Motion

3.1 Parameterization Method to Generate the Knot Vector

According to Eq. (4), the basis functions are established by the knot vector \mathbf{U} as shown in Eq. (3). For the number of boundary conditions at $u_j, u_k, u_l,$ and $u_h,$ the input angle vector of camshaft, denoted by \mathbf{D} , is arranged from small to big value of the cam rotation in the order $u_j, u_k, u_l,$ and $u_h.$ Thus, for $n + 1$ input angles, \mathbf{D} can be written as

$$\mathbf{D} = [D_0, D_1, \dots, D_n]. \tag{12}$$

The vector, denoted by $\mathbf{t} = [t_0, t_1, \dots, t_n],$ has $n + 1$ parameters. To compute these parameters, we present three methods such as the uniformly space method, the chord length method, and the centripetal method. From Eq. (1), the angle of camshaft as u is in the parameter domain $[a, b],$ with $a = D_0$ and $b = D_n.$

The uniformly space method has been presented in [6]. With the end parameters $t_0 = a$ and $t_n = b,$ the remaining parameters are computed by

$$\begin{cases} t_0 = a \\ t_i = a + i \frac{b - a}{n} \text{ for } i = 1, \dots, n - 1. \\ t_n = b \end{cases} \tag{13}$$

The detail of chord length parameterization method can be found in [14]. The end parameters are $t_0 = a$ and $t_n = b.$ The other parameters are calculated by

$$\begin{cases} t_0 = a \\ t_i = a + \frac{\sum_{i=1}^k |D_i - D_{i-1}|}{\sum_{i=1}^n |D_i - D_{i-1}|} (b - a) \text{ for } k = 1, \dots, n - 1. \\ t_n = b \end{cases} \tag{14}$$

Respectively, the centripetal parameterization method can be found in [7]. The first and the end parameters are $t_0 = a$ and $t_n = b.$ The remaining parameters are expressed as

$$\begin{cases} t_0 = a \\ t_i = a + \frac{\sum_{i=1}^k |D_i - D_{i-1}|^\alpha}{\sum_{i=1}^n |D_i - D_{i-1}|^\alpha} (b - a) \text{ for } k = 1, \dots, n - 1, \\ t_n = b \end{cases} \tag{15}$$

with the positive power as α is in $[0, 1].$ Selecting the value α affects the shape of the displacement, velocity, acceleration, and jerk curves. In this paper, we

do not discuss the effect of the parameter α . For calculating the parameters t_i according to the centripetal method, we choose the value $\alpha = 1/2$ that is the square root of chord length method.

3.2 Knot Vector Generation

To generate the knot vector for NURBS after a set of parameters t_i is obtained. Using NURBS with degree p for motion curves, we need to compute $m + 1$ knots from $n + 1$ parameters in \mathbf{t} , where $m = n + p + 1$. According to the knot vector in Eq. (3), we have $p + 1$ knots with $u_0 = u_1 = \dots = u_p = a$ and $u_{m-p} = u_{m-p+1} = \dots = u_m = b$. The remaining $n - p$ interval knots ($u_{p+1}, \dots, u_{m-p-1}$) are computed from the parameters t_i .

The uniformly spaced knot vector can be calculated by [6]

$$\begin{cases} u_0 = u_1 = \dots = u_p = a \\ u_{j+p} = t_0 + \frac{j}{n-p+1}(b-a) & \text{for } j = 1, 2, \dots, n-p. \\ u_{m-p} = u_{m-p+1} = \dots = u_m = b \end{cases} \quad (16)$$

For the chord length and centripetal method, knots are computed by the average method [5]

$$\begin{cases} u_0 = u_1 = \dots = u_p = a \\ u_{j+p} = t_0 + \frac{1}{p} \sum_{i=j}^{j+p-1} t_i & \text{for } j = 1, 2, \dots, n-p. \\ u_{m-p} = u_{m-p+1} = \dots = u_m = b \end{cases} \quad (17)$$

4 Results and Discussions

This section presents two examples with a large number of boundary conditions. In the first example, the follower of the cam mechanism satisfies 20 boundary conditions (see in [8]) of the displacement, velocity, and acceleration as shown by start signs in Fig. 1. From the given angles of camshaft, the input angle vector is expressed as $\mathbf{D} = [0, 0, 0, 0.7854, 0.7854, 1.5708, 1.5708, 1.5708, 2.3562, 2.3562, 2.6180, 3.1416, 3.1416, 3.1416, 3.6652, 3.9270, 3.9270, 4.7124, 4.7124, 4.7124]$. The knot vectors for the uniform space, chord length and centripetal methods are computed in Sect. 3.

From the knot vector, basis functions $N_{i,p}$ and rational basis functions $R_{i,p}$ are established (see Eqs. (4) and (5)). The displacement function is computed from calculating the control points in Eq. (8). The results of the displacement, velocity, acceleration, and jerk diagram (SVAJ diagram) show in Fig. 1. It is seen that the difference of the displacement curves is not changed much. However, the velocity, acceleration, and jerk curves are much different. The maximum values of velocity, acceleration, and jerk using chord length method are much smaller than others.

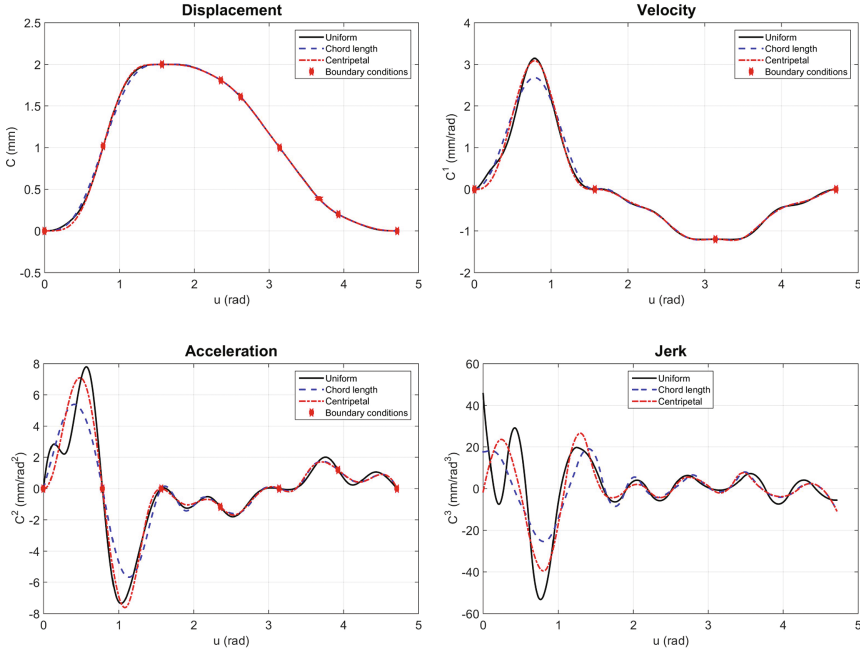


Fig. 1. Comparison of motion curves for three cases of knot vector

As the second example, we consider the cardiovascular mock loop where the motion of the human heart is simulated. The measurement of the displacement follower is shown by star signs in Fig. 2 with 27 values of the displacement. Because of the discontinuity of the velocity and acceleration, the infinite values of the acceleration and jerk will occur, respectively. Thus, to avoid the discontinuity of the velocity, acceleration, and jerk, some boundary conditions are added at the start and the end points of the velocity, acceleration, and jerk, such that their values are equal to zero. Respectively, the input angle vector with 33 elements is written as $\mathbf{D} = [0, 0, 0, 0, 0.2417, 0.4833, 0.725, 0.9666, 1.2083, 1.45, 1.6916, 1.9333, 2.1749, 2.4166, 2.6583, 2.8999, 3.1416, 3.3833, 3.6249, 3.8666, 4.1082, 4.3499, 4.5916, 4.8332, 5.0749, 5.3165, 5.5582, 5.7999, 6.0415, 6.2832, 6.2832, 6.2832, 6.2832]$.

Figure 2 shows SVAJ diagram in one cycle of the cam mechanism. The displacement, velocity, acceleration, and jerk curves in case of the chord length and the centripetal method are coincided because of the same as vector \mathbf{t} , also the knot vector \mathbf{U} . As \mathbf{D} above, the difference between two elements, $|D_i - D_{i-1}| (i = 5, \dots, 30)$, does not change, and the remaining elements are equal to zero. In this case, the parameters t_i are not affected by the power α of the centripetal method. Thus, they have similar values in both the chord length method and the centripetal method, likewise the value of knots u_i . As shown in Fig. 2, the displacement for the uniformly spaced method

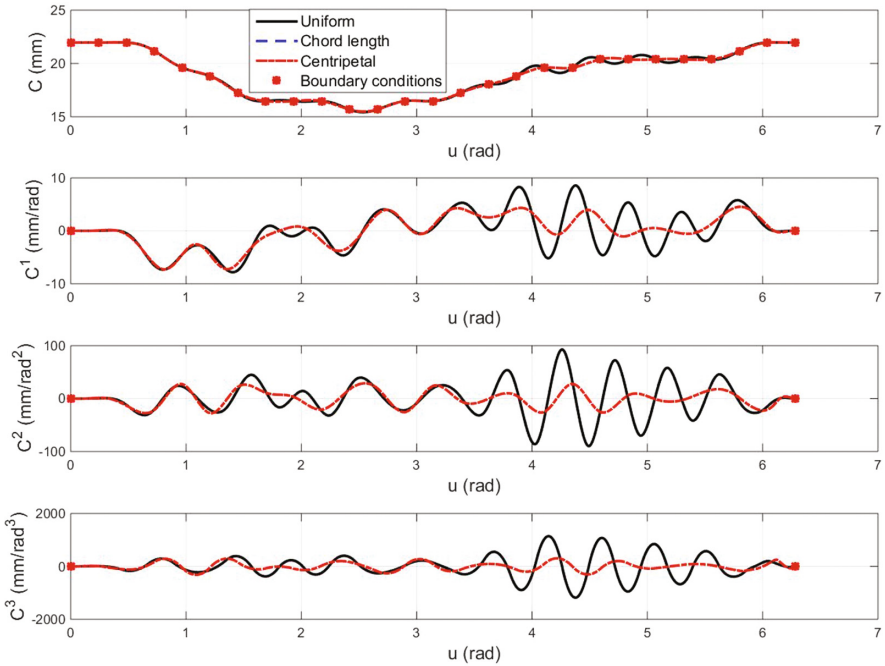


Fig. 2. SVAJ diagram comparison of uniform, chord length, and centripetal methods

is slightly oscillating. Therefore, the peak values of the velocity, acceleration, and jerk curves occur. The maximum values of velocity, acceleration, and jerk with the chord length and the centripetal methods are much smaller than the uniformly spaced method.

5 Conclusions

Using NURBS curve for cam motion synthesis is flexible and robust because it satisfies arbitrary boundary conditions of displacement, velocity, acceleration, and jerk constraints. Furthermore, NURBS curve and its derivative are controlled by several parameters such as knot vector, control points, and weights. The evaluation of effecting the knot vector on the displacement, velocity, acceleration, and jerk curves is presented in this paper. Several methods for computing the knot vector of NURBS used to synthesize the motion curves are presented. The results show that the maximum values of acceleration and jerk in case of the chord length method are smaller than the other methods. Especially, these values for chord length method are much smaller than the uniform method.

References

1. Shigley, J.E., Uicker, J.: Theory of Machines and Mechanisms. McGraw-Hill Inc., New York (1981)
2. Norton, R.L.: Design of Machinery: An Introduction to the Synthesis and Analysis of Mechanisms and Machines, 2nd edn. McGraw-Hill, New York (1999)
3. Norton, R.L.: Cam Design and Manufacturing Handbook. Industrial Press, New York (2002)
4. Piegl, L., Tiller, W.: The Nurbs Book, 2nd edn. Springer, Heidelberg (1997)
5. De Boor, C.R.: A Practical Guide to Splines. Springer, New York (1978)
6. Shamsuddin, S.M.H., Ahmed, M.A.: A hybrid parameterization method for NURBS. In: Proceedings of the International Conference on Computer Graphics, Imaging and Visualization (CGIV'04), pp. 15–20 (2004)
7. Saux, E., Daniel, M.: Estimating criteria for fitting B-spline curves: Application to data compression. In: International Conference Graphicon, pp. 225–232 (1998)
8. Tsay, D.M., Huey, C.O.: Cam motion synthesis using spline function. *J. Mech. Transmissions Autom. Des.* **110**, 161–165 (1988)
9. Tsay, D.M., Lin, B.J.: Improving the geometry design of cylindrical cams using nonparametric rational B-splines. *Comput.-Aided Des.* **28**, 5–15 (1996)
10. Sateesh, N.: Improvement in motion characteristics of cam-follower systems using NURBS. *Int. J. Des. Manuf. Technol.* **8**, 15–21 (2014)
11. Sahu, L.K., Gupta, O.P., Sahu, M.: Design of cam profile using higher order B-spline. *Int. J. Innovative Sci. Eng. Technol.* **13**, 327–335 (2016)
12. Sandgren, E., West, R.L.: Shape optimization of cam profile using a B-spline representation. *J. Mech. Transmissions Autom. Des.* **111**, 195–201 (1989)
13. Naskar, T.K., Mishra, R.: Introduction of control points in B-spline for synthesis of ping finite optimized cam motion program. *J. Mech. Sci. Technol.* **26**, 489–494 (2012)
14. Lee, E.T.Y.: Choosing nodes in parametric curve interpolation. *Comput.-Aided Des.* **6**, 363–370 (1989). Boeing Comerial Airplanes

Kinematics of Biplanetary Epicyclic Gears

J. Drewniak¹, A. Deptuła², T. Kądziołka³, and S. Zawisłak⁴(✉)

¹ Department of Fundamentals of Machine Building,
Faculty of Machine Building and Computer Science,
University of Bielsko-Biala, Bielsko-Biala, Poland
jdrewniak@ath.bielsko.pl

² Department of Knowledge Engineering,
Faculty of Production Engineering and Logistic,
Opole University of Technology, Opole, Poland
a.deptula@po.opole.pl

³ Vocational High School, Nowy Sącz, Poland
tkadziolka@pwsz-ns.edu.pl

⁴ Department of Informatics and Automation,
Faculty of Machine Building and Computer Science,
University of Bielsko-Biala, Bielsko-Biala, Poland
szawislak@ath.bielsko.pl

Abstract. In the present paper, the biplanetary gears are analysed. They have complex layouts and their functioning is not too easy to recognize based upon these general schemes. However, it has been proved that two methods i.e. Willis and Kutzbach could be useful for their detailed kinematical analysis, enclosing e.g. directions of rotation of particular geared wheels. The exemplary gears analysed e.g. kinematical ratios have been calculated. The analysis of these gears could be a good training for mechanism understanding by students and researchers.

Keywords: Biplanetary gear · Kinematical gear ratio · Willis equation · Scheme of velocities

1 Introduction

Planetary gears are mechanisms consisting – among other – of geared wheels, in which at least the symmetry axis of one wheel encircles the main symmetry axis of the system. The wheel, which is going round, is called a planetary wheel or even just a planet or a satellite gear. In practice, more frequently the mechanical system is a three-shaft-gear which consists of a central geared wheel (sun wheel) 1, an outer ring (annulus) with inward-facing teeth that mesh with the planet gear 3 and (at least) three planet gears are joined and displaced regularly in the space by means of an arm (carrier) h (Fig. 1a). In this gear, the arm h and two central geared wheels 1 and 3 consists the set of the basic elements. It is described by a code 2WH (2 wheels i.e. W plus an arm H). Depending on fixing or braking of one of its elements, the gear can work as a mechanism of one degree of freedom (1 DOF) however it represents three possible variants of operation. In case when all three basic gear parts are movable, then a planetary gear has two degrees of freedom and there is a demand for driving of two

different basic elements. Therefore, in such a case, a system serves as a differential gear. This case was analyzed by the authors in [6]. Besides Willis method, graph-based approaches were there effectively utilized.

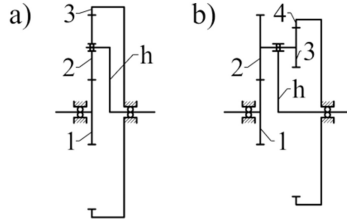


Fig. 1. Schemes of planetary gears - 2WH type (a) and 2WH-EI (b)

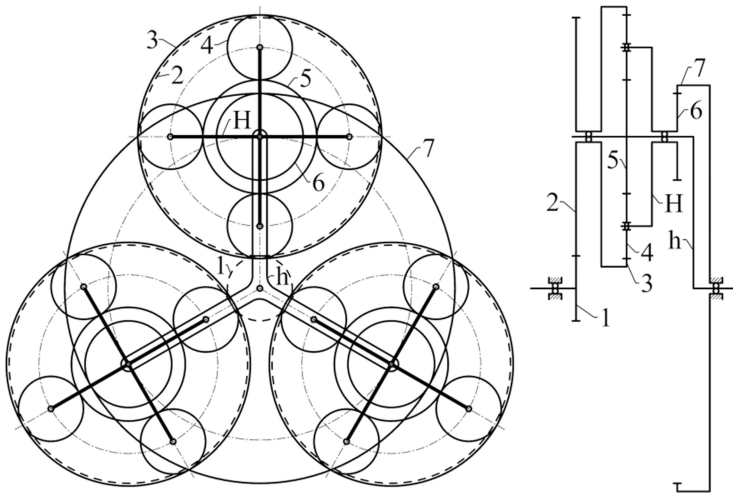


Fig. 2. Front view and scheme of biplanetary gear [5]

In case, when the satellite gears 2 and 3 - for the gear described as 2WH-EI (in Fig. 1b) - are connected via an additional kinematic chain, called the internal planetary mechanism. Moreover, we obtain the double planetary gear (biplanetary gear). The biplanetary gears are described e.g.: in books [1, 3, 5], some of them have been edited recently so there is an interest in this type of mechanisms not only in teaching curricula but also in industry. Namely, just recently it has been described special applications of biplanetary gears [2, 7] in power transmissions and chemical equipment. The exemplary scheme of this gear is presented in Fig. 2. It consists of one main planetary gear having the sun wheel 1 geared with the planetary gears 2, the outer arm is denoted by h . Moreover, the system has the second pair of wheels consisting of planetary wheels/number 3 in Fig. 1b/geared with braked central wheel 7 (number 4 in Fig. 1b). The additional kinematic chain is created by the planetary gears 2 and 6 which create

an epicyclic gear called as an internal planetary mechanism. It consists of the ring gear 3, planet 4, sun wheel 5 and an inner arm H . The arm H drives the planetary wheel 6 – belonging however to the main gear sub-mechanism. The sun wheel 5, belonging to the inner planetary sub-mechanism, is simultaneously in the considered design variant – the arm h of the main planetary gear.

The value of DoF can be calculated based on the following Kutzbach criterion:

$$W = 3 \cdot n - 2 \cdot p_5 - p_4 = 3 \cdot 5 - 2 \cdot 5 - 4 = 1, \quad (1)$$

where: $n = 5$ - number of moving links, $p_5 = 5$ - number of kinematic pairs of 5-th class (bearings), $p_4 = 4$ - number of kinematic pairs of 4-th class (described as: meshing, geared, in mesh or in gear). Characteristic feature of this gear is that the satellite gears of the epicyclic satellite sub-mechanism performs a complex movement rotating around three axes – own, central of planetary sub-mechanism and central of the main planetary gear. Therefore, the kinematical analysis of the whole system is difficult and complex. These gears – due to the character of their internal movements – are utilized mainly in mine machines (cross-cutters, shearer) as well as agricultural machinery.

2 Kinematic Ratio of Biplanetary Gear

2.1 Calculations Performed by Means of Willis Formula

According to the definition of kinematical ratio, we consider the ratio $i_{1,h}^7$ (from pinion 1 to arm h , in case when the wheel 7 is braked/in general immobilized/). The ratio is expressed by means of the following formula:

$$i_{1,h}^7 = \left(\frac{n_1}{n_h} \right)_{n_7=0}, \quad (2)$$

where:

$n_1 = n_{in}$ velocity of pinion 1 - i.e. an input velocity of the considered gear, $n_h = n_{out}$ velocity of arm h - i.e. an output velocity of the gear (Fig. 2).

Aiming for determination of kinematic ratio $i_{1,h}^7$, at the beginning, the basic ratio of the inner gear have to be calculated - in case when the rotational speed is equal to $-n_h$ (i.e. considerations of kinematics in relation to the arm h). In this case, the relative angular velocities of particular wheels of the gear are equal to: $n_j^h = n_j - n_h$ for $j = 1, 2, \dots, 7$ (Fig. 2). Similarly, the relative angular velocity of the internal (inner) arm H in relation to the external arm h is equal to: $n_H^h = n_H - n_h$ (Fig. 2). The basic ratio of the inner planetary gear consisting of the wheels 3, 4, 5 and arm H , in case of known relative velocities: n_3^h, n_4^h, n_5^h and n_H^h - the ratio could be calculated by means of the Willis formula:

$$i_{3,5}^H = \frac{n_3^h - n_H^h}{n_5^h - n_H^h} \quad (3)$$

additionally, based on the formulas for ratios related to the set of wheels 3, 4 and 5 in relations to arm H , we obtain the underneath relationship, depending on adequate teeth numbers:

$$i_{3,5}^H = \left(\frac{n_3^h - n_H^h}{n_4^h - n_H^h} \right) \cdot \left(\frac{n_4^h - n_H^h}{n_5^h - n_H^h} \right) = \left(\frac{n_3^h - n_H^h}{n_5^h - n_H^h} \right) = \left(-\frac{z_4}{z_3} \right) \cdot \left(-\frac{z_5}{z_4} \right) = \left(\frac{z_5}{z_3} \right), \quad (4)$$

optionally it could be expressed by means of other considered notions:

$$i_{3,5}^H = \left(\frac{z_5}{z_3} \right) = \frac{n_3^h - n_H^h}{-n_H^h}, \quad (5)$$

because $n_5^h = n_5 - n_h = 0$ in case when $n_5 = n_h$ (Fig. 2).

Furthermore, aiming for determination of the unknown ratio of the biplanetary gear – the unknown relative angular velocities n_3^h and n_H^h /utilized in the formula (5) - have to be determined as functions of: n_h and/or n_1 . It could be done upon two conditions related to the ratio $i_{H,7}^h$ (i.e. ratio from the arm H to the wheel 7) as well as the ratio $i_{3,1}^h$ (i.e. ratio from the wheel 3 to the wheel 1):

$$i_{H,7}^h = \frac{n_H^h}{n_7^h} = \frac{n_6^h}{n_7^h} = -\frac{z_7}{z_6}, \quad (6)$$

Because $n_H = n_6$, therefore additionally we can write $n_H^h = n_H - n_h = n_6 - n_h = n_6^h$, in turn, therefore consecutive formulas can be calculated:

$$n_H^h = n_7^h \cdot \left(-\frac{z_7}{z_6} \right) = n_h \cdot \frac{z_7}{z_6}, \quad (7)$$

Because $n_7^h = n_7 - n_h = -n_h$ in case $n_7 = 0$, moreover

$$i_{3,1}^h = \frac{n_3^h}{n_1^h} = \frac{n_2^h}{n_1^h} = -\frac{z_1}{z_2}, \quad (8)$$

Because $n_3 = n_2$ and the following equalities can be considered as proper for the considered scheme and the assumption made: $n_3^h = n_3 - n_h = n_2 - n_h = n_2^h$. Moreover, taking into account the former considerations–the underneath formula can be obtained:

$$n_3^h = n_1^h \cdot \left(-\frac{z_1}{z_2} \right) = (n_1 - n_h) \cdot \left(-\frac{z_1}{z_2} \right). \quad (9)$$

Therefore, for the ratio of teeth numbers z_5/z_3 considered in the formula (5) – after some transformations/e.g. considering formula (9)/ – can be expressed by the following relationship:

$$\left(\frac{z_5}{z_3}\right) = \frac{(n_1 - n_h) \cdot \left(-\frac{z_1}{z_2}\right) - n_h \cdot \frac{z_7}{z_6}}{-n_h \cdot \frac{z_7}{z_6}} = \frac{\left(\frac{n_1}{n_h} - 1\right) \cdot \left(-\frac{z_1}{z_2}\right) - \frac{z_7}{z_6}}{-\frac{z_7}{z_6}}, \quad (10)$$

Finally, the formula(2) for determination of the ratio of the biplanetary gear– can be written in the following form:

$$i_{1,h}^7 = \left(\frac{n_1}{n_h}\right)_{n_7=0} = 1 - \frac{z_7}{z_6} \cdot \frac{z_2}{z_1} \cdot \left(1 - \frac{z_5}{z_3}\right) = 1 - \frac{-108}{24} \cdot \frac{132}{36} \cdot \left(1 - \frac{42}{-90}\right) = 25.20. \quad (11)$$

The calculations were done for the assumed number of teeth for the biplanetary gear: $z_1 = 36$, $z_2 = 132$, gear module $m_{1,2} = 1$, $z_3 = -90$, $z_4 = 24$, $z_5 = 42$, gear module $m_{3,4,5} = 1, 5$, $z_6 = 24$, $z_7 = -108$, $m_{6,7} = 2$. The notation style has been utilized that teeth number of geared rings are considered as negative.

2.2 Schemes of Velocities of Particular Gear Elements

An analysis of tangential velocities of the biplanetary gear could be done independently on the other calculation methods via graphical approach. In the considered case, we introductory assume the value of the rotational velocity ω_h of the arm h (e.g.: $\omega_h = 1 \text{ rad/s}$) for the main planetary gear [1, 5]. In this case, it is possible to determine the tangential velocity v_h of the arm– via the following formula:

$$v_h = \omega_h \cdot r_h = 1 \cdot 84 \cdot 10^{-3} = 0.084 \text{ m/s}, \quad (12)$$

where: r_h -radius of the arm h , in the main planetary gear:

$$r_h = 0.5 \cdot (d_1 + d_2) = 0.5 \cdot m_{1,2} \cdot (z_1 + z_2) = 0.5 \cdot 1 \cdot (36 + 132) = 84 \text{ mm}. \quad (13)$$

Vector of this velocity is graphically determined in the way shown in (Fig. 3). Point of gearing (meshing) of the satellite 6 with the immobilized wheel 7 is the temporary central point of rotation of the wheel 6; i.e. the tangential velocity of the wheel 6 in this point is equal to $v_{6,7} = 0$. Therefore, the vector v_H (i.e. velocity of the arm H) is determined by the straight line going from the end of the vector v_h via the point relevant to the zero velocity of the wheel 6, in the temporary center of rotational movement. Its value is derived from the proportion:

$$\frac{v_h}{r_6} = \frac{v_H}{r_H - r_6}; v_H = v_h \cdot \frac{r_H - r_6}{r_6} = 0.084 \cdot \frac{49.5 - 24}{24} = 0.08925 \text{ m/s} \quad (14)$$

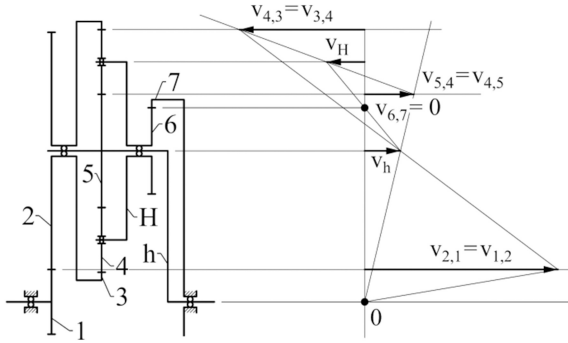


Fig. 3. Scheme of tangential velocities

where: r_H - radius of the external arm H and r_6 - pitch radius of the satellite 6:

$$r_h = 0.5 \cdot (d_5 + d_4) = 0.5 \cdot m_{3,4,5} \cdot (z_5 + z_4) = 0.5 \cdot 1.5 \cdot (42 + 24) = 49.5 \text{ mm}, \quad (15)$$

$$r_6 = 0.5 \cdot m_{6,7} \cdot z_6 = 0.5 \cdot 2 \cdot 24 = 24 \text{ mm}. \quad (16)$$

The sun wheel 5 creates a common element with the arm h , therefore the vector of velocity $v_{5,4}$ of the sun wheel 5 in the point of meshing with the satellite 4 is determined by the straight line going from the point O i.e. the center of rotation of the arm h via the endpoint of the velocity vector v_h . The value of velocity $v_{5,4} = v_{4,5}$ can be calculated upon the proportion:

$$\frac{v_h}{r_h} = \frac{v_{5,4}}{r_h + r_5}; v_{5,4} = v_h \cdot \frac{r_h + r_5}{r_h} = 0.084 \cdot \frac{84 + 31.5}{84} = 0.1155 \text{ m/s} \quad (17)$$

where: r_5 - pitch radius r_5 of the sun wheel 5:

$$r_5 = 0.5 \cdot m_{3,4,5} \cdot z_5 = 0.5 \cdot 1.5 \cdot 42 = 31.5 \text{ mm}. \quad (18)$$

Knowing the velocity $v_{4,5} = v_{5,4}$ of the satellite 4 in the touch point with the sun wheel 5 and velocity v_H of the central point of the satellite 4; - it is possible to establish velocity $v_{4,3}$ of the satellite 4 in the touch point with the ring gear 3. In consequence, the value of vector $v_{4,5}$ is analytically determined based upon the proportion:

$$\frac{v_{4,5} + v_H}{r_4} = \frac{v_{4,3} - v_H}{r_4}, \quad (19)$$

therefore:

$$v_{4,3} = v_{4,5} + 2 \cdot v_H = 0.1155 + 2 \cdot 0.08925 = 0.294 \text{ m/s}, \quad (20)$$

where: $r_4 = 0.5 \cdot m_{3,4,5} \cdot z_4 = 0.5 \cdot 1.5 \cdot 24 = 18 \text{ mm}$ - pitch radius of the satellite wheel 4.

Based on relationships from vector analysis $v_{3,4} = v_{4,3}$ and $v_{2,1} = v_{1,2}$ we have;

$$\frac{v_{2,1} - v_h}{r_2} = \frac{v_{3,4} + v_h}{|r_3|}, \quad (21)$$

we have the formula:

$$v_{2,1} = (v_{3,4} + v_h) \cdot \frac{r_2}{|r_3|} + v_h = (0.294 + 0.084) \cdot \frac{66}{|-67.5|} + 0.084 = 0.4536 \text{ m/s}, \quad (22)$$

where: r_2, r_3 - pitch radiuses of the satellite wheel 2 and the ring 3, respectively:

$$r_2 = 0.5 \cdot m_{1,2} \cdot z_2 = 0.5 \cdot 1 \cdot 132 = 66 \text{ mm}, \quad (23)$$

$$r_3 = 0.5 \cdot m_{3,4,5} \cdot z_3 = 0.5 \cdot 1,5 \cdot (-90) = -67.5 \text{ mm}. \quad (24)$$

Finally, the searched (unknown) angular velocity ω_1 of the sun wheel 1, for the assumed angular velocity $\omega_h = 1 \text{ rad/s}$ of the external (outer) arm H , is equal to:

$$\omega_1 = \frac{v_{1,2}}{r_1} = \frac{0.4536}{18.5} \cdot 10^3 = 25.20 \text{ rad/s}, \quad (25)$$

where: $r_1 = 18 \text{ mm}$ -pitch radius of pinion (i.e. sun wheel).

Finally it was obtained the same value of kinematic ratio:

$$i_{1,h}^7 = \left(\frac{\omega_1}{\omega_h} \right)_{\omega_7=0} = \frac{25.20}{1} = 25.20. \quad (26)$$

The analysis was performed for an exemplary gear but the applied approach could be used in analysis of these types of planetary gear, in general.

3 Conclusions

The discussed methods i.e.: Willis's and Kutzbach's belong to the most effective and general approaches. Therefore, they are useful for an analysis of velocities (kinematics) of biplanetary gears which are rarely considered, despite the applications in control and chemical devices. Based on the utilized methodology, it is not only possible to established velocities of particular parts but also one can calculate the kinematic ratio(s) as well as directions of rotation of all wheels. Furthermore, these approaches are useful – in general, for other complex planetary gears [6].

References

1. Kolovsky, M.Z., Evgrafov, A.N., Semenov, Y.A., Slousch, A.V.: *Advanced Theory of Mechanisms and Machines*. Springer Science & Business Media, Heidelberg (2012)
2. Bin, S., Pengkai, J.: The analysis and modeling of active front steering system. In: 2nd International Conference on IEEE Computing, Control and Industrial Engineering (CCIE), pp. 237–242 (2011)
3. Bostan, I.: Planetary precessional transmissions: synthesis and generation technologies. In: *Power Transmissions*, pp. 21–44. Springer Netherlands (2013)
4. Russian Patent: Coaxial twin-rotor engine biplanetary drive. Opened 25 Jan 2017. <http://russianpatents.com/patent/245/2455192.html>
5. Cyplakov, J.C.: *Bi-Planetary Mechanisms*. Mas'instroenie, Moscow (1966)
6. Drewniak, J., Zawiślak, S.: Linear-graph and contour-graph-based models of planetary gears. *J. Theor. Appl. Mech.* **48**(2), 415–433 (2010)
7. Karimov, R.I., Nurmatov, A.S.: Simulating the dynamics of a biplanetary oil processing mechanism. *Chem. Pet. Eng.* **37**(11), 559–561 (2001)

Optimization

Dynamic Synthesis of a Multibody System: A Comparative Study Between Genetic Algorithm and Particle Swarm Optimization Techniques

Mohamed Amine Ben Abdallah¹(✉), Imed Khemili²,
Med Amine Laribi³, and Nizar Aifaoui¹

¹ Laboratory of Mechanical Engineering (LGM),
National Engineering School of Monastir, University of Monastir,
5000 Monastir, Tunisia
amine.abdallah@yahoo.fr

² Mechanical Laboratory of Sousse (LMS),
National Engineering School of Sousse, University of Sousse,
4000 Sousse, Tunisia
kemili_imed@yahoo.fr

³ Department of GMSC, Pprime Institute,
CNRS - University of Poitiers - ENSMA - UPR 3346, Poitiers, France
med.amine.laribi@univ-poitiers.fr

Abstract. This paper proposes a dynamic synthesis of a flexible multibody systems, mainly, a slider crank mechanism incorporating a flexible connecting rod. Differently to classical synthesis, the mechanism design variables are identified by means of the mechanism dynamic responses such as, the velocity and the acceleration of the slider, and the flexible connecting rod transversal deflection. A comparative study between two optimization techniques, the genetic algorithm (GA) and the Particle Swarm Optimization (PSO), has been established. The two approaches employ different strategies and computational effort to find a solution to a given objective function. Thus, we are interested in the comparison of their implementation. The comparative study asserts that the PSO technique is more suitable for the dynamic synthesis.

Keywords: Flexible slider crank mechanism · Dynamic synthesis · PSO · GA

1 Introduction

Synthesis of multibody systems presents a stiff problem. Thus, regard to the tremendous constraints required for this problem resolution, representing a burdensome task to handle with. For some industrial applications, such as medical applications, welding and manufacturing robot, the mechanism reliability is highly required. Usually, the multibody synthesis is established by means of a kinematic modelling. Thereby, the described path of the mechanism is optimized subject to a desired path. Consequently, the mechanism parameters, involved in the described path, are optimized in order to

handle as maximum as possible with the desired path. However, for the applications mentioned above, the kinematic synthesis presents many shortcomings. This is referred to the non consideration of the inevitable clearance in the joint, also, the elastic behaviour of its different components. For high velocity, the clearance has a significant impact on the mechanism response [1]. Thus, the mechanism synthesis deploying simply the generated path has major drawbacks.

Many works has been completely devoted to multibody synthesis by means of optimization techniques. Laribi et al. [2] have focused on a four bar mechanism synthesis. An hybrid algorithm coupling the genetic algorithm to the fuzzy logic has been developed for this aim. Recently, Essomba et al. [3] have deployed the genetic algorithm for a spherical parallel mechanism, used in medical applications, synthesis. Kucuk [4] has used the particle swarm optimization in order to reduce the consumed energy for a 3-RRR parallel manipulator.

This work deals with a dynamic synthesis of a flexible slider crank mechanism. The optimal mechanism design variables are defined based on a desired dynamic response for more reliability. The main advantage of the dynamic synthesis is that, it take into account the real imperfections subsumed in a real mechanism and involve them in the optimization process.

A comparative study between two optimization techniques is presented in this work. The genetic algorithm and the particle swarm optimization have been performed for the mechanism synthesis. The slider velocity and acceleration, as well as, the transversal deflection of the connecting rod have been chosen as dynamic responses deployed for the mechanism identification.

2 Mathematical Modelling

The dynamic modelling of the multibody systems has been the object of numerous works.

The differential algebraic equations combine both, ordinary differential equations (ODE) and algebraic equations. Ordinary differential equations describe the multibody systems responses. Thereby, algebraic equations are responsible for geometrical modelling of the mechanism.

In this work, a flexible slider crank mechanism is used as a demonstrative example. The synthesis of the mechanism design variables is carried out based on the mechanism dynamic response.

Lagrangian coordinates for the used mechanism are depicted in Fig. 1.

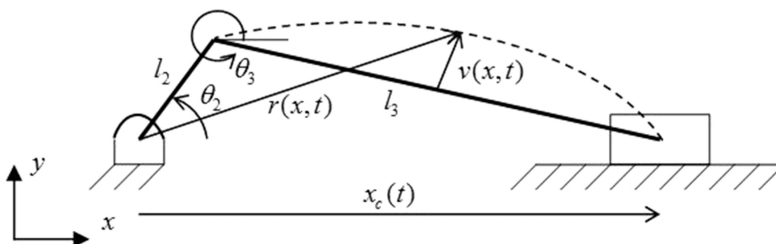


Fig. 1. Flexible slider crank mechanism

The Hamilton principle yields:

$$\begin{bmatrix} M & \Phi_q^T \\ \Phi_q & 0 \end{bmatrix} \begin{bmatrix} \ddot{q} \\ \dot{\lambda} \end{bmatrix} = \begin{bmatrix} Q_e + Q_v \\ Q_c \end{bmatrix} \tag{1}$$

$$\Phi(q, t) = 0 \tag{2}$$

$$Q_{vi} = \sum_{j=1}^2 \lambda_j \frac{\partial \phi_j}{\partial q_i} \tag{3}$$

Wherein, Q_v, Q_e are respectively The total constrained forces and The total applied forces.

The constraint equations, for the slider crank mechanism, which are a system of one degree of freedom, with holonomic constraints based on general coordinates, is as follow:

$$\Phi(q, t) = \begin{pmatrix} \phi_1(q, t) \\ \phi_2(q, t) \end{pmatrix} = \begin{pmatrix} l_2 \cos \theta_2 + l_3 \cos \theta_3 - x_c \\ l_2 \sin \theta_2 + l_3 \sin \theta_3 \end{pmatrix} = \begin{pmatrix} 0 \\ 0 \end{pmatrix} \tag{4}$$

3 Objective Function

The synthesis problem, is formulated as an optimization problem. Thus, the design parameters (the crank and flexible connecting rod lengths) involved in the dynamic response are obtained in order to reduce the error between the desired response and the optimal one, by mean of the used optimizations techniques.

The mechanism response, mainly the slider velocity or the acceleration or the midpoint transversal deflection of the connecting rod, has been represented for, about two crank revolutions.

The error is measured between every point of the optimal solution obtained with the optimization technique and the target one.

The objective function is presented in the following form:

$$F = \min (Error) \tag{5}$$

$$Error = \sqrt{\frac{1}{n} \sum_i [x_i - x_{i \text{ target}} / \text{Max}(x_i) - \text{Min}(x_i)]^2} \tag{6}$$

Where, $x_b, x_{itarget}$ and n represent respectively the proposed design variables response, the target response and the number of measured points in the response.

The error value is dimensionless, therefore, the proposed objective function can be applied for different dynamic responses involved along the identification process.

4 Optimization Approaches

In this work, two optimization techniques have been carried out. A comparative study has been made between the genetic algorithm and the particle swarm optimization.

The genetic algorithm has been the most used heuristic optimization technique for a long time, mainly due, to the simplicity of its implementation. It is divided into the following steps:

Initial population choice:

The initial population in this work is constituted of 20 individuals. Each individual is a vector of two parameters. These parameters are the crank length and the flexible connecting rod length.

Evaluation and selection:

All the initial chosen individuals are evaluated by means of the objective function. A selection probability will be then affected to each individual referring to its performance [5]. Consequently, a high selection probability will be attributed to better individual to favourite their selection for the crossover. However, the selections of low performance individuals remain possible.

Crossover:

Along the crossover process, the two selected individuals exchange each other some characteristics. The crossover probability is equal to 0.9 in this work.

Mutation:

The mutation aim to ensure that the proposed solution is a global optimum. Thus through modifying just a single component of the design variables vector, the individual can be situated in a position far away to its vicinity in the search space. This lead to investigate a broader area of potential global optimum. The mutation probability is equal to 0.3.

The PSO (particle swarm optimization) technique is inspired from the swarm displacement phenomenon. It has been proved that, for a swarm, every particle moves beyond and toward particles in its neighbourhood. Thus, these particles are called informers. Referring to these informers, the velocity and position can be updated. In accordance to the natural swarm, for the optimization using PSO, every particle is matched to her own informers. A confidence coefficients are involved for the communication as well as, the particles positions and velocities update. In fact, thanks to informants, all the swarm particles are connected together. Thus, the swarm is similar to a network allowing the communication between the leader of the swarm (best located particle) with the rest of the swarm. The evolution of every particle performance contributes for the swarm guidance in order to reach the best existent position. Indeed, every particle contains a number of parameters to optimize. In this work, the crank and the connecting rod length are the parameters to optimize. Each position represents a solution, and the swarm moves among the defined search space. In every iteration for the PSO algorithm, the positions and the velocities of all particles are updated as the following equation [6]:

$$v_d = c_1 v_d + c_2(p_d - x_d) + c_3(g_d - x_d) \tag{7}$$

$$x_d = x_d + v_d \tag{8}$$

Where, c_1 , c_2 and c_3 are confidences coefficient, x_d , v_d , are respectively the position and the velocity p_d , g_d are respectively the best position found by the particle and the best position found by informants of the particle.

5 Results and Discussion

The dynamic synthesis has been carried out by means of three different dynamic responses. Two design variables are involved in the mechanism synthesis, mainly, the crank and the flexible connecting rod lengths. An enlarged search interval has been chosen for the aforementioned design variables. The synthesis is made regard to a reference mechanism of a crank length of 50 mm and a flexible connecting rod of 350 mm.

Genetic algorithm results

The interval search has been chosen as [10; 90] and [100; 900] respectively for the crank and the flexible connecting rod lengths. A set of 20 individuals has been randomly considered from the search interval mentioned above.

Based on the mechanism response, the design variables identification has been established. In each iteration, the algorithm evaluates the proposed design variables (11, 12) performance, and error between the proposed and the reference mechanism responses is measured thanks to the objective function.

As illustrated in Fig. 2a the minimization evolution of the objective function subject to iteration number reaches an error of about $6.68 \cdot 10^{-3}$. The proposed lengths after 250 iterations, are 49.09 and 361.2 mm, respectively for the crank and the connecting rod. Using an intel I7 3.4 GHz with 8 Gb of RAM, the CPU time is about 909 s.

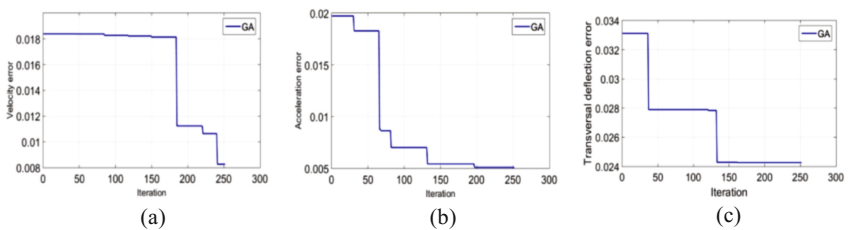


Fig. 2. Optimization error evolution: (a) based on the velocity, (b) based on the acceleration, (c) based on the transversal deflection

It is worth mentioning that the mechanism synthesis can be also conducted using the slider acceleration. As it can be seen in Fig. 2b, an error of $5.105 \cdot 10^{-3}$ has been reached after 250 iterations. The algorithm proposes a couple of 49.292 mm and 339.06 mm respectively for the crank and the connecting rod lengths for a CPU time of 1092 s. The mechanism synthesis deploying the transversal deflection of the connecting rod presents the most onerous synthesis for the proposed algorithm. Thus, based only on a single body elastic deformation (due to eigenmode excitation), doesn't allow to the mechanism to carter for the required reliability. Therefore, the algorithm reaches an error of $1.99 \cdot 10^{-2}$ after 250 iterations as shown in Fig. 2c. Otherwise, a couple of 47.54 mm and 363.18 mm respectively for the crank and the connecting rod lengths are proposed for a CPU time of 1148 s.

As it can be drawn, for the proposed interval search, the genetic algorithm doesn't match perfectly with high accuracy, in spite of, an exhibited convergence (Table 1).

Table 1. Proposed design variables using the genetic algorithm optimization

	The crank length (mm)	The connecting rod length (mm)	Error	CPU time (s)
Acceleration synthesis	49.29	339.06	$5.105 \cdot 10^{-3}$	1092.7
Velocity synthesis	49.09	361.2	$6.68 \cdot 10^{-3}$	909.54
Transversal deflection synthesis	47.54	363.18	$1.99 \cdot 10^{-2}$	1148.9

A higher performance optimization technique should be investigated to overcome the genetic algorithm weakness, in order to propose better accurate results.

PSO optimization results

This section is completely devoted to the dynamic synthesis using the particle swarm optimization.

In order to perform a comparative study between the GA and PSO, a set of 20 particles as well as 250 iterations has been fixed along the particle PSO algorithm execution. As evident in Fig. 3a, for the PSO optimization, the algorithm converges in almost 50 iterations beside 170 for the genetic algorithm. Moreover, the proposed design variables are exactly the same ones of the reference mechanism in about $5.19 \cdot 10^3$ s. However, the required CPU time is significantly higher than time consumed for the GA. This represents an interesting trade off accuracy/CPU time.

Similarly to the dynamic synthesis deploying the GA, the PSO synthesis is able also to identify the mechanism response, based on the slider acceleration. Figure 3b exhibits the mechanism synthesis based on the slider acceleration. The algorithm convergence is reached in about 25 iterations. Beside an error of $5.105 \cdot 10^{-3}$ for the GA, the PSO guarantees an error of $5.851 \cdot 10^{-9}$, matching perfectly with the reference mechanism dimensions.

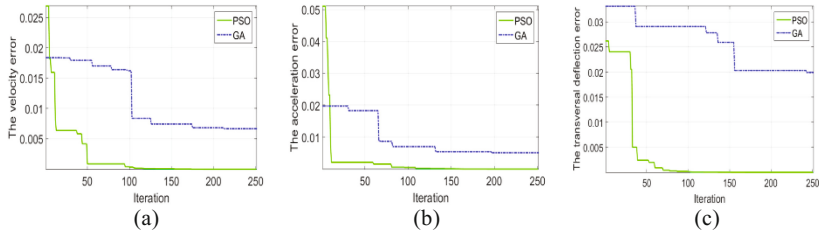


Fig. 3. Optimization error evolution: (a) based on the velocity, (b) based on the acceleration, (c) based on the transversal deflection

Regarding to the most burdensome synthesis type for the GA, based on the transversal deflection of the connecting rod, the PSO algorithm overcomes the difficulties faced, proposing exactly the same design variables as these of the reference mechanism. As illustrated in Fig. 3c, for an error of $1.6193 \cdot 10^{-8}$ beside $1.995 \cdot 10^{-2}$ for the GA, the PSO presents a very performant tool for the mechanism optimization in spite of its high consumed calculation time (Table 2).

Table 2. Proposed design variables using the PSO optimization

	The crank length(mm)	The connecting rod length(mm)	Error	CPU time (s)
The velocity synthesis	50	350	$2.7345e-08$	$5.19 \cdot 10^3$
The acceleration synthesis	50	350	$5.851e-09$	$7.27 \cdot 10^3$
The transversal deflection synthesis	50	350	$1.6193e-08$	$7.29 \cdot 10^3$

6 Conclusion

This work denotes an insight into the multibody system synthesis. For this purpose, the flexible slider crank mechanism has been deployed as a demonstrative example. Some conclusions can be drawn:

- For an enlarged interval search, the mono-objective optimization using the genetic algorithm do not provide reliable results for the dynamic synthesis, mainly, for the transversal deflection synthesis. The genetic algorithm provides the best design variables results based on the slider acceleration.
- The PSO optimization provides more accurate results comparing to the GA. Moreover, the algorithm convergence is reached in almost few iterations, and the algorithm converges exactly to the reference mechanism parameters.

It is observed that, from an evolutionary point of view, the performance of the PSO is better than that of GA. The PSO seems to arrive at its final parameter values in fewer generations than the GA. Compared to GA, the advantages of PSO are that it is easy to implement and there are few parameters to adjust.

References

1. Ben Abdallah, M.A., Khemili, I., Aifaoui, N.: Multibody SystDyn **38**, 173 (2016). doi:[10.1007/s11044-016-9526-7](https://doi.org/10.1007/s11044-016-9526-7)
2. Laribi, M.A., Mlika, A., Romdhane, L., Zegloul, S.: Combined genetic algorithm-fuzzy logic method (GA-FL) in mechanisms synthesis. Mech. Mach. Theory **39**, 717–735 (2004)
3. Essomba, T., Laribi, M.A., Zegloul, S., Poissonrobotica, G.: Optimal synthesis of a spherical parallel mechanism for medical application. doi:<https://doi.org/10.1017/S0263574714001805>
4. Kucuk, S.: Energy minimization for 3-RRR fully planar parallel manipulator using particle swarm optimization. Mech. Mach. Theory **62**, 129–149 (2013)
5. Goldberg, D.: Genetic Algorithms in Search, Optimization, and Machine Learning. Addison-Wesley Longman Publishing Co, Boston (1989)
6. Maurice clerc particle, swarm optimization. Wiley-ISTE, February 2006

Robust Design Methodology of Topologically Optimized Components Under the Effect of Uncertainties

Joshua Amrith Raj and Arshad Javed^(✉)

Department of Mechanical Engineering, BITS-Pilani Hyderabad Campus,
Hyderabad 500078, India

{f2013469, arshad}@hyderabad.bits-pilani.ac.in

Abstract. In the present work, a robust design methodology is presented for topologically optimized components. An integrated methodology combining design of experiment and reliability based topology optimization is proposed to capture the performance of optimized components in realistic environment including various uncertainties. In the present work, Mechanical Advantage, output displacement and the maximum von-Mises stress values are considered as performance functions. Volume fraction, force and aspect ratio are set as design-factors. The uncertainties of design factors are incorporated in the design using reliability method. The uncertainties of non-controllable factors are simulated by creating random field of material properties. Considering uncertainties, the performance of the topology optimization problem is simulated for a space of design factors. The simulated results are analyzed using statistical tools such as, analysis of mean. This technique helps to identify statistical significance and the effect on the performance variations. The proposed methodology is illustrated on a Force inverter. This analysis provides a design methodology in a realistic environment that helps in achieving targeted performance and robust design.

Keywords: Topology optimization · Robust design · Uncertainty · RBTO · Design of experiments · Reliability

1 Introduction

Topology optimization is a useful tool for minimization of structural and machine components [1, 2]. This is done taking into consideration a set of boundary conditions with an objective to maximize the performance of the component.

The performance of a topologically optimized structure is characterized by the mechanical advantage, output displacement and the maximum stress developed. These factors depend on parameters like input force, volume fraction, elasticity of the workpiece, dimension of the material etc. However, in reality there is a considerable amount of uncertainty involved. Consequently, this would affect the performance of the structure. Therefore to deal with this problem, Reliability based Topology Optimization (RBTO) is utilized.

In this paper we consider input force, volume fraction and aspect ratio as the input factors. These are controllable input factors, since they can be modified after each

experiment. The elasticity of the material is a non-controllable input factor. The general approach followed in RBTO is to consider the uncertainty in design factors and to generate the performance values for the worst case scenario. In this approach however, it is difficult to take into account the uncertainties in the non-controllable factors. In addition, it is difficult to conduct the performance analysis of the experiment for all values of the design factors. Hence, to simplify these issues we integrate the method of Design of Experiment (DOE) with Reliability based Topology Optimization (RBTO) [6, 7, 14, 16]. Using DOE helps us to establish the relation between the performance function values and the input factors. It also enables us to perform the simulations in the created design factor domain systematically, thereby reducing the number of simulations. The performance function values are analyzed using statistical techniques like Analysis of Mean (ANOM). In the present work, all the above-mentioned techniques have been carried out for a force inverter.

The manuscript is organized in following manner. The descriptions of DOE and RBTO are presented in Sects. 2 and 3 respectively. The overall methodology of simulation is given in Sect. 4. The analyses of the simulated results are discussed in Sect. 5. The performance values are verified for the structure in COMSOL and finally a conclusion is drawn.

2 Design of Experiments

Design of Experiments (DOE) is a systematic process to frame efficient experiments [10]. The objective of the experiments would be to analyze the effects of several factors on the response or performance of a product or a process. Factors are the parameters that affect the performance of the process or product. These are initially set by the designer while commencing his study. Using the normal experimental process, the number of experiments may be very large to generate the factor-response relation in a generalized way. Here, the DOE offers a scientific way to choose numbers and type of experiment to reduce the cost of experiment without any loss in efficiency. This is achieved by merging several design factors in one study in spite of conducting separate study of each factor. In this way, number of experiments decreases and detailed understating of the product performance is got. In addition to the above, DOE approach helps in steering performance in a desired direction. Therefore, statistically significant factors can easily be identified, and the treatment combinations that have reduced variations in the performance can be identified.

We have chosen input force, volume fraction and aspect ratio as the input parameters. Their uncertainties are selected based on the literature available [11]. Since we have chosen three factors there are a total of 27 combinations possible. From these values we have selected 9 combinations to perform the simulation based on Taguchi method [12]. The uncertainties in the non-controllable factors are also included while carrying out the simulation.

The overall framework of a DOE is represented in Fig. 1. Here, the overall experiment is designed by DOE approach and simulations of performance functions are carried by RBTO method [4, 13]. The responses (performance) corresponding to this combination will be the outcome of this experiment. Using the available ANOM,

ANOVA, SNR and Response Surface method the analysis of the simulated result can be performed. The detailed discussions on each of these techniques, with the actual results are given in subsequent sections. As mentioned earlier, the approach of DOE as integrated with the RBTO method is discussed in the next section.

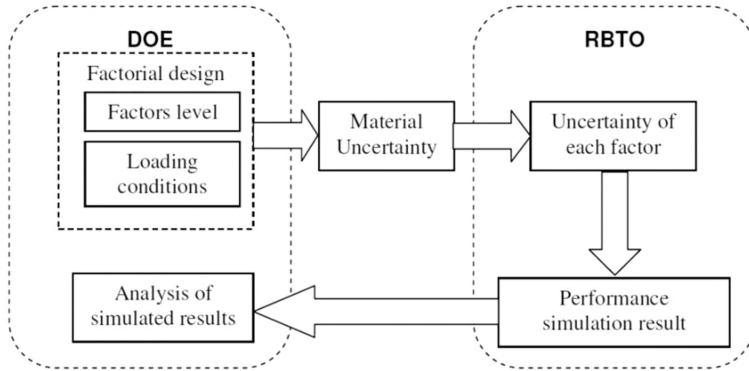


Fig. 1. Framework of integrated DOE and RBTO approach

3 Design of Experiments Integrated to Reliability Based Topology Optimization

In the present work, DOE method is integrated with RBTO. The overall experiment is designed by DOE approach and simulations of performance functions carried by RBTO method. The responses (performance) corresponding to this combination will be the outcome of the experiment (Fig. 1).

The probability of failure of the design [3, 15] is included through the extra probability constant, typical of any RBTO problem. Different types of optimal topologies can be generated based on the type of RBTO approach [4, 13]. However, we follow the approach proposed by Kharmanda et al. [8, 9], since this method minimizes the computation time involved in solving RBTO problems. Thus the present investigation of simulating the compliance and deflection values of reliable optimal topology, employing the Kharmanda [8, 9] approach would involve the following steps.

The design variables are represented by means of variables x and the random variables are represented as y . The reliability index (β) is introduced with a normalized vector U that defines the relation between x and y [5]. The variables x and y can be related to each other by the normalized vector U . The vector U is used to relate random values with mean and also random values with spread (or standard deviation).

The spread S is related to the standard deviation σ as $S = 6\sigma$.

The next step is to evaluate the reliability index β . This is done by solving a constrained optimization problem shown below. The solution of this is called the design point.

$$\begin{aligned} \min : \beta &= \left(U_g^T U_g \right)^{\frac{1}{2}} \\ \text{subject to : } \beta &\geq \beta^* \end{aligned}$$

Now the reliability index when used with the normalized vector U , defines the change in the value of the design variables. Using these values the topology optimization problem is carried out, with an additional constraint to satisfy a target reliability index β .

4 Methodology

In the present work as explained in Sects. 2 and 3, we follow the procedure given below to analyze the performance of the topology optimized component with respect to different levels of factors, including uncertainties.

The set of controllable factors for the problem in our study are applied force, volume fraction and aspect ratio. Using the reliability index and spread values the uncertainties are calculated. Taking these uncertainties into consideration the optimal topology is generated and the performance functions namely compliance, output displacement and von- Mises stress values are determined. Compliance is calculated taking the ratio of the reaction force at the output point to the force exerted at the input. Von Mises stress is calculated by taking the deflection in each direction and substituting it in Eq. (1), where 1, 2, 3 are the stresses in individual directions.

$$\sigma = \sqrt{\sigma_1^2 + \sigma_2^2 + \sigma_3^2 - \sigma_1\sigma_2 - \sigma_1\sigma_3 - \sigma_2\sigma_3} \tag{1}$$

The above mentioned steps are carried out taking the problem of a force inverter and simulated using MATLAB.

4.1 Reliability Based Topology Optimization for a Force Inverter

To illustrate this work we use a force inverter. The design domain for a force inverter is shown in Fig. 2. Force inverter is an example of a compliant mechanism. For certain applications in MEMS there is a need to convert contraction forces to expansion forces. We use a force inverter for this.



Fig. 2. Design domain with load scheme for force inverter

The goal of the optimization problem is to maximize the mechanical advantage so that the energy stored as strain energy is minimum. Strain energy uses a portion of the input energy hence the output energy reduces making the force inverter less efficient. A spring is attached at the output and the input port to simulate the resistance offered by the workpiece. The optimal topology for the force inverter is to be generated for a required material volume so that the mechanical advantage is maximum.

As shown in the figure the dimensions of the design domain is $300 \mu\text{m} \times 300 \mu\text{m}$ and the thickness is $10 \mu\text{m}$. We take the material of the mechanism as silicon which has Young's modulus 160GPa and poisson ratio 0.22 . An input force is applied at the middle of the left edge and an output force is obtained at the middle of the right edge. The left top and the left bottom corners are fixed. Now for a given volume constraint we have to maximize the mechanical advantage. Let us say we require only 30% of the total volume of the domain. We assume the spring constant (elasticity) of the workpiece as $30 \text{ N}/\mu\text{m}$. The maximum allowed displacement at the input end is set as $2 \mu\text{m}$. The values of the design factors which we employ to generate the optimized topology and to calculate the value of performance functions are given.

Table 1. Level of factors

Force (Newton)	Volume fraction	Number of elements in the x-direction
0.001	0.30	30
0.001	0.35	32
0.001	0.40	34
0.002	0.30	34
0.002	0.35	30
0.002	0.40	32
0.003	0.30	32
0.003	0.35	34
0.003	0.40	30

5 Analysis

This analysis helps us identify the mutual interaction of the factors and their relative influence on the performance functions. It can also be used to decide the value of the factor for which the targeted performance can be achieved [10].

5.1 Analysis of Mean

The analysis of mean (ANOM) is carried out by calculating the mean of the performance functions for each level of factors. These values are then plotted. The Figs. 3(a)–(c) shows the level versus the plotted performance values for different values of reliability index (β), and the spread (S). In engineering applications the preferred values of reliability index are chosen as 3 or 3.8 which is 99.99% and 99.97% reliable [10]. Therefore we have chosen 3 and 3.8 as the reliability index for illustration. The spread

values chosen are 10% and 20% of the nominal value of the factor. To keep the manuscript short, all curves are not included.

Figures 3(a), (b) and (c) show the ANOM for the force inverter. It is observed that all three factors are dependent on one another. It is observed that the influences of the factors on performance functions are varying significantly, from deterministic to the reliable cases. These changes are observed because of the significant change in the optimal topologies for reliable case. However, within the reliable cases, the factor influences remain same. As a whole, aspect ratio is observed as the highly influencing factor leaving few exclusions. The ANOM analysis depicts the complex nature of the force inverter problem. It also reflects the lack of similarity in the performance for different cases of deterministic and reliable values.

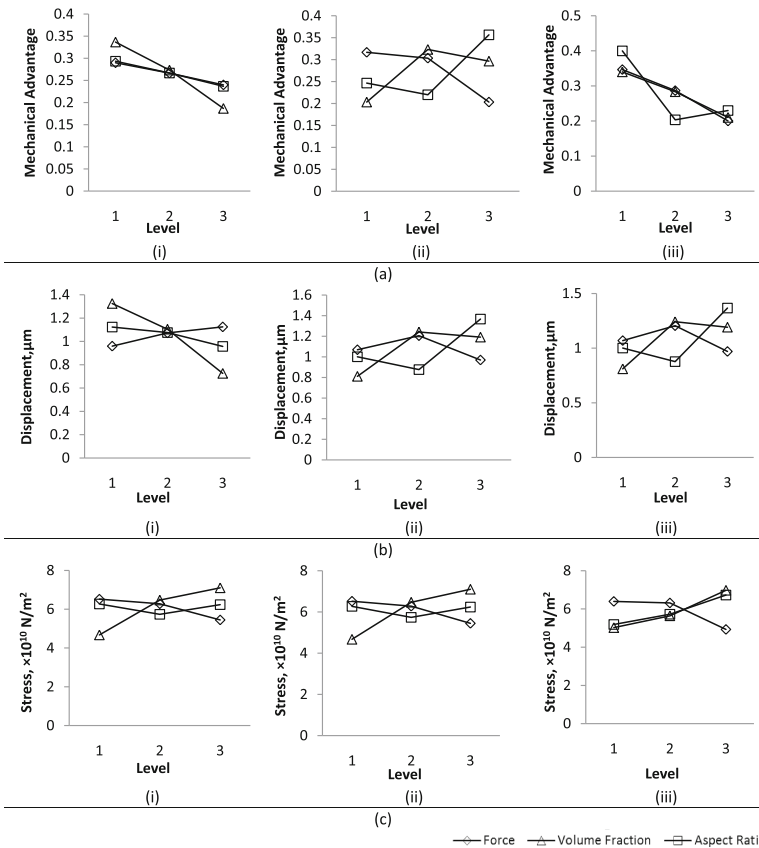


Fig. 3. (a) For force inverter, ANOM of Mechanical Advantage considering, (i) deterministic, (ii) b = 3, S = 10%, (iii) b = 3.8, S = 20% (b) For force inverter, ANOM of deflection (μm), considering, (i) deterministic, (ii) b = 3, S = 10%, (iii) b = 3.8, S = 20% (c) For force inverter, ANOM of Von-Mises stress (N/m^2), (i) deterministic, (ii) b = 3, S = 10%, (iii) b = 3.8, S = 20%

In addition to these observations, it is also seen that with the increased values of reliability index and spread, the effects of aspect ratio and force come closer, when compliance is the performance function. While for deflection, the effect of aspect ratio and force became more distinct. This can be attributed to factor values that come from reliability index and spread. The observations made here can therefore be taken as guidelines to design a topologically optimized structure. It shows the different characteristics of factors under uncertainties.

5.2 Targeted Value Performances

From a designer’s perspective, it is desired to achieve a targeted value of performance with high reliability. However, when the selected RBTO scheme is applied to topology optimization problem, the value of performance functions are altered. In such a scenario, the intended performance cannot be achieved with desired reliability. To achieve a targeted performance with reliability, the design factor must be selected properly. This selection of controllable factors is done using mean performance value analysis. The mean values of performances are computed for each combination of factors. In Fig. 4, the mean Mechanical advantage values with respect to the different combinations are shown. The mean compliance values are computed corresponding to the different values of reliability index and spread.

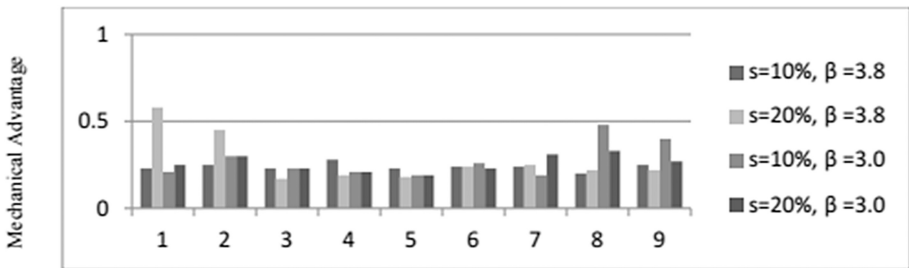


Fig. 4. Values of mechanical advantage for different values of s,β

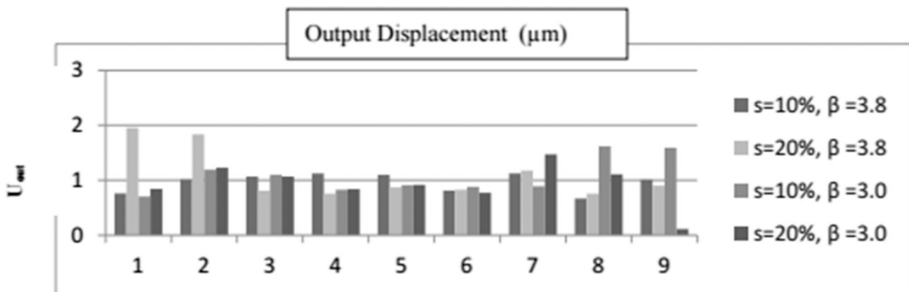


Fig. 5. Values of output displacement for different values of s, β

In Fig. 4, variation of Mechanical advantage value with respect to different β and S can be seen corresponding to each combination. It can be observed that for a desired value of Mechanical advantage or deflection, there are different combination of factors available. A targeted performance value can be achieved by selecting the available combination of controllable factors, reliability index, and spread value.

From Fig. 5, the variation of deflection value with respect to different β and S is seen corresponding to each combination. All observations are similar to that of compliance. It is observed that with increased β and S values, the mean deflection also varies similar to the previous case. In order to observe the behavior of stress variations the mean values of maximum Von-Mises stress is presented in Fig. 6.

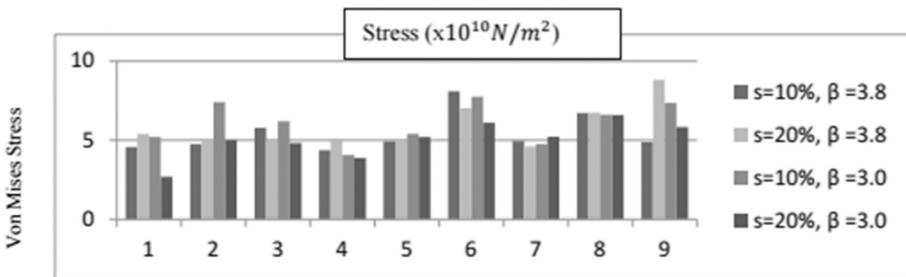


Fig. 6. Values of von Mises stress for different values of s, β

Table 2. Optimal topologies along with the performance function values for $\beta = 3.8$

S. No	Force (N)	Volume Fraction	Number of elements in x-direction	Spread & Reliability	Mechanical Advantage	Output Displacement	Stress	Optimal Topologies
1.	0.0010	0.30	30	10%, 3.8	0.23	0.7644	4.5789	
2.	0.0012	0.35	30	10%, 3.8	0.25	1.0153	4.7517	
3.	0.0014	0.40	30	10%, 3.8	0.23	1.0688	5.7813	
4.	0.0012	0.30	32	10%, 3.8	0.28	1.1246	4.3763	
5.	0.0014	0.35	32	10%, 3.8	0.23	1.1006	4.9356	
6.	0.0010	0.40	32	10%, 3.8	0.24	0.8127	8.100	
7.	0.0014	0.30	34	10%, 3.8	0.24	1.1279	4.9495	
8.	0.0010	0.35	34	10%, 3.8	0.20	0.6702	6.7190	
9.	0.0012	0.40	34	10%, 3.8	0.25	1.0126	4.8844	

From Fig. 6, it is observed that the variation of stress over the different combinations is similar to that of mechanical advantage and deflection. As discussed earlier, the varying optimal topologies at different values, are the reason such variations. Similar to the previous performance function, few observations are also made here. The changes in performance values are lesser with respect to β , compared to that with respect to S . In addition, the effect of change of S value is high when $\beta = 3.8$ compared to that of $\beta = 3$. The observation regarding the performance versus β and S are because of their level values and the specific characteristic of RBTO method.

The optimal topologies along with the performance function values are shown in Table 2 for $s = 10\%$, $\beta = 3.8$

6 Validation of Results with COMSOL

The maximum von Mises stress in the force inverter is found to be 2.3×10^4 when calculated using the MATLAB code. The optimal topology generated using MATLAB was imported to COMSOL.

For the same design factor values the force inverter was simulated in COMSOL. The results are shown in Figs. 7 and 8. The maximum stress as obtained in COMSOL is $2.6 \times 10^4 \text{ MPa}$, which is close to the value computed using MATLAB.

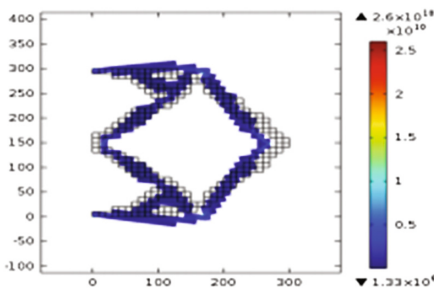


Fig. 7. Von-Mises stress diagram in COMSOL

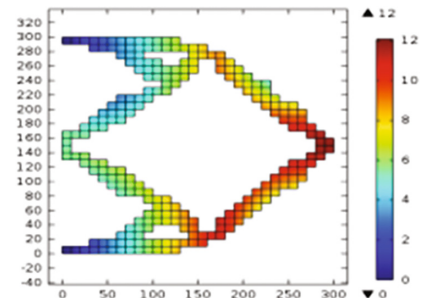


Fig. 8. Displacement diagram in COMSOL

7 Conclusions

The RBTO method assures the design of structural members against the realistic environment. However, to select the input parameter efficiently, the sensitivities of the factors are required to be known. In addition, the performance of the topology-optimized structure varies from its deterministic value, when RBTO is applied. In the present work, a methodology based on DOE and RBTO has been integrated to simulate the

performance in realistic scenarios, in a desired domain of factors including the uncertainties of controllable and non-controllable factors. Current work also addresses the issues of achieving targeted performance for a given problem. The methodology has been illustrated using force inverter. The results are analyzed using ANOM. The sensitivity and the statistical significance of the factors are obtained. Present analysis will be helpful to predict the behavior of performance function in realistic scenarios and to identify the relative robustness of the factor-combinations. Especially in the case of complex real time problems, where the input factor and uncertainties are difficult to directly relate with the output performances, this analysis can also be used to carry out targeted performance function problems of topology optimization.

References

1. Bendsøe, M.P.: Optimization of Structural Topology: Shape and Material, 1st edn. Springer, Berlin (1995)
2. Bendsøe, M.P., Sigmund, O.: Topology Optimization: Theory, Methods and Applications, 2nd edn. Springer, Berlin (2003)
3. Deaton, J.D., Grandhi, R.V.: A survey of structural and multidisciplinary continuum topology optimization: post 2000. *Struct. Multidiscip. Optim.* **49**, 1–38 (2000)
4. Enevoldsen, I., Sørensen, J.D.: Reliability-based optimization in structural engineering. *Struct. Saf.* **15**, 169–196 (1994)
5. Hasofer, A.M., Lind, N.C.: An exact and invariant first order reliability format. *ASCE J. Eng. Mech.* **100**, 111–121 (1974)
6. Javed, A., Rout, B.K.: Tolerance range selection of topologically optimized structure using combined array design of experiments approach. *Proc. Inst. Mech. Eng. C J. Mech. Eng. Sci.* **227**, 2023–2038 (2013)
7. Javed, A., Rout, B.K.: Tolerance range selection of topologically optimized structures with the effects of uncertainties of manufacturing process. *Proc. Inst. Mech. Eng. C J. Mech. Eng. Sci.* **228**, 3441–3461 (2014)
8. Kharrmanda, G., Olhohoff, N.: Reliability-based topology optimization as a new strategy to generate different structural topologies, In: Proceedings of Fifteenth Nordic Seminar on Computational Mechanics, Aalborg, Denmark (2002)
9. Kharmanda, G., Olhohoff, N., Mohamed, A., Lemaire, M.: Reliability-based topology optimization. *Struct. Multidiscip. Optim.* **26**, 295–307 (2004)
10. Montgomery, D.C.: Design and Analysis of Experiments, 5th edn. John Wiley & Sons, Asia (2007)
11. Sigmund, Ole: On the design of compliant mechanisms using topology optimization (1997). *Mech. Struct. Mach.* **25**(4), 493–524 (2007)
12. Ranjit, K.: Roy: Design of Experiments (DOE) Using the Taguchi Approach. Wiley & Sons, New York (2001)
13. Tu, J., Choi, K.K., Park, Y.H.: A new study on reliability-based design optimization. *J. Mech. Des. (ASME)* **121**, 557–564 (1999)

14. Yoo, K.S., Eom, Y.S., Park, J.Y., Im, M.G., Han, S.Y.: Reliability-based topology optimization using successive standard response surface method. *Finite Elem. Anal. Des.* **47**, 843–849 (2011)
15. Youn, B.D., Choi, K.K.: Selecting probabilistic approaches for reliability-based design optimization. *AIAA J.* **42**, 124–131 (2004)
16. Zhao, Q., Chen, X., Ma, Z.D., Lin, Y.: Reliability-based topology optimization using stochastic response surface method with sparse grid design. *Mathematical Problems in Engineering*, 2015, Article ID 487686 (2015)

Parallel Robots

Kinematic and Dynamic Modeling and Base Inertial Parameters Determination of the Quadrupteron Parallel Manipulator

Behzad Danaei, Alaleh Arian, Mehdi Tale Masouleh^(✉), and Ahmad Kalhor

Human and Robot Interaction Laboratory, School of Electrical and Computer Engineering, University of Tehran, Tehran, Iran

{behzad.danaei, aarian, m.t.masouleh, akalhor}@ut.ac.ir

Abstract. This paper deals with the kinematic analysis, dynamic modeling and base inertial parameter determination of a member of multipteron parallel manipulator family, namely, Quadripteron. First, as a prerequisite for dynamic analysis, kinematic relations are obtained. By using a new geometric approach, the solution of the inverse kinematic problem is made equivalent to solve the problem of determining the intersection of two circles within a plane. Compared to other proposed methods, this approach yields more compact and closed-form solutions. The instantaneous kinematic problem is solved via employing the screw theory. Based on foregoing kinematic relations and the concept of link Jacobian matrices, the dynamic model is formulated by means of the principle of virtual work. Furthermore, in order to obtain a more compact formulation for the dynamic analysis, a reduced dynamic model is obtained by determining the base inertial parameters of the under study manipulators.

Keywords: Parallel robots · Kinematics · Screw theory · Dynamic model · Base inertial parameters

1 Introduction

It is well known that, compared to serial robots, parallel manipulators can offer several advantages in terms of better rigidity, higher precision and better dynamic performances. Due to the widespread application of industrial robots performing Schönflies motion pattern, several researches have been conducted on the synthesis and prototyping of parallel or hybrid manipulators featuring the Schönflies motions.

The H4 robot, a fully parallel Schönflies motion generator, was introduced [1]. Also, the (fully parallel) Kanuk and the (hybrid) Manta architectures were proposed [2]. All of the aforementioned architectures were developed mainly based on intuition. In [3], a synthesis method based on screw theory was presented and a large number of other new architectures were discovered. In [4], a quasi-decoupled 4-DOF Schönflies motion generator was proposed, based on the type

synthesis presented in [3]. This architecture, referred to as the Quadrupteron, is of the 4-PRRU type. Here and throughout this paper, in order to represent the kinematic arrangement of a limb, P, R and U stand for a revolute, prismatic and universal joints, respectively, where the actuated one is underlined.

Several studies concerning the Quadrupteron have been carried out over the last decade, however, most of researches are related to their kinematic properties, namely, direct and inverse kinematics, workspace and singularity analysis [4–6]. While the kinematic analysis is an essential and indispensable step in studying a multibody system, in many applications such as simulation and model-based control strategies, an accurate knowledge of the dynamic behavior of the manipulator is a definite asset. To the best knowledge of the authors, as far as Quadrupteron is concerned, there is still a gap on the dynamic analysis of this type of mechanism. There are several approaches for formulating the dynamic model of a multibody system, some of which are: Newton-Euler, the Euler-Lagrange formulation, the principle of virtual work, Kane’s method and Natural Orthogonal Complement (NOC) approach [7].

While the mathematical structure of the dynamic model can be formulated with the above-mentioned approaches, one of the main factors affecting the accuracy of the results, is the exactness of the values of the physical parameters used in the model. It is well-known that not all the inertial parameters have a direct effect on the dynamic response of the system. Therefore, only a set of identifiable parameters can be estimated. The minimal set of identifiable parameters, which are often referred to as *base inertial parameters*, can be determined symbolically or numerically [8,9]. The determination of the base inertial parameters also contributes in reducing the computational cost of the dynamic models, as it eliminates or groups the original inertial parameters [8].

The main contribution of the this paper can be regarded as: (1) Proposing a new geometric approach to solve the position analysis of the under study manipulators which leads to a compact solution for the inverse position problem. (2) Obtaining the dynamic model of a member of multipteron parallel manipulator family, namely, Quadrupteron, in a closed and unified form. (3) Minimizing the computational cost of the dynamic model by obtaining the base inertial parameters of the under study manipulator and reducing the dynamic models without losing the accuracy of the models.

2 Position Analysis

The Quadrupteron, represented schematically in Fig. 1(a), is a 4-DoF parallel mechanism capable of producing the Schönflies motions. The Quadrupteron is composed of 4 legs of the PRRU type attached to an end-effector. In one of the legs (Leg 1 in Fig. 1)(a), the last U joint degenerates into an R joint.

In this section, as the first step of obtaining the kinematic relationships, the Inverse Displacement Problem (IDP) is addressed. Even though the Quadrepteron have been studied before [5,6], a simple closed-form analytical solution is clearly preferred. Such a solution is not only more efficient with regard

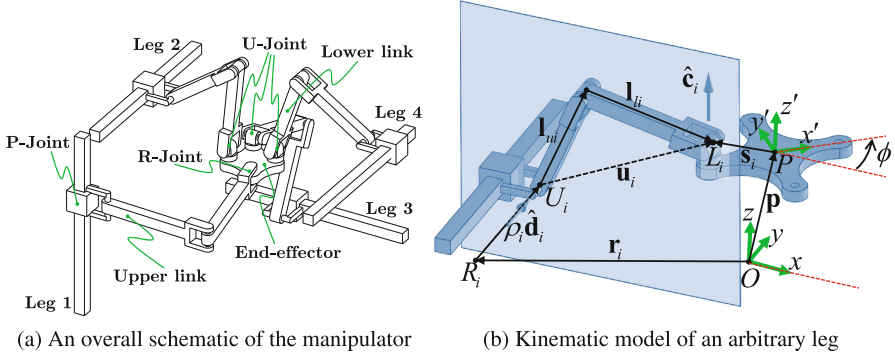


Fig. 1. The Quadrupteron: a 4-DOF Schönflies-motion parallel mechanism.

to computational cost, but also gives a valuable geometric insight for the design. In this regard, a new geometrical method is proposed which results in a general closed-form solutions for the IDP. Before proceeding with the analysis, the following lemma is presented:

Lemma 1. *Suppose $\hat{\mathbf{d}}$ is a known unit vector and \mathbf{u} , \mathbf{l}_u and \mathbf{l}_l are vectors in a plane perpendicular to $\hat{\mathbf{d}}$, satisfying $\mathbf{l}_u + \mathbf{l}_l = \mathbf{u}$. Assuming that \mathbf{u} and length of \mathbf{l}_u and \mathbf{l}_l are known, there are two possible solutions for \mathbf{l}_u and \mathbf{l}_l :*

$$\mathbf{l}_u = \frac{1}{2\|\mathbf{u}\|} \left\{ \left(\|\mathbf{u}\|^2 + l_u^2 - l_l^2 \right) \hat{\mathbf{u}} \pm \sqrt{\left(\|\mathbf{u}\| + l_u + l_l \right) \left(-\|\mathbf{u}\| + l_u + l_l \right) \left(\|\mathbf{u}\| - l_u + l_l \right) \left(\|\mathbf{u}\| + l_u - l_l \right)} \left(\hat{\mathbf{d}} \times \hat{\mathbf{u}} \right) \right\} \quad (1)$$

$$\mathbf{l}_l = \frac{1}{2\|\mathbf{u}\|} \left\{ \left(\|\mathbf{u}\|^2 + l_l^2 - l_u^2 \right) \hat{\mathbf{u}} \mp \sqrt{\left(\|\mathbf{u}\| + l_u + l_l \right) \left(-\|\mathbf{u}\| + l_u + l_l \right) \left(\|\mathbf{u}\| - l_u + l_l \right) \left(\|\mathbf{u}\| + l_u - l_l \right)} \left(\hat{\mathbf{d}} \times \hat{\mathbf{u}} \right) \right\} \quad (2)$$

where l_u and l_l are respectively the length of \mathbf{l}_u and \mathbf{l}_l ¹.

Remark 1: The solution given in Lemma 1 is the same as finding the intersection of two circles in given plane with known diameters.

Remark 2: If the expression under the radical sign in Eqs. (1) and (2) become negative there is no real solution for \mathbf{l}_u and \mathbf{l}_l . From a geometrical standpoint, this condition takes place when the two circles have no intersection.

¹ This lemma can be easily verified by substituting Eqs. (1) and (2) into $\mathbf{l}_u + \mathbf{l}_l = \mathbf{u}$, $\hat{\mathbf{d}} \cdot \mathbf{l}_u = \hat{\mathbf{d}} \cdot \mathbf{l}_l = \hat{\mathbf{d}} \cdot \mathbf{u} = 0$ and $\frac{l_u}{\|\mathbf{l}_u\|} = \frac{l_l}{\|\mathbf{l}_l\|} = 1$. To the best knowledge of the authors, content of this lemma is not available in the literature.

In what follows, we will illustrate how Lemma 1 is used to solve the IDP of the under study manipulators. Referring to Fig. 1(b), the following equation can be established for the i^{th} leg:

$$\mathbf{r}_i + \rho_i \hat{\mathbf{d}}_i + \mathbf{u}_i = \mathbf{p} + \mathbf{s}_i \tag{3}$$

By dot multiplying both sides of Eq. (3) with $\hat{\mathbf{d}}_i$ and considering the fact that \mathbf{u}_i is perpendicular to $\hat{\mathbf{d}}_i$, the following equation is obtained:

$$\rho_i = (\mathbf{p} + \mathbf{s}_i - \mathbf{r}_i) \cdot \hat{\mathbf{d}}_i \tag{4}$$

The latter equation represents the relationship between the pose of the end-effector and position of the i^{th} actuated P-joint. In addition, by substituting Eq. (4) into Eq. (3), \mathbf{u}_i can be obtained as:

$$\mathbf{u}_i = \left(\mathbf{1}_{3 \times 3} - \hat{\mathbf{d}}_i \hat{\mathbf{d}}_i^T \right) (\mathbf{p} + \mathbf{s}_i - \mathbf{r}_i) \tag{5}$$

According to Fig. 1(b), \mathbf{u}_i , \mathbf{l}_{ui} and \mathbf{l}_{li} are vectors in a plane perpendicular to $\hat{\mathbf{d}}_i$, satisfying $\mathbf{l}_u + \mathbf{l}_l = \mathbf{u}$. Hence, by using Lemma 1 one can obtain \mathbf{l}_{ui} and \mathbf{l}_{li} as:

$$\mathbf{l}_{ui} = \frac{1}{2 \|\mathbf{u}_i\|} \left\{ \left(\|\mathbf{u}_i\|^2 + l_{ui}^2 - l_{li}^2 \right) \hat{\mathbf{u}}_i \pm \sqrt{\left(\|\mathbf{u}_i\| + l_{ui} + l_{li} \right) \left(-\|\mathbf{u}_i\| + l_{ui} + l_{li} \right) \left(\|\mathbf{u}_i\| - l_{ui} + l_{li} \right) \left(\|\mathbf{u}_i\| + l_{ui} - l_{li} \right)} \left(\hat{\mathbf{d}}_i \times \hat{\mathbf{u}}_i \right) \right\} \tag{6}$$

$$\mathbf{l}_{li} = \frac{1}{2 \|\mathbf{u}_i\|} \left\{ \left(\|\mathbf{u}_i\|^2 + l_{li}^2 - l_{ui}^2 \right) \hat{\mathbf{u}}_i \mp \sqrt{\left(\|\mathbf{u}_i\| + l_{ui} + l_{li} \right) \left(-\|\mathbf{u}_i\| + l_{ui} + l_{li} \right) \left(\|\mathbf{u}_i\| - l_{ui} + l_{li} \right) \left(\|\mathbf{u}_i\| + l_{ui} - l_{li} \right)} \left(\hat{\mathbf{d}}_i \times \hat{\mathbf{u}}_i \right) \right\} \tag{7}$$

3 Instantaneous Kinematics Analysis

One of the requirements for obtaining the dynamic model by using the virtual work principal, is to derive the relationship between the twist of all of the manipulator’s parts with a suitable reference, such as twist of the end-effector. In this section, by employing the screw theory, the instantaneous twist of each link and the input velocities will be calculated with respect to end-effector’s twist.

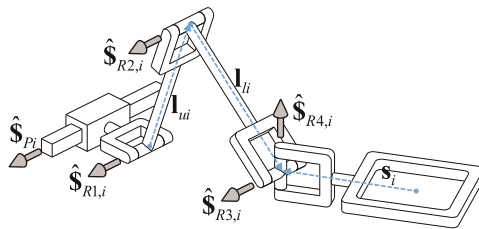


Fig. 2. Screw axes associated with PRR(RR) kinematic structure.

According to Fig. 2, which depicts a kinematic chain with $\underline{PRR}(\text{RR})$ structure which resembles the i^{th} leg of Quadrupteron, the unit joints screws of the i^{th} leg can be written as:

$$\begin{aligned} \hat{\mathbf{S}}_{Pi} &= \begin{bmatrix} \mathbf{0} \\ \hat{\mathbf{d}}_i \end{bmatrix}; & \hat{\mathbf{S}}_{R1,i} &= \begin{bmatrix} \hat{\mathbf{d}}_i \\ (\mathbf{s}_i - \mathbf{l}_{ui} - \mathbf{l}_{li}) \times \hat{\mathbf{d}}_i \end{bmatrix}; & \hat{\mathbf{S}}_{R2,i} &= \begin{bmatrix} \hat{\mathbf{d}}_i \\ (\mathbf{s}_i - \mathbf{l}_{li}) \times \hat{\mathbf{d}}_i \end{bmatrix} \\ \hat{\mathbf{S}}_{R3,i} &= \begin{bmatrix} \hat{\mathbf{d}}_i \\ \mathbf{s}_i \times \hat{\mathbf{d}}_i \end{bmatrix}; & \hat{\mathbf{S}}_{R4,i} &= \begin{bmatrix} \hat{\mathbf{c}}_i \\ \mathbf{s}_i \times \hat{\mathbf{c}}_i \end{bmatrix}; \end{aligned} \quad (8)$$

Now, considering each branch as an open-loop chain and expressing the instantaneous twist of the end-effector, \mathbf{S}_E , in terms of the joint screws, gives:

$$\mathbf{S}_E = \hat{\mathbf{S}}_{Pi}\dot{\rho}_i + \hat{\mathbf{S}}_{R1,i}\dot{\theta}_{R1,i} + \hat{\mathbf{S}}_{R2,i}\dot{\theta}_{R2,i} + \hat{\mathbf{S}}_{R3,i}\dot{\theta}_{R3,i} + \hat{\mathbf{S}}_{R4,i}\dot{\theta}_{R4,i} \quad (9)$$

In order to obtain the relationship between the output twist, \mathbf{S}_E , and the input joint velocities, one should eliminate the passive joint screws from Eq. (9). To do so, both sides of Eq. (9) is left multiplied by a wrench, reciprocal to the passive joints, i.e., $\boldsymbol{\xi}_i^T = [(\mathbf{s}_i \times \hat{\mathbf{d}}_i)^T \quad \hat{\mathbf{d}}_i^T]$. Hence, the relationship between the twist of the end-effector and the linear velocity of the prismatic joints can be obtained as:

$$\begin{bmatrix} \dot{\rho}_1 \\ \vdots \\ \dot{\rho}_4 \end{bmatrix} = \begin{bmatrix} \hat{\mathbf{d}}_1^T (\hat{\mathbf{d}}_1 \times \hat{\mathbf{c}}_1) \cdot \mathbf{s}_1 \\ \vdots \\ \hat{\mathbf{d}}_4^T (\hat{\mathbf{d}}_4 \times \hat{\mathbf{c}}_4) \cdot \mathbf{s}_4 \end{bmatrix} \begin{bmatrix} \dot{\rho} \\ \dot{\phi} \end{bmatrix} = \mathbf{J} \begin{bmatrix} \dot{\rho} \\ \dot{\phi} \end{bmatrix} \quad (10)$$

where \mathbf{J} is called the *input-output Jacobian matrix*.

Also, taking the time derivative of Eq. (3) and dot multiplying both sides of the resulting equation by \mathbf{l}_{li} and \mathbf{l}_{ui} results in:

$$\begin{bmatrix} \mathbf{v}_{Ui} \\ \dot{\theta}_{ui}\hat{\mathbf{d}}_i \end{bmatrix} = \begin{bmatrix} \frac{\hat{\mathbf{d}}_i\hat{\mathbf{d}}_i^T}{\hat{\mathbf{d}}_i\mathbf{l}_{li}^T} & \frac{\hat{\mathbf{d}}_i\hat{\mathbf{d}}_i^T(\hat{\mathbf{c}}_i \times \mathbf{s}_i)}{\hat{\mathbf{d}}_i\mathbf{s}_i^T(\mathbf{l}_{li} \times \hat{\mathbf{c}}_i)} \\ \frac{\mathbf{l}_{ui} \times \hat{\mathbf{d}}_i}{(\mathbf{l}_{ui} \times \mathbf{l}_{li}) \cdot \hat{\mathbf{d}}_i} & \frac{(\mathbf{l}_{ui} \times \mathbf{l}_{li}) \cdot \hat{\mathbf{d}}_i}{(\mathbf{l}_{ui} \times \mathbf{l}_{li}) \cdot \hat{\mathbf{d}}_i} \end{bmatrix} \begin{bmatrix} \dot{\rho} \\ \dot{\phi} \end{bmatrix} = \mathbf{J}_{ui} \begin{bmatrix} \dot{\rho} \\ \dot{\phi} \end{bmatrix} \quad (11)$$

$$\begin{bmatrix} \mathbf{v}_{Li} \\ \dot{\theta}_{li}\hat{\mathbf{d}}_i \end{bmatrix} = \begin{bmatrix} \mathbb{1}_{3 \times 3} & \hat{\mathbf{k}} \times \mathbf{s}_i \\ \frac{\hat{\mathbf{d}}_i\mathbf{l}_{ui}^T}{(\mathbf{l}_{li} \times \mathbf{l}_{ui}) \cdot \hat{\mathbf{d}}_i} & \frac{\hat{\mathbf{d}}_i\mathbf{s}_i^T(\mathbf{l}_{ui} \times \hat{\mathbf{c}}_i)}{(\mathbf{l}_{li} \times \mathbf{l}_{ui}) \cdot \hat{\mathbf{d}}_i} \end{bmatrix} \begin{bmatrix} \dot{\rho} \\ \dot{\phi} \end{bmatrix} = \mathbf{J}_{li} \begin{bmatrix} \dot{\rho} \\ \dot{\phi} \end{bmatrix} \quad (12)$$

where \mathbf{J}_{ui} and \mathbf{J}_{li} are respectively the i^{th} *upper and lower link Jacobian matrices*. Also, $\dot{\theta}_{ui}$ and $\dot{\theta}_{li}$ are respectively the magnitude of angular velocities of the i^{th} upper and lower link.

4 Dynamics Analysis

In this section, the dynamic model of the under study manipulators are formulated by means of d'Alembert's form of the principle of virtual work. Figure 3

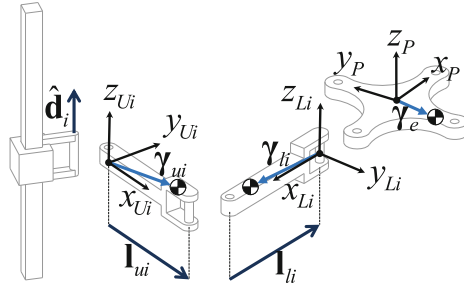


Fig. 3. Local coordinate frames assigned to each link.

depicts the coordinate frames attached to the i^{th} upper and lower links. The position of the center of mass of the i^{th} upper link, lower links and end-effector relative to their reference points are respectively denoted by γ_{ui} , γ_{li} and γ_e . Assuming that the friction forces and torques at the joints are negligible, using the principle of virtual work, referring to the manipulator Jacobian matrix, given in Eq. (10), and link Jacobian matrices given in Eqs. (11) and (12), dynamics of the under study manipulator can be stated as:

$$\mathcal{F}_a = -\tilde{\mathcal{F}}_p - \mathbf{J}^{-\text{T}} \left(\sum_{i=1}^4 \mathbf{J}_{ui}^{\text{T}} \mathcal{F}_{ui} + \sum_{i=1}^4 \mathbf{J}_{li}^{\text{T}} \mathcal{F}_{li} + \mathcal{F}_e \right) \quad (13)$$

where $\mathcal{F}_a = [F_{a1} \cdots F_{aj}]^{\text{T}}$ is the vector of input forces and $\tilde{\mathcal{F}}_p$ is:

$$\tilde{\mathcal{F}}_p = [m_{p1}(\hat{\mathbf{d}}_1 \cdot \mathbf{g} - \ddot{\rho}_1) \cdots m_{pj}(\hat{\mathbf{d}}_4 \cdot \mathbf{g} - \ddot{\rho}_4)]^{\text{T}} \quad (14)$$

And \mathcal{F}_{ui} , \mathcal{F}_{li} and \mathcal{F}_e represent the resultant of applied and inertia forces exerted to the reference point of the i^{th} upper link, i^{th} lower link and the end-effector.

Equation (13) denotes the relation between the actuators' forces and the applied and inertia wrenches acting on the manipulator.

Now by using a method based on principle of virtual work [10], the dynamic model given in Eq. (13) is rewritten in a linear form:

$$\mathcal{F}_a = \mathbf{J}^{-\text{T}} [\mathbf{J}^{\text{T}} \Omega_p \quad \mathbf{J}_{u1}^{\text{T}} \Omega_{u1} \cdots \mathbf{J}_{uj}^{\text{T}} \Omega_{uj} \quad \mathbf{J}_{l1}^{\text{T}} \Omega_{l1} \cdots \mathbf{J}_{lj}^{\text{T}} \Omega_{lj} \quad \Omega_e] \mathbf{P} \quad (15)$$

where Ω_p , Ω_{ui} , Ω_{li} and Ω_e are matrices which are functions of kinematic properties of the manipulator and $\mathbf{P} = [\mathbf{p}_p \quad \mathbf{p}_{u1} \cdots \mathbf{p}_{uj} \quad \mathbf{p}_{l1} \cdots \mathbf{p}_{lj} \quad \mathbf{p}_e]$ in which the entries are defined as:

$$\mathbf{p}_p = [m_{p1} \cdots m_{pj}]^{\text{T}}; \mathbf{p}_{ui} = \begin{bmatrix} m_{ui} \\ m_{ui} U^i \gamma_{ui} \\ U^i I_{ui(z)} \end{bmatrix}; \mathbf{p}_{li} = \begin{bmatrix} m_{li} \\ m_{li} L^i \gamma_{li} \\ L^i I_{li(z)} \end{bmatrix}; \mathbf{p}_e = \begin{bmatrix} m_e \\ m_e^P \gamma_e \\ P I_{e(z)} \end{bmatrix}; \quad (16)$$

Table 1. Base inertial parameters of the Quadrupteron parallel manipulator.

Base inertial parameters	Linear combination	Base inertial parameters	Linear combination
P_{b1}	$m_{p1} + m_{u1} + 20.11^{L^1} I_{l1(z)}$	P_{b14}	$U^4 I_{u4(z)} + 0.91^{L^4} I_{l4(z)}$
P_{b2}	$m_{p2} + m_{u2} + 38.58^{L^2} I_{l2(z)}$	P_{b15}	$m_{l1} - 20.11^{L^1} I_{l1(z)} + m_{l4} - 38.58^{L^4} I_{l4(z)} + 12.5m_e^P \gamma_{e(x)} - 12.5m_e^P \gamma_{e(y)} + 312.5^P I_{e(z)}$
P_{b3}	$m_{p3} + m_{u3} + 35.86^{L^3} I_{l3(z)}$	P_{b16}	$m_{l1}^{L^1} \gamma_{l1(x)} + 4.48^{L^1} I_{l1(z)}$
P_{b4}	$m_{p4} + m_{u4} + 38.58^{L^4} I_{l4(z)}$	P_{b17}	$m_{l1}^{L^1} \gamma_{l1(y)}$
P_{b5}	$U^1 I_{u1(z)} + 0.83^{L^1} I_{l1(z)}$	P_{b18}	$m_{l2} - 38.58^{L^2} I_{l2(z)} - m_{l4} + 38.58^{L^4} I_{l4(z)} - 25m_e^P \gamma_{e(x)}$
P_{b6}	$m_{u2} U^2 \gamma_{u2(x)} + 5.94^{L^2} I_{l2(z)}$	P_{b19}	$m_{l2}^{L^2} \gamma_{l2(x)} + 6.21^{L^2} I_{l2(z)}$
P_{b7}	$m_{u2} U^2 \gamma_{u2(y)}$	P_{b20}	$m_{l2}^{L^2} \gamma_{l2(y)}$
P_{b8}	$U^2 I_{u2(z)} + 0.91^{L^2} I_{l2(z)}$	P_{b21}	$m_{l3} - 35.85^{L^3} I_{l3(z)} + m_{l4} - 38.58^{L^4} I_{l4(z)} + 12.5m_e^P \gamma_{e(x)} + 12.5m_e^P \gamma_{e(y)} + 312.5^P I_{e(z)}$
P_{b9}	$m_{u3} U^3 \gamma_{u3(x)} + 5.99^{L^3} I_{l3(z)}$	P_{b22}	$m_{l3}^{L^3} \gamma_{l3(x)} + 5.99^{L^3} I_{l3(z)}$
P_{b10}	$m_{u3} U^3 \gamma_{u3(y)}$	P_{b23}	$m_{l3}^{L^3} \gamma_{l3(y)}$
P_{b11}	$U^3 I_{u3(z)} + L^3 I_{l3(z)}$	P_{b24}	$m_{l4}^{L^4} \gamma_{l4(x)} + 6.21^{L^4} I_{l4(z)}$
P_{b12}	$m_{u4} U^4 \gamma_{u4(x)} + 5.94^{L^4} I_{l4(z)}$	P_{b25}	$m_{l4}^{L^4} \gamma_{l4(y)}$
P_{b13}	$m_{u4} U^4 \gamma_{u4(y)}$	P_{b26}	$m_e - 625^P I_{e(z)}$

5 Base Inertial Parameter Determination

The dynamic model given in Eq. (15) is linear with respect to inertial parameters and it can be rewritten as $\boldsymbol{\tau} = \mathcal{D}\mathbf{P}$, where \mathbf{P} is the vector of inertia parameters and \mathcal{D} is called the dynamic matrix. As aforementioned, not all of the parameters will directly affect the dynamic model. Thus, by eliminating or grouping the parameters, one can reduce the number of inertial parameters. This reduced set of parameters is known as the *base inertial parameters*. In this section, the SVD-based approach given in [8] was used to determine the base inertial parameters of the Quadrupteron manipulator. The relation between the base inertial parameters and the original parameters is shown in Table 1. It should be noted that, the parameters given in the aforementioned tables are not the only possible set for base inertial parameters and any invertible linear combination of them can be regarded as a new set of base inertial parameters.

By using the base inertial parameters, the dynamic model represented by Eq. (15) is reduced to $\boldsymbol{\tau} = \mathcal{D}_{\text{red}}\mathbf{P}_{\text{red}}$, where \mathcal{D}_{red} is the reduced dynamic matrix after eliminating and grouping the inertial parameters and \mathbf{P}_{red} is the vector containing the base inertial parameters. It is worth mentioning that by compar-

ing the computational time of the reduced dynamic model with the complete dynamic model, it follows that the reduced dynamic model is approximately 41% faster than the original virtual work model.

6 Conclusion

In this paper, the kinematic and dynamic model of Quadrupteron parallel manipulator was derived. As a prerequisite to dynamic analysis, the kinematic analysis was performed which was investigated by resorting to the screw theory. The reason for which screw theory was adopted as kinematic investigation tool is that it provides a Jacobian-base formulation for mapping of the time rate changes of all joints, including passive and actuated, which is essential for dynamic analysis based on virtual work concept. Also, a new geometrical approach based on the intersection of two circles within a plane, was presented which resulted in a compact closed-form solution for inverse kinematic problems. The dynamics of the manipulator was modeled using virtual work principle. Expressing the dynamic model in a linear form with respect to inertial parameters enabled us to determine the base inertial parameters and reduce the dynamic model which reduced the computation time by 41%.

References

1. Pierrot, F., Marquet, F., Company, O., Gil, T.: H4 parallel robot: modeling, design and preliminary experiments. In: IEEE International Conference on Robotics and Automation, Proceedings 2001 ICRA, vol. 4, pp. 3256–3261. IEEE (2001)
2. Rolland, L.: The manta and the kanuk: Novel 4-dof parallel mechanisms for industrial handling. In: Proceedings of ASME Dynamic Systems and Control Division IMECE 1999, pp. 14–19 (1999)
3. Kong, X., Gosselin, C.M.: Type synthesis of 3t1r 4-dof parallel manipulators based on screw theory. IEEE Trans. Robot. Autom. **20**(2), 181–190 (2004)
4. Richard, P.-L., Gosselin, C.M., Kong, X.: Kinematic analysis and prototyping of a partially decoupled 4-dof 3t1r parallel manipulator. J. Mech. Design **129**(6), 611–616 (2007)
5. Kong, X., Gosselin, C.: Forward displacement analysis of a quadratic 4-dof 3t1r parallel manipulator. Meccanica **46**(1), 147–154 (2011)
6. Gosselin, C.M., Tale Masouleh, M., Duchaine, V., Richard, P.-L., Foucault, S., Kong, X.: Parallel mechanisms of the multipteron family: kinematic architectures and benchmarking. In: Proceedings 2007 IEEE International Conference on Robotics and Automation, pp. 555–560. IEEE (2007)
7. Angeles, J., Lee, S.K.: The formulation of dynamical equations of holonomic mechanical systems using a natural orthogonal complement. J. Appl. Mech. **55**(1), 243–244 (1988)
8. Shome, S.S., Beale, D.G., Wang, D.: A general method for estimating dynamic parameters of spatial mechanisms. Nonlinear Dyn. **16**(4), 349–368 (1998)
9. Ebrahimi, S., Kövecses, J.: Unit homogenization for estimation of inertial parameters of multibody mechanical systems. Mech. Mach. Theor. **45**(3), 438–453 (2010)
10. Codourey, A., Burdet, E.: A body-oriented method for finding a linear form of the dynamic equation of fully parallel robots. In: 1997 IEEE International Conference on Robotics and Automation, Proceedings, vol. 2, pp. 1612–1618. IEEE (1997)

Forward Kinematics of the General Triple-Arm Robot Using a Distance-Based Formulation

Nicolas Rojas¹ and Federico Thomas²(✉)

¹ Dyson School of Design Engineering, Imperial College, London SW7 1NA, UK
n.rojas@imperial.ac.uk

² Institut de Robòtica i Informàtica Industrial (CSIC-UPC), Barcelona, Spain
fthomas@iri.upc.edu

Abstract. Distance-based formulations have successfully been used to obtain closure polynomials for planar mechanisms without relying, in most cases, on variable eliminations. The methods resulting from previous attempts to generalize these techniques to spatial mechanisms exhibit some limitations such as the impossibility of incorporating orientation constraints. For the first time, this paper presents a complete satisfactory generalization. As an example, it is applied to obtain a closure polynomial for the general triple-arm parallel robot (that is, the 3-RPS 3-DOF robot). This polynomial, not linked to any particular reference frame, is obtained without variable eliminations or tangent-half-angle substitutions.

Keywords: Triple-arm parallel robot · Distance-based formulations · Forward kinematics

1 Introduction

The distance-based formulation introduced in this paper generalizes the ideas developed in [1] for the position analysis of planar kinematic chains to solve the position analysis of spatial mechanisms. The methods resulting from previous attempts to attain this generalization were limited in scope [2], or were unable to obtain closure polynomials of minimum degree for mechanisms with orientation constraints [3]. The proposed formulation permits the incorporation of this kind of constraints so that it can be applied to general spatial linkages. Besides being general, it is shown how it highly simplifies the algebraic manipulations needed to obtain closure polynomials up to the point in which no variable eliminations are needed in many non-trivial cases. As an example, it is applied to obtain a closure polynomial for the general triple-arm parallel robot (see Fig. 1). This robot consists of a moving platform connected to a fixed base through three revolute-prismatic-spherical kinematic chains, the prismatic joint of each chain being actuated. The forward kinematics problem of this robot consists in finding the possible poses of the moving platform, with respect to the fixed base, for specified values of the actuated prismatic joints. Several researchers have studied

this problem (e.g., [4–7]), but their solutions assume that the axes of the revolute joints attached to the fixed base are arranged forming a triangle. In this paper, using the aforementioned distance-based formulation, the forward kinematics of the triple-arm parallel robot with skew revolute joints is solved. It will be shown how this formulation allows obtaining a closure univariate polynomial that is not linked to any particular reference frame, and is straightforwardly obtained without variable eliminations or tangent-half-angle substitutions.

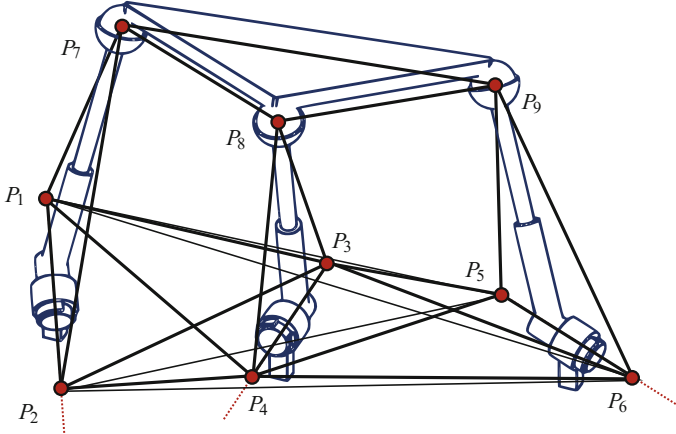


Fig. 1. Triple-arm parallel robot in which the axes supporting the segments P_1P_2 , P_3P_4 , and P_5P_6 are skew and its corresponding bar-and-joint framework model.

The rest of this paper is organized as follows. Section 2 introduces the basics of the distance-based formulation and its corresponding properties and operations. These ideas are then applied to obtain a closure polynomial for the general triple-arm robot in Sect. 3 which is then applied to solve, in Sect. 4, its forward kinematics for a particular instance. Finally, we conclude in Sect. 5.

2 Preliminaries

In what follows, P_i will denote a point in \mathbb{E}^3 , $\mathbf{p}_{i,j} = \overrightarrow{P_iP_j}$, $\mathbf{p}_{i,j,k} = \mathbf{p}_{i,j} \times \mathbf{p}_{i,k}$, and $s_{i,j} = \|\mathbf{p}_{i,j}\|^2$. Vector coordinates will be arranged as column vectors. Vectors $\mathbf{p}_{i,j}$, $\mathbf{p}_{i,k}$, and $\mathbf{p}_{i,j,k}$ represent, in general, a non-orthonormal reference frame which will be denoted by the column vector of nine components $\mathbf{q}_{i,j,k} = (\mathbf{p}_{i,j}^T \ \mathbf{p}_{i,k}^T \ \mathbf{p}_{i,j,k}^T)^T$.

The tetrahedron defined by P_i , P_j , P_k , and P_l will be denoted by $\Delta_{i,j,k,l}$, and it will be said that its *origin* is located at P_i , its *base* is given by then triangle $\Delta_{i,j,k}$, its *base vectors* are $\mathbf{p}_{i,j}$ (*first*) and $\mathbf{p}_{i,k}$ (*second*), and its *output vectors* are $\mathbf{p}_{i,l}$, $\mathbf{p}_{j,l}$, and $\mathbf{p}_{k,l}$.

2.1 Trilateration in Matrix Form

Given the tetrahedron $\triangle_{i,j,k,l}$, its output vector $\mathbf{p}_{i,l}$ can be expressed as a function of the base vectors $\mathbf{p}_{i,j}$ and $\mathbf{p}_{i,k}$ and its squared edge distances as follows (see [8] for details):

$$a_{i,j,k} \mathbf{p}_{i,l} = b_{i,j,k,l} \mathbf{p}_{i,j} + c_{i,j,k,l} \mathbf{p}_{i,k} + \sigma_{i,j,k,l} d_{i,j,k,l} \mathbf{p}_{i,j,k}, \tag{1}$$

where

$$a_{i,j,k} = -\frac{1}{4} \begin{vmatrix} 0 & 1 & 1 & 1 \\ 1 & 0 & s_{i,j} & s_{i,k} \\ 1 & s_{i,j} & 0 & s_{j,k} \\ 1 & s_{i,k} & s_{j,k} & 0 \end{vmatrix}, \quad b_{i,j,k,l} = \frac{1}{4} \begin{vmatrix} 0 & 1 & 1 & 1 \\ 1 & 0 & s_{i,k} & s_{i,l} \\ 1 & s_{i,j} & s_{j,k} & s_{j,l} \\ 1 & s_{i,k} & 0 & s_{k,l} \end{vmatrix},$$

$$c_{i,j,k,l} = -\frac{1}{4} \begin{vmatrix} 0 & 1 & 1 & 1 \\ 1 & 0 & s_{i,j} & s_{i,l} \\ 1 & s_{i,j} & 0 & s_{j,l} \\ 1 & s_{i,k} & s_{j,k} & s_{k,l} \end{vmatrix}, \quad d_{i,j,k,l} = \sqrt{\frac{1}{8} \begin{vmatrix} 0 & 1 & 1 & 1 & 1 \\ 1 & 0 & s_{i,j} & s_{i,k} & s_{i,l} \\ 1 & s_{i,j} & 0 & s_{j,k} & s_{j,l} \\ 1 & s_{i,k} & s_{j,k} & 0 & s_{k,l} \\ 1 & s_{i,l} & s_{j,l} & s_{k,l} & 0 \end{vmatrix}},$$

and $\sigma_{i,j,k,l}$ accounts for the two possible locations of P_l with respect to the plane supporting $\triangle_{j,k,l}$ such that $\sigma_{i,j,k,l} = +1$ if $|\mathbf{p}_{i,j} \mathbf{p}_{i,k} \mathbf{p}_{i,l}| > 0$, and $\sigma_{i,j,k,l} = -1$ otherwise.

Equation (1) can be expressed in matrix form as

$$\mathbf{p}_{i,l} = \mathbf{W}_{i,j,k,l} \mathbf{q}_{i,j,k}, \tag{2}$$

where $\mathbf{W}_{i,j,k,l} = \begin{pmatrix} b_{i,j,k,l} \mathbf{I} & c_{i,j,k,l} \mathbf{I} & d_{i,j,k,l} \mathbf{I} \\ a_{i,j,k} & a_{i,j,k} & a_{i,j,k} \end{pmatrix}$, \mathbf{I} being the 3×3 identity matrix. Thus, the output vector $\mathbf{p}_{j,l}$ can be expressed as

$$\mathbf{p}_{j,l} = \mathbf{p}_{i,l} - \mathbf{p}_{i,j} = (\mathbf{W}_{i,j,k,l} - \mathbf{K}_{\text{IOO}}) \mathbf{q}_{i,j,k}, \tag{3}$$

where $\mathbf{K}_{\text{IOO}} = (\mathbf{I} \ \mathbf{O} \ \mathbf{O})$, \mathbf{O} being the 3×3 null matrix. Similarly, for the case of the output vector $\mathbf{p}_{k,l}$ we have that

$$\mathbf{p}_{k,l} = \mathbf{p}_{i,l} - \mathbf{p}_{i,k} = (\mathbf{W}_{i,j,k,l} - \mathbf{K}_{\text{OIO}}) \mathbf{q}_{i,j,k}, \tag{4}$$

with $\mathbf{K}_{\text{OIO}} = (\mathbf{O} \ \mathbf{I} \ \mathbf{O})$.

Since $\mathbf{q}_{i,j,k}$ represents, in general, a non-orthogonal reference frame, any vector \mathbf{v} can be expressed as $\mathbf{v} = \boldsymbol{\Omega} \mathbf{q}_{i,j,k}$, where $\boldsymbol{\Omega} = (\omega_1 \mathbf{I} \ \omega_2 \mathbf{I} \ \omega_3 \mathbf{I})$ with ω_i being a scalar. Moreover, it can be checked that $\|\mathbf{v}\|^2 = \mathbf{q}_{i,j,k}^T \boldsymbol{\Omega}^T \boldsymbol{\Omega} \mathbf{q}_{i,j,k}$.

2.2 Reference Frame Change

Let us suppose that \mathbf{v} can be expressed in the reference frame defined by $\mathbf{q}_{l,m,n}$ as $\mathbf{v} = \boldsymbol{\Omega}_1 \mathbf{q}_{l,m,n}$, where $\boldsymbol{\Omega}_1 = (\omega_1^1 \mathbf{I} \ \omega_2^1 \mathbf{I} \ \omega_3^1 \mathbf{I})$. Let us also assume that the base

vectors of $\mathbf{q}_{l,m,n}$, $\mathbf{p}_{l,m}$ and $\mathbf{p}_{l,n}$, can be expressed in the reference frame defined by $\mathbf{q}_{i,j,k}$ as $\mathbf{p}_{l,m} = \Omega_2 \mathbf{q}_{i,j,k}$ and $\mathbf{p}_{l,n} = \Omega_3 \mathbf{q}_{i,j,k}$, where $\Omega_2 = (\omega_1^2 \mathbf{I} \ \omega_2^2 \mathbf{I} \ \omega_3^2 \mathbf{I})$, and $\Omega_3 = (\omega_1^3 \mathbf{I} \ \omega_2^3 \mathbf{I} \ \omega_3^3 \mathbf{I})$, respectively. Then, it is possible to express \mathbf{v} in the reference frame defined by $\mathbf{q}_{i,j,k}$ as:

$$\mathbf{v} = \Omega_1 \mathbf{q}_{l,m,n} = \Omega_1 \Lambda_{i,j,k}^{\Omega_2 \Omega_3} \mathbf{q}_{i,j,k}, \tag{5}$$

where

$$\Lambda_{i,j,k}^{\Omega_2 \Omega_3} = \begin{pmatrix} \omega_1^2 \mathbf{I} & \omega_2^2 \mathbf{I} & \omega_3^2 \mathbf{I} \\ \omega_1^3 \mathbf{I} & \omega_2^3 \mathbf{I} & \omega_3^3 \mathbf{I} \\ k_1 \mathbf{I} & k_2 \mathbf{I} & k_3 \mathbf{I} \end{pmatrix},$$

with

$$\begin{aligned} k_1 &= \frac{1}{2}(\omega_1^2 \omega_3^3 - \omega_3^2 \omega_1^3)(s_{i,j} + s_{i,k} - s_{j,k}) + (\omega_2^2 \omega_3^3 - \omega_3^2 \omega_2^3) s_{i,k}, \\ k_2 &= -((\omega_1^2 \omega_3^3 - \omega_3^2 \omega_1^3) s_{i,j} + \frac{1}{2}(\omega_2^2 \omega_3^3 - \omega_3^2 \omega_2^3)(s_{i,j} + s_{i,k} - s_{j,k})), \\ k_3 &= \omega_1^2 \omega_2^3 - \omega_2^2 \omega_1^3. \end{aligned}$$

$\Lambda_{i,j,k}^{\Omega_2 \Omega_3}$ is defined as a *reference frame change matrix*. In the particular case in which $\omega_1^2 = 1, \omega_2^2 = \omega_3^2 = 0$, this matrix will be explicitly denoted as $\Lambda_{i,j,k}^{\mathbf{K}_{100} \Omega_3}$. Likewise, if $\omega_2^3 = 1, \omega_1^3 = \omega_3^3 = 0$, this matrix will be denoted as $\Lambda_{i,j,k}^{\Omega_2 \mathbf{K}_{010}}$.

3 Deriving a Closure Polynomial for the General Triple-Arm Robot

A link connecting two skew revolute axes can be modeled by taking two points on each of these axes and connecting them all with edges to form a tetrahedron. Similarly, a link connecting a revolute axis and a ball joint can be modeled by taking two points on the axis and the center of rotation of the spherical pair and connecting them all with edges to form a triangle, and a link connecting two ball joints can be modeled by connecting the centers of rotation of the spherical pairs by an edge. Thus, a triple arm mechanism with skew revolute joints can be modeled as the bar-and-joint framework shown in Fig. 1. The geometry of this robot is then completely determined by 9 points, namely $P_1 \dots P_9$; 24 squared distances, namely $s_{1,2}, s_{1,3}, s_{1,4}, s_{1,5}, s_{1,6}, s_{1,7}, s_{2,3}, s_{2,4}, s_{2,5}, s_{2,6}, s_{2,7}, s_{3,4}, s_{3,5}, s_{3,6}, s_{3,8}, s_{4,5}, s_{4,6}, s_{4,8}, s_{5,6}, s_{5,9}, s_{6,9}, s_{7,8}, s_{7,9}$, and $s_{8,9}$; and the orientation of 3 tetrahedra, namely $\Delta_{1,2,3,4}, \Delta_{1,2,4,5}$, and $\Delta_{1,2,5,6}$.

According to the notation of Fig. 1, and applying the operations introduced in Sect. 2, next we derive a closure condition for this particular robot. To this end, we are going to express $s_{6,9}$ as a function of $s_{3,7}$. In other words, $s_{3,7}$ is going to be used as a parameter in terms of which the configuration of the robot can be expressed.

For the fixed base, which involves points $P_1 \dots P_6$ and tetrahedra $\triangle_{1,2,3,4}$, $\triangle_{1,2,4,5}$, and $\triangle_{1,2,5,6}$, we have

$$\mathbf{p}_{1,4} = \mathbf{W}_{1,2,3,4} \mathbf{q}_{1,2,3}, \quad (6)$$

$$\mathbf{p}_{1,5} = \mathbf{W}_{1,2,4,5} \mathbf{q}_{1,2,4} = \mathbf{W}_{1,2,4,5} \mathbf{A}_{1,2,3}^{\mathbf{K}_{\text{IOO}}} \mathbf{W}_{1,2,3,4} \mathbf{q}_{1,2,3}, \quad (7)$$

$$\mathbf{p}_{1,6} = \mathbf{W}_{1,2,5,6} \mathbf{q}_{1,2,5} = \mathbf{W}_{1,2,5,6} \mathbf{A}_{1,2,4}^{\mathbf{K}_{\text{IOO}}} \mathbf{W}_{1,2,4,5} \mathbf{A}_{1,2,3}^{\mathbf{K}_{\text{IOO}}} \mathbf{W}_{1,2,3,4} \mathbf{q}_{1,2,3}. \quad (8)$$

Equations (6), (7), and (8) correspond to a representation of the vectors $\mathbf{p}_{1,4}$, $\mathbf{p}_{1,5}$, and $\mathbf{p}_{1,6}$ in the non-orthonormal reference frame defined by $\mathbf{q}_{1,2,3}$. Now, we derive a representation of $\mathbf{p}_{1,7}$ and $\mathbf{p}_{7,9}$ in the same reference frame to compute the closure vector equation $\mathbf{p}_{6,9} = -\mathbf{p}_{1,6} + \mathbf{p}_{1,7} + \mathbf{p}_{7,9}$. For the case of vector $\mathbf{p}_{1,7}$, we straightforwardly have

$$\mathbf{p}_{1,7} = \mathbf{W}_{1,2,3,7} \mathbf{q}_{1,2,3}. \quad (9)$$

For the case of vector $\mathbf{p}_{7,9}$, we first compute

$$\mathbf{p}_{7,3} = -\mathbf{p}_{3,7} = -(\mathbf{W}_{1,2,3,7} - \mathbf{K}_{\text{OIO}}) \mathbf{q}_{1,2,3} = \boldsymbol{\Omega}_{73} \mathbf{q}_{1,2,3}. \quad (10)$$

Similarly, from Eqs. (6) and (9), we get

$$\mathbf{p}_{7,4} = -\mathbf{p}_{1,7} + \mathbf{p}_{1,4} = (\mathbf{W}_{1,2,3,4} - \mathbf{W}_{1,2,3,7}) \mathbf{q}_{1,2,3} = \boldsymbol{\Omega}_{74} \mathbf{q}_{1,2,3}. \quad (11)$$

Then,

$$\mathbf{p}_{7,8} = \mathbf{W}_{7,3,4,8} \mathbf{q}_{7,3,4} = \mathbf{W}_{7,3,4,8} \mathbf{A}_{1,2,3}^{\boldsymbol{\Omega}_{73} \boldsymbol{\Omega}_{74}} \mathbf{q}_{1,2,3} = \boldsymbol{\Omega}_{78} \mathbf{q}_{1,2,3}. \quad (12)$$

Moreover, from Eqs. (7) and (9), we obtain

$$\mathbf{p}_{7,5} = -\mathbf{p}_{1,7} + \mathbf{p}_{1,5} = \left(\mathbf{W}_{1,2,4,5} \mathbf{A}_{1,2,3}^{\mathbf{K}_{\text{IOO}}} \mathbf{W}_{1,2,3,4} - \mathbf{W}_{1,2,3,7} \right) \mathbf{q}_{1,2,3} = \boldsymbol{\Omega}_{75} \mathbf{q}_{1,2,3}, \quad (13)$$

and from Eqs. (7), (9), and (12),

$$\begin{aligned} \mathbf{p}_{5,8} &= -\mathbf{p}_{1,5} + \mathbf{p}_{1,7} + \mathbf{p}_{7,8} \\ &= \left(-\mathbf{W}_{1,2,4,5} \mathbf{A}_{1,2,3}^{\mathbf{K}_{\text{IOO}}} \mathbf{W}_{1,2,3,4} + \boldsymbol{\Omega}_{78} + \mathbf{W}_{1,2,3,7} \right) \mathbf{q}_{1,2,3} = \boldsymbol{\Omega}_{58} \mathbf{q}_{1,2,3}. \end{aligned} \quad (14)$$

Then, using Eqs. (12) and (13), we have

$$\mathbf{p}_{7,9} = \mathbf{W}_{7,8,5,9} \mathbf{q}_{7,8,5} = \mathbf{W}_{7,8,5,9} \mathbf{A}_{1,2,3}^{\boldsymbol{\Omega}_{78} \boldsymbol{\Omega}_{75}} \mathbf{q}_{1,2,3}. \quad (15)$$

Using Eqs. (8), (9), and (15), we can now write $\mathbf{p}_{6,9}$ in the reference frame defined by $\mathbf{q}_{1,2,3}$ as:

$$\mathbf{p}_{6,9} = -\mathbf{p}_{1,6} + \mathbf{p}_{1,7} + \mathbf{p}_{7,9} = \boldsymbol{\Omega}_{69} \mathbf{q}_{1,2,3}, \quad (16)$$

with

$$\boldsymbol{\Omega}_{69} = -\mathbf{W}_{1,2,5,6} \mathbf{A}_{1,2,4}^{\mathbf{K}_{\text{IOO}}} \mathbf{W}_{1,2,4,5} \mathbf{A}_{1,2,3}^{\mathbf{K}_{\text{IOO}}} \mathbf{W}_{1,2,3,4} + \mathbf{W}_{7,8,5,9} \mathbf{A}_{1,2,3}^{\boldsymbol{\Omega}_{78} \boldsymbol{\Omega}_{75}} + \mathbf{W}_{1,2,3,7}.$$

Thus, we finally conclude that

$$s_{6,9} = \mathbf{q}_{1,2,3}^T \boldsymbol{\Omega}_{69}^T \boldsymbol{\Omega}_{69} \mathbf{q}_{1,2,3}. \quad (17)$$

The right hand side of the above equation is a function of the unknown squared distances $s_{3,7}$, $s_{4,7}$, $s_{5,7}$ and $s_{5,8}$. However, from Eqs. (11), (13), and (14), we have that

$$s_{4,7} = \mathbf{q}_{1,2,3}^T \boldsymbol{\Omega}_{74}^T \boldsymbol{\Omega}_{74} \mathbf{q}_{1,2,3}, \quad (18)$$

$$s_{5,7} = \mathbf{q}_{1,2,3}^T \boldsymbol{\Omega}_{75}^T \boldsymbol{\Omega}_{75} \mathbf{q}_{1,2,3}, \quad (19)$$

$$s_{5,8} = \mathbf{q}_{1,2,3}^T \boldsymbol{\Omega}_{58}^T \boldsymbol{\Omega}_{58} \mathbf{q}_{1,2,3}. \quad (20)$$

Then, the substitution of these expressions in (17) yields a scalar radical equation in a single variable: $s_{3,7}$. The real roots of this closure condition determine the assembly modes of the analyzed robot. These roots can be computed, for instance, from the univariate polynomial resulting from clearing the radicals in this expression, as explained in [9]. For each real root, we can determine the location of the three points of the moving platform by computing, for example, the following sequence of trilaterations: obtaining $\mathbf{p}_{1,7}$ from $\mathbf{p}_{1,2}$ and $\mathbf{p}_{1,3}$, then $\mathbf{p}_{3,8}$ from $\mathbf{p}_{3,7}$ and $\mathbf{p}_{3,4}$, and finally $\mathbf{p}_{5,9}$ from $\mathbf{p}_{5,7}$ and $\mathbf{p}_{5,8}$. This leads to up to eight locations for P_9 . At least one of them necessarily satisfies the distance constraint imposed by $s_{6,9}$ and hence corresponds to a valid assembly mode.

4 Numerical Example

According to the notation of Fig. 1, let us consider the triple arm mechanism with the following known squared lengths: $s_{1,2} = 1$, $s_{1,3} = 17$, $s_{1,4} = 10$, $s_{1,5} = 26$, $s_{1,6} = 20$, $s_{1,7} = 101$, $s_{2,3} = 16$, $s_{2,4} = 11$, $s_{2,5} = 19$, $s_{2,6} = 13$, $s_{2,7} = 102$, $s_{3,4} = 3$, $s_{3,5} = 11$, $s_{3,6} = 13$, $s_{3,8} = 126$, $s_{4,5} = 20$, $s_{4,6} = 18$, $s_{4,8} = 101$, $s_{5,6} = 2$, $s_{5,9} = 145$, $s_{6,9} = 123$, $s_{7,8} = 10$, $s_{7,9} = 26$, and $s_{8,9} = 10$; with $\sigma_{1,2,3,4} = +1$, $\sigma_{1,2,4,5} = -1$, and $\sigma_{1,2,5,6} = +1$. Substituting these values in (17), using the expressions for $s_{4,7}$, $s_{5,7}$ and $s_{5,8}$ in terms of $s_{3,7}$, and clearing radicals, we obtain the following polynomial:

$$\begin{aligned} & 4.3635 \cdot 10^{12} s_{3,7}^{16} - 1.1184 \cdot 10^{16} s_{3,7}^{15} + 1.3683 \cdot 10^{19} s_{3,7}^{14} - 1.0517 \cdot 10^{22} s_{3,7}^{13} \\ & + 5.6413 \cdot 10^{24} s_{3,7}^{12} - 2.2259 \cdot 10^{27} s_{3,7}^{11} + 6.6546 \cdot 10^{29} s_{3,7}^{10} - 1.5332 \cdot 10^3 \cdot 2 \cdot s_{3,7}^9 \\ & + 2.7456 \cdot 10^3 \cdot 4 \cdot s_{3,7}^8 - 3.8296 \cdot 10^3 \cdot 6 \cdot s_{3,7}^7 + 4.1433 \cdot 10^3 \cdot 8 \cdot s_{3,7}^6 - 3.4390 \cdot 10^{40} s_{3,7}^5 \\ & + 2.1463 \cdot 10^{42} s_{3,7}^4 - 9.7358 \cdot 10^{43} s_{3,7}^3 + 3.0275 \cdot 10^{45} s_{3,7}^2 - 5.7676 \cdot 10^{46} s_{3,7} \\ & + 5.0725 \cdot 10^{47}. \end{aligned} \quad (21)$$

This polynomial has six real roots: 126.00, 140.93, 186.75, 190.26, 193.73, and 198.13. The corresponding robot configurations for the case in which P_1 is located at the origin, and $\mathbf{p}_{1,2} = (1, 0, 0)^T$, $\mathbf{p}_{1,3} = (1, 4, 0)^T$, $\mathbf{p}_{1,4} = (0, 3, 1)^T$, $\mathbf{p}_{1,5} = (4, 3, -1)^T$, and $\mathbf{p}_{1,6} = (4, 2, 0)^T$, appear in Fig. 2.

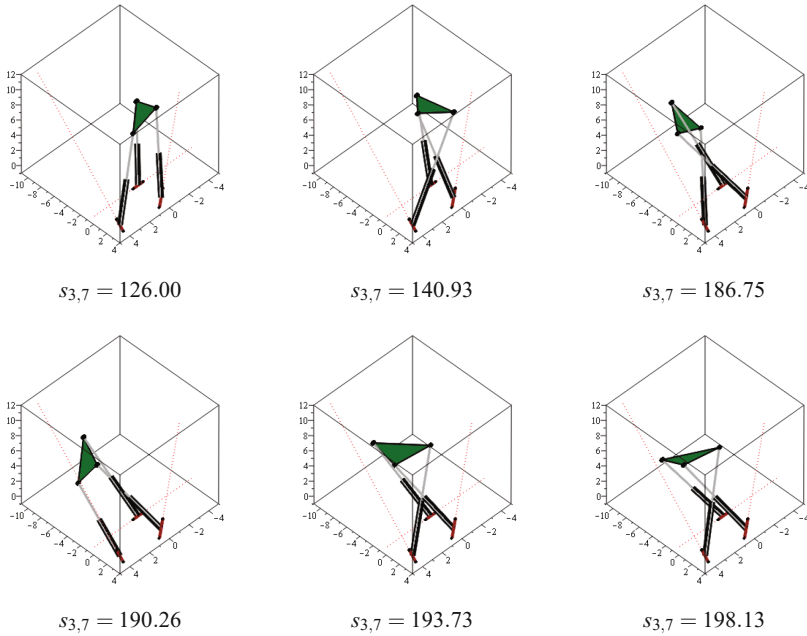


Fig. 2. The six real solutions to the forward kinematics of the analyzed triple-arm robot.

5 Conclusion

Solving the position analysis of kinematic chains based on the idea of obtaining closure conditions using n -laterations and constructive geometry arguments has been quite successful for the planar case. However, the extension of this approach to three dimensions, to solve the position analysis of spatial mechanisms, remained elusive despite the efforts to generalize the planar techniques. The main drawbacks of these previous attempts include the impossibility of dealing with orientation constraints, the limited range of mechanisms that can be analyzed using them, and the complexity of the algebraic manipulation needed to solve even relatively simple problems. This paper has introduced the basic concepts and properties of a distance-based matrix formulation that clears all these disadvantages. The technique has been applied to solve the forward kinematics of the triple arm mechanism with skew revolute joints.

Acknowledgements. This work has been partially supported by the Spanish Ministry of Economy and Competitiveness under project DPI2014-57220-C2-2-P.

References

1. Rojas, N.: Distance-based formulations for the position analysis of kinematic chains. Ph.D. thesis, Universitat Politècnica de Catalunya (2012)
2. Rojas, N., Thomas, F.: The closure condition of the double banana and its application to robot position analysis. In: Proceedings of the IEEE International Conference on Robotics and Automation, pp. 4641–4646 (2013)
3. Thomas, F., Porta, J.M.: Closure polynomials for strips of tetrahedra. In: Advances in Robot Kinematics (2016)
4. Gosselin, C.: Kinematic analysis optimization and programming of parallel robotic manipulators. Ph.D. Thesis, McGill University (1988)
5. Waldron, K.J., Raghavan, M., Roth, B.: Kinematics of a hybrid series-parallel manipulation system. ASME J. Mech. Transm. Autom. Des. **111**(2), 211–221 (1989)
6. Kim, J., Park, F.C.: Direct kinematic analysis of 3-RS parallel mechanisms. Mech. Mach. Theory **36**(10), 1121–1134 (2001)
7. Schadlbauer, J., Walter, D., Husty, M.: A complete analysis of the 3-RPS manipulator. In: Bandyopadhyay, G., Ramu, P. (eds.) Machines and Mechanisms, pp. 410–419. Narosa Publishing House, New Delhi (2011)
8. Thomas, F., Ros, L.: Revisiting trilateration for robot localization. IEEE Trans. Robot. **21**(1), 93–101 (2005)
9. Porta, J.M., Thomas, F.: Closed-form position analysis of variable geometry trusses. Mechanism and Machine Theory (to appear)

Parallel Manipulators in Terms of Dual Cayley-Klein Parameters

G. Nawratil^(✉)

Institute of Discrete Mathematics and Geometry,
Vienna University of Technology, Vienna, Austria
nawratil@geometrie.tuwien.ac.at

Abstract. Cayley-Klein parameters are an alternative to Euler parameters for describing the spherical motion group. Based on Study's and Kotelnikov's "Principle of Transference" one can use dual Cayley-Klein parameters for the motion study of oriented lines in Euclidean 3-space. In this paper we focus on the transformation of points in terms of dual Cayley-Klein parameters and show that these parameters imply a very compact symbolic expression of the sphere condition, which is the central equation for computational algebraic kinematics of parallel manipulators of Stewart-Gough type. Moreover it is shown that the compactness of this formulation is passed on to the symbolic expression of the singularity loci. We also adopt our results to the analogue in planar kinematics and point out the difference to the well-known approach of isotropic coordinates.

Keywords: Dual cayley-klein parameters · Sphere condition · Circle condition · Singularity loci

1 Introduction

It is well-known that planar displacements of the Euclidean plane can be written as:

$$\begin{pmatrix} x \\ y \end{pmatrix} \mapsto \begin{pmatrix} x_0 \\ y_0 \end{pmatrix} = \begin{pmatrix} \cos \varphi & -\sin \varphi \\ \sin \varphi & \cos \varphi \end{pmatrix} \begin{pmatrix} x \\ y \end{pmatrix} + \begin{pmatrix} m \\ n \end{pmatrix}, \quad (1)$$

where $(x_0, y_0)^T$ (resp. $(x, y)^T$) are the coordinates of a point P with respect to the fixed frame (resp. moving frame), φ is the angle of rotation and $(m, n)^T$ the translation vector. By interpreting the Euclidean plane as Gaussian plane, Eq. (1) can be rewritten as:

$$x + yi \mapsto x_0 + y_0i = e^{i\varphi}(x + yi) + (m + ni), \quad (2)$$

where i denotes the complex unit. In addition one can set:

$$p_0 := x_0 + y_0i, \quad \bar{p}_0 := x_0 - y_0i \quad (3)$$

and replace the original coordinates x_0 and y_0 by:

$$x_0 = (p_0 + \bar{p}_0)/2, \quad y_0 = (p_0 - \bar{p}_0)/(2i). \quad (4)$$

The obtained pair (p_0, \bar{p}_0) are the so-called isotropic coordinates of \mathbf{P} with respect to the fixed system. Analogously one gets the isotropic coordinates $(p, \bar{p}) := (x + yi, x - yi)$ of \mathbf{P} with respect to the moving system and the isotropic coordinates $(\tau, \bar{\tau}) := (m + ni, m - ni)$ of the translation. Thus Eq. (2) equals $p \mapsto p_0 = e^{i\varphi}p + \tau$. In order to make this formulation algebraic, we replace $e^{i\varphi}$ by the complex number κ , which has to fulfill the normalizing condition $\kappa\bar{\kappa} = 1$. Hence we get the compact notation:

$$p \mapsto p_0 = \kappa p + \tau \quad \text{with} \quad \kappa\bar{\kappa} = 1. \tag{5}$$

A historical overview on planar kinematics based on isotropic coordinates is given in the work [21] by Wampler, in which these coordinates are used to determine the degree and circularity of curves traced by planar linkages. Further references and historical remarks can be found in the book of Wunderlich [23] where these coordinates are called minimal coordinates. Beside [18] most of the recent work using isotropic coordinates was done by Wampler (cf. [22] and all self-references therein).

1.1 Motivation and Outline of the Paper

Based on the algebraic formulation Eq. (5) we can derive the basic equation for the study of planar parallel manipulators with RPR legs (Fig. 1 left); namely the condition that a point \mathbf{P} of the moving system is located on a circle with radius R centered at the point \mathbf{B} with fixed coordinates $(u_0, v_0)^T$. This so-called circle condition reads as follows:

$$(\kappa p + \tau - b_0)(\bar{\kappa} \bar{p} + \bar{\tau} - \bar{b}_0) - R^2 = 0, \tag{6}$$

where $(b_0, \bar{b}_0) := (u_0 + v_0i, u_0 - v_0i)$ denote the isotropic coordinates of \mathbf{B} with respect to the fixed system. Expanding this equation shows that it has 10 terms and that it is inhomogeneous quadratic in the motion parameters $\kappa, \bar{\kappa}, \tau, \bar{\tau}$.

Nevertheless the symbolic expression of Eq. (6) is very compact, a lot of recent publications (e.g. [2, 7, 9, 11, 19]) use the circle condition formulated in terms of Blaschke-Grünwald (BG) parameters, which has 26 terms. A motive for doing this is that one ends up with a homogenous quadratic equation in the BG parameters, thus methods of projective algebraic geometry can be applied. This gives reason to ask for a formulation, which has both benefits (compactness and homogeneity). We present such a formulation as a special case of a more general approach taken for spatial kinematics. In detail the paper is structured as follows:

We close Sect. 1 by giving a very brief review on the quaternionic formulation of displacements in Euclidean spaces of dimension 2 and 3. In Sect. 2 we discuss the transformation of points with respect to dual Cayley-Klein (CK) parameters and use them in Sect. 3 for presenting the most compact symbolic expression of the sphere condition and the singularity loci of Stewart-Gough (SG) manipulators (Fig. 1 right), which is known to the author. Moreover, the obtained results can easily be adopted for planar kinematics, thus we also get a solution to our motivating question; namely a homogenous circle condition with only 10 terms.

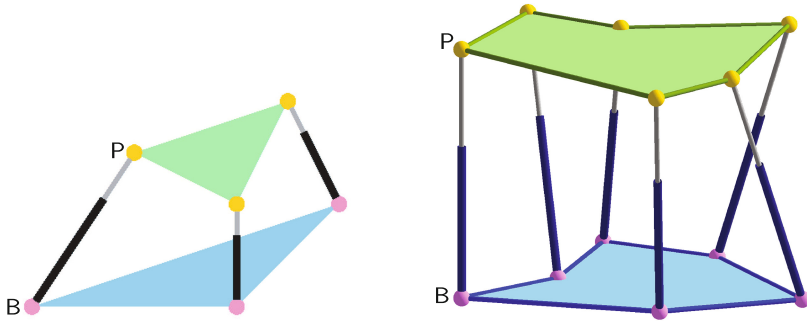


Fig. 1. (Left) 3-dof RPR planar parallel manipulator: The platform is connected via three RPR-legs to the base. (Right) SG manipulator: The platform is connected via six SPS-legs to the base. For the planar as well as the spatial mechanism the anchor points of the legs are denoted by P and B, respectively, and in both cases only the prismatic joints are active.

1.2 Quaternionic Formulation of Displacements

$\mathfrak{Q} := q_0 + q_1\mathbf{i} + q_2\mathbf{j} + q_3\mathbf{k}$ with $q_0, \dots, q_3 \in \mathbb{R}$ is an element of the skew field of quaternions \mathbb{H} , where $\mathbf{i}, \mathbf{j}, \mathbf{k}$ are the so-called quaternion units. The conjugated quaternion to \mathfrak{Q} is given by $\tilde{\mathfrak{Q}} := q_0 - q_1\mathbf{i} - q_2\mathbf{j} - q_3\mathbf{k}$. Moreover, \mathfrak{Q} is called unit-quaternion for $q_0^2 + q_1^2 + q_2^2 + q_3^2 = 1$.

Displacements in spatial kinematics can be formulated in terms of dual quaternions $\mathbb{H} + \varepsilon\mathbb{H}$, where ε is the dual unit with the property $\varepsilon^2 = 0$. An element $\mathfrak{C} + \varepsilon\mathfrak{T}$ of $\mathbb{H} + \varepsilon\mathbb{H}$ with $\mathfrak{C} := e_0 + e_1\mathbf{i} + e_2\mathbf{j} + e_3\mathbf{k}$ and $\mathfrak{T} := t_0 + t_1\mathbf{i} + t_2\mathbf{j} + t_3\mathbf{k}$ is called dual unit-quaternion if \mathfrak{C} is an unit-quaternion and following condition holds:

$$e_0t_0 + e_1t_1 + e_2t_2 + e_3t_3 = 0. \tag{7}$$

It is well-known (e.g. [10, Sect. 3.3.2.2]) that displacements of points in the Euclidean 3-space can be expressed by dual unit-quaternions $\mathfrak{C} + \varepsilon\mathfrak{T}$ as follows:

$$\mathfrak{P} \mapsto \mathfrak{P}_0 = \mathfrak{C} \circ \mathfrak{P} \circ \tilde{\mathfrak{C}} + (\mathfrak{T} \circ \tilde{\mathfrak{C}} - \mathfrak{C} \circ \tilde{\mathfrak{T}}), \tag{8}$$

where \circ denotes the quaternion multiplication and $\mathfrak{P} := xi + yj + zk$ (resp. $\mathfrak{P}_0 := x_0\mathbf{i} + y_0\mathbf{j} + z_0\mathbf{k}$) is the embedding of a point P with Cartesian coordinates $\mathbf{p} = (x, y, z)^T$ (resp. $\mathbf{p}_0 = (x_0, y_0, z_0)^T$) with respect to the moving (resp. fixed) frame into \mathbb{H} .

As both dual unit-quaternions $\pm(\mathfrak{C} + \varepsilon\mathfrak{T})$ correspond to the same Euclidean motion, one considers the homogeneous 8-tuple $(e_0, \dots, e_3, t_0, \dots, t_3)\mathbb{R}$, which are the well-known Study parameters [20] of the Euclidean motion group $SE(3)$. Note that $(e_0, \dots, e_3)\mathbb{R}$ are the so-called Euler parameters of the spherical motion group.

Restricting the Study parameters to planar Euclidean displacements within the plane $x_3 = 0$ implies $e_1 = e_2 = t_0 = t_3 = 0$ (cf. [10, Remark 3.38]), thus one ends up with the homogenous quadruple $(e_0, e_3, t_1, t_2)\mathbb{R}$, which are the already mentioned BG parameters [1, 6].

2 Dual Cayley-Klein Parameters

According to the recently published work [17], which also contains a historical overview and a detailed list of references on CK parameters, the formulation of spherical displacements of points based on Euler parameters $(e_0, \dots, e_3)\mathbb{R}$; i.e.

$$\mathfrak{P} \mapsto \mathfrak{E} \circ \mathfrak{P} \circ \tilde{\mathfrak{E}} \quad \text{with} \quad e_0^2 + e_1^2 + e_2^2 + e_3^2 = 1 \tag{9}$$

can be rewritten in terms of CK parameters $\alpha, \beta \in \mathbb{C}$ as follows:

$$\mathbf{P} \mapsto \mathbf{EPE}^* \quad \text{with} \quad \alpha\bar{\alpha} + \beta\bar{\beta} = 1, \tag{10}$$

where

$$\mathbf{P} := \begin{pmatrix} z & \bar{p} \\ p & -z \end{pmatrix}, \quad \mathbf{E} := \begin{pmatrix} \bar{\alpha} & -\beta \\ \beta & \alpha \end{pmatrix} \quad \text{and} \quad \mathbf{E}^* := \begin{pmatrix} \alpha & \beta \\ -\bar{\beta} & \bar{\alpha} \end{pmatrix}. \tag{11}$$

Note that the upper index $*$ denotes the transposed conjugate of a matrix. Moreover, \mathbf{P} is the embedding of the point \mathbf{P} with Cartesian coordinates $\mathbf{p} = (x, y, z)^T$ into the set of complex 2×2 matrices, which can be seen as a spatial generalization of isotropic coordinates according to [17]. The introduction of CK parameters can be completed by giving their relations to the Euler parameters, which read as follows:

$$\alpha := e_0 + e_3i \quad \text{and} \quad \beta := e_2 + e_1i. \tag{12}$$

Remark 1. Note that there exists the alternative formulation $\mathbf{P} \mapsto \mathbf{E}^*\mathbf{PE}$, where the matrix \mathbf{P} of Eq. (11) and the formula for β of Eq. (12) are replaced by:

$$\mathbf{P} := \begin{pmatrix} zi & pi \\ -\bar{p}i & -zi \end{pmatrix} \quad \text{and} \quad \beta := -e_2 + e_1i. \tag{13}$$

We prefer the other convention, as the connection with the isotropic coordinates in case of planar kinematics is straightforward. Moreover, one can compute $\|\mathbf{p}\|^2$ simply as $-\det \mathbf{P}$. ◇

Due to the ‘‘Principle of Transference’’, which dates back to Kotelnikov [12] and Study [20], this formulation of a spherical displacement of points can also be applied to the spatial displacements of oriented lines by dualizing the complete framework; i.e. complex numbers are substituted by dual complex numbers. Up to the author’s knowledge the resulting dual CK parameters have only been used for this purpose [3, 17], but never for the description of displacements of points in Euclidean 3-space. For doing this, we use the relation to quaternions and a more detailed formulation of Eq. (8), which reads as follows (cf. [10, page 498]):

$$1 + \varepsilon\mathfrak{P} \mapsto 1 + \varepsilon\mathfrak{P}_0 = (\mathfrak{E} + \varepsilon\mathfrak{T}) \circ (1 + \varepsilon\mathfrak{P}) \circ (\tilde{\mathfrak{E}} - \varepsilon\tilde{\mathfrak{T}}). \tag{14}$$

A straightforward translation into terms of complex 2×2 matrices yields:

$$(\mathbf{I}i + \varepsilon\mathbf{P}) \mapsto (\mathbf{I}i + \varepsilon\mathbf{P}_0) = (\mathbf{E} + \varepsilon\mathbf{T})(\mathbf{I}i + \varepsilon\mathbf{P})(\mathbf{E}^* - \varepsilon\mathbf{T}^*), \tag{15}$$

where \mathbf{I} denotes the 2×2 identity matrix and

$$\mathbf{P}_0 := \begin{pmatrix} z_0 & \bar{p}_0 \\ p_0 & -z_0 \end{pmatrix}, \quad \mathbf{T} := \begin{pmatrix} \bar{\gamma} & -\delta \\ \delta & \gamma \end{pmatrix} \quad \text{with} \quad \gamma := t_0 + t_3i, \quad \delta := t_2 + t_1i. \quad (16)$$

Expanding and simplifying Eq. (15) implies:

$$(\mathbf{I}i + \varepsilon\mathbf{P}) \mapsto (\mathbf{I}i + \varepsilon\mathbf{P}_0) = \mathbf{I}i + \varepsilon(\mathbf{EPE}^* + i\mathbf{TE}^* - i\mathbf{ET}^*). \quad (17)$$

In order that our later obtained symbolic expressions (e.g. Eq. (26)) are free of the complex unit i we make the following redefinition:

$$\mathbf{S} := i\mathbf{T} = \begin{pmatrix} \lambda & \bar{\mu} \\ \mu & -\bar{\lambda} \end{pmatrix} \quad \text{and} \quad \mathbf{S}^* := -i\mathbf{T}^* = \begin{pmatrix} \bar{\lambda} & \bar{\mu} \\ \mu & -\lambda \end{pmatrix} \quad (18)$$

with

$$\lambda := t_3 + t_0i \quad \text{and} \quad \mu := t_1 + t_2i, \quad (19)$$

thus we finally get the desired representation, which is summarized next.

Theorem 1. *Any spatial displacement of points \mathbf{P} can be written as:*

$$\mathbf{P} \mapsto \mathbf{P}_0 = \mathbf{EPE}^* + \mathbf{SE}^* + \mathbf{ES}^*, \quad (20)$$

where the four involved parameters $\alpha, \beta, \lambda, \mu \in \mathbb{C}$ fulfill the normalizing condition $\Phi = 1$ with

$$\Phi := \alpha\bar{\alpha} + \beta\bar{\beta} \quad (21)$$

and the analogue of the Study condition (7), which is given by $\Psi = 0$ with

$$\Psi := (\alpha\lambda - \bar{\alpha}\bar{\lambda}) + (\beta\mu - \bar{\beta}\bar{\mu}). \quad (22)$$

Moreover, the mapping of Eq. (20) is a spatial displacement of points for each quadruple $\alpha, \beta, \lambda, \mu \in \mathbb{C}$ fulfilling $\Phi = 1$ and $\Psi = 0$.

For the planar case we get $\beta = 0$ and $\lambda = 0$ due to $e_1 = e_2 = 0$ and $t_0 = t_3 = 0$, respectively (cf. end of Sect. 1.2). Therefore the following corollary holds:

Corollary 1. *Any planar displacement of points \mathbf{P} can be written as:*

$$p \mapsto p_0 = \alpha(\alpha p + 2\mu) \quad \text{with} \quad \alpha, \mu \in \mathbb{C} \quad \text{and} \quad \alpha\bar{\alpha} = 1. \quad (23)$$

Moreover, the mapping of Eq. (23) is a planar displacement of points for each bituple $\alpha, \mu \in \mathbb{C}$ fulfilling $\alpha\bar{\alpha} = 1$.

Remark 2. Based on Corollary 1 we can point out the relation

$$\kappa = \alpha^2 \quad \text{and} \quad \tau = 2\alpha\mu \quad (24)$$

between the parameters $\kappa, \tau \in \mathbb{C}$ of Eq. (5) and the parameters $\alpha, \mu \in \mathbb{C}$ of Eq. (23), which is a non-linear one. \diamond

3 Application to Parallel Manipulators

For symbolic computations in robotics, we consider $\bar{\alpha}, \bar{\beta}, \bar{\lambda}, \bar{\mu}$ as independent variables; i.e. they are uncoupled from $\alpha, \beta, \lambda, \mu$. Under this assumption Study's kinematic mapping (e.g. [16, Sect. 2]) can be reformulated as follows:

Corollary 2. *There is a bijection between $SE(3)$ and 8-tuples of complex numbers $(\alpha, \beta, \lambda, \mu, \bar{\alpha}, \bar{\beta}, \bar{\lambda}, \bar{\mu}) \in \mathbb{R}$ fulfilling $\Psi = 0$ with $(\alpha, \beta, \bar{\alpha}, \bar{\beta}) \neq (0, 0, 0, 0)$ and the condition that the quadruple $(\bar{\alpha}, \bar{\beta}, \bar{\lambda}, \bar{\mu})$ is the conjugate quadruple of $(\alpha, \beta, \lambda, \mu)$.*

Based on this result the sphere condition, that the platform point \mathbf{P} is located on a sphere with radius R centered in the base point \mathbf{B} with fixed coordinates $\mathbf{b}_0 = (u_0, v_0, w_0)^T$, can be computed as (cf. end of Remark 1):

$$\Phi^2 R^2 + \det(\mathbf{P}_0 - \mathbf{B}_0) = 0 \quad \text{with} \quad \mathbf{B}_0 := \begin{pmatrix} w_0 & \bar{b}_0 \\ b_0 & -w_0 \end{pmatrix}, \quad (25)$$

where the coefficient Φ^2 of R^2 homogenizes the equation. Doing the corresponding tricky summation of Husty [8] (see also [15]) by adding Ψ^2 to the left hand-side, shows that Φ factors out. The remaining quadratic factor Σ reads as follows:

$$\begin{aligned} & \alpha^2 p \bar{b}_0 - \beta^2 p b_0 + \bar{\alpha}^2 \bar{p} b_0 - \bar{\beta}^2 \bar{p} \bar{b}_0 + (\alpha \bar{\alpha} + \beta \bar{\beta})(R^2 - z^2 - w_0^2 - b_0 \bar{b}_0 - p \bar{p}) \\ & + 2(\alpha \bar{\alpha} - \beta \bar{\beta}) z w_0 - 2\alpha \beta p w_0 + 2\alpha \bar{\beta} z \bar{b}_0 + 2\bar{\alpha} \beta z b_0 - 2\bar{\alpha} \bar{\beta} \bar{p} w_0 \\ & - 2(\beta \mu + \bar{\beta} \bar{\mu})(w_0 + z) + 2(\alpha \lambda + \bar{\alpha} \bar{\lambda})(w_0 - z) + 2(\bar{\alpha} \bar{\mu} + \beta \lambda) b_0 \\ & + 2(\alpha \mu + \bar{\beta} \bar{\lambda}) \bar{b}_0 + 2(\beta \bar{\lambda} - \alpha \bar{\mu}) p + 2(\bar{\beta} \lambda - \bar{\alpha} \mu) \bar{p} - 4(\lambda \bar{\lambda} + \mu \bar{\mu}). \end{aligned} \quad (26)$$

Therefore the sphere condition $\Sigma = 0$ has only 38 terms in contrast to its formulation based on Study parameters, which has 80 terms (cf. [8]). An example for pointing out the beneficial effects of this reduction of terms is the symbolic elimination process in the direct kinematics of SG platforms.

Example 1. As each leg imply a sphere condition we get six sphere equations $\Sigma_i = 0$ with $i = 1, \dots, 6$. It is well-known [8] that the differences of two sphere conditions are only linear in the translational parameters. Therefore the system of five equations $\Psi = \Sigma_5 - \Sigma_1 = \Sigma_4 - \Sigma_1 = \Sigma_3 - \Sigma_1 = \Sigma_2 - \Sigma_1 = 0$ linear in $\lambda, \mu, \bar{\lambda}, \bar{\mu}$ can only have a non-trivial solution if the determinant of the 5×5 coefficient matrix vanishes. This determinant splits up into Φ and a factor with 53 280 terms, which is homogenous of degree 4 in $\alpha, \beta, \bar{\alpha}, \bar{\beta}$. In contrast, the corresponding quartic expression based on Study parameter has 258 720 terms (cf. [5, Sect. 3.2]). \diamond

By setting $z = w_0 = \beta = \bar{\beta} = \lambda = \bar{\lambda} = 0$ we get from Eq. (26) the circle condition, which can be written similarly to Eq. (6) as:

$$(\alpha p + 2\mu - \bar{\alpha} b_0)(\bar{\alpha} \bar{p} + 2\bar{\mu} - \alpha \bar{b}_0) - \alpha \bar{\alpha} R^2 = 0. \quad (27)$$

This equation has both benefits; i.e. the compactness of the isotropic formulation and the homogeneity of the approach based on BG parameters (cf. Sect. 1.1).

In the following we show that the compactness of the proposed formulation passes on to the symbolic expression of the singularity loci of SG platforms. Therefore we compute the Plücker coordinates of the line spanned by the base anchor point and the corresponding platform anchor point. The direction vector $\mathbf{l} = (l_1, l_2, l_3)^T$ is given by $(\mathbf{p}_0 - \Phi \mathbf{b}_0)$, where the coefficient Φ is again used for homogenization, and the moment vector $\mathbf{m} := (m_1, m_2, m_3)^T$ reads as $\mathbf{b}_0 \times \mathbf{l}$. Thus each entry of the 6-tuple $(\mathbf{l}, \mathbf{m})\mathbb{R}$ fulfilling the Plücker condition $\langle \mathbf{l}, \mathbf{m} \rangle = 0$ is homogenous of degree 2 in the dual CK parameters $\alpha, \beta, \lambda, \mu, \bar{\alpha}, \bar{\beta}, \bar{\lambda}, \bar{\mu}$. By defining:

$$\begin{aligned}
 l &:= l_1 + l_2 i = \alpha^2 p - \bar{\beta}^2 \bar{p} - \alpha \bar{\alpha} b_0 - \beta \bar{\beta} b_0 + 2\alpha \bar{\beta} z + 2\bar{\lambda} \bar{\beta} + 2\mu \alpha, \\
 m &:= m_2 + m_1 i = (\bar{\alpha}^2 \bar{p} - \beta^2 p) w_0 + (\bar{\beta} \bar{\alpha} \bar{p} + \beta \alpha p) \bar{b}_0 + (\beta \bar{\beta} - \alpha \bar{\alpha}) z \bar{b}_0 \\
 &\quad + 2(\bar{\alpha} \beta z + \bar{\alpha} \bar{\mu} + \beta \lambda) w_0 + (\beta \mu + \bar{\beta} \bar{\mu} - \alpha \lambda - \bar{\alpha} \bar{\lambda}) \bar{b}_0, \\
 n &:= 2m_3 i = 2(\alpha \mu + \bar{\beta} \bar{\lambda} + \alpha \bar{\beta} z_0) \bar{b}_0 - 2(\bar{\alpha} \bar{\mu} + \beta \lambda + \bar{\alpha} \beta z_0) b_0 \\
 &\quad + (\alpha^2 \bar{b}_0 + \beta^2 b_0) p - (\bar{\alpha}^2 b_0 + \bar{\beta}^2 \bar{b}_0) \bar{p},
 \end{aligned} \tag{28}$$

we can replace $(\mathbf{l}, \mathbf{m})\mathbb{R}$ by the more compact 6-tuple $\mathbf{f} := (l, \bar{l}, l_3, m, \bar{m}, n)\mathbb{R}$ with

$$l_3 = \alpha \bar{\alpha} (z - w_0) - \beta \bar{\beta} (z + w_0) - \alpha \beta b_0 - \bar{\alpha} \bar{\beta} \bar{b}_0 + \alpha \lambda + \bar{\alpha} \bar{\lambda} - \beta \mu - \bar{\beta} \bar{\mu} \tag{29}$$

fulfilling $lm - \bar{l}\bar{m} + l_3 n = 0$. As each leg of the SG platform implies such a 6-tuple, we get $\mathbf{f}_1, \dots, \mathbf{f}_6$. As a consequence the manipulator is in a singular pose (cf. [14]), if and only if:

$$\det(\mathbf{F}) = 0 \quad \text{with} \quad \mathbf{F} := (\mathbf{f}_1, \dots, \mathbf{f}_6). \tag{30}$$

The expression $\det(\mathbf{F})$ splits up into Φ^2 and a homogenous octic factor F in the dual CK parameters. Moreover, F has 542 496 terms if the platform and base anchor points are chosen as follows with respect to the moving and fixed frame: the first anchor point is located in the origin, the second one on the x -axis and the third one in the xy -plane. In contrast, F reformulated in Study parameters has 1 748 184 terms.

Note that $F = 0$ can be seen as an alternative singularity locus expression to [4, 13]. Finally, the singularity loci of the planar analogue (Fig. 1 left) can be computed as the determinant of a 3×3 matrix (cf. [9]), as $m = \bar{m} = l_3 = 0$ hold.

4 Conclusion

We discussed the transformation of points in terms of dual CK parameters (Sect. 2) and showed that these parameters imply a very compact symbolic expression of the sphere condition and the singularity loci of SG platforms (Sect. 3). These parameters cannot only be restricted to planar motions, but they can also be extended for kinematics in Euclidean 4-space according to [16]. The proposed representation is especially of interest for the determination of SG platforms with self-motions (e.g. [5]), but maybe it is also beneficial for the symbolic study of other mechanisms.

Acknowledgements. The author is supported by Grant No. P 24927-N25 of the Austrian Science Fund FWF within the project “Stewart Gough platforms with self-motions”.

References

1. Blaschke, W.: Euklidische Kinematik und nichteuklidische Geometrie. *Zeitschrift für Mathematik und Physik* **60**, 61–91 and 203–204 (1911)
2. Brunthaler, K., Pfurner, M., Husty, M.L.: Synthesis of planar four-bar mechanisms. *CSME Trans.* **30**(2), 297–313 (2006)
3. Denavit, J.: Displacement analysis of mechanisms based on (2×2) matrices of dual numbers. *VDI-Berichte* **29**, 81–88 (1958)
4. DiGregorio, R.: Singularity-locus expression of a class of parallel mechanisms. *Robotica* **20**, 323–328 (2002)
5. Gallet, M., Nawratil, G., Schicho, J.: Liaison linkages. *J. Symbolic Comput.* **79**(1), 65–98 (2017)
6. Grünwald, J.: Ein Abbildungsprinzip, welches die ebene Geometrie und Kinematik mit der räumlichen Geometrie verknüpft. *Sitz.-Ber. der math.-nat. Klasse der kaiserlichen Akademie der Wissenschaften Wien* **120**, 677–741 (1911)
7. Hayes, M.J.D., Husty, M.L.: On the kinematic constraint surfaces of general three-legged planar robots. *Mech. Mach. Theory* **38**(5), 379–394 (2003)
8. Husty, M.: An algorithm for solving the direct kinematics of general Stewart-Gough platforms. *Mech. Mach. Theory* **31**(4), 365–380 (1996)
9. Husty, M., Gosselin, C.: On the singularity surface of planar 3-RPR parallel mechanisms. *Mech. Based Des. Struct. Mach.* **36**, 411–425 (2008)
10. Husty, M., Karger, A., Sachs, H., Steinhilper, W.: *Kinematik und Robotik*. Springer, Heidelberg (1997)
11. Husty, M., Mielczarek, S., Hiller, M.: Constructing an overconstrained planar 4RPR manipulator with maximal forward kinematics solution set. In: *CD-ROM Proceedings of the 10th International Workshop on Robotics in Alpe-Adria-Danube Region RAAD* (2001)
12. Kotelnikov, A.P.: Screw calculus and some applications to geometry and mechanics. *Annals of the Imperial University of Kazan* (1895)
13. Li, H., Gosselin, C.M., Richard, M.J., Mayer-St-Onge, B.: Analytic form of the six-dimensional singularity locus of the general gough-stewart platform. *J. Mech. Des.* **128**, 279–287 (2006)
14. Merlet, J.-P.: Singular configurations of parallel manipulators and grassmann geometry. *Int. J. Robot. Res.* **8**(5), 45–56 (1989)
15. Nawratil, G.: Kinematic mapping of $SE(4)$ and the hypersphere condition. In: Lenarcic, J., Khatib, O. (eds.) *Advances in Robot Kinematics*, pp. 11–19. Springer (2014)
16. Nawratil, G.: Fundamentals of quaternionic kinematics in euclidean 4-space. *Adv. Appl. Clifford Algebras* **26**(2), 693–717 (2016)
17. Pennestri, E., Valentini, P.P., Figliolini, G., Angeles, J.: Dual cayley-klein parameters and Möbius transform: Theory and applications. *Mech. Mach. Theory* **106**, 50–67 (2016)
18. Plecnik, M.M., McCarthy, J.M.: Numerical synthesis of six-bar linkages for mechanical computation. *J. Mech. Robot.* **6**, 031012 (2014)

19. Schröcker, H.-P., Husty, M., McCarthy, J.M.: Kinematic mapping based assembly mode evaluation of planar four-bar mechanisms. *J. Mech. Des.* **129**(9), 924–929 (2007)
20. Study, E: *Geometrie der Dynamen*. Teubner, Leipzig (1903)
21. Wampler, C.W.: Isotropic coordinates, circularity, and Bezout numbers: Planar kinematics from a new perspective. In: *Proceedings of ASME Design Engineering Technical Conference and Computers in Engineering Conference*, 96-DETC/MECH-1210 (1996)
22. Wampler, C.W.: The geometry of singular foci of planar linkages. *Mech. Mach. Theory* **39**, 1139–1153 (2004)
23. Wunderlich, W.: *Ebene Kinematik*. Hochschultaschenbücher-Verlag (1970)

An Approach for Type Synthesis of Overconstrained 1T2R Parallel Mechanisms

C. Dong¹, H. Liu^{1(✉)}, Q. Liu¹, T. Sun¹, T. Huang^{1,2},
and D.G. Chetwynd²

¹ Key Laboratory of Mechanism Theory and Equipment Design of State
Ministry of Education, Tianjin University, Tianjin 300072, China
liuht@tju.edu.cn

² School of Engineering, The University of Warwick, Coventry CV4 7AL, UK

Abstract. This paper presents a simple and illustrative approach for type synthesis of a family of overconstrained parallel mechanisms having one translational and two rotational movement capability. This family features a spatial limb plus a member of a class of planar symmetrical linkages, connected by a revolute joint either with the machine frame at the base link or with the platform at the output link. Criteria for selecting suitable structures among numerous candidates are proposed by considering the realistic and practical requirements of reconfigurability, movement capability, component design rationality, etc. Exploiting the structures obtained and examined by the criteria proposed leads to a novel 5-DOF hybrid module named TriMule, which offers a lightweight, cost effective, and flexible design particularly suitable for configuring various robotized manufacturing cells.

Keywords: Parallel robots · Conceptual design · Type synthesis

1 Introduction

Overconstrained 1T2R (T-translation; R-rotation) parallel mechanisms can have several advantages over their counterparts that lack overconstraints: higher stiffness, greater cost-effectiveness, and easier-to-obtain explicit inverse/forward kinematics, for example, because the common constraints allow fewer joints to be used. However, type synthesis for parallel mechanisms of this kind is by no means an easy task because the Grübler–Kutzbach formula is unable to identify the virtual constraints produced by the special geometric arrangements of joint axes, and is thereby no longer valid to determine the number of degrees of freedom (DOF) in the structure.

The last few decades have seen tremendous efforts towards type synthesis of lower mobility overconstrained parallel mechanisms in general [1, 2] and those having 1T2R movement capability in particular [3, 4]. Methods currently available include those based upon screw theory [1, 5], group theory [3, 4, 6], linear transformation [7], and many others [8]. These methods are general by first creating individual limbs and then setting the assembly conditions at the final step. However, the procedures are not easily understandable due to their abstraction and/or complicated mathematics. Therefore, it is highly beneficial to develop a simple, illustrative and effective approach that is easily

understood not only by academia but also and even more importantly by design engineers. Another challenging issue encountered in type synthesis is that although a large number of structures have been generated, there is a lack of criteria to evaluate which are the better ones even if they have the same 1T2R movement capability [3]. Therefore, the development of criteria to select suitable structures for specific applications is also an open issue to be investigated.

This paper presents a simple, easily visualized yet effective approach for type synthesis of a family of overconstrained 1T2R parallel mechanisms. By fully exploiting the common constraints provided by a plane, Sect. 2 presents a methodology to synthesize 1T2R overconstrained parallel mechanisms featuring a spatial limb plus a member of a class of planar symmetrical linkages, resulting in two subfamilies with and without a properly constrained non-actuated limb. Focused on realistic mechanism design, Sect. 3 investigates the criteria for selecting suitable structures among numerous candidates. Exploiting the structures obtained and equipped with the criteria proposed, Sect. 4 presents a novel 5-DOF hybrid PKM module before the conclusions are drawn in Sect. 5.

2 Methodology

Viewed in terms of kinematic inversion [5], Fig. 1 demonstrates a general structure of the proposed family of overconstrained 1T2R parallel mechanisms. Members belonging to this family feature a spatial limb plus a planar linkage lying in a plane denoted by Π . The two end links of the spatial limb are represented by Body I and Body III, whilst those of the planar linkage are denoted by Body II and Body III, respectively. Body I and Body II are connected by a revolute joint, denoted by R, with its joint axis n - n parallel to Π . In addition, there are actuated prismatic joints for achieving high rigidity, each denoted by \underline{P} , in the spatial limb and in each of two identical limbs of the planar linkage. The planar linkage may also have one properly constrained non-actuated limb. The term ‘properly constrained’ here means that the number and type of degrees of freedom of the limb is exactly the same as those of the output link.

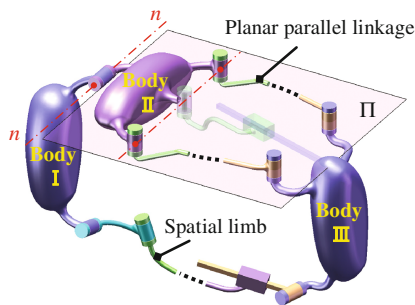


Fig. 1. General structure of a family of overconstrained 1T2R parallel mechanisms

Using these descriptions, two subfamilies of overconstrained 1T2R parallel mechanisms can be synthesized by giving Body I (or Body III) either of two roles in the system. In the first subfamily, Body I is taken as the machine frame, and Body III thereby as the output link of the planar linkage to which the platform is attached, leading to Body II being the base link of the linkage. Kinematic inversion produces the second subfamily where Body I is taken as the platform, Body II as the output link, and Body III as the machine frame to which the base link is attached. Hence, 1T2R platform motion arises from 1T1R internal motion of the output link and 1R motion of the platform about the axis n - n with respect to either the output link or the machine frame.

As shown in Fig. 2(a), assume that the planar linkage has a basic form represented by a six-bar linkage with a single-loop closure. In each actuated limb, the joint connecting the limb to the output link is an R joint, while the inner joint and the joint connecting the limb with the base link are either a \underline{P} or an R joint. Then, the axis n - n is confined to be parallel to the common normal to the two R joints at either the base link or the output link as shown in Fig. 1. Note that the output link in the basic form has 2T1R internal mobility. Hence, a 1T internal motion must be restricted by imposing one additional constraint wrench $\$_{wc}$ (a pure force) with its axis parallel to Π . Then, 1T2R movement capability of the platform can be achieved by simultaneously adding a 1R motion about the axis n - n . The required constraint wrench can be generated by either of two ways: (i) the use of a properly constrained non-actuated limb embedded between two actuated limbs for achieving structural symmetry as shown in Fig. 2(b), or (ii) the use of a 5-DOF spatial limb as shown in Fig. 2(c). Consequently, two classes of overconstrained 1T2R parallel mechanisms in each subfamily can be generated with ease using the procedures introduced as follows.

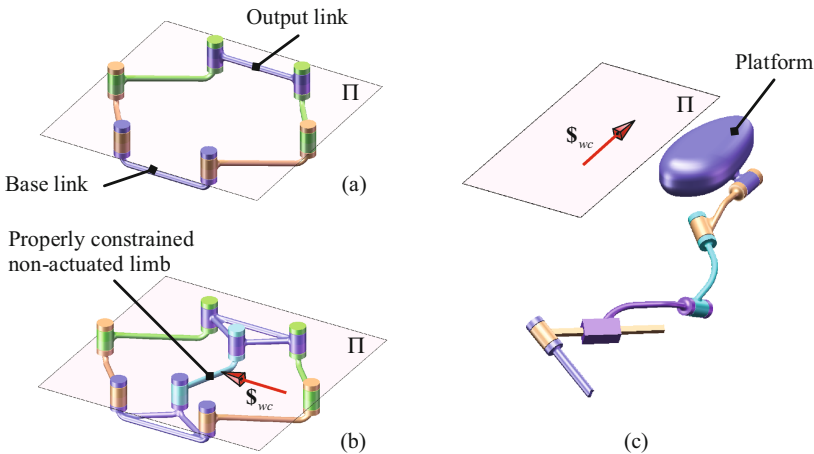


Fig. 2. (a) A basic form of planar linkage, (b) A properly constrained non-actuated limb, (c) A 5-DOF spatial limb

Class A: mechanism using a properly constrained non-actuated limb

Members belonging to this class feature a 6-DOF spatial limb plus a stand-alone 1T1R planar parallel mechanism containing a properly constrained non-actuated limb, connected by an R joint to the machine frame at the base link in the first subfamily, or to the platform at the output link in the second. Two types of such constrained limbs, denoted by RP and PR (P stands for a non-actuated prismatic joint), are available for achieving structural symmetry. Both provide the output link with a constraint wrench (a force) $\$_{wc}$ lying in Π , passing through the R joint axis, and being normal to the P joint direction as depicted in Fig. 3. As a result, the 1T internal motion of the output link parallel to the wrench axis is restricted. This class uses a 6-DOF spatial limb to provide the platform with an actuation to generate 1R motion about the axis $n-n$. Considering only those structures simultaneously actuated by three internal or external \underline{P} joints, Fig. 4 shows four overconstrained 1T2R parallel mechanisms, where S and U denote a spherical and universal joint.

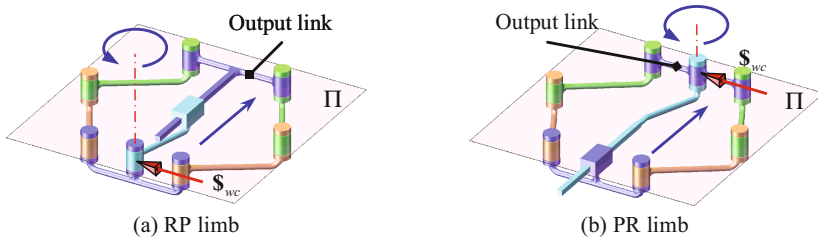


Fig. 3. Constraint wrench imposed by a properly constrained non-actuated limb

Class B: mechanism without properly constrained non-actuated limb

Members belonging to this class generally feature a 5-DOF spatial limb plus the 2T1R six-bar under-constrained planar linkage as shown in Fig. 2(a), connected by an R joint as discussed in Class A. Numerous 5-DOF spatial limbs are available to do this [5], but we here consider only those having four R joints and one \underline{P} joint for practical use. Within this category, the location and direction of the constraint wrench can uniquely be determined by the conditions: (i) the axis of one R joint, denoted by R_1 , is parallel to the wrench axis, (ii) the axes of the other three R joints, each denoted by R_2 , intersect the wrench axis at a common point, and (iii) the axis of the \underline{P} joint is normal to the wrench axis, namely normal to the R_1 joint axis. By sequentially ordering all joints from the machine frame to the platform and utilizing joint substitutions, these conditions reveal four possible limb structures, denoted respectively by $\underline{S}PR_1$, $\underline{U}PR_2R_1$, $R_1\underline{P}S$ and $\underline{P}R_1S$.

To assemble the spatial limb with the planar linkage, the direction of the R_1 joint axis must be placed correctly with respect to its location and the direction of the permitted 1T internal motion of the output link. For example, if the R_1 joint connects the spatial limb with the platform, the joint axis should be parallel to the common normal of the axes of the two R joints connecting the output link as shown in Fig. 5(a).

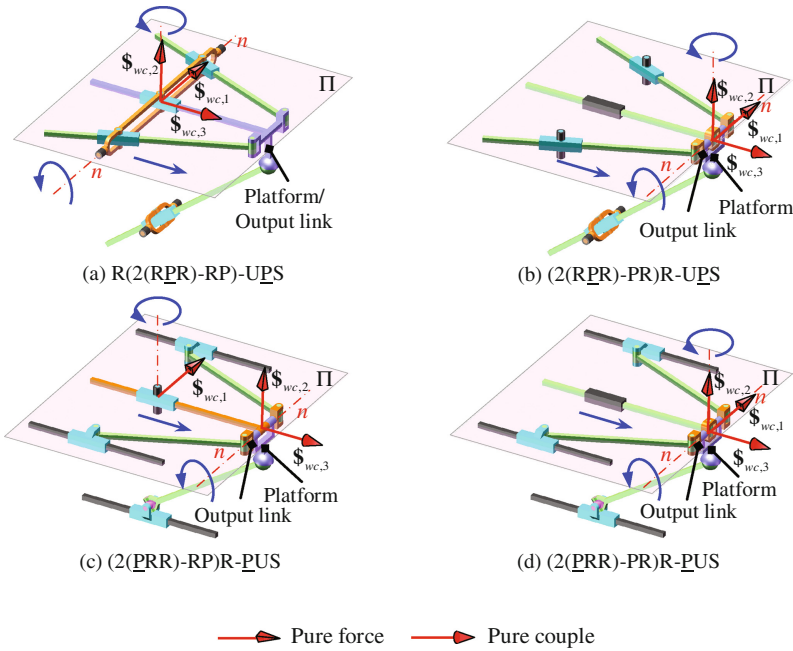


Fig. 4. Typical overconstrained 1T2R parallel mechanisms of class A

But if the R_1 joint connects the spatial limb with the machine frame, the joint axis should be parallel to Π and normal to the direction of the 1T permitted motion as shown in Fig. 5(b). Similarly, if the P joint connects the spatial limb with the machine frame, the P joint axis should be parallel to the direction of the 1T permitted motion and the R_1 joint axis parallel to Π as shown by the dashed line in Fig. 5(b). Figure 6 shows some typical overconstrained 1T2R parallel mechanisms, all integrating three R_2 joints into an S joint to achieve a two-link limb design and only considering those simultaneously actuated by three internal \underline{P} joints though many other possibilities exist.

3 Criteria for Selecting Suitable Structures

Selecting suitable structures for 1T2R parallel mechanisms from among the huge number of candidates is a challenging issue in developing 5-DOF hybrid robotized modules where high rigidity, high dynamic responses are the essential requirements. By considering the realistic and practical requirements of reconfigurability, movement capability, component design rationality, etc., four important criteria are proposed as follows.

- *Criterion 1:* A suitable structure should have a relatively large ratio of workspace volume against footprint so that the relevant PKM can be integrated into a rigid yet compact module, as exactly exhibited by the Sprint Z3 head, the Tricept as well as the Exechon, for configuring various manufacturing cells.

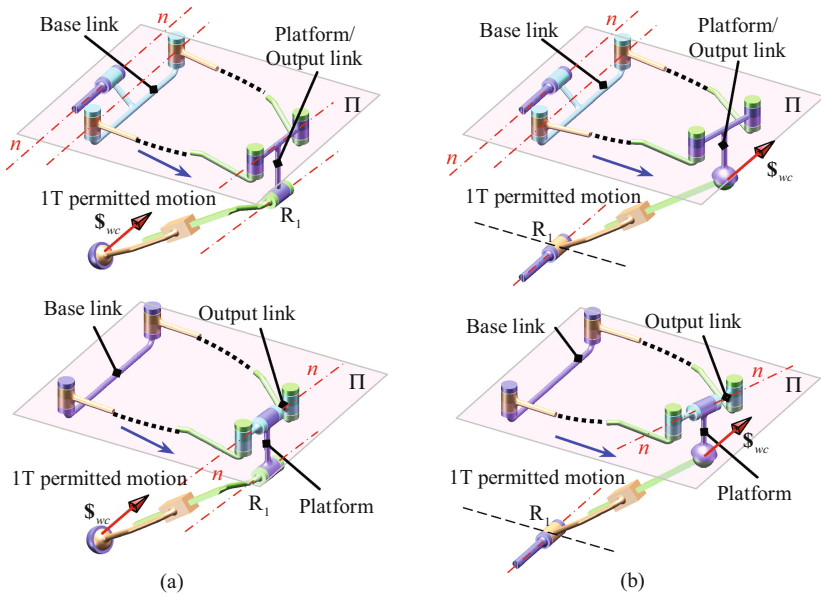


Fig. 5. Location and direction of the constraint wrench and the R_1 joint axis

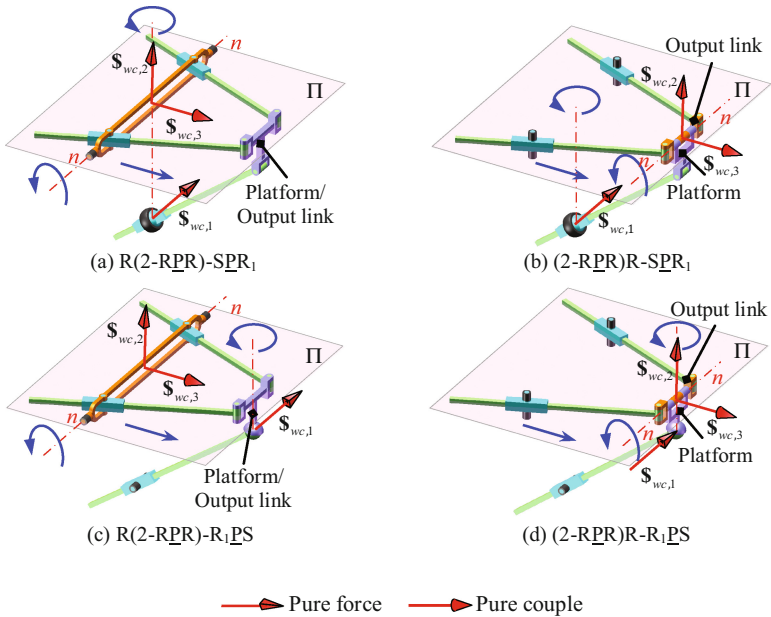


Fig. 6. Typical overconstrained 1T2R parallel mechanisms of class B

- *Criterion 2:* A suitable structure should have identical or nearly identical actuated limbs (due to the overconstraints). This not only leads to cost effective designs but also is valuable for achieving an appropriate movement capability.
- *Criterion 3:* A suitable structure must allow the main body of all lower mobility limbs to be given shapes having high bending and/or torsional stiffness/mass ratios.
- *Criterion 4:* A suitable structure should have an explicit solution to its inverse kinematics, an important issue for CNC control. An explicit solution to the forward kinematics is not essential, but is very useful for rapid online monitoring of the platform poses.

4 An Example

Exploiting the structures obtained in Sect. 2 and the criteria presented in Sect. 3, we propose a novel 5-DOF hybrid module, named TriMule [9], shown in Fig. 7(a). Its essential structure is the overconstrained 1T2R parallel mechanism shown in Fig. 4(a). A critical feature is that this base link is elaborately designed into a three-in-one part that locates the rear R joints of the two actuated R_{PR} limbs, and the R and P joints of the RP limb. Compared with the non-constrained 1T2R parallel mechanism used in the Tricept (see Fig. 7(b)), the new design can theoretically save up to six R joints. This can be done by replacing the front S joints of two UPS limbs by R joints, and integrating the rear U joints of the two UPS limbs and the U joint of UP limb into the three-in-one component. However, by the criteria proposed in Sect. 3, it is preferable in practice to use two R_{PS} limbs instead of two R_{PR} limbs in the planar linkage. This is because constraint bending and torsional moments imposed on these limbs can then be avoided completely though these loads will anyway be carried to a great extent by the properly constrained non-actuated RP limb. A significant potential advantage of the TriMule over the Tricept arises from its integration of the joints connecting the base link and the machine frame into a three-in-one part supported at each side by a roller bearing requiring only a small outer frame. It is this novelty that indeed offers a lightweight, cost effective and flexible design of a 5-DOF hybrid module particularly suitable for configuring various robotized manufacturing cells.



Fig. 7. 3D view of (a) TriMule and (b) Tricept

5 Conclusions

An approach is proposed for type synthesis of overconstrained 1T2R parallel mechanisms, resulting in a family comprising a spatial limb plus a member of a class of planar linkages, connected by a revolute joint. By considering the realistic and practical requirements of reconfigurability, movement capability, component design rationality, *etc.*, four important criteria are proposed for selecting suitable structures from numerous candidates, leading to a lightweight, cost effective and flexible design of a novel 5-DOF hybrid module named TriMule.

Acknowledgments. The research is partially supported by National Key Basic Research Program (2014CB046603) and National Natural Science Foundation of China (51420105007).

References

1. Huang, Z., Li, Q.: General methodology for type synthesis of symmetrical lower-mobility parallel manipulators and several novel manipulators. *Int. J. Robot. Res.* **21**(2), 131–145 (2002)
2. Fang, Y., Tsai, L.-W.: Structure synthesis of a class of 4-DOF and 5-DOF parallel manipulators with identical limb structures. *Int. J. Robot. Res.* **21**(9), 799–810 (2002)
3. Li, Q., Hervé, J.-M.: 1T2R parallel mechanisms without parasitic motion. *IEEE Trans. Robot.* **26**(3), 401–410 (2010)
4. Li, Q., Hervé, J.-M.: Type synthesis of 3-DOF RPR-equivalent parallel mechanisms. *IEEE Trans. Robot.* **30**(6), 1333–1343 (2014)
5. Fang, Y., Tsai, L.-W.: Structure synthesis of a class of 3-DOF rotational parallel manipulators. *IEEE Trans. Robot. Autom.* **20**(1), 117–121 (2004)
6. Hervé, J.-M.: The Lie group of rigid body displacements, a fundamental tool for mechanism design. *Mech. Mach. Theory* **34**(5), 719–730 (1999)
7. Gogu, G.: Structural synthesis of fully-isotropic parallel robots with Schönflies motions via theory of linear transformations and evolutionary morphology. *Eur. J. Mech. A/Solids* **26**(2), 242–269 (2007)
8. Yang, T., Liu, A., Jin, Q., Luo, Y., Shen, H., Hang, L.: Position and orientation characteristic equation for topological design of robot mechanisms. *J. Mech. Des.* **131**(2), 021001.1–021001.17 (2009)
9. Huang, T., et al.: A novel 5-DOF hybrid robot with multi-axes gimbal holder, China Patent, No. ZL201510401279.9 (2015)

Transmission Quality Evaluation for a Class of Four-limb Parallel Schönflies-motion Generators with Articulated Platforms

Guanglei Wu¹(✉), Shaoping Bai², and Stéphane Caro³

¹ School of Mechanical Engineering,
Dalian University of Technology, Dalian 116024, China
gwu@dlut.edu.cn

² Department of Mechanical and Manufacturing Engineering,
Aalborg University, 9220 Aalborg, Denmark
shb@make.aau.dk

³ CNRS, Laboratoire des Sciences du Numérique de Nantes,
UMR CNRS 6004, Ecole Centrale de Nantes, 44321 Nantes, France
stephane.caro@ls2n.fr

Abstract. This paper investigated the motion/force transmission quality for a class of parallel Schönflies-motion generators built with four identical RR/RRR-type limbs. It turns out that the determinant of the forward Jacobian matrices for this class of parallel robots can be expressed as the scalar product of two vectors, the first vector being the cross product of the four unit vectors along the parallelograms, the second one being related to the rotation of the mobile platform. The pressure angles, derived from the determinants of forward and inverse Jacobians, respectively, are used for the evaluation of the transmission quality of the robots. Four robots are compared based on the proposed method as illustrative examples.

Keywords: Schönflies motion · Jacobian · Pressure angle · Transmission

1 Introduction

Parallel robots performing Schönflies motions are well adapted to high-speed pick-and-place (PnP) operations [4, 10], thanks to their lightweight architecture and high stiffness. A typical robot is the Quattro robot [1] by Adept Technologies Inc., the fastest industrial robot available. Its latest version can reach an acceleration up to $15G$ with a 2 kg payload, allowing to accomplish four standard PnP cycles per second. Its similar version is the H4 robot [9] that consists of four identical limbs and an articulated traveling plate [6]. Recently, the Veloce. robot [2] with a different articulated platform that is connected by a screw pair has been developed. Besides, the four-limb robots with single-platform architecture have also been reported [13, 14]. Four-limb parallel robots with an articulated mobile platform are displayed in Fig. 1. It is noteworthy that the H4 robot with the modified

mobile platform can be mounted vertically instead of the horizontal installation for the reduced mounting space, to provide a rotation around an axis of vertical direction, which is named as “V4” for convenience in the following study.

In the design and analysis of a manipulator, its kinematic Jacobian matrix plays an important role, since the dexterity/manipulability of the robot can be evaluated by the condition number of Jacobians as well as the accuracy/torque capability [8] between the actuators and end-effector. On the other hand, a problem usually encountered in this procedure is that the parallel manipulators with mixed input or/and output motions, i.e., compound linear and angular motions, will result in dimensionally inhomogeneous Jacobians, thus, the conventional performance indices associated with the Jacobian matrix, such as norm or condition number, will lack in physical significance [7]. As far as Schönflies-motion generators are concerned, their end-effector generates a mixed motion of three translations and one rotation (3T1R), for which the terms of the kinematic Jacobian matrix do not have the same units. A common approach to overcome this problem is to introduce a *characteristic length* [3] to homogenize the Jacobian matrix, whereas, the measurement significantly depends on the choice of the *characteristic length* that is not unique, resulting in biased evaluation, although a “best” one can be found by optimization technique [5]. Alternatively, an efficient approach to accommodate this dimensional inhomogeneity is to adopt the concept of the virtual coefficient, namely, the transmission index, which is closely related to the transmission/pressure angle. The pressure angle based transmission index will be adopted in this work.

This paper presents a uniform evaluation approach for transmission quality of a family of four-limb 3T1R parallel robots with articulated mobile platforms. The pressure angles, derived from the forward and inverse Jacobians straightforward, are used for the evaluation of the transmission quality of the robots. The defined transmission index is illustrated with four robot counterparts for the performance evaluation and comparison.

2 Manipulator Architecture

Figure 2(a) depicts a simplified CAD model of the parallel Schönflies-motion generator, which is composed of four identical $\underline{\text{R}}\text{RI}\text{I}\text{RR}^1$ -type limbs connecting the base and an articulated mobile platform (MP). The generalized base platform and the different mobile platforms of the four robots are displayed in Figs. 2(b) and (c), respectively.

The global coordinate frame \mathcal{F}_b is built with the origin located at the geometric center of the base platform. The x -axis is parallel to the segment A_2A_1 (A_3A_4), and the z -axis is normal to the base-platform plane pointing upwards. The moving coordinate frame \mathcal{F}_p is attached to the mobile platform and the origin is at the geometric center, where X -axis is parallel to segment C_2C_1 (C_3C_4). Vectors \mathbf{i} , \mathbf{j} and \mathbf{k} represent the unit vectors of x -, y - and z -axis, respectively. The axis of rotation of

¹ R and II stand for revolute joint and parallelogram (II joint), respectively, and the underlined letter indicates the actuated joint.

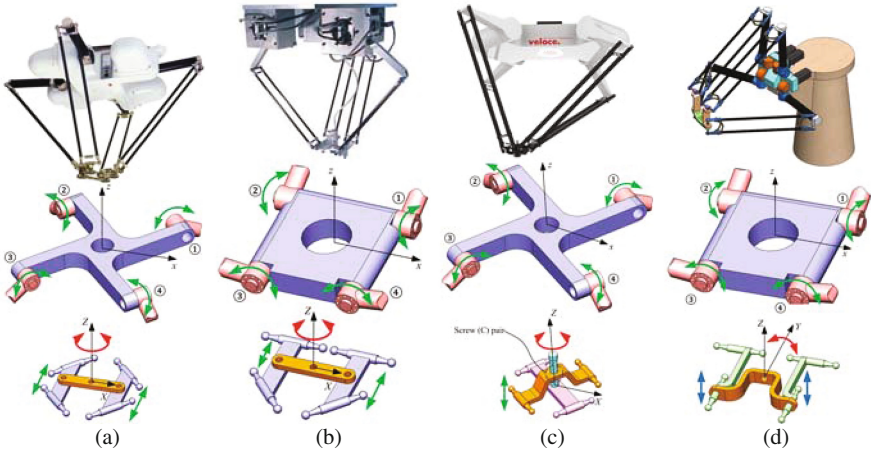


Fig. 1. The four-limb PnP robots with different base and mobile platforms: (a) Quattro [1]; (b) H4 [9]; (c) Veloce. [2]; (d) “V4” [12].

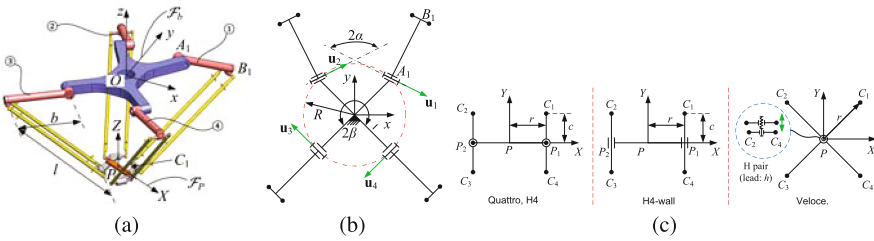


Fig. 2. The parameterization of the four-limb robots: (a) simplified CAD model; (b) a generalized base platform; (c) three different mobile platforms for the four robots.

the i th actuated joint is parallel to unit vector $\mathbf{u}_i = \mathbf{R}_z(\alpha_i)\mathbf{i}$, where \mathbf{R} stands for the rotation matrix, and $\alpha_1 = -\alpha_2 = \alpha - \pi/2$, $\alpha_3 = -\alpha_4 = \beta + \pi/2$. Moreover, unit vectors \mathbf{v}_i and \mathbf{w}_i are parallel to the segments $\overline{A_iB_i}$ and $\overline{B_iC_i}$, respectively, namely, the unit vectors along the proximal and distal links, respectively.

3 Kinematics and Jacobian Matrix of the Robots

The Cartesian coordinates of points A_i and B_i expressed in the frame \mathcal{F}_b are respectively derived by

$$\mathbf{a}_i = R [\cos \eta_i \sin \eta_i 0]^T \tag{1}$$

$$\mathbf{b}_i = b\mathbf{v}_i + \mathbf{a}_i; \mathbf{v}_i = \mathbf{R}_z(\alpha_i)\mathbf{R}_x(\theta_i)\mathbf{j} \tag{2}$$

where $\eta_i = (2i - 1)\pi/4$, $i = 1, \dots, 4$, and θ_i is the input angle.

Let the mobile platform pose be denoted by $\chi = [\mathbf{p}^T \phi]^T$, $\mathbf{p} = [x \ y \ z]^T$, the Cartesian coordinates of point C_i in frame \mathcal{F}_b are expressed as

$$\mathbf{c}_i = \begin{cases} \text{sgn}(\cos \eta_i)r\mathbf{R}_z(\phi)\mathbf{i} + \text{sgn}(\sin \eta_i)c\mathbf{j} + \mathbf{p}, & \text{Quattro (H4)} \\ -\text{sgn}(\cos \eta_i)r\mathbf{R}_y(\phi)\mathbf{i} + \text{sgn}(\cos \eta_i)c\mathbf{j} + \mathbf{p}, & \text{V4} \\ r\mathbf{R}_z(\eta_i)\mathbf{i} + \text{mod}(i, 2)h\phi/(2\pi)\mathbf{k} + \mathbf{p}, & \text{Veloce.} \end{cases} \quad (3)$$

where $\text{sgn}(\cdot)$ stands for the sign function of (\cdot) , and mod stands for the modulo operation, h being the lead of the screw pair of the Veloce. robot.

The inverse geometric problem has been well documented [10]. It can be solved from the following the kinematic constraint equations:

$$(\mathbf{c}_i - \mathbf{b}_i)^T(\mathbf{c}_i - \mathbf{b}_i) = l^2, \quad i = 1, \dots, 4 \quad (4)$$

Differentiating Eq. (4) with respect to time, one obtains

$$\dot{\phi}r\mathbf{w}_i^T\mathbf{s}_i + \mathbf{w}_i^T\dot{\mathbf{p}} = \dot{\theta}_i b\mathbf{w}_i^T(\mathbf{u}_i \times \mathbf{v}_i) \quad (5)$$

with

$$\mathbf{w}_i = \frac{\mathbf{c}_i - \mathbf{b}_i}{l}; \quad \mathbf{s}_i = \begin{cases} \text{sgn}(\cos \eta_i)\mathbf{R}_z(\phi)\mathbf{j}, & \text{Quattro (H4)} \\ \text{sgn}(\cos \eta_i)\mathbf{R}_y(\phi)\mathbf{k}, & \text{V4} \\ \text{mod}(i, 2)h\phi/(2\pi)\mathbf{k}, & \text{Veloce.} \end{cases} \quad (6)$$

Equation (5) can be cast in a matrix form, namely,

$$\mathbf{A}\dot{\chi} = \mathbf{B}\dot{\theta} \quad (7)$$

with

$$\mathbf{A} = [\mathbf{e}_1 \ \mathbf{e}_2 \ \mathbf{e}_3 \ \mathbf{e}_4]^T; \quad \dot{\chi} = [\dot{x} \ \dot{y} \ \dot{z} \ \dot{\phi}]^T \quad (8a)$$

$$\mathbf{B} = \text{diag} [h_1 \ h_2 \ h_3 \ h_4]; \quad \dot{\theta} = [\dot{\theta}_1 \ \dot{\theta}_2 \ \dot{\theta}_3 \ \dot{\theta}_4]^T \quad (8b)$$

where \mathbf{A} and \mathbf{B} are the forward and inverse Jacobian matrices, respectively, and

$$\mathbf{e}_i = [\mathbf{w}_i^T \ r\mathbf{w}_i^T\mathbf{s}_i]^T; \quad h_i = b\mathbf{w}_i^T(\mathbf{u}_i \times \mathbf{v}_i) \quad (9)$$

As along as \mathbf{A} is nonsingular, the kinematic Jacobian matrix is obtained as

$$\mathbf{J} = \mathbf{A}^{-1}\mathbf{B} \quad (10)$$

According to the inverse Jacobian matrix, each limb can have two working modes, which is characterized by the sign “-/+” of h_i . In order for the robot not to reach any serial singularity, the mode $h_i < 0$, $i = 1, \dots, 4$, is selected as the working mode for all the robots.

4 Transmission Quality Analysis

Our interests are the transmission quality, which is related to the robot Jacobian. The determinant $|\mathbf{B}|$ of the inverse Jacobian matrix \mathbf{B} is expressed as

$$|\mathbf{B}| = \prod_{i=1}^4 h_i = b^4 \prod_{i=1}^4 \mathbf{w}_i^T (\mathbf{u}_i \times \mathbf{v}_i) \tag{11}$$

sequentially, the pressure angle μ_i associated with the motion transmission in the i th limb, i.e., the motion transmitted from the actuated link to the parallelogram, is defined as:

$$\mu_i = \cos^{-1} \mathbf{w}_i^T (\mathbf{u}_i \times \mathbf{v}_i), \quad i = 1, \dots, 4 \tag{12}$$

namely, the pressure angle between the velocity of point B_i along the vector of $\mathbf{u}_i \times \mathbf{v}_i$ and the pure force applied to the parallelogram along \mathbf{w}_i , as shown in Fig. 3(a).

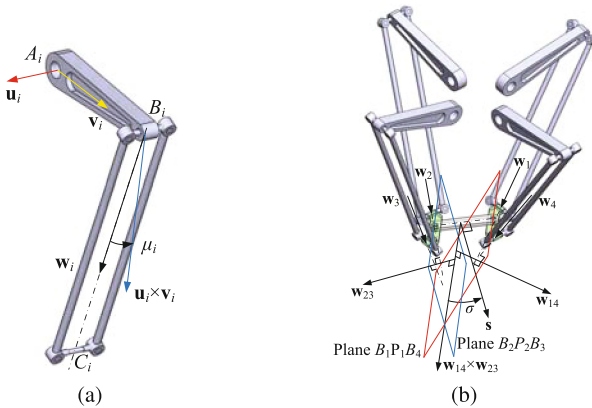


Fig. 3. The pressure angles of the four-limb robots in the motion/force transmission: (a) μ_i for all robots; (b) σ for Quattro.

Likewise, with the Laplace expansion, the determinant $|\mathbf{A}|$ of the forward Jacobian matrix \mathbf{A} is simplified as

$$|\mathbf{A}| = \begin{cases} -2r(\mathbf{w}_{14} \times \mathbf{w}_{23})^T \mathbf{s}, \mathbf{s} = \mathbf{R}_z(\phi)\mathbf{j}; & \text{Quattro (H4)} \\ 2r(\mathbf{w}_{14} \times \mathbf{w}_{23})^T \mathbf{s}, \mathbf{s} = \mathbf{R}_y(\phi)\mathbf{k}; & \text{V4} \\ h\phi/(2\pi)(\mathbf{w}_{13} \times \mathbf{w}_{24})^T \mathbf{k}; & \text{Veloce.} \end{cases} \tag{13}$$

where $\mathbf{w}_{mn} = \mathbf{w}_m \times \mathbf{w}_n$. Taking the Quattro robot as an example, the pressure angle σ amongst limbs, namely, the force transmitted from the end-effector to the passive parallelograms in the other limbs, provided that the actuated joints in these limbs are locked, is derived below:

$$\sigma = \cos^{-1} \frac{(\mathbf{w}_{14} \times \mathbf{w}_{23})^T \mathbf{s}}{\|\mathbf{w}_{14} \times \mathbf{w}_{23}\|} \tag{14}$$

where the of angle σ can be interpreted as the angle between the minus Y -axis (\mathbf{s} is normal to segment $\overline{P_1P_2}$) and the intersection line of planes $B_1P_1B_4$ and $B_2P_2B_3$, where plane $B_1P_1B_4$ ($B_2P_2B_3$) is normal to the common perpendicular line between the two skew lines along \mathbf{w}_1 and \mathbf{w}_4 (\mathbf{w}_2 and \mathbf{w}_3), as depicted in Fig. 3(b). To illustrate the angle σ physically, $(\mathbf{w}_{14} \times \mathbf{w}_{23})^T \mathbf{s}$ can be rewritten in the following form:

$$\begin{aligned} (\mathbf{w}_{14} \times \mathbf{w}_{23})^T \mathbf{s} &= \mathbf{w}_{14}^T [\mathbf{w}_3(\mathbf{w}_2 \cdot \mathbf{s}) - \mathbf{w}_2(\mathbf{w}_3 \cdot \mathbf{s})] \\ &= \mathbf{w}_{23}^T [\mathbf{w}_4(\mathbf{w}_1 \cdot \mathbf{s}) - \mathbf{w}_1(\mathbf{w}_4 \cdot \mathbf{s})] \end{aligned} \quad (15)$$

The angle σ now can be interpreted as the pressure angle between the velocity in the direction of $\mathbf{w}_1 \times \mathbf{w}_4$ and the forces along $\mathbf{w}_2 \times \mathbf{w}_3$ imposed by the parallelograms in limbs 2 and 3 to point P , under the assumption that the actuated joints in limbs 1 and 4 are locked simultaneously. The same explanation is applicable for the case when the actuated joints in limbs 2 and 3 are locked.

By the same token, the pressure angle for the remaining robot counterparts can be defined. Consequently, the motion κ and force ζ transmission indices (TI) in a prescribed configuration are defined as the minimum value of the cosine of the pressure angles, respectively,

$$\kappa = \min(|\cos \mu_i|), \quad i = 1, \dots, 4; \quad \zeta = |\cos \sigma| \quad (16)$$

To this end, the local transmission index (LTI) [11] is defined as

$$\eta = \min\{\kappa, \zeta\} = \min\{|\cos \mu_i|, |\cos \sigma|\} \in [0, 1] \quad (17)$$

The larger the value of the index η , the better the transmission quality of the manipulator. This index can also be applicable for the detection of robot singularity, where $\eta = 0$ means a singular configuration.

5 Transmission Evaluation of PnP Robots

In this section, the transmission index over the regular workspace, for the Quattro, H4, Veloce. and V4 robots, will be mapped to analyzed their motion/force transmission qualities. According to the technical parameters of the Quattro robot [1], the parameters of the robots' base and mobile platforms are given in Table 1, and other parameters are set to $R = 275$ mm, $b = 375$ mm and $l = 800$ mm, respectively.

The LTI isocontours of the four robots with different rotation angles of mobile platform are visualized in Fig. 4, from which it is seen that the minimum LTI of the Quattro and Veloce. robots are much higher than those of H4 and V4. Moreover, the volumes of the formers with $\text{LTI} \geq 0.7$ are larger, to formulate larger operational workspace with high transmission quality. This means that the four-limb robots with a fully symmetrical structure have much better transmission performance than the asymmetric robot counterparts. Another observation is that the transmission performance of the robots decreases with the increasing MP rotation angle.

Table 1. Geometrical parameters of the base and mobile platforms of the four-limb robots.

Robots	Base	Mobile platform
Quattro	$\alpha = -\pi/4, \beta = 3\pi/4$	$r = 80 \text{ mm}, c = 70 \text{ mm}$
H4, V4	$\alpha = 0, \beta = \pi/2$	$r = 80 \text{ mm}, c = 70 \text{ mm}$
Veloce	$\alpha = -\pi/4, \beta = 3\pi/4$	$r = 100 \text{ mm}, \gamma = (2i - 1)\pi/4, h$

As displayed in Fig. 4(a), the transmission index of the Quattro robot have larger values in the central region, which admits a singularity-free workspace with rotational capability $\phi = \pm 45^\circ$. Similarly, Fig. 4(c) shows that the Veloce. robot can also have a high-transmission workspace free of singularity with smaller lead

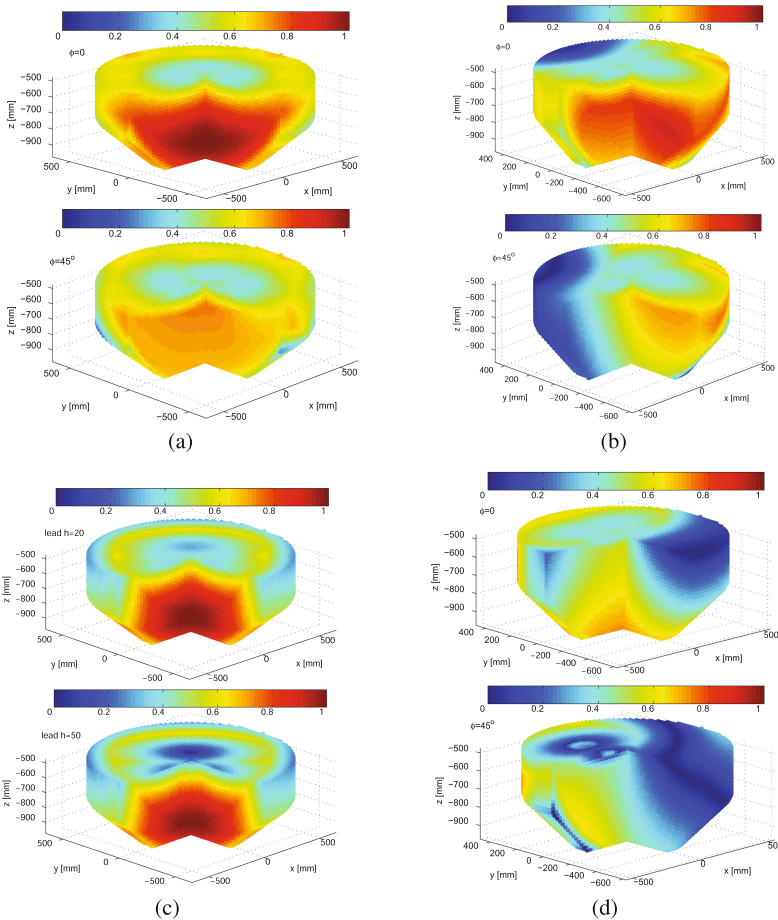


Fig. 4. The LTI isocontours of the robots: (a) Quattro, $\phi = 0$ and $\phi = 45^\circ$; (b) H4, $\phi = 0$ and $\phi = 45^\circ$; (c) Veloce. with $\phi = 2\pi$, screw lead $h = 20$ and $h = 50$; (d) V4, $\phi = 0$ and $\phi = 45^\circ$.

of screw pair, which means that this type of mobile platform allows the robot to have high performance in terms of transmission quality and rotational capability of full-circle rotation. By contrast, the asymmetric H4 and V4 robots result in relatively small operational workspace and relatively low transmission performance, as illustrated in Figs. 4(b) and (d), but similar mechanism footprint ratio with same link dimensions and close platform shapes.

6 Conclusions

This paper presents the transmission analysis for a class of four-limb parallel Schönflies-motion robots with articulated mobile platforms, closely in connection with two pressure angles derived from the forward and inverse Jacobian matrices, wherein the determinant of the forward Jacobian matrices was simplified in an elegant manner, i.e., the scalar product between two vectors, through the Laplace expansion. The cosine function of the pressure angles based indices are defined to evaluate the transmission quality. It appears that the robot with the screw-pair-based mobile platform, namely, the Veloce., is the best in terms of transmission quality for any orientation of the mobile-platform.

Acknowledgements. The reported work is partly supported by the Fundamental Research Funds for the Central Universities (DUT16RC(3)068) and by Innovation Fund Denmark (137-2014-5).

References

1. Adept Quattro Parallel Robots. <http://www1.adept.com/main/ke/data/Archived/Quattro/sQuattro.UG.pdf>
2. Penta Veloce. <http://pentarobotics.com/products/#brochure>
3. Altuzarra, O., Hernandez, A., Salgado, O., Angeles, J.: Multiobjective optimum design of a symmetric parallel Schönflies-motion generator. *ASME J. Mech. Des.* **131**(3), 031002 (2009)
4. Amine, S., Masouleh, M.T., Caro, S., Wenger, P., Gosselin, C.: Singularity conditions of 3 T1 R parallel manipulators with identical limb structures. *ASME J. Mech. Robot.* **4**(1), 011011 (2012)
5. Angeles, J.: Is there a characteristic length of a rigid-body displacement? *Mech. Mach. Theory* **41**(8), 884–896 (2006)
6. Company, O., Krut, S., Pierrot, F.: Internal singularity analysis of a class of lower mobility parallel manipulators with articulated traveling plate. *IEEE Trans. Robot.* **22**(1), 1–11 (2006)
7. Kim, S.G., Ryu, J.: New dimensionally homogeneous Jacobian matrix formulation by three end-effector points for optimal design of parallel manipulators. *IEEE Trans. Robot. Autom.* **19**(4), 731–736 (2003)
8. Merlet, J.P.: Jacobian, manipulability, condition number, and accuracy of parallel robots. *ASME J. Mech. Des.* **128**(1), 199–206 (2006)
9. Pierrot, F., Company, O.: H4: a new family of 4-dof parallel robots. In: *IEEE/ASME International Conference on Advanced Intelligent Mechatronics*, pp. 508–513 (1999)

10. Pierrot, F., Nabat, V., Company, O., Krut, S., Poignet, P.: Optimal design of a 4-dof parallel manipulator: from academia to industry. *IEEE Trans. Robot.* **25**(2), 213–224 (2009)
11. Wang, J., Wu, C., Liu, X.: Performance evaluation of parallel manipulators: motion/force transmissibility and its index. *Mech. Mach. Theory* **45**(10), 1462–1476 (2010)
12. Wu, G.: Kinematic analysis and optimal design of a wall-mounted four-limb parallel Schönflies-motion robot for pick-and-place operations. *J. Intell. Robot. Syst* **85**, 663–667 (2016)
13. Wu, G., Bai, S., Hjørnet, P.: Architecture optimization of a parallel schönflies-motion robot for pick-and-place applications in a predefined workspace. *Mech. Mach. Theory* **106**, 148–165 (2016)
14. Xie, F., Liu, X.: Design and development of a high-speed and high-rotation robot with four identical arms and a single platform. *ASME J. Mech. Robot.* **7**(4), 041015 (2015)

Study of Redundantly Actuated DELTA-Type Parallel Kinematic Mechanisms

Burkhard Corves, Seyed Amirreza Shahidi^(✉), Michael Lorenz,
Sami Charaf Eddine, and Mathias Hüsing

Department of Mechanism Theory and Dynamics of Machines,
RWTH Aachen University, 52072 Aachen, Germany
{corves,shahidi,lorenz,charaf_eddine,huesing}@igm.rwth-aachen.de

Abstract. Due to their high precision and dynamic properties, parallel kinematic manipulators (PKM) are particularly suited for high-speed and high-accuracy object handling. In order to improve their stiffness, their payload capacity and their accuracy PKM can be optimized using a redundant actuator configuration. Accordingly, additional actuators are added to PKM to generate an optimized performance. The objectives, in this context, are highly task oriented and can involve a wide range of the robot's topological and morphological parameters. Based on different tasks and optimization objectives, robots with unique specifications can be designed. In this study redundancy is used to show the effect of topological parameters of redundantly actuated DELTA-type parallel manipulators on general performance characteristics, such as the energy consumption of the robot. The topological characteristics of n -RRPaR manipulators in combination with actuator capabilities are considered as variables. It is shown that optimal torque distribution, chosen a proper topology, would enhance the manipulator's performance and may result in a more efficient energy consumption.

Keywords: Actuation redundancy · PKM · n -RRPaR · DELTA-type Robot · Force capability

1 Introduction

The quality and performance of industrial robots and manipulators commonly is measured by their maximum payload, maximum handling velocity or by their precision in a given workspace. In terms of accuracy in fast object handling, parallel kinematic manipulators (PKM) are preferred to their serial counterparts due to their excellent precision, dynamics characteristics and stiffness, regardless of their relatively small workspace [1]. Generally, these manipulators are equipped with a task-dependent number of actuators represented by the required degree of freedom (DoF) [2]. In contrast, redundantly actuated parallel kinematic manipulators (RA-PKM) use more actuators than needed (over-actuated) in trade-off for a higher stiffness resulting in a higher precision and a more homogeneous and efficient torque distribution.

Over actuating parallel kinematic manipulators can be achieved by means of *branch* and *in-branch* actuation redundancy [3,4]. In the context of the current study, an n -RRPaR ($n \geq 3$) structure is analyzed, which is also known as a DELTA-type branch-redundant PKM. n -RRPaRs are able to execute motion tasks in three translational

degrees of freedom (DoF) as a result of their specific structure including parallelogram members [5].

Time-based characterization of the manipulator is of importance to optimize their performance in many aspects, such as object handling and assembly [6]. For the presented manipulator, the inverse kinematics and dynamics are elaborated in Sects. 2 and 3.

The objective to be pursued in current study is the effect of redundancy on general performance characteristics, such as the force capability of n -RRPaRs. Two topologies with one and three degrees of redundancy ($DoR = n - 3$) are introduced [4], of which the one with four arms is supposed to be reconfigurable. There are different methods to study the force capability of (redundant)-PKM in which the screw theory is widely used [7–9]. The procedure used in this contribution is mainly bottomed on the one introduced by [4].

2 Inverse Kinematics

Determining the joint space parameters q_i of the n -RRPaR given operational space position of the end-effector is discussed in this section. The special case of $n = 3$ with uniformly distributed arms characterises the conventional DELTA robot. The joint space parameters q of the manipulator can be extracted in the same way as DELTA robot. The kinematic parameters of the active and passive joints are as (see Fig. 1):

$$\phi_{3,i} = \cos^{-1} \left(\frac{{}^i r_{i,y}}{l_{2,i}} \right) \tag{1a}$$

$$\phi_{2,i} = \cos^{-1} \left(\frac{{}^i r_{i,x}^2 + {}^i r_{i,y}^2 + {}^i r_{i,z}^2 - l_{1,i}^2 - l_{2,i}^2}{2 l_{1,i} l_{2,i} \sin(\phi_{3,i})} \right) \tag{1b}$$

$$q_i = \tan^{-1} \left(\frac{-\kappa^i r_{i,x} + \zeta^i r_{i,z}}{\zeta^i r_{i,x} + \kappa^i r_{i,z}} \right) \text{ with: } \begin{cases} \zeta = l_{2,i} \sin(\phi_{3,i}) \cos(\phi_{2,i}) + l_{1,i} \\ \kappa = l_{2,i} \sin(\phi_{3,i}) \sin(\phi_{2,i}) \end{cases} \tag{1c}$$

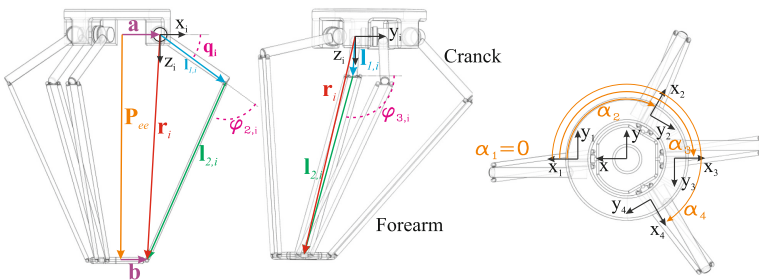


Fig. 1. Kinematic description of n -RRPaR

The time differentiation of closed form equation of the end-effector position can be exploited to determine the angular velocity of the crank and forearms of linkages:

$$\mathbf{P}_{ee} = \mathbf{l}_{1,i} + \mathbf{l}_{2,i} + \mathbf{a} - \mathbf{b} \quad \therefore \quad \dot{\mathbf{P}}_{ee} = \dot{\mathbf{q}}_i \times \mathbf{l}_{1,i} + \omega_{2,i} \times \mathbf{l}_{2,i}, \quad (2)$$

where $\dot{\mathbf{q}}_i$ and $\omega_{2,i}$ are the rotational velocities of the crank and forearm of branch i respectively. The vector $\omega_{2,i} \times \mathbf{l}_{2,i}$ turns to zero by post dot multiplying both sides of (2) by $\mathbf{l}_{2,i}$ due to perpendicularity. Using the equation for angular velocity of the active joint (\mathbf{R}_i is the rotation matrix of branch i of the manipulator to the global coordinate system and $\mathbf{R}_{i|2}$ represents the second column of matrix \mathbf{R}_i):

$$\dot{\mathbf{q}}_i = \mathbf{R}_i \dot{q}_i [0, 1, 0]^T = \dot{q}_i \mathbf{R}_{i|2}, \quad (3)$$

and replacing the cross multiplication by the asymmetric matrix product (represented by $[\bullet]^c$), (2) can be rewritten in algebraic form:

$$\mathbf{l}_{2,i}^T \cdot \dot{\mathbf{P}}_{ee} = \mathbf{l}_{2,i}^T (\dot{q}_i [\mathbf{R}_{i|2}]^c \mathbf{l}_{1,i}). \quad (4)$$

Stacking (4) for different linkages results in (the dimensions are inserted for clarity):

$$\begin{aligned} \left[[\mathbf{l}_{2,r}^T]_{(1,3)} \otimes \mathbf{1}_{(n,1)} \right]_{(n,3)} \cdot \dot{\mathbf{P}}_{ee(3,1)} &= \left[\dot{q}_r \otimes \mathbf{I}_n \right]_{(n,n)} \cdot \left[[\mathbf{l}_{2,r}^T]_{(1,3)}, \otimes \mathbf{I}_n \right]_{(n,3n)} \\ &\quad \cdot \left[[\mathbf{R}_{i|2}]^c \otimes \mathbf{I}_n \right]_{(3n,3n)} \cdot \left[[\mathbf{l}_{1,r}]_{(1,3)} \otimes \mathbf{1}_{(n,1)} \right]_{(3n,1)}, \end{aligned} \quad (5)$$

where the operator \otimes represents the Kronecker product and the subscript r determines the row-index of the succeeding matrix. In order to simplify (5), the auxiliary matrix $[\mathbf{J}_{aux}]$ can be introduced as:

$$\left[[\mathbf{l}_{2,r}^T]_{(1,3)} \otimes \mathbf{1}_{(n,1)} \right]_{(n,3)} \cdot \dot{\mathbf{P}}_{ee(3,1)} = \left[\dot{q}_r \otimes \mathbf{I}_n \right]_{(n,n)} \cdot [\mathbf{J}_{aux}]_{(n,1)}. \quad (6)$$

Since the relation between workspace and joint space velocities is of interest, the right hand side of (6) is rearranged according to:

$$\left[[\mathbf{l}_{2,r}^T]_{(1,3)} \otimes \mathbf{1}_{(n,1)} \right]_{(n,3)} \cdot \dot{\mathbf{P}}_{ee(3,1)} = [\mathbf{J}_{aux}(r, 1) \otimes \mathbf{I}_n]_{(n,n)} \cdot \left[\dot{q}_r \otimes \mathbf{1}_{(n,1)} \right]_{(n,1)}. \quad (7)$$

The matrix $[\mathbf{J}_{aux}(r, 1) \otimes \mathbf{I}_n]_{(n,n)}$ in (7) is a full rank diagonal matrix. Therefore, pre-multiplying both sides of (7) by $[\mathbf{J}_{aux}(r, 1) \otimes \mathbf{I}_n]_{(n,n)}^{-1}$ results in the Jacobian matrix:

$$\left[\dot{q}_r \otimes \mathbf{1}_{(n,1)} \right]_{(n,1)} = [\mathbf{J}_{aux}(r, 1) \otimes \mathbf{I}_n]_{(n,n)}^{-1} \left[[\mathbf{l}_{2,r}^T]_{(1,3)} \otimes \mathbf{1}_{(n,1)} \right]_{(n,3)} \cdot \dot{\mathbf{P}}_{ee(3,1)}, \quad (8)$$

$$[\dot{\mathcal{Q}}]_{(n,1)} = [\mathbf{J}_v]_{(n,3)} \cdot \dot{\mathbf{P}}_{ee(3,1)}. \quad (9)$$

3 Inverse Dynamics

Considering the n -RRPaR as a time-invariant holonomic mechanical system, the principle of virtual works can be used to generalize the inverse dynamic. Acceleration of active and passive joints can be derived by second time derivation of (2):

$$\ddot{\mathbf{P}}_{ee} = \ddot{\mathbf{q}}_{1,i} \times \mathbf{l}_{1,i} + \dot{\mathbf{q}}_i \times (\dot{\mathbf{q}}_i \times \mathbf{l}_{1,i}) + \dot{\omega}_{2,i} \times \mathbf{l}_{2,i} + \omega_{2,i} \times (\omega_{2,i} \times \mathbf{l}_{2,i}). \quad (10)$$

Post dot-multiplying (10) by $\mathbf{l}_{2,i}$ and performing algebraic simplifications, the joint space acceleration given work space acceleration can be presented:

$$\ddot{q}_i = \frac{\mathbf{l}_{2,i}^T (\ddot{\mathbf{P}}_{ee} + (\dot{\mathbf{q}}_i \cdot \dot{\mathbf{q}}_i) \mathbf{l}_{1,i} + (\dot{\mathbf{q}}_i \cdot \dot{\mathbf{q}}_i) \mathbf{l}_{2,i})}{\mathbf{l}_{2,i}^T [\mathbf{R}_i]_c \mathbf{l}_{1,i}} \quad \therefore \quad \ddot{\mathbf{q}}_{1,i} = \ddot{q}_i \mathbf{R}_i. \quad (11)$$

The angular acceleration of the forearm can be obtained, rearranging (10).

After defining the velocity and acceleration vectors, the force and moments associated to the end-effector and linkages can basically be driven in the same manner as the one for conventional topology of DELTA structures (for details see [10]):

$$\begin{aligned} 0 = & \delta[\mathcal{Q}]_{(1,n)}^T [\boldsymbol{\tau}]_{(n,1)} + \delta[\mathbf{X}_{ee}]_{(1,3)}^T [m_{ee} (\mathbf{g} - \ddot{\mathbf{P}}_{ee})]_{(3,1)} \\ & + \sum_{i=1}^n \left(\delta^i[\mathbf{X}_{l_{1,i}}]_{(1,6)}^T \left[\begin{array}{c} m_{l_{1,i}} ({}^i\mathbf{g} - {}^i\mathbf{a}_{1,i,c}) \\ {}^i\mathbf{l}_{1,i} {}^i\ddot{\mathbf{q}}_{1,i} + {}^i\dot{\mathbf{q}}_i \times ({}^i\mathbf{l}_{1,i} {}^i\dot{\mathbf{q}}_i) \end{array} \right]_{(6,1)} \right. \\ & \left. + 2 \delta^i[\mathbf{X}_{l_{2,i}}]_{(1,6)}^T \left[\begin{array}{c} m_{l_{2,i}} ({}^i\mathbf{g} - {}^i\mathbf{a}_{2,i,c}) \\ {}^i\mathbf{l}_{2,i} {}^i\dot{\omega}_{2,i} + {}^i\omega_{2,i} \times ({}^i\mathbf{l}_{2,i} {}^i\omega_{2,i}) \end{array} \right]_{(6,1)} \right). \end{aligned} \quad (12)$$

In (12) $\boldsymbol{\tau}$ is the vector of manipulator torques, \mathbf{g} represents the gravity, \mathbf{I} is the inertia matrix, \mathbf{a} stands for accelerations and subscript c refers to the center of mass. $\delta[\mathbf{X}_{ee}]$, $\delta^i[\mathbf{X}_{l_{1,i}}]$ and $\delta^i[\mathbf{X}_{l_{2,i}}]$ refer to infinitesimal deviations of the end-effector and the center of mass of the cranks and forearms respectively. $\delta[\mathbf{X}_{ee}]$ can be defined by means of the system Jacobian matrix as shown in (9). The link Jacobians \mathbf{J}_{v1}^* and \mathbf{J}_{v2}^* , which relate the velocities of each link's center of mass to the work space velocity vector, are deployed for simplification:

$$\{\delta[\mathcal{Q}], \delta^i[\mathbf{X}_{l_{1,i}}], \delta^i[\mathbf{X}_{l_{2,i}}]\} = \{[\mathbf{J}_v], [\mathbf{J}_{v1}^*], [\mathbf{J}_{v2}^*]\} \delta[\mathbf{X}_{ee}]. \quad (13)$$

Shortening the summation (Σ) part of (12) as link dynamics (LD) results in:

$$0 = \delta[\mathbf{X}_{ee}]_{(1,3)}^T [\mathbf{J}_v]_{(3,n)}^T [\boldsymbol{\tau}]_{(n,1)} + \delta[\mathbf{X}_{ee}]_{(1,3)}^T [m_{ee} (\mathbf{g} - \ddot{\mathbf{P}}_{ee})]_{(3,1)} + \delta[\mathbf{X}_{ee}]_{(1,3)}^T LD. \quad (14)$$

Thus, the dynamic burden of actuators can be concisely formulated as:

$$[\boldsymbol{\tau}]_{(n,1)} = -[\mathbf{J}_v]_{(3,n)}^{+T} ([m_{ee} (\mathbf{g} - \ddot{\mathbf{P}}_{ee})]_{(3,1)} + LD), \quad (15)$$

where $[\]^+$ symbolizes the pseudo inverse.

4 Force Capability

The topological structure of the n -RRPaR can be optimized with regard to different tasks considering an appropriate objective function. One of the possible objectives can be considered as the applicable force of the manipulator. In this section, the overall procedure in order to compute the force capability of the manipulator, with a concise formulation for the general structure, is sketched and discussed.

The classical relation between torque and force can be written for the cranks:

$${}^i\mathbf{M}_i = {}^i\mathbf{l}_{1,i} \times {}^i\mathbf{F}_i. \quad \therefore \quad {}^i\mathbf{F}_i = -\frac{1}{l_{1,i}^2} {}^i\mathbf{l}_{1,i} \times {}^i\mathbf{M}_i. \quad (16)$$

In (16), ${}^i\mathbf{F}_i$ represents the resultant force of the actuator in the local coordinate system and:

$${}^i\mathbf{l}_{1,i} = l_{1,i} [c(q_i), 0, s(q_i)]^T, \quad {}^i\mathbf{M}_i = T_i [0, 1, 0]^T, \quad (17)$$

with T_i the applicable torque of the i^{th} actuator. To transfer the equation to algebraic form, cross multiplication is replaced with the asymmetric matrix product. Simultaneously, the forces are transferred to the global coordinate system:

$$\mathbf{F}_i = -\frac{1}{l_{1,i}^2} \mathbf{R}_i [{}^i\mathbf{l}_{1,i}]^c {}^i\mathbf{M}_i = \mathbf{J}_{F,i} {}^i\mathbf{M}_i, \quad (18)$$

where $\mathbf{J}_{F,i}$ refers to the force Jacobian.

Considering the rods of the forearm as rigid bodies, which prevents the energy loss, the contribution of each actuator to the end-effector's force capability is equal to \mathbf{F}_i . Thus, summing the individual forces up, the force capability of the manipulator on the end-effector results from:

$$\mathbf{F}_{(3,1)} = \left[\mathbf{I}_3 \otimes \mathbf{1}_{1,n} \right]_{(3,3n)} \cdot \left[\mathbf{J}_{F,r} \otimes \mathbf{I}_n \right]_{(3n,3n)} \cdot \left[\text{Conversion Matrix} \right]_{(3n,n)} \cdot \left[\boldsymbol{\tau} \right]_{(n,1)}, \quad (19)$$

where index r in $\mathbf{J}_{F,r}$ refers to the row index of the succeeding matrix and $[\text{Conversion Matrix}]$ is a sparse matrix containing ones at the indices $(3(i-1)+2, i)$ with $i = 1, \dots, n$.

The method of scaling factors can be used to compute the maximum force capability of the manipulator [4, 7, 8]. In this method, the required torque to impose a force in a predefined direction of interest is computed by means of (19). The computed torques can be scaled by the factors resulting from the ratio of maximum applicable torques to the required amount and lastly the force is to be recalculated by (19). In the present study, the Jacobian's null-space resolution is also used to optimize the maximum force as introduced in [9].

5 Results

To examine the presented idea two types of structure topologies are introduced in this section. The first structure is a 4-armed manipulator with varying torque capacity of

actuators and adjustable configuration. The second structure is a 6-armed manipulator and considered to have a variable torque capacity of actuators. Different topologies and actuator capacities are listed in Table 1. The 4-armed manipulators in the three scenarios $4n - 1$ to $4n - 3$ have evenly distributed branches (i.e. α in Fig. 1) and are supposed to have actuators with different torque capacities (the nominal torque of actuators are supposed to be $100 Nm$). The remaining scenarios involve manipulators with varying topological configurations, with all actuators working with 100% capacity. The topology of the 6-armed manipulator is supposed to be unique (with evenly distributed arms) with varying capacities of actuators. For clarity, manipulators of the cases $4n - 3$ to $4n - 6$ are shown in Fig. 2.

Table 1. Percentage of applicable torque of actuators in different simulation configurations

α	0	$\frac{\pi}{8}$	$\frac{\pi}{4}$	$\frac{\pi}{3}$	$\frac{3\pi}{8}$	$\frac{\pi}{2}$	$\frac{5\pi}{8}$	$\frac{2\pi}{3}$	$\frac{3\pi}{4}$	$\frac{7\pi}{8}$	π	$\frac{9\pi}{8}$	$\frac{5\pi}{4}$	$\frac{4\pi}{3}$	$\frac{11\pi}{8}$	$\frac{3\pi}{2}$	$\frac{13\pi}{8}$	$\frac{5\pi}{3}$	$\frac{7\pi}{4}$	$\frac{15\pi}{8}$	
$4n - 1$	100					10					100					10					
$4n - 2$	50					50					50					50					
$4n - 3$	100					100					100					100					
$4n - 4$		100								100		100									100
$4n - 5$			100						100				100								100
$4n - 6$					100		100								100		100				
$6n - 1$	100			10				100			10			100					10		
$6n - 2$	50			50				50			50			50					50		
$6n - 3$	100			50				100			50			100					50		
$6n - 4$	100			100				100			100			100					100		

Figure 2 shows the force distribution of a 4-armed manipulator, in which all the actuators are working with full capacity, in a plane in the middle of the workspace ($z = -0.775 m$). Two main topologies are selected, which are oriented complimentary to each other (i.e. $4n - 3$ with $4n - 5$ and $4n - 4$ with $4n - 6$). A preliminary examination exhibits choosing an appropriate orientation of the manipulator in a specific application can enhance the force capability of the manipulator in a direction of desire considerably. For instance, although the manipulators of cases $4n - 3$ and $4n - 5$ have a similar topology and the actuator capacities are the same, with a same z -force capability, there is an almost 42% improvement in x and y -force capabilities for $4n - 5$. The fact also holds for the manipulator with non-homogeneously distributed arms.

The force capabilities for the 4-armed manipulators are also computed all over the workspaces. The force expectations in different directions are shown in Fig. 3. A comparison between $4n - 1$ and $4n - 2$ emphasizes the importance of a well torque distribution and proves the advantages of task-oriented manipulator design.

The statistical study of the cases with 6 arms are also presented in Fig. 3. The results are obtained from the examination of force capabilities in the effective workspace of the manipulator. Cases $6n - 1$ and $6n - 2$ show comparable force capabilities with a smoothly distributed torque capacity in case $6n - 2$. Doubling the actuation of three actuators in $6n - 2$ results in almost 50% higher force capability in case $6n - 3$, but further doubling the actuation of remaining actuators would result in almost 32% more improvement (the force capability of $6n - 4$ is twice as $6n - 2$).

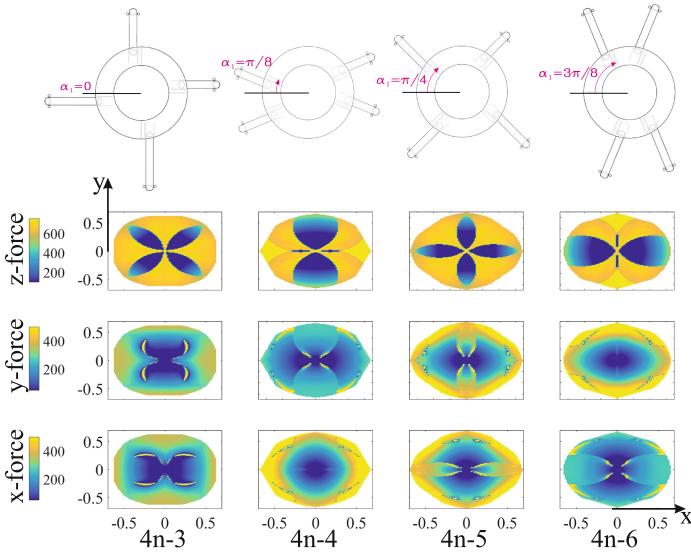


Fig. 2. 4-armed manipulators with configurations $4n - 3$ to $4n - 6$

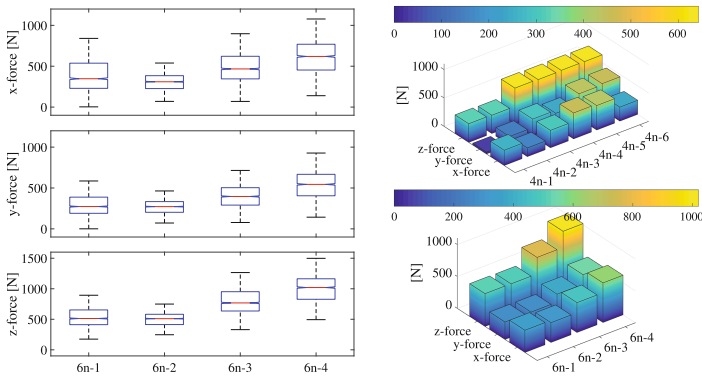


Fig. 3. Statistical examination of selected structures presented in Table 1

6 Conclusions

This study intends to examine the effect of actuation redundancy and topological configuration of a DELTA-type parallel manipulator on its kineto-statics performance. It is shown that a task-oriented topological design of the robot can remarkably enhance its force capability. Furthermore, over-actuated manipulators proved to have a smooth torque distribution for specific performances, which may lead to a more resource-efficient processes.

Further research in this field is accomplished by examining the manipulator flexibility by different topologies. Optimizations are performed to achieve high precision

manipulators, adhering a high performance and energy-efficient task-oriented manipulation. Furthermore, corresponding control strategies in terms of actuation redundancy have to be implemented in order to avoid inner tensioning.

References

1. Merlet, J.P.: Parallel robots, vol. 74. Springer Science & Business Media (2012)
2. Corves, B., Brinker, J., Lorenz, M., Wahle, M.: Design methodology for translational parallel manipulators exhibiting actuation redundancy. *Proc. Inst. Mech. Eng. Part C: J. Mech. Eng. Sci.* **230**(3), 425–436 (2016)
3. Pierrot F.: Parallel mechanisms and redundancy. In: 1st International Colloquium, Collaborative Research Centre 562, pp. 261–277, Braunschweig, 29–30 Mai 2002
4. Lorenz, M., Corves, B., Riedel, M.: Kinetostatic performance analysis of a redundantly driven parallel kinematic manipulator. In: ASME 2014 International Design Engineering Technical Conferences and Computers and Information in Engineering Conference, pp. V05BT08A080–V05BT08A080. American Society of Mechanical Engineers, August 2014
5. Clavel, R.: U.S. Patent No. 4,976,582. Washington, DC: U.S. Patent and Trademark Office (1990)
6. Biagiotti, L., Melchiorri, C.: Trajectory planning for automatic machines and robots. Springer Science & Business Media (2008)
7. Garg, V., Nokleby, S.B., Carretero, J.A.: Force-moment capabilities of redundantly-actuated spatial parallel manipulators using two methods. In: Proceedings of the 2007 CCToMM Symposium on Mechanisms, Machines, and Mechatronics, Montral, QC, Canada, p. 12, May 2007
8. Firmani, F., Zibil, A., Nokleby, S.B., Podhorodeski, R.P.: Force-moment capabilities of revolute-jointed planar parallel manipulators with additional actuated branches. *Trans. Can. Soc. Mech. Eng.* **31**(4), 469–481 (2007)
9. Nokleby, S.B., Fisher, R., Podhorodeski, R.P., Firmani, F.: Force capabilities of redundantly-actuated parallel manipulators. *Mech. Mach. Theory* **40**(5), 578–599 (2005)
10. Brinker, J., Corves, B., Wahle, M.: A comparative study of inverse dynamics based on clavel's delta robot. In: Proceedings of the 14th World Congress in Mechanism and Machine Science, Taipei, Taiwan, pp. 25–30, October 2015

3-RRR Spherical Parallel Robot Optimization with Minimum of Singularities

Asma Jelassi, Abdelbadia Chaker^(✉), and Abdelfattah Mlika

Mechanical Laboratory of Sousse (LMS), National Engineering
School of Sousse, University of Sousse, 4000 Sousse, Tunisia
asma_jlassi23@yahoo.fr, abdelbadi3@gmail.com,
abdeflattah.mlika@gmail.com

Abstract. This paper deals with the optimization of the 3-RRR Spherical parallel Manipulator SPM. In addition to workspace constraints and dexterity performance; singularity positions and distribution appeared to have considerable effects when treating control issues. Thus, this additional parameter is integrated in a Genetic Algorithm (GA) Based synthesis process. A multi objective problem is then formulated and results were analysed. The effect of self rotation φ was also explored through three different values. Results were finally discussed.

Keywords: SPM · Optimization · Dexterity · Singularity · GA · Self rotation

1 Introduction

Multiple criteria were considered in sphericalparallel Manipulator (SPM) design such as workspace [1], dexterity [2], precision [3], and singularity free space [4].

In addition to serial singularities; the 3-RRR SPM has parallel singularities within its workspace [5], this generates many control problems and has negatives effects on the dexterity. The serial singularities could be avoided by enlarging the workspace through bigger manipulator in order to largely cover the desired workspace. However; singularities inside the workspace have to be treated differently by optimizing the manipulator design parameters. For a teleoperation application [2], a 3-RRR architecture (Fig. 1) was adopted in order to realize surgical tasks through the reproduction of a surgery expertmotion. This application needs a high precision; dexterity and especially an optimal control of the system. This can be only with a free singularity workspace.

In this scope; this paper presents an optimization process of the 3-RRR SPM in order to obtain the design parameters that give high level dexterity and a singularity free workspace.

In the next section, the kinematics of the SPM is presented and the design parameters are identified the Optimization problem is then detailed and multiple iterations with different conditions were realized. The first optimization aimed a prescribed workspace with maximum dexterity; the second one considered additionally obtaining a singularity free workspace. Results were finally discussed.

2 Kinematics of the 3-RRR

The 3-RRR SPM is based on a mobile platform over three identical open kinematic chains or legs (Fig. 1). Every chain is composed of three revolute joints with axes intersecting in one point called center of the robot. The axes of the base joints are orthogonal while, on the mobile platform, they are at a 120° angle.

The orientation of the platform is given by the ZXZ configuration of the EULER angles: $[\psi, \theta, \varphi]$.(Boudreau, 2004)

For a leg k the three joints are distributed as shown in Fig. 2 with Z_{ik} the axe of the i^{th} joint and Z_E axe of the platform given by

$$Z_E = \begin{bmatrix} \sin(\Psi)\sin(\theta) \\ -\cos(\Psi)\sin(\theta) \\ \cos(\theta) \end{bmatrix} \tag{1}$$

The joints parameters of each leg are $\theta_{1k}\theta_{2k}, \theta_{3k}(k = 1, 2, 3)$.

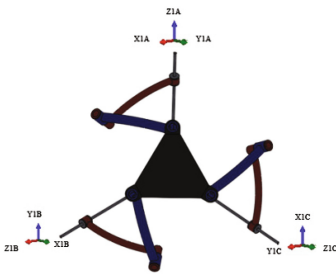


Fig. 1. Kinematics of 3-RRR

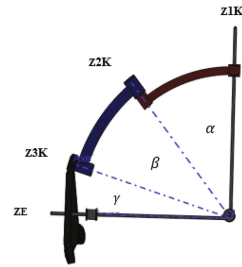


Fig. 2. One Leg parameters of 3-RRR

2.1 Inverse Geometric Model

The inverse geometric model of the SPM developed previously in (A. Chaker, 2012) was obtained through the relation:

$$Z_{3K}.Z_{2K} = \cos(\beta) \tag{2}$$

A three equations system was then derived:

$$\begin{cases} f_1 = A_1.\cos(\theta_{1A}) + B_1.\sin(\theta_{1A}) + C_1 \\ f_2 = A_2.\cos(\theta_{1B}) + B_2.\sin(\theta_{1B}) + C_2 \\ f_3 = A_3.\cos(\theta_{1C}) + B_3.\sin(\theta_{1C}) + C_3 \end{cases} \tag{3}$$

With C_i : as constants ($i = 1..3$). The solutions of this system are conditioned with the relation that defines workspace frontiers:

$$\left(\frac{C_i^2}{A_i^2 + B_i^2} \right) \leq 1 \quad (4)$$

2.2 Kinematics Model

The kinematic formulation is derived from Eq. 2 (A. Chaker, 2012):

$$\dot{\mathbf{Z}}_{2K} \cdot \dot{\mathbf{Z}}_{3K} + \dot{\mathbf{Z}}_{3K} \cdot \dot{\mathbf{Z}}_{2K} = 0 \quad (5)$$

The following system is then obtained:

$$\mathbf{B} \cdot \dot{\mathbf{q}} = \mathbf{A} \cdot \boldsymbol{\omega} \quad (6)$$

With $\dot{\mathbf{q}} = [\dot{\theta}_{1A} \dot{\theta}_{1B} \dot{\theta}_{1C}]^T$ the joints velocity and

$\mathbf{B} = \text{diag} [(Z_{1A} \wedge Z_{2A}) \cdot Z_{3A} (Z_{1B} \wedge Z_{2B}) \cdot Z_{3B} (Z_{1C} \wedge Z_{2C}) \cdot Z_{3C}]$

$\mathbf{A} = [(Z_{3A} \wedge Z_{2A})^T (Z_{3B} \wedge Z_{2B})^T (Z_{3C} \wedge Z_{2C})^T]^T$

And $\boldsymbol{\omega}$ the angle velocity of the platform defined in the global basis

The kinematics of the robot can be written as function of the jacobian matrix \mathbf{J} as follow

$$\boldsymbol{\omega} = (\mathbf{A}^{-1} \cdot \mathbf{B}) \cdot \dot{\mathbf{q}} = \mathbf{J} \cdot \dot{\mathbf{q}} \quad (7)$$

3 Optimization

The optimization is realized for a desired workspace having the platform axis \mathbf{Z}_E able to evaluate on a cone with a 30° half angle. The considered objective functions in this optimization process are: the prescribed workspace accessibility function, the power function, the dexterity function and the singularity function.

3.1 The Accessibility Objective Function

This function is based on the accessibility constraint and helps verifying either the platform position belongs to the desired workspace or not. It is described as:

$$F1 = \sum_j^N \sum_i^3 \omega_i(\mathbf{Y}, \mathbf{P}_j) \quad (8)$$

$$\text{With } \omega_i(\mathbf{Y}, \mathbf{P}_j) = \begin{cases} 0 & \text{si } CDi(\mathbf{Y}, \mathbf{P}_j) \leq 0 \\ cf & \text{si } CDi(\mathbf{Y}, \mathbf{P}_j) > 0 \end{cases}$$

Y is the design vector $Y = [\alpha\beta]$, $\text{CDi}(Y, P_j) = (C_i^2 - (A_i^2 + B_i^2))$

P_j is a given orientation of the platform

$j = 1..N$: the number of orientations of the platform defined by $P_j = \psi, \theta, \varphi$ and cf a high value constant attributed as penalty to candidate manipulate or enable to reach the prescribed conic workspace.

3.2 The Power Objective Function

This function is used to evaluate the distance between the SPM reachable workspace and the prescribed one. Minimizing this function leads to a manipulator which workspace is as close as possible to the desired one. It is formulated as follow:

$$\mathbf{F2} = \sum_j^N \sum_i^3 \left| \frac{C_i^2(Y, P_j)}{A_i^2(Y, P_j) + B_i^2(Y, P_j)} \right| \quad (9)$$

3.3 Dexterity Objective Function

The dexterity traduces the capacity of a robot to realize, with high precision, small and arbitrary displacements around a position in a desired workspace. The inverse of the local condition number of the Jacobian matrix $K(J)$ is used as index to measure dexterity

$$\mathbf{K}(J) = \|J\| \cdot \|J^T\| \quad (10)$$

The manipulator dexterity is then represented as function of the sum of the condition numbers:

$$\mathbf{F3} = \sum_{\Psi_{min}}^{\Psi_{max}} \sum_{\theta_{min}}^{\theta_{max}} 1/K(Y, P(\Psi, \theta)) \quad (11)$$

With Ψ_{min}, Ψ_{max} the limit values of the Ψ angle range; $\theta_{min}, \theta_{max}$: the limit values of the θ angle range;

3.4 Singularity Objective Function

This function ensures the requirement of a singularity free desired workspace. They are tolerated only outside of the prescribed workspace where kinematic performance has to be optimal. We focus on parallel singularities defined as orientations distance that reduces the $\text{Det}(A)$ to zero. The function $\mathbf{F4}$ calculates the number of singularity positions for every candidate manipulator by verifying the condition ($\text{Det}(A) = 0$). This function is written as follow:

$$\mathbf{F4} = \sum_{\Psi_{min}}^{\Psi_{max}} \sum_{\theta_{min}}^{\theta_{max}} S(Y, P(\Psi, \theta)) \quad (12)$$

$$\text{with: } S(Y, P(\psi, \theta)) = \begin{cases} 0 & \text{if } \text{Det}(A) \neq 0 \\ 1 & \text{if } \text{Det}(A) = 0 \end{cases}$$

4 First Optimization : Dexterity

The first optimization, named Optimization 1, is operated with the three objective functions **F1**, **F2** et **F3**. The aim is to have an optimal structure able to cover all the desired workspace and guarantee a high level of local dexterity. The optimization problem is then written as:

$$\text{Min } \mathbf{f} = \min[\mathbf{f}(1) \mathbf{f}(2)]$$

- $\mathbf{f}(1) = \mathbf{F1} + \mathbf{F2}$
- $\mathbf{f}(2) = \mathbf{F3}$

Optimization 1 with $\varphi = 0^\circ$

We obtain the design parameter vector: $Y_{opt} = [38.86^\circ \ 31.07^\circ \ 17.31^\circ]$

Figure 3 shows the dexterity distribution in the workspace. The maximum dexterity value is 0.42 with a mean value of 0.2127. The desired workspace, represented in yellow on the Fig. 4, is completely reachable and is free of singularities.

Other self rotation angles were tested with the resulting manipulator, for a value of $\varphi = 50^\circ$ we have the workspace in Fig. 5. We notice the reduction of the manipulator workspace size which affects the prescribed workspace accessibility and the appearance of a consistent singularity zone (in red) in the center of the workspace.

Local dexterity falls to a maximum of 0.22 and a dissymmetrical distribution appears with very low values in the center of the workspace Fig. 6. This corresponds clearly to the singularity zone.

These results make clear the effect of self rotation angle on the SPM performance. Examining the effect of this parameter on the optimization results is then a necessity. Two symmetrical values were taken: $\varphi = \pm 50^\circ$ in order to enlarge the range of optimization and find better design vector candidates with angles α, β, γ leading to better dexterity performance and singularity free workspace

Optimization 1 pour $\varphi = 50^\circ$

The design vector resulting is $Y_{opt} = [38.76^\circ \ 37.76^\circ \ 29.99^\circ]$

With a maximum value of dexterity 0.39 and 0.1357 as mean value (Fig. 7)

We notice also a dissimmetrical distribution of the dexterity; but we have a desired workspace completely reachable (Fig. 8).

Optimization pour $\varphi = -50^\circ$

In this case; the resulting vector is $Y_{opt} = [39.79^\circ \ 39.7^\circ \ 29.16^\circ]$. The maximum dexterity value is 0.5 with a mean of 0.2830 (Fig. 9) and a resulting workspace covering the entire desired one (Fig. 10).

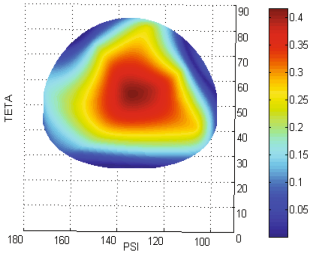


Fig. 3. Dexterity distribution for $\varphi = 0$

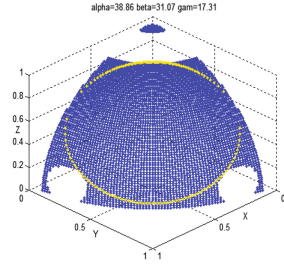


Fig. 4. Workspace for $\varphi = 0$. (Color figure online)

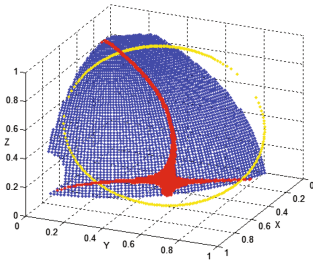


Fig. 5. Workspace for $\varphi = 50$. (Color figure online)

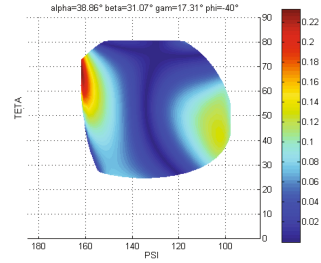


Fig. 6. Dexterity distribution for $\varphi = 50$

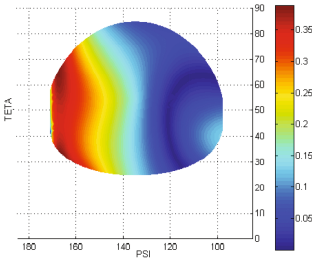


Fig. 7. Dexterity distribution for $\varphi = 50^\circ$

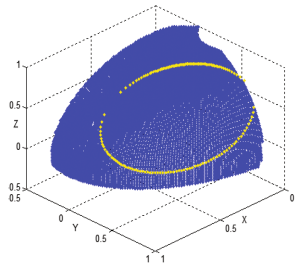


Fig. 8. Workspace for $\varphi = 50^\circ$

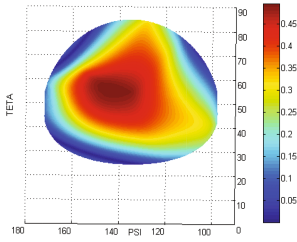


Fig. 9. Dexterity for optimization 1 and $\varphi = -50$

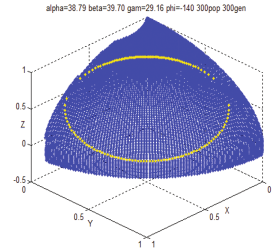


Fig. 10. Workspace for optimization 1 $\varphi = -50^\circ$

5 Second Optimization: Dexterity

The second optimization, named Optimization 2, is launched considering the three objective functions to minimize **F1**, **F2** and **F4**.we formulate the problem as follow:

$$\text{Min } \mathbf{f} = \min[\mathbf{f}(1) \mathbf{f}(2)]$$

- $\mathbf{f}(1) = \mathbf{F1} + \mathbf{F2}$
- $\mathbf{f}(2) = \mathbf{F4}$

the same desired workspace is aimed and the three self rotation values $\varphi = 0^\circ, 50^\circ, -50^\circ$ are considered.

Optimization 2 for $\varphi = 0^\circ$

The optimum solution resultis $Y_{opt} = [38.88^\circ \ 38.6^\circ \ 20.58^\circ]$

Considering Fig. 11, dexterity reaches a maximum of 0.49 and the mean value is 0.2452. Figure 12 shows that the prescribed workspace is totally covered and singularity zones were discarded out of the useful workspace.

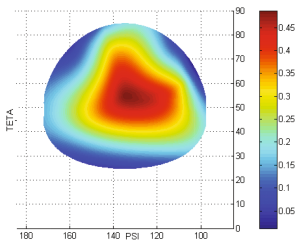


Fig. 11. Dexterity for optimization 2, $\varphi = 0$

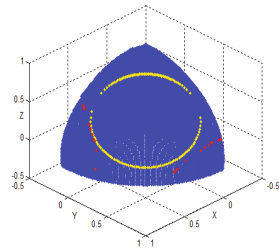


Fig. 12. Workspace for optimization 2, $\varphi = 0$

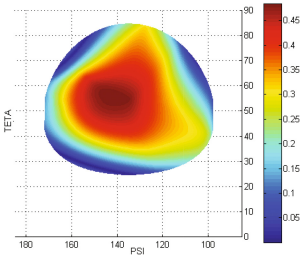


Fig. 13. Dexterity for optimization 2, $\varphi = -50^\circ$

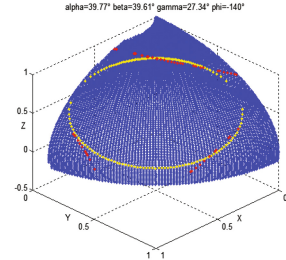


Fig. 14. Workspace for optimization 2, $\varphi = -50^\circ$

Optimization 2 for $\varphi = -50^\circ$

The optimum solution obtained is: $Y_{opt} = [39.77^\circ \ 39.61^\circ \ 27.34^\circ]$

The dexterity distribution regain in symmetry with a maximum value of 0.49, (Fig. 13). Figure 14 shows the prescribed workspace covered by the manipulator

6 Conclusion

This paper discussed the optimization process if a 3-RRR SPM. We concluded that all the three parameters have to be considered: the prescribed task workspace; the dexterity and avoiding singularity zones. Design vectors were determined for the two first parameters and performances were discussed. A clear effect of the self rotation angle on the dexterity and the singularity zone was noticed. The optimization process where then reconducted for three values of φ . The optimum design vector showed better performance by reaching the desired workspace with better dexterity and a singularity free workspace. Otherwise, discarding singularity out of the useful workspace induces a rise of the design parameters and then a bigger manipulator.

References

1. Bai, S.: Optimum design of spherical parallel manipulator for a prescribed workspace. *Mech. Mach. Theor.* **45**, 200–211 (2010)
2. Chaker, A.: Synthesis of spherical parallel manipulator for dexterous task. *Front. Mech. Eng.* **7**(2), 150–162 (2012)
3. Al-Widyan, K.M.X.: The robust design of parallel. *Mech. Mach. Theor.* **46**(3), 335–343 (2011)
4. Boudreau, M.A.: The synthesis of three degree of freedom planar parallel mechanisms with revolute joints (3-RRR) for an optimal singularity-free workspace. *J. Robot. Syst.* **21**(5), 259–274 (2004)
5. Saafi, H.: Forward kinematic model of a new spherical parallel manipulator used as a master device. In *Recent Advances in Mechanism Design for Robotics*. Mechanisms and Machine Science, vol. 33, pp. 399–406 (2015)

4haptic: A Dexterous 4 d.o.fs Haptic Device Based on Delta Architecture

Celestin Preault^(✉), Housseem Saafi, Med Amine Laribi, and Said Zegloul

Department of GMSC, Pprime Institute,
CNRS - University of Poitiers - ENSMA - UPR 3346, Poitiers, France
{celestin.preault,housseem.saafi,
med.amine.laribi,said.zegloul}@univ-poitiers.fr

Abstract. This paper introduces a novel kinematic of 4 d.o.fs haptic device based on Delta architecture. A fourth leg is added to the Delta structure to convert translations into rotations and to provide translation of the handle allowing 3 rotations and 1 translation of the end effector. The fourth leg is linked to the base and to the moving platform by two spherical joints. The kinematic model of the new structure, called 4haptic, is presented. The novel device has a better dexterity distribution compared with previous developed master device based on spherical parallel manipulator architecture. The 4haptic device offers a singularity free useful workspace which makes it a suitable candidate to perform tele-operated Minimally Invasive surgery.

Keywords: Delta robot · Haptic devices · Minimally Invasive surgery · Teleoperation system

1 Introduction

Haptic devices are developed to simulate interaction between the user and a virtual environment, by applying force and torque feedback on a master device. Such devices are widely used in virtual reality [1], gaming [2] and tele-robotics [3]. In medicine, haptic devices are used for training in virtual environment the practice of surgical techniques [4, 5] or for tele-operation [6, 7].

A previous study [8] highlights that Minimally Invasive Surgery (MIS) gesture requires at least four degrees of freedom (d.o.fs) to perform a suture. Therefore, the haptic controller should have three rotations around the Remote Center of Motion (RCM) and a translation along its self rotation axis.

A previous haptic interface based on spherical parallel architecture has been developed for MIS procedure. This Spherical Parallel Manipulator (SPM) suffers from the presence of the singularity inside the useful workspace. The solution proposed is to use a Delta structure to convert 3 translational d.o.fs to 2 rotational d.o.fs. The third rotation as well as the translation along the self rotation axis is provided by the fourth leg.

This paper focuses on the kinematic model and the kinematic performances of this new interface based on Delta structure called 4haptic since it has 4 d.o.fs.

This paper is organized as follows. In Sect. 2, an overview of a tele-operation system for MIS is presented. The kinematic model of the new device is explained in Sect. 3. Section 4 compares the dexterity of the new interface to the one of the previous structure. Section 5 concludes this paper.

2 Gesture in Minimally Invasive Surgery and Teleoperation

The main goal of tele-surgery is not to develop an autonomous system but to assist the surgeon during his task by adding accuracy, safety and comfort. Teleoperation systems consist of a slave surgery robot controlled by a master interface (with or without haptic feedback).

Minimally Invasive Surgery uses instruments inserted into patient's body through tiny incisions points. Unlike open surgery which generally requires up to six d.o.fs, minimally invasive procedure requires only four d.o.fs: three rotation around incision point and one translation along the instrument axis (Fig. 1). This is due to the constraints imposed by the trocar.

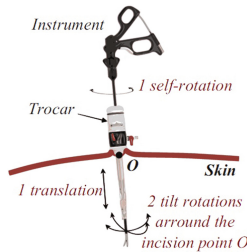


Fig. 1. Minimally Invasive surgery motions

A previous study of MIS gesture using a motion capture system has revealed the useful workspace needed by a surgeon to perform arterial anastomosis [8]. Using these results a slave robot (Fig. 2) was designed and optimized to perform MIS tasks. To reach the useful workspace, the slave robot was designed with a serial spherical architecture. To implement haptic feedback on the master interface, a six-axis force sensor has been inserted between the effector and the slave robot.

A master interface (see Fig. 3) has been designed based on a spherical parallel architecture. Multiple prototypes of the interface have been developed. The first prototypes (see Fig. 3) suffer from the presence of parallel singularity in its workspace. This singularity is located in the center of useful workspace and depends on the self-rotation of the moving platform. It induces errors during Forward Kinematic Model (FKM) evaluation and requires high motor torques for haptic feedback [9]. Due to this singularity and a lack of dexterity, the first prototype doesn't allow us to properly control the slave robot.

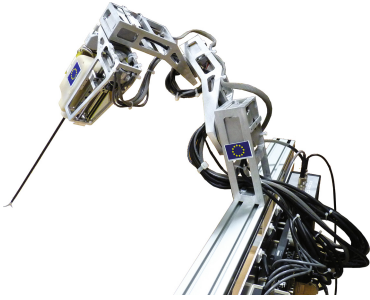


Fig. 2. MIS slave robot



Fig. 3. 1st prototype of master interface

To reduce effects of the singularity on haptic feedback, a redundant actuator has placed on the moving platform [10,11]. This setup allows to obtain the needed torques for haptic feedback, however it increases the weight of the moving platform. The interface is not transparent anymore, it's not a suitable solution to control the slave robot.

A novel kinematic architecture based on Delta structure is proposed in this work in order to cope with these drawback.

3 4haptic Device Architecture

3.1 A New Kinematic Structure

The intended MIS procedure requires three rotational and one translational d.o.fs. However, classical Delta device allows three translational d.o.fs. To convert

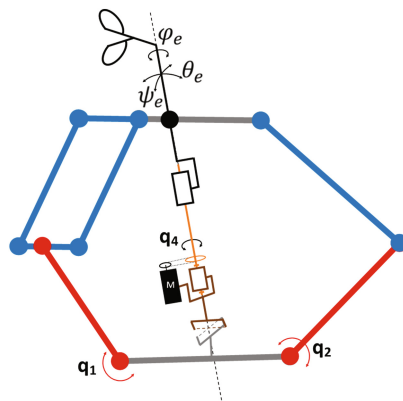


Fig. 4. New Kinematic based on Delta robot architecture

translation into rotations, a fourth leg is added to the structure. This extensible leg is linked thanks to two spherical joints on the base and the moving platform. The three rotational d.o.fs are given by the orientation of the fourth leg with respect to the base. The translational d.o.fs is given by a prismatic joint located in the fourth leg as shown in Fig. 4.

The spherical joint on the base is composed of an universal joint and a revolute joint which allows to control self-rotation φ_e .

A CAD model and a 3D printed prototype have been designed to validate the kinematic behavior.

3.2 Forward Kinematic Model

To evaluate the position of the moving platform, we have to determine the coordinates of vector $\mathbf{OD} = [x_d, y_d, z_d]$ in R_0 where O is the origin of the fixed frame attached to the base of the Delta and D is the center of the moving platform.

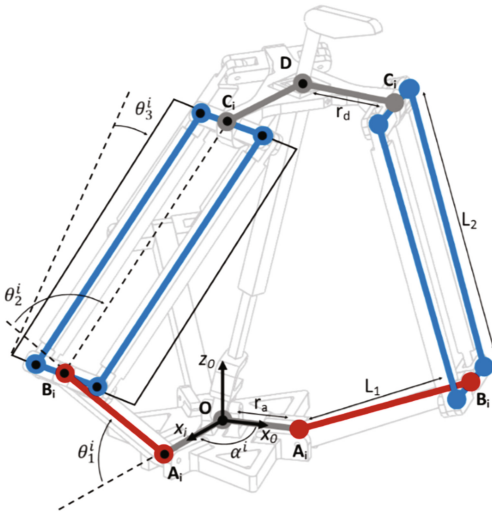


Fig. 5. Geometric parameters of Delta robot

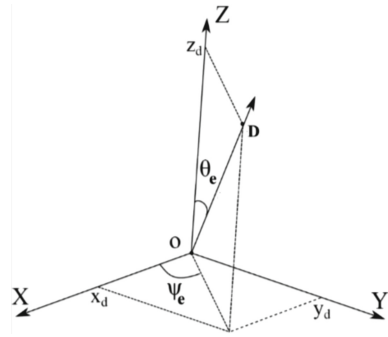


Fig. 6. Orientations of the 4th leg (vector \mathbf{OD})

The geometric parameters of Delta structure are L_1, L_2, r_a, r_d and α^i as described in the Fig. 5. θ_1^i defines the active joint angle while θ_2^i, θ_3^i define the passive joint angles of each leg. The coordinate of the moving platform (point D) are given by the FKM written as follows for each leg of the Delta:

$$\begin{cases} x_d = C\alpha^i(r + L_1C\theta_1^i + L_2C\theta_3^iC\theta_{12}^i) - L_1S\alpha^iS\theta_3^i \\ y_d = S\alpha^i(r + L_1C\theta_1^i + L_2C\theta_3^iC\theta_{12}^i) + L_1C\alpha^iS\theta_3^i \\ z_d = L_1S\theta_1^i + L_2C\theta_3^iS\theta_{12}^i \end{cases} \quad \text{for } i = 1, 2, 3 \quad (1)$$

with $r = r_a - r_d$ and $C\theta = \text{Cos}(\theta)$; $S\theta = \text{Sin}(\theta)$; $C\theta_{12} = \text{Cos}(\theta_1 + \theta_2)$.

The forward model determines the position x_d, y_d, z_d of the moving platform for any given configuration of actuated revolute joints θ_1^i . The position of point D can be obtained by solving the following equations (for $i = 1, 2, 3$):

$$(x_d - x_i)^2 + (y_d - y_i)^2 + (z_d - z_i)^2 = L_2^2 \quad (2)$$

$$\text{where } \begin{cases} x_i = \cos(\alpha^i)(r + L_1 \cos(\theta_1^i)) \\ y_i = \sin(\alpha^i)(r + L_1 \cos(\theta_1^i)) \\ z_i = -L_1 \sin(\theta_1^i) \end{cases} \quad (3)$$

The orientation of the handle created by the fourth leg and the two spherical joints is described using Euler ZYZ angles $(\psi_e, \theta_e, \varphi_e)$. A fourth active joint θ_4 is introduced to control the self-rotation (φ_e) .

One can describe the coordinates of vector OD using $\psi_e, \theta_e, \varphi_e$ and L_d as follows (see Fig. 6):

$$\mathbf{OD} = L_d \cdot R_z(\psi_e) \cdot R_y(\theta_e) \cdot Z = L_d \cdot \begin{bmatrix} \cos\psi_e \sin\theta_e \\ \sin\psi_e \sin\theta_e \\ \cos\theta_e \end{bmatrix} = \begin{bmatrix} x_d \\ y_d \\ z_d \end{bmatrix} \quad (4)$$

$$\begin{cases} L_d = \|OD\| = \sqrt{x_d^2 + y_d^2 + z_d^2} \\ \theta_e = a \cos\left(\frac{z_d}{L_d}\right) \\ \psi_e = a \tan 2\left(-\frac{y_d}{L_d \sin\theta_e}, -\frac{x_d}{L_d \sin\theta_e}\right) \\ \varphi_e = \theta_4 \end{cases} \quad (5)$$

The self rotation φ_e is directly given by the fourth active joint θ_4 .

These two models combined gives the FKM model of the 4haptic interface using $\theta_1^1, \theta_1^2, \theta_1^3, \theta_4$ as input to evaluate $\theta_e, \psi_e, \varphi_e$ and L_d .

4 Dexterity Analysis and Comparison Between SPM and 4haptic Devices

Kinematic performances evaluate the ability of moving and applying forces to the handle. In order to measure the kinematic performances we use dexterity criteria. The dexterity describes the amplification of the errors due to the kinematic and static transformations between Cartesian and joints spaces. The dexterity is evaluated using the Condition number of Jacobian matrix $\kappa(J)$ that describe the kinematic of the master device [12].

The dexterity is evaluated as follows:

$$\eta(J) = \frac{1}{\kappa(J)} \quad \text{where } \kappa(J) = \|J\| \cdot \|J^{-1}\| \quad (6)$$

4.1 SPM Dexterity

The Spherical Parallel Manipulator (SPM) dexterity has been evaluated in previous work [9–11]. On this architecture, the distribution of dexterity depends on self rotation φ .

For MIS task, the center of the workspace is the most important region. According to the previous study of the SPM interface [9], for $\varphi = 0^\circ$, the dexterity is maximum on the center of the workspace but still low (about 0.4, see Fig. 7), however for $\varphi = 50^\circ$, the dexterity on the center of the workspace vanishes (see Fig. 8). The presence of this singularity in the workspace amplifies the error during FKM evaluation and requires high actuator torque for haptic feedback. Due to this singularity, the self-rotation is not controllable anymore when the dexterity is too low.

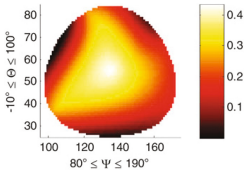


Fig. 7. Dexterity distribution for $\varphi = 0^\circ$

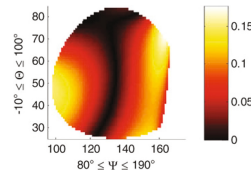


Fig. 8. Dexterity distribution for $\varphi = 50^\circ$

A solution with a redundant actuator installed on a joint of the platform has been studied [10,11]. This modification of the device improves the dexterity of the interface (up to 0.5), however it increases the weight of the moving platform. For this reason, the solution is not suitable.

4.2 4haptic Dexterity

By differentiating Eq. (2), the Jacobian matrix of the 4haptic device can be obtained. The fourth d.o.f. (self rotation φ_e) is excluded from the study since this rotation is totally decoupled from the rest of the system.

$$\dot{x}_d(x_d - x_i) + \dot{y}_d(y_d - y_i) + \dot{z}_d(z_d - z_i) = \dot{x}_i(x_d - x_i) + \dot{y}_i(y_d - y_i) + \dot{z}_i(z_d - z_i) \quad (7)$$

This equation can be written as follows:

$$J_v v_d = J_\theta \dot{q} \quad (8)$$

Where $v_d = [\dot{x}_d, \dot{y}_d, \dot{z}_d]^T$ (platform velocity) and $\dot{q} = [\dot{\theta}_1^1, \dot{\theta}_1^3, \dot{\theta}_1^3]^T$ (joints velocities)

$$J_v = \begin{bmatrix} x_d - x_1 & y_d - y_1 & z_d - z_1 \\ x_d - x_2 & y_d - y_2 & z_d - z_2 \\ x_d - x_3 & y_d - y_3 & z_d - z_3 \end{bmatrix} \quad J_\theta = \begin{bmatrix} J_1 & & \\ & J_2 & \\ & & J_3 \end{bmatrix} \quad (9)$$

with

$$J_i = -L_1 C \alpha^i S \theta_1^i (x_d - x_i) - L_1 S \alpha^i S \theta_1^i (y_d - y_i) - L_1 c \theta_1^i (z_d - z_i) \quad \text{for } i = 1, 2, 3 \quad (10)$$

The global Jacobian matrix used to evaluate dexterity is defined by $J = (J_v)^{-1} J_\theta$.

The dexterity of the new interface has been evaluated (Fig. 9) using different fixed values of the fourth leg length L_d , which correspond to the fourth joint parameter.

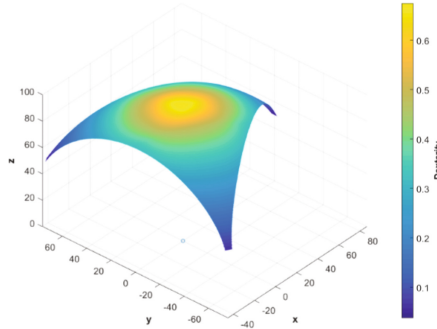


Fig. 9. Dexterity distribution of the 4haptic device in Cartesian space for $L_d = 100$ mm

The new haptic interface has a maximum dexterity of 0.7. This value is greater than the one obtained for previous SPM [9], which was limited to 0.4. The dexterity is maximum in the center of workspace. Unlike SPM, it doesn't depend on the self-rotation φ since this rotation is decoupled from the rest. This makes the new architecture better and suitable haptic interface for the intended surgical task.

5 Conclusion

This paper presents a novel kinematic architecture of a 4 d.o.fs haptic interface based on Delta structure, called 4haptic. A fourth leg is added to the Delta structure to convert translations into rotations and translations. This solution provides 3 rotations and 1 translation of the handle. The kinematic model as well as the dexterity distribution of the novel architecture has been evaluated in this paper. For the intended task, the dexterity of this device is higher than the existing haptic controller (Spherical Parallel Manipulator) [9]. In addition, the new interface has no singularity in the useful workspace. A higher dexterity and absence of singularity in the workspace will improve the force feedback of the novel device, which will be a suitable haptic interface for MIS teleoperation system. In future works, a prototype will be designed and built based on the results of this study in order to control efficiently a surgical slave robot.

Acknowledgements. This research is supported by ROBOTEX, the French national network of robotics platforms (N° ANR-10-EQPX-44-01).

References

1. Gosselin, F., Jouan, T., Brisset, J., Andriot, C.: Design of a wearable haptic interface for precise finger interactions in large virtual environments. In: Eurohaptics Conference, 2005 and Symposium on Haptic Interfaces for Virtual Environment and Teleoperator Systems, 2005. World Haptics 2005. First Joint, pp. 202–207. IEEE (2005)
2. Park, W., Kim, L., Cho, H., Park, S.: Design of haptic interface for brickout game. In: IEEE International Workshop on Haptic Audio Visual Environments and Games, 2009. HAVE 2009, pp. 64–68. IEEE (2009)
3. Son, H., Franchi, A., Chuang, L., Kim, J., Bulthoff, H., Giordano, P.: Human-centered design and evaluation of haptic cueing for teleoperation of multiple mobile robots. *IEEE Trans. Cybern.* **43**(2), 1247–1250 (2013)
4. Broeren, J., Rydmark, M., Sunnerhagen, K.: Virtual reality and haptics as a training device for movement rehabilitation after stroke: a single-case study. *Arch. Phys. Med. Rehabil.* **85**(8), 1247–1250 (2004)
5. Seo, Y., Chowriappa, A., Guru, K., Kesavadas, T.: Medical simulator for trocar insertion procedure. In: Medicine Meets Virtual Reality Conference, San Diego, CA, February 2013
6. van den Bedem, L., Hendrix, R., Rosielle, N., Steinbuch, M., Nijmeijer, H.: Design of a minimally invasive surgical teleoperated master-slave system with haptic feedback. In: International Conference on Mechatronics and Automation, 2009. ICMA 2009, pp. 60–65. IEEE (2009)
7. Tobergte, A., Helmer, P., Hagn, U., Rouiller, P., Thielmann, S., Grange, S., Albuschaffer, A., Conti, F., Hirzinger, G.: The sigma. 7 haptic interface for mirosurge: a new bi-manual surgical console. In: 2011 IEEE/RSJ International Conference on Intelligent Robots and Systems (IROS), pp. 3023–3030. IEEE (2011)
8. Chaker, A., Mlika, A., Laribi, M.A., Romdhane, L., Zeghloul, S.: Synthesis of spherical parallel manipulator for dexterous medical task. *Front. Mech. Eng.* **7**(2), 150–162 (2012)
9. Saafi, H., Laribi, M.A., Zeghloul, S.: Forward kinematic model improvement of a spherical parallel manipulator using an extra sensor. *Mech. Mach. Theory* **91**, 102–119 (2015)
10. Saafi, H., Laribi, M.A., Zeghloul, S.: Redundantly actuated 3-RRR spherical parallel manipulator used as a haptic device: improving dexterity and eliminating singularity. *Robotica* **33**(05), 1113–1130 (2015)
11. Saafi, H., Laribi, M.A., Zeghloul, S.: Optimal torque distribution for a redundant 3-RRR spherical parallel manipulator used as a haptic medical device. *Robot. Auton. Syst.* **89**, 40–50 (2017)
12. Laribi, M.A., Romdhane, L., Zeghloul, S.: Analysis and dimensional synthesis of the delta robot for a prescribed workspace. *Mech. Mach. Theory* **42**(7), 859–870 (2007)

Error Modelling and Sensitivity Analysis of a Planar 3-PRP Parallel Manipulator

Jayant K. Mohanta¹, Santhakumar Mohan^{1(✉)}, Mathias Huesing²,
and Burkhard Corves²

¹ Mechanical Engineering, Indian Institute of Technology (IIT) Indore,
Indore 453552, India

{phd1401103005, santhakumar}@iiti.ac.in

² Department of Mechanism Theory and Dynamics of Machines,
RWTH Aachen University, Aachen 52072, Germany
{huesing, corves}@igm.rwth-aachen.de

Abstract. This paper presents an analytical error prediction model of a 3PRP planar parallel manipulator using the screw theory. This analytical approach is used to find the effect of mechanical inaccuracies contributing to the end-effector pose errors and their sensitivity coefficients. Finally, parameter sensitivity analysis of non-compensable errors of two different configurations based on their fixed base shape namely Δ -shape and U-shape fixed bases are analysed and compared.

Keywords: Planar parallel manipulator · Error modelling · Sensitivity analysis · Non-compensable errors · Mechanical inaccuracies

1 Introduction

Planar parallel manipulators (PPMs) are having higher attention in the recent years due to their simplicity in design and other potential advantages over serial manipulators [6]. In specific, manipulators having first joint as active prismatic joint in each leg has several advantages than others [5]. In this respect, one of the commercially available manipulators namely Hephaist [3] is a 3PRP U-shape PPM and the manipulator proposed by Damien Chablat *et al.* is a Δ -shape 3-PRP PPM [1], both of them are promising in terms of their kinematic and dynamic performances. This 3PRP configuration has shown potential advantage in industrial usage but which of these two base configurations is better in terms of accuracy in presence of mechanical inaccuracies are yet to be explored. Accuracy analysis of these configurations due to the actuator inaccuracies using the geometric approach is presented by Yu *et al.* [8], but in this work, effect of other non-compensable errors and kinematic parameter errors are not included. It is significant to quantify the sources of errors which are contributing the end-effector pose errors in order to find the quality of task performed by the manipulator, which directly affects the positional accuracy of the manipulator. These pose errors can be of three kinds: kinematic errors, encoder errors and the errors due to joint clearances.

The kinematic errors are due to the misalignments and the manufacturing imperfections and tolerances. These kinematic errors for manipulators can be estimated and many researches has found methods to quantify and compensate them [3, 4]. Encoder errors can be of two types, the first one is due to least count of the encoders and other one is due to incorrect index of the encoder reading. Index errors can be corrected by zero point confirmation, but least count errors are non-compensable. Similarly, error due to joint clearances and backlashes are also non-compensable in nature.

Therefore, in this paper, a complete error prediction model considering all possible errors i.e., due to mechanical inaccuracies (including the kinematic parameter errors and error due to joint clearances in the rotary and prismatic joints which are non-compensable in nature) based on screw theory [2] is derived and presented. This technique is already been utilized and verified by G. Wu *et al.* [7] for modelling the error prediction model for 3-PPR configuration. This configuration has a simple model due to its forward kinematics relationship, which is independent of its end-effector orientation. But, in case of 3-PRP configuration, the kinematic relationship is dependent on the end effector orientation. The proposed mathematical error model has incorporated all these changes and used it for the error sensitivity analysis. This errors estimation is done for the xy -plane only, the error z -axis is not derived in this model as manipulator functioning is restricted to xy -plane only. Further, the effects of the non-compensable errors are compared to identify the best configuration among U-shape and Δ -shape fixed base configurations (which one is less susceptible to the non-compensable errors).

2 Kinematic Model of the Manipulator

Here in this section, a generalized kinematic solution for the 3PRP configuration is presented. This kinematic model is established on the basis of screw theory. The kinematic arrangement of the 3PRP configuration is presented in Fig. 1. In Fig. 1, the point T is the position of the end-effector and φ is its orientation angle, the point O represents the origin of the frame of reference, points G_i , P_i , R_i and F_i represent the beginning limit of the linear actuators, the current position of the linear actuators, the point where the passive prismatic joint starts and the point at which the prismatic link connects to the end effector of the i^{th} link, respectively. The vectors \mathbf{i}_i , \mathbf{j}_i , \mathbf{k}_i , \mathbf{l}_i and \mathbf{m}_i are the vectors leading from the fixed reference frame (origin) to the end-effector (moving reference frame). Representation of the each vector for the first kinematic chain (leg) is shown in Fig. 1, and it is similar to the other kinematic chains with corresponding index number. These vectors are characterized by the angles α_i , β_i , γ_i , θ_i , φ and ψ_i , where angles α_i , β_i , γ_i , θ_i and φ are with respect to the origin reference frame while ψ_i is with respect to end-effector's reference frame and $i = 1, 2, 3$, which is the index of the kinematic link chain.

From the closed looped kinematic chain $O - G_i - P_i - R_i - F_i - T - O$

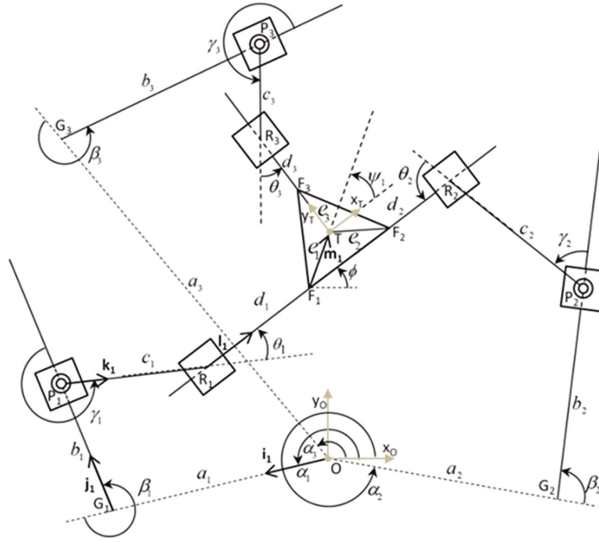


Fig. 1. Generalized kinematic parameter diagram for 3PRP manipulator

Forward kinematics equation for the position vector of the end-effector, \mathbf{T} , is given as:

$$\mathbf{T} = a_i \mathbf{i}_i + b_i \mathbf{j}_i + c_i \mathbf{k}_i + d_i \mathbf{l}_i + e_i \mathbf{m}_i, i = 1, 2, 3 \tag{1}$$

With, $\mathbf{i}_i = [\cos \alpha_i \sin \alpha_i]^T$, $\mathbf{j}_i = [\cos \beta'_i \sin \beta'_i]^T$, $\mathbf{k}_i = [\cos \gamma'_i \sin \gamma'_i]^T$,

$$\mathbf{l}_i = [\cos \theta'_i \sin \theta'_i]^T, \mathbf{m}_i = [\cos(\phi + \psi_i) \sin(\phi + \psi_i)]^T \text{ and}$$

$$\beta'_i = \alpha_i + \beta_i, \gamma'_i = \alpha_i + \beta_i + \gamma_i + \phi, \theta'_i = \alpha_i + \beta_i + \gamma_i + \phi + \theta_i$$

The inverse kinematics solution for the manipulator can be derived from Eq. (1)

$$\begin{aligned} b_i &= (\mathbf{l}_i^T \mathbf{E} \mathbf{j}_i)^{-1} \mathbf{l}_i^T \mathbf{E} (\mathbf{T} - a_i \mathbf{i}_i - c_i \mathbf{k}_i - e_i \mathbf{m}_i) \\ d_i &= (\mathbf{j}_i^T \mathbf{E} \mathbf{l}_i)^{-1} \mathbf{j}_i^T \mathbf{E} (\mathbf{T} - a_i \mathbf{i}_i - c_i \mathbf{k}_i - e_i \mathbf{m}_i) \end{aligned} \tag{2}$$

where, \mathbf{E} is the right angle rotation matrix and defined as: $\mathbf{E} = \begin{bmatrix} 0 & -1 \\ 1 & 0 \end{bmatrix}$

Geometric parameters for the U-shape and Δ -shape fixed base 3-PRP manipulators are given in Tables 1 and 2. The CAD models are presented in Fig. 2.

Table 1. Geometric parameters for the U-shape fixed base 3PRP manipulator

Parameters	α_i (in degrees)	β_i (in degrees)	γ_i (in degrees)	θ_i (in degrees)
$i = 1$	180°	-90°	-90° + ϕ	0°
$i = 2$	0°	+90°	+90° + ϕ	0°
$i = 3$	90°	-90°	-90° + ϕ	0°

Table 2. Geometric parameters for the Δ -shape fixed base 3PRP manipulator

Parameters	α_i (in degrees)	β_i (in degrees)	γ_i (in degrees)	θ_i (in degrees)
$i = 1$	0°	120°	-90° + ϕ	0°
$i = 2$	0°	60°	+90° + ϕ	0°
$i = 3$	90°	-90°	-90° + ϕ	0°

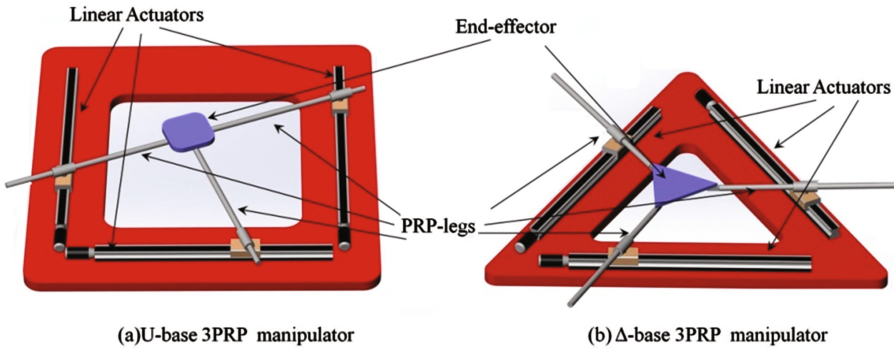


Fig. 2. CAD models of the U-shape and Δ -shape fixed base 3-PRP manipulators

3 Jacobian and Singularities of the Manipulator

Velocity expression can be derived from the Eq. (1) by taking time derivative and eliminating the coefficient of \mathbf{l}_i , as below:

$$\mathbf{A} [\dot{\mathbf{T}} \quad \dot{\phi}]^T = \mathbf{B}\mathbf{b} \tag{3}$$

where, \mathbf{A} and \mathbf{B} are the forward and inverse Jacobian of the manipulators, respectively. These matrices are analytically given as follows:

$$\mathbf{A} = \begin{bmatrix} \mathbf{l}_1^T \mathbf{E}^T & -d_1 - c_1 \mathbf{l}_1^T \mathbf{k}_1 - e_1 \mathbf{l}_1^T \mathbf{m}_1 \\ \mathbf{l}_2^T \mathbf{E}^T & -d_2 - c_2 \mathbf{l}_2^T \mathbf{k}_2 - e_2 \mathbf{l}_2^T \mathbf{m}_2 \\ \mathbf{l}_3^T \mathbf{E}^T & -d_3 - c_1 \mathbf{l}_1^T \mathbf{k}_1 - e_1 \mathbf{l}_2^T \mathbf{m}_2 \end{bmatrix}, \mathbf{B} = \begin{bmatrix} \mathbf{l}_1^T \mathbf{E}^T \mathbf{j}_1 & 0 & 0 \\ 0 & \mathbf{l}_2^T \mathbf{E}^T \mathbf{j}_2 & 0 \\ 0 & 0 & \mathbf{l}_3^T \mathbf{E}^T \mathbf{j}_3 \end{bmatrix}$$

The kinematic Jacobain of the manipulator is given as:

$$\mathbf{J} = \mathbf{A}^{-1}\mathbf{B} \tag{4}$$

where, Matrix \mathbf{A} is never singular while matrix \mathbf{B} is singular only when the angle $\phi = \pm 90^\circ$, which is not possible for the manipulator within workspace, so neither serial nor parallel singularity is present in the manipulator. So this configuration is a singularity-free within its given workspace.

4 Error Modelling

In order to include the effect of joint clearances, the rotary joint the clearance is characterized by using a small distance $\delta\rho_i$ between the points \mathbf{P}_i and \mathbf{P}'_i in the i^{th} link as shown in Fig. 3. To obtain the error for the end effector at point \mathbf{T} Eq. (1) is differentiated to obtain Eq. (5).

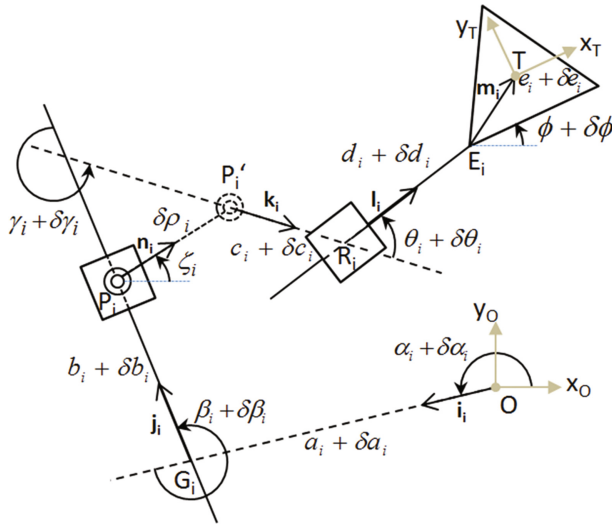


Fig. 3. Error variables in the joint parameters of 3PRP manipulator

$$\delta\mathbf{T} = \delta a_i \mathbf{i}_i + a_i \delta \alpha_i \mathbf{E} \mathbf{i}_i + \delta b_i \mathbf{j}_i + b_i \delta \beta'_i \mathbf{E} \mathbf{j}_i + \delta \rho_i \mathbf{n}_i + \delta c_i \mathbf{k}_i + c_i \delta \gamma'_i \mathbf{E} \mathbf{k}_i + \delta d_i \mathbf{l}_i + d_i \delta \theta'_i \mathbf{E} \mathbf{l}_i + e_i (\delta \phi + \delta \psi_i) \mathbf{E} \mathbf{m}_i, \quad i = 1, 2, 3 \tag{5}$$

$$\begin{aligned} \delta \beta'_i &= \delta \alpha_i + \delta \beta_i \\ \delta \gamma'_i &= \delta \alpha_i + \delta \beta_i + \delta \gamma_i + \delta \phi \\ \delta \theta'_i &= \delta \alpha_i + \delta \beta_i + \delta \gamma_i + \delta \phi + \delta \theta_i \end{aligned} \tag{6}$$

where, $\delta\mathbf{T}$ and $\delta\phi$ are the positioning and orientation error at the end effector.

Other variables namely, δa_i , $\delta \alpha_i$, δb_i , $\delta \beta_i$, δc_i , $\delta \gamma_i$, δd_i , $\delta \theta_i$, δe_i and $\delta \psi_i$ show the variations in the geometric parameters of the link arrangement. Other than these effects, it is also introduced a joint distance which represents the joint clearance of a rotary joint and denoted as $\delta \rho_i$. The associated vector with this distance variable is $\mathbf{n}_i = [\cos \zeta_i \quad \sin \zeta_i]^T$, by substituting the values of Eq. (6) in Eq. (5) and eliminating the variable δd_i , it gives

$$\begin{aligned} \mathbf{l}_i^T \mathbf{E}^T \delta \mathbf{T} = & \delta a_i \mathbf{l}_i^T \mathbf{E}^T \mathbf{i}_i + \delta \alpha_i [\mathbf{l}_i^T (a_i \mathbf{i}_i + b_i \mathbf{j}_i + c_i \mathbf{k}_i) + d_i] + \delta b_i \mathbf{l}_i^T \mathbf{E}^T \mathbf{j}_i \\ & + \delta \beta_i [\mathbf{l}_i^T (b_i \mathbf{j}_i + c_i \mathbf{k}_i) + d_i] + \delta \rho_i \mathbf{l}_i^T \mathbf{E}^T \mathbf{n}_i + \delta c_i \mathbf{l}_i^T \mathbf{E}^T \mathbf{k}_i + \delta \gamma_i (c_i \mathbf{l}_i^T \mathbf{k}_i + d_i) \\ & + d_i \delta \theta_i + \delta \phi (c_i \mathbf{l}_i^T \mathbf{k}_i + d_i + e_i \mathbf{l}_i^T \mathbf{m}_i) + \delta e_i \mathbf{l}_i^T \mathbf{E}^T \mathbf{m}_i + \delta \psi_i e_i \mathbf{l}_i^T \mathbf{m}_i \end{aligned} \quad (7)$$

If substituting the values of $i = 1, 2, 3$ in Eq. (7) and arrange it in vector form as:

$$\begin{aligned} \mathbf{A} \begin{bmatrix} \delta x \\ \delta y \\ \delta \phi \end{bmatrix} = & \mathbf{H}_a \begin{bmatrix} \delta a_1 \\ \delta a_2 \\ \delta a_3 \end{bmatrix} + \mathbf{H}_\alpha \begin{bmatrix} \delta \alpha_1 \\ \delta \alpha_2 \\ \delta \alpha_3 \end{bmatrix} + \mathbf{B} \begin{bmatrix} \delta b_1 \\ \delta b_2 \\ \delta b_3 \end{bmatrix} + \mathbf{H}_\beta \begin{bmatrix} \delta \beta_1 \\ \delta \beta_2 \\ \delta \beta_3 \end{bmatrix} + \mathbf{H}_\rho \begin{bmatrix} \delta \rho_1 \\ \delta \rho_2 \\ \delta \rho_3 \end{bmatrix} \\ & + \mathbf{H}_c \begin{bmatrix} \delta c_1 \\ \delta c_2 \\ \delta c_3 \end{bmatrix} + \mathbf{H}_\gamma \begin{bmatrix} \delta \gamma_1 \\ \delta \gamma_2 \\ \delta \gamma_3 \end{bmatrix} + \mathbf{H}_\theta \begin{bmatrix} \delta \theta_1 \\ \delta \theta_2 \\ \delta \theta_3 \end{bmatrix} + \mathbf{H}_e \begin{bmatrix} \delta e_1 \\ \delta e_2 \\ \delta e_3 \end{bmatrix} + \mathbf{H}_\psi \begin{bmatrix} \delta \psi_1 \\ \delta \psi_2 \\ \delta \psi_3 \end{bmatrix} \end{aligned} \quad (8)$$

By multiplying \mathbf{A}^{-1} on both sides, using Eq. (4) and replacing \mathbf{J}_q with $\mathbf{A}^{-1} \mathbf{H}_q$, where $q \in \{a, \alpha, \beta, \rho, c, \gamma, d, \theta, e, \psi\}$. The error sensitivity equation for the manipulator is given as:

$$\begin{aligned} \begin{bmatrix} \delta x \\ \delta y \\ \delta \phi \end{bmatrix} = & \mathbf{J}_a \begin{bmatrix} \delta a_1 \\ \delta a_2 \\ \delta a_3 \end{bmatrix} + \mathbf{J}_\alpha \begin{bmatrix} \delta \alpha_1 \\ \delta \alpha_2 \\ \delta \alpha_3 \end{bmatrix} + \mathbf{J} \begin{bmatrix} \delta b_1 \\ \delta b_2 \\ \delta b_3 \end{bmatrix} + \mathbf{J}_\beta \begin{bmatrix} \delta \beta_1 \\ \delta \beta_2 \\ \delta \beta_3 \end{bmatrix} + \mathbf{J}_\rho \begin{bmatrix} \delta \rho_1 \\ \delta \rho_2 \\ \delta \rho_3 \end{bmatrix} \\ & + \mathbf{J}_c \begin{bmatrix} \delta c_1 \\ \delta c_2 \\ \delta c_3 \end{bmatrix} + \mathbf{J}_\gamma \begin{bmatrix} \delta \gamma_1 \\ \delta \gamma_2 \\ \delta \gamma_3 \end{bmatrix} + \mathbf{J}_\theta \begin{bmatrix} \delta \theta_1 \\ \delta \theta_2 \\ \delta \theta_3 \end{bmatrix} + \mathbf{J}_e \begin{bmatrix} \delta e_1 \\ \delta e_2 \\ \delta e_3 \end{bmatrix} + \mathbf{J}_\psi \begin{bmatrix} \delta \psi_1 \\ \delta \psi_2 \\ \delta \psi_3 \end{bmatrix} \end{aligned} \quad (9)$$

The coefficients of the error vectors in the above relation are the corresponding sensitivity matrices related to each error variables. These analytical expressions are validated using the virtual prototype with the help of MSC ADAMS software. Further, these relations are used for accuracy and sensitivity analyses in the following section.

5 Error Sensitivity Analysis

Errors due to joint (bearing) clearances and the actuator inaccuracies (least count errors) may cause alteration in the end-effector's pose which cannot be compensated. Other structural parameter errors related to the link lengths and actuator indexing errors can

be compensated by the help of the calibration techniques or parameter identification methods suggested for parallel manipulators. But the error caused due to the presence of clearances, actuator inaccuracies and encoder least count errors are non-compensable by such calibration techniques. Therefore, pose errors are estimated due to the joint clearances, actuator inaccuracies and encoder least count errors using commercially available data for rotary and prismatic joints and, encoder resolution. For the rotary joint, joint clearances are assumed as:

$0 \text{ mm} \leq \delta\rho_i \leq 0.016 \text{ mm}$ and the contact angle ζ_i can vary from 0 to 2π radians, where $\delta\rho_i$ is the center to center distance of the mating bodies of the rotary joints. The error variable $\delta\theta_i$ depends on the joint clearance of the prismatic joint and angular deviation because of that which is $-0.04^\circ \leq \delta\theta_i \leq 0.04^\circ$ and the least count error is taken as half of the least count which cannot be detected by the encoders here taken as $0 \text{ mm} \leq \delta b_i \leq 0.025 \text{ mm}$. The analytical error prediction model is solved simultaneously as an optimization problem using the genetic algorithms. For numerical computation, the Matlab function namely, “*ga*” an in-built genetic algorithms optimization solver is used. The test region for the error sensitivity analysis is considered as a square area of $80 \text{ mm} \times 80 \text{ mm}$ for the given actuator span of 200 mm in all three legs. To compare the effect of the non-compensable errors in U-shape and Δ -shape fixed base parallel configurations the data for joint clearances and encoder resolutions are taken from the industrial product catalogues [7]. Local maximum possible pose errors of the end-effector are obtained through the optimization code for the given workspace region for the constant end-effector orientation. Error contour plots are presented in Figs. 4 and 5.

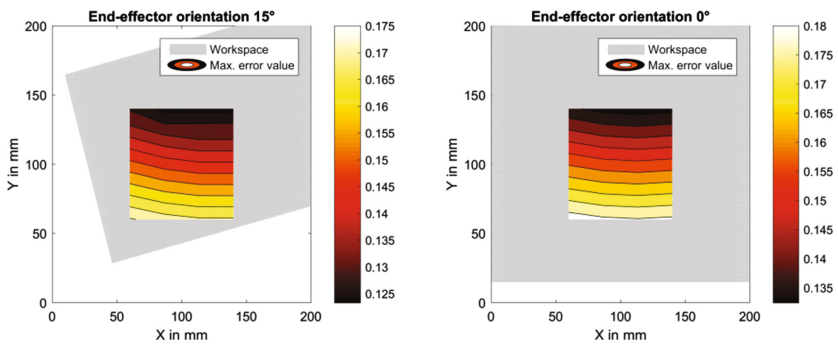


Fig. 4. Non-compensable error contour plots of the U-shape fixed base 3-PRP PPM

The local maximum position errors due to the non-compensable errors in U-shape and Δ -shape fixed base parallel configurations are presented in Figs. 4 and 5, respectively. The result shows that the pose errors due the non-compensable errors for the selected workspace region are varying from $110 \mu\text{m}$ to $150 \mu\text{m}$ for U-shape 3-PRP PPM and $70 \mu\text{m}$ to $95 \mu\text{m}$ for Δ -shape 3-PRP PPM. From the results, it is observed that Δ -shape (symmetric shape) fixed base configuration performs better than U-shape fixed base configurations in presence of non-compensable errors for 3-PRP kinematic arrangement.

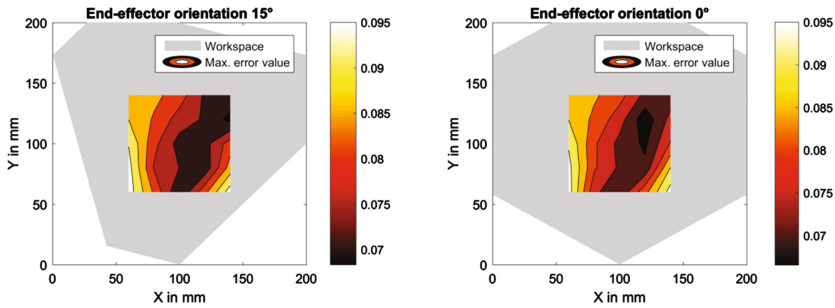


Fig. 5. Non-compensable error contour plots of the Δ -shape fixed base 3-PRP PPM

6 Conclusions

In this paper, an analytical error prediction model for the planar 3-PRP parallel configuration is derived by considering all possible mechanical inaccuracies. Solution for the joint parameter's dependency on the orientation angle of the end-effector is solved and demonstrated. From the results, it is found that the Δ -shape fixed base configuration is less sensitive to the non-compensable errors. These non-compensable errors cannot be compensated by the offline calibration method. But, it can be minimized or compensated by using a task-space motion control strategy in trajectory tracking, which would be considered as a future work.

Acknowledgments. This research was supported and funded in part by the Council of Scientific & Industrial Research (CSIR) India, (22(0698)/15/EMR-II/5767).

References

1. Chablat, D., Staicu, S.: Kinematics of A 3-PRP planar parallel robot. *UPB Sci. Bull. Ser. D Mech. Eng.* **71**, 3–16 (2009)
2. Huang, Z., Li, Q., Ding, H.: *Theory of Parallel Mechanisms*. Springer, Dordrecht (2012)
3. Joubair, A., Slamani, M., Bonev, I.A.: A novel XY-Theta precision table and a geometric procedure for its kinematic calibration. *Robot. Comput. Integr. Manuf.* **28**, 57–65 (2012)
4. Liu, Y., Wu, J., Wang, L., Wang, J.: Parameter identification algorithm of kinematic calibration in parallel manipulators. *Adv. Mech. Eng.* **8**, 1–16 (2016)
5. Singh, Y.: Performance investigations on mechanical design and motion control of planar parallel manipulators, Ph.D. thesis, Indian Institute of Technology Indore (2016)
6. Wijk, V.V., Herder, J.L.: Guidelines for low mass and low inertia dynamic balancing of mechanisms and robotics. In: *Advances in Robotics Research*, pp. 21–30. Springer (2009)
7. Wu, G., Bai, S., Kepler, J.A., Caro, S.: Error modeling and experimental validation of a planar 3-PPR parallel manipulator with joint clearances. *J. Mech. Robot.* **4**, 041008-1–041008-12 (2012)
8. Yu, A., Bonev, I.A., Zsombor-Murray, P.: Geometric approach to the accuracy analysis of a class of 3-DOF planar parallel robot. *Mech. Mach. Theor.* **43**, 364–375 (2008)

Determination of Workspace Volume of Parallel Manipulators Using Monte Carlo Method

Arkadeep Narayan Chaudhury and Ashitava Ghosal^(✉)

Department of Mechanical Engineering, Indian Institute of Science,
Bangalore 560012, Karnataka, India
{arkadeep, asitava}@mecheng.iisc.ernet.in

Abstract. In this paper, we present a Monte Carlo simulation based method to determine the workspace of spatial parallel and hybrid manipulators. The method does not need the solution of the forward kinematics problem which is often difficult for spatial multi-degree-of-freedom parallel and hybrid manipulators. The method uses the solution of the inverse kinematics problem, which is often much simpler. The method can also readily incorporate joint limits and obtain the well-conditioned workspace. The approach is illustrated with a six-degree-of-freedom hybrid parallel manipulator which is a model for a human hand with three fingers. A typical human hand geometry and the range of motion at the joints are incorporated and the inverse kinematics equations for each finger is derived and used to obtain the volume of the hybrid parallel manipulator.

Keywords: Workspace of parallel manipulators · Monte Carlo method · Human hand inspired hybrid parallel manipulator

1 Introduction

The workspace of a parallel or a hybrid manipulator is much more difficult to find in comparison to that of a serial manipulator. In a serial manipulator, the workspace is determined by the geometry of the manipulator, its Denavit-Hartenberg parameters and the limits on the actuated joints. In a parallel or hybrid manipulators, in addition, the ranges of the motion of the passive joints need to be determined by solving the forward kinematics problem – if there are no real solutions to the forward kinematics problem, then the parallel manipulator cannot be assembled for the given actuated joint variables. Additionally, the self collisions of the links of the robot and the singularities which may split the workspace thereby restricting the motion across them increase the complexity of determining the workspace. Merlet [11, 12] summarizes the approaches for determining the workspace of parallel manipulators. These approaches are search based – an estimated region in space is discretized, the inverse kinematics is solved at discrete points to obtain the joint variable and then the joint variables are checked for joint limit constraints. To obtain better resolution, the 3D workspace is discretized finer. One can also obtain the orientation workspace [7, 13] and also obtain

regions where the manipulator Jacobian is not rank deficient [8]. In this work we use a Monte-Carlo based approach to obtain the well-conditioned workspace of a parallel hybrid manipulator. The main advantage of using Monte-Carlo based approach as described later, involves solving only the inverse kinematics problem for a manipulator and various other checks may be accommodated to ensure that the *well-conditioned* workspace is obtained without violating any joint limits. To illustrate the Monte-Carlo method based approach, we use a model of the human hand where the palm, the thumb, the index and the middle finger, grasping an object, is modeled as a hybrid parallel manipulator. There exists several models of multi-fingered human hand (see, for example, Stanford-JPL hand [15], Utah-MIT hand [9], DLR hand [1] and Metahand [2]). In this paper we present a six-degree-of-freedom model of a three-fingered hand, each finger with three degrees of freedom, with two joints actuated in each finger. For the kinematic model we use the anatomical dimensions of a typical human hand from available literature. The joint limit constraints in the fingers are also used in determining the workspace boundary and the volume. The Monte-Carlo based approach also uses the condition number of the Jacobian to determine the well-conditioned workspace. The paper is organized as follows. Section 2 gives a brief overview of the Monte-Carlo method and discusses why it may be useful for obtaining workspaces of manipulators. Section 3 describes the kinematic model of the hybrid parallel manipulator modeling the three-fingered human hand. In Sect. 4 we describe two general results pertaining to the workspace of the manipulator and conclude with Sect. 5 by summarizing the paper and proposing a possible avenue for future extension of the current work.

2 A Review of the Monte Carlo Method

The Monte-Carlo method can be used to evaluate integrals of arbitrary functions (vector or scalar, smooth or non-smooth) over an arbitrary domain [5]. The integral

$$\mathcal{I} = \int_{[0,1]^d} f(\mathbf{x}) \, d\mathbf{x}$$

where $f(\cdot)$ is a bounded real valued function, can be obtained as $\mathbf{E}(f(\mathbf{U}))$ where $\mathbf{E}(\cdot)$ is the expectation of a variable taking a particular probabilistic value, and $\mathbf{U} = [u_1, u_2, \dots, u_d]^T$ a $1 \times d$ vector taking random values of $u_i \in [0, 1] \forall i = 1, 2, \dots, d$. From the strong law of large numbers the average,

$$S_N = \frac{1}{n} \sum_{i=1}^n f(U_i) \tag{1}$$

converges to $\mathbf{E}(f(\mathbf{U}))$ as $n \rightarrow \infty$ with probability 1.0.

We use the Monte Carlo method to obtain the *well-conditioned* and *reachable* workspace of a parallel manipulator, by recognizing that it is an integration problem in \mathbb{R}^d where d is the dimensionality of the joint space of the parallel

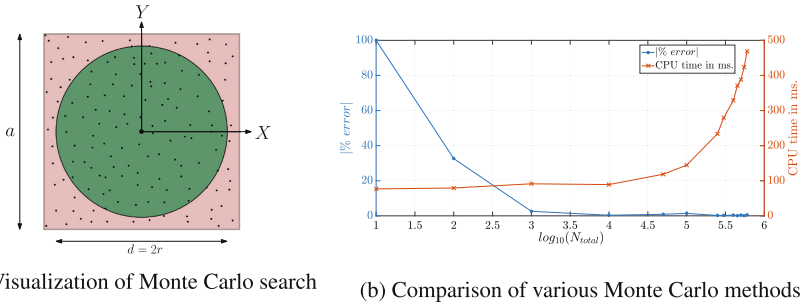


Fig. 1. Demonstration of the Monte Carlo method

manipulator. For this we formulate a function $f(\mathbf{j}) = \begin{cases} 0 \\ 1 \end{cases}$, where $\mathbf{j} = \{\theta_i, \phi_j\}^T$, $\forall i = 1, 2, \dots, n$ actuated joint variables and $\forall j = 1, 2, \dots, m$ passive joint variables and $m + n = d$. At a given position and orientation of a chosen end-effector of the manipulator, the function f assumes either 0 or 1 depending on whether the said position and orientation of the parallel manipulator is well conditioned¹ and inverse kinematics of the manipulator is possible at that position and orientation with all the joint values within permissible joint limits.

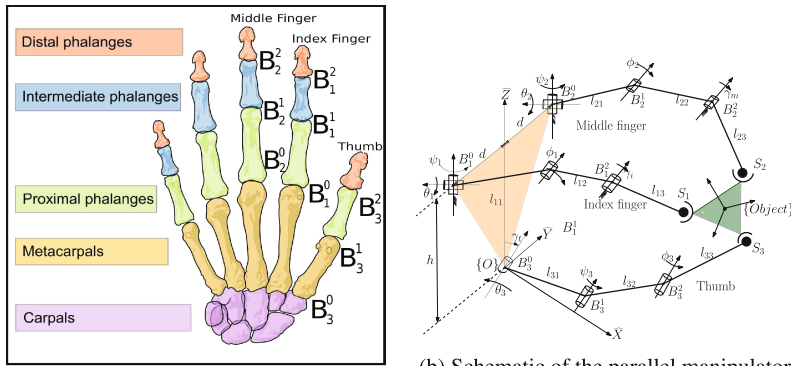
We demonstrate the above by the following example. We assume that the well conditioned reachable workspace of a certain manipulator is a sphere with center at the origin $\{0, 0, 0\}$ and of radius r units. Therefore, the function $f(\mathbf{p})$, $\mathbf{p} = \{x, y, z\}^T$ is used to classify whether a randomly selected point p is in, on or outside the permissible workspace. For this case, the check is very simple being, $f(\mathbf{p}) = \begin{cases} 1 & \forall x^2 + y^2 + z^2 \leq r^2 \\ 0 & \text{otherwise} \end{cases}$. We test the method by fixing $r = 2$ units and searching *uniformly* through a cube of sides $a = 5$ units, centered at the origin. A schematic view of the *workspace* and *search-space* is given in Fig. 1a. An approximation of the probability that a uniformly selected random point lies in or on the workspace is $\frac{N_{in}}{N_{total}}$ where N_{in} is the total number of points in/on the workspace (selected by ensuring $f(\mathbf{p}) = 1$), and N_{total} is the total number of points searched through. Since, by assumption, the points were randomly distributed, the volume of the workspace can be approximated by $V_W = \frac{N_{in}}{N_{total}} \times a^3$. A comparison of Monte Carlo methods with different iteration depths is given in Fig. 1b. We observe that the Monte Carlo method with $N_{total} = 10 \times 5^6 = 156,250$ samples is quite accurate (accuracy is $\geq 99.8\%$) and takes fairly low computation time² of less than 2 s.

¹ We have used a definition of the condition number which encompasses both linear and angular motion of the manipulator at the said position and orientation. The *well conditioned*-ness is ensured by restricting the condition number to be less than 100 at all times.

² The CPU times are for Matlab[®] R2015a running on a Windows 7 PC with an Intel XEON quad core processor at 3.10 GHz and 16 GB of RAM.

3 Description of the Parallel Manipulator

In this section, we first consider an anatomical representation of the human hand (see Fig. 2a) and then present a schematic representation of the proposed manipulator (see Fig. 2b). For the kinematic model, we consider only the thumb, index and middle finger. In Fig. 2a and b, all the joints of interest are labeled. For the index and middle fingers, the labels with a suffix 0, i.e. B_1^0 & B_2^0 represent the *metacarpo-phalangeal joints*, B_3^0 is the trapezium joint between the carpals and metacarpal bone of the thumb. For the index and middle fingers, the joints with suffix one, i.e. B_1^1 & B_2^1 are the joints between the proximal and intermediate phalanges, for the thumb, the joint B_3^1 indicates the joint between the metacarpal and the proximal phalanx bone. Finally, B_1^2 & B_2^2 indicate the joints between the intermediate and distal phalanges, for the thumb, the joint B_3^2 indicates the joint between proximal and distal phalanx of the thumb. The main difference between the proposed model and that of the Salisbury hand (see [15]) is that we are considering the *metacarpo-phalangeal* joint for the index and middle fingers to be a two degree of freedom joint, as opposed to a single revolute joint, as considered by Salisbury and co-workers. The joint was realized by 2 intersecting orthogonal revolute joints. To obtain analytical solutions of the inverse kinematic problems of all the joint values during a given motion of the manipulator, we realize that we can have at most 9 joints with 6 active joints for the targeted 6 degrees of freedom and 3 passive joint, distributed as one passive joint per finger.



(a) Anatomy of human hand {<https://en.wikipedia.org/wiki/Hand>}

(b) Schematic of the parallel manipulator

Fig. 2. Anatomical and schematic representation of the human hand

Kinesiological studies (see the work by Nakamura et al. [14] and the references contained therein for more details) have shown that all the joints in the human finger do not equally participate in the prehensile movements of the human hand. For a given grasping task, the motion is generally started from the proximal joints B_1^0, B_2^0 & B_3^0 and end in the distal joints B_1^2, B_2^2 & B_3^2 , with the proximal joints

being active for most of the time. Therefore, we choose the proximal joints to be actuated and we fix the distal joints of the index and middle fingers B_1^2, B_2^2 and make B_3^2 passive.

Table 1. Joint notations in Fig. 2b and permissible motions

Joint center	Joint variable	Nature	Range of motion/Joint value
B_1^0 and B_2^0	θ_1 and θ_2	Active	0° to 90°
B_3^0	θ_3	Active	-45° to 45°
B_1^1 and B_2^1	ϕ_1 and ϕ_2	Active	0° to 90°
B_3^1	ψ_3	Active	0° to 90°
B_1^0 and B_2^0	ψ_1 and ψ_2	Passive	0° to 15°
B_3^2	ϕ_3	Passive	0° to 90°
B_1^2 and B_2^2	γ_i and γ_m	Fixed	0°
B_3^0	γ_t	Fixed	$\gamma_t = 45^\circ$
S_1, S_2 and S_3	$\{\xi_X^i, \xi_Y^i\} \forall i = 1, 2, 3$	Passive	$\pm 45^\circ$

We conservatively choose the joint limit ranges to be ranging from 0° to 90° . This is somewhat less to that specified by Lin et al. [10], Degeorges and Oberlin [4], and Degeorges et al. [3]. This was done to exclude the joint values greater than 0° and less than 90° , which may be introducing singularities, and increasing the computational time by checking the equivalent condition number for more number of points.

A brief formulation and solution of the inverse kinematics (IK) problem is given in Appendix A. It maybe noted that the inverse kinematics of the manipulator, for the index, middle and thumb, can be solved analytically since the eliminant obtained is a quartic function of the angle ψ_i (see, Ghosal [6]). The solution of the direct kinematics problem requires the solution of a sixteenth degree polynomial.

4 Results: Workspaces of the Manipulator

For simulation we use the following dimensions measured off the right hand of an adult male individual. The dimensions shown in Table 2, along with the abbreviations used correspond to the same in Fig. 2b. For determining the workspace of the manipulator, we have considered 200,000 random points in the Cartesian space bounded by $X \in [0, 80]$ mm, $Y \in [0, 80]$ mm and $Z \in [0, 80]$ mm. At each of these points we have assigned a random configuration of the object, $\Delta S_1 S_2 S_3$ in Fig. 2b and checked the inverse kinematics solution of the manipulator. If the IK problem was solvable by satisfying the joint limits in Table 1, the *equivalent*³ was less than 10^2 and the motions of the S joints were within the prescribed limits, the point is counted and used for the representation as shown in Fig. 3a.

³ Obtained by combining the linear and angular velocity Jacobian matrices by scaling the lengths by $\{l_{11} + l_{12} + l_{13}\}$ as shown in Fig. 2b.

Table 2. Sample finger and hand segment lengths

Hand part	Symbols in Fig. 2b	Values in mm.
Index finger	$\{l_{11}, l_{12}, l_{13}\}$	$\{35.45, 23.92, 17.6\}$
Middle finger	$\{l_{21}, l_{22}, l_{23}\}$	$\{41.33, 22.3, 18.26\}$
Thumb	$\{l_{31}, l_{32}, l_{33}\}$	$\{45.7, 36.23, 20.52\}$
Palm	$\{d, h\}$	$\{15, 68.83\}$

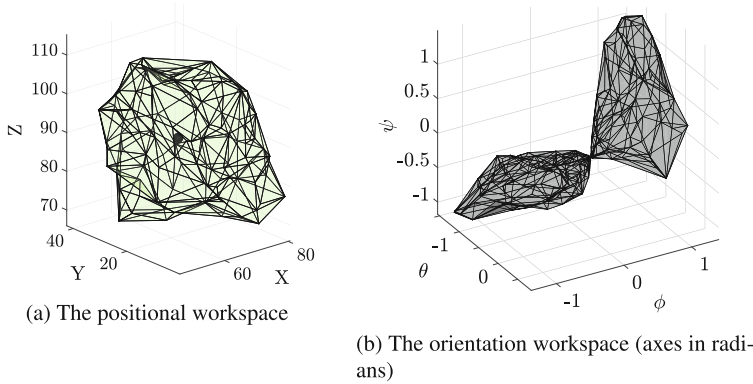


Fig. 3. Position and orientation workspaces of the manipulator

Using the data from Table 2 we obtain the volume of the workspace of the manipulator as $1.4 \times 10^3 \text{ mm}^3$. The orientations workspace, in terms of $X - Y - Z$ Euler angles, at a point (marked by a black dot) is shown in Fig. 3b. The shape and volume of the workspaces shown in Fig. 3 was obtained in less than 50 s. It may be noted that the range of the Euler angles are chosen to be $\pm 90^\circ$. The top part of Fig. 4 shows the workspace of the Salisbury hand ([15]) for the same

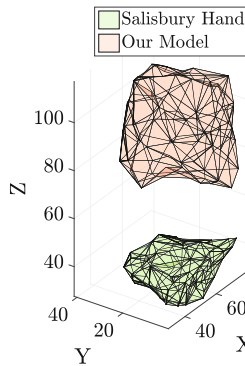


Fig. 4. Comparison of well-conditioned workspaces between the proposed manipulator and the Salisbury hand (see [15])

set of parameters and it can be seen that the *well conditioned* workspace for the proposed manipulator is larger than the workspace of the Salisbury hand.

5 Conclusions

In this paper, we have used the Monte-Carlo method to determine the workspace of a six-degree-of-freedom hybrid-parallel manipulator. The hybrid-parallel manipulator is a model of a three-fingered human hand grasping an object with the contact between the object and the fingers modeled with spherical joint which implies that there is no rolling at the contact. Each finger has two actuated and one passive joint. The dimensions of the link, the geometry and the joint limits of the hybrid-parallel manipulator are derived from a typical human hand. The general shape and measure of the workspace has been obtained using the Monte Carlo method. However, a majority of dexterous manipulation tasks are realized by rolling type of contact between the finger-tips and the object, and we are attempting to extend this approach to include rolling contact between the fingers and the object.

A Appendix I: Solution of the IK Problem of the Proposed Manipulator

For the most general case, the position vector of the point S_1 (see Fig. 2a) is given as the expressions of X, Y and Z below. From the expressions in Eqs. 2, 3 and 4 we obtain $E_1 = X^2 + (Y + d)^2 + (Z - h)^2$ as given in Eq. 5. Using the expressions for E_1 and Z from Eqs. 4 and 5, in Sylvester's dialytic method we can obtain the eliminant for ψ_1 as a quartic function of the angular variable. The value of θ_1 may be obtained by solving the expression for $-X + (Y + d)$ symbolically and the value of ϕ_1 is obtained by using terms from the expressions of Z and E_1 as discussed in [6].

$$X = \frac{1}{2}(l_{11} \cos(\psi_1 - \theta_1) + l_{11} \cos(\psi_1 + \theta_1) + l_{12} \cos(\phi_1 - \psi_1 + \theta_1) + l_{12} \cos(\phi_1 + \psi_1 + \theta_1) + l_{13} \cos(\gamma_i + \phi_1 - \psi_1 + \theta_1) + l_{13} \cos(\gamma_i + \phi_1 + \psi_1 + \theta_1)) \quad (2)$$

$$Y = \frac{1}{2}(l_{11} \sin(\psi_1 + \theta_1) + l_{11} \sin(\psi_1 - \theta_1) + l_{12} \sin(\phi_1 + \psi_1 + \theta_1) - l_{12} \sin(\phi_1 - \psi_1 + \theta_1) + l_{13} \sin(\gamma_i + \phi_1 + \psi_1 + \theta_1) - l_{13} \sin(\gamma_i + \phi_1 - \psi_1 + \theta_1)) - d \quad (3)$$

$$Z = -\sin(\phi_1 + \gamma_i + \theta_1) l_{13} - \sin(\theta_1 + \phi_1) l_{12} - \sin(\theta_1) l_{11} + h \quad (4)$$

$$E_1 = (2 \cos(\gamma_i) l_{11} l_{13} + 2 l_{12} l_{11}) \cos(\phi_1) - 2 l_{13} \sin(\gamma_i) \sin(\phi_1) l_{11} + 2 l_{13} \cos(\gamma_i) l_{12} + l_{11}^2 + l_{12}^2 + l_{13}^2 \quad (5)$$

References

1. Butterfaß, J., Grebenstein, M., Liu, H., Hirzinger, G.: DLR-Hand II: Next generation of a dextrous robot hand. In: 2001 Proceedings of the IEEE International Conference on Robotics and Automation, ICRA 2001, vol. 1, pp. 109–114. IEEE (2001)
2. Dai, J.S., Wang, D., Cui, L.: Orientation and workspace analysis of the multifingered metamorphic hand-metahand. *IEEE Trans. Rob.* **25**(4), 942–947 (2009)
3. Degeorges, R., Laporte, S., Pessis, E., Mitton, D., Goubier, J.N., Lavaste, F.: Rotations of three-joint fingers: a radiological study. *Surg. Radiol. Anat.* **26**(5), 392–398 (2004)
4. Degeorges, R., Oberlin, C.: Measurement of three-joint-finger motions: reality or fancy? A three-dimensional anatomical approach. *Surg. Radiol. Anat.* **25**(2), 105–112 (2003)
5. Dunn, W.L., Shultis, J.K.: *Exploring Monte Carlo Methods*. Elsevier, Amsterdam (2011)
6. Ghosal, A.: *Robotics: Fundamental Concepts and Analysis*. Oxford University Press, Oxford (2006)
7. Gosselin, C.: Determination of the workspace of 6-DOF parallel manipulators. *ASME J. Mech. Des.* **112**(3), 331–336 (1990)
8. Haug, E.: *Workspace analysis of multibody mechanical systems using continuation methods* (1989)
9. Jacobsen, S., Iversen, E., Knutti, D., Johnson, R., Biggers, K.: Design of the Utah/MIT dextrous hand. In: 1986 Proceedings of the IEEE International Conference on Robotics and Automation, vol. 3, pp. 1520–1532. IEEE (1986)
10. Lin, J., Wu, Y., Huang, T.S.: Modeling the constraints of human hand motion. In: 2000 Proceedings of the Workshop on Human Motion, pp. 121–126. IEEE (2000)
11. Merlet, J.P.: Determination of the orientation workspace of parallel manipulators. *J. Intell. Rob. Syst.* **13**(2), 143–160 (1995)
12. Merlet, J.P.: A generic trajectory verifier for the motion planning of parallel robots. *Trans. Am. Soc. Mech. Engg.* **123**(4), 510–515 (2001)
13. Merlet, J.P.: *Parallel Robots*, vol. 74. Springer Science & Business Media, Dordrecht (2012)
14. Nakamura, M., Miyawaki, C., Matsushita, N., Yagi, R., Handa, Y.: Analysis of voluntary finger movements during hand tasks by a motion analyzer. *J. Electromyogr. Kinesiol.* **8**(5), 295–303 (1998)
15. Salisbury, J.K., Craig, J.J.: Articulated hands: force control and kinematic issues. *Int. J. Robot. Res.* **1**(1), 4–17 (1982)

Kinematics of a 6-RUU Parallel Robots with Reconfigurable Platforms

Guanglei Wu^(✉) and Huimin Dong

School of Mechanical Engineering, Dalian University of Technology,
Dalian 116024, China
{gwu,donghm}@dlut.edu.cn

Abstract. This paper presents a HEXA parallel robots with reconfigurable platforms of Schönflies motion and its kinematic study. Four limbs of the robot forms a fully parallel Schönflies-motion robot, with a six-bar linkage to locate the second end-effector. The second end-effector is constrained by a four-bar linkage subject to a prescribed pose of the first end-effector as well as the two remaining limbs. The kinematic issues of the robot, i.e., the inverse geometry, kinematic constraints of the reconfigurable platforms and Jacobian matrices, are studied. Some transmission indices are defined to investigate the robot performance and the reachable workspace for both end-effectors are identified. The isocontours of the transmission indices over the regular workspace are visualized for graphical presentation of the robot's transmission performance.

Keywords: Pick-and-place robot · Schönflies motion · HEXA · Reconfigurable platforms

1 Introduction

High-speed parallel robots with Schönflies motion are dedicated to fast pick-and-place (PnP) operations, serving in the light industries of food handling and electronic board assembly, etc. Amongst this type of robots [3, 7, 10, 14], most of them inherit the architecture from the Adept Quattro robot [1], which has a symmetrical base platform and four identical limbs.

With the increasing requirement on grasping capabilities of this type of robots, a number of fully parallel robots were modified and improved for performance enhancement. For instance, the FANUC M-3iA/6A robot [2] adopts the structure of the translational Delta robot, with three actuators mounted on the ends of the three actuated links to actuate its wrist-mechanism end-effector. To reduce the dynamic inertia, a double Delta robot was proposed by fixing all the actuators [12], towards high acceleration. This design concept was inspired by the approach of coupling two planar parallel translational robots to generate the Schönflies motion [6]. Actuation redundancy was also considered as a way to enhance the acceleration capability of the PnP robots [5] as well as reconfiguration [4]. The previous robots were improved in the kinematic or dynamic

aspects, resulting in one end-effector. To improve the PnP efficiency, a strategy is to make the robot have reconfigurable platforms to install multiple grippers. A 5-dof RRIIRR robot [8], with two translational end-effectors, was developed for electric board assembly, for which the connecting bars of the mobile platforms constitute a six-bar linkage. Sequentially, architectural modifications can be made to the previous reconfigurable platforms to generate an additional rotation around an axis of vertical direction for each end-effector, as the Schönflies motion is more and more popular in material handling.

On the basis of the design of reconfigurable platforms [8], this paper will present a HEXA [9] base 6-RUU parallel robots with reconfigurable platforms of Schönflies motion as shown in Fig. 1(a) and preliminary kinematic study. The displacement group of the mobile platforms is studied. Moreover, the reachable workspace is identified and some transmission indices are defined to investigate the robot's performance, where the isocontours of the transmission indices over the regular workspace are visualized to show the robot's transmission performance.

2 Manipulator Under Study and Displacement Group

The parameterizations of the robot are depicted in Figs. 1(b) and (c). Limbs 1 and 6 are connected by a sub-platform as well as limbs 2 and 3, which behaves similar to the articulated platform of Quattro robot [1], the rotation of the end-effector 1 being realized by their relative movements. Moreover, limbs 4 and 5 are coupled by the end-effector 2 that is located in a six-bar linkage formed by limbs 1, 2, 3 and 6.

The global coordinate frame \mathcal{F}_b is built with the origin located at the geometric center of the base platform, namely, point O , where the x -axis is parallel to the axes of rotation of the first two actuated joints. The moving coordinate frames \mathcal{F}_1 and \mathcal{F}_2 are located at the geometric centers of the two end-effectors, namely, points P_1 and P_2 , where x_1 and x_2 -axes are parallel to the segments C_2C_1 and C_4C_5 , respectively. The angle between \mathbf{u}_i and x -axis is represented by μ_i , $\mu_1 = \mu_2 = 0$, $\mu_3 = \mu_4 = 2\pi/3$, $\mu_5 = \mu_6 = -2\pi/3$. Moreover, unit vectors \mathbf{v}_i and \mathbf{w}_i are parallel to the segments $\overline{A_iB_i}$ and $\overline{B_iC_i}$, respectively, namely, the unit vectors along the active link and parallelogram in the i th limb. Here and after, vectors \mathbf{i} , \mathbf{j} and \mathbf{k} represent the unit vectors of x -, y - and z -axis, respectively. In the following study, the vertical offsets in the platforms are supposed to be zero for convenience, as they do not affect the planar motion of the end-effector.

Figure 2(a) depicts the joint-and-loop graph of the robot, wherein the gray and white boxes represent the actuated and passive joints, respectively. With the Group Theory, the kinematic bond \mathcal{L}_i of the RUU chain in i th limb, as displayed in Fig. 2(b), is the product as below:

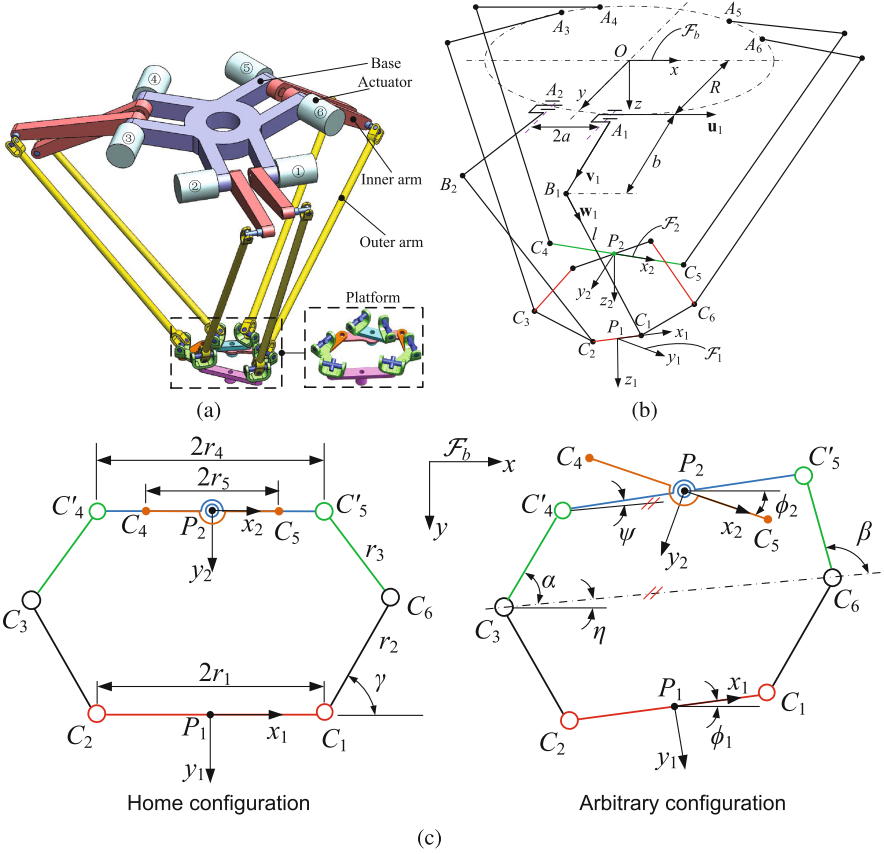


Fig. 1. The 6-RUU robot: (a) CAD model; (b) parameterization; (c) top view of the platform.

$$\mathcal{L}_i = \mathcal{R}(\mathcal{A}_i) \cdot \mathcal{R}(\mathcal{B}_i) \cdot \mathcal{T}(\mathbf{n}_i) \cdot \mathcal{R}(\mathcal{C}_i) = \mathcal{X}(\mathbf{u}_i) \quad (1)$$

and the kinematic bonds of the joint 1st and 6th limbs \mathcal{L}_{16} is

$$\mathcal{L}_{16} = \mathcal{T} \cdot \mathcal{R}(N, \mathbf{k}) = \mathcal{X}(\mathbf{k}) \quad (2)$$

Similarly, the kinematic bonds of the 2nd and 3rd limbs \mathcal{L}_{23} is $\mathcal{X}(\mathbf{k})$. Subsequently, the intersection of the subgroups for platform 1 results in a Schönflies subgroup $\mathcal{X}(\mathbf{k})$, namely, the Schönflies motion.

On the other hand, the kinematic bonds \mathcal{L}_{45} of the closed loop $A_4-B_4-C_4-C_5-B_5-A_5$ is

$$\mathcal{L}_{45} = \mathcal{T} \cdot \mathcal{S}(N) \quad (3)$$

and the subgroups of the coupler in the closed loop six-bar linkage is $\mathcal{X}(\mathbf{k}) \cdot \mathcal{G}(\mathbf{k})$, where $\mathcal{G}(\mathbf{k})$ is the planar motion subgroup. Therefore, the intersection of all the

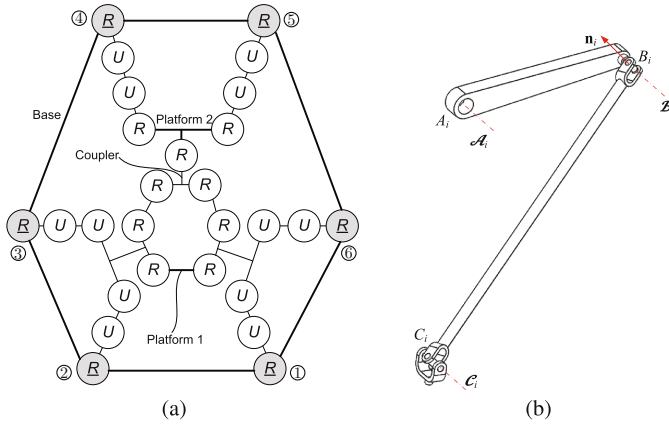


Fig. 2. The loop structure of the robot: (a) joint-and-loop graph; (b) one limb with rotational input.

subgroups for platform 2 leads to $\mathcal{X}(\mathbf{k}) \cdot \mathcal{G}(\mathbf{k}) \cap \mathcal{T} \cdot \mathcal{S}(N) = \mathcal{X}(\mathbf{k})$, meaning that platform 2 performs the Schönflies motion.

3 Kinematic Modeling of the Robot

3.1 Inverse Geometry

The inverse geometry problem of the robot can be readily solved from the following kinematic constraint equation:

$$\|\mathbf{c}_i - \mathbf{b}_i\| - l = 0 \tag{4}$$

To this end, the angular displacement of the i th actuated joint is solved as

$$\theta_i = 2 \tan^{-1} \frac{-I_i \pm \sqrt{I_i^2 + J_i^2 - K_i^2}}{K_i - J_i} \quad \text{where} \quad \begin{cases} I_i = -2bm_{iz} \\ J_i = 2b(m_{ix} \sin \mu_i - m_{iy} \cos \mu_i) \\ K_i = \|\mathbf{m}_i\|^2 + b^2 - l^2 \end{cases} \tag{5}$$

where $\mathbf{m}_i = [m_{ix} \ m_{iy} \ m_{iz}]^T = \mathbf{c}_i - \mathbf{a}_i$, and \mathbf{a}_i and \mathbf{c}_i , respectively, are the Cartesian coordinates of points A_i and C_i in \mathcal{F}_b :

$$\mathbf{a}_i = \mathbf{R}_z(\mu_i)[(-1)^{i+1}\mathbf{a}_i + R\mathbf{j}] \tag{6a}$$

$$\mathbf{c}_i = \begin{cases} \mathbf{p}_1 + (-1)^{i+1}r_1\mathbf{Q}_1\mathbf{i}, & i = 1, 2 \\ \mathbf{p}_1 + (-1)^i r_1\mathbf{Q}_1\mathbf{i} - r_2[(-1)^{i+1} \cos \gamma \ \sin \gamma \ 0]^T, & i = 3, 6 \\ \mathbf{p}_2 + (-1)^{i+1}r_5\mathbf{Q}_i, & i = 4, 5 \end{cases} \tag{6b}$$

and $\mathbf{p}_j = [x_j \ y_j \ z]^T$, $j = 1, 2$, are the Cartesian coordinates of points P_j , i.e., the end-effector position, and $\mathbf{Q}_j = \mathbf{R}_z(\phi_j)$ are the rotation matrices of the end-effectors.

Moreover, the poses of the two end-effectors are kinematically constrained:

$$k_1 + k_2 \cos \beta - k_3 \cos \alpha - \cos \alpha \cos \beta - \sin \alpha \sin \beta = 0 \quad (7a)$$

$$\mathbf{c}_3 + \mathbf{R}_\eta [r_3 \mathbf{R}_z(\alpha) \mathbf{i} + r_4 \mathbf{R}_z(\psi) \mathbf{i}] - \mathbf{p}_2 = 0 \quad (7b)$$

$$\mathbf{c}_6 + \mathbf{R}_\eta [r_3 \mathbf{R}_z(\beta) \mathbf{i} - r_4 \mathbf{R}_z(\psi) \mathbf{i}] - \mathbf{p}_2 = 0 \quad (7c)$$

with

$$\mathbf{R}_\eta = \begin{bmatrix} \cos \eta & \sin \eta & 0 \\ \sin \eta & -\cos \eta & 0 \\ 0 & 0 & 1 \end{bmatrix}, \quad k_1 = \frac{\|\mathbf{c}_6 - \mathbf{c}_3\|^2 + 2r_3^2 - 4r_4^2}{2r_3^2}, \quad k_2 = k_3 = \frac{\|\mathbf{c}_6 - \mathbf{c}_3\|}{r_3} \quad (8)$$

3.2 Kinematic Jacobian Matrix and Transmission Index

Differentiating Eq. (4) with respect to time leads to

$$\mathbf{A} \dot{\boldsymbol{\chi}} = \mathbf{B} \dot{\boldsymbol{\theta}} \quad (9)$$

with

$$\mathbf{A} = [\mathbf{e}_1^T \dots \mathbf{e}_6^T]^T; \quad \dot{\boldsymbol{\chi}} = [\dot{x}_1 \ \dot{y}_1 \ \dot{z} \ \dot{\phi}_1 \ \dot{x}_2 \ \dot{y}_2 \ \dot{\phi}_2]^T \quad (10a)$$

$$\mathbf{B} = \text{diag} [h_1 \ h_2 \ \dots \ h_6]; \quad \dot{\boldsymbol{\theta}} = [\dot{\theta}_1 \ \dot{\theta}_2 \ \dots \ \dot{\theta}_6]^T \quad (10b)$$

where \mathbf{A} and \mathbf{B} are the forward and inverse Jacobian matrices, respectively, and

$$\mathbf{e}_i = \begin{cases} [\mathbf{w}_i^T \ \mathbf{w}_i^T \ \mathbf{s}_i \ 0_{1 \times 3}]^T, & i = 1, 2, 3, 6 \\ [0_{1 \times 2} \ w_{iz} \ 0 \ w_{ix} \ w_{iy} \ \mathbf{w}_i^T \ \mathbf{s}_i]^T, & i = 4, 5 \end{cases}; \quad h_i = b \mathbf{w}_i^T (\mathbf{u}_i \times \mathbf{v}_i) \quad (11)$$

here, $\mathbf{w}_i = [w_{ix} \ w_{iy} \ w_{iz}]^T = (\mathbf{c}_i - \mathbf{b}_i)/l$, $\mathbf{s}_{1(6)} = -\mathbf{s}_{2(3)} = r_1 \mathbf{Q}_1 \mathbf{j}$, $\mathbf{s}_5 = -\mathbf{s}_4 = r_5 \mathbf{Q}_2 \mathbf{j}$.

From Eqs. (10a) and (10b), it is seen that the number of output parameters is not equal to that of input ones, for which the reason lies in the kinematic constraints of the two end-effectors.

For performance evaluation, some transmission indices will be defined, in order to accommodate the dimensional inhomogeneity of the forward Jacobian matrix due to the mixed linear and rotational motions of end-effectors.

From the determinant $|\mathbf{B}|$ of the inverse Jacobian matrix \mathbf{B} below:

$$|\mathbf{B}| = \prod_{i=1}^6 h_i = b^6 \prod_{i=1}^6 \mathbf{w}_i^T (\mathbf{u}_i \times \mathbf{v}_i) \quad (12)$$

the input transmission index λ_i of the i th limb is defined as [13]

$$\lambda_i = |\cos \vartheta_i| = |\mathbf{w}_i^T (\mathbf{u}_i \times \mathbf{v}_i)| \in [0, 1], \quad i = 1, \dots, 6 \quad (13)$$

where ϑ_i is the pressure angle [11] associated with the motion transmission, i.e., the motion transmitted from the actuated link to the parallelogram.

The limbs 1, 2, 3, 6 and the end-effector 1 determines a fully Schönflies-motion robot, for which the input and output twists are mapped by the following equation:

$$\mathbf{A}_1 \dot{\chi}_1 = \mathbf{B}_1 \dot{\theta}_1; \mathbf{A}_1 = \begin{bmatrix} \mathbf{w}_1 & r_1 \mathbf{w}_1^T \mathbf{s}_1 \\ \mathbf{w}_2 & r_1 \mathbf{w}_2^T \mathbf{s}_2 \\ \mathbf{w}_3 & r_1 \mathbf{w}_3^T \mathbf{s}_3 \\ \mathbf{w}_6 & r_1 \mathbf{w}_6^T \mathbf{s}_6 \end{bmatrix}, \dot{\chi}_1 = \begin{bmatrix} \dot{x}_1 \\ \dot{y}_1 \\ \dot{z} \\ \dot{\phi}_1 \end{bmatrix}, \mathbf{B}_1 = \begin{bmatrix} h_1 & & & \\ & h_2 & & \\ & & h_3 & \\ & & & h_6 \end{bmatrix}, \dot{\theta}_1 = \begin{bmatrix} \dot{\theta}_1 \\ \dot{\theta}_2 \\ \dot{\theta}_3 \\ \dot{\theta}_6 \end{bmatrix} \quad (14)$$

With the Laplace expansion, the determinant of the forward Jacobian \mathbf{A}_1 is [13]:

$$|\mathbf{A}_1| = 2r_1(\mathbf{w}_1 \times \mathbf{w}_6) \times (\mathbf{w}_2 \times \mathbf{w}_3) \cdot \mathbf{s}_1 \quad (15)$$

then the output transmission index σ for the end-effector 1 is defined as

$$\sigma = |\cos \omega| = \frac{|(\mathbf{w}_1 \times \mathbf{w}_6) \times (\mathbf{w}_2 \times \mathbf{w}_3) \cdot \mathbf{s}_1|}{\|(\mathbf{w}_1 \times \mathbf{w}_6) \times (\mathbf{w}_2 \times \mathbf{w}_3)\|} \in [0, 1] \quad (16)$$

where ω is the pressure angle amongst limbs, namely, the force transmitted from the end-effector to the passive parallelograms in the other limbs, provided that the actuated joints in these limbs are locked.

Moreover, the output transmission index for limbs 4 and 5 are defined by [14]

$$\xi_k = \frac{|\hat{\mathbf{S}}_{Ok} \circ \hat{\mathbf{S}}_{Tk}|}{|\hat{\mathbf{S}}_{Ok} \circ \hat{\mathbf{S}}_{Tk}|_{\max}} \in [0, 1]; \quad \hat{\mathbf{S}}_{Ok} = \begin{bmatrix} \mathbf{k} \\ r_5 \mathbf{Q}_2 \mathbf{i} \end{bmatrix}, \hat{\mathbf{S}}_{Tk} = \begin{bmatrix} \mathbf{w}_k \\ b \mathbf{v}_k \times \mathbf{w}_k \end{bmatrix}, k = 4, 5 \quad (17)$$

where $\hat{\mathbf{S}}_{Ok}$ and $\hat{\mathbf{S}}_{Tk}$ are the unit output twist screw (OTS) and transmission wrench screw (TWS) of the i th limb, respectively.

The larger value of the indices defined in Eqs. (13), (16) and (17) indicates better transmission quality and while index value 0 means singular configuration.

4 Workspace and Transmission Analysis of the Robot

The workspace of the robot under study can be obtained from Eqs. (4) and (5), either by CAD approach or numerical searching method. Here, the numerical searching method is adopted, where the geometric parameters are given in mm: $R = 200$, $a = 60$, $b = 260$, $l = 550$, $r_1 = r_2 = r_3 = r_4 = r_5 = 60$.

With a prescribed position of point P_1 , the maximum reachable positions of the end-effector 2, namely, point P_2 , are displayed in Fig. 3(a). The reachable workspace of the end-effector 1 (green) and the end-effector 2 (red) of the mobile platforms with a constant orientation $\phi_1 = \phi_2 = 0$ are shown in Fig. 3(b) together with a fitted regular common workspace for the two end-effectors.

Figure 4 shows the transmission indices defined in previous section over the regular workspace with constant orientations. From these figures, it can be seen that the input transmission indices are larger than 0.2, which are relatively larger than the output transmission indices of both end-effectors. The output transmission indices of end-effector 1 which are close to 0 appear in the workspace boundaries, while some smaller indices ξ of end-effector 2 occurs inside the workspace,

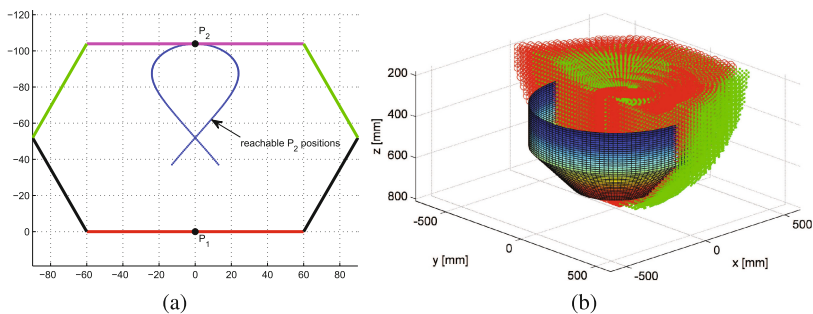


Fig. 3. The workspace of the robot with $\phi_1 = \phi_2 = 0$: (a) possible positions of end-effector 2 relative to end-effector 1; (b) reachable workspace of both end-effectors. (Color figure online)

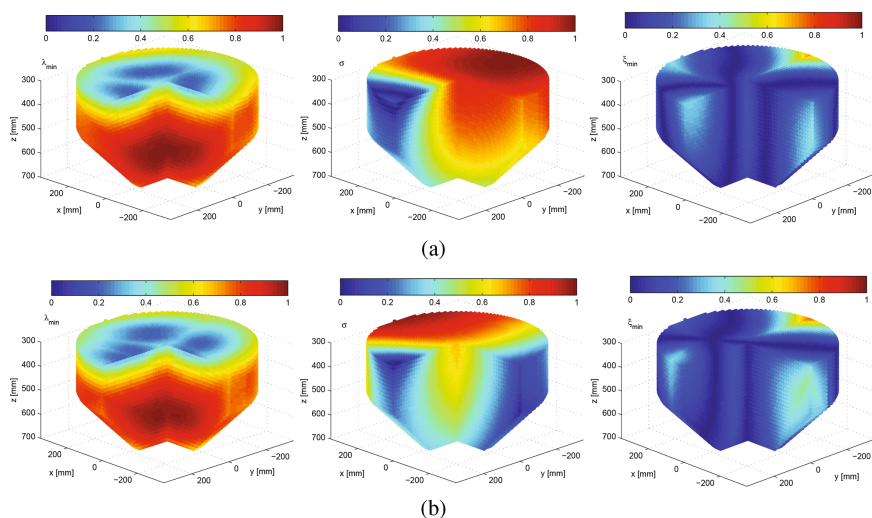


Fig. 4. Transmission indices of the robot over the regular workspace with constant orientations: (a) $\phi_1 = \phi_2 = 0$; (b) $\phi_1 = -\phi_2 = \pi/4$.

showing that the transmission quality for end-effector 1 are better than end-effector 2 in most region of the workspace. This means that the end-effector 2 will encounter parallel singularities inside the workspace, thus, the motors of the robot needs to be arranged for singularity-free design. Another observation is that the robot can have better transmission with Cartesian coordinates of $y \leq 0$. Moreover, the first end-effector admits a relatively larger operational workspace with transmission indices larger than $LTI \geq 0.7$ for high transmission quality.

5 Conclusions

This paper presents a HEXA parallel robots with reconfigurable platforms, of which both end-effectors perform Schönflies motions. Four limbs of the robot constitute a fully parallel Schönflies-motion robot and the second end-effector is kinematically constrained by the former. The Jacobian matrices are derived to define the transmission indices and the corresponding isocontours are plotted to show the transmission quality of the translational workspace with rotational capability $\pm 45^\circ$. The first end-effector is almost free of singularity within the identified regular workspace, while the second one will encounter parallel singularities inside the workspace. In the future, singularity-free design will be conducted.

Acknowledgements. The reported work is supported by the Fundamental Research Funds for the Central Universities under grant No. DUT16RC(3)068.

References

1. Adept Quattro Parallel Robots. <http://www1.adept.com/main/ke/data/Archived/Quattro/sQuattro.UG.pdf>
2. M-3i A Delta robot. <http://www.fanuc.eu/se/en/robots/robot-filter-page/m3-series/m-3ia-6a>
3. Altuzarra, O., Şandru, B., Pinto, C., Petuya, V.: A symmetric parallel Schönflies-motion manipulator for pick-and-place operations. *Robotica* **29**, 853–862 (2011)
4. Balmaceda-Santamaría, A., Castillo-Castaneda, E., Gallardo-Alvarado, J.: A novel reconfiguration strategy of a Delta-type parallel manipulator. *Int. J. Adv. Robot. Syst.* **13**, 1 (2016)
5. Corbel, D., Gouttefarde, M., Company, O., Pierrot, F.: Actuation redundancy as a way to improve the acceleration capabilities of 3 T and 3T1R pick-and-place parallel manipulators. *ASME J. Mech. Robot.* **2**(4), 041002 (2010)
6. Gosselin, C., Isaksson, M., Marlow, K., Laliberté, T.: Workspace and sensitivity analysis of a novel nonredundant parallel SCARA robot featuring infinite tool rotation. *IEEE Robot. Autom. Lett.* **1**(2), 776–783 (2016)
7. Krut, S., Nabat, V., Company, O., Pierrot, F.: A high-speed parallel robot for SCARA motions. In: *International Conference on Robotics Automation*, vol. 4, pp. 4109–4115 (2004)
8. Lambert, P.: Parallel robots with configurable platforms. Ph.D. thesis, Delft University of Technology (2013)
9. Pierrot, F., Dauchez, P., Fournier, A.: HEXA: a fast six-dof fully-parallel robot. In: *Fifth International Conference on Advanced Robotics*, pp. 1158–1163 (1991)
10. Pierrot, F., Nabat, V., Company, O., Krut, S., Poignet, P.: Optimal design of a 4-dof parallel manipulator: From academia to industry. *IEEE Trans. Robot.* **25**(2), 213–224 (2009)
11. Takeda, Y., Funabashi, H.: A transmission index for in-parallel wire-driven mechanisms. *JSME Inter. J. Series C Mech. Syst. Mach. Elem. Manuf.* **44**(1), 180–187 (2001)
12. Wu, G.: Conceptual design and analysis of a 6-axis double Delta robot towards high acceleration. In: *Proceedings of ASIAN MMS 2016 & CCMMS 2016*, pp. 389–401 (2016)

13. Wu, G.: Kinematic analysis and optimal design of a wall-mounted four-limb parallel Schönflies-motion robot for pick-and-place operations. *J. Intell. Robot. Syst.* **85**, 663–667 (2016)
14. Wu, G., Bai, S., Hjørnet, P.: Architecture optimization of a parallel schönflies-motion robot for pick-and-place applications in a predefined workspace. *Mech. Mach. Theory* **106**, 148–165 (2016)

On the Motion/Force Transmissibility and Constrainability of Delta Parallel Robots

Jan Brinker¹(✉), Burkhard Corves¹, and Yukio Takeda²

¹ Department of Mechanism Theory and Dynamics of Machines,
RWTH Aachen University, Aachen, Germany

brinker@igm.rwth-aachen.de

² Department of Mechanical Engineering,
Tokyo Institute of Technology, Tokyo, Japan

takeda@mech.titech.ac.jp

Abstract. The motion and force transmission is highly important for the analysis and design of parallel manipulators. Recent advances in research have led to generally applicable formulations for transmission indices based on the notion of power coefficient. Analyses of limited-dof parallel manipulators however require separate consideration of constraint characteristics. Conversely, the design parameters of parallel manipulators are highly coupled. Thus, such separation may distort the performance evaluation and optimization of parallel manipulators. In this context, indices based on pressure angles of fully parallel manipulators are revisited and applied to the performance evaluation of the Delta robot, one of the lower-dof parallel robots. The resulting index is physically appropriate and allows for simultaneous assessment of both, the motion and force transmission and the constraint characteristics.

Keywords: Transmission indices · Pressure angle · Power coefficient · Constraint singularity · Delta parallel robot

1 Introduction

The geometries of parallel manipulators can be optimized such that specified workspace requirements are met. Manipulators that were optimized by workspace and occupied space requirements only may however suffer from poor kinematic and dynamic characteristics. Thus, kinematic and dynamic performance measures are commonly taken into account for the optimization of manipulators. The main kinematic concepts for performance measurement are the concepts of condition number, manipulability, and motion/force transmissibility and constrainability [1].

Both measures, the condition number as well as the manipulability, are based on the characteristics of the Jacobian. The condition number [2] is a local measure of the Jacobian-induced distortion of the motion and force transmission from the active joint to the end-effector space. The product of the singular values of the Jacobian matrix corresponds to the volume of the so-called manipulability ellipsoid [3]. However, information on the directionality get lost. In addition, for translational and rotational dof of the moving platform, the Jacobian matrix contains inhomogeneous units and

further modification, e.g. normalization or separate analyses of position and orientation [4], is required. Moreover, for limited-dof manipulators the input-output Jacobian may not be sufficient to predict all possible singularities [5]. Finally, Jacobian-based indices are frame-dependent. As a result, the values of the indices vary with the choice of coordinates [6]. To overcome the aforementioned problems, the performance of parallel manipulators can alternatively be assessed analyzing the quality of transmissibility and constrainability.

Analyses of transmissibility date back to Alt [7] proposing the transmission angle in planar mechanisms. Following the theory of screws [8], the first transmission indices of spatial manipulators were proposed by Yuan et al. [9] using the virtual coefficient between the transmission wrench screw (TWS) and the output twist screws (OTS). Sutherland and Roth [10] normalized the initial approach. Shimojima et al. [11] proposed a unique definition of TWS, which is dependent on the output link's load condition. Further generalizations were proposed by Tsai and Lee [12] taking into account a generalized transmission wrench screw (GTWS) and the related virtual coefficients to the input and output screw. Later Chen and Angeles [13] proposed the generalized transmission index (GTI). The three approaches can be distinguished by the different definitions of the maximum value of the virtual coefficient (as used for normalization).

Takeda and Funabashi [14] proposed a transmission index (TI) taking into account the virtual power transmitted from the input links to the output link. In their approach, single-dof mechanisms are generated by fixing all input links except one and analyzed in respect of the resulting pressure angles at the connection between input and output link. The approach is only feasible for TWS with a zero pitch (i.e. a transmission force line) and thus represents a special case of the GTI. In other words, in order to define the pressure angle in a simple definition, the TWS can be represented at a (spherical) joint where no moment is applied as constraint. This approach was extended to cable driven parallel mechanism [15] and spherical parallel mechanism [16]. Briot et al. [17] investigated the determination of the maximum reachable workspace of planar parallel manipulators based on the transmission angle and the position of the instantaneous center of rotation.

Based on the concept of virtual coefficient and following Takeda's approach of fixing all inputs except one, Wang et al. [18] proposed a general procedure for non-redundant spatial parallel manipulators including new transmission indices based on the input transmission index (ITI) and output transmission index (OTI), where the normalized virtual coefficient is called power coefficient. Additionally, the minimum of all indices are defined as local transmission index (LTI). The concept was extended for redundant and/or overconstrained parallel manipulators [6, 19]. Further indices are e.g. the global transmission index (GTI) ensuring good performance throughout the entire workspace of a manipulator and the good-transmission workspace (GTW) defined by a minimum value for the LTI [20]. In fact, the proposed indices are able to detect a manipulator's closeness to actuation (transmission) singularities, but cannot be applied to measure the closeness to constraint singularities [21, 22]. Thus, constraint transmission indices (CTI) were developed as shown in [21, 23] and further refined and discussed extensively in [24]. At the same time, Liu et al. [25] proposed a novel approach for the derivation of the maximum value of the virtual coefficient.

In the present paper, transmission indices based on the approaches of both the pressure angles and the power coefficient for the Delta robot, one of the lower-dof parallel robots, are formulated. Assessments are given to support the kinematic design of the Delta robot with high transmission and constraint capability.

2 Transmissibility of Delta Parallel Robots

The Delta robot is one of the best known and most widely spread parallel robots in academia and industry [26]. The output link or moving platform of the Delta robot is restricted to purely translational dof. Usually, the architecture is represented by three symmetric kinematic chains of the type $\underline{R}(SS)_2$. Accordingly, the parallelogram contains four spherical joints and four links pairwise of the same length. With this, the connecting rods only need to transmit axial forces allowing for light-weight design. Figure 1 shows the schematic representation of the Delta robot and the related kinematic relations. The vector $r_{F,i}$ denotes the position of the revolute joint of the i -th kinematic chain on a circle with radius r_F . Similarly, the attachment point of the parallelogram on the output link is denoted by $r_{P,i}$. The distance D_s between the spherical joints is the same for all joint pairs. The vectors $l_{PL,i}$ and $l_{DL,i}$ point along the i -th proximal and distal links, respectively. The workspace prescribed for the following analyses is represented by a cylindrical base (with radius D_1 and height Z_1) and a conical portion (with radius D_2 and height Z_2) adjacent to it. The centre of their connecting surface determines the relative position $P_0 = [0, 0, Z_0]$ of the workspace to the origin of frame O. Table 1 summarizes the related parameters. The fundamentals are presumed to be known.

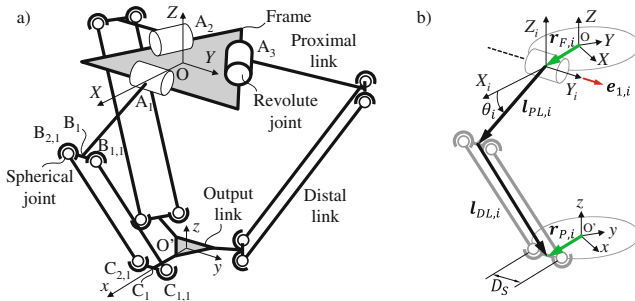


Fig. 1. Schematic representation and definition of kinematic parameters

Table 1. Parameters: delta robot and prescribed workspace

Parameter	$r_{F,i}$	$r_{P,i}$	D_s	$l_{PL,i}$	$l_{DL,i}$	D_1	D_2	Z_1	Z_2	Z_0
Value [m]	0.20	0.05	0.10	0.40	0.80	1.00	0.80	0.25	0.05	-0.80

2.1 Transmission Indices Based on Pressure Angles

The two connecting rods j within a chain i solely transmit axial forces denoted by the unit vector $\hat{\mathbf{f}}_{j,i}$. Hence, the direction of these forces is given by the vector $\mathbf{l}_{DL,i}$ (Fig. 1b). The angle between the velocity $\mathbf{v}_{B,i}$ of the spherical joint $B_{j,i}$ and the direction of the force transmitted to the output link along the distal link can be interpreted as pressure angle γ_i of the input transmission. Its cosine value is thus

$$\lambda_{i,PA} = \cos(\gamma_i) = \mathbf{v}_{B,i}^T \hat{\mathbf{f}}_{j,i} / \|\mathbf{v}_{B,i}\| \quad (1)$$

Accordingly, the best transmission occurs when the directions of velocity and force coincides. The input transmission index ITI is given as the minimum of the absolute pressure angles' cosine among all three kinematic chains, i.e.

$$ITI = \min(|\lambda_{i,PA}|) \forall i = \{1, 2, 3\} \quad (2)$$

In respect of the output transmission, a transmission wrench screw (TWS) can be introduced at each of the six spherical joints $C_{j,i}$ where no moment is applied as constraint [14, 27]. With this a simple definition of an output-related pressure angle is obtained. The TWS of rod (j, i) with respect to $C_{k,m}$ are then given by

$$\hat{\mathcal{S}}_{TWS,j,i} = \begin{bmatrix} \hat{\mathbf{f}}_{j,i} \\ (\mathbf{r}_{P,j,i} - \mathbf{r}_{P,k,m}) \times \hat{\mathbf{f}}_{j,i} \end{bmatrix} \quad (3)$$

Imagine the virtual motion of a single-dof mechanism by removing one of the six connecting rods k of a chain m (Fig. 2b, $k = 1$) [14]. The instantaneous motion of the output link is the given by

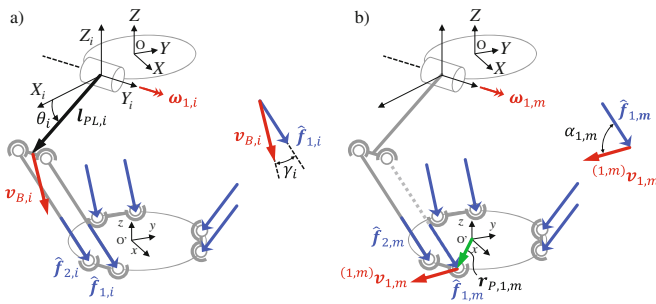


Fig. 2. Pressure angles of input and output transmission (with six supporting links)

$${}^{(k,m)}\mathcal{S}_{OTS} = \begin{bmatrix} {}^{(k,m)}\boldsymbol{\omega} \\ {}^{(k,m)}\mathbf{v}_{j,i} \end{bmatrix} \quad (4)$$

with ${}^{(k,m)}\boldsymbol{\omega}$ as angular velocity and ${}^{(k,m)}\mathbf{v}_{j,i}$ as translational velocity at joint $C_{j,i}$ of the output link. Among $\hat{\$}_{TWS,j,i}$, all except $\hat{\$}_{TWS,k,m}$ are constraint wrenches applying no work to the output link [18]. Then, the virtual power can be derived as

$$\delta W_{j,i} = \hat{\$}_{TWS,j,i} \circ {}^{(k,m)}\$_{OTS} = \$_{TWS,j,i} \circ \begin{bmatrix} {}^{(k,m)}\boldsymbol{\omega} \\ {}^{(k,m)}\mathbf{v}_{j,i} \end{bmatrix} = 0 \quad (5)$$

where one entry of ${}^{(k,m)}\$_{OTS}$ can be chosen arbitrarily. Finally, the instantaneous velocity ${}^{(k,m)}\mathbf{v}_{j,i}$ at joint $C_{k,m}$ can be extracted to compute the pressure angle $\alpha_{k,m}$ of the output transmission. The angle can be physically interpreted as pressure angle at the respective connection point to the output link (Fig. 2b). Its cosine value is given by

$$\eta_{k,m,PA} = \cos(\alpha_{k,m}) = \frac{{}^{(k,m)}\mathbf{v}_{k,m}^T \hat{\mathbf{f}}_{k,m}}{\|{}^{(k,m)}\mathbf{v}_{k,m}\|} \quad (6)$$

The output transmission index can then be derived as

$$OTI_{PA,6} = \min(|\eta_{k,m,PA}|) \forall m = \{1, 2, 3\}, \forall k = \{1, 2\} \quad (7)$$

2.2 Transmission Indices Based on Power Coefficients

Alternative approaches are based on the notion of power coefficient. In general, the orthogonal product of a wrench and twist screw ($\$_{WS}$ and $\$_{TS}$) related to a body is called virtual coefficient and can be interpreted as instantaneous power caused by the wrench acting on the moving body [24]. The higher the virtual coefficient, the better is the kinematic performance or the less wrench is required to transmit power [25]. The power coefficient is the normalized virtual coefficient

$$\rho = \left| \hat{\$}_{WS} \circ \hat{\$}_{TS} \right| / \left| \hat{\$}_{WS} \circ \hat{\$}_{TS} \right|_{max} \quad (8)$$

Following this definition, the input transmission index corresponds to Eq. (1).

For the output transmission index, the unit output twist screw (OTS) is related to the TWS. The general derivation in [25], and in particular the derivation of the maximum characteristic length, can be simplified for the Delta robot. The axis of the TWS passes through the spherical joint for any configuration. More importantly, presuming that the output link performs translational motion only, the angular velocity of the OTS is set to zero (disregarding potential constraint singularities). Then, for infinite pitch screws (pure translation), the maximum virtual coefficient is simply given by the maximum value of the dot product of the wrench and twist axes, which is one in this case [13].

Delta-related analyses of the output transmission based on power coefficients can, for example, be found for the four-legged 4-dof-variants X4 [28] and Ragnar robot [29]. Presuming three supporting links and translational motion of the output only, the system of Eq. (5) can be solved releasing one input link while blocking the other two. For instance, if the first chain is removed the output link might move in the direction

$$\mathbb{S}_{OTS,1} = \begin{bmatrix} \mathbf{0}_3 \\ \mathbf{v}_1 \end{bmatrix} = \begin{bmatrix} \mathbf{0}_3 \\ \hat{\mathbf{f}}_3 \times \hat{\mathbf{f}}_2 / \|\hat{\mathbf{f}}_3 \times \hat{\mathbf{f}}_2\| \end{bmatrix} \quad (9)$$

Then, an alternative formulation for the output transmission index is given as

$$\eta_{1,PC,3} = |\mathbb{S}_{TWS,1} \circ \mathbb{S}_{OTS,1}| = \left| \hat{\mathbf{f}}_1^T (\hat{\mathbf{f}}_3 \times \hat{\mathbf{f}}_2) \right| / \|\hat{\mathbf{f}}_3 \times \hat{\mathbf{f}}_2\| \quad (10)$$

which, since the maximum virtual coefficient is one, corresponds to the orthogonal product of wrench and twist screw. The same applies for the second and third chain. As mentioned before, the orientation of the output link cannot be kept constant if one complete chain is removed since one constraint moment is removed as well. Compared to the *OTI* taking into account all six supporting links, cf. Eq. (3), Eq. (10) disregards the constraint moment and thus prevents a physically appropriate definition as pressure angle. Still, in recent Delta-related studies (e.g. [21, 30, 31]) the index is introduced as pressure angle among the three supporting links where three unit forces $\hat{\mathbf{f}}_i$ apply to the output link from the three chains. Then, for the 3-dof variant, the absolute value of the cosine of the pressure angle among the links corresponds to Eq. (10). Inevitably, the constraint singularities must be tackled separately using constraint transmission indices as shown in [23].

3 Results and Discussion

The transmission characteristics are analyzed based on the parameters as shown in Table 1. The input transmission characteristics (*ITI*) are unequivocal, whereas two distinct approaches are found for the output transmission. These are (A1) based on physically appropriate pressure angles of six supporting links covering constraint singularities ($OTI_{PA,6}$) and (A2) based on the power coefficient presuming translational (virtual) motion of the output link with three supporting links ($OTI_{PC,3}$). Figure 3a) displays the distributions of *ITI* for the symmetry planes of the prescribed workspace and the $Z = Z_0$ -plane. Figure 3b) shows the distribution of the *OTI* for $Z = -0.24$ and unrestricted swing angles. Regions where *OTI* become less than 0.1 are highlighted in red. Here, based on the relationship between the output pose error and the transmission index (*TI*) for the 6-SPS mechanism in [32], the threshold value to identify the neighborhoods of singularity is set to 0.1.

For (A1), the $OTI_{PA,6}$ are close to zero in neighborhoods where actuation (dashed line) or constraint (dotted line) singularities occur. Accordingly, (A2) fails to detect the internal (constraint) singularities. However, minimal values ($OTI_{PC,3} \leq 0.1$) correspond to singular point-curves of actuation. Thus, for thorough analyses with (A2) separate investigations of constraint transmission indices are unavoidable. Then, the same singular point-curves can be obtained as for $OTI_{PA,6}$. Nonetheless, in contrast to $OTI_{PA,6}$, the definition of *OTI* and *CTI* is based on virtual situations which are not physically appropriate. For instance, for the *CTI*, the relation between the constraint wrench moment and the (virtual) rotational motion of the output link is evaluated. In practice, such situation does not exist. Moreover, difficulties may arise for the determination of a

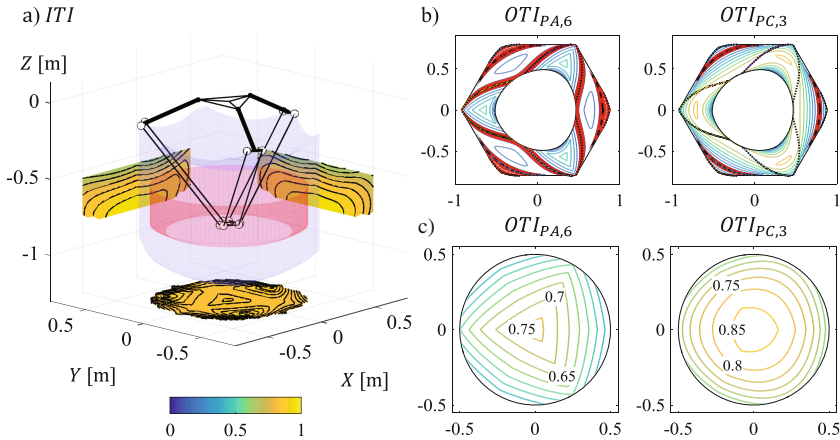


Fig. 3. Distribution of the input and two alternative output transmission indices

unique index, which may be the minimum or the product of OTI and CTI including weightings. Accordingly, the distributions of the OTI on the $Z = Z_0$ -plane within the prescribed workspace are different (Fig. 3c). In summary, (A1) seems to be the most appropriate approach for the analyses and understanding of the motion/force transmissibility and constrainability of Delta parallel robots.

4 Conclusions

This study demonstrated different approaches to assess the transmission and constraint capabilities of Delta robots. Recent advances based on the power coefficient can be used for the analyses with three supporting legs. However, for lower-dof parallel manipulators, constraint characteristics must be assessed together with actuation (output transmission) characteristics. Therefore, an alternative approach based on pressure angles is introduced. The resulting index is physically meaningful and simultaneously takes into account actuation as well as constraint characteristics. Moreover, using this index, the distance between the spherical joints in a parallelogram of the distal links can be considered as an additional design parameter in future kinematic optimization of Delta parallel robots. Future work includes the generalization of the proposed approach based on the pressure angles for the evaluation of the transmission and constraint characteristics of lower-dof parallel robots.

Acknowledgments. This work is supported by the German Academic Exchange Service (DAAD) with funds from the Federal Foreign Office (FFO).

References

1. Angeles, J.: Fundamentals of robotic mechanical systems. Springer (2014)
2. Gosselin, C., Angeles, J.: The optimum kinematic design of a planar three-degree-of-freedom parallel manipulator. *J. Mech. Trans. Autom. Des.* **110**(1) (1988)
3. Yoshikawa, T.: Manipulability of robotic mechanisms. *Int. J. Robot. Res.* **4**(2), 3–9 (1985)
4. Cardou, P., et al.: Kinematic-sensitivity indices for dimensionally nonhomogeneous Jacobian matrices. *IEEE Trans. Robot.* **26**(1), 166–173 (2010)
5. Joshi, S.A., Tsai, L.-W.: Jacobian analysis of limited-DOF parallel manipulators. *J. Mech. Des.* **124**(2), 254–258 (2002)
6. Xie, F., et al.: Performance evaluation of redundant parallel manipulators assimilating motion/force transmissibility. *Int. J. Adv. Robot. Sys.* **8**(5), 113–124 (2011)
7. Alt, H.: Der Übertragungswinkel und seine Bedeutung für das Konstruieren periodischer Getriebe. *Werkstatttechnik* **26**, 61–64 (1932)
8. Ball, R.S.: A treatise on the theory of screws (1900)
9. Yuan, M.S.C., et al.: Kinematic analysis of spatial mechanism by means of screw coordinates. Part 2 – analysis of spatial mechanisms. *J. Eng. Ind.* **91**(1), 67–73 (1971)
10. Sutherland, G., Roth, B.: A transmission index for spatial mechanisms. *J. Eng. Ind.* **95**(2), 589–597 (1973)
11. Shimojima, H., et al.: A transmissibility for single-loop spatial mechanism. *Bull. JSME* **22** (165), 405–411 (1997)
12. Tsai, M.J., Lee, H.W.: The transmissivity and manipulability of spatial mechanisms. *J. Mech. Des.* **116**, 137–143 (1994)
13. Chen, C., Angeles, J.: Generalized transmission index and transmission quality for spatial linkages. *Mech. Mach. T.* **42**, 1225–1237 (2007)
14. Takeda, Y., Funabashi, H.: Motion transmissibility of in-parallel actuated manipulators. *JSME Int. J. Series C* **38**(4), 749–755 (1995)
15. Takeda, Y., Funabashi, H.: A transmission index for in-parallel wire-driven mechanisms. *JSME Int. J. Series C* **44**(1), 180–187 (2001)
16. Takeda, Y., et al.: Development of a spherical in-parallel actuated mechanism with three DoF with large working space and high motion transmissibility. *JSME Int. J. Series C* **39**(3), 541–548 (1996)
17. Briot, S., et al.: Investigation of the effort transmission in planar parallel manipulators. *J. Mech. Robot.* **7** (2013)
18. Wang, J., et al.: Performance evaluation of parallel manipulators: motion/force transmissibility and its index. *Mech. Mach. T.* **45**, 1462–1476 (2010)
19. Liu, H.: Force/motion/stiffness transmissibility analyses of redundantly actuated and overconstrained parallel manipulators. In: Proceedings 14th World Congress in MMS, Taipei (2015)
20. Wu, C., et al.: Optimal design of spherical 5R parallel manipulators considering the motion/force transmissibility. *J. Mech. Des.* **132**(3) (2010)
21. Liu, X.-J., et al.: A new approach for singularity analysis and closeness measurement to singularities of parallel manipulators. *J. Mech. Robot.* **4**(4) (2012)
22. Wu, C., et al.: New measure for ‘Closeness’ to singularities of parallel robots. In: Proceedings of the ICRA, Shanghai (2011)
23. Liu, X.-J., et al.: Motion/force constrainability analysis of lower-mobility parallel manipulators. *J. Mech. Robot.* **6** (2014)
24. Chen, X., et al.: Screw theory based singularity analysis of lower-mobility parallel robots considering the motion/force transmissibility and constrainability. *Math. Prob. Eng.* **3** (2015)

25. Liu, H., et al.: A Generalized approach for computing the transmission index of parallel mechanisms. *Mech. Mach. T.* **74**, 245–256 (2014)
26. Brinker, J., Corves, B.: A survey on parallel robots with delta-like architecture. In: *Proceedings 14th World Congress in MMS, Taipei* (2015)
27. Takeda, Y., et al.: Development of spatial in-parallel actuated manipulators with six degrees of freedom with high motion transm. *JSME Int. J. Series C* **40**(2), 299–308 (1997)
28. Xie, F., Liu, X.-J.: Design and development of a high-speed and high-rotation robot with four identical arms and a single platform *J. Mech. Robot.* **7** (2015)
29. Wu, G., et al.: Multi-objective design optimization of a parallel Schönflies-motion robot. In: *Advances in Reconfigurable Mechanisms and Robots II*, pp. 657–667 (2016)
30. Zhang, L., et al.: Dimensional synthesis of the delta robot using transmission angle constraints. *Robotica* **30**, 343–349 (2011)
31. Liu, S., et al.: Optimal design of a 4-DOF SCARA type parallel robot using dynamic performance indices and angular constraints. *J. Mech. Robot.* **4** (2012)
32. Takeda, Y., Funabashi, H.: Kinematic and static characteristics of in-parallel actuated manipulators at singular points and in their neighborhood. *JSME Int J. Ser. C* **39**(1), 85–93 (1996)

A Geometrical Approach for the Singularity Analysis of a 3-RRS Parallel Manipulator

Halil Tetik and Gokhan Kiper^(✉)

Department of Mechanical Engineering,
Izmir Institute of Technology, Izmir, Turkey
{halilтетик, gokhankiper}@iyte.edu.tr

Abstract. Identifying singularity manifolds of parallel manipulators analytically is a hard task due to their complex kinematics and passive joints. This study proposes to use the geometrical conditions of singularities in order to identify the singularity manifolds for a 3-RRS parallel manipulator. The singularity surfaces for both inverse and forward kinematics singularities are obtained and plotted.

Keywords: Parallel manipulators · Jacobian analysis · Singularity analysis · Singularity surfaces

1 Introduction

At a singular configuration of a manipulator, the end effector loses its rigidity or has uncontrollable degrees-of-freedom (dof) [5]. When considering the parallel manipulators (PM), it should be noticed that the singular configurations can be observed inside the workspace and it is highly undesirable to lose the stiffness or gain an uncontrollable dof while performing a task with the PM [9].

For the case of closed loop kinematic chains, the velocity input-output relationship is defined in [3] as $\mathbf{A}\dot{\mathbf{x}} + \mathbf{B}\dot{\boldsymbol{\theta}} = 0$, where $\dot{\mathbf{x}}$ represents task space velocities and $\dot{\boldsymbol{\theta}}$ represents joint space velocities. Using the velocity input-output relationship equation, 3 types of singularities are defined. The first type occurs when $\det(\mathbf{B}) = 0$. For this type of singularity, the mechanism reaches either its internal or external limit of the workspace. This type of singularity is called as inverse kinematic singularity (IKS) or loss type singularity. The second type of singularity is observed when $\det(\mathbf{A}) = 0$. This type of singularity occurs within the workspace, rather than at the boundary, and it is called as forward kinematic singularities (FKS) or gain type singularities. The third type of singularity is observed when $\det(\mathbf{A}) = \det(\mathbf{B}) = 0$. This type of singularities are called as combined singularities.

The PM investigated in this study is a 3-dof manipulator which can achieve 1 dof translational and 2 dof rotational motion (1T2R). All the limbs have same kinematic structure and they are symmetrically connected to the base and moving platforms. In the literature, there are several studies investigating the singularities of PMs which have the same motion characteristics. For a 3-PRRU PM (the P3 Robot) the singularity analysis is performed in [2] by evaluating the determinants of the Jacobian matrices.

The singularity conditions were issued in [6] by obtaining the Jacobian matrices of a 3-PSP PM. They mention the difficulty of analytically determining the singularity equations for PMs by using the Jacobian matrices. So, instead of evaluating the Jacobian matrices, they provide the geometrical condition for the singularities. The singularities of a 3-PRS PM were investigated in [4]. Instead of evaluating the determinants of the Jacobian matrices, they investigated the geometrical conditions for the singularities of the PM. For platform type multiloop spatial mechanisms, several mechanisms were examined in [1], providing the geometrical conditions of the mechanisms at which the gain type singularities will occur.

This study investigates both IKS and FKS of a 3-RRS PM. To achieve this, firstly the geometry of the PM is explained. Then the Jacobian matrices for the inverse and forward kinematics are formulated. Using the Jacobian matrices, the singularity conditions of the PM and their physical meaning are examined. Finally, using the geometrical singularity conditions, both IKS and FKS surfaces in terms of the independent task space parameters are constructed using Mathematica[®] software.

2 Manipulator Geometry

The manipulator investigated in this study is a 3-dof PM located at Izmir Institute of Technology and it has 3 identical limbs. All the limbs have an active revolute (R) joint, a passive R joint and a spherical (S) joint. In Fig. 1, active R joints are shown with O_{0i} , passive R joints shown with O_{ij} and S joints are shown with O_{7j} for $i = 1, 2, 3$ and $j = i + 3$. The R joint axes on each limb are parallel to each other, and therefore each limb has a planar motion. θ_i and ϕ_i are respectively the active and passive R joint variables on the i^{th} link. The length of the bottom and upper links are $l_1 = 0.7$ m and $l_2 = 0.775$ m, respectively.

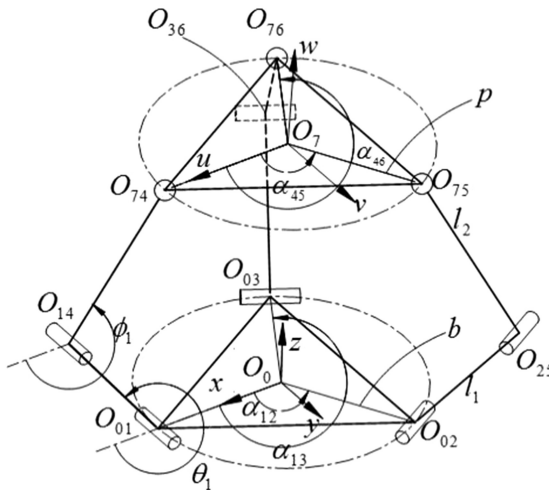


Fig. 1. Geometry of the 3-RRS parallel manipulator

Both base and platform are in the shape of an equilateral triangle with circumcircle radii $b = p = 0.544$ m. The axes of the active R joints are tangential to the base circumcircle. The centers of the base and platform circumcircles are shown with O_0 and O_7 , respectively. A fixed coordinate frame (O_0 -xyz) is attached to O_0 and its x-axis is along $\overrightarrow{O_0O_{01}}$ direction. A moving coordinate frame (O_7 -uvw) is attached to O_7 and its u axis is along $\overrightarrow{O_7O_{74}}$ direction. The limbs are attached to the corners of the base and platform triangles such that $\alpha_{11} = \alpha_{44} = 0^\circ$; $\alpha_{12} (\angle O_{01}O_0O_{02}) = \alpha_{45} (\angle O_{74}O_7O_{75}) = 120^\circ$; $\alpha_{13} (\angle O_{01}O_0O_{03}) = \alpha_{46} (\angle O_{74}O_7O_{76}) = 240^\circ$.

The position of the moving platform origin O_7 , with respect to (O_0 -xyz) is defined with a position vector:

$$\vec{O}_7 = [O_{7,x} \quad O_{7,y} \quad O_{7,z}]^T \quad (1)$$

To define the platform orientation, a rotation matrix is generated using x-y-z Euler rotation sequence with orientation angles ψ_x , ψ_y and ψ_z of the platform:

$$\mathbf{R} = \begin{bmatrix} c\psi_y c\psi_z & -c\psi_y s\psi_z & s\psi_y \\ s\psi_x s\psi_y c\psi_z + c\psi_x s\psi_z & c\psi_x c\psi_z - s\psi_x s\psi_y s\psi_z & -s\psi_x c\psi_y \\ s\psi_x s\psi_z - c\psi_x s\psi_y c\psi_z & s\psi_x c\psi_z + c\psi_x s\psi_y s\psi_z & c\psi_x c\psi_y \end{bmatrix} \quad (2)$$

where c and s stand for sine and cosine, respectively. Since the PM has 3-dof, three of the pose parameters given in Eqs. (1) and (2) are selected as independent task space parameters and the remaining three are found by solving the constraint equations. Considering the motion characteristics of the 3-RRS PM, the independent pose parameters are selected as $O_{7,z}$, ψ_x and ψ_y . The constraint equations to obtain the dependent task space parameters are given in [8].

3 Jacobian Analysis

For the i^{th} limb of the PM, the platform location can be expressed as:

$$\overrightarrow{O_0O_7} + \overrightarrow{O_7O_{7j}} = \overrightarrow{O_0O_{0i}} + \overrightarrow{O_{0i}O_{ij}} + \overrightarrow{O_{ij}O_{7j}} \quad (3)$$

By differentiating Eq. (3), the velocity loop equation for the i^{th} limb is obtained:

$$\vec{v}_{O_7} + \vec{\omega}_p \times \overrightarrow{O_7O_{7j}} = (\vec{y}_i \times \overrightarrow{O_{0i}O_{ij}}) \dot{\theta}_i + (\vec{y}_i \times \overrightarrow{O_{ij}O_{7j}}) \dot{\phi}_i \quad (4)$$

where $\vec{y}_i = [-sa_{1i} \ ca_{1i} \ 0]^T$, \vec{v}_{O_7} is the linear velocity of O_7 and $\vec{\omega}_p$ is angular velocity of the moving platform. The passive joint velocity on i^{th} limb, $\dot{\phi}_i$, should be eliminated from Eq. (4) in order to obtain the relation between input and output velocities. Taking the scalar product of both sides of Eq. (4) with $\overrightarrow{O_{ij}O_{7j}}$ and rearranging:

$$\overrightarrow{O_{ij}O_{7j}} \cdot \vec{v}_{O_7} + \left(\overrightarrow{O_7O_{7j}} \times \overrightarrow{O_{ij}O_{7j}} \right) \cdot \vec{\omega}_p - \left(\overrightarrow{O_{0i}O_{ij}} \times \overrightarrow{O_{ij}O_{7j}} \right) \cdot \vec{y}_i \dot{\theta}_i = 0 \quad (5)$$

Three of the velocity components, $v_{O7,x}$, $v_{O7,y}$, ω_z , depend on the task space velocities ω_x , ω_y (there is no dependency on $v_{O7,z}$) as [7]:

$$\begin{aligned}
 v_{O7,x} &= g_{xx}\omega_x + g_{xy}\omega_y = -\frac{p\mathbf{c}\psi_y\mathbf{S}\psi_y(\mathbf{c}\psi_x + \mathbf{c}\psi_y\mathbf{S}\psi_x\mathbf{S}\psi_y)}{2(1 + \mathbf{c}\psi_x\mathbf{c}_y)^2}\omega_x - \frac{p\mathbf{c}\psi_y\mathbf{S}\psi_x(\mathbf{c}\psi_x + \mathbf{c}\psi_y + \mathbf{S}\psi_x\mathbf{S}\psi_y)}{2(1 + \mathbf{c}\psi_x\mathbf{c}_y)^2}\omega_y \\
 v_{O7,y} &= g_{yx}\omega_x + g_{yy}\omega_y = -\frac{p\mathbf{c}\psi_y\mathbf{S}\psi_y(\mathbf{c}\psi_x + \mathbf{c}\psi_y)}{(1 + \mathbf{c}\psi_x\mathbf{c}_y)^2}\omega_x + \frac{p\mathbf{S}\psi_x \left(\begin{array}{l} s^2\psi_x s^4\psi_y - c^4\psi_y + c^2\psi_x c 2\psi_y - \\ \frac{\mathbf{c}\psi_x}{4}(5\mathbf{c}\psi_y + 3\mathbf{c}3\psi_y) \end{array} \right)}{2(1 + \mathbf{c}\psi_x\mathbf{c}_y)^2}\omega_y \\
 \omega_z &= g_{zx}\omega_x + g_{zy}\omega_y = \frac{-\mathbf{S}\psi_y}{1 + \mathbf{c}\psi_x\mathbf{c}_y}\omega_x - \frac{\mathbf{S}\psi_x}{1 + \mathbf{c}\psi_x\mathbf{c}_y}\omega_y
 \end{aligned} \tag{6}$$

Substituting Eq. (6) in Eq. (5) for all limbs results in:

$$\mathbf{J}_X \begin{bmatrix} v_{O7,z} \\ \omega_x \\ \omega_y \end{bmatrix} + \mathbf{J}_Q \begin{bmatrix} \dot{\theta}_1 \\ \dot{\theta}_2 \\ \dot{\theta}_3 \end{bmatrix} = \begin{bmatrix} 0 \\ 0 \\ 0 \end{bmatrix} \tag{7}$$

where

$$\mathbf{J}_Q = \begin{bmatrix} \left(\overrightarrow{O_{01}O_{14}} \times \overrightarrow{O_{14}O_{74}} \right) \cdot \vec{y}_1 & 0 & 0 \\ 0 & \left(\overrightarrow{O_{02}O_{25}} \times \overrightarrow{O_{25}O_{75}} \right) \cdot \vec{y}_2 & 0 \\ 0 & 0 & \left(\overrightarrow{O_{03}O_{36}} \times \overrightarrow{O_{36}O_{76}} \right) \cdot \vec{y}_3 \end{bmatrix}_{3 \times 3} \tag{8}$$

$$\mathbf{J}_X = \begin{bmatrix} A_1^z & A_1^x g_{xx} + A_1^y g_{yx} + B_1^x + B_1^z g_{zx} & A_1^x g_{xy} + A_1^y g_{yy} + B_1^y + B_1^z g_{zy} \\ A_2^z & A_2^x g_{xx} + A_2^y g_{yx} + B_2^x + B_2^z g_{zx} & A_2^x g_{xy} + A_2^y g_{yy} + B_2^y + B_2^z g_{zy} \\ A_3^z & A_3^x g_{xx} + A_3^y g_{yx} + B_3^x + B_3^z g_{zx} & A_3^x g_{xy} + A_3^y g_{yy} + B_3^y + B_3^z g_{zy} \end{bmatrix} \tag{9}$$

with $\overrightarrow{O_{ij}O_{7j}} = [A_i^x A_i^y A_i^z]^T$ and $\overrightarrow{O_7O_{7j}} \times \overrightarrow{O_{ij}O_{7j}} = [B_i^x B_i^y B_i^z]^T$.

4 Inverse Kinematics Singularities

The inverse kinematics singularity condition is satisfied if $\det[\mathbf{J}_Q] = 0$, or equivalently if $\overrightarrow{O_{0i}O_{ij}} \times \overrightarrow{O_{ij}O_{7j}} = \vec{0}$ for any limb i . This configuration refers to the positions when the bottom $\left(\overrightarrow{O_{0i}O_{ij}} \right)$ and upper $\left(\overrightarrow{O_{ij}O_{7j}} \right)$ links on limb i are collinear. Such a configuration is obtained when a double root is obtained during the inverse kinematics solution where two different assembly modes of a limb converges to each other. Instead of working with the determinants of Jacobian matrices, the IKS can geometrically be expressed in terms of the task space parameters using the collinearity condition of the limbs. Since all limbs of the PM have a planar motion, local planar coordinate frames $(O_0-x^i z)$ can be attached to each limb i (Fig. 2).

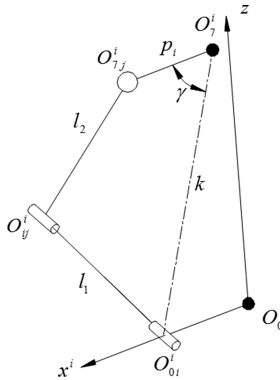


Fig. 2. Geometry of the 3-RRS parallel manipulator

The global coordinates of any point P on the PM can be projected onto the local planar coordinates as:

$$\vec{O_P} = [O_{P,x} \quad O_{P,y} \quad O_{P,z}]^T \rightarrow \vec{O_P^i} = [O_{P,x}c\alpha_{1i} + O_{P,y}s\alpha_{1i} \quad O_{P,z}]^T \quad (10)$$

The lengths p^i and k (projections of $\vec{O_7O_{7j}^i}$ and $\vec{O_{0i}O_{7j}^i}$ on the $x^i z$ -plane), and the angle γ in Fig. 2 can be expressed in terms of task space parameters as:

$$p^i = |\vec{O_7^i O_{7j}^i}|, \quad k = |\vec{O_{0i}^i O_{7j}^i}|, \quad \cos \gamma = \left(\vec{O_7^i O_{7j}^i} \cdot \vec{O_{0i}^i O_{7j}^i} \right) / p^i k \quad (11)$$

The collinearity condition of the bottom and upper links of limb i can geometrically be expressed by making use of the cosine theorem for $O_{0i}^i O_{7j}^i O_7^i$ triangle:

$$\cos \gamma = \left[p_i^2 + k^2 - (l_1 + l_2)^2 \right] / (2p_i k) \quad (12)$$

Equation (12) is written for the extended dead-center configuration of the links. For the folded dead-center configuration, $l_1 + l_2$ in Eq. (12) should be replaced by $l_2 - l_1$, but this case never occurs for our manipulator due to link collisions. Combining Eqs. (11) and (12), the inverse kinematics singularity equation for the 3-RRS PM can be formulated in terms of the task space parameters as:

$$2\vec{O_7^i O_{7j}^i} \cdot \vec{O_{0i}^i O_{7j}^i} + (l_1 + l_2)^2 - p_i^2 - k^2 = 0 \quad (13)$$

Equation (13) represents a surface in the task space parametrized by ψ_x, ψ_y and $O_{7,z}$. Using Mathematica[®], the IKS surface given by Eq. (13) for all the limbs of the 3-RRS PM can be constructed (Eq. (13) is written three times for $i = 1, 2, 3$). Considering the motion characteristics of the PM, it is preferred to plot the surface in spherical

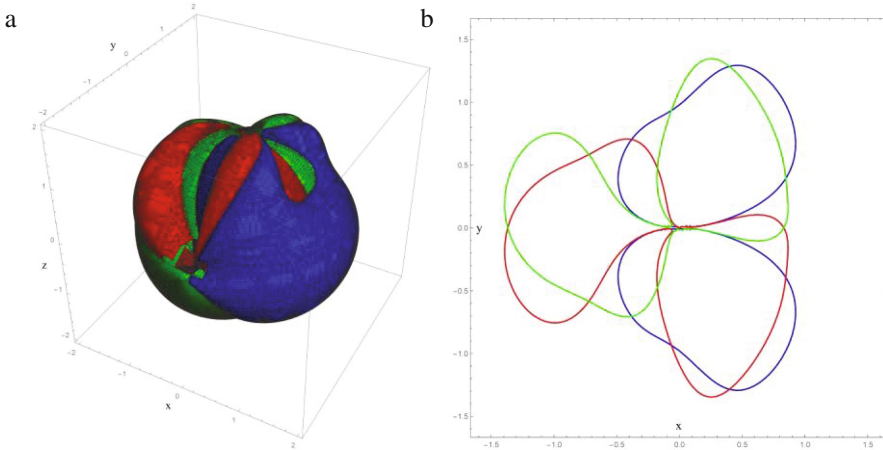


Fig. 3. IKS surface: (a) Full view, (b) $z = 1$ section view

coordinates: $O_{7,z} = \sqrt{x^2 + y^2 + z^2}$ (in meters), $\psi_x = \text{atan2}(-\sqrt{x^2 + y^2}, y)$ and $\psi_z = \text{atan2}(z, x)$. The IKS surface of the 3-RRS PM is presented in Fig. 3a. The singularity manifold has mirror symmetry about the xz -plane. In order to illustrate the contours inside, a cross section for $z = 1$ is given in Fig. 3b.

5 Forward Kinematics Singularities

The forward kinematic singularities of the 3-RRS PM are obtained $\det[\mathbf{J}_X] = 0$. It is not straightforward to extract the geometrical conditions which make the determinant zero. However, when the $\det[\mathbf{J}_X] = 0$ is formulated and plotted, it is seen that the singular configurations correspond to the cases where at least one of the upper links of a limb is coplanar with the platform plane, i.e. $\overrightarrow{O_7O_{7j}} \times \overrightarrow{O_{ij}O_{7j}} = \vec{0}$, or equivalently $B_i^x = B_i^y = B_i^z = 0$ for any $i = 1, 2, 3$. Coplanarity of an upper link and the platform corresponds to a double root during the forward kinematics solution. Instead of evaluating the Jacobian determinant, the coplanarity condition can be expressed in the local coordinate frame of the i^{th} limb using cosine theorem for $O_{0i}^iO_{ij}^iO_7^i$ triangle (Fig. 2):

$$\cos \gamma = \left[(p_i + l_2)^2 + k^2 - l_1^2 \right] / [2k(p_i + l_2)] \tag{14}$$

Singularity also occurs when the upper link is folded on the platform, in which case the $l_2 + p_i$ term should be replaced by $l_2 - p_i$. Combining Eqs. (11) and (14), the FKS equation for a limb can be formulated in terms of the task space parameters as:

$$2(p_i + l_2) \left(\overrightarrow{O_7^iO_{7j}^i} \cdot \overrightarrow{O_7^iO_{0i}^i} \right) - p_i \left[(p_i + l_2)^2 + k^2 - l_1^2 \right] = 0 \tag{15}$$

Using Mathematica[®], the singularity surface for all limbs is constructed in spherical coordinates (Fig. 4). Although the FKS surface is plotted in the task space, it is possible to plot the surface in the joint space using inverse kinematics formulation.

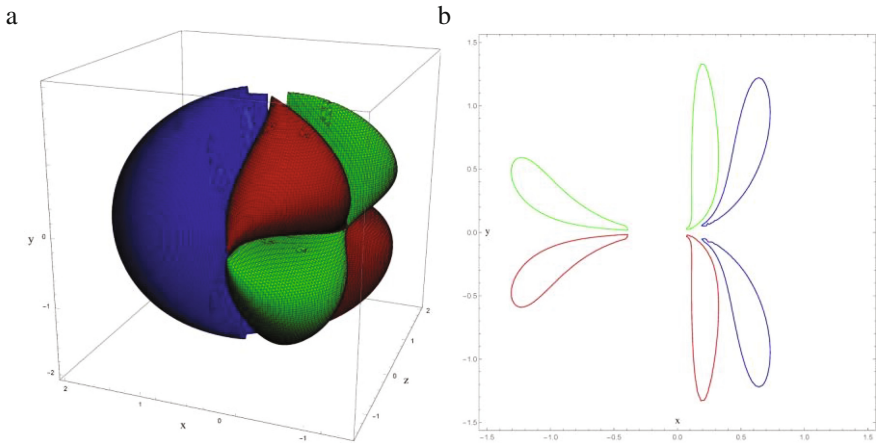


Fig. 4. FKS surface: (a) Full view, (b) $z = 1$ section view

6 Conclusions

This study presents a geometrical approach to determine the inverse and forward singularity manifolds of a 3-RRS PM. For the IKS, the Jacobian matrix \mathbf{J}_Q is a diagonal matrix and each diagonal element being equal to zero corresponds to IKS configurations due to one of the limbs of the PM. However, it is not straightforward to express the diagonal elements in terms of the task space parameters. On the other hand, using the physical interpretation of the singularity condition and by simply writing a cosine theorem for each limb, the singularity surfaces can be very easily obtained in terms of the task space parameters.

In general, for the FKS of PMs, it is an hard task to relate the physical interpretation of the singular configurations with the determinant of the Jacobian matrix \mathbf{J}_X . For the 3-RRS manipulator issued in this study, although each of the three limbs independently contribute to the FKS, decomposing the Jacobian determinant into three is a challenging task. Instead of using the Jacobian matrix, the FKS surfaces due to each limb is constructed independently in this study by making use of the geometrical conditions which result in singularities.

Another contribution of this study is expressing the singularity surfaces of a 1T2R PM in spherical coordinates.

Acknowledgments. The authors acknowledge the discussions with Prof. Sandipan Bandyopadhyay from IIT Madras, India.

References

1. Basu, D., Ghosal, A.: Singularity analysis of platform-type multi-loop spatial mechanisms. *Mech. Mach. Theory* **32**, 375–389 (1997)
2. Chen, Q.H., Chen, Z., Chai, X.X., Li, Q.C.: Kinematic analysis of a 3-axis parallel manipulator: the P3. *Adv. Mech. Eng.* (2013). doi:[10.1155/2013/589156](https://doi.org/10.1155/2013/589156)
3. Gosselin, C., Angeles, J.: Singularity analysis of closed-loop kinematic chains. *Robot. Autom. IEEE Trans.* **6**, 281–290 (1990)
4. Li, Y., Xu, Q.: Kinematic analysis of a 3-PRS parallel manipulator. *Robot. Comput. Integr. Manuf.* **23**, 395–408 (2007)
5. Merlet, J.-P.: *Parallel Robots*. Springer, Berlin (2001)
6. Rezaei, A., Akbarzadeh, A., Nia, P.M., Akbarzadeh-T, M.R.: Position, Jacobian and workspace analysis of a 3-PSP spatial parallel manipulator. *Robot. Comput. Integr. Manuf.* **29**, 158–173 (2013)
7. Tetik H.: *Modelling and Control of a 3-RRS Parallel Manipulator*. MSc Thesis, İzmir Institute of Technology (2016)
8. Tetik, H., Kalla, R., Kiper, G., Bandyopadhyay, S.: Position kinematics of a 3-RRS parallel manipulator. In: Parenti-Castelli, V., Schiehlen, W. (eds.) *ROMANSY 21—Robot Design, Dynamics and Control*. Springer, pp. 65–72 (2016)
9. Tsai, L.-W.: *Robot Analysis: The Mechanics of Serial and Parallel Manipulators*. Wiley, New York (1999)

The Collision-Free Workspace of the Tripteron Parallel Robot Based on a Geometrical Approach

Zolfa Anvari¹, Parnyan Ataei¹, and Mehdi Tale Masouleh²(✉)

¹ Human-Robot Interaction Laboratory, University of Tehran, Tehran, Iran
{zolfa.anvari,parnyan.ataei}@taarlab.com

² Human-Robot Interaction Laboratory, School of Electrical and Computer,
University of Tehran, Tehran, Iran
m.t.masouleh@ut.ac.ir

Abstract. Parallel robots, despite many kinematic features, generally have limited workspace. Therefore, it is paramount importance to obtain the workspace by considering the mechanical interference. In this paper, the mechanical interference, including collision of links, collision of links with obstacles, collision of the end-effector with obstacles, are investigated by using a new geometrical reasoning. For this purpose, a new geometric method is proposed which is based on the segment to segment intersection test. This method can be well extended to a wide range of robotic mechanical systems, including, among others, parallel robots. Moreover, in this paper, an index is introduced which can be used to examine the workspace with respect to mechanical interference. Furthermore, the aforementioned index provides some insight into obtaining a well-conditioned workspace. For the sake of validation, as case study, the proposed method is implemented to a spatial 3-DOF parallel robot, known as the Tripteron.

Keywords: Mechanical interference · Parallel robot · Collision-free workspace · Performance index

1 Introduction

The workspace of parallel robots is more constrained compared to their serial counterparts. Some of the contributing factors rendering a significant amount of workspace useless are collision of links to each other, collision of links with obstacles, collision of the end-effector with obstacles and also mechanical limitations of the joints [2]. Researches conducted on this subject are limited and most of them are concerned with avoiding collision with obstacles, on mobile robots or the end-effector of serial manipulators [4]. Despite its significance, there have been few studies examining the workspace and the mechanical interference among the links and between the links and the end-effector with obstacles; the reason might be that in most simulations the volume and mass of the robot's

components are ignored, in order to simplify the problem. The significance of such collisions is highlighted during implementation and use of the robots, where without appropriate collision prevention measures between the components, the robot might sustain serious damages. The present study aims at improving the workspace, by taking into account the problem of collision-free workspace. This can be achieved by eliminating those parts of the workspace wherein any kind of mechanical collisions might happen. This method is applied to the so-called Tripteron robot, which is a linearly independent 3-DOF parallel robot performing translational motion. The parameters used for implementing the proposed approach are based on the parameters of the actual prototype in the Human and Robot Interaction Laboratory, University of Tehran. The remainder of the paper is organized as follows. In Sect. 2, the Tripteron parallel robot is introduced. As the main contribution of this paper, a new algorithm is presented in Sect. 3 which can identify mechanical collisions of the robot. In Sect. 4, the collisions in the workspace of the Tripteron is examined and the proportion of the practical to theoretical workspace is calculated as an index. Finally, the paper concluded with some remarks and hints as ongoing works.

2 Tripteron

The Tripteron, as shown in Fig. 1, is a 3-DOF translational parallel mechanism, whose end-effector is connected by three kinematically identical chains. From the type synthesis performed for this kind of mechanisms, it follows that all the revolute joints and the prismatic actuators have parallel axes in each arm which together form an orthogonal set. One of the remarkable kinematic features of the Tripteron consists in its decoupling properties among its DOF. The latter leads to have an identical Jacobian matrix which results in having a singularity-free workspace [3, 5].

3 A New Algorithm Based on Segments Collision

The mechanical collisions depend on design properties, such as dimensions of the links, the fixed frame, and the end-effector. Moreover, if there is an obstacle in the workspace, it can influence the movement of the end-effector considerably. In fact, existence of one or more obstacles in the workspace can limit not only the end-effector but also the movement of the links. Under such circumstances, the detection of collision of links with an obstacle is as important as the collision of end-effector with an obstacle. The obstacles may have different shapes, which they can be inscribed inside a polyhedron.

By dividing the workspace into its constituent parts (meshing), placing the end-effector in all these points, and calculate the inverse kinematics for all these positions, all possible configurations of the robot are obtained. Upon determining the configuration, as shown in the first to the 15th line of Algorithm 1, and after checking the condition of the angle between robot mechanical components, if the angle is not within the allowable range, the robot end-effector is not allowed to

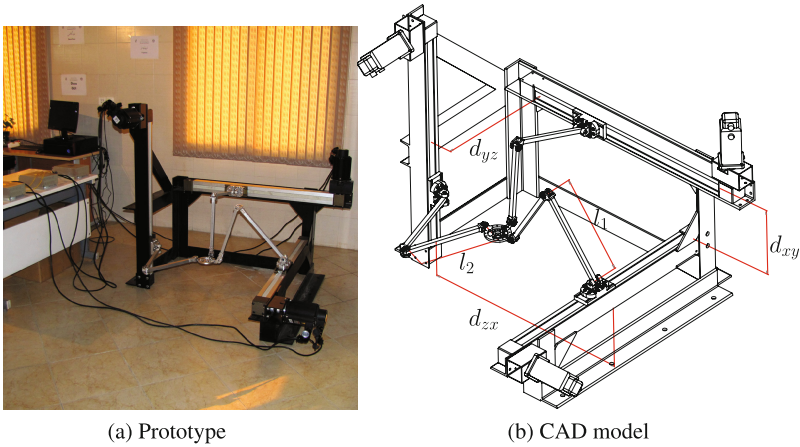


Fig. 1. The 3-DOF Tripteron parallel robot, built at the Human and Robot Interaction Laboratory, University of Tehran.

go to that part of the workspace and check collision is not necessary, based on lines 16 to 20 of Algorithm 1. However, if the angle is within the allowable range and there is at least one mechanical collision among the links, end-effector, and obstacles, the corresponding coordinate will be considered as a non admissible point for the end-effector. Thus the robot's end-effector is not allowed to go to that part of the workspace, as indicate in lines 22 to 32 of Algorithm 1. By repeating this algorithm for all points of the workspace, a set of coordinates will be obtained for which a collision will take place. Then, this set can be eliminated from the workspace, or considered as an obstacle. From the outset, the geometrical examination of mechanical collisions, can be solved readily using one of the following approaches:

1. Examining the intersection of two line segments in space at any given time;
2. Calculating the common perpendicular of two line segments and comparing it to a permissible value that equals the total radius of the two links.

However, since in this method the space is meshed, the configuration of the robot at any moment is one step apart from its next and previous moment. In other words, the positions are discreted. In such a discrete space, it is not possible to calculate all the collision points, because a collision might happen between two selected points. As presented in Fig. 2a, a discrete space will cause L_1 to be on the edge of collision at a given moment t but at the moment $t + 1$ it will leave the collision position behind and the collision will not be detected. Moreover, in this case, one cannot take into account the thickness of the links; therefore, the first approach is rejected. The second approach can not be regarded as a comprehensive method. As shown in Fig. 2b, when the line segments are part of the two intersecting lines and do not collide, the length of the common perpendicular is zero, and it seems that there has been a collision. Therefore, it

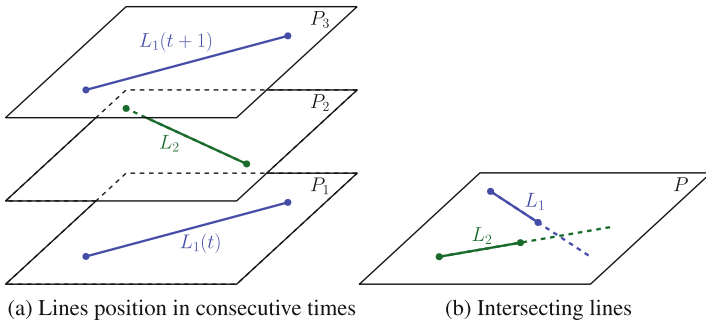


Fig. 2. Two failed conventional approaches.

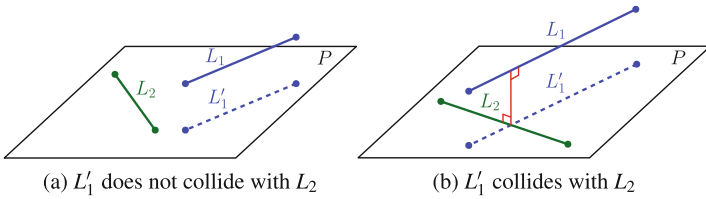


Fig. 3. Two cases which arise by projecting two lines in space.

is important to provide a comprehensive algorithm which can be generalized to any line segment in the space, and consider the thickness of the links and other mechanical parts.

In the proposed geometrical method, for detecting the collision among the links, the first line segment is projected into a plane that includes the second line segment and is parallel to the first line segment (the surface normal is the common perpendicular of the two lines). Now, two cases arise:

1. The projection of the first line segment does not collide with the second line segment, Fig. 3a, where the two lines do not collide;
2. The projection of the first line segment collides with the second line segment; as shown in Fig. 3b. Obviously, the former situation does not necessarily mean collision of the links and it is necessary to calculate the length of the common perpendicular, if it was less than the permissible value (sum of the thickness of both links), it can be concluded a collision occurs.

As it was claimed and shown in lines 33 to 42 of Algorithm 1, this algorithm can be generalized to all relative positions of the lines. If two lines intersect, the plane in which the collision is examined is their common plane; and if the two line segments are parallel, upon projecting, they should be matched and the second condition (the length of common perpendicular), should be analysed. Therefore, through analysis of the two geometrical conditions, the collision of two mechanical components or lack thereof, with arbitrary thickness and length at any position in the space is obtained. The collision of links is not the only

mechanical limitation in robots. For instance, in the prismatic joints, the slider can move in a specified range, and most of the revolute joints do not support 360° orientation.

The Collision-Free Workspace (CFW) index is defined as the ratio of practical workspace to theoretical workspace after calculating the available workspace of the parallel robot in every configuration. The index is used for identification of the most effective factor in designing and ultimately improving the workspace of parallel robots. In fact, this index, η , ranged between 0 and 1 stands for the ratio of collision-free workspace to the theoretical workspace [1]:

$$\eta = \frac{W_p}{W_t} \approx \frac{n_{W_p}}{n_{W_t}} \tag{1}$$

In the above relation, W_p is the practical workspace, W_t is the theoretical workspace, and n is the number of discrete workspaces of the parallel robot.

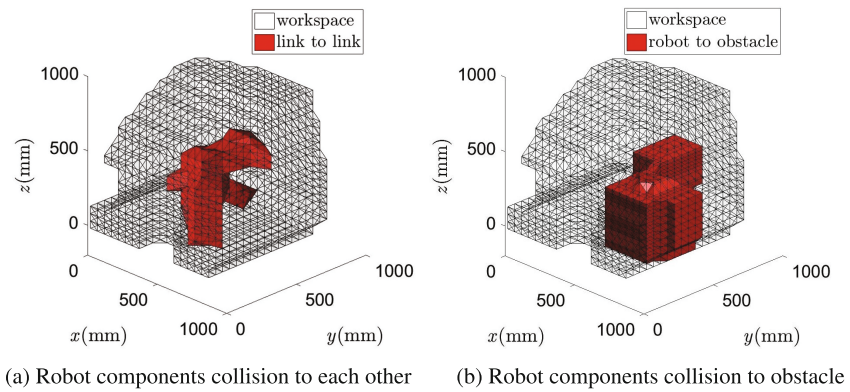


Fig. 4. Collision within the workspace of the Tripterion robot.

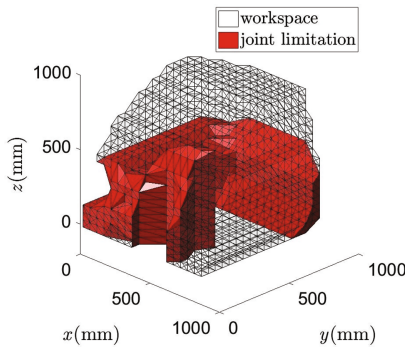


Fig. 5. Joint limitation in the workspace of the Tripterion robot.

input : l_1 and l_2 : Length of links.
 d_{xy} , d_{yz} and d_{zx} : Distance between axis of prismatic joints and coordinates axis.

R : Radius of end-effector.
 w : Allowed threshold between links.

output: modified workspace.

```

1  F: Collision matrix.
2   $i \leftarrow 0$ 
3  for Whole of possible space do
4  |   for 3 kinematic chains do
5  |   |   Check kinematic constraints
6  |   |   if The conditions holds. then
7  |   |   |    $i \leftarrow i + 1$ 
8  |   |   |   [ $X(i), Y(i), Z(i)$ ]: Save  $(x, y, z)^T$  as the coordinates point of the workspace.
9  |   |   end
10 |   end
11 end
12 for  $j = 1 : i$  do
13 |   Solve IK for  $X(j), Y(j), Z(j)$ .
14 |   Results are:  $\theta_1, \theta_2, \theta_3$  and  $\rho_1, \rho_2, \rho_3$ .
15 |   So obtained configuration of robot.
16 end
17 Check angle.
18 Calculate the angle between the segments by using law of cosines.
19 if Angel isn't in allowable angle range. then
20 |   Save  $X, Y, Z$  in a new matrix.
21 |    $F(j, 1) \leftarrow X(j), F(j, 2) \leftarrow Y(j), F(j, 3) \leftarrow Z(j)$ .
22 |   else
23 |   |   Check collision.
24 |   |   Lines collision detection by using collisioncheck, function.
25 |   |   [OUTPUT] = collisioncheck(2segment).
26 |   |   Returns  $\langle 1 \rangle$  if at least there is a collision. If not, returns  $\langle 0 \rangle$  by default.
27 |   |   Check every 2 segments (include links to each other, links to end-effector,
28 |   |   |   end-effector to obstacle and links to obstacle) in robot.
29 |   |   if There is atleast a collision. then
30 |   |   |   Save  $X, Y, Z$  in a new matrix.
31 |   |   |    $F(j, 1) \leftarrow X(j), F(j, 2) \leftarrow Y(j), F(j, 3) \leftarrow Z(j)$ .
32 |   |   end
33 |   end
34 Function [OUTPUT] = collisioncheck(2segment)
35 OUTPUT  $\leftarrow 0$ 
36  $L_1$ : First segment.
37  $L_2$ : Second segment.
38  $L_1$  Project on the plate that is parallel to  $L_1$  and includes  $L_2$  which is labelled as  $L_1'$ 
39 if Intersection occur between  $L_1'$  and  $L_2$  then
40 |   if Common perpendicular  $\leq w$  then
41 |   |   OUTPUT  $\leftarrow 1$ 
42 |   end
43 end

```

Algorithm 1. Collision detection algorithm.

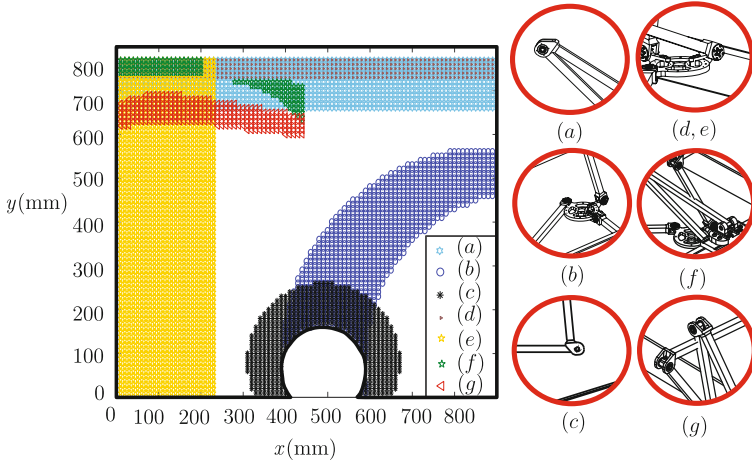


Fig. 6. All types of collisions in a horizontal section at $z = 0$.

Table 1. The effect of collisions in the useless space of the Tripteron in $z = 0$. In $\text{link}(i, j)$, i and j stand for the number of link and kinematic chain, respectively.

	Involved components	Percentage
<i>a</i>	link(1,1) to link(2,1)	26.94
<i>b</i>	link(2,3) to EE	25.55
<i>c</i>	link(3,1) to link(3,2)	11.22
<i>d</i>	link(2,1) to EE	13.39
<i>e</i>	link(2,2) to EE	44.67
<i>f</i>	link(1,1) to link(2,2)	3.68
<i>g</i>	link(2,1) to link(2,1)	6.60

4 Results

In this section, the performance of the proposed collision algorithm is examined for different kinds of mechanical collisions in the workspace, the limitation of revolute joints and the CFW index in the Tripteron robot is presented. Useless parts of the robot's workspace has been detected by collision algorithm. If the end-effector is placed in this space, collision will occur between mechanical components of robot with each other and with obstacle. The 3D appearance of this space in the primary workspace, is illustrated in Fig. 4a and b, respectively. In this case, the considered obstacle is a rectangular cube, located at $P_o(635, 370, 160)^T$, length, width and height of this rectangular cube are 100, 100 and 400, respectively. It should be noted that, from a practical stand point, since a revolute joint can not rotate freely, thus for a given working mode a range of motion is considered less than 160° for all the revolute joints of the Tripteron.

The latter leads to have a restricted range of motion for the end-effector, as shown in Fig. 5. The index of practical workspace to theoretical workspace ratio, η , in this case is 0.734 without an obstacle and 0.498 with obstacle.

In Fig. 6, each area represents a type of collision or mechanical limits of the joints in the robot's workspace. Table 1 provides some information about the percentage of collision occurred within the workspace by each components. From the foregoing Table 1 it can be inferred that which parts of the robots have a greater percentage of collision and should be subject of further investigation to be improved for an optimum design of this robot.

5 Conclusions

This paper proposed a new geometrical algorithm which can be used for all serial, parallel, and cable-driven robots. Previously, this problem was solved by meshing and final elements, which was far more complicated, required large quantities of data for comparison and was slower. The provided CFW index is very useful for design stage. For instance, measuring the value of this index for each component of the robot, provides a clear understanding of the relation between these variations and the collision-free workspace of the robot which can be regarded as a definite asset in practice. In this way, an optimum design for workspace could be obtained. In addition, the forbidden coordinates can be used as fixed obstacles in the obstacle avoidance algorithms. As ongoing work, this approach will be merged with optimization algorithms to synthesis collision-free workspace parallel robot for a prescribed workspace.

References

1. Danaei, B., Karbasizadeh, N., Tale Masouleh, M.: A general approach on collision-free workspace determination via triangle-to-triangle intersection test. *Robot. Comput. Integr. Manuf.* **44**, 230–241 (2017)
2. Gosselin, C.: Determination of the workspace of 6-DOF parallel manipulators. *ASME J. Mech. Des.* **112**(3), 331–336 (1990)
3. Gosselin, C.M., Tale Masouleh, M., Duchaine, V., Richard, P.L., Foucault, S., Kong, X.: Parallel mechanisms of the multipteron family: kinematic architectures and benchmarking. In: 2007 IEEE International Conference on Robotics and Automation, pp. 555–560. IEEE (2007)
4. Merlet, J.P.: *Parallel Robots*, vol. 74. Springer Science & Business Media, Cham (2012)
5. Tale Masouleh, M., Gosselin, C.: Kinematic analysis and singularity representation of 5-rprrr parallel mechanisms. In: ASME 2007 International Design Engineering Technical Conferences and Computers and Information in Engineering Conference, pp. 1125–1132. American Society of Mechanical Engineers (2007)

A Novel 3T1R Parallel Manipulator 2PaRSS and Its Kinematics

Huiping Shen¹(✉), Guowei Shao¹, Jiaming Deng¹, and Ting-li Yang²

¹ School of Mechanical Engineering, Changzhou University,
213164 Jiangsu, People's Republic of China

shp65@126.com, czdydjm@126.com, 898618909@qq.com

² Research Center for Advanced Mechanism Theory, Changzhou University,
213164 Jiangsu, People's Republic of China

yangtl@126.com

Abstract. By using the topological structure synthesis theory and method based on POC (Position and Orientation Characteristic) equations, a novel 4-DOF 3T1R parallel manipulator (PM) with low coupling degree, **2PaRSS**, is presented. First, the modeling and numerical solutions for forward and inverse position of the PM is established. Then, the workspace and rotation capacity of the PM are analyzed based on inverse solutions. This work shows 2PaRSS has simple structure, larger workspace and rotation capacity compared to H4, I4 etc.

Keywords: Parallel manipulator · POC · Coupling degree · Kinematics · SOC

1 Introduction

On type synthesis of three-translation and one-rotation (3T1R) PMs, F. Pierrot and O. Company *et al.* proposed a class of famous 4-DOF parallel robots that have been widely industrial used such as H4 [1], I4L [2], I4R [3], Par4 [4] and Heli4 [5], all of those are composed of four identical complex chains containing a parallelogram between the static and moving platform. Meanwhile, the coupling degrees of all these PMs mentioned are larger, which are $k = 2$ [6].

The coupling degree is used to describe the complexity of the topological structure of a mechanism [7]. It is represented by k ($k \geq 0$) that reflects the independence of the kinematic variables among loops of a PM, and also reflects the complexity of kinematics and dynamics solutions for the mechanism. It has been proved that the larger the value k , the higher of the complexity will be [6–8]. Therefore, the forward position solutions of all these existing 3T1R PMs are very difficult, which influences their real-time control and path planning.

By using topological structure synthesis theory and method for PMs based on POC equations [6, 8], the authors proposed a class of novel 4-DOF 3T1R PMs [6]. Among them, one is a novel **2PaRSS** PM presented in this paper. The PM features simple structure, large workspace and rotational ability. But its coupling degree is low, i.e., $k = 1$. The PM is composed of only two parallelogram complex chains containing 4S and two nonconstraint RSS chains (S-spherical joint, R-rotation joint). Therefore, the PM is not only simpler in the structure but also easier both in the solutions for

kinematics and dynamics and in manufacturing as well as assembly than that of H4 etc. The reason is that these existing PMs contain four parallelogram complex chains containing 4S and their coupling degrees are larger ($k = 2$) [6].

2 Structural Analysis

As shown in Fig. 1, the 2PaRSS PM [6, 9] consists of a moving platform 1, a static platform 0, two nonconstraint RSS chains and a hybrid chain whose end link 2 produces three-translation output.

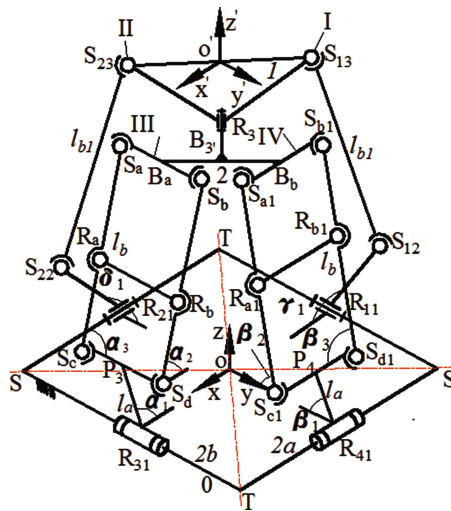


Fig. 1. A novel 2PaRSS PM and kinematic modeling

The hybrid chain has two parallelogram sub-chains III and IV which have four spherical joints (S_a, S_b, S_c, S_d) connected by the link 2. A rod with two rotating joints R_a and R_b shall be in the parallelogram configuration to make the four joints S_a, S_b, S_c, S_d in the same plane. The length of the rod $R_a R_b$ is equal to $S_a S_b$ or $S_c S_d$. The axis of the rotation pair R_3 must be perpendicular to the moving platform 1. Joint R_{11}, R_{21}, R_{31} and R_{41} are four actuated joints, and they are located in the midpoint of each side in the static platform 0. Two parallelogram sub-chains should satisfy $R_{31} \perp R_{41}$, while two nonconstraint RSS chains may take any arrangement relation, say $R_{11} \perp R_{21}$. “ \perp ” stands for perpendicular. Thus, the moving platform 1 can realize three translations and one rotation around the R_3 axis [6].

The topological analysis for the 2PaRSS PM can be found in [6], which shows that the PM contains only one Assur Kinematic Chain (AKC) and its coupling degree is only 1. Therefore all of the numerical solutions for the forward position can be found by using one dimensional search method.

3 Position Analysis

3.1 The Coordinate System and Annotation

Given the input angles $(\alpha_1, \beta_1, \gamma_1, \delta_1)$ of the actuated joints, the forward position solution is to solve the position (x, y, z) and the attitude angle (γ) of the moving platform 1, as in Fig. 1.

The static coordinate system O-XYZ is in the geometric center of the static platform 0, X axis is collinear with the connection line between R_{11} and R_{31} , Y axis is collinear with the connection line between R_{21} and R_{41} , and the direction of Z axes are determined by the law of the right hand. The origin of the coordinate $o'-X'Y'Z'$ is located in the midpoint of the hypotenuse ($S_{13}S_{23}$) of the platform 1, X' axis is parallel to the connection line between S_{13} and R_3 , and Y' axis is parallel to the connection line between S_{23} and R_3 . Since the static platform 0 is rectangular, its length and width are $2a$ and $2b$ respectively. Moving platform 1 is isosceles right triangle and the length of the right side is $2m_2$.

The orientation angle γ is the rotation angle of the moving platform 1 around the rotation pair R_3 , which is expressed by the angle between the OX axis and the connection line from R_3 to o' . The counter-clockwise direction of the angles is positive. The point B_3 is the midpoint of the rod B_aB_b . Let $R_3B_3 = q_l$, $B_aB_b = l$. The angle between the B_aB_b and the rod of S_aS_b or $S_{a1}S_{b1}$ is φ , respectively. Let $R_{11}S_{12} = R_{21}S_{22} = l_{a1}$, $S_{12}S_{13} = S_{22}S_{23} = l_{b1}$, $R_{31}P_3 = R_{41}P_4 = l_a$, $P_3B_a = P_4B_b = l_b$.

The angles between the parallelogram plane and the static platform plane are α_2 and β_2 respectively, while the interior angles of two parallelograms are respectively α_3 and β_3 , as shown in Fig. 1.

The position of the rod $S_{13}S_{12}$ and $S_{23}S_{22}$ in the space are expressed by three angles between them with the X, Y, Z axes in the static platform 0 respectively, which are $\gamma_2, \gamma_3, \gamma_4$ and $\gamma_5, \gamma_6, \gamma_7$, as shown in Fig. 2.

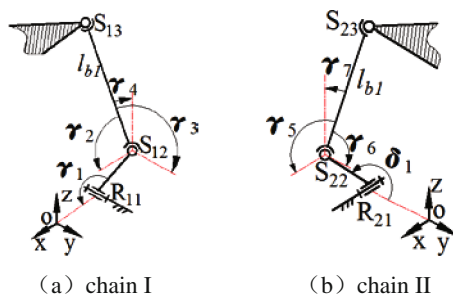


Fig. 2. Calculation model of chain I and II

3.2 Forward Position Modeling

The principle of modeling of forward position analysis based on SOC method can be found in [8].

3.2.1 The Modeling of the SOC₁

(1) The first SOC, i.e.SOC₁, of the PM is composed of two sub-chains III and IV, joint R₃ and S₁₃-S₁₂-R₁₁ chain, as in Fig. 1. By SOC₁, the coordinates of point O', S₁₃, S₂₃ can be obtained by D-H matrix as follows

$$\begin{bmatrix} x_{O'} \\ y_{O'} \\ z_{O'} \end{bmatrix} = \begin{bmatrix} a - l_a \cos \alpha_1 - l_b \sin \alpha_3 \cos \alpha_2 - l/2 \cos \varphi - \sqrt{2}m_2 \cos (\pi/4 + \gamma) \\ l_b \cos \alpha_3 - l/2 \sin \varphi - \sqrt{2}m_2 \sin (\pi/4 + \gamma) \\ l_a \sin \alpha_1 + l_b \sin \alpha_3 \sin \alpha_2 + q_1 \end{bmatrix} \quad (1)$$

$$\begin{bmatrix} x_{O'} \\ y_{O'} \\ z_{O'} \end{bmatrix} = \begin{bmatrix} l_b \cos \beta_3 + l/2 \cos 45^0 - \sqrt{2}m_2 \cos (\pi/4 + \gamma) \\ -l_a \cos \beta_1 - l_b \sin \beta_3 \cos \beta_2 - l/2 \sin 45^0 - \sqrt{2}m_2 \sin (\pi/4 + \gamma) \\ l_a \sin \beta_1 + l_b \sin \beta_3 \sin \beta_2 + q_1 \end{bmatrix} \quad (2)$$

$$\begin{bmatrix} x_{S_{13}} \\ y_{S_{13}} \\ z_{S_{13}} \end{bmatrix} = \begin{bmatrix} a - l_a \cos \alpha_1 - l_b \sin \alpha_3 \cos \alpha_2 - l/2 \cos \varphi - 2m_2 \cos \gamma \\ l_b \cos \alpha_3 - l/2 \sin \varphi - 2m_2 \sin \gamma \\ l_a \sin \alpha_1 + l_b \sin \alpha_3 \sin \alpha_2 + q_1 \end{bmatrix} \quad (3)$$

$$\begin{bmatrix} x_{S_{23}} \\ y_{S_{23}} \\ z_{S_{23}} \end{bmatrix} = \begin{bmatrix} a - l_a \cos \alpha_1 - l_b \sin \alpha_3 \cos \alpha_2 - l/2 \cos \varphi - 2m_2 \cos \gamma \\ l_b \cos \alpha_3 - l/2 \sin \varphi - 2m_2 \sin \gamma \\ l_a \sin \alpha_1 + l_b \sin \alpha_3 \sin \alpha_2 + q_1 \end{bmatrix} \quad (4)$$

By using Eqs. (1) and (2), we have the equation as

$$(k + t_1)k_1^2 + 2t_3k_1 + k - t_1 = 0$$

Then we get

$$k_1 = \frac{-t_3 \pm \sqrt{t_3^2 - k^2 + t_1^2}}{k + t_1}$$

where

$$k_1 = \tan \alpha_2/2 \quad (5)$$

$$t_1 = a - l_a \cos \alpha_1 - l \cos \varphi; t_2 = -l_a \cos \beta_1; t_3 = l_a \sin \alpha_1 - l_a \sin \beta_1$$

$$k = \frac{t_1^2 + t_2^2 + t_3^2 - 2t_2l_b \cos \alpha_3}{2l_b \sin \alpha_3}$$

We assign the angle α_3 as the virtual variable, i.e. α_3^* . Then, by Eq. (5), α_2 is a function of the virtual variable α_3^* .

(2) By the chain I, as in Fig. 2, the coordinates of S₁₂ can be easily obtained.

Further, by Eq. (3) and the link-length constraint $S_{12}S_{13} = l_{b1}$, we can obtain

$$A_1 \sin \gamma + B_1 \cos \gamma + C_1 = 0$$

Where

$$\begin{aligned} A_1 &= -4m_2(l_b \cos \alpha_3 - l/2 \sin \varphi) \\ B_1 &= -4m_2(a - l_a \cos \alpha_1 - l_b \sin \alpha_3 \cos \alpha_2 - l/2 \cos \varphi + l_{a1} \cos \gamma_1); \\ C_1 &= (a - l_a \cos \alpha_1 - l_b \sin \alpha_3 \cos \alpha_2 - l/2 \cos \varphi + l_{a1} \cos \gamma_1)^2 + \\ &\quad (2m_2)^2 + (l_b \cos \alpha_3 - l/2 \cos \varphi)^2 + (l_a \sin \alpha_1 + l_b \sin \alpha_3 \sin \alpha_2 + q_1 - l_{a1} \sin \gamma_1)^2 - l_{b1}^2; \end{aligned}$$

And let

$$k_2 = \tan(\gamma/2) \tag{6}$$

We have

$$k_2 = \frac{-A_1 \pm \sqrt{A_1^2 + B_1^2 - C_1^2}}{C_1 - B_1} \tag{7}$$

It is known from Eqs. (6) and (7) that angle γ^* is also a function of virtual variable α_3^* .

3.2.2 The Modeling of SOC₂

The second SOC, i.e., SOC₂, is S₂₃-S₂₂-R₂₁, as in Fig. 2, by which the coordinates of S₂₂ are easily obtained. Further, according to Eq. (4) and the link-length constraint S₂₂S₂₃ = l_{b1}, we have

$$\begin{aligned} f(\alpha_3^*) &= (a - l_a \cos \alpha_1 - l_b \sin \alpha_3^* \cos \alpha_2 - l/2 \cos \varphi + 2m_2 \sin \gamma^*)^2 \\ &\quad + (l_b \cos \alpha_3^* - l/2 \sin \varphi - 2m_2 \cos \gamma^* - l_{a1} \cos \delta_1)^2 + (l_a \sin \alpha_1 + l_b \sin \alpha_3^* \sin \alpha_2 + q_1 - l_{a1} \sin \delta_1)^2 - l_{b1}^2 \end{aligned} \tag{8}$$

By continuously changing α_3^* from 0 to 360 until $f(\alpha_3^*) = 0$, the value of α_3 is the real value. Then, the coordinates of point O', o'(x, y, z), can be obtained when the real α_3 is substituted into Eqs. (1) and (5). Further, by taking into Eq. (6), the real angle γ of the moving platform 1 can be obtained.

When the position (x, y, z) and angle γ of the moving platform 1 are known, the input angle $\alpha_1, \beta_1, \gamma_1, \delta_1$ of the driving arm is easily solved, which is the inverse position solutions for the PM. Both the forward and inverse position solutions of 2PaRSS PM have been testified to be correct by using an numerical example, which is omitted for the limited space.

4 Workspace and Rotation Capacity Analysis

The method of limit boundary searching based on inverse position solutions [10] is used to analyze the workspace of the **2PaRSS** PM. Namely, the height in the Z direction of the workspace is pre-determined, the boundary of workspace will be found by changing the search radius ρ and angle θ . This paper chooses the parameters such as $550 \leq z \leq 1200$ and $\Delta z = 10$, $-\pi \leq \theta \leq \pi$, $0 \leq \rho \leq 1000$. The range of the input angle $\alpha_1, \beta_1, \gamma_1, \delta_1$ are $[0, \pi]$.

4.1 Workspace Analysis

Using the MATLAB, the three-dimension graph of the workspace of the **2PaRSS** is shown in Fig. 3, and each X-Y cross-section is shown in Fig. 4. We find:

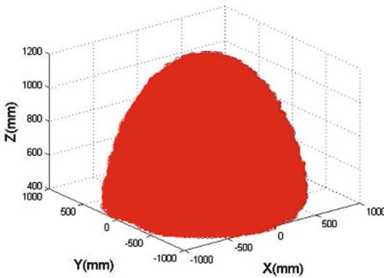


Fig. 3. Workspace of 2PaRSS

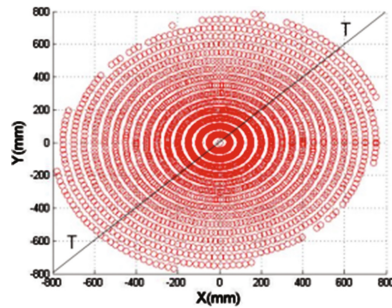


Fig. 4. X-Y section of workspace when $Z = 850$ mm

- (a) When $400 \text{ mm} \leq z \leq 550 \text{ mm}$, the internal space has an empty hole. The empty hole will disappear while increasing height Z.
- (b) When $z \in [550, 1000]$, the X-Y cross-section of the workspace is symmetric about the T-T line.
- (c) The workspace is a regular one, while increasing Z, the cross-section area will decrease.
- (d) Without considering the interference of the links, the workspace is bigger than that of I4R (H4) etc. in the same parameters and the search scope. The specific data are as follows:
 - ① Using the parameters of [11] and giving the search scope such as $0 \leq \rho \leq 1000$ and $500 \leq z \leq 1150$, the workspace volume of I4R is $6.1668 \cdot 10^8 (\text{mm}^3)$, and that of **2PaRSS** is $7.0070 \cdot 10^8 (\text{mm}^3)$. Therefore, the workspace of **2PaRSS** is increased by 13.6% compared to I4R robot.

- ② Using the parameters of [12], the workspace volume of CrossIV-3 is $4.4274 \cdot 10^8 (\text{mm}^3)$ and that of the **2PaRSS** is $4.6464 \cdot 10^8 (\text{mm}^3)$. Therefore, the workspace of **2PaRSS** is increased by 4.95% compared to CrossIV-3 robot.

4.2 Rotation Capacity Analysis

The rotation capacity of the moving platform is defined as the rotation range of the end effector in the workspace [13]. Its size is also an important indicator to measure the rotating performance of the **2PaRSS** PM.

Considering the scope of $z \in [550, 1000]$, at any X-Y cross-section, we can get the rotation ability of the moving platform. For clarity, we use $z = 1000 \text{ mm}$ as an example. Then the X-Y cross-section of the **2PaRSS** is got as shown in Fig. 5. And the rotation capacity of H4 is shown in Fig. 6, from which we observe as follows.

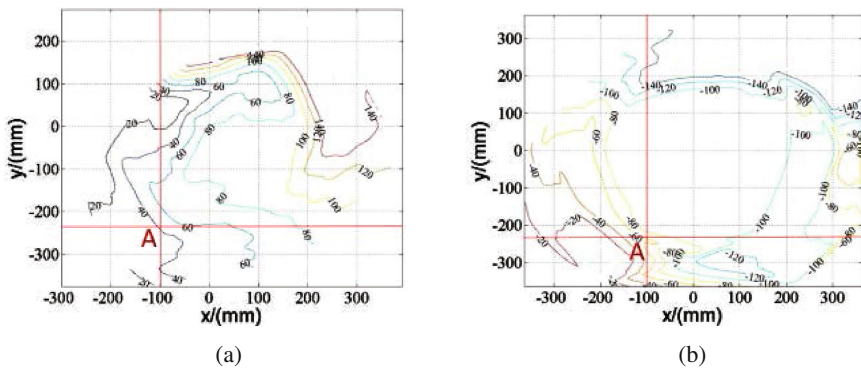


Fig. 5. Rotational capacity of 2PaRSS when $Z = 1000 \text{ mm}$ (a) Distribution of γ_{\max} (b) Distribution of γ_{\min}

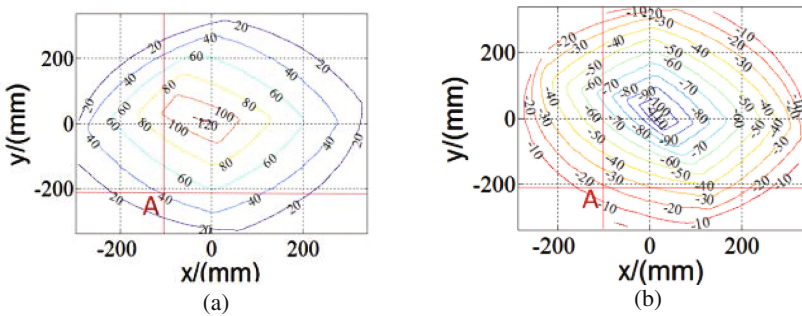


Fig. 6. Rotational capacity of H4 when $Z = 1000 \text{ mm}$ (a) Distribution of γ_{\max} (b) Distribution of γ_{\min}

The rotation range of the **2PaRSS** in the X-Y plane is $-140^{\circ} \leq \gamma \leq +140^{\circ}$ when $z = 1000$, while the rotation range of H4 is $-120^{\circ} \leq \gamma \leq +110^{\circ}$. Comparing with H4, the distribution of γ_{\max} is increased by 30° , and the distribution of γ_{\min} is increased by 20° . Therefore, the total value of **2PaRSS** will increase by 21.74% relative to H4. Specific comparisons are given as follows:

When using the point A($-100, -237, 1000$) as an example, the rotation output of the H4 is $\gamma_{\max} = 40^{\circ}$ and $\gamma_{\min} = -20^{\circ}$, while **2PaRSS** is $\gamma_{\max} = 40^{\circ}$ and $\gamma_{\min} = -60^{\circ}$. Therefore, it is easy to find that rotation capacity of the **2PaRSS** is larger than that of H4.

5 Conclusions

A novel 4-DOF 3T1R **2PaRSS** manipulator with simple structure and low coupling degree is presented.

The modeling of the forward position solutions based on the SOC method is established. A position constraint equation (Eq. (8)) with only one variable is derived, from which all numerical solutions of forward position are obtained by using one-dimension search method.

Based on inverse position solutions, the performance of the workspace is also analyzed. It is proved that the workspace of the **2PaRSS** is increased by 13.6% and 4.95% respectively compared with that of H4(I4) etc. The rotation capacity of the **2PaRSS** is increased by 21.74% compared with that of H4. This work shows the **2PaRSS** PM has potential applications.

Acknowledgments. This research is sponsored by NSFC (No.51475050, 51375062) and Jiangsu Key Development Pro-ject (No.BE2015043) and Jiangsu Scientific and Technology Transformation Fund Project (No. BA2015098).

References

1. Pierrot, F.: H4: a new family of 4-DOF parallel robots. In: Proceedings of 1999 IEEE/ASME International Conference on Advanced Intelligent Mechatronics, pp. 508–513 (1999)
2. Krut, S., Benoit, M., Ota, H., et al.: 14: a new parallel mechanism for Scara motions. In: Proceedings of IEEE International Conference on Robotics and Automation, vol. 2, pp. 1875–1880 (2003)
3. Krut, S., Nabat, V., Pierrot, F.: A high-speed parallel robot for Scara motions. In: Proceedings of 2004 IEEE International Conference on Robotics and Automation, vol. 4, pp. 4109–4115 (2004)
4. Nabat, V., de la O Rodriguezm, M., Krut, S., et al.: Par4: very high speed parallel robot for pick-and-place. In: Proceedings of 2005 IEEE/RSJ International Conference on Intelligent Robots and Systems, pp. 553–558 (2005)
5. Krut, S., Nabat, V., Pierrot, F.: Heli4: a parallel robot for Scara motions with a very compact traveling plate and a symmetrical design. In: Proceedings of International Conference on Intelligent Robots and Systems, pp. 1656–1661 (2006)

6. Yang, T., Liu, A., Shen, H., Hang, L.: Topological structure synthesis of 3T1R parallel mechanism based on POC equations. In: Proceedings of 9th International Conference on Intelligent Robotics and Applications. LNCS, vol. 9834, pp. 147–161. ICIRA (2016). doi:[10.1007/978-3-319-43506-0_13](https://doi.org/10.1007/978-3-319-43506-0_13)
7. Yang T.L.: Structural analysis and number synthesis of spatial mechanisms. In: Proceedings of the 6th World Congress on Mechanisms and Machines Theory, New Delhi, vol. 1, pp. 280–283 (1983)
8. Yang, T.: Topology Structure Design of Robot Mechanisms. China Machine Press, Beijing (2004)
9. Shen, H., Yang, T., Shao, G., et al.: A parallel robot hand with three translations and one rotation. Patent application number:201510640394.X (2015)
10. Xu, Z.: Studies and application of workspace and trajectory planning for 3-PCR parallel mechanism. Shandong University of Technology (2009)
11. Pingsong, L.: Study on Global Performance and Optimization of I4R Parallel Robot. Nanjing University of Science and Technology, Nanjing (2013)
12. Li, Y., Mei, J., Liu, S., et al.: Dynamic dimensional synthesis of a 4-DOF high-speed parallel manipulator. Chin. J. Mech. Eng. **19**, 32–40 (2014)
13. Xie, F., Liu, X.J.: Design and development of a high-speed and high-rotation robot with four identical arms and a single platform. J. Mech. Robot. **7**(4), 041015 (2015)

Multi-objective Optimization of a Tripod Parallel Mechanism for a Robotic Leg

Matteo Russo^{1(✉)}, Saioa Herrero², Oscar Altuzarra²,
and Marco Ceccarelli¹

¹ LARM – Laboratory of Robotics and Mechatronics,
University of Cassino and South Latium, Cassino, Italy
{matteo.russo, ceccarelli}@unicas.it

² Mechanical Engineering Department,
UPV/EHU University of the Basque Country, Bilbao, Spain
{saioa.herrero, oscar.altuzarra}@ehu.es

Abstract. This paper presents the multi-objective optimization of a three-degree-of-freedom parallel manipulator. First, the geometry of the mechanism is described and its kinematic and static performance is characterized with closed-form expressions of workspace volume and force efficiency. These indices are used as objective functions of the optimization, which is then conducted in order to compute the optimal design of the manipulator. Finally, the results of the multi-objective optimization are reported and discussed.

Keywords: Multi-objective optimization · Robot design · Leg mechanisms · Parallel robots

1 Introduction

Parallel mechanisms in robotic legs are seldom used, since they usually have a smaller workspace than serial mechanisms of the same size. However, parallel architectures perform better in accuracy and payloads [1, 2] and therefore they can substitute serial mechanisms when they fulfil workspace requirements. Some examples of parallel mechanisms used as robot legs can be found in [3–6]. The novel tripod architecture that is analysed in this paper is proposed in [7–9] while its kinematics is briefly described in Sect. 2. In order to find an optimal design for the mechanism, a multi-objective optimization is proposed in this work. The objective functions for the optimization of parallel mechanisms are discussed in many research works, such as [10–16]. In these studies, several indices have been proposed in order to characterize the workspace of the manipulator, its kinematic and dynamic performance and its stiffness. Among them, the workspace volume and the efficiency in force transmission are the most relevant ones for a robotic leg mechanism. Therefore, these two functions are evaluated in their closed-form expressions in Sect. 3 for the proposed structure, while Sect. 4 shows the multi-objective optimization solution by mapping the objective functions in the parameter space and discussing the results in order to find an optimal design.

2 Mechanism Description

The subject of the paper is the 3 degrees-of-freedom mechanism shown in Fig. 1 and introduced in [7–9]. It is composed by a fixed frame and by an end-effector body that are connected by three UPR chains. Referring to Fig. 1a, each chain consists of a linear actuator with length l_i that is connected to the fixed frame by a universal joint in A_i and to the end-effector by a revolute joint, in H. The structure is characterized by the fact that the three revolute joints are located at the end-effector point H thanks to the mechanism shown in Fig. 1b: link 1 rotates around the x-axis of the end-effector mechanism, while link 2 and link 3 can only rotate around the Y-axis. The position of point H can be found as the intersection of three spheres centred in A_i with radius equal to l_i , for $i = \{1, 2, 3\}$. Thus, this particular configuration of the end-effector notably simplifies the kinematics of the structure. According to this, if the frame is an equilateral triangle with side length a and characterized by Eq. (1),

$${}^0A_1 = \begin{pmatrix} 0 \\ 0 \\ 0 \end{pmatrix}; {}^0A_2 = \begin{pmatrix} a \\ 0 \\ 0 \end{pmatrix}; {}^0A_3 = \begin{pmatrix} a/2 \\ \sqrt{3}a/2 \\ 0 \end{pmatrix}, \tag{1}$$

the direct kinematic problem of the structure is solved as Eq. (2),

$$x = \frac{1}{2a} (l_1^2 - l_2^2 + a^2) \tag{2}$$

$$y = \frac{1}{2\sqrt{3}a} (l_1^2 + l_2^2 - 2l_3^2 + a^2)$$

$$z = -\sqrt{\frac{-l_1^4 - l_2^4 - l_3^4 - a^4 + l_1^2 l_2^2 + l_1^2 l_3^2 + l_2^2 l_3^2 + a^2 (l_1^2 + l_2^2 + l_3^2)}{3a^2}}$$

where x, y, z are the coordinates of the end point H.

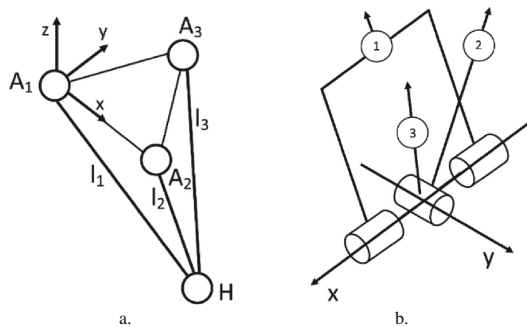


Fig. 1. Kinematic diagrams of the proposed mechanism: a. tripod structure; b. end-effector mechanism

This paper analyses and gives the optimization for a configuration with an equilateral triangle as base frame. Non-equilateral configuration for the base frame have also been investigated but held worse results. The kinematic problem of the structure is written in position only and not in orientation because the end-effector is analytically described as a punctiform body. Since the end-effector is the mechanism in Fig. 1b, it is possible to evaluate its orientation with Euler angles as Eq. (3),

$$\begin{aligned} \alpha &= \tan^{-1} \frac{(l_1^2 + l_2^2 - 2l_3^2 + a^2)}{2\sqrt{-l_1^4 - l_2^4 - l_3^4 - a^4 + l_1^2 l_2^2 + l_1^2 l_3^2 + l_2^2 l_3^2 + a^2(l_1^2 + l_2^2 + l_3^2)}} \\ \beta &= \arctan \frac{l_1 - l_2}{\sqrt{4a^2 l_3^2 - l_2^4 - l_1^4 + 2l_1^2 l_2^2}} \\ \gamma &= 0 \end{aligned} \tag{3}$$

where α is the rotation angle of the end effector around the X-axis, β is the intrinsic rotation around the Y-axis and γ is the one around the Z-axis.

Nevertheless, its Jacobian can be written as a 3×3 matrix as Eq. (4).

$$\mathbf{J}_p = \begin{bmatrix} \frac{l_1}{a} & -\frac{l_2}{a} & 0 \\ \frac{l_1}{\sqrt{3}a} & \frac{l_2}{\sqrt{3}a} & -\frac{2l_3}{\sqrt{3}a} \\ \frac{l_1(-2l_1^2 + l_2^2 + l_3^2 + a^2)}{3a^2z} & \frac{l_2(l_1^2 - 2l_2^2 + l_3^2 + a^2)}{3a^2z} & \frac{l_3(l_1^2 + l_2^2 - 2l_3^2 + a^2)}{3a^2z} \end{bmatrix} \tag{4}$$

The inverse Jacobian can be computed from Eq. (4) as Eq. (5).

$$\mathbf{J}_p^{-1} = \begin{bmatrix} \frac{x}{l_1} & \frac{y}{l_1} & \frac{z}{l_1} \\ \frac{x-a}{l_2} & \frac{y}{l_2} & \frac{z}{l_2} \\ \frac{x-\frac{a}{2}}{l_3} & \frac{y-\frac{\sqrt{3}a}{2}}{l_3} & \frac{z}{l_3} \end{bmatrix} \tag{5}$$

The singularities of the mechanism are evaluated by using Eq. (4). The Jacobian matrix is singular only in the plane $z = 0$ that the end-effector cannot physically reach because of the angular limitations of the universal joints on the base frame. Therefore, the reachable workspace of the mechanism can be obtained by computing Eq. (6),

$$\mathbf{H} = (x, y, z)^T \text{ for } l_1, l_2, l_3 \in [l_0, l_0 + s] \tag{6}$$

and it is coincident with its singularity-free workspace.

3 Kinematic and Dynamic Performance

In order to optimise the mechanism design, kinematic and dynamic performances have to be evaluated. Several functions have been proposed as numerical indices to compute both kinematic and dynamic performances of parallel mechanisms [1, 10–16]. Basic performance for the optimal design of the proposed mechanism can be evaluated in terms of workspace and force transmission, since these two parameters are the most important ones for the application of the manipulator as a robotic leg.

3.1 Workspace Volume

The workspace volume is the first parameter that can be used as objective function for optimization [1]. For the proposed 3-DoF manipulator the workspace can be evaluated as maximal or reachable workspace, which includes all the points that can be reached by the end-effector with at least one orientation. An example of reachable workspace for the proposed mechanism can be computed by discretising the actuation variables [2] and it is shown in Fig. 2.

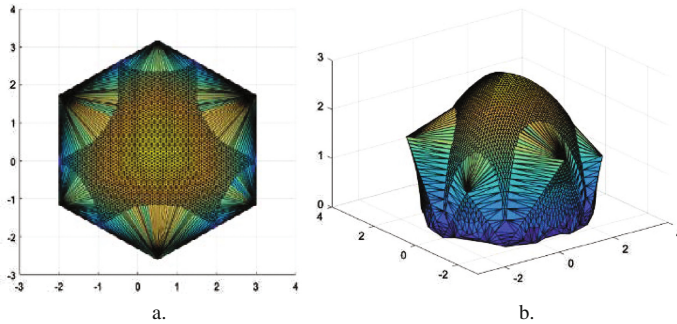


Fig. 2. Reachable workspace of the mechanism for $a = 1$, $l_{min} = 2a$, $l_{max} = 3a$; a. upper view; b. lateral view.

The shape of the reachable workspace of the mechanism, however, is irregular and its implementation in control algorithm for particular trajectories can be difficult. Therefore, a workspace formed of simple geometrical shapes is preferred. Since the proposed mechanism has axial symmetry, it is possible to obtain the operational workspace as part of a circular trajectory on the XY plane that is contained in the workspace itself. Figure 3 illustrates an example of operational workspace for the particular geometry that was already used for Fig. 2.

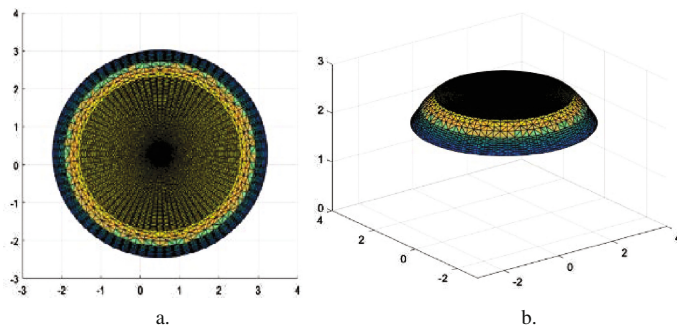


Fig. 3. Workspace as maximum circular trajectories of the mechanism for $a = 1$, $l_{min} = 2a$, $l_{max} = 3a$; a. upper view; b. lateral view

3.2 Force Transmission

In order to evaluate the static performance of the manipulator, it is necessary to write the actuation forces and the reaction forces on the foot respectively as Eq. (7).

$$\boldsymbol{\tau} = (\tau_1 \ \tau_2 \ \tau_3)^T, \quad \boldsymbol{w} = (f_1 \ f_2 \ f_3)^T \tag{7}$$

It is possible to define an index to evaluate the efficiency of the leg as Eq. (8).

$$\eta = \frac{\boldsymbol{w}}{\sum_{i=1}^3 \tau_i} \tag{8}$$

This efficiency index is position dependent and it allows to evaluate the ratio between a force applied on the end-effector and the actuation needed to balance it. In a static condition, the reaction force vector can be defined as Eq. (9),

$$\boldsymbol{w}_s = (0 \ 0 \ R)^T \tag{9}$$

where the only non-zero component is the reaction force between end-effector and ground, which is along the z -axis. Thus, it is possible to compute Eq. (8) for the proposed leg mechanism as Eq. (10).

$$\eta = \frac{|a^2 z|}{\sum_{i=1}^3 |l_i k_i|} \tag{10}$$

with $k_1 = -2l_1^2 + l_2^2 + l_3^2 + a^2$; $k_2 = l_1^2 - 2l_2^2 + l_3^2 + a^2$;
 $k_3 = l_1^2 + l_2^2 - 2l_3^2 + a^2$.

4 A Multi-objective Optimization Design Procedure

A multi-objective optimization is the search of an optimal set of parameters, which are subject to constraint functions, with regards to two or more objective functions. The problem can be defined as Eq. (11),

$$\min \boldsymbol{F}(\boldsymbol{r}) = \min [f_1(\boldsymbol{r}) f_2(\boldsymbol{r}) \cdots f_n(\boldsymbol{r})]^T, \quad \boldsymbol{r} = [r_1 r_2 \cdots r_m]^T \tag{11}$$

with $\boldsymbol{F} : \mathbb{R}^m \rightarrow \mathbb{R}^n$, $\boldsymbol{F}(\boldsymbol{r}) = [f_1(\boldsymbol{r}) f_2(\boldsymbol{r}) \cdots f_n(\boldsymbol{r})]^T$

subject to Eq. (12),

$$\begin{aligned} \boldsymbol{g}(\boldsymbol{r}) &\leq 0, \quad \boldsymbol{h}(\boldsymbol{r}) = 0 \\ \boldsymbol{g}(\boldsymbol{r}) &= [g_1(\boldsymbol{r}) g_2(\boldsymbol{r}) \cdots g_p(\boldsymbol{r})]^T \\ \boldsymbol{h}(\boldsymbol{r}) &= [h_1(\boldsymbol{r}) h_2(\boldsymbol{r}) \cdots h_t(\boldsymbol{r})]^T \end{aligned} \tag{12}$$

where \boldsymbol{F} is the vector that contains the objective functions f_i , \boldsymbol{r} is the vector of the design parameters of the entire system, \boldsymbol{g} is the disequality constraint function vector and \boldsymbol{h} the equality constraint function vector. The numbers n , m , p and t describe

respectively the number of objective functions, design parameters, disequality constraints and equality constraints. The problem is solved by finding the optimal solutions to the problem, which are called *Pareto-optimal* or *non-dominated* and are those solutions which cannot be improved in any of the objectives without degrading at least another one. The objective functions that are chosen for the analysis are operational workspace volume and force efficiency as in Eq. (10).

The multi-optimization problem only has two parameters: the ratio of the stroke of the actuator s over the base dimension a and the ratio of the minimum length of each leg l_0 over the base dimension a . Thus, it is possible to employ an exhaustive method that directly generates all the solutions by computing all the objective functions for each possible combination of the design parameters.

The constraint functions for the attached problem can be written as Eq. (13),

$$\frac{l_{0,min}}{a} \leq \frac{l_0}{a} \leq \frac{l_{0,max}}{a}; \quad \frac{s_{min}}{a} \leq \frac{s}{a} < \frac{l_0}{a} \tag{13}$$

where the maximum length of the stroke is limited by the minimum length of the actuator for feasibility reasons. Given the numerical constraints

$$0.9 \leq \frac{l_0}{a} \leq 2; \quad 0.9 \leq \frac{s}{a} < \frac{l_0}{a} \tag{14}$$

it is possible to map the values of each objective function in the whole parameter space. Figure 4 illustrates how the objective functions vary with regards to different configurations by mapping their displacement from the mean value, computed as Eq. (15).

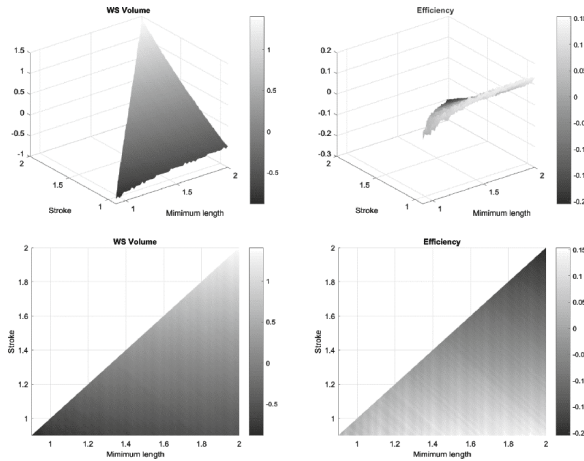


Fig. 4. Objective functions in the parameter space: a. Operational workspace volume; b. Force efficiency from Eq. (10)

$$\Delta f_i \left(\frac{l_0}{a}, \frac{s}{a} \right) = \frac{f_i \left(\frac{l_0}{a}, \frac{s}{a} \right)}{f_{i,mean}} \tag{15}$$

As shown in Fig. 4, objective functions are influenced in different ways by the two optimization parameters.

In particular, the efficiency function presented in Eq. (10) is characterized by a maximum variation of 20% from its average value (Fig. 4c), workspace volume varies over 100% of its average value in the parameter space, as shown in Fig. 4a and b. Furthermore, the optimum of each objective function is located in a different region of the parameter space. A good efficiency can be found for small values of the stroke but it does not show a strong dependency on the minimum length of the link. The workspace volume is optimized in a different region, characterized by high values of both the optimization parameters. Therefore, optimal solutions should be studied in order to find a compromise between the different objectives.

The influence of the design parameters on the operational workspace volume is too different to the one on the force efficiency index to detect a proper set of solutions on the Pareto front, which is characterized by points scattered in the whole parameter space. Therefore, another kind of solution has been chosen. The diagram in Fig. 5 maps the number of objective functions above their average value in each region of the parameter space. In particular, a black region is characterized by 0 objective functions above average, a grey region has one objective function above average and a white region is characterized by both objective functions above their average. Therefore, two optimal solutions for the mechanism design can be found in the two white regions around points (1.46; 1.30) and (1.96; 1.24).

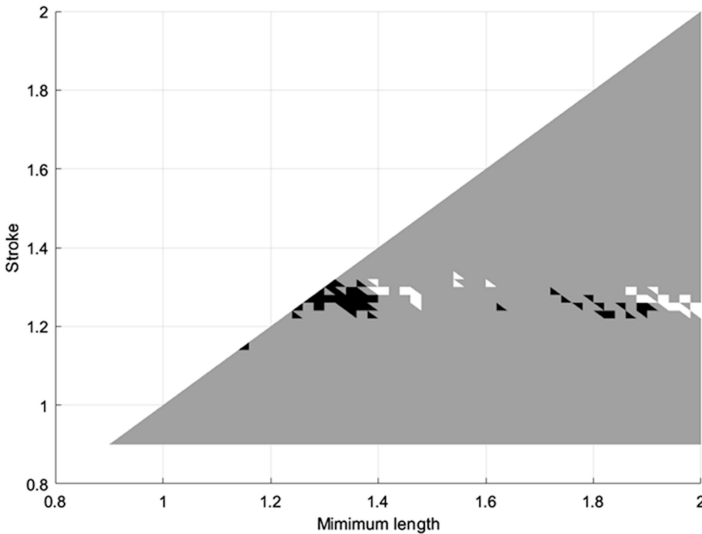


Fig. 5. Map of the parameter space with number of objective functions above average – black region: 0; grey region: 1; white region: 2

5 Conclusions

This paper describes the procedure for the optimization procedure of a parallel leg mechanism. First of all, the mechanism is introduced and its kinematics and dynamics are described. Then, its performance is evaluated in terms of workspace volume and force transmission. Finally, the main variables of the design are chosen as parameters and an optimization procedure is presented in order to select a set of solutions with the optimal performance indices. Furthermore, the performance of the mechanism is evaluated and mapped in the whole parameter space.

Acknowledgments. The first author wants to acknowledge the support received from the Erasmus+ program of the European Union for his stay at the University of the Basque Country, in Bilbao, in the year 2016.

References

1. Merlet, J.P.: *Parallel Robots*, vol. 74. Springer, Dordrecht (2012)
2. Ceccarelli, M.: *Fundamentals of Mechanics of Robotic Manipulation*, vol. 27. Springer, Dordrecht (2004)
3. Wang, H., Sang, L., Zhang, X., Kong, X., Liang, Y., Zhang, D.: Redundant actuation research of the quadruped walking chair with parallel leg mechanism. In *IEEE International Conference on Robotics and Biomimetics (ROBIO)*, pp. 223–228 (2012)
4. Xin, G., Zhong, G., Deng, H.: Dynamic analysis of a hexapod robot with parallel leg mechanisms for high payloads. In: *Proceedings of the 10th Asian Control Conference (ASCC)*, pp. 1–6 (2015)
5. Lim, H.O., Takanishi, A.: Biped walking robots created at Waseda University: WL and WABIAN family. *Philos. Trans. R. Soc. Lond. A Math. Phys. Eng. Sci.* **365**(1850), 49–64 (2007)
6. Wang, M., Ceccarelli, M.: Design and simulation of walking operation of a Cassino biped locomotor. In: *New Trends in Mechanism and Machine Science*, pp. 613–621. Springer International Publishing (2015)
7. Russo, M., Ceccarelli, M.: Kinematic design of a tripod parallel mechanism for robotic legs. In: *Proceedings of the 4th IFToMM Conference on Mechanisms, Transmissions and Applications, Trabzon* (2017, Submitted)
8. Ceccarelli, M., Russo, M.: Device for the spherical connection of three bodies, Italian Patent Application no. 10201600009369 (2016). (in Italian)
9. Russo, M., Cafolla, D., Ceccarelli, M.: Device for tripod leg, Italian Patent Application no. 102016000097258 (2016). (in Italian)
10. Carbone, G., Ottaviano, E., Ceccarelli, M.: An optimum design procedure for both serial and parallel manipulators. *Proc. Inst. Mech. Eng. Part C J. Mech. Eng. Sci.* **221**(7), 829–843 (2007)
11. Zhang, D., Gao, Z.: Forward kinematics, performance analysis, and multi-objective optimization of a bio-inspired parallel manipulator. *Robot. Comput. Integr. Manuf.* **28**(4), 484–492 (2012)
12. Gao, Z., Zhang, D., Hu, X., Ge, Y.: Design, analysis, and stiffness optimization of a three degree of freedom parallel manipulator. *Robotica* **28**(03), 349–357 (2010)

13. Unal, R., Kiziltas, G., Patoglu, V.: Multi-criteria design optimization of parallel robots. In: 2008 IEEE Conference on Robotics, Automation and Mechatronics, pp. 112–118, September 2008
14. Kelaiaia, R., Company, O., Zaatri, A.: Multiobjective optimization of a linear Delta parallel robot. *Mech. Mach. Theory* **50**, 159–178 (2012)
15. Altuzarra, O., Pinto, C., Sandru, B., Hernandez, A.: Optimal dimensioning for parallel manipulators: Workspace, dexterity, and energy. *J. Mech. Des.* **133**(4), 041007 (2011)
16. Altuzarra, O., Hernandez, A., Salgado, O., Angeles, J.: Multiobjective optimum design of a symmetric parallel Schönflies-motion generator. *J. Mech. Des.* **131**(3), 031002 (2009)

Robust Optimization of the RAF Parallel Robot for a Prescribed Workspace

M.A. Laribi¹(✉), A. Mlika², L. Romdhane^{2,3}, and S. Zeghloul¹

¹ Department of GMSC, Pprime Institute, CNRS - University of Poitiers - ENSMA - UPR, 3346 Poitiers, France

{med.amine.laribi,said.zegloul}@univ-poitiers.fr

² Mechanical Laboratory of Sousse (LMS), National Engineering School of Sousse, University of Sousse, 4000 Sousse, Tunisia

{abdelfattah.mlika,lotfi.romdhane}@gmail.com

³ Mechanical Engineering Department, American University of Sharjah, PO Box 26666, Sharjah, United Arab Emirates

Abstract. This paper deals with the optimal synthesis of the RAF robot for a prescribed workspace. The RAF (Romdhane-Affi-Fayet) robot is a three translational parallel manipulator (3TPM). A method based on the genetic algorithm is used to solve the optimization problem. A multi-objective function, based on the mathematical concept of the power of a point with respect to a surface, is formulated. The suggested method is simple and effective in defining the geometry of the robot having the smallest workspace that includes a specified volume and the best kinematic performance.

Keywords: Optimal design · Synthesis · RAF parallel robot · Genetic algorithm · Workspace · Power of a point · Dexterity index

1 Introduction

The interest in parallel manipulators (PM) arises from the fact that they exhibit high stiffness in nearly all configurations and a high dynamic performance. The RAF (Romdhane-Affi-Fayet) parallel manipulator is also a 3TPM and it consists of a mobile platform connected to the base by three active legs and two passive kinematics' chains [1–3].

The design problem has been addressed in many previous works [6, 11–14, 16–19]. In [9], we showed using the mathematical concept of the power of a point, how to design a DELTA robot for a prescribed workspace. In this paper, we will solve the problem of designing the three translational dof RAF robot to have a specified workspace and the highest dexterity. A multi-objective genetic algorithm (MOGA) is used to solve the optimization problem, because of its robustness and simplicity.

This paper is organized as follows: Sect. 2 presents the architecture of the RAF robot. Section 3, is devoted to the kinematic analysis and the determination of the workspace of the RAF parallel robot. The dexterity index of the robot is presented in Sect. 3. In Sect. 4, we carry out the formulation of the optimization problem using the genetic algorithm. Section 5 contains the results and discussion. Finally, Sect. 6 contains some conclusions.

2 Architecture of the RAF Parallel Robot

The RAF robot consists of a mobile platform connected to the base by 3 legs. These three legs constitute the actuators of the manipulator, whereas two other kinematic chains with passive joints are used to eliminate the three rotations of the mobile platform with respect to the base (Fig. 1) [1, 2].

Let $R_b(O_B, x_B, y_B, z_B)$ and $R_P(P, x_P, y_P, z_P)$ represent two references frames, which are fixed on the base and on the platform, respectively (see Fig. 1). The active legs are connected to the base through spherical joints. These spherical joints are centered in points $B_i, i = 1, 2, 3$, with the base and in points $C_i, i = 1, 2, 3$, with the platform.

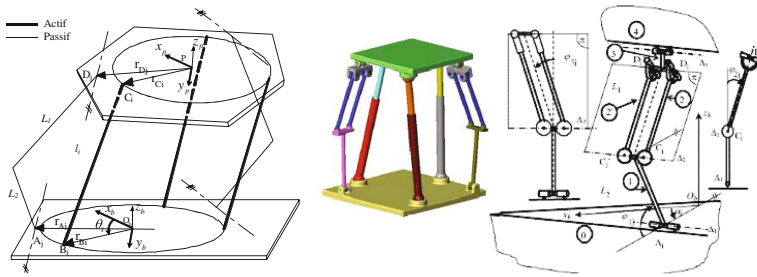


Fig. 1. The RAF robot parameters.

In this work, a standard configuration is selected for the active legs as follows :

- $r_{B_i} = r_B; r_{C_i} = r_C (i = 1, 2, 3)$ which means that the centers of the spherical joints relating the three legs to the base, respectively the platform, are located on a circle centered in O_B , respectively P , and with a radius r_B , respectively r_C .
- $\theta_{C_1} = \theta_{B_1} = \theta_1 = 0; \theta_{C_2} = \theta_{B_2} = \theta_2 = \frac{2\pi}{3}; \theta_{C_3} = \theta_{B_3} = \theta_3 = \frac{4\pi}{3}$ which means that the three centers are arranged at 120° from each other.

The parameters of the active kinematics' chains are:

- l_{max} : The maximum extension of the active legs.
- l_{min} : The minimum extension of the active legs.

Figure 1 shows the architecture of one of the passive kinematics chains [2]. Each kinematic chain is made of an arm (1) connected to the base (0) by a revolute joint. More details on the RAF architecture are presented and discussed in [1–3].

The parameters of the passive kinematics' chains are L_1 and L_2 (see Fig. 1). We will take the case where $L_1 = L_2 = L$. Points A_j , respectively $D_j (j = 1, 2)$, are located on a circle with a radius r_A , respectively r_D . We also have $(A_1 \widehat{O_B} A_2) = 120^\circ$ (see Fig. 1).

3 Workspace of the RAF Robot

The workspace of the RAF robot is the intersection of two workspaces of the two imbricated robots, respectively, the passive part and the active part.

3.1 Active and Passive Workspaces of the Platform

The active workspace of the RAF robot is defined by a volume, in the Cartesian space, reachable by the center of the platform $P[X_P, Y_P, Z_P]$. The geometrical model of the active kinematic chain is described by the following equation for each actuator (for $i = 1, \dots, 3$):

$$(R\cos\theta_i - X_P)^2 + (R\sin\theta_i - Y_P)^2 - Z_P^2 - l_i^2 = 0 \tag{1}$$

It is assumed that the actuators are identical and their lengths vary between the minimal value, l_{min} , and the maximum value, l_{max} ($l_{min} = l_{max}/3$). The reachable points of each one of these legs are confined within a volume delimited by two concentric spheres given by (for $i = 1, \dots, 3$):

$$(R\cos\theta_i - X_P)^2 + (R\sin\theta_i - Y_P)^2 - Z_P^2 - l_{max}^2 = 0 \tag{2}$$

$$(R\cos\theta_i - X_P)^2 + (R\sin\theta_i - Y_P)^2 - Z_P^2 - l_{min}^2 = 0 \tag{3}$$

The intersection of the three volumes delimited by the three pairs of concentric spheres, represents the active workspace of the manipulator for a given orientation.

A slice of the active workspace at $z = z_k$ is shown on Fig. 2. This space is similar to that presented by [10] in the case of a Stewart platform of the 6-SPS type. However, our problem is less complex, since we have only three actuators instead of six.

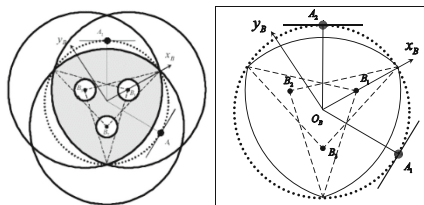


Fig. 2. Slice of the active workspace at XY plane

Considering the same point $P[X_P, Y_P, Z_P]$ on the platform. The kinematic model for the passive chains can be written as, with $j = 1, 2$:

$$\mathbf{O}_B\mathbf{P} = \mathbf{O}_B\mathbf{A}_j + \mathbf{A}_j\mathbf{C}_j + \mathbf{C}_j\mathbf{D}_j + \mathbf{D}_j\mathbf{P} \tag{4}$$

$$\mathbf{O}_B\mathbf{P} = \begin{bmatrix} r \cos \alpha_j \\ r \sin \alpha_j \\ 0 \end{bmatrix} + \begin{bmatrix} L_2 \cos \varphi_{1j} \cos \alpha_j \\ L_2 \cos \varphi_{1j} \sin \alpha_j \\ -L_2 \sin \varphi_{1j} \end{bmatrix} + \begin{bmatrix} L_1 \cos \varphi_{3j} \cos(\varphi_{1j} + \varphi_{2j}) \cos \alpha_j \\ L_1 \cos \varphi_{3j} \cos(\varphi_{1j} + \varphi_{2j}) \sin \alpha_j \\ L_1 \cos \varphi_{3j} \sin(\varphi_{1j} + \varphi_{2j}) \end{bmatrix} + \begin{bmatrix} -L_1 \sin \alpha_j \sin \varphi_{3j} \\ L_1 \cos \alpha_j \sin \varphi_{3j} \\ 0 \end{bmatrix}$$

where, φ_{3j} is the angle between the direction of the 2 forearms and the plane generated by the direction of z-axis and that of the arm, φ_{2j} is the angle between the projection of the forearms on the previously defined plane and the direction of the arm, and φ_{1j} is the angle between the direction of the arm and that of the straight line through O and A_j . In order to eliminate the passive joint variable, we square and add these equations

$$\begin{aligned} [(r + L_2 \cos \varphi_{1j}) \cos \alpha_j - X_P]^2 + [(r + L_2 \cos \varphi_{1j}) \sin \alpha_j - Y_P]^2 \\ + [L_2 \sin \varphi_{1j} - Z_P]^2 - L_1^2 = 0 \end{aligned} \tag{5}$$

where, $r = r_A - r_D$. Equation (5) can be expressed as a function of $\cos \varphi_{1j}$ and $\sin \varphi_{1j}$, as follows:

$$\begin{aligned} (2rL_2 - 2L_2X_P \cos \alpha_j - 2L_2Y_P \sin \alpha_j) \cos \varphi_{1j} - 2rX_P \cos \alpha_j + 2L_2Z_P \sin \varphi_{1j} - 2rY_P \sin \alpha_j \\ + X_P^2 + r^2 + L^2 + Z_P^2 + Y_P^2 - L_1^2 = 0 \end{aligned} \tag{6}$$

which can be written as:

$$l_j \cos \varphi_{1j} + m_j \sin \varphi_{1j} - n_j = 0 \tag{7}$$

where,

$$u_j = 2rL_2 - 2L_2X_P \cos \alpha_j - 2L_2Y_P \sin \alpha_j; \quad m_j = 2L_2Z_P; \quad n_j = -2rY_P \sin \alpha_j + X_P^2 + r^2 + L_2^2 + Z_P^2 + Y_P^2 - L_1 - 2rX_P \cos \alpha_j$$

Equation (7) can have a solution if and only if for $j = 1, 2$:

$$\left| \frac{n_j}{\sqrt{u_j^2 + m_j^2}} \right| \leq 1 \Leftrightarrow n_j^2 - (u_j^2 + m_j^2) \leq 0 \tag{8}$$

3.2 Workspace of the RAF Robot

The workspace of the RAF parallel manipulator is defined by the intersection of the active workspace and the passive one. (see Fig. 3).

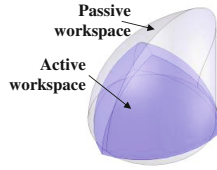


Fig. 3. Workspace of the RAF robot

- Point P is inside the active workspace then, for $i = 1, 2, 3$:

$$ha_i^{\max}(P) = (R\cos\theta_i - X_P)^2 + (R\sin\theta_i - Y_P)^2 - Z_P^2 - L_{max}^2 \leq 0 \quad (9)$$

$$ha_i^{\min}(P) = (R\cos\theta_i - X_P)^2 + (R\sin\theta_i - Y_P)^2 - Z_P^2 - L_{min}^2 \geq 0 \quad (10)$$

- Point P is inside the passive workspace then, for $j = 1, 2$:

$$\begin{aligned} hp_j(P) = & (X_P\cos\alpha_j + Y_P\sin\alpha_j - r)^2 \\ & + (X_P\cos\alpha_j + Y_P\sin\alpha_j)^2 + Z_P^2 + L_2^2 - L_1^2)^2 \\ & - 4L_2^2((X_P\cos\alpha_j + Y_P\sin\alpha_j - r)^2 + Z_P^2) \leq 0 \end{aligned} \quad (11)$$

4 Singularity Analysis of the RAF Robot

Due to the complexity of the kinematic model of parallel mechanisms, most of the authors proposed numerical methods to analyze their singularities. The approach proposed by Romdhane et al. [2] to analyze the singularity of the 3-translational-DOF parallel manipulator, is a combination of vector analysis and geometric analysis. Romdhane shows that this method allows to elucidate and physically explain the different singular configurations. The platform can only translate due to the two passive chains even in the absence of the active legs. The architecture of the passive chains is made such that the axis of the revolute joint with the platform is always parallel to the axis of the revolute joint with the base, i.e., the line maintains a constant orientation. The velocity of any point of the platform is the same, i.e.,

$$\mathbf{V}(C_1 \in \wp/B) = \mathbf{V}(C_2 \in \wp/B) = \mathbf{V}(C_3 \in \wp/B) = \mathbf{V}(M \in \wp/B) \quad (12)$$

We can also write that :

$$\dot{l}_i = \frac{V(M \in \wp/B) \cdot B_i P_i^T}{\| B_i P_i \|} = \mathbf{u}_i^T \cdot \mathbf{V}(M \in \wp/B) \tag{13}$$

where \mathbf{u}_i is a unit vector along the leg i and \dot{l}_i is the velocity of the linear actuator located between C_i and B_i . Using matrix representation, we obtain:

$$\begin{bmatrix} \dot{l}_1 \\ \dot{l}_2 \\ \dot{l}_3 \end{bmatrix} = [\mathbf{u}_1^T \mathbf{u}_2^T \mathbf{u}_3^T] [\mathbf{V}(M \in \wp/B)] = \mathbf{J}^T [\mathbf{V}(M \in \wp/B)] \tag{14}$$

where \mathbf{J} is a jacobian matrix whose columns are the unit vectors $(\mathbf{u}_1, \mathbf{u}_2, \mathbf{u}_3)$. We have the following relation

$$\mathbf{B}_i \mathbf{C}_i = l_i \mathbf{u}_i \tag{15}$$

Where for $i = 1, 2, 3$,

$$\mathbf{B}_i \mathbf{C}_i = \mathbf{B}_i \mathbf{O}_B + \mathbf{O}_B \mathbf{P} + \mathbf{P} \mathbf{C}_i = \begin{bmatrix} x_P - R \cos \alpha_i \\ y_P - R \sin \alpha_i \\ z_P \end{bmatrix} \tag{16}$$

with $\mathbf{O}_B \mathbf{B}_i = \begin{bmatrix} r_B \cos \alpha_i \\ r_B \sin \alpha_i \\ 0 \end{bmatrix}$, $\mathbf{O}_B \mathbf{P} = \begin{bmatrix} x_P \\ y_P \\ z_P \end{bmatrix}$, $\mathbf{P} \mathbf{C}_i = \begin{bmatrix} x_P + r_C \cos \alpha_i \\ y_P + r_C \sin \alpha_i \\ 0 \end{bmatrix}$

Using Eq. 17 the unit vector \mathbf{u}_i can be expressed as follows :

$$\mathbf{u}_i = \frac{B_i C_i}{\| B_i C_i \|} \tag{17}$$

To evaluate the kinematic performances of robot, researchers have introduced several criteria. The dexterity is a measure reflecting the amplification of error due to the kinematic and statistic transformations between the joints and the Cartesian space. It is of utmost importance that the proposed robot maintains a certain level of dexterity over its workspace. Several criteria were proposed in the literature to quantify the dexterity of robot manipulators. In this work, we propose the most used one, which is the condition number $\kappa(\mathbf{J})$ of the Jacobean matrix that describes the overall kinematic behavior of a robot [15]. The problem of non homogeneity of the Jacobean matrix is not encountered in our case since the 3-translational-DOF parallel manipulator has only translation degrees of freedom. The local dexterity is defined as :

$$\kappa(\mathbf{J}) = \|\mathbf{J}\| \cdot \|\mathbf{J}\|^T \tag{18}$$

The Jacobian describes the overall kinematic behavior of the considered robot. We adopted for the representation the inverse of the condition number, $\eta = \frac{1}{\kappa(J)}$, ranging between 0 and 1 (isotropy is reached when $\eta = 1$).

The manipulator under study is in a singular configuration if and only if the set of the three vectors $(\mathbf{B}_1\mathbf{C}_1, \mathbf{B}_2\mathbf{C}_2, \mathbf{B}_3\mathbf{C}_3)$ are linearly dependent [2]. This condition depend only on the value of the geometric parameter, the radius R , which appears in the expression of the unit vector \mathbf{u}_i . In order to explore the evolution on the local dexterity for a given design vector and over the manipulator workspace, Fig. 4 illustrates the distribution of the inverse of the condition number in the (x, y) plane and for a given value of the radius R .

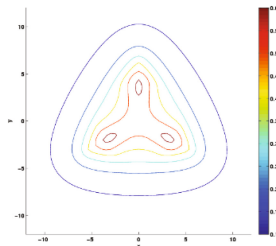


Fig. 4. The local dexterity distribution for $R = 5$ and $z = 5$

5 Synthesis of the RAF Robot for a Prescribed Workspace

5.1 Formulation of the Problem

The aim of this section is to formulate the multidimensional optimization problem of selecting the design variables for the RAF robot having a specified workspace with the best kinematic performance distribution. The desired workspace is given by a volume Ω in space.

The optimization problem can be formulated as follows:

Given: A specified volume in space Ω .

Find: The parameters of the RAF robot having the smallest workspace that includes the specified volume and best kinematic performance.

The general associated optimization problem, with n parameters for a suitably chosen objective function $F(\mathbf{I}, P)$, can be stated as:

$$\min F(\mathbf{I}, P) = [f_1 \quad f_2]^T \tag{19}$$

Subject to,

$ha_i^{\max}(I, P_k) \leq 0, i = 1, \dots, 3; k = 1, \dots, N_{pt}$: for active workspace constraints.

$ha_i^{\min}(I, P_k) \geq 0, i = 1, \dots, 3; k = 1, \dots, N_{pt}$: for active workspace constraints.

$hp_j(I, P_k) \leq 0, j = 1, 2; k = 1, \dots, N_{pt}$: for passive workspace constraints.

For all the points P inside the specified workspace Ω where $\mathbf{I} = [x_1, x_2, \dots, x_n]$ is the unknown vector of parameters, and $x_i \in [x_{i\min}, x_{i\max}]$, $i = 1, 2, \dots, n$ specify the allowable parameters range for each variable.

In this work, we will take the case where Ω is a cube given by $N_{pt} = 8$ points (see Fig. 5).

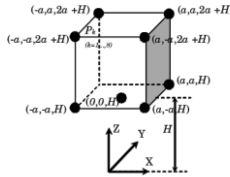


Fig. 5. The scheme of the prescribed workspace

For every workspace to be generated by the RAF robot, the independent design variables are:

$$\mathbf{I} = [r, l_{max}, L, R, H] \tag{20}$$

where, $r = r_A - r_D$: The difference in radius of the passive kinematic chain. $R = r_B - r_C$: The difference in radius of the active kinematic chain. l_{max} : The maximum length of the actuator. L : The length of the leg. H : is a parameter defining how far is the specified volume from the base of the RAF robot. The center of the cube is taken on the z axis because of the symmetry of the workspace.

5.1.1 Power Function Ratio

In a previous work [8], the performed optimization proved that one of the passive workspace or the active workspace can have a great influence on the quality of the optimal solution. This formulation ensures that the desired workspace is obtained but leads to a cumbersome structure. A large difference between the dimensions of the two chains, passive and active, should be noted. Indeed, the two obtained design vectors for the RAF robot present a large base or a large platform. The quality of the obtained results depends on the choice of the value of the aggregation coefficient used in the definition of the objective function. In order to overcome this formulation problem and to obtain the passive and active workspaces with similar sizes, a new formulation based on the use of power function ratio, is proposed. This ratio is defined as:

$$\frac{f_p}{f_a} \simeq 1$$

The corresponding objective function is defined as follows:

$$f_1(\mathbf{I}, P_k) = \left| \frac{f_p}{f_a} - 1 \right|$$

where,

$$f_a = \frac{\sum_{i=1}^3 |ha_i^{\max}(\mathbf{I}, P_k)|}{\sqrt{\sum_{i=1}^3 (ha_i^{\max}(\mathbf{I}, P_k))^2}} + \frac{\sum_{i=1}^3 |ha_i^{\min}(\mathbf{I}, P_k)|}{\sqrt{\sum_{i=1}^3 (ha_i^{\min}(\mathbf{I}, P_k))^2}} \text{ and } f_p = \frac{\sum_{j=1}^2 |hp_j(\mathbf{I}, P_k)|}{\sqrt{\sum_{j=1}^2 (hp_j(\mathbf{I}, P_k))^2}}$$

5.1.2 Dexterity

veral methods and dexterity indices can be found in the literature, e.g., Yoshikawa [1], Angeles [2], and Gosselin [3]. To compute the kinematic performance of a structure, we chose the global dexterity method proposed by Gosselin as it characterizes the isotropy of the robot. A commonly used criterion to evaluate this kinematic performance is the global conditioning index η^G , which describes the isotropy of the kinematic performance. The index, for a given structure described by the design vector \mathbf{I} , is defined over a workspace Ω as:

$$\eta^G = \frac{\int_{\Omega} \eta^L dw}{\int_{\Omega} dw} = \frac{\int_{\Omega} 1/\kappa(\mathbf{J}) dw}{\int_{\Omega} dw} \quad (21)$$

Where η^L is the local dexterity and $\kappa(\mathbf{J})$ is the condition number of the kinematic Jacobian matrix (19). The corresponding objective function is defined as follows: $f_2(\mathbf{I}) = \eta^G$

5.2 Results

The objective is to find the smallest set of parameters, given by \mathbf{I}^* , that can yield a RAF robot having a workspace with smallest passive/active workspace that includes the given volume in space Ω , while, simultaneously, achieving the best kinematic performances over the whole workspace. The methodology followed here to solve this problem is based on minimizing the multiple design objectives. This minimization problem is solved using the Multi-Objective Genetic Algorithm (MOGA) method. The solutions are called Pareto-optimal solutions when an improvement in one objective requires a degradation of another. Figure 6 shows the surface representing the Pareto front. Each point represents the values of the two objective functions, respectively f_1 and f_2 , obtained by a given design vector.

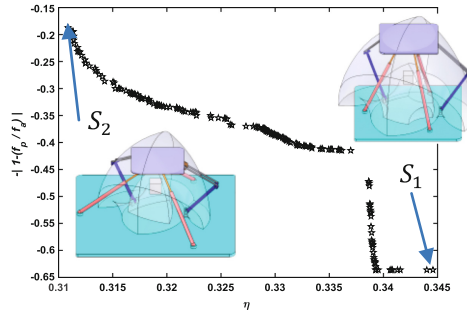


Fig. 6. Pareto front

6 Conclusions

In this work, the workspace of the RAF parallel manipulator having three linear actuators, was determined. An optimal dimensional synthesis method suited for the RAF robot was presented and solved. In this approach, two objective functions were considered. The first one aims at finding the smallest robot having a desired workspace and the second one is to ensure the best overall dexterity over this workspace. The first objective function is based on the concept of the power of a point, which was used to calculate the ratio of the passive to the active workspaces. The optimum value of the ratio is unity, which ensures the two workspaces having similar sizes. The second objective function is based on the condition number of the jacobian matrix. The MOGA method was used to find the optimal solutions represented by the Pareto front. Two extreme solutions from the Pareto front were taken and their CAD models were presented.

It was shown that favoring the dexterity could lead to a bulky robot and a robot with similar workspaces could have a relatively low dexterity. However, the presented solutions all have a value of dexterity ranging from 0.3 to 0.35, which is relatively low.

References

1. Romdhane, L.: Design and analysis of a hybrid serial-parallel manipulator. *Mech. Mach. Theory* **34**(7), 1037–1055 (1999)
2. Romdhane, L., Affi, Z., Fayet, M.: Design and singularity analysis of a 3 translational-DOF in-parallel manipulator. *ASME J. Mech. Des.* **124**, 419–426 (2002)
3. Affi Z., Romdhane L., Maalej, A.: Dimensional synthesis of a 3-translational-DOF in-parallel manipulator for a desired workspace. *Euro. J. Mech. - A/Solids* **23**, 311–324 (2004). I. 2
4. Ceccarelli, M., Carbone, G., Ottaviano, E.: An optimization problem approach for designing both serial and parallel manipulators. In: *The International Symposium on Multibody Systems and Mechatronics Uberlandia, Brazil*, 6–9 March 2005
5. Clavel, R.: Delta, a fast robot with parallel geometry. In: *Proceedings of the 18th International Symposium of Robotic Manipulators*. IFR Publication, pp. 91–100 (1988)

6. Clavel, R.: Une nouvelle structure de manipulation parallèle pour la robotique légère, R.A.I. R.O. APII, vol. 23, 6 (1986)
7. Lallemant, J.P., Goudali, A., Zeghloul, S.: The 6 - D.o.f. 2 - Delta parallel robot. *Robotica J.* **15**, 407–416 (1997)
8. Laribi, M.A., Mlika, A., Romdhane, L., Zeghloul, S.: Multi criteria optimum design of 3 dof translational parallel manipulators (3TPM). In: 13th IFToMM World Congress, Guanajuato, Mexico, 19–23 June (2011)
9. Laribi, M.A., Romdhane, L., Zeghloul, S.: Analysis and dimensional synthesis of the DELTA robot for a prescribed workspace. *Mech. Mach. Theory* **42**, 859–870 (2007). I. 7
10. Gosselin, C.: Determination of the workspace of 6-dof parallel manipulators. *ASME J. Mech. Des.* **112**, 331–336 (1990)
11. Boudreau, R., Gosselin, C.M.: *Mech. Mach. Theory* **36**, 327–342 (2001)
12. Boudreau, R., Gosselin, C.M.: *ASME. J. Mech. Design* **121**, 533–537 (1999)
13. Gallant, M., Boudreau, R.: The synthesis of planar parammel manipulators with prismatic joints for an optimal singularity-free workspace. *J. Robot. Syst.* **19**(1), 13–24 (2002)
14. Snyman, J.A., Hay, A.M.: Optimal synthesis for a continuous prescribed dexterity interval of 3-DOF parallel planar manipulator for different prescribed output workspaces. In: *Proceeding of CK 2005, Cassino, May 4–6*
15. Yang, G., et al.: Design, and kinematic an analysis of modular reconfigurable parallel robots. In: *Proceedings of the IEEE. ICRA, Michigan (1999)*
16. Tsai, L.-W.: *Previous Robot Analysis: The Mechanics of Serial and previous Parallel Manipulator*, John Wiley & Sons, Inc., New York (1999)
17. Chablat, D., Wenger, P.: Architecture optimization of a 3-DOF previous parallel mechanism for machining applications: the orthoglide. *IEEE Trans. Rob. Aut.* **19–3**, 403–410 (2003)
18. Liu, X.-J., Jeong, J., Kim, J.: A three translational DoFs previous parallel cube-manipulator. *Robotica* **21**(6), 645–653 (2003)
19. Jamwal, P.K., Xie, S., Aw, K.C.: Kinematic design optimization of a parallel ankle rehabilitation previous robot using modified genetic algorithm. *Robot. Auton. Syst.* **57**(10), 1018–1027 (2009)

Optimal Design of N- \mathcal{UU} Parallel Mechanisms

Yuanqing Wu^(✉) and Marco Carricato

Department of Industrial Engineering, University of Bologna, Bologna, Italy
{yuanqing.wu,marco.carricato}@unibo.it

Abstract. In this paper, we present the optimal design of N- \mathcal{UU} (\mathcal{U} stands for universal joints) parallel mechanisms (PM) with general geometry, for the achievement of maximal singularity-free tilt angle. We first briefly recall the synthesis condition and constraint analysis of the general N- \mathcal{UU} PM, showing that static singularities may be factorized into active and passive constraint singularities. We then formulate the optimal design problem as the maximization of the end-effector tilt angle subject to closeness to active and passive constraint singularities. We conclude the paper by illustrating how an angle-equalizing device on the inner revolute pairs of the \mathcal{UU} legs may help avoiding passive constraint singularities and increasing the maximal tilt angle.

Keywords: Symmetric subspace · Parallel mechanism · Singularity analysis · Workspace optimization

1 Introduction

It is well known that N- \mathcal{UU} PMs are kinematically equivalent to a well known class of constant-velocity couplings with two rotational degrees of freedom (DoF) [8]. A special-geometry N- \mathcal{UU} PM was first proposed in [6], followed by several rediscoveries of the same mechanism until recently [10–12]. Carricato [4] made a further clarification of the synthesis condition of the N- \mathcal{UU} PM, which may be summarized as follows:

- (C1) The two \mathcal{U} joints in each \mathcal{UU} leg must be identical and remain in a mirror symmetric configuration during full-cycle motion; see Fig. 1(b).
- (C2) all \mathcal{UU} legs share the same plane of symmetry and the revolute axes of the proximal (distal) \mathcal{U} joints of all legs intersect at one point \mathbf{s}^+ (\mathbf{s}^-); see Fig. 1(c).

A comprehensive kinematic and singularity analysis of general-geometry N- \mathcal{UU} PMs is conducted in [14]. In this paper, instead, we study the optimal design of these mechanisms for the maximization of the end-effector singularity-free tilt angle (simply referred to as tilt angle hereafter).

The paper is organized as follows. Section 2 recalls the most relevant results presented in [14]. We show that N- \mathcal{UU} PMs may equivalently be studied as purely spherical mechanisms, so that their static singularities may be factorized into

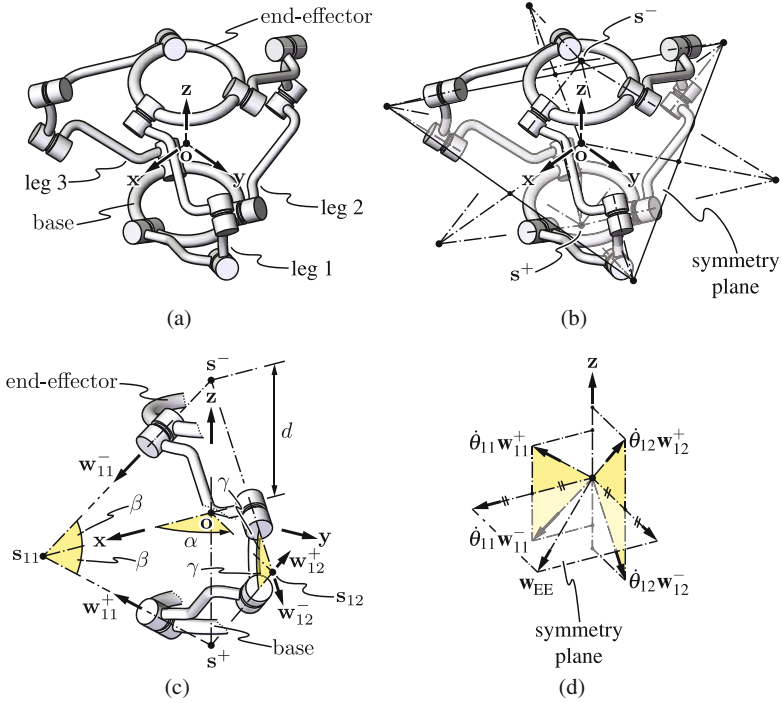


Fig. 1. Schematic of a general 3-UU PM: (a) components of the PM; (b) synthesis condition of the PM: the two \mathcal{U} joints in each leg are mirror symmetric about the \mathbf{xy} -plane, and the revolute axes of all proximal (or distal) \mathcal{U} joints in all legs intersect at a point \mathbf{s}^+ (or \mathbf{s}^-); (c) geometry of the first leg; (d) end-effector angular velocity \mathbf{w}_{EE} under an instantaneous symmetric movement ($\dot{\theta}_{1j}^+ = \dot{\theta}_{1j}^- = \dot{\theta}_{1j}$, $j = 1, 2$).

the degeneracy of a force bundle (active constraint singularity) and a torque bundle (passive constraint singularity). In Sect. 3, we propose two formulations for the optimal design of N-UU PMs; in particular, results for 3- and 4-UU PMs are presented. Finally, Sect. 4 presents a simple yet effective way of generating additional constraints for avoiding passive constraint singularities, namely by applying an angle-equalizing device on the inner revolute joints of each UU leg.

2 Constraint and Singularity Analysis of N-UU PMs

In reference to (C1) and (C2) in Sect. 1, the most general N-UU PMs may have a geometry as illustrated in Fig. 1(c). Without loss of generality, we assume that the mechanism has N-fold axial symmetry about the \mathbf{z} -axis (the fixed reference frame $\mathbf{o}\text{-}\mathbf{xyz}$ is shown in Fig. 1, with \mathbf{xy} being the symmetry plane in the home configuration). The direction vectors of the revolute joints in leg i will be denoted as \mathbf{w}_{i1}^+ , \mathbf{w}_{i2}^+ , \mathbf{w}_{i2}^- and \mathbf{w}_{i1}^- , and their joint angles will be correspondingly denoted as θ_{i1}^+ , θ_{i2}^+ , θ_{i2}^- and θ_{i1}^- . Due to mirror symmetry, the two pairs $(\mathbf{w}_{i1}^+, \mathbf{w}_{i1}^-)$ and

$(\mathbf{w}_{i2}^+, \mathbf{w}_{i2}^-)$ intersect on the symmetry plane at \mathbf{s}_{i1} and \mathbf{s}_{i2} , respectively. As long as only rotational motion is concerned, a total of three angular parameters, namely α, β and γ , are needed to specify the kinematics of the mechanism.

It was proved in [15] that the N-UU PM is a zero-torsion mechanism [3], so that its rotation matrix has the form $e^{2\psi\hat{\mathbf{w}}}$, where $\mathbf{w} = \mathbf{x}\cos\phi + \mathbf{y}\sin\phi, \phi \in [0, 2\pi], \psi \in [0, \pi/2]$ and $\hat{\mathbf{w}}$ is a 3×3 skew-symmetric matrix satisfying $\hat{\mathbf{w}}\mathbf{v} = \mathbf{w} \times \mathbf{v}, \forall \mathbf{v} \in \mathbb{R}^3$. We refer to $e^{2\psi\hat{\mathbf{w}}}$ as the *tilt motion* about the *tilt axis* \mathbf{w} , with the *tilt angle* being 2ψ . By utilizing symmetric space theory [16], we characterized the geometric properties of the N-UU motion in [14], as follows. The symmetric chain $(\mathbf{w}_{i1}^+, \mathbf{w}_{i2}^+, \mathbf{w}_{i2}^-, \mathbf{w}_{i1}^-)$ generates the tilt motion under the symmetric movement condition

$$\theta_{ij}^+ = \theta_{ij}^- = \theta_{ij}, \quad i = 1, \dots, N, j = 1, 2 \tag{1}$$

i.e., for any tilt axis $\mathbf{w} = \mathbf{x}c_\phi + \mathbf{y}s_\phi, \phi \in [0, 2\pi]$ and half-tilt angle ψ (within a singularity-free workspace), there is a unique pair $(\theta_{11}, \theta_{12}) \in [0, 2\pi]^2$ such that

$$e^{\theta_{i1}\hat{\mathbf{w}}_{i1}^+} e^{\theta_{i2}\hat{\mathbf{w}}_{i2}^+} e^{\theta_{i2}\hat{\mathbf{w}}_{i2}^-} e^{\theta_{i1}\hat{\mathbf{w}}_{i1}^-} = e^{2\psi\hat{\mathbf{w}}} \tag{2}$$

The symmetry plane passes through \mathbf{o} , the instantaneous location of \mathbf{o} , and is perpendicular to $e^{\psi\hat{\mathbf{w}}}\mathbf{z}$ at a generic configuration $e^{2\psi\hat{\mathbf{w}}}$. The distal center \mathbf{s}^- rotates about the fixed proximal center \mathbf{s}^+ , with unit direction \mathbf{w} of the end-effector, but with a magnitude ψ being half that of the end-effector; \mathbf{o} remains the center of the line segment $\mathbf{s}^- - \mathbf{s}^+ = e^{\psi\hat{\mathbf{w}}}(2d\mathbf{z})$ (with a fixed length of $2d$) under full-cycle motion (see Fig. 2(a)).

Each UU leg contributes to a 2-D constraint wrench system spanned by two zero-pitch wrenches, with one (denoted ζ_{i1}) passing through \mathbf{s}_{i1} and \mathbf{s}_{i2} and the other (denoted ζ_{i2}) passing through \mathbf{s}^+ and \mathbf{s}^- ; ζ_2 is identical for all legs [4].

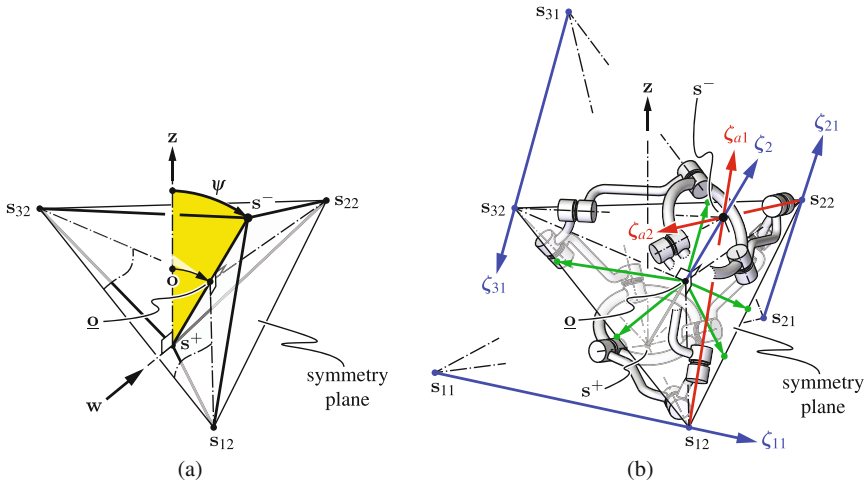


Fig. 2. (a) displacement kinematics of the 3-UU PM; (b) twists (green), constraint wrenches (blue) and actuation wrenches (red) of the 3-UU PM. (Color figure online)

The constraint wrenches are denoted by blue arrows in Fig. 2(b). When choosing \mathbf{w}_{11}^+ and \mathbf{w}_{21}^+ as the actuation joints, the actuation wrenches ζ_{a1} and ζ_{a2} may be chosen as the zero-pitch wrenches lying on $\mathbf{s}_{12}\mathbf{s}^-$ and $\mathbf{s}_{22}\mathbf{s}^-$ respectively, as illustrated by the red arrows in Fig. 2. For convenience, we shall denote the unit force vector of a constraint wrench $\zeta_{(\cdot)}$ by $\mathbf{f}_{(\cdot)}$. More details can be found in [14].

Using the aforementioned notation for active and passive constraint wrenches, we can formulate the *static singularity* (leading to a loss of control of the PM, [5]) of a N- \mathcal{UU} PM as

$$\sigma_1 (\zeta_{11} \zeta_{21} \cdots \zeta_{N1} \zeta_2 \zeta_{a1} \zeta_{a2}) = 0 \quad (3)$$

where σ_1 denotes the smallest singular value of a matrix. Since all constraint and actuation wrenches have zero pitch, we can readily apply the Grassmann-Cayley Algebra (GCA) techniques [1,9] to further decompose the static singularity. It is proved in [14] that the static singularity may be decomposed into an *active constraint singularity* (ACS) characterized by:

$$\sigma_1 (\mathbf{f}_2 \mathbf{f}_{a1} \mathbf{f}_{a2}) = 0 \quad (4)$$

and a *passive constraint singularity* (PCS) characterized by:

$$\sigma_1 (\boldsymbol{\tau}_{11} \boldsymbol{\tau}_{21} \cdots \boldsymbol{\tau}_{N1}) = 0 \quad (5)$$

where $\boldsymbol{\tau}_{i1}$ is the normalized torque (about \mathbf{s}^-) generated by ζ_{i1} , and therefore is given by $\mathbf{w}_{i1}^- \times \mathbf{w}_{i2}^- / \|\mathbf{w}_{i1}^- \times \mathbf{w}_{i2}^-\|$.

3 Optimal Design of General Geometry N- \mathcal{UU} PMs

As shown in Sect. 2, ACS and PCS may be characterized by the rank degeneracy of a bundle of forces and a bundle of torques, respectively. Geometrically, this corresponds to the force or torque bundles degenerating to a pencil. In the former case, there exists a vector $\mathbf{v} \in \mathbb{R}^3$ (perpendicular to the pencil) such that

$$\mathbf{v}^T \mathbf{f}_{a1} = \mathbf{v}^T \mathbf{f}_{a2} = \mathbf{v}^T \mathbf{f}_2 = 0 \quad (6)$$

The closeness to an ACS may then be measured by the following index:

$$\begin{aligned} i_a &\triangleq \sigma_1 (\mathbf{f}_{a1} \mathbf{f}_{a2} \sqrt{N}\mathbf{f}_2) = \min_{\|\mathbf{v}\|=1} \left(\mathbf{v}^T \left(\mathbf{f}_{a1}\mathbf{f}_{a1}^T + \mathbf{f}_{a2}\mathbf{f}_{a2}^T + \sum_{i=1}^N \mathbf{f}_2\mathbf{f}_2^T \right) \mathbf{v} \right)^{1/2} \\ &= \min_{\|\mathbf{v}\|=1} \left((\mathbf{v}^T \mathbf{f}_{a1})^2 + (\mathbf{v}^T \mathbf{f}_{a2})^2 + \sum_{i=1}^N (\mathbf{v}^T \mathbf{f}_2)^2 \right)^{1/2} \end{aligned} \quad (7)$$

which equals the minimum value, over all possible choices of \mathbf{v} , of the root sum square of the projected length of \mathbf{f}_{a1} , \mathbf{f}_{a2} and (N copies of) \mathbf{f}_2 onto \mathbf{v} (see Fig. 3(a)) [13]. Similarly, the PCS measure, denoted as i_p , can be defined as:

$$i_p \triangleq \sigma_1 (\boldsymbol{\tau}_{11} \boldsymbol{\tau}_{21} \cdots \boldsymbol{\tau}_{N1}) = \min_{\|\mathbf{w}\|=1} \left(\mathbf{w}^T \left(\sum_{i=1}^N \boldsymbol{\tau}_{i1}\boldsymbol{\tau}_{i1}^T \right) \mathbf{w} \right)^{1/2} \quad (8)$$

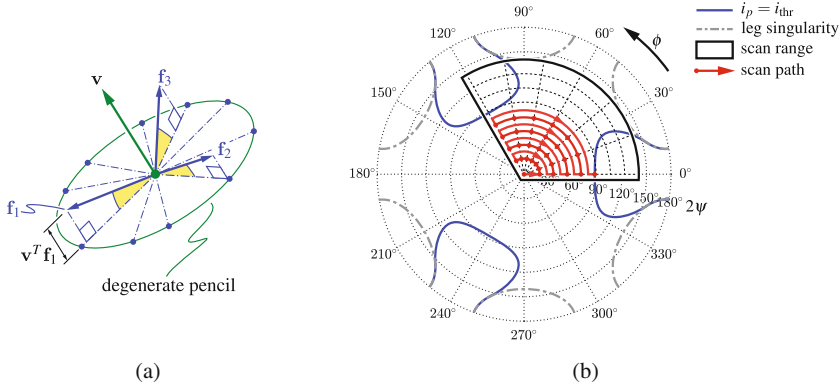


Fig. 3. (a) Least square approximation of a subbundle of unit vectors f_i 's to a degenerate pencil with normal v ; (b) sequential scan over the workspace of a 3- \mathcal{UU} PM for maximal PCS-free tilt angle.

The advantage of adopting the above singularity measures is two-fold. First, their definition is independent of the number of \mathcal{UU} legs in the PM. Second, since only pure forces or pure torques are involved, it is obviously frame and scale independent.

The optimal design may be formulated as follows:

(O1) Maximization of the tilt angle subject to a singularity margin constraint:

$$\max_{(\alpha, \beta, \gamma)} 2\psi_S \tag{9}$$

where

$$\begin{aligned} 2\psi_A &= \max \{2\psi \mid i_A(\phi, \psi) \geq i_{thr}, \forall \phi \in [0, 2\pi]\} \\ 2\psi_P &= \max \{2\psi \mid i_P(\phi, \psi) \geq i_{thr}, \forall \phi \in [0, 2\pi]\} \\ 2\psi_S &= \min \{2\psi_A, 2\psi_P\} \end{aligned} \tag{10}$$

Once a singularity margin i_{thr} is designated, we may proceed with (O1) as follows. First, we set the parameter space $\{(\alpha, \beta, \gamma)\}$ to a bounded cube $[\alpha_{min}, \alpha_{max}] \times [\beta_{min}, \beta_{max}] \times [\gamma_{min}, \gamma_{max}]$, and discretize it to a reasonably fine grid. Next, for a particular point (α, β, γ) on the grid, we may sequentially scan a grid of configurations (ϕ, ψ) for a minimal tilt angle 2ψ that violates the ACS or PCS margin i_{thr} for a certain ϕ . This value corresponds exactly to $2\psi_A$ or $2\psi_P$. To accelerate the scan process, we utilize the N-fold symmetry of the PCS (resulting from that of the N- \mathcal{UU} PM) by restricting ϕ to $[0, 2\pi/N]$ (see Fig. 3(b)). The distribution of $2\psi_A, 2\psi_P$ and $2\psi_S$ versus $(\beta, \gamma) \in [-50^\circ, 50^\circ]^2, \alpha = 90^\circ$ are illustrated in Fig. 4 for the case $N = 3$. Note from the \mathcal{UU} leg geometry that $(\alpha, \beta, \gamma), (\alpha, -\beta, -\gamma), (\pi - \alpha, \beta, -\gamma)$ and $(\pi - \alpha, -\beta, \gamma)$ all lead to the same singularity behavior (as can be observed in Fig. 4). To resolve such redundancy, we shall hereafter narrow down the parameter space to $\alpha \in [45^\circ, 90^\circ], \beta \in [-45^\circ, 45^\circ]$ and $\gamma \in [0, 45^\circ]$. It may be inferred from Fig. 4(a) that a larger ACS-free tilt angle is achieved with β and γ taking values closer to zero. However, such

parameter values lead to a very low PCS-free tilt angle (Fig. 4(b)). A compromise is achieved with β remaining close to and γ substantially deviating from zero (Fig. 4(c)).

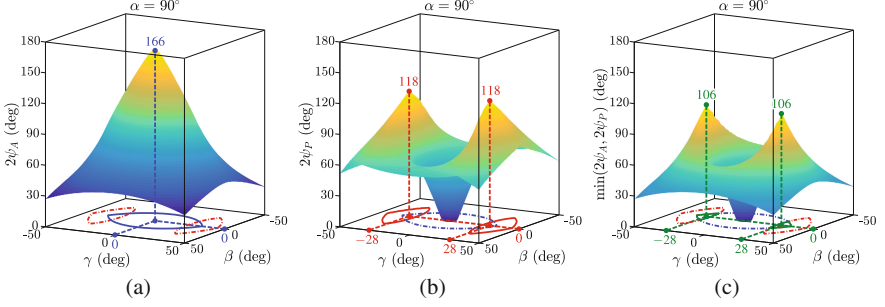


Fig. 4. Distribution of maximal tilt angle of a 3- \mathcal{UU} PM over $(\beta, \gamma) \in [-50^\circ, 50^\circ]^2$ with α fixed at 90° and $i_{\text{thr}} = 0.1$. (a) $2\psi_A$; (b) $2\psi_P$; (c) $2\psi_S$.

We emphasize that an optimal design for N- \mathcal{UU} PMs following (O1) should be based on a physically meaningful (see [13] for some discussion) singularity margin value i_{thr} , which are usually not available at conceptual design stage [2, Ch. 6]. Alternatively, we may seek to maximize the minimal singularity measure over a fixed prescribed workspace (e.g. $2\psi \in [0, \pi/2]$):

(O2) **Maximization of the minimal singularity measure over a prescribed work-space:**

$$\begin{aligned} & \max_{(\alpha, \beta, \gamma)} i_{\text{thr}} \\ & \text{s.t.} \quad \begin{cases} i_{\text{thr}} \leq \min_{(\phi, \psi)} i_A(\phi, \psi) \\ i_{\text{thr}} \leq \min_{(\phi, \psi)} i_P(\phi, \psi) \end{cases} \quad \begin{cases} 0 \leq \phi \leq 2\pi \\ 0 \leq 2\psi \leq \pi/2 \end{cases} \end{aligned} \quad (11)$$

(O2) can be solved with an approach similar to that of (O1). The optimal margin value and corresponding parameters for 3- and 4- \mathcal{UU} PMs are given in Table 1.

4 Angle-Equalizing Device

According to the symmetric movement condition (1), each revolute joints pair $(\mathbf{w}_{ij}^+, \mathbf{w}_{ij}^-)$ is instantaneously equivalent to a single revolute joint along $\mathbf{w}_{ij}^+ + \mathbf{w}_{ij}^-$ (see Fig. 1(d)). However, as the symmetric movement condition is enforced by the loop-closure constraint of the N- \mathcal{UU} PM, such equivalence does not hold in constraint analysis.

Table 1. Optimal design results of 3- and 4- \mathcal{UU} PMs for formulation (O2).

Number of legs	Angle-Eq. device	$\max i_{thr}$	α	β	γ
3	No	0.210	90	0	29
	Yes	0.454	90	0	14
4	No	0.521	82	12	20
	Yes	0.637	88	-2	13

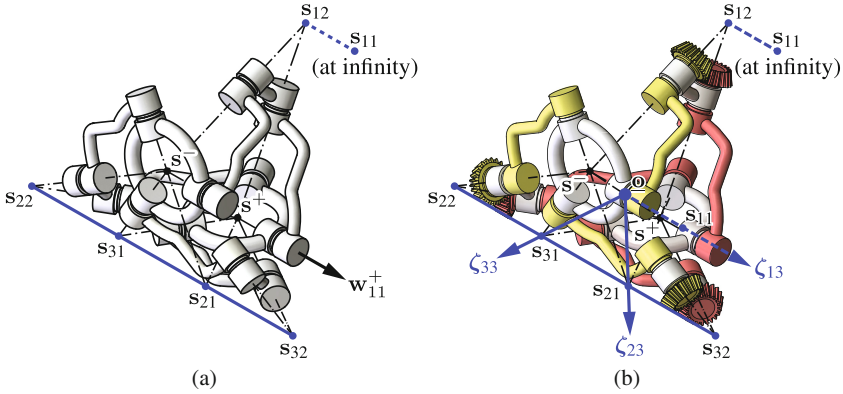


Fig. 5. (a) A configuration of PCS for a 3- \mathcal{UU} PM ($\alpha = 90^\circ$, $\beta = 0^\circ$, $\gamma = 20^\circ$); (b) avoidance of the PCS configuration by imposing angle-equalizing devices.

Motivated by the above observation, we consider imposing an angle-equalizing device onto the inner revolute pair $(\mathbf{w}_{i2}^+, \mathbf{w}_{i2}^-)$ of each leg i , via for example a bevel gear pair. This does turn each \mathcal{UU} leg into a 3-DoF leg that is instantaneously equivalent to a \mathcal{RRR} leg with unit direction vectors $(\mathbf{w}_{i1}^+, \mathbf{w}_{i2}, \mathbf{w}_{i1}^-)$, $\mathbf{w}_{i2} = (\mathbf{w}_{i2}^+ + \mathbf{w}_{i2}^-) / \|\mathbf{w}_{i2}^+ + \mathbf{w}_{i2}^-\|$. It is easy to verify for each \mathcal{UU} leg that an additional constraint wrench, denoted as ζ_{i3} , emerges, and it can be identified as the zero-pitch wrench along \mathbf{os}_{i1} . Since ζ_{i3} , $i = 1, \dots, N$ all lie in the symmetry plane, they help to avoid PCSs. Figure 5(a) illustrates a 3- \mathcal{UU} PM at a configuration of PCS. In this particular case, \mathbf{s}_{21} , \mathbf{s}_{22} , \mathbf{s}_{31} and \mathbf{s}_{32} become collinear and therefore ζ_{21} and ζ_{31} become linearly dependent. With the imposition of an angle-equalizing devices on the PM, as illustrated in Fig. 5(b), the PCS is avoided with the presence of three extra passive constraint wrenches ζ_{13} , ζ_{23} and ζ_{33} . Consequently, the definition for the PCS measure given in Eq. (8) may be changed to:

$$\begin{aligned}
 i_p &\triangleq \sigma_1 \left(\boldsymbol{\tau}_{11} \ \boldsymbol{\tau}_{13} \ \boldsymbol{\tau}_{21} \ \boldsymbol{\tau}_{23} \ \dots \ \boldsymbol{\tau}_{N1} \ \boldsymbol{\tau}_{N3} \right) \\
 &= \min_{\|\mathbf{w}\|=1} \left(\mathbf{w}^T \left(\sum_{i=1}^N (\boldsymbol{\tau}_{i1} \boldsymbol{\tau}_{i1}^T + \boldsymbol{\tau}_{i3} \boldsymbol{\tau}_{i3}^T) \right) \mathbf{w} \right)^{1/2} \tag{8'}
 \end{aligned}$$

where τ_{i3} is a normalized torque (about \mathbf{s}^-) generated by ζ_{i3} , and is given by $(\mathbf{s}_{i1} - \mathbf{o}) \times (\mathbf{s}^- - \mathbf{o}) / \|(\mathbf{s}_{i1} - \mathbf{o}) \times (\mathbf{s}^- - \mathbf{o})\|$. The optimal design results, for (O2), of 3- and 4- \mathcal{UU} PMs with angle-equalizing devices are also presented in Table 1. The 4- \mathcal{UU} PM with or without angle-equalizing device has higher singularity margin than its three-legged counterpart. Second, since the angle-equalizing device helps to avoid PCSs, γ is allowed to take a smaller value to increase the ACS margin (Cf. the discussion about Fig. 4).

5 Conclusions

We conclude our paper with two remarks. First, the optimal parameter values of general-geometry N- \mathcal{UU} PMs listed in Table 1, to some extent, agree with those acquired with a special geometry ($\alpha = 90^\circ, \beta = 0^\circ$; see [14]). Second, the actual workspace of N- \mathcal{UU} PMs is also limited by potential link collisions. In practice, this issue may be solved by iterative design/collision checking in CAD modeling software. Otherwise, a systematic solution may be derived by following the approach proposed in [7].

Acknowledgements. The authors gratefully acknowledge the financial support of the Italian Ministry of Education, Universities and Research through the PRIN Grant no. 20124SMZ88. This work is also in partial fulfillment to China National Natural Science Foundation Grant no. 51375413, which supported Dr. Wu when he was working at HKUST.

References

1. Ben-Horin, P., Shoham, M.: Application of Grassmann-Cayley algebra to geometrical interpretation of parallel robot singularities. *Int. J. Robot. Res.* **28**(1), 127–141 (2009)
2. Bohigas, O.: Numerical computation and avoidance of manipulator singularities. Ph.D. thesis, Universidad Polit cnica de Catalu na (2013)
3. Bonev, I., Zlatanov, D., Gosselin, C.: Advantages of the modified Euler angles in the design and control of PKMs. In: 2002 Parallel Kinematic Machines International Conference, pp. 171–188. Citeseer (2002)
4. Carricato, M.: Decoupled and homokinetic transmission of rotational motion via constant-velocity joints in closed-chain orientational manipulators. *J. Mech. Robot.* **1**(4) (2009). 041,008
5. Conconi, M., Carricato, M.: A new assessment of singularities of parallel kinematic chains. *IEEE Trans. Robot.* **25**(4), 757–770 (2009)
6. Culver, I.H.: Constant velocity universal joint. US Patent 3,477,249 (1969)
7. Gosselin, C.M., Hamel, J.F.: The agile eye: a high-performance three-degree-of-freedom camera-orienting device. In: 1994 IEEE International Conference on Robotics and Automation Proceedings, pp. 781–786. IEEE (1994)
8. Hunt, K.: Constant-velocity shaft couplings: a general theory. *J. Eng. Ind.* **95**(2), 455–464 (1973)
9. Kanaan, D., Wenger, P., Caro, S., Chablat, D.: Singularity analysis of lower mobility parallel manipulators using Grassmann-Cayley algebra. *IEEE Trans. Robot.* **25**(5), 995–1004 (2009)

10. Kong, X., Yu, J., Li, D.: Reconfiguration analysis of a two degrees-of-freedom 3–4R parallel manipulator with planar base and platform. *J. Mech. Robot.* **8**(1) (2016). 011,019
11. Rosheim, M.E., Sauter, G.F.: New high-angulation omni-directional sensor mount. In: *International Symposium on Optical Science and Technology*, pp. 163–174. International Society for Optics and Photonics (2002)
12. Sone, K., Isobe, H., Yamada, K.: High angle active link. *Special Issue Special Supplement to Industrial Machines* (2004)
13. Voglewede, P.A., Ebert-Uphoff, I.: Overarching framework for measuring closeness to singularities of parallel manipulators. *IEEE Trans. Robot.* **21**(6), 1037–1045 (2005)
14. Wu, Y., Carricato, M.: Synthesis and singularity analysis of n - \mathcal{UU} parallel wrists: a symmetric subspace approach. In: *International Design Engineering Technical Conferences & Computers and Information in Engineering Conference*. American Society of Mechanical Engineers (2017, Submitted)
15. Wu, Y., Li, Z., Shi, J.: Geometric properties of zero-torsion parallel kinematics machines. In: *2010 IEEE/RSJ International Conference on Intelligent Robots and Systems (IROS)*, pp. 2307–2312. IEEE (2010)
16. Wu, Y., Löwe, H., Carricato, M., Li, Z.: Inversion symmetry of the Euclidean group: theory and application to robot kinematics. *IEEE Trans. Robot.* **32**(2), 312–326 (2016)

Robust Multi-objective Design Optimization of the 3-UPU TPM Based on the GA-Krawczyk Method

S. El Hraiech¹(✉), A.H. Chebbi¹, Z. Affi¹, and L. Romdhane²

¹ LGM, National Engineering School of Monastir,
University of Monastir, Monastir, Tunisia
safa_el_hraiech@hotmail.fr,
ahmed.h.chebbi@gmail.com, zouhaier.affi@gmail.com

² Department of Mechanical Engineering,
American University of Sharjah, Sharjah, UAE
lromdhane@aus.edu

Abstract. This paper deals with the robust design optimization of the 3-UPU translational parallel manipulator. An approach, that regroups the genetic algorithm multi-objective optimization and the Krawczyk operator (GAMOK), is used to represent the optimal design vector of parameters and their uncertainties. This optimization leads to minimize the position error and relax the parameters intervals of tolerance. Based on this GAMOK algorithm, the designer can pick out the optimal design vector according to the desired accuracy in the workspace of the manipulator.

Keywords: Interval analysis · Krawczyk operator · Genetic algorithm · Uncertainties · Optimization

1 Introduction

Parallel manipulators have many advantages such as, greater rigidity, higher stiffness and essentially higher accuracy compared to serial ones. There are several types of parallel manipulators; the translational robot, the rotational robot and the mixed ones [9, 10]. The position error of parallel manipulator caused by design parameters uncertainties cannot be neglected. Therefore, it is quite important to optimize the design parameters and their uncertainties as function of the robot performances. Several optimization methods have been used. Genetic algorithm (GA) is an evolutionary algorithm inspired from natural evolution, used to solve optimization problems [1]. The main advantages of the genetic algorithm are the capability to escape local optima and its powerful searching ability. Laribi et al. proposed a combined GA-fuzzy algorithm in order to find the optimal dimensions of a five bare mechanism for a desired closed curve [5]. El Kribi et al. developed a multi-objective genetic algorithm of a mechatronic system with continuous and discrete variables [2].

In this paper, an approach that couples the genetic algorithm and the “Krawczyk” method used for the robust design optimization of the 3-UPU TPM. In fact, the robot

optimal design vector is given simultaneously by the design parameters nominal values (DPNV) and the parameters uncertainties. The rest of this paper is organized as follow: in Sect. 2, the structure of the manipulator is described and its kinematic modeling is presented. In Sect. 3, an hybrid GA-”Krawczyk” algorithm is presented. A case study is finally presented which shows the efficiency of the proposed algorithm. In Sect. 4, some concluding remarks are presented.

2 Architecture of the Manipulator

The 3-UPU translational parallel manipulator (Fig. 1) is composed of three kinematic chains of type UPU (U and P stand for universal and prismatic joint respectively) that connect the base to the platform. This manipulator has extensible legs which are connected to the base by universal joints. Each universal joint comprises two revolute pairs with intersecting and perpendicular axes. To restrict the platform motions to only translations, the following conditions have to be satisfied [4, 8]: the axes of the two intermediate revolute pairs are parallel to each other and the axes of the two ending revolute pairs are parallel to each other.

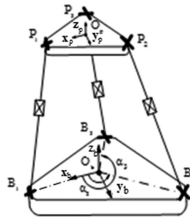


Fig. 1. Architecture of the 3-UPU translational parallel manipulator

2.1 Modeling of the 3-UPU Translational Manipulator

Let $S_b(O_b, x_b, y_b, z_b)$ and $S_p(O_p, x_p, y_p, z_p)$ two reference systems fixed on the base and the platform, respectively. The origin O_b (O_p) corresponds to the reference point of the base (platform). The first axis x_b goes through point B_1 ; z_b axis is normal to the plane defined by the points B_i and pointing from the base to the platform, while y_b axis is taken according to the right hand rule. The position of the moving platform expressed in the reference system S_b is given as:

$$\mathbf{x} = \mathbf{b}_i + \mathbf{l}_i - \mathbf{Q}\mathbf{p}_i \quad i = 1, 2, 3 \tag{1}$$

where:

$$\mathbf{b}_i = [O_b B_i]_{S_b}; \mathbf{p}_i = [O_p P_i]_{S_p}; \mathbf{l}_i = [B_i P_i]_{S_b}; \mathbf{x} = [O_b O_p]_{S_b} \tag{2}$$

\mathbf{Q} is the rotation matrix that takes \mathbf{S}_p to \mathbf{S}_b . Since the 3-UPU manipulator has only translations, the rotation matrix \mathbf{Q} is constant and can be considered as the identity. According to Eq. (1), the inverse kinematic model is given by:

$$l_i = \sqrt{(x - (r_b - r_p) \cdot \cos(\alpha_i))^2 + (y - (r_b - r_p) \cdot \sin(\alpha_i))^2 + z^2} \quad (3)$$

where l_i is the length of the i -th leg; α_i is the angular position of the i -th leg; x , y and z are the coordinates of the reference point of the platform O_p in \mathbf{S}_b .

2.2 Prediction of the Position Error

In this section, the method of intervals is applied to predict the upper and lower bounds of the orientation error of the manipulator. The interval operations are implemented using Matlab library INTLAB [6]. To reduce the overestimation, several contractors based on fixed-point iteration can be used. In this work, the ‘‘Krawczyk’’ contractor will be used. Let f be a function with variables (position error of the manipulator) and parameters given by vector \mathbf{q} . The variables and the parameters intervals are presented by $[\mathbf{x}]$ and $[\mathbf{q}]$ respectively. The solution of the system of equation $\mathbf{f}(\mathbf{q}, \mathbf{x}) = 0$ is given as:

$$\sum(\mathbf{f}, [\mathbf{p}], \tilde{\mathbf{x}}) = \{\mathbf{x} \in \mathbb{R}^n : \exists \mathbf{p} \in [\mathbf{p}], \mathbf{f}(\mathbf{p}, \mathbf{x}) = 0\} \quad (4)$$

These solutions are closed to the nominal solution when the values of the parameters changes in its intervals. To avoid the overestimation, we will use the inverse kinematic model in its quadratic form:

$$l_i^2 - (x - (r_b - r_p) \cdot \cos(\alpha_i))^2 - (y - (r_b - r_p) \cdot \sin(\alpha_i))^2 - z^2 \quad (5)$$

The system of equation given above takes the following form $\mathbf{f}(\mathbf{q}, \mathbf{x}) = 0$.

Let $(\tilde{\mathbf{q}}, \tilde{\mathbf{x}})$ be a nominal solution of the equation given above. The linearization of the function in the neighborhood of the nominal solution is given as:

$$\mathbf{f}(\tilde{\mathbf{q}}, \tilde{\mathbf{x}}) + \mathbf{f}_x(\tilde{\mathbf{q}}, \tilde{\mathbf{x}})(\mathbf{x} - \tilde{\mathbf{x}}) + \mathbf{f}_q(\tilde{\mathbf{q}}, \tilde{\mathbf{x}})(\mathbf{q} - \tilde{\mathbf{q}}) = 0 \quad (6)$$

where \mathbf{f}_x and \mathbf{f}_q are the derivative of the function \mathbf{f} with respect to \mathbf{x} and \mathbf{q} , respectively. Thus, the solution of $\mathbf{f}(\mathbf{q}, \mathbf{x}) = 0$ can be computed by the following equation:

$$\mathbf{x} = \tilde{\mathbf{x}} - \mathbf{C} \cdot \mathbf{f}(\tilde{\mathbf{q}}, \tilde{\mathbf{x}}) - (\mathbf{C} \cdot \mathbf{f}_x(\mathbf{q}, \mathbf{x}) - \mathbf{I})(\mathbf{x} - \tilde{\mathbf{x}}) - \mathbf{C} \cdot \mathbf{f}_q(\mathbf{q}, \tilde{\mathbf{x}})(\mathbf{q} - \tilde{\mathbf{q}}) \quad (7)$$

where \mathbf{C} is a preconditioning nonsingular matrix [3, 7]

The mathematical concept of the ‘‘Krawczyk’’ operator can be written as:

$$\mathbf{K}_{f, [\mathbf{q}]}([\mathbf{x}]) = \tilde{\mathbf{x}} - (\mathbf{C} \cdot [\mathbf{X}] - \mathbf{I}) \cdot ([\mathbf{x}] - \tilde{\mathbf{x}}) - [\mathbf{Y}] \quad (8)$$

where:

$$\mathbf{C} = \text{mid}([\mathbf{X}])^{-1}, [\mathbf{A}] = \left[\frac{df}{dq} \right]([\mathbf{q}], \tilde{\mathbf{x}}), [\mathbf{Y}] = \mathbf{C} \cdot [\mathbf{f}](\tilde{\mathbf{q}}, \tilde{\mathbf{x}}) + \mathbf{C} \cdot [\mathbf{A}] \cdot ([\mathbf{q}] - \tilde{\mathbf{q}}) \quad (9)$$

3 Multi-objective Design Optimization

A combined GA-“Krawczyk” algorithm will be used to determine the (DPNV) and their relative uncertainties that guarantee a good accuracy (E_p) with the maximal tolerance intervals of design parameters (IT). The population is evaluated by the interval linearization method: In fact, the position error of each design vector of the population is calculated with the “Krawczyk” algorithm (Fig. 2).

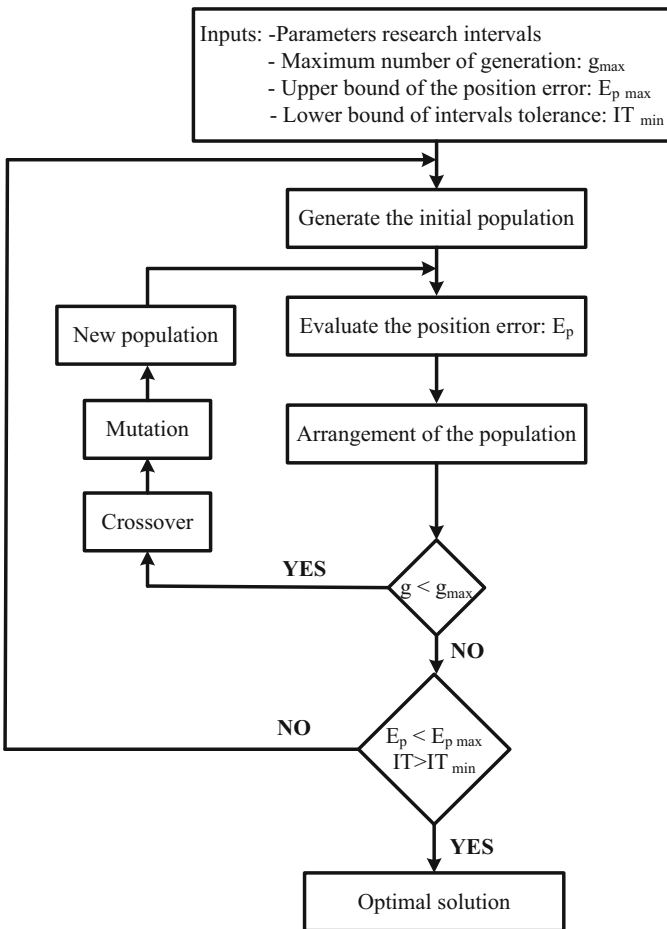


Fig. 2. Scheme of optimization process with genetic algorithm

Let the vector \mathbf{q} regroups the (DPNV) and their uncertainties:

$$[\mathbf{q}] = \left[\tilde{r}_b + \Delta r_{b \max}, \tilde{r}_b - \Delta r_{b \min}, \tilde{r}_p + \Delta r_{p \max}, \tilde{r}_p - \Delta r_{p \min}, \tilde{\alpha}_1 + \Delta \alpha_{1 \min}, \tilde{\alpha}_1 - \Delta \alpha_{1 \max}, \tilde{\alpha}_2 + \Delta \alpha_{2 \min}, \tilde{\alpha}_2 - \Delta \alpha_{2 \max}, \tilde{\alpha}_3 + \Delta \alpha_{3 \min}, \tilde{\alpha}_3 - \Delta \alpha_{3 \max} \right] \quad (10)$$

where \tilde{q}_i is the nominal value of the corresponding design parameter and $\Delta q_{i \max}$ and $\Delta q_{i \min}$ are the upper and lower uncertainties values. The uncertainties of the design parameters nominal values are defined by an interval vector $[\mathbf{q}]$ and the position error of the manipulator by $[\mathbf{X}]$.

The optimization problem can be formulated as:

$$\min \mathbf{F}(\mathbf{X}) = \min [f_j(\mathbf{X})]^T, (j = 1..n) \quad (11)$$

Subjected to

$$\mathbf{g}(\mathbf{X}) < 0 \quad (12)$$

where T is the transpose operator, n is the number of objective functions, \mathbf{X} is the vector of design variables, $\mathbf{F}(\mathbf{x})$ is the vector of objective functions and $\mathbf{g}(\mathbf{X})$ is the vector of constraint functions [11].

The goal of this work is to minimize the robot position error and maximize the design parameters tolerances' intervals simultaneously within a given workspace. The first objective function f_1 to be minimized corresponds to the platform position error, given by:

$$f_1 = \text{Max} \left(\sqrt{E_{px}^2 + E_{py}^2 + E_{pz}^2} \right) \quad (13)$$

where: $E_{px} = \text{Max}(|x_{\min} - x|, |x_{\max} - x|)$, $E_{py} = \text{Max}(|y_{\min} - y|, |y_{\max} - y|)$,

$$E_{pz} = \text{Max}(|z_{\min} - z|, |z_{\max} - z|) \quad (14)$$

where x_{\min} , y_{\min} and z_{\min} are the lower bounds of the interval vector $[\mathbf{x}]$, x_{\max} , y_{\max} and z_{\max} are the upper bounds of the interval vector $[\mathbf{x}]$.

The second objective f_2 to be minimized corresponds to the inverse of normalized interval tolerance some. This objective function can be expressed as:

$$f_2 = \frac{1}{\frac{\Delta r_{b \min} + \Delta r_{b \max}}{r_b} + \frac{\Delta r_{p \min} + \Delta r_{p \max}}{r_p} + \frac{\Delta \alpha_{1 \min} + \Delta \alpha_{1 \max}}{\alpha_1} + \frac{\Delta \alpha_{2 \min} + \Delta \alpha_{2 \max}}{\alpha_2} + \frac{\Delta \alpha_{3 \min} + \Delta \alpha_{3 \max}}{\alpha_3}} \quad (15)$$

To avoid the singularity related to the manipulator architecture, the following constraints have to be fulfilled:

$$r_b > r_p, \alpha_i \neq \alpha_j, i \neq j, i, j = 1, 2, 3 \quad (16)$$

To avoid the problem of normalization of α_1 , we choose a configuration where the angle first axe $\alpha_1 \neq 0$.

4 Case Study

The desired workspace of the manipulator is a cube defined by:

$$-150 \leq x, y[\text{mm}] \leq 150 \text{ and } 100 \leq z[\text{mm}] \leq 400 \tag{17}$$

The uncertainties of the actuators lengths is chosen to be constant even the actuator lengths are variables: $\Delta l_{i\min} = \Delta l_{i\max} = 0.01 \text{ mm}$. The bounds of the design parameters and their uncertainties are defined in Table 1.

Table 1. Bounds of the design parameters and their uncertainties

Design parameters	Bounds	Uncertainties of the parameters	Bounds
r_b [mm]	[250 350]	Δr_b [mm]	[-0.3 0.3]
r_p [mm]	[20 80]	Δr_p [mm]	[-0.05 0.05]
α_1 [degree]	[80 100]	$\Delta \alpha_1$ [degree]	[-1 1]
α_2 [degree]	[210 230]	$\Delta \alpha_2$ [degree]	[-1 1]
α_3 [degree]	[320 340]	$\Delta \alpha_3$ [degree]	[-1 1]

A predefined function of genetic algorithm ‘gamultiobj’ is used to minimize the position error of the manipulator and to maximize the uncertainties of the design parameters. The parameters of the optimization algorithm are the population size $N_p = 200$, the maximum generation number $g_{max} = 100$, the crossover probability $P_c = 0.8$ and the mutation probability $P_m = 0.2$. The Pareto front is used to represent the optimal solutions of the problem for the two competitive objective functions f_1 and f_2 . The main difficulty of a multi-objective problem is that the notion of optimal solution does not exist. The designer can simply accept the fact that one solution is preferable to another, so it is a question of finding satisfactory solutions. The Pareto front is given by Fig. 3.

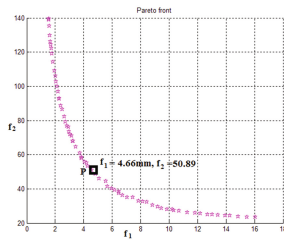


Fig. 3. The optimal design vectors

Hence, the designer can choose an optimal robust design vector from the Pareto front that suite his application. For example, if the designer chooses the solution P as presented in Fig. 3, the allowed magnitude of the position error will be 4.66 mm. In

this case, the chosen solution of design parameters nominal values and their uncertainties is given by:

$$[\mathbf{q}] = [271, 28mm_{-0.23}^{+0.17}, 53.59mm_{-0.04}^{+0.03}, 87.64^{\circ}_{-0.57}^{+0.58}, 203.07^{\circ}_{-0.24}^{+0.24}, 330.0^{\circ}_{-0.2}^{+0.13}] \quad (18)$$

For the chosen solution P, the distribution of the position error of the manipulator is presented in two sections of the workspace defined by $y = 0$ and $z = 200$. As it is shown in Fig. 4, the maximum position error does not exceed 4.66 mm in the defined workspace.

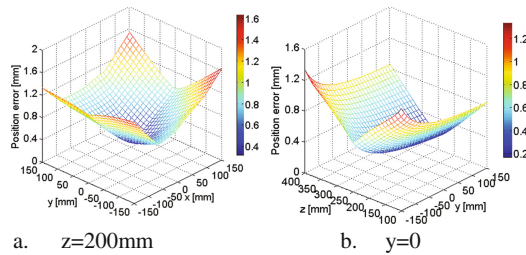


Fig. 4. Distribution of the position error of the manipulator a. $z = 200$ mm b. $y = 0$

5 Conclusion

In this paper, an hybrid GA-“Krawczyk” has been developed. The proposed method aims to determine the optimal design vector composed of the nominal design parameters and their uncertainties in order to minimize the position error of the manipulator. The proposed method is tested on the 3-UPU translational parallel manipulator and has proved its efficiency by determining the manipulator’s design vector, in order to guarantee a better accuracy of the manipulator.

References

1. Boudreau, R., Gosselin, C.M.: The synthesis of planar parallel manipulators with a genetic algorithm. *ASME J. Mech. Des.* **121**, 533–537 (1999)
2. EL-Kribi, B., Houidi, A., Affi, Z., Romdhane, L.: Application of multi-objective genetic algorithms to the mechatronic design of a four bar system with continuous and discrete variables. *Mech. Mach. Theory* **61**, 68–83 (2013)
3. Goldzstejn, A.: Sensitivity Analysis Using a Fixed Point Interval Iteration, HAL report number: hal-00339377 (2008)
4. Ping, J., Hongtao, W.: Kinematics analysis of an offset 3-UPU translational parallel robotic manipulator. *Robot. Auton. Syst.* **42**, 117–123 (2003)

5. Laribi, M.A., Mlika, A., Romdhane, L., Zeghloul, S.: A combined genetic algorithm–fuzzy logic method (GA–FL) in mechanisms synthesis. *Mech. Mach. Theory* **39**, 717–735 (2004)
6. Rump, S.: INTLAB – INTerval LABoratory. In: Cendes, T. (ed.) *Developments in Reliable Computing*, pp. 77–104. Kluwer Academic Publishers, Dordrecht (1999)
7. Tannous, M., Caro, S., Goldsztejn, A.: Sensitivity analysis of parallel manipulators using an interval linearization method. *Mech. Mach. Theory*, Elsevier **71**, 93–114 (2014)
8. Tsai, L.W., Joshi, S.: Kinematic and optimization of a spatial 3-UPU parallel manipulator. *ASME J. Mech. Des.* **122**, 439–446 (1999)
9. Liu, X.-J., Wang, J., Wu, C., Kim, J.: A new family of spatial 3DOF parallel manipulators with two translational and one rotational DOFs. *Robotica* **27**, 241–247 (2009)
10. Zhen Huang, Z., Chen, Z., Liu, J., Liu, S.: A 3DOF rotational parallel manipulator without intersecting axes. *Mech. Robot.* **3** (2011). doi:[10.1115/1.4003848](https://doi.org/10.1115/1.4003848)
11. Ceccarelli, M., Carbone, G., Ottaviano, E.: Multi criteria optimum design of manipulators. *Bull. Polish Acad. Sci. Tech. Sci.* **53**, 9–18 (2005)

Planar Robots

Topology Optimization of a Reactionless Four-Bar Linkage

Sebastien Briot^(✉) and Alexandre Goldsztejn

Laboratoire des Sciences du Numérique de Nantes (LS2N),
UMR CNRS 6004, Nantes, France
{Sebastien.Briot,Alexandre.Goldsztejn}@ls2n.fr

Abstract. Most of existing works on the optimal design of balanced four-bar linkages deal essentially with the minimization of their inertia or input torques under balancing constraints. These approaches are not suitable to include constraints based on the elastic behavior of the mechanism. In order to solve this issue, we propose in this paper to perform the topology optimization of a reactionless four-bar linkage. Conditions for balancing the mechanism are first recalled and a topology optimization algorithm is run in order to maximize the first natural frequency while ensuring the balancing and constraining the mechanism compliance. We show that in order to obtain an interesting design solution, it is necessary to modify the balancing constraints in order to penalize them. Interesting design solutions are obtained in a rather short computational time.

Keywords: Four-bar linkage · Shaking force and shaking moment balancing · Optimal design · Topology optimization

1 Introduction

Transmitting no reactions to the ground is very appealing in many applications such that space robotics or high-speed manipulation [10]. However, complete shaking force and shaking moment balancing is usually obtained by using both counterweights and counter-rotations, thus leading to an increase in the design complexity and to noise and backlash issues due to the use of gears [10].

In order to avoid the drawbacks in using counter-rotations, a reactionless four-bar linkage without them was proposed in [12]. For obtaining this property, conditions on both the geometry and the mass distribution of the linkage must be respected. It was later shown in [9] that this reactionless linkage can be used as an elementary block in order to design reactionless robots.

In [10], the optimal design of the reactionless four-bar linkage was carried out for minimizing its input torques under balancing conditions constraints only. In this work, the shape of the links and counterweights is fixed and the authors focus on the optimal positioning of the counterweights. Other works deal with the optimal design of balanced four-bar linkages for allowing the full [8] or partial [5, 7] dynamic balancing while optimizing energy consumption or input torque amplitude. More complete list of reference can be found in [1].

The main issue with the aforementioned methods comes from the fact that the shape of the links is already fixed (the design variables are their dimension) and deformation or vibration constraints may lead to an unfeasible design in practice (bulky mechanism to resist to the external efforts while ensuring the balancing conditions). For avoiding this issue, it is necessary to optimize the shape of the links. This was done in [5] for the partial balancing of the four-bar linkage, however the approach proposed allows for finding only the external shape of the links. No voids can be included, which is not optimal w.r.t. the minimization of the link deformation while ensuring the decrease of the link mass.

Performing a Topology Optimization (TO) of the linkage can solve this issue [15]. This technique aims at optimizing the material distribution in a link in order to satisfy performance criteria including deformations or vibration constraints.

Our contribution in the present paper is to perform the TO of the reaction-less four-bar linkage for ensuring its full balancing conditions while constraining elastic performance criteria. To the best of our knowledge, this is the first time that the TO of a fully force and moment balanced mechanism is performed. Furthermore, we show that balancing constraints must be partially penalized in order to obtain meaningful designs.

2 Problem Formulation

The general scheme of the four-bar linkage is given in Fig. 1(a). In what follows,

- body \mathcal{B}_1 is the body between joints at O_1 and O_2 , body \mathcal{B}_2 is the body between joints at O_2 and O'_2 and body \mathcal{B}_3 is the body between joints at O_3 and O'_2 ,
- l_1 is the distance between O_1 and O_2 , l_2 is the distance between O_2 and O'_2 and l_3 is the distance between O_3 and O'_2 , l_4 is the distance between O_1 and O_3 ,

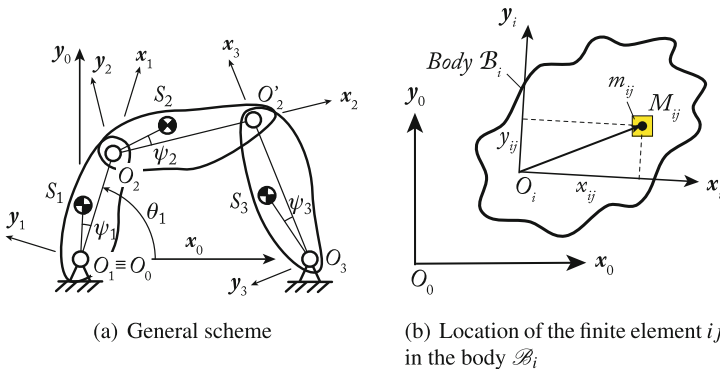


Fig. 1. A general four-bar linkage.

- r_i is the distance between O_i and S_i ($i = 1, 2, 3$)
- for body i , S_i is the center of mass, m_i is its mass, zz_i is the moment of inertia expressed at O_i , mx_i (my_i , resp.) is the static moment around x_i (y_i , resp.), i.e.

$$\begin{bmatrix} mx_i \\ my_i \end{bmatrix} = \int_{\mathcal{B}_i} \overrightarrow{O_i M_{ij}} dm = m_i r_i \begin{bmatrix} \cos \psi_i \\ \sin \psi_i \end{bmatrix}. \tag{1}$$

2.1 Shaking Force and Shaking Moment Balancing Conditions

The conditions given in [12] for achieving the full shaking force and shaking moment balancing of the four-bar linkage without counter-rotations involve both constraints on the mechanism geometry and mass distribution. Three different set of links lengths are possible: Set 1: $\ell_1 = \ell_3$ and $\ell_2 = \ell_4$; Set 2: $\ell_1 = \ell_2$ and $\ell_3 = \ell_4$; Set 3: $\ell_1 = \ell_4$ and $\ell_2 = \ell_3$.

In what follows, we focus only on mechanisms designed with the first set of geometric constraints, which is the set most often studied in the papers (see for instance [9,10]) and corresponds to the anti-parallelogram linkage. In this case, the conditions on the mass distribution given in [12] for the full balancing can be rewritten as:

$$my_1 = 0 \quad \text{and} \quad my_2 = 0 \quad \text{and} \quad my_3 = 0 \tag{2}$$

$$mx_1/\ell_1 + m_2 - mx_2/\ell_2 = 0 \quad \text{and} \quad mx_3/\ell_3 + mx_2/\ell_2 = 0 \tag{3}$$

$$zz_1 - mx_1\ell_1 + zz_2 - mx_2\ell_2 = 0 \quad \text{and} \quad zz_3 - mx_3\ell_3 + zz_2 - mx_2\ell_2 = 0 \tag{4}$$

2.2 Modeling of the Linkage Elastic Behavior

Topology optimization uses the same physical model as in the finite element method for modeling bodies and linkages: each body is meshed using finite elements. The presence or absence of an element ij (i.e. the element j of the body \mathcal{B}_i) is parameterized with a material density variable ρ_{ij} which can take values between 0 (which represents the absence of material) and 1 (which represents the presence of material).

Based on these density variables, we use an interpolation scheme in order to define an artificial material. This method is called the Solid Isotropic Material with Penalization (SIMP, [2]) and is known to be the most effective and the most widely used material interpolation scheme. This interpolation scheme is adopted in order to avoid having optimization results with too much intermediate material density, i.e. in order to have a final design solution with densities only equal to $\rho_{ij} = 1$ or $\rho_{ij} = 0$ without too many intermediate values ($0 < \rho_{ij} < 1$) that are difficult to manage by the designer.

The SIMP scheme is used to parameterize the Young's modulus associated with the stiffness matrix of the element ij and it is defined as follows:

$$E_{ij} = E_{\min} + \rho_{ij}^p (E_0 - E_{\min}), \text{ with } \rho_{ij} \in [0, 1] \quad (5)$$

where E_0 is the Young's modulus of the material, E_{\min} is a very small stiffness value assigned to void regions in order to prevent the stiffness matrix from becoming singular, p (typically $p = 3$) is the penalization factor, and E_{ij} is the Young's modulus of element j of the body i corresponding to the density variable ρ_{ij} .

Then, based on this definition of the Young's modulus for the element ij , we build its stiffness matrix. Finally, once all elementary matrices are defined, the computation of the body and linkage stiffness matrices is the same as in the traditional methodology [13].

The computation of the body and linkage mass matrices (necessary for the computation of the elastodynamic performance) is also based on the use of elementary mass matrices \mathbf{M}_{ij} equal to

$$\mathbf{M}_{ij} = \rho_{ij} \mathbf{M}_{ij}^0 \quad (6)$$

where \mathbf{M}_{ij}^0 is the mass matrix of the element ij computed for a density $\rho_{ij} = 1$.

Once the linkage stiffness and mass matrices are obtained, the elastic performance of the mechanism can be defined, such that the deformations or natural frequencies [13].

It should be mentioned that, in order to decrease the time for computing the elastic performance of the linkage, a Craig-Bampton model reduction technique [6] is applied on each body independently, as done in [4].

2.3 Optimization Problem

The general formulation of a mono-objective TO problem is given by:

$$\min_{\boldsymbol{\rho}} f(\boldsymbol{\rho}) \text{ subject to } \boldsymbol{\rho} \in [0, 1]^n, \mathbf{g}(\boldsymbol{\rho}) \leq \mathbf{0}, \mathbf{h}(\boldsymbol{\rho}) = \mathbf{0}, \quad (7)$$

where

- $\boldsymbol{\rho}$ is the decision variable vector containing all element densities ρ_{ij} ,
- f , \mathbf{g} and \mathbf{h} are functions of $\boldsymbol{\rho}$ characterizing performance indices or structure constraints.

Several optimization algorithms can be used, among which we can cite the Optimality Criteria method [17], the Method of Moving Asymptotes [16] or the Linearization Method [11] (LM) only recently used in the context of TO in [4]. We used the latter in this work. All these techniques have the same specificity: they require the symbolic computation of the functions and their gradients.

Here, we decided to maximize the first natural frequency for the linkage under the following constraints:

- the balancing equalities (2) to (4) must be respected. As shown in [4], the inertial parameters used in these equalities are all linear with respect to the decision variables in \mathfrak{P} .
- the compliance (i.e. twice the potential elastic energy or also the dot product of the nodal wrenches by the nodal displacements) must be lower than a given threshold under a given loading (as often done in TO, see for instance [15]).

For computing the compliance and natural frequency, we consider that the body \mathcal{B}_1 is actuated in O_1 and that the computation of these performances is made for $\theta_1 = \pi/2$ (Fig. 1(a)).

3 Topology Optimization

3.1 Initial Domain

The initial design domain for the proximal and distal links is represented in Figs. 2(a), (c) and (e). Four-bar geometric parameters are taken at $\ell_1 = \ell_3 = 60$ mm and $\ell_2 = \ell_4 = 200$ mm. Each link has got two holes (voids) in which

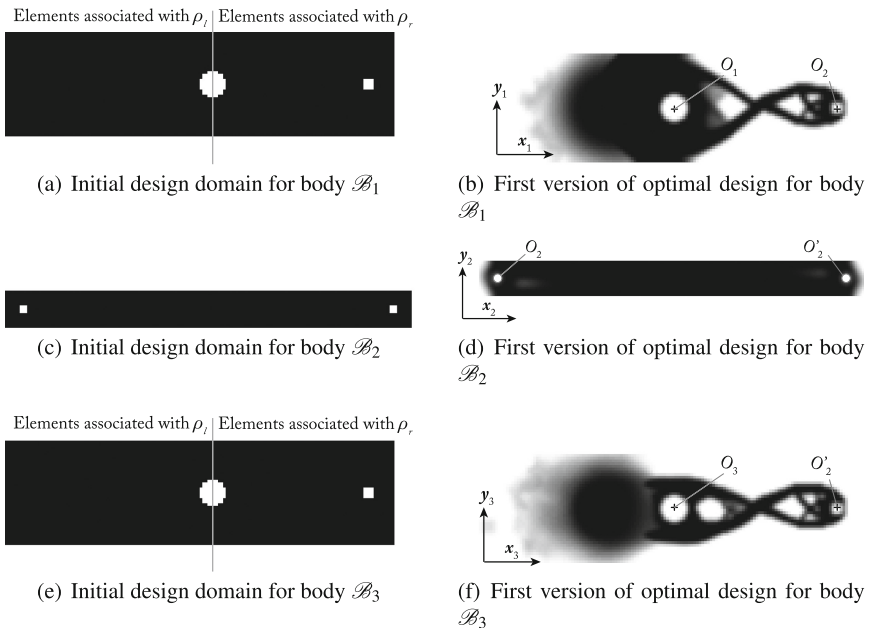


Fig. 2. Initial design domain and first tentative optimal design for all bodies (black elements correspond to $\rho_{ij} = 1$, white elements to $\rho_{ij} = 0$, and gray elements to $0 < \rho_{ij} < 1$)

the joints will be inserted. Bodies \mathcal{B}_1 and \mathcal{B}_3 external shapes are rectangles of dimension (150×40) mm and thickness of 10 mm, while body \mathcal{B}_2 external shape is a rectangle of size (220×20) mm and thickness of 1 mm. For the meshing of the links, QUA4 finite elements (i.e. four-nodes rectangular planar elements) of size 1×1 mm. Links are considered to be made of steel with Young's modulus $E_0 = 210$ GPa, Poisson's ratio $\nu = 0.3$ and density of 7800 kg/m³. As a result, 6000 elements are used for meshing the bodies \mathcal{B}_1 and \mathcal{B}_3 while the body \mathcal{B}_2 is made of 4400 elements (Figs. 2(a), (c) and (e)).

3.2 Optimization Results

We run the TO algorithm with a fixed threshold for the compliance value of $1.6 \cdot 10^{-3}$ Nm for the assembled linkage under the following loading:

- at O_2 : a force of 15 N along \mathbf{x}_0 , a force of 15 N along \mathbf{y}_0 , a moment of 2 Nm around \mathbf{z}_0 on body \mathcal{B}_1 , a moment of 1 Nm around \mathbf{z}_0 on body \mathcal{B}_2 ,
- at O'_2 : a force of 15 N along \mathbf{x}_0 , a force of 15 N along \mathbf{y}_0 , a moment of 2 Nm around \mathbf{z}_0 on body \mathcal{B}_3 , a moment of 1 Nm around \mathbf{z}_0 on body \mathcal{B}_2 ,
- at O_3 : a moment of 2 Nm around \mathbf{z}_0 on body \mathcal{B}_3 .

As usually done in TO, in order to obtain a smoother layout without checkerboards problem, we modified the density variables assigned to the elements with the information of its neighborhoods as was proposed in [3].

All functions have been encoded with Matlab in the Windows 7 environment. The LM optimization algorithm is available under request to the second author.

The optimization process is run and we considered that the algorithm converged when the maximal change between two sequential iterations for any component of the density vector ρ is lower than 0.01. First results of optimization are shown in Figs. 2(b), (d) and (f). The algorithm stopped after 524 iterations, with a maximal constraint violation of $5 \cdot 10^{-3}$ %¹. In totality, the optimization procedure took 28 minutes with a Pentium 4 2.70 GHz, 16 GB of RAM. However, the algorithm had difficulty to converge (large oscillations in the value of the objective function, not displayed for reasons of page limitations) and finally attained a first natural frequency of 67 Hz (which is quite low, as will be shown below).

Obtained results showed that on the left-hand area of the points O_1 and O_3 , the material density for bodies \mathcal{B}_1 and \mathcal{B}_3 is between 0 and 1 (gray elements), thus leading to bodies which are not easy to design by engineers [14]. We increased the number of allowed optimization iterations and obtained no improvement: These portions of materials are mostly here to fulfill the balancing constraints and have less impact on the compliance constraint or the frequency of the full linkage.

We propose here a way to improve this solution which is based on a partial penalization of the balancing constraint equations. As said in Sect. 2.3, the

¹ Constraints are normalized using their values computed for the initial design, except for Eq. (2) whose initial values are null.

equality constraints (2), (3) and (4) are linear, i.e. they can be written under the form:

$$\mathbf{A}\boldsymbol{\rho} = \mathbf{A}_l\boldsymbol{\rho}_l + \mathbf{A}_r\boldsymbol{\rho}_r = \mathbf{0} \quad (8)$$

in which $\boldsymbol{\rho}_l$ contains the decision variables associated with the elements on the left-hand side of the gray lines in Figs. 2(a) and (e) for bodies \mathcal{B}_1 and \mathcal{B}_3 while $\boldsymbol{\rho}_r$ contains all other variables, including those of the body \mathcal{B}_2 . Thus, the vector $\boldsymbol{\rho}_l$ contains the variables associated with the portions of materials which are almost here to fulfill the balancing constraints, which have few impacts on the linkage elastic performance, and which takes intermediary values for density.

In order to force the values of the variables in $\boldsymbol{\rho}_l$ to be only 0 or 1, we modify the balancing equality (8) by raising the variables $\boldsymbol{\rho}_l$ at the power of q as follows:

$$\mathbf{A}_l\boldsymbol{\rho}_l^q + \mathbf{A}_r\boldsymbol{\rho}_r = \mathbf{0} \quad (9)$$

In our code, we put $q = 2$ or 3 . To the best of our knowledge, this is the first time that penalization method is applied in order to achieve balancing constraints. Based on this new formulation, condition (9) does well represent the balancing equality (8) if all elements in $\boldsymbol{\rho}_l$ are equal to 0 or 1. Thanks to this penalization of the variables $\boldsymbol{\rho}_l$, a small removal of material has a considerable impact on the balancing of the system, thus forcing the algorithm to impose 0 or 1 values to the variables $\boldsymbol{\rho}_l$ in order to counterbalance the effect of the variables $\boldsymbol{\rho}_r$. The optimization results by taking into account the constraints (9) instead of (8) are shown in Figs. 3(a), (c) and (e) (results obtained in 20 min, objective: first natural frequency of 646 Hz, constraint violation of $1.4 \cdot 10^{-4}$ %). Results were obtained without any instability of the optimization algorithm and it can be observed that gray elements have been removed from the design solution.

Figures 3(b), (d) and (f) show the same optimization problem but the difference comes from a change in the initial domain for body \mathcal{B}_2 which was increased (body's height is now of 30 mm instead of 20 mm). Final objective was of 763 Hz and was attained in around 10 h. It can be observed that a slight change in the design domain may lead to a totally different design solution.

3.3 Discussion

This work was made in order to show that TO can be used in order to obtain solutions in a rather short time of a complicated design problem which was to balance a four-bar linkage while ensuring deformation, compliance or frequency constraints.

However, in this paper, some issues have not been solved, which should be investigated later. First, the optimization is performed for compliance and frequency computed at $\theta_1 = \pi/2$. Thus, our optimization will be local by default. A more global optimization procedure ensuring the performance for any linkage configuration could be used (see [4] for instance) and some other optimization problems could be envisaged: objective and constraints could be changed.

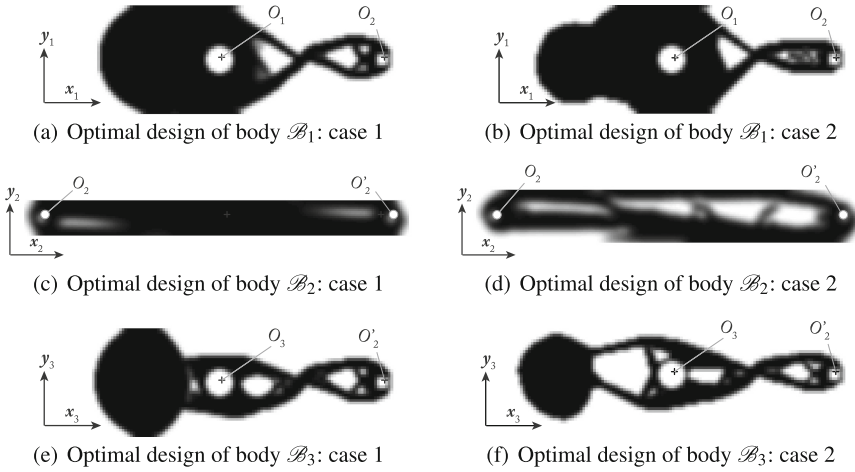


Fig. 3. Optimal design of bodies \mathcal{B}_1 , \mathcal{B}_2 and \mathcal{B}_3 in two cases; case 1: the initial design domain of body \mathcal{B}_2 is the one depicted in Fig. 2; case 2: the initial design domain of body \mathcal{B}_2 is changed: the body’s height is now of 30 mm instead of 20 mm as in case 1 (black elements correspond to $\rho_{ij} = 1$, white elements to $\rho_{ij} = 0$, and gray elements to $0 < \rho_{ij} < 1$)

It should be finally mentioned that our simulations have shown that the convergence of the algorithm is considerably sensitive by the threshold on the inequality constraints. In case all constraints are not achievable (i.e. there is no solution to the problem), the algorithm may become unstable.

4 Conclusion

Most of existing works on the optimal design of balanced four-bar linkages deal essentially with the minimization of their inertia or input torques under balancing constraints. These approaches are not suitable to include constraints based on the elastic behavior of the mechanism. In order to solve this issue, we performed in this paper the topology optimization of a reactionless four-bar linkage.

In our paper, a topology optimization algorithm was run in order to maximize the first natural frequency while ensuring the balancing and constraining the mechanism compliance. We showed that in order to obtain an interesting design solution, it was necessary to modify the balancing constraints in order to penalize them. Interesting design solutions were obtained in a rather short computational time.

Future works include solving the problem in 3-D and also carrying out multi-material topology optimization in order to ensure the balancing conditions by partially using materials with higher density leading thus to smaller mechanism footprint. The design of a prototype is also envisaged.

Acknowledgements. This work was supported by the project RobEcolo funded by the French Région Pays de la Loire (Convention No. 2015-10773).

References

1. Arakelian, V., Briot, S.: *Balancing of Linkages and Robot Manipulators - Advanced Methods with Illustrative Examples*. Springer (2015). ISBN: 978-3-319-12489-6
2. Bendsoe, M., Sigmund, O.: Material interpolation schemes in topology optimization. *Arch. Appl. Mech.* **69**, 635–654 (1999)
3. Bourdin, B.: Filters in topology optimization. *Int. J. Numer. Meth. Eng.* **50**, 2143–2158 (2001)
4. Briot, S., Goldsztejn, A.: Global topology optimization of industrial robots with the linearization method. *Mech. Mach. Theory* (2017). <http://www.irccyn.ec-nantes.fr/~briot/Download/BriotGoldsztejn.pdf>
5. Chaudhary, K., Chaudhary, H.: Shape optimization of dynamically balanced planar four-bar mechanism. *Procedia Comput. Sci.* **57**, 519–526 (2015)
6. Craig, R.R., Bampton, M.C.C.: Coupling of substructures for dynamic analysis. *AIAA J.* **6**(7), 1313–1319 (1968)
7. Erkaya, S.: Investigation of balancing problem for a planar mechanism using genetic algorithm. *J. Mech. Sci. Technol.* **27**(7), 2153–2160 (2013)
8. Farmani, M., Jaamialahmadi, A., Babaie, M.: Multiobjective optimization for force and moment balance of a four-bar linkage using evolutionary algorithms. *J. Mech. Sci. Technol.* **25**(12), 2971–2977 (2011)
9. Gosselin, C., Vollmer, F., Côté, G., Wu, Y.: Synthesis and design of reactionless three-degree-of-freedom parallel mechanisms. *IEEE Trans. Robot. Autom.* **20**(2), 191–199 (2004)
10. Jiang, Q., Gosselin, C.: Dynamic optimization of reactionless four-bar linkages. *J. Dyn. Syst. Measur. Control* **132**, 041006 (2010)
11. Pshenichnyj, B.: *The Linearization Method for Constrained Optimization*. Computational Mathematics. Springer, Heidelberg (1994)
12. Ricard, R., Gosselin, C.: On the development of reactionless parallel manipulators. In: *Proceedings of the ASME Design Engineering Technical Conferences and Computers and Information in Engineering Conference (IDETC/CIE 2000)*, Baltimore, Maryland (2000)
13. Shabana, A.: *Dynamics of Multibody Systems*. Cambridge University Press, Cambridge (2005)
14. Sigmund, O.: A 99 line topology optimization code written in MATLAB. *Struct. Multi. Optim.* **21**(2), 120–127 (2001)
15. Sigmund, O., Maute, K.: Topology optimization approaches: a comparative review. *Struct. Multi. Optim.* **48**(6), 1031–1055 (2013)
16. Svanberg, K.: The method of moving asymptotes - a new method for structural optimization. *Numer. Methods Eng.* **24**(2), 359–373 (1987)
17. Yin, L., Yang, W.: Optimality criteria method for topology optimization under multiple constraints. *Comput. Struct.* **79**(20–21), 1839–1850 (2001)

Kinetostatic Analysis and Solution Classification of a Planar Tensegrity Mechanism

P. Wenger^(✉) and D. Chablat

Laboratoire des Sciences du Numérique de Nantes, UMR CNRS 6004,
Ecole Centrale de Nantes, 1, Rue de La Noe, 44321 Nantes, France
{philippe.wenger,damien.chablat}@ls2n.fr

Abstract. Tensegrity mechanisms have several interesting properties that make them suitable for a number of applications. Their analysis is generally challenging because the static equilibrium conditions often result in complex equations. A class of planar one-degree-of-freedom (dof) tensegrity mechanisms with three linear springs is analyzed in detail in this paper. The kinetostatic equations are derived and solved under several loading and geometric conditions. It is shown that these mechanisms exhibit up to six equilibrium configurations, of which one or two are stable. Discriminant varieties and cylindrical algebraic decomposition combined with Groebner base elimination are used to classify solutions as function of the input parameters.

Keywords: Tensegrity mechanism · Kinetostatic model · Geometric design · Algebraic computation

1 Introduction

A tensegrity structure is an assembly of compressive elements (struts) and tensile elements (cable, springs) held together in equilibrium [1–3]. Their inherent interesting features (low inertia, natural compliance and deployability) make them suitable in several applications. They can also be used as preliminary models in musculo-skeleton systems to analyze animal and human movements [4, 5]. A spine can be modelled by stacking a number of suitable tensegrity modules. Accordingly, the frame of this work is a preliminary step of a large collaborative project with the Museum National d’Histoire Naturelle (MNHN) to model bird necks.

A tensegrity mechanism can be obtained by actuating one or several elements. Most results on tensegrity mechanisms have been published recently, see for example [6–8] and references therein. Deriving the input/output equations of a tensegrity mechanism needs to solve the equilibrium conditions. They are generally obtained by minimizing the potential energy, which often leads to complex equations. Planar tensegrity mechanisms (PTM) are simpler to analyze and are more suitable for algebraic computations. A 2-DOF PTM was analyzed by Arsenault [6] in terms of its kinetostatics, dynamics and workspace. Recently, Boehler [8] proposed a more complete definition of the workspace of that 2-DOF PTM, along with a method with higher-order continuation tools to

evaluate it. This work focuses on a one-DOF PTM made of one base telescopic rod, two crossed fixed-length rods and three connecting springs (see Fig. 1). This mechanism was studied in [9] in the particular case of symmetric geometric and loading conditions. The equilibrium configurations were solved for a set of geometric parameters and for one actuator input value. Here, this class of PTM is analyzed in a more systematic way and in more details, with the goal of understanding in depth the evolution of the number of stable and unstable solutions as function of the geometric parameters, the loading conditions and the actuated joint inputs. It turns out that the algebra involved in the stability analysis may prove very complicated while the PTM at hand is rather simple. Discriminant varieties and cylindrical algebraic decomposition are used to classify the number of stable solutions as function of some input parameters. It is shown that there are always up to six equilibrium solutions, of which at most one or two are stable.

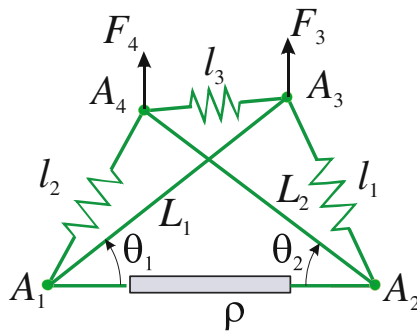


Fig. 1. Planar tensegrity mechanism

2 Mechanism Description and Basic Equations

The studied mechanism is shown in Fig. 1. It is composed of two rigid rods A_1A_3 and A_2A_4 of lengths L_1 and L_2 and three identical linear springs of stiffness k connecting A_1A_4 , A_2A_3 and A_3A_4 , respectively. A reference frame is attached to point A_1 with the x -axis oriented along A_1A_2 . Point A_1A_2 is fixed and A_2 can be translated along the x -axis by a prismatic actuator. This mechanism has three dof, one is controlled by the actuator (ρ) and the other two result from the compliant rotations of the two struts about A_1 and A_2 denoted by θ_1 and θ_2 , respectively.

Two vertical forces F_3 and F_4 are applied at nodes A_3 and A_4 , respectively. We first consider the case of zero free length springs. This is not a purely theoretical hypothesis since equivalent zero free lengths springs can be designed as shown for example in [6, 9]. Assuming no friction and infinite stiffness in the rods and in the prismatic joint, the potential energy U of this mechanism can be written as:

$$U = \frac{k}{2} \sum_{i=1}^3 l_i^2 - F_3 y_3 - F_4 y_4 \tag{1}$$

where y_3 and y_4 are the ordinates of A_3 and A_4 , respectively. After expressing the spring lengths l_i as function of the other geometric parameters, U can be shown to take the form:

$$U = \frac{k}{2}(3\rho^2 - 4L_1\rho \cos(\theta_1) + 2L_1^2 + 2L_2^2 - 4L_2\rho \cos(\theta_2) + 2L_1L_2 \cos(\theta_1 + \theta_2) - F_3L_1\rho \sin(\theta_1) - F_4L_2\rho \sin(\theta_2)) \quad (2)$$

The mechanism is in equilibrium when the two derivatives of U with respect to θ_1 and θ_2 vanish simultaneously, which yields the following two equations:

$$L_1 \sin(\theta_2 + \theta_1) - 2\rho \sin(\theta_2) + F'_4 \cos(\theta_2) = 0 \quad (3)$$

$$L_2 \sin(\theta_2 + \theta_1) - 2\rho \sin(\theta_1) + F'_3 \cos(\theta_1) = 0 \quad (4)$$

where $F'_4 = F_4/k$ and $F'_3 = F_3/k$. The solutions to the direct kinetostatic problem (DKSP) of the mechanism for a given input ρ , are obtained by solving Eqs. (3) and (4) for θ_1 and θ_2 . Note that both stable and unstable solutions will be obtained at this stage.

3 Solutions to the DKSP

Equations (3) and (4) above are transformed into polynomial equations by resorting to the tan-half-angle substitutions $t_1 = \tan(\theta_1/2)$ and $t_2 = \tan(\theta_2/2)$:

$$F'_3 t_1^2 t_2^2 + 2L_2 t_1^2 t_2 + 2L_2 t_2^2 t_1 + 4\rho t_2^2 t_1 + F'_3 t_1^2 - F'_3 t_2^2 - 2L_2 t_1 - 2L_2 t_2 + 4\rho t_1 - F'_3 = 0 \quad (5)$$

$$F'_4 t_1^2 t_2^2 + 2L_1 t_1^2 t_2 + 2L_1 t_2^2 t_1 + 4\rho t_1^2 t_2 + F'_4 t_1^2 - F'_4 t_2^2 - 2L_1 t_1 - 2L_1 t_2 + 4\rho t_2 - F'_4 = 0 \quad (6)$$

After elimination of one of the variables (say t_1) in the above two equations, a polynomial of degree 6 is obtained after clearing the factor $(1 + t_1^2)$. For each root, Eqs. (5) and (6) can be combined to eliminate the terms of degree 2 and t_2 is then solved with a linear equation. Thus, the mechanism may have up to 6 solutions to the DKSP.

It is clear that not all the solutions are stable equilibrium configurations in general. Stable solutions can be sorted out by verifying that the 2×2 Hessian matrix H is definite positive, namely, if its leading principal minors are greater than zero: $H(1,1) > 0$ and $\det(H) > 0$.

We now inspect particular conditions that lower the degree of the above polynomial or lead to interesting special cases.

3.1 No External Loading ($F_3 = F_4 = 0$)

When $F_3 = F_4 = 0$, Eqs. (3) and (4) simplify to:

$$L_1 \sin(\theta_2 + \theta_1) - 2\rho \sin(\theta_2) = 0 \quad (7)$$

$$L_2 \sin(\theta_2 + \theta_1) - 2\rho \sin(\theta_1) = 0 \quad (8)$$

Thus, $\theta_i = 0$ or π , $i = 1, 2$ are solutions to the above system, which give four singular configuration (the mechanism is fully flat and cannot resist any force along the vertical direction). There are two more solutions of the form:

$$\begin{aligned} (\theta_1 = \arctan(Q/R_1), \theta_2 = \arctan(Q/R_2)), \\ (\theta_1 = -\arctan(Q/R_1), \theta_2 = -\arctan(Q/R_2)) \end{aligned} \quad (9)$$

Moreover, when the coordinates of A_3 and A_4 are calculated with the above solutions, it is found that $y_3 = y_4$ and $x_3 - x_4 = \rho$, which means that the mechanism remains always in a parallelogram configuration, even when $L_1 \neq L_2$.

3.2 Symmetric Design and Equal Forces

When $L_1 = L_2$ and $F_3 = F_4$, the system is fully symmetric. This situation was studied by Arsenault [9] under the assumption that all solutions satisfy $\theta_1 = \theta_2$. Accordingly, the DKSP was solved with only one equation (the derivative of U w.r.t. $\theta = \theta_1 = \theta_2$), resulting in a 4th degree polynomial equation. In fact, it is not proven that the solutions are always of the form $\theta_1 = \theta_2$ and the DKSP is solved here with $\theta_1 \neq \theta_2$ a priori. Thus, we use the two Eqs. (7) and (8). To get simpler expressions, the second equation is subtracted to the first one. Then the tan-half substitution is done in this new equation and the following new system is obtained:

$$(t_1 - t_2)(F_4(t_1 + t_2) + 2k\rho(1 - t_1 t_2)) = 0 \quad (10)$$

$$F_4(t_1^2 t_2^2 - 1) + 2L_1 k(t_1^2 t_2 + t_1 t_2^2) + 4k\rho(t_1^2 t_2 + t_2) + F_4(t_2^2 - t_1^2) - 2L_1 k(t_1 + t_2) = 0 \quad (11)$$

The first factor $(t_1 - t_2)$ appearing in (10) confirms that solutions $\theta_1 = \theta_2$ exist but the second factor indicates that solutions with distinct angles may also appear. Eliminating t_1 from the second factor of (10) and (11) leads to a polynomial of degree 2 in t_2 :

$$4F_4 k^2 t_2^2 (L\rho + \rho^2) + 16k^3 \rho^3 t_2 + F_4^3 (t_2^2 - 1) + 4F_4^2 k \rho t_2 + 4F_4 k^2 (L\rho - \rho^2) = 0 \quad (12)$$

Since t_1 can then be solved linearly using the second factor of (10), there are up to two solutions of $\theta_1 \neq \theta_2$. Moreover, the two solutions are of the form (t_1, t_2) and (t_2, t_1) since the same polynomial as (12) could have been obtained in t_1 by eliminating t_2 instead of t_1 . The equal solutions obtained from the first factor in (10) are calculated by substituting $t_2 = t_1$ in Eq. (11), which yields up to 4 distinct solutions.

3.3 Stability Analysis

The leading principal minors of the Hessian matrix H must be calculated and their sign must be positive for an equilibrium solution to be stable. Their expression is large and is not reported here.

In the symmetric case, ($L_1 = L_2$ and $F_3 = F_4$), the symbolic calculation of $\det(H)$ for the solutions $\theta_1 \neq \theta_2$ is tractable. Solving the second factor of (10) for t_2 and replacing the solution in $\det(H)$ leads to the following expression:

$$\det(H) = -\frac{4(t_2^2 + 1)^2(4k^2\rho^2 + F_4^2)^2(-k\rho t_2^2 + F_4 t_2 + k\rho)^2}{(-2k\rho t_2 + F_4)^4} \quad (13)$$

which is always negative. Thus, the two equilibrium solutions satisfying $\theta_1 \neq \theta_2$ are always unstable.

For the unloaded case ($F_3 = F_4 = 0$), it can be easily shown by reporting $\theta_{1,2} = 0$ or π into $\det(H)$ and $H(1,1)$ that three solutions of the four flat ones are always unstable.

Regarding the other cases, symbolic calculations did not succeed and no general results could be obtained at this stage.

In the next section, the number of solutions according to the inputs parameters is investigated using more sophisticated tools, namely, cylindrical algebraic decomposition (CAD).

4 Solutions Classification Using CAD

In this section the number of stable equilibrium solutions is classified as function of the geometric and physical parameters of the PTM. The algebraic problem relies on solving a polynomial parametric system of the form:

$$E = \{\mathbf{v} \in \mathbb{R}^n, p_1(\mathbf{v}) = 0, \dots, p_m(\mathbf{v}) = 0, q_1(\mathbf{v}) > 0, \dots, q_l(\mathbf{v}) > 0\} \quad (14)$$

Such systems can be solved in several ways. Discriminant varieties (DV) [10, 12, 13] and CAD [11–13] are used here. They provide a formal decomposition of the parameter space through an algebraic variety that is known exactly. These tools have already been applied successfully in similar classes of problems [12, 13]. Roughly speaking, DV generate a set of separating hyper-surfaces in the parameters space of the parametric system at hand, such that the number of solutions in each resulting connected components or cells is known and constant. The DV can be computed with known tools like Groebner bases using the Maple sub-package *RootFinding[Parametric]*. Once the DV are obtained, an open CAD is computed to provide a description of all the cells. The number of solutions in each cell is determined by solving the polynomial system for one arbitrary point in each cell. Finally, adjacent cells with the same number of solutions are merged.

The equilibrium solutions depend on three geometric parameters (the rod lengths L_1 and L_2 and the input variable ρ) and two physical parameters (the spring stiffness k and the forces F_3 and F_4). However, the lengths parameters can be normalized with L_1 and F_3 and F_4 can be replaced by F_3/k and F_4/k , without loss of generality. Finally our system depends on 4 independent parameters only. In what follows, L_1 and k are fixed to 1 and 100, respectively.

4.1 No External Loading

We start with the simplest situation where $F_3 = F_4 = 0$.

We were able to show in the preceding section that three of the four flat solutions were unstable but no general information regarding the two non-flat solutions could be obtained. Since $F_3 = F_4 = 0$, the parameter space is a plane (L_2, ρ) . Computing the DV and the CAD for this case leads to the existence of a region in the parameter plane where the PTM has two stable solutions. Outside this region, the PTM has one stable solution. Figure 2 (left) shows a representation of the CAD for L_2 and ρ in $[0, 4]$. The 2-solution region is the red one. The DV that bound the regions are defined by $2\rho - L_2 - 1 = 0$, $2\rho - L_2 + 1 = 0$ and $2\rho + L_2 - 1 = 0$. Here it can be easily verified with geometric arguments that these boundaries correspond to the fully flat (singular) configurations of the PTM. In the 1-solution regions, the PTM has one stable fully flat solution and in the 2-solution regions, it has two stable (non-flat) solutions, one being the mirrored image of the other as shown in Fig. 2 (right). The 2-solution region is of constant width equal to 1 (in fact L_1) when $L_2 > 1$, while it decreases linearly with L_2 when $L_2 < 1$.

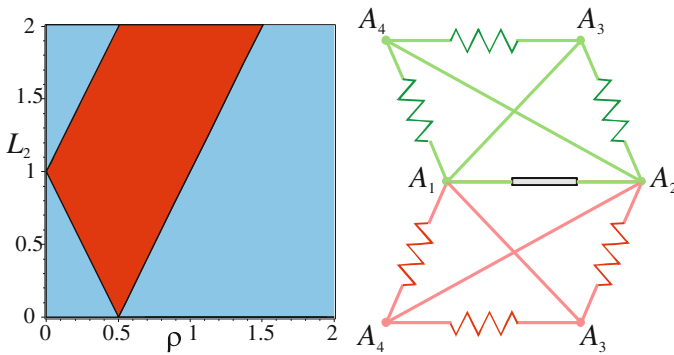


Fig. 2. Unloading case: CAD (left) and stable solutions for $\rho = 1, L_2 = 3/2$ (right)

4.2 Fully Symmetric Case

We now study the case $L_1 = L_2$ and $F_3 = F_4$. We could show in the preceding section that the two solutions $\theta_1 \neq \theta_2$ are always unstable but we could not conclude for the four solutions $\theta_1 = \theta_2$. Here the parameter space is the plane (ρ, F_4) . The computed DV and CAD is illustrated in Fig. 3 (left) for $0 < \rho < 2$ and $-10 < F_4 < 0$ (a symmetric pattern is obtained for $0 < F_4 < 10$).

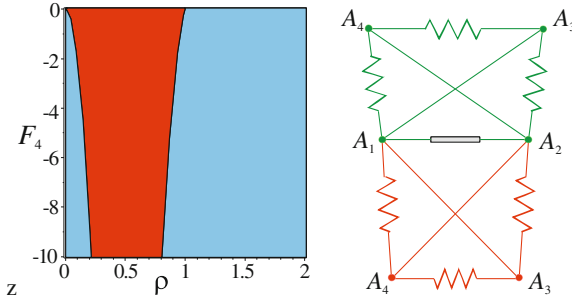


Fig. 3. Symmetric case: CAD (left) and stable solutions for $\rho = 3/4, F_4 = -10$ (right)

It reveals that there exists a region with two stable solutions in the parameter plane. Figure 3 (right) shows two stable solutions for $\rho = 3/4$ and $F_4 = -10$.

The boundaries here are two curves of degree 6 defined by:

$$F_4^6 + 12 \times 10^4 F_4^4 \rho^2 + 48 \times 10^8 F_4^2 \rho^4 + 64 \times 10^{12} \rho^6 - 16 \times 10^8 F_4^2 \rho^2 = 0 \quad (15)$$

$$F_4^6 + 12 \times 10^4 F_4^4 \rho^2 + 48 \times 10^8 F_4^2 \rho^4 + 64 \times 10^{12} \rho^6 - 12 \times 10^4 F_4^4 + 336 \times 10^8 F_4^2 \rho^2 - 192 \times 10^{12} \rho^4 + 48 \times 10^8 F_4^2 + 192 \times 10^{12} \rho^2 - 64 \times 10^{12} = 0 \quad (16)$$

In the 1-solution region, it can be shown that the PTM operates always in a reverse configuration, namely, y_3 and y_4 are negative. Assuming that the mechanism starts from a configuration with y_3 and y_4 positive, the operation range for a given F_4 is thus determined by the 2-solution region. The operation range decreases when the external force increases (in magnitude). It can be verified that for $F_4 = 0$, the operation range reaches its maximal value, which is equal to 1 (or L_1) in accordance with the preceding result. Note that in the presence of pulling forces ($F_4 > 0$), the operation range of the PTM would be full because in this case y_3 and y_4 turn out to be positive in the one-solution region.

4.3 General Case

The parameter space is now defined by (ρ, L_2, F_3, F_4) . Two parameters are first assigned in order to have a parameter space of dimension 2. Accordingly, the DV and the CAD are computed for $F_3 = F_4 = -10$. Figure 4 (left) shows the obtained partition of the parameter plane (ρ, L_2) for $0 < \rho < 2$ and $0 < L_2 < 2$. It looks similar to the unloaded case but the boundaries here are three curves of degree 12 in ρ and in L_2 . Their equations contain hundreds of terms. There are two stable solutions in the red region and only one in the blue regions. Figure 4 (right) shows two stable solutions for $L_2 = 3/2$ and $\rho = 7/10$.

Like in the preceding case, the operation range is determined by the 2-solution region if the PTM starts with $y_3 > 0$ and $y_4 > 0$. The operation range reaches its maximal width for $L_2 = 1$, which is the fully symmetric case (it can be verified that this

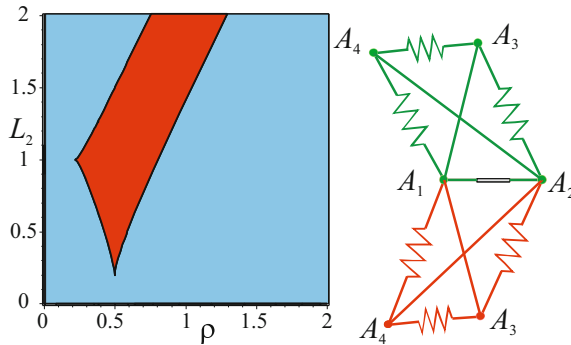


Fig. 4. General case with $F_3 = F_4 = -10$: CAD (left) and stable solutions for $L_2 = 3/2$ and $\rho = 7/10$ (right)

range is exactly the same as the one calculated from the DV above for $F_4 = -10$). The operation range decreases slowly when L_2 increases from 1 but the decrease is much more significant when L_2 decreases from 1.

We now compute the DV and the CAD with $F_3 = -10$ and $L_2 = 3/2$ in the parameter plane (ρ, F_4) . The result is shown in Fig. 5 for $0 < \rho < 2$ and $-30 < F_4 < 0$, where the red region contains 2 stable solutions and the blue region only 1. The boundaries are defined by curves of degree 12 in ρ^2 and in F_4 .

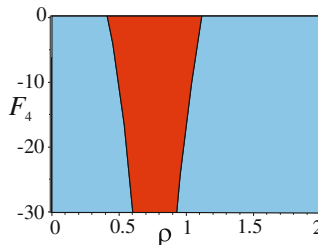


Fig. 5. CAD for the general case with $F_3 = -30$ and $L_2 = 1$ (Color figure online)

5 Discussion on More General Cases

5.1 Adding Horizontal Force Components

When horizontal force components F_{3x} and F_{4x} are added, it can be shown that this does not change the global nature of the algebraic equations and of the results. Indeed the only changes are the additional term $2F_{3x}$ (resp. $2F_{4x}$) appearing in the coefficients of $t_2^2 t_1$ and of t_1 in Eq. (5) (resp. of $t_1^2 t_2$ and of t_2 in Eq. (6)). Globally one comes up with a system yielding 6 solutions, of which 1 or 2 are stable like above.

5.2 Springs with Non-Zero Free Lengths

Zero free length springs have been assumed so far. It is interesting to investigate the changes induced on the algebraic complexity of the systems when non-zero free lengths are introduced in the springs. Crane et al. reported an amazing increase in complexity for a planar pre-stressed parallel manipulator made of a triangular base and platform connected by one extensible RPR leg and two springs [7]. When a free length l_0 is introduced in all springs, Eq. (1) becomes:

$$U = \frac{k}{2} \sum_{i=1}^3 (l_i - l_0)^2 - F_3 y_3 - F_4 y_4 \quad (17)$$

The point is that l_i is calculated using a square root, which disappears if $l_0 = 0$ but remains when $l_0 \neq 0$. The two derivatives of U now contain several square roots, which can be cleared after squaring two times. As a result, Eqs. (5) and (6) become extremely complex and their degree is now 28. Due to the complex algebra, parameters must be specified before proceeding to the elimination. We could keep ρ as such and all remaining parameters were assigned arbitrary values. The univariate polynomial after elimination of t_1 turned out to be of degree 328 in t_2 but could be divided by $(1 + t_2^2)^{56}$, thus reducing the degree to 272. Attempts to solve the polynomial for some values of ρ resulted in 12 to 30 real solutions. After verification of the vanishing of the two derivatives of U to eliminate all spurious solutions, no more than 6 solutions remained. Note that for a solution to be acceptable finally, the lengths of all springs must be verified to be greater than l_0 in addition to the stability condition. Deeper investigations will be the subject of future work to obtain more results but it is clear that a classification study as in the case $l_0 = 0$ will be difficult because of high calculation times.

6 Conclusions

The goal of this paper was to investigate in depth the direct kinetostatic solutions of a family of planar tensegrity mechanisms composed of a prismatic base, two crossed rods and three springs. With zero-free length springs, the problem can be treated using computer algebra tools like for the direct kinematics of parallel manipulator. We have used discriminant varieties and cylindrical algebraic decomposition to study the evolution of the number of solutions as function of the input parameters. Basically, a univariate polynomial of degree 6 must be solved in the general case, resulting in one to two stable solutions. In the unloaded case, there are always two stable symmetric solutions for a range of the input prismatic joint which is of constant width and whose limits vary with the rod lengths. Moreover, the mechanism remains always in a parallelogram configuration even when the two rod lengths are different. The mechanism can also reach one flat stable solution, which is singular. Such a stable flat solution might be of interest to store the mechanism when it is not used. When the two external forces and the two rod lengths are equal, there are still 6 solutions, including 4 unstable, non-symmetric solutions. The case of springs with non-zero free lengths was discussed and shown to lead to very large equations with high degree but no more than 6 solutions were found in our numerical experiments.

Acknowledgments. This work is partially funded by the French ANR project “AVINECK: an arm for the bird”, ANR-16-CE33-0025-02, 2017-2020.

References

1. Fuller, R.B.: Tensile-integrity structures. United States Patent 3063521 (1962)
2. Skelton, R., de Oliveira, M.: Tensegrity Systems. Springer, Heidelberg (2009)
3. Motro, R.: Tensegrity systems: the state of the art. *Int. J. Space Struct.* **7**(2), 75–83 (1992)
4. Vogel, S.: *Cats Paws and Catapults: Mechanical Worlds of Nature and People*. W.W. Norton and Company, New York (2000)
5. Levin, S.: The tensegrity-truss as a model for spinal mechanics: biotensegrity. *J. Mech. Med. Biol.* **2**(3), 375–388 (2002)
6. Arsenault, M., Gosselin, C.M.: Kinematic, static and dynamic analysis of a planar 2-DOF tensegrity mechanism. *Mech. Mach. Theory* **41**(9), 1072–1089 (2006)
7. Crane, C., Bayat, J., Vikas, V., Roberts, R.: Kinematic analysis of a planar tensegrity mechanism with pres-stressed springs. In: Lenarcic, J., Wenger, P. (eds.) *Advances in Robot Kinematics: Analysis and Design*, pp. 419–427. Springer (2008)
8. Boehler, Q., Charpentier, I., Vedrines, M., Renaud, P.: Definition and computation of tensegrity mechanism workspace. *ASME J. Mech. Robot.* **7**(4), 044502–044502-4 (2015)
9. Arsenault, M.: Développement et analyse de mécanismes de tensegrité. Ph.D thesis, Université Laval, Québec, Canada (2006)
10. Lazard, D., Rouillier, F.: Solving parametric polynomial systems. *J. Symb. Comput.* **42**(6), 636–667 (2007)
11. Collins, G.E.: Quantifier elimination for real closed fields by cylindrical algebraic decomposition. Springer (1975)
12. Corvez, S., Rouillier, F.: Using computer algebra tools to classify serial manipulators. In: *Automated Deduction in Geometry. Lecture Notes in Computer Science*, vol. 2930, pp. 31–43 (2002)
13. Manubens, M., Moroz, G., Chablat, D., Wenger, P., Rouillier, F.: Cusp points in the parameter space of degenerate 3-RPR planar parallel manipulators. *ASME J. Mech. Robot.* **4**(4), 041003–041003-8 (2012)

Design Optimization and Accuracy Analysis of a Planar 2PRP-PRR Parallel Manipulator

Santhakumar Mohan¹(✉), Burkhard Corves², and Philippe Wenger³

¹ Discipline of Mechanical Engineering, Indian Institute of Technology Indore, Indore 453552, India

santhakumar@iiti.ac.in

² Department of Mechanism Theory and Dynamics of Machines, RWTH Aachen University, 52072 Aachen, Germany

corves@igm.rwth-aachen.de

³ IRCCyN - UMR CNRS 6597, Ecole Centrale de Nantes, 44321 Nantes, France
Philippe.Wenger@ls2n.fr

Abstract. This paper addresses the dimensional synthesis and design optimization of a three-degree-of-freedom planar U-shape fixed base 2PRP-PRR parallel manipulator to maximize its workspace. Two kinematic design solutions are proposed and their link parameters are optimized to maximize the workspace. Furthermore, accuracy analysis of the optimized manipulator configurations for the actuator inaccuracies is performed and the results are compared with the well-known planar 3PRP and 2PRP-PPR parallel configurations.

Keywords: Design optimization · Planar parallel manipulator · 2PRP-PPR · Workspace · Accuracy analysis · Error analysis

1 Introduction

Planar parallel manipulators are getting great attention and interest for industrial applications namely positioning and tracking in recent years. Although planar parallel manipulators have several advantages such as higher accuracy, speed, rigidity and payload capability, they have shortcomings due to smaller workspace and presence of singularities [1, 2]. Therefore, several researchers are working towards identifying the best possible (optimal) configuration to overcome these shortcomings [2]. In order to identify the optimal configuration, there are several methods applied and quantifiers used in the literature [2–4]. For example, the dexterity or isotropy index, global conditioning index, payload index, accuracy measures, etc. are being used to quantify the performance of the manipulator [2–4]. From the literature, it is found that usage of unsymmetrical fixed base (U-shape fixed base) provides larger singularity-free workspace and simple kinematic relations rather than symmetrical fixed base (Δ -shape fixed base) [4, 7]. Furthermore it is found that planar parallel manipulators having their first joint actuated and prismatic arranged in a U-shape fixed base provide better performance and few advantages over other configurations [4, 7]. The detailed kinematic and dynamic performance analyses of this particular family was performed and it was found that the planar 2PRP-PRR parallel configuration has better performance in terms

of isotropy and payload indices [4]. The 2PRP-PRR manipulator kinematics and its kinematic performance measures were presented in [5]. In [5], the optimum kinematic design of the configuration, i.e., the optimal link parameters were not considered, but the performance results confirmed the influence and sensitivity of the link parameters in overall performance. During the initial design procedure, the analysis of the performance sensitivity to uncertainties is an important task and sensitivity analysis of planar parallel manipulators was performed using the screw theory [8]. In [8], the end-effector pose errors due to dimensions and actuators errors were calculated and compared for different configurations.

Therefore, in this paper the design optimization of the planar 2PRP-PRR parallel configuration is performed with two cases namely the PRR leg connections with and without offset distance between active prismatic joint (slider block) to the RR link. The configurations of these cases are given in Figs. 1(a) and (b). Furthermore the optimal configuration workspaces are compared with well-known planar 3PRP and 2PRP-PPR parallel configurations. In addition, accuracy analyses of the optimal configuration for the actuator inaccuracies are performed and compared through the help of analytical approach [7] based on forward kinematic relations. For the accuracy measure analysis, the local maximum position errors of the end-effector for a given actuator inaccuracies and a common test region within the singularity-free workspace are considered.

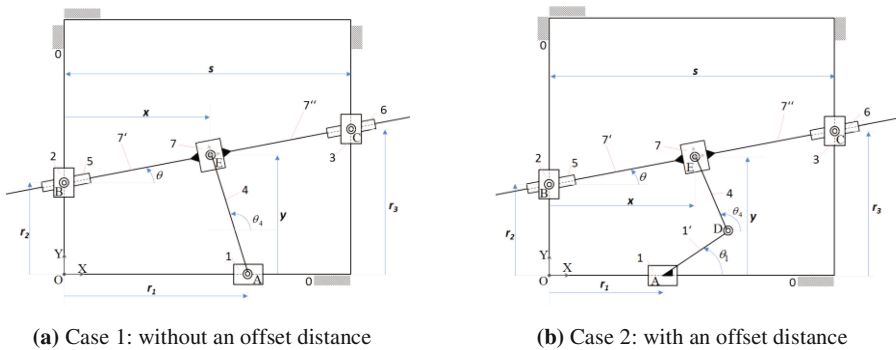


Fig. 1. Schematic arrangements of the planar 2PRP-PRR parallel manipulator

The remainder of this paper is arranged as follows: the next section presents the mathematical background which includes kinematic relations of the manipulator whose workspace will be studied in this paper. Section 3 presents the design optimization results obtained from the genetic algorithms and Sect. 4 presents the accuracy measure in terms of error analysis which computing the local maximum position errors for the given actuator inaccuracies. Conclusions and scope of future work are given in the last section.

2 Mathematical Background

The kinematic arrangements (both cases) of the manipulator are shown in Figs. 1(a) and (b). The fixed base, 0, and the moving platform (end-effector), 7 are connected through three legs. In these three legs: two of them have prismatic, revolute and prismatic joints and the third leg has prismatic, revolute and revolute joints. In all three legs, the starting prismatic joint is actuated and other joints are passive. The vector of actuator coordinates (joint displacements) is $\mathbf{q} = [r_1 \ r_2 \ r_3]^T$ and these joint displacements are considered as positive values, i.e., $r_1 \geq 0, r_2 \geq 0$ and $r_3 \geq 0$. The vector of task coordinates of the end-effector is $\boldsymbol{\mu} = [x \ y \ \theta]^T$. The forward kinematic relation of the manipulator is as follows:

$$\boldsymbol{\mu} = \begin{bmatrix} x \\ y \\ \theta \end{bmatrix} = \begin{bmatrix} r_1 + l_4 \cos \theta_4 + l_{1'} \cos \theta_1 \\ r_2 + \left(\frac{r_3 - r_2}{s}\right) (r_1 + l_4 \cos \theta_4 + l_{1'} \cos \theta_1) \\ \tan^{-1} \left(\frac{r_3 - r_2}{s}\right) \end{bmatrix} \tag{1}$$

where, $\theta_4 = \text{atan2} \left(\frac{y - l_{1'} \sin \theta_1}{l_4}, \sqrt{1 - \left(\frac{y - l_{1'} \sin \theta_1}{l_4}\right)^2} \right)$, s is the longitudinal span. $l_{1'}$ and l_4 are the link lengths of link 1' and link 4.

The inverse kinematic relations of the manipulator are given as follows:

$$\mathbf{q} = [r_1 \ r_2 \ r_3]^T = [x - l_4 \cos \theta_4 - l_{1'} \cos \theta_1 \quad y - x \tan \theta \quad y + [s - x] \tan \theta]^T \tag{2}$$

Velocity relations can be obtained by differentiating (2) with respect to time, as

$$\dot{\mathbf{q}} = \mathbf{J}(\boldsymbol{\mu})\dot{\boldsymbol{\mu}} \tag{3}$$

where, $\mathbf{J}(\boldsymbol{\mu})$ is the Jacobian matrix of the kinematic configuration and given as:

$$\mathbf{J}(\boldsymbol{\mu}) = \begin{bmatrix} 1 & \tan \theta_4 & 0 \\ -\tan \theta & 1 & -x \sec^2 \theta \\ -\tan \theta & 1 & (s - x) \sec^2 \theta \end{bmatrix} \tag{4}$$

where, $\mathbf{J}(\boldsymbol{\mu})$ is singular at $(1 - \tan \theta \tan \theta_4) = 0$, in other words, singularity is encountered whenever rod 4 is perpendicular to rods 7' and 7". In this case the moving platform can perform infinitesimal translation motions along the direction of 7' and 7". Therefore singularity-free workspace computation is performed and described in the next section.

3 Design Optimization and Workspace Analysis

Manipulator design is one of the complex subjects and the overall performance heavily depends on the manipulator geometry and the performance quantifiers are almost depend on the geometry as well [2, 6]. Therefore, design optimization is an essential

process in manipulator design and this is an iterative process. In this paper, the manipulator's geometry is optimized by maximizing the singularity free workspace. One of the design parameters can be fixed without loss of generality. Here the longitudinal span (s) is assumed to be 0.2 m. The design optimization of the configuration 1 (without offset distance) is performed with the help of a simple scanning method. In this method, the link length (L_{AE}) is varied from 0.05 m to 0.2 m and the area of the singularity-free workspace is calculated for the constant end-effector orientation in $[-15^\circ, +15^\circ]$. That is, the set of points reachable for any orientation within $[-15^\circ, +15^\circ]$. The area of the singularity-free workspace as function of the link length is plotted in Fig. 2. It shows that the largest area is obtained for $L_{AE} = 0.148$ m and its numerical value is 0.0136 m². This value still decreases when increasing the value of L_{AE} above 0.2 m. However, it is limited to the longitudinal span of the manipulator.

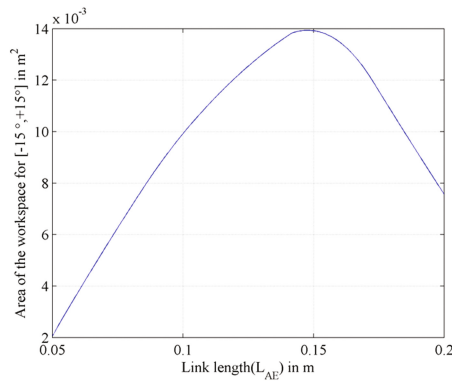


Fig. 2. Area of the workspace of the 2PRP-PRR (case 1) as function of the link length variations

Design optimization of configuration 2 is not as simple as the earlier. This configuration has three design variables namely, θ_I , L_{AD} and L_{DE} . The influence of each parameter's variations on the workspace is presented in Fig. 3. It shows that each design variable has a significant contribution. Therefore, in this work the design optimization is performed with the help of genetic algorithms for maximizing the workspace. The area of the singularity-free workspace is calculated for the given entire stroke length of each joints (it is considered as 0 to 0.2 m for all joints) and finding the points which give non-zero determinant value of the Jacobian matrix. Here for the optimization, the end-effector positions, x and y are varied from -0.1 m to 0.3 m and the end-effector orientation θ is varied from -15° to $+15^\circ$. The genetic algorithm optimization toolbox in matlab is used for the numerical computation. The optimized values of design variables for the constant end-effector orientation in $[-15^\circ, +15^\circ]$ are obtained as follows: $\theta_I = 47.15^\circ$, $L_{AD} = 0.1376$ m and $L_{DE} = 0.1045$ m. The area of singularity-free workspace is 0.0239 m². The constant workspace optimization process is also performed for different orientations of the end-effector. The variations in the optimized design values are very minimal. These configurations based on their optimized design values are compared with well-known planar 3PRP and 2PRP-PRR

manipulators and, their kinematic arrangements are presented in Figs. 4 and 5. For better comparison, the span (s) is considered as 0.2 m for all manipulators. The singularity-free constant orientation workspaces of these configurations are presented in Fig. 6. Areas of the singularity-free workspace of the manipulators are given in Table 1.

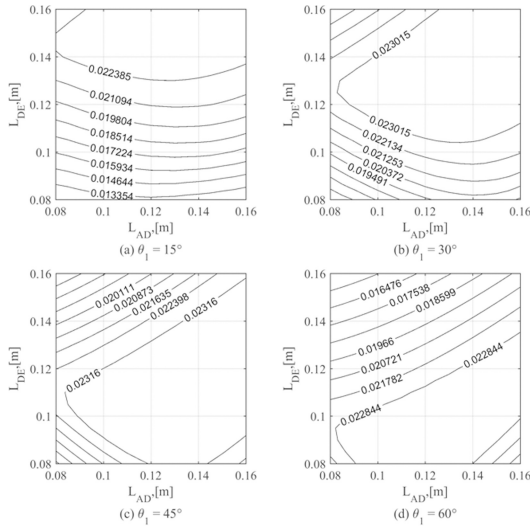


Fig. 3. Contour plots of the workspace area of the 2PRP-PRR (case 2) configuration for the parameter variations

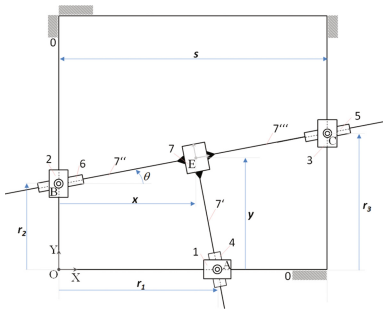


Fig. 4. Schematic arrangement of the planar 3PRP parallel manipulator

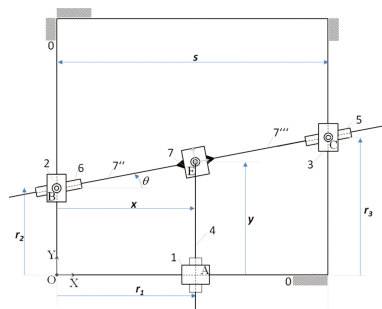


Fig. 5. Schematic arrangement of the planar 2PRP-PPR parallel manipulator

4 Error Analysis

Most of the kinematic performance measures depend on the Jacobian matrix which may not be appropriate for overall performance comparison and they are generally not appropriate to manipulators with mixed units. Therefore, accuracy measure based on kinematic error analysis is performed. In this error analysis, the end-effector position errors due to actuator inaccuracies (index errors) are only considered [7]. Since the end-effector position error of the 2PRP-PPR is constant in its entire workspace for a given end-effector orientation [7], the error analysis is carried out only for 3PRP and 2PRP-PPR (case 2) configurations. The test regions are chosen within the singularity-free workspace and presented in Fig. 7. The limit of actuator inaccuracies (maximum) of all active joints are considered to be equal to $\pm 50 \mu\text{m}$. For obtaining the local maximum end-effector pose errors based on the above range of error parameters is considered as a maximization (optimization) problem. In this paper, the maximization of local position and orientation errors of the end-effector is carried out using one of the popular optimization methods namely genetic algorithms. In this method, the local position errors are maximized based on the forward kinematic model, actuator inaccuracies range. To find the maximum value of the pose error, the in-built MATLAB function namely 'ga' is used. The error contours of these manipulators for different end-effector orientations are presented in Fig. 8. The maximum, minimum and mean values of local maximum end-effector position errors of the manipulators are given in Table 2.

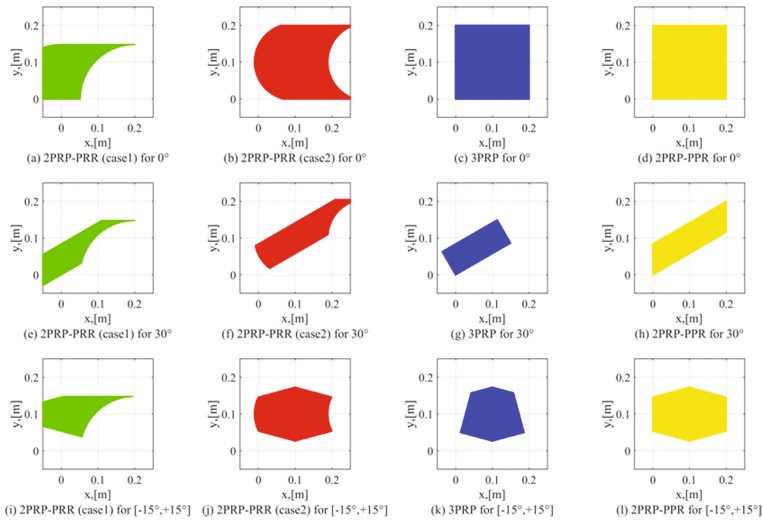


Fig. 6. Singularity-free workspace plots of planar parallel manipulators

From the results, it is found that 2PRP-PPR configuration is better in terms of accuracy in all three cases as compared to 3PRP configuration. Not only smaller values but also the range of smaller values is much larger as well. Further, error values of 2PRP-PPR depend on the location of the end-effector in the workspace.

Table 1. Singularity-free workspace of the planar parallel manipulators

Configuration	Singularity-free workspace in m ²		
	$\theta = 0^\circ$	$\theta = +30^\circ$	$\theta = [-15^\circ, +15^\circ]$
3PRP	0.0400	0.0127	0.0185
2PRP-PPR	0.0400	0.0169	0.0240
2PRP-PPR (case 1)	0.0196	0.0122	0.0137
2PRP-PPR (case 2)	0.0400	0.0175	0.0239

Further, an experimental study on energy consumption with payload of these three manipulators was carried out in [4]. The values of energy consumption for a circular-path tracking task with full payload (50 N) of the 3PRP, 2PRP-PPR and 2PRP-PPR (case 2) are 0.846 Wh, 1.349 Wh and 0.739 Wh [4]. The 2PRP-PPR configuration is better in terms of accuracy but the PPR leg has a moving passive prismatic joint which requires more energy and driving force compare to PRR leg [4]. Therefore, in overall, it is found that the optimized 2PRP-PPR configuration with the offset distance is could be better as compared to other configurations.

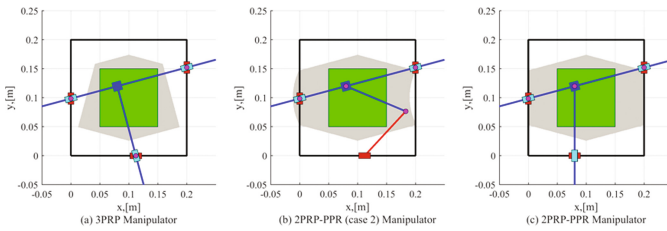


Fig. 7. Singularity-free workspace for $[-15^\circ, +15^\circ]$ along with the accuracy test region

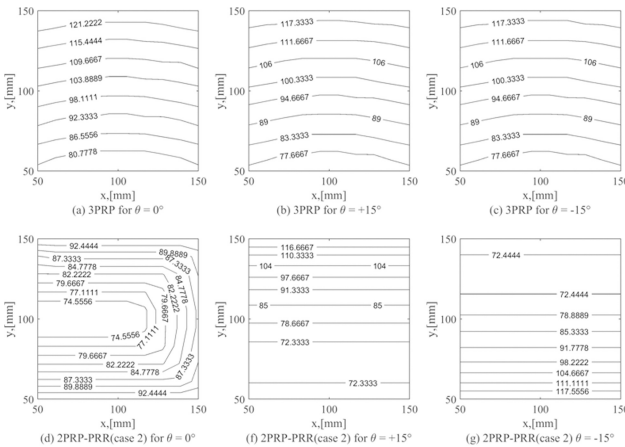


Fig. 8. Contour plots of the maximum position error (in μm)

Table 2. Local maximum end-effector position errors of the planar parallel manipulators

Configuration		Local maximum end-effector position errors (in μm)				
		$\theta = 0^\circ$	$\theta = +15^\circ$	$\theta = +30^\circ$	$\theta = -15^\circ$	$\theta = -30^\circ$
3PRP	Maximum	127.48	123.15	110.42	123.14	110.42
	Minimum	75.05	72.47	65.01	72.45	64.98
	Mean	101.28	97.83	87.72	97.83	87.72
2PRP-PRR (case 2)	Maximum	95.74	123.74	177.13	124.51	179.04
	Minimum	68.73	66.31	59.33	66.15	61.63
	Mean	84.62	87.43	102.28	87.65	102.95
2PRP-PPR	Constant	70.71	80.74	93.38	80.74	93.38

5 Conclusions

In the present paper, the design optimization of the planar 2PRP-PRR parallel manipulator was performed. Two different configurations were considered and their parameters were optimized. The constant orientation workspaces of these configurations were found and compared. Based on workspace results, it was found that configuration 2 (with offset distance) has better performance than the configuration 1 (without offset distance). Further error analysis was performed for the configuration 2 and compared with well-known 3PRP and 2PRP-PPR configurations. From the overall results, the optimized 2PRP-PRR design could be a better planar parallel platform for precise and accurate positioning applications. The use of the proposed optimum 2PRP-PRR manipulator in conjunction with the mechanical error compensation motion control would be the next research objective.

Acknowledgments. This research was supported in part by the Humboldt Fellowship funded by the Alexander von Humboldt (AvH) Foundation, Germany.

References

1. Briot, S., Bonev, I.-A.: Are parallel robots more accurate than serial robots? *Transaction of the Canadian Society for Mechanical Engineering* **31**, 445–455 (2007)
2. Merlet, J.-P.: *Parallel Robots (Solid Mechanics and Its Applications)*. Springer, Secaucus (2006)
3. Patel, S., Sobh, T.: Manipulator performance measures a comprehensive literature survey. *J. Intell. Rob. Syst.* **77**, 547–570 (2015)
4. Singh, Y.: Performance investigations on mechanical design and motion control of planar parallel manipulators. Ph.D. thesis, Indian Institute of Technology Indore (2016)
5. Singh, Y., Mohan, S.: Kinematic performance analysis of a new 2PRP-PRR planar parallel robotic manipulator. In: *Proceedings of the 4th Joint International Conference on Multibody System Dynamics*, Montreal (2016)

6. Ur-Rehman, R., Caro, S., Chablat, D., Wenger, P.: Multi-objective design optimization of 3PRR planar parallel manipulators. In: Proceedings of the 20th CIRP Design Conference, Nantes (2010)
7. Yu, A., Bonev, I.-A., Zsombor-Murray, P.: Geometric approach to the accuracy analysis of a class of 3-DOF planar parallel robots. *Mech. Mach. Theory* **43**, 364–375 (2008)
8. Binaud, N., Caro, S., Wenger, P.: Sensitivity comparison of planar manipulators. *Mech. Mach. Theory* **45**, 1477–1490 (2010)

Operation Modes of the Planar 3-RRR Manipulator

Aravind Baskar and Sandipan Bandyopadhyay^(✉)

Department of Engineering Design, Indian Institute of Technology Madras,
Chennai 600036, India

krishna.arvind91@gmail.com, sandipan@iitm.ac.in

Abstract. The planar 3-RRR parallel manipulator is known to have six assembly modes. However, analysing it in the framework of spatial kinematics reveals that it has a total of twelve assembly modes, six in each of the two possible operation modes. The modes are derived using a Study parameter formulation first, and later confirmed in another formulation in the joint-space, and finally visualised in terms of the planar constraint curves generated by the sub-chains of the manipulator. Numerical results show that all the twelve modes can be real for certain inputs.

Keywords: Operation modes · Study's kinematic mapping · Discrete Screw Axis (DSA) · Forward Kinematic Univariate (FKU)

1 Introduction

The planar 3-RRR manipulator has six assembly modes, as mentioned in many existing reports, e.g., Gosselin *et al.* [1]. However, if the forward kinematic analysis of this manipulator is performed in the joint space, it shows twelve assembly modes. In this work, this problem is investigated from multiple perspectives, namely: the kinematic mapping of Study; the constraints in the joint space; and the constraints generated by the sub-chains of the manipulator. This work is similar to the study of the 3-RPR manipulator by Husty [3], using the Study parameter representation of $\mathbb{SE}(2)$. However, in the current work, the full spatial setup is used in the kinematic modelling, as in [4], which leads to results that are strikingly similar. On the other hand, this work is also motivated by [6], where the kinematic analysis is performed on the basis of the constraint equations in the joint-space of the 3-RPS. Analogous results are obtained in this case as well, and nice inferences can be drawn based on these to present a consistent interpretation of the results obtained from various approaches. The main results are that the manipulator has six assembly modes in each of the two of its operation modes, though only one mode is apparent at a time, as unlike in the 3-RPS, a transition between the modes is not (physically) possible in this case. It is (mathematically) possible for all the assembly modes to be real at the same time, as shown with the help of a numerical example. Also, the solutions can

be explained geometrically in terms of the intersections of the constraint curves generated by the sub-chains of the manipulator.

The rest of the paper is presented as follows: Sect. 2 describes the forward kinematic analysis of the problem in the task space while Sect. 3 discusses the same problem in the joint space. Section 4 concludes the paper.

2 Forward Kinematic Analysis Using Study Parameters

The forward kinematic problems of planar 3-degrees-of-freedom parallel manipulators have been studied using the planar kinematic mapping (see, e.g., [3] in case of 3-RPR manipulator). In the following, spatial kinematic mapping is used to study the planar 3-RRR manipulator, leading to certain new and interesting observations.

2.1 Kinematic Model

The manipulator is shown in Fig. 1. The fixed base $b_1 b_2 b_3$ and the moving platform $p_1 p_2 p_3$ are both equilateral triangles, of side lengths b and a respectively. Three limbs of R-R-R architecture, each having an actuated link of length l and a passive link of length r , connect the two platforms. The active joint angles are given by $\theta = [\theta_1, \theta_2, \theta_3]^T$, and the passive joint angles by $\phi = [\phi_1, \phi_2, \phi_3]^T$. The frame $\{A\}$, given by $O_A-X_A Y_A Z_A$, serves as the global frame of reference. Likewise, frame $\{B\}$, attached to the moving platform, denotes the moving frame. The vertices of the two platforms are expressed in projective coordinates: ${}^B p_1 = [0, 0, 0, 1]^T$, ${}^B p_2 = [a, 0, 0, 1]^T$, ${}^B p_3 = [\frac{a}{2}, \frac{\sqrt{3}a}{2}, 0, 1]^T$, and

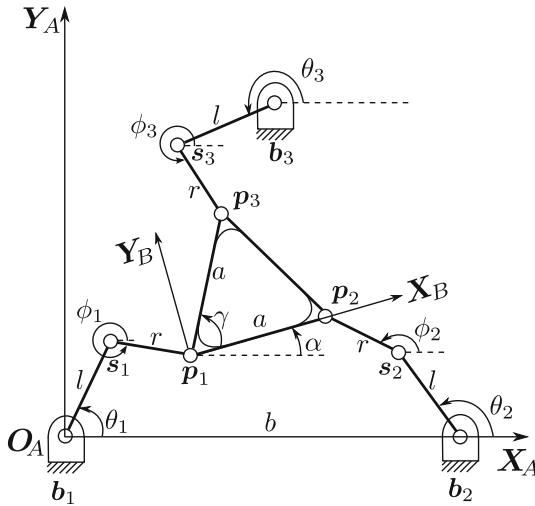


Fig. 1. Planar 3-RRR parallel manipulator

${}^A\mathbf{b}_1 = [0, 0, 0, 1]^\top$, ${}^A\mathbf{b}_2 = [b, 0, 0, 1]^\top$, ${}^A\mathbf{b}_3 = \left[\frac{b}{2}, \frac{\sqrt{3}}{2}b, 0, 1 \right]^\top$, where the fourth coordinate, 1, is the projective coordinate, and the leading superscripts A and B indicate the frame of reference. The frame $\{B\}$ is related to $\{A\}$ through a 4×4 homogeneous transformation matrix, ${}^A_B\mathbf{T}$, expressed in terms of the *Study-parameters*. The Study parameters, namely, $x_0 : x_1 : x_2 : x_3 : y_0 : y_1 : y_2 : y_3$, represent spatial motions of a rigid-body via the *kinematic map* $\kappa : \mathbb{P}^7 \rightarrow \mathbb{SE}(3)$, when they satisfy the following constraints (see, e.g., [5]):

$$\text{Equation of the Study quadric: } x_0y_0 + x_1y_1 + x_2y_2 + x_3y_3 = 0, \quad (1)$$

$$\text{Normalisation constraint: } x_0^2 + x_1^2 + x_2^2 + x_3^2 = 1. \quad (2)$$

2.2 Kinematic Constraint Equations and the Operation Modes

The *loop-closure* constraints are derived from the fact that the passive links are rigid, and have a constant length r each:

$$\|{}^A\mathbf{p}_i - {}^A\mathbf{s}_i\|^2 - r^2 = 0, \quad i = 1, 2, 3, \quad (3)$$

where ${}^A\mathbf{s}_i$ locate the tip of the active links, given by ${}^A\mathbf{s}_1 = [l \cos \theta_1, l \sin \theta_1, 0, 1]^\top$, ${}^A\mathbf{s}_2 = [b + l \cos \theta_2, l \sin \theta_2, 0, 1]^\top$, ${}^A\mathbf{s}_3 = \left[\frac{b}{2} + l \cos \theta_3, \frac{\sqrt{3}}{2}b + l \sin \theta_3, 0, 1 \right]^\top$.

Equations (3) locate each of the points \mathbf{p}_i on a sphere centered at \mathbf{s}_i . To incorporate the planar nature of the manipulator, additional constraints are generated, by setting the Z component of ${}^A\mathbf{p}_i - {}^A\mathbf{s}_i$ to zero, and manipulating them a little:

$$\eta_1 : x_3y_0 + x_2y_1 - x_1y_2 - x_0y_3 = 0, \quad (4)$$

$$\eta_2 : x_1x_3 - x_0x_2 = 0, \quad (5)$$

$$\eta_3 : x_0x_1 + x_2x_3 = 0. \quad (6)$$

The forward kinematic problem is represented by the set of Eqs. (1–6). An analysis of the planarity constraints (Eqs. (4–6)) along with the Study quadric equation (Eq. (1)) and the normalisation constraint (Eq. (2)) lead to two distinct *operation modes* (see [4] for a similar analysis of the 3-RPS manipulator):

- Mode 1, characterised by $x_1 = x_2 = 0$, $x_0^2 + x_3^2 \neq 0$:
 From Eqs. (1) and (4), one finds that $y_0 = y_3 = 0$, as the non-trivial solution leads to $x_0^2 + x_3^2 = 0$, which cannot be admitted. Thus, the variables x_1, x_2, y_0, y_3 are eliminated from the equations in this mode, and the normalising constraint (in Eq. (2)) gets reduced to $x_0^2 + x_3^2 = 1$.
- Mode 2, characterised by $x_0 = x_3 = 0$, $x_1^2 + x_2^2 \neq 0$:
 Using a similar argument, it can be established that $y_1 = y_2 = 0$ in this operation mode; the normalising constraint (Eq. (2)) becomes $x_1^2 + x_2^2 = 1$.

It may be noted that the two modes described above cover *all* the possible solutions of the forward kinematics problem. Furthermore, the two modes are *dis-joint*, as their intersection would lead to the *exceptional generator*, characterised by $x_0 = x_1 = x_2 = x_3 = 0$, which is physically inadmissible.

2.3 Derivation of the Forward Kinematic Univariate (FKU)

In the following, the loop-closure equations are reduced to a univariate polynomial equation (termed as the *Forward Kinematic Univariate (FKU)* [6]) following a sequence of elimination of variables. For the sake of brevity, only mode 1 is explained.

In mode 1, Eqs. (2 and 3) reduce to:

$$g_1 : l^2 - r^2 + 4l \sin \theta_1(x_0y_2 + x_3y_1) + 4l \cos \theta_1(x_0y_1 - x_3y_2) + 4(y_1^2 + y_2^2) = 0, \quad (7)$$

$$g_2 : (a - b)^2 + l^2 - r^2 + 2l \cos \theta_2(a(2x_3^2 - 1) + b + 2x_0y_1 - 2x_3y_2) + 4abx_3^2 - 4x_3y_2(a + b) + 4l \sin \theta_2(-ax_0x_3 + x_0y_2 + x_3y_1) - 4ax_0y_1 + 4bx_0y_1 + 4(y_1^2 + y_2^2) = 0, \quad (8)$$

$$g_3 : (a - b)^2 + l^2 - r^2 + l \sin \theta_3(a(\sqrt{3}(2x_3^2 - 1) - 2x_0x_3) + \sqrt{3}b + 4x_0y_2 + 4x_3y_1) + l \cos \theta_3(a(2x_3(\sqrt{3}x_0 + x_3) - 1) + b + 4x_0y_1 - 4x_3y_2) + 4abx_3^2 + 2x_3(a + b)(\sqrt{3}y_1 - y_2) - 2ax_0y_1 - 2\sqrt{3}ax_0y_2 + 2bx_0y_1 + 2\sqrt{3}bx_0y_2 + 4(y_1^2 + y_2^2) = 0, \quad (9)$$

$$g_4 : x_0^2 + x_3^2 - 1 = 0. \quad (10)$$

Therefore, mode 1 is represented by the ideal $\langle g_1, g_2, g_3, g_4 \rangle$. The steps to derive the FKU from this are:

1. Compute $h_1 = g_2 - g_1$, and $h_2 = g_3 - g_1$, which are linear in y_1, y_2 .
2. Obtain y_1, y_2 from $h_1 = 0, h_2 = 0$.
3. Substitute the values of y_1, y_2 in $g_1 = 0$, to obtain the equation $g'_1 = 0$ in x_0 and x_3 . The polynomial g'_1 is of degree six in x_3 .
4. Divide the polynomial g'_1 by g_4 , treating both as polynomials in x_3 , and obtain an expression for x_3 by solving the linear equation resulting from setting the remainder to zero.
5. Substitute x_3 back in g_4 to obtain the univariate in x_0 .

The FKU is of degree 6 in x_0^2 , hence there are a maximum of 6 real assembly modes, as each root is counted twice due to the nature of the kinematic map. A similar analysis leads to analogous results in mode 2.

2.4 Numerical Results and Interpretations

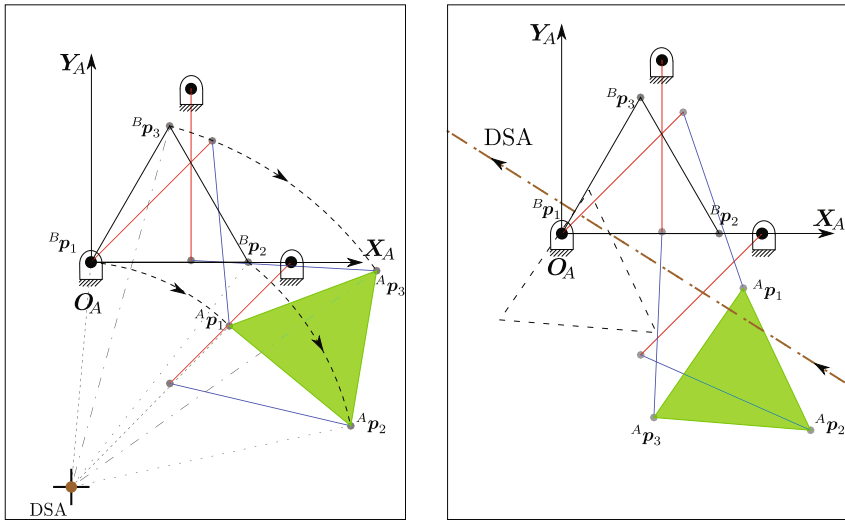
The above formulation is demonstrated via a numerical example, for the architecture parameters¹ $l = 6/7, r = 13/14, a = 11/14$ and $b = 1$. The set of input joint angles given by $\theta = [\pi/4, 5\pi/4, 3\pi/2]^T$ is found to produce 6 real solutions for each of the modes, which are listed in Table 1.

¹ All the linear dimensions are scaled by the base length, b , and are therefore unit-less; all angles are in radians.

Table 1. Twelve real solutions to forward kinematics

Operation mode	Assembly mode	x_0	x_1	x_2	x_3	y_0	y_1	y_2	y_3
Mode 1	1	-0.985	0	0	-0.172	0	-0.057	0.025	0
	2	-0.941	0	0	0.338	0	0.379	-0.033	0
	3	-0.852	0	0	0.523	0	-0.360	0.353	0
	4	-0.381	0	0	0.925	0	0.060	-0.011	0
	5	-0.350	0	0	-0.937	0	-0.058	-0.299	0
	6	-0.169	0	0	0.986	0	-0.116	0.795	0
Mode 2	1	0	-0.983	-0.185	0	-0.155	0	0	0.178
	2	0	-0.941	0.338	0	0.278	0	0	-0.335
	3	0	-0.845	0.535	0	-0.456	0	0	-0.127
	4	0	-0.369	0.930	0	0.028	0	0	-0.835
	5	0	-0.341	-0.940	0	-0.099	0	0	0.544
	6	0	-0.172	0.985	0	-0.133	0	0	-0.083

It is of interest to study the operation modes of the manipulator in terms of the finite screw motions generated by them. In mode 1, the motion is equivalent to a *pure* rotation about the *discrete screw axis (DSA)* [4], which is parallel to the Z axis and intersects the XY plane at $x = y_2/x_3, y = -y_1/x_3$. The pitch of the screw is null, as expected. Figure 2a shows the screw motion, using the numerics corresponding to assembly mode 2 of operation 1 from Table 1.



(a) Mode 1: The triangle ${}^B p_1 {}^B p_2 {}^B p_3$ represented in local frame, when rotated about the DSA, transforms to the final position ${}^A p_1 {}^A p_2 {}^A p_3$ (filled triangle), indicating a pure-rotation.

(b) Mode 2: The interim position (dashed) is reached through π -rotation about the DSA from the home position ${}^B p_1 {}^B p_2 {}^B p_3$. The final position ${}^A p_1 {}^A p_2 {}^A p_3$ (filled) is then attained through translation along the DSA.

Fig. 2. Screw motion characteristics of the operation modes

The motion generated in mode 2 is not physically realisable without a disassembly of the manipulator, as it involves a rotation through π about a *horizontal* DSA. The equation of the DSA in the plane is found to be $y = (x_2x + y_3)/x_1$. Such screws have been termed as the π -screws in [4]. Figure 2b depicts the motion and the corresponding DSA for the assembly mode 3 of operation mode 2 listed in Table 1.

3 Forward Kinematic Analysis in the Joint Space

In this section, the forward kinematic analysis is performed in terms of the passive joint angles. Existence of the operation modes is brought out and the relationship between the two modes is established in terms of certain properties of the FKU.

3.1 Derivation of the FKU and Its Interpretation

In this case, the end-points of the passive links are expressed in terms of the active and the passive joint angles as follows: ${}^A\mathbf{p}_1 = {}^A\mathbf{s}_1 + [r \cos \phi_1, r \sin \phi_1, 0, 1]^T$, ${}^A\mathbf{p}_2 = {}^A\mathbf{s}_2 + [r \cos \phi_2, r \sin \phi_2, 0, 1]^T$, ${}^A\mathbf{p}_3 = {}^A\mathbf{s}_3 + [r \cos \phi_3, r \sin \phi_3, 0, 1]^T$, where ${}^A\mathbf{s}_i, i = 1, 2, 3$ are given in Sect. 2.2. Equating the distance between each distinct pair of vertices of the moving platform to the known value a , the loop-closure constraints are obtained as:

$$f_1(\phi_1, \phi_2) \triangleq ({}^A\mathbf{p}_1 - {}^A\mathbf{p}_2) \cdot ({}^A\mathbf{p}_1 - {}^A\mathbf{p}_2) - a^2 = 0, \tag{11}$$

$$f_2(\phi_2, \phi_3) \triangleq ({}^A\mathbf{p}_2 - {}^A\mathbf{p}_3) \cdot ({}^A\mathbf{p}_2 - {}^A\mathbf{p}_3) - 2a^2(1 - \cos \gamma) = 0, \tag{12}$$

$$f_3(\phi_1, \phi_3) \triangleq ({}^A\mathbf{p}_3 - {}^A\mathbf{p}_1) \cdot ({}^A\mathbf{p}_3 - {}^A\mathbf{p}_1) - a^2 = 0, \tag{13}$$

where $\gamma = \pi/3$ is the interior angle of the triangular moving platform. The parameter γ is retained in its symbolic form to facilitate certain inferences drawn later in the paper. Equations (11–13) are linear in the sine and cosine of each of the passive angles, from which an FKU in $t_2 = \tan(\phi_2/2)$ can be obtained easily following the elimination/transformation sequence depicted below²:

$$\left. \begin{array}{l} f_1(\phi_1, \phi_2) = 0 \\ f_3(\phi_1, \phi_3) = 0 \end{array} \right) \xrightarrow{\times \phi_1} \left. \begin{array}{l} u(\phi_2, \phi_3) = 0 \\ f_2(\phi_2, \phi_3) = 0 \end{array} \right) \begin{array}{l} \xrightarrow{\phi_3 \rightarrow t_3} v_1(t_3, \phi_2) = 0 \\ \xrightarrow{\phi_3 \rightarrow t_3} v_2(t_3, \phi_2) = 0 \end{array} \xrightarrow{\times t_3} w(\phi_2) = 0.$$

The notation ‘ $\xrightarrow{\times x}$ ’ denotes the elimination of the variable x from two algebraic equations preceding it, while ‘ $\xrightarrow{\phi_i \rightarrow t_i}$ ’ indicates the conversion of an equation in ϕ_i to its polynomial equivalent in the variable $t_i = \tan(\phi_i/2)$. The equation $w(\phi_2) = 0$, when converted to a polynomial in $t_2 = \tan(\phi_2/2)$, is of degree 12,

² The derivation of this FKU is neither difficult, nor novel; hence the details are omitted for the sake of brevity.

indicating the possibility of existence of 12 real assembly modes—a result that matches with the previous analysis. The FKU decomposes into two factors as follows:

$$w(\gamma, t_2) = j_1(\gamma, t_2)j_2(\gamma, t_2), \text{ where } j_1(\gamma, t_2) = j_2(-\gamma, t_2). \quad (14)$$

Equation (14) confirms the relation between the two modes, as mode 2 corresponds to a moving platform that has been *flipped* up-side down, or equivalently, one in which the sequence of the vertices have been changed from CCW to CW. Also, it has been verified symbolically, that $j_i(\gamma, t_2) = 0$ is the FKU for the mode i , $i = 1, 2$.

3.2 Geometric Interpretation of the Operation Modes

It is well-known that the forward kinematics of certain planar three degrees-of-freedom parallel manipulators is equivalent to the problem of intersection of the *coupler curve* of a four-bar mechanism and a circle, which leads to a maximum of six assembly modes (see, e.g., [2]). In Fig. 3a, the dotted (blue) curve is the locus of p_3 as a part of the four-bar sub-chain $s_1p_1p_2s_2s_1$, with s_1s_2 as its ground link, corresponding to mode 1 of operation, superimposed over the assembly mode shown in Fig. 2a. The circle represents the locus of p_3 as a part of the sub-chain $b_3s_3p_3$, once the input θ_3 is given. The solid (red) curve in Fig. 3b corresponds to the mode 2, and is obtained by rotating the coupler link p_1p_2 about the axis X_B by π -radians, and then performing a similar analysis. The solutions marked on Fig. 3b correspond to the numerics presented in Sect. 2.4. These figures can be thought of as a visual interpretation of Eq. (14).

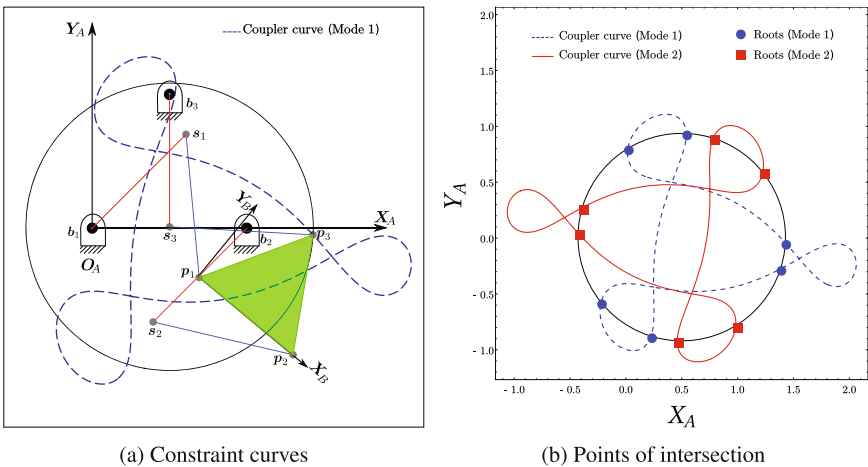


Fig. 3. Location of p_3 as the intersection of the two planar curves. (Color figure online)

4 Conclusion

This paper analyses the planar 3-RRR manipulator, to establish its two operation modes, and the six assembly modes in each. This result is first derived using the Study parameters, and then corroborated with the results obtained from the study of the kinematics of the manipulator in its joint space. Finally, the results are unified using a graphical visualisation of the assembly modes, in terms of the intersection of the constraint curves generated by the sub-chains of the manipulator. It is shown, that mathematically all the twelve assembly modes can be real at the same time, though physically it is impossible for the manipulator to transit from one operation mode to the other, and hence only one operation mode is apparent any time.

References

1. Gosselin, C., Sefrioui, J.: Polynomial solutions for the direct kinematic problem of planar three-degree-of-freedom parallel manipulators. In: *Robots in Unstructured Environments, 1991 ICAR, Fifth International Conference on Advanced Robotics*, pp. 1124–1129. IEEE (1991)
2. Hunt, K.: Structural kinematics of in-parallel-actuated robot-arms. *J. Mech. Transm. Autom. Des.* **105**(4), 705–712 (1983)
3. Husty, M.L.: Non-singular assembly mode change in 3-RPR-parallel manipulators. In: *Computational Kinematics*, pp. 51–60. Springer (2009)
4. Schadlbauer, J., Walter, D., Husty, M.: The 3-RPS parallel manipulator from an algebraic viewpoint. *Mechanism Mach. Theory* **75**, 161–176 (2014)
5. Selig, J.: *Geometric Fundamentals of Robotics*. Springer Science+Business Media Inc., Berlin (2005)
6. Srivatsan, R.A., Bandyopadhyay, S.: Analysis of constraint equations and their singularities. In: *Advances in Robot Kinematics*, pp. 429–436. Springer (2014)

The Impact of Kinematic Redundancies on the Conditioning of a Planar Parallel Manipulator

Joao Vitor C. Fontes^(✉), Hiparco L. Vieira, and Maíra M. da Silva

Department of Mechanical Engineering, São Carlos School of Engineering,
University of São Paulo - USP, São Carlos, São Paulo, Brazil
{joao.fontes,hiparcolins}@usp.br, mairams@sc.usp.br

Abstract. Parallel manipulators present drawbacks such as singularities inside their workspace. In order to measure these drawbacks, the condition number of the Jacobian matrix can be used either as a measurement of the distance between the end effector and singularities or as an isotropy index. In this paper, a study of the impact of kinematic redundancies on the improvement of a planar manipulator's isotropicity and on the reduction of singularities is presented. In order to do so, conditioning maps are exploited for the non-redundant 3RRR and for the kinematically redundant 3PRRR manipulators. The outcome of this evaluation supports evidences in favor of kinematic redundancies regarding kinematic characteristics.

Keywords: Parallel kinematic manipulator (PKM) · Kinematic redundancy · Singularity avoidance · Conditioning maps · Isotropy index

1 Introduction

Parallel kinematic manipulators (PKMs) can be promising industrial alternatives to serial manipulators due to their higher dynamic capabilities, higher accuracy and better payload/self-weight ratio [4]. Nevertheless, they present important drawbacks regarding real applications [5]. Some of these drawbacks are caused by the presence of singularities in the parallel manipulator's workspace. For instance, the accuracy of a PKM may rapidly decrease near singularities during a task. Kinematic redundancy can be applied to avoid or attenuate this problem. It consists in the introduction of an active joint in a kinematic chain allowing the self-motion of the manipulator. Due to the inclusion of the redundant actuator, the inverse kinematic model of kinematically redundant PKMs presents infinite solutions. A proper selection of a solution may enforce the avoidance of undesirable behaviour. In fact, kinematic redundancy has been used not only for the singularities' avoidance but also for the improvement of manipulator's kinematic and dynamic characteristics [2, 3, 6].

Additionally, PKMs present highly coupled dynamics which can become an issue for designing and implementing real-time control strategies for industrial

applications [7]. The coupling of the mechanism can be measured by an isotropic index that can be defined by the condition number of the Jacobian matrix as described by [8]. This index is also exploited as a measurement of the distance between the end effector and singularities [1].

In this manuscript, a study of the impact of kinematic redundancies on the enhancement of the manipulator's isotropy and on the reduction of singular regions. This is accomplished by identifying the behaviour of the condition number of the Jacobian matrix of planar parallel kinematic manipulators with kinematic redundancy. In order to do that, the non-redundant manipulator, the 3RRR , and the kinematically redundant manipulator, the 3PRRR are investigated. These manipulators, illustrated in Fig. 1, present three kinematic chains composed of one active revolute joint (\underline{R}) and two passive revolute joints (RR). The inclusion of extra active prismatic joints (\underline{P}) is responsible for the kinematic redundancies.

The comparison of the behaviour of the condition number of the Jacobian matrix for predefined tasks could yield misleading interpretations, since this outcome is task dependent. In this way, conditioning maps are proposed and depicted over the manipulator's workspace. In this proposal, the kinematic redundancy is properly treated.

This paper is organized as follows. The kinematic model of the 3PRRR manipulator is described in Sect. 2. Section 3 presents the methodology addressing the conditioning maps. The results are presented and discussed in Sect. 4. Finally, conclusions are drawn in Sect. 5.

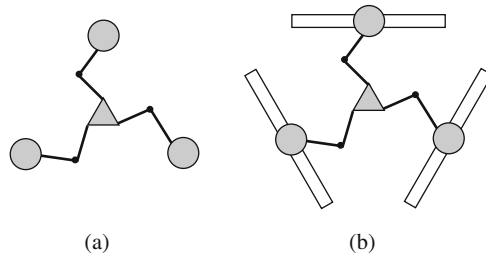


Fig. 1. Illustrations of (a) the non-redundant manipulator 3RRR and (b) the kinematically redundant manipulator 3PRRR .

2 Kinematic Model

In this section, the kinematic model of the 3PRRR manipulator is presented. This model can be used to represent the non-redundant manipulator 3RRR by imposing the input values of the redundant actuators. Figure 2 illustrates a scheme of the geometry of the 3PRRR . The subscript $i = 1, \dots, 3$ describes the kinematic chain. There are revolute joints in A_i , B_i and C_i , where A_i is active and B_i and C_i are passive. The angles θ_i and β_i represent the orientation

of the links A_iB_i and B_iC_i , respectively. The lengths of links A_iB_i and B_iC_i are, respectively, l_1 and l_2 . Active prismatic joints can modify the position of the point A_i . Using this linear actuators the position of A_i can be modified according to the position δ_i and the orientation γ_i (see Fig. 2b). The distance between the manipulator's center and the central position of the linear actuators is represented by a . The Cartesian position of the end effector is (x, y) with orientation α . The distance of C_i to the center of the end effector is h . Details on this description can be found in [3].

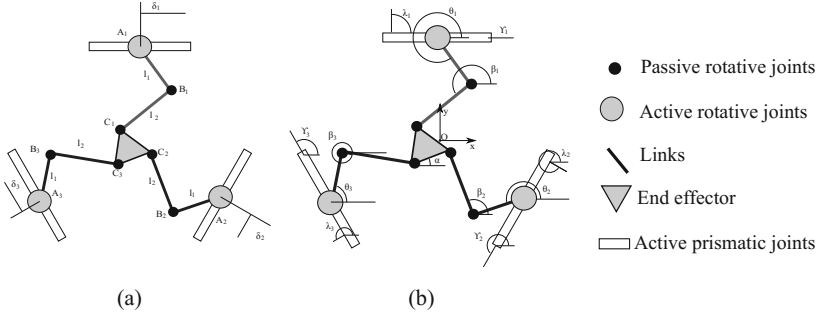


Fig. 2. Model parameters of the redundant manipulator 3PRRR: (a) points and link lengths; (b) angles and coordinate system.

2.1 Inverse Kinematics

The inverse kinematic model is used to determine the active joints' inputs $\Theta = [\theta_1, \theta_2, \theta_3, \delta_1, \delta_2, \delta_3]^T$ that yield a desired end effector's pose $\mathbf{X} = [x, y, \alpha]^T$. Due to the kinematic redundancies, this task is not simple since the mechanism presents six actuators while the end effector presents only three DOFs. As a consequence, this problem, usually denoted as redundancy resolution, presents infinite solutions. So, considering that the values of the redundant actuators' inputs δ_1, δ_2 and δ_3 are known, the inverse kinematics of the manipulator is defined.

First, the variables ρ_{xi} and ρ_{yi} are introduced as:

$$\begin{bmatrix} \rho_{xi} \\ \rho_{yi} \end{bmatrix} = \begin{bmatrix} x \\ y \end{bmatrix} + h \begin{bmatrix} \cos(\alpha + \lambda_i) \\ \sin(\alpha + \lambda_i) \end{bmatrix} - \delta_i \begin{bmatrix} \cos(\gamma_i) \\ \sin(\gamma_i) \end{bmatrix} - a \begin{bmatrix} \cos(\lambda_i) \\ \sin(\lambda_i) \end{bmatrix}. \quad (1)$$

The following geometrical constraint can be imposed according to the length of the links:

$$\left\| \begin{bmatrix} \rho_{xi} - l_1 \cos(\theta_i) \\ \rho_{yi} - l_1 \sin(\theta_i) \end{bmatrix} \right\| = l_2. \quad (2)$$

Expanding the norm in Eq. 2 and rearranging its result, the following relation can be obtained:

$$e_{i1} + e_{i2} \cos(\theta_i) + e_{i3} \sin(\theta_i) = 0, \quad (3)$$

where

$$e_{i1} = -2l_1\rho_{yi}, \tag{4}$$

$$e_{i2} = -2l_1\rho_{xi} \tag{5}$$

$$e_{i3} = \rho_{xi}^2 + \rho_{yi}^2 + l_1^2 - l_2^2 = 0. \tag{6}$$

The tangent half-angle substitution is employed to solve Eq. 3 for θ_i yielding:

$$\theta_i = 2 \tan^{-1} \left(\frac{-e_{i1} \pm \sqrt{e_{i1}^2 + e_{i2}^2 - e_{i3}^2}}{e_{i3} - e_{i2}} \right). \tag{7}$$

Using Eq. 2 and the result of θ_i , the angle β_i can also be determined by

$$\beta_i = \tan^{-1} \left(\frac{\rho_{yi} - l_1 \sin(\theta_i)}{\rho_{xi} - l_1 \cos(\theta_i)} \right). \tag{8}$$

2.2 Jacobian Matrix

The Jacobian matrix \mathbf{J} , which relates $\dot{\mathbf{X}} = [\dot{x}, \dot{y}, \dot{\alpha}]^T$ with $\dot{\Theta} = [\dot{\theta}_1, \dot{\theta}_2, \dot{\theta}_3, \dot{\delta}_1, \dot{\delta}_2, \dot{\delta}_3]^T$, needs to be determined as well for the calculation of the manipulators' conditioning. This relation is defined as

$$\dot{\mathbf{X}} = \mathbf{J}\dot{\Theta} \tag{9}$$

One way to determine it is by taking the time derivative of the constraint relation described by Eq. 3. This approach yields:

$$\begin{aligned} \dot{x}[l_2 \cos(\beta_i)] + \dot{y}[l_2 \sin(\beta_i)] + \dot{\alpha}[l_2 h \sin(\beta_i - \lambda_i - \alpha)] = \\ = \dot{\theta}_i[l_1 l_2 \sin(\beta_i - \theta_i)] + \dot{\delta}_i[l_2 \cos(\beta_i - \gamma_i)]. \end{aligned} \tag{10}$$

Equation 10 can be rewritten in a matrix form yielding

$$\mathbf{A}\dot{\mathbf{X}} = \mathbf{B}\dot{\Theta}. \tag{11}$$

The matrices \mathbf{A} and \mathbf{B} can be defined as:

$$\mathbf{A} = \begin{bmatrix} a_{11} & a_{12} & a_{13} \\ a_{21} & a_{22} & a_{23} \\ a_{31} & a_{32} & a_{33} \end{bmatrix} \text{ and} \tag{12}$$

$$\mathbf{B} = \begin{bmatrix} b_{11} & 0 & 0 & b_{14} & 0 & 0 \\ 0 & b_{22} & 0 & 0 & b_{25} & 0 \\ 0 & 0 & b_{33} & 0 & 0 & b_{36} \end{bmatrix}. \tag{13}$$

where $a_{i1} = l_2 \cos(\beta_i)$, $a_{i2} = l_2 \sin(\beta_i)$, $a_{i3} = l_2 h \sin(\beta_i - \lambda_i - \alpha)$, $b_{ii} = l_1 l_2 \sin(\beta_i - \theta_i)$ and $b_{ii+3} = l_2 \cos(\beta_i - \gamma_i)$.

3 Conditioning Map

The mathematical definition of singularities in PKMs is described by the determinant of the Jacobian matrices \mathbf{A} and \mathbf{B} [4]. Singular Jacobian matrices indicate singularities. Nevertheless, regions near to singularities can also be problematic for real applications and should be avoided. According to [1], the inverse of the condition number of the matrix \mathbf{A} can be used to evaluate the closeness between the end effector and singularities.

From the kinematic model, one can notice that the matrix \mathbf{A} is heterogeneous, thus its condition number has no physical meaning. This characteristic is due to the presence of translational and rotational DOFs. Therefore, in order to compensate and homogenize the matrix \mathbf{A} , [1] have proposed a new homogenized matrix $\bar{\mathbf{A}}$ defined as:

$$\bar{\mathbf{A}} = \begin{bmatrix} a_{11} & a_{12} & a_{13}/Lc \\ a_{21} & a_{22} & a_{23}/Lc \\ a_{31} & a_{32} & a_{33}/Lc \end{bmatrix}, \quad (14)$$

where $Lc = \sqrt{2}h$ is the manipulator's characteristic length.

The condition number κ of the matrix $\bar{\mathbf{A}}$ can be defined as

$$\kappa(\bar{\mathbf{A}}) = \frac{\max \sigma(\bar{\mathbf{A}})}{\min \sigma(\bar{\mathbf{A}})}, \quad (15)$$

where $\sigma(\bar{\mathbf{A}})$ is the vector of singular values of the matrix $\bar{\mathbf{A}}$.

By definition, the index κ^{-1} is bounded, ($0 \leq \kappa^{-1} \leq 1$). And, the following physical interpretation can be realized: $\kappa^{-1} = 0$ means that the manipulator is on a singularity and $\kappa^{-1} = 1$ means that it is on an ideal isotropic configuration. In this way, [1] have demonstrated that the index κ^{-1} indicates the distance between the end effector and the singularities.

Since the index κ^{-1} is dependent on the manipulators' configuration, its value is not constant over the manipulators' workspace. In this way, the values of the index κ^{-1} can be calculated in a mesh over the manipulator's workspace. Conditioning maps can be depicted by plotting these values over the workspace.

For non-redundant manipulator, the 3RRR manipulator, a single kinematic configuration is derived by the inverse kinematic model. In this way, a single value of the index κ^{-1} is found for each configuration defined by the mesh. For the kinematically redundant manipulator, the 3PRRR manipulator, infinite configurations can be derived for a single pose of the end effector. In this work, the conditioning map for the redundant manipulator is derived by dividing each input of the active prismatic joints (the redundant actuators, δ_i) in k possible positions. The best inputs are found by extensive search for the higher value of the index κ^{-1} . The higher values of the index κ^{-1} are depicted yielding the conditioning maps for the redundant case.

4 Results

In this comparison, the parameters for both manipulator are the same. Moreover, these values have been selected in order to match a real setup built by our research group [9]. The lengths of each link l_1 and l_2 are 0.191 m and 0.232 m, respectively. The limits of the linear actuators are $\delta_{min} = -0.3$ m and $\delta_{max} = 0.3$ m. The lengths a_i and h_i are the same for all kinematic chains and are equal to 0.260 m and 0.060 m, respectively.

Figure 3 depicts the conditioning map of the $3\underline{R}RR$ manipulator. There are three unreachable circles inside the workspace due to the difference in the lengths of links l_1 and l_2 . Moreover, the dark blue areas near to these circles present low condition numbers. This indicates that these regions are close to singularities. In general, the conditioning map of the $3\underline{R}RR$ shows that the manipulator conditioning is lower than 0.8 in a large amount of the workspace. Conditioning values higher than 0.8 can only be found at regions near to the center of the workspace.

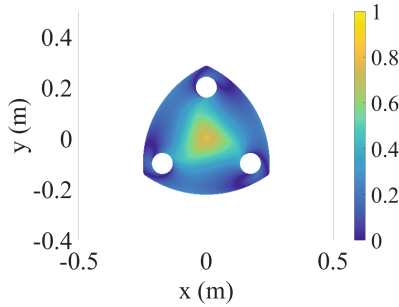


Fig. 3. Conditioning map of the non-redundant manipulator $3\underline{R}RR$. (Color figure online)

Figure 4 illustrates the conditioning map of the $3\underline{P}RRR$ manipulator. One can notice that there is no unreachable area inside the workspace, which is considerable larger than the $3\underline{R}RR$'s workspace. Moreover, there is no area that presents a conditioning index lower than 0.2 and there is a wide area with conditioning index higher than 0.8 in the center of the workspace.

Comparing Figs. 3 and 4, one can notice that the region with index values higher than 0.8 (yellow area) presents the same size of the $3\underline{R}RR$ workspace. This suggests that kinematic redundancy promotes the improvement of the manipulator's conditioning, since the $3\underline{P}RRR$ manipulator generally presents higher conditioning values than the $3\underline{R}RR$ manipulator.

Although the redundant manipulator has shown a better conditioning map, these aforementioned values can only be achieved in specific inputs of the active prismatic joints (the redundant actuators 1, 2 and 3). These optimal inputs are depicted in the workspace in Figs. 5(a), (b) and (c). One can observe that there are some important discontinuities regions in these maps leading to unfeasible

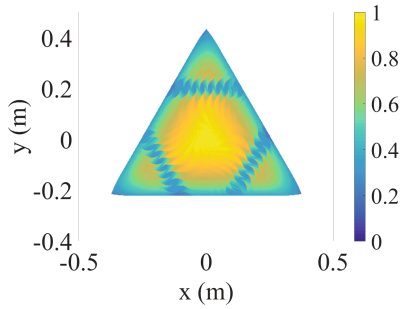


Fig. 4. Conditioning map of the redundant manipulator 3PRRR. (Color figure online)

trajectories for the redundant actuators. Indeed, this fact shows that the proposal of a strategy to design smooth optimal position maps can be helpful for the design of redundant manipulators. These maps can be useful for deriving redundancy resolution scheme for real applications.

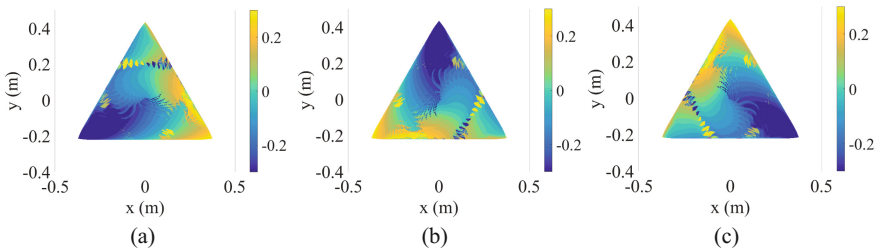


Fig. 5. Optimal inputs for the redundant actuators (a) δ_1 , (b) δ_1 and (c) δ_1 .

5 Conclusions

In general, PKMs present singularities in the workspace. In order to avoid these drawbacks, kinematic redundancy can be applied as stated in the literature. In this manuscript, the impact of kinematic redundancy on the conditioning of PKMs was addressed. In order to do that, two manipulators were compared: the non-redundant 3RRR and the redundant 3PRRR manipulators. This comparison was carried out by contrasting the conditioning maps of both manipulators. These maps were depicted by plotting the inverse of the condition number of the homogenized Jacobian matrix in the manipulator’s workspace.

The results demonstrated a considerable increase in the area where the conditioning index is larger than 0.8 when kinematic redundancies are considered. This indicates that kinematic redundancies can be an alternative for improving the performance of PKMs. Finally, the authors believe that these conditioning maps could be applied to the development of a redundancy resolution scheme improving the conditioning of redundant manipulators for real applications.

Acknowledgements. This research is supported by FAPESP 2014/01809-0, FP7-ITN Grant Agreement 315967 - EMVeM (Energy Efficiency Management for Vehicles and Machines) and CNPq.

References

1. Alba-Gomez, O., Wenger, P., Pamanes, A.: Consistent kinetostatic indices for planar 3-DOF parallel manipulators, application to the optimal kinematic inversion. In: 29th Mechanisms and Robotics Conference, Parts A and B, vol. 7, pp. 765–774. ASME. (2005). doi:[10.1115/DETC2005-84326](https://doi.org/10.1115/DETC2005-84326)
2. Do Thanh, T., Kotlarski, J., Heimann, B., Ortmaier, T.: Dynamics identification of kinematically redundant parallel robots using the direct search method. *Mech. Mach. Theory* **55**, 104–121 (2012). doi:[10.1016/j.mechmachtheory.2012.03.011](https://doi.org/10.1016/j.mechmachtheory.2012.03.011)
3. Fontes, J.V., da Silva, M.M.: On the dynamic performance of parallel kinematic manipulators with actuation and kinematic redundancies. *Mech. Mach. Theory* **103**, 148–166 (2016). doi:[10.1016/j.mechmachtheory.2016.05.004](https://doi.org/10.1016/j.mechmachtheory.2016.05.004)
4. Gosselin, C., Angeles, J.: Singularity analysis of closed-loop kinematic chains. *IEEE Trans. Robot. Autom.* **6**(3), 281–290 (1990). doi:[10.1109/70.56660](https://doi.org/10.1109/70.56660)
5. Merlet, J.P.: *Parallel Robots*. Springer (2006)
6. Mohamed, M.G., Gosselin, C.M.: Design and analysis of kinematically redundant parallel manipulators with configurable platforms. *IEEE Trans. Robot.* **21**(3), 277–287 (2005). doi:[10.1109/TRO.2004.837234](https://doi.org/10.1109/TRO.2004.837234)
7. Paccot, F., Andreff, N., Martinet, P.: A review on the dynamic control of parallel kinematic machines: theory and experiments. *Int. J. Robot. Res.* **28**(3), 395–416 (2009). doi:[10.1177/0278364908096236](https://doi.org/10.1177/0278364908096236)
8. Patel, S., Sobh, T.: Manipulator performance measures - a comprehensive literature survey. *J. Intell. Robot. Syst.* **77**(3–4), 547–570 (2015). doi:[10.1007/s10846-014-0024-y](https://doi.org/10.1007/s10846-014-0024-y)
9. Santos, J.C., Frederice, D., Fontes, J.V.C., da Silva, M.M.: Numerical analysis and prototyping details of a planar parallel redundant manipulator. In: 2015 12th Latin American Robotics Symposium and 2015 3rd Brazilian Symposium on Robotics (LARS-SBR), pp. 55–60. IEEE (2015). doi:[10.1109/LARS-SBR.2015.30](https://doi.org/10.1109/LARS-SBR.2015.30)

Holistic Modular Multilayer Synthesis of Planar Linkages Using Parameterized Mass Properties

S. Heinrich^(✉) and M. Berger

Dept. of Mechanical Engineering, Professorship Assembly and Handling Technologies,
Chemnitz University of Technology,
Reichenhainer Straße 70, 09126 Chemnitz, Germany
{stefan.heinrich,maik.berger}@mb.tu-chemnitz.de

Abstract. This paper shows that new opportunities and areas of development arise from using a module-based layer synthesis and description of mass properties combined with a domain spanning system simulation software. That allows for a holistic mechanism synthesis with a continuous analysis-synthesis-parameter-adjustment (ASPA). Hence, the user may perform both mechanism analysis and synthesis employing one single program interface with, what is also possible, an identification of the ideal mechanism in terms of dynamics during an optimization process.

Keywords: Modular multilayer synthesis · Planar linkages · Parameterized mass properties · Rigid body dynamics

1 Introduction

For applying state of the art techniques to determine a dynamically favorable design of nonlinear mechanisms, it is necessary to know their characterizing parameters, such as structure related dimensions, mass, stiffness and damping matrices. In order to optimize a preferred nonlinear drive assembly by using high-performance programs (e.g. PTC Creo Elements/Mechanism, ESI ITI SimulationX or Altair HyperWorks) today's methods offer solutions like mass or power balancing. Despite their certain functions, these software tools sparsely answer typical synthesis questions to fulfill arbitrary motion demands or dynamical boundary conditions. Therefore, a new method has been developed based on a local cross-linking of an analysis, synthesis and optimization to close the gap between the demands and already existing functions within a chosen software environment as shown in Fig. 1. In order to obtain this cross-linking, one main objective was to create a flexible method for everyday engineering practice. Hence, the principle of module based system engineering (as used in the software ITI SimulationX) was retrieved [1] which posed two main challenges. Firstly, it was necessary to develop a library of standardized synthesis modules that can easily be implemented within the aforementioned software environments and that provides the geometrical dimensions of a mechanism. The mathematical concept of this library is described in Sect. 2.

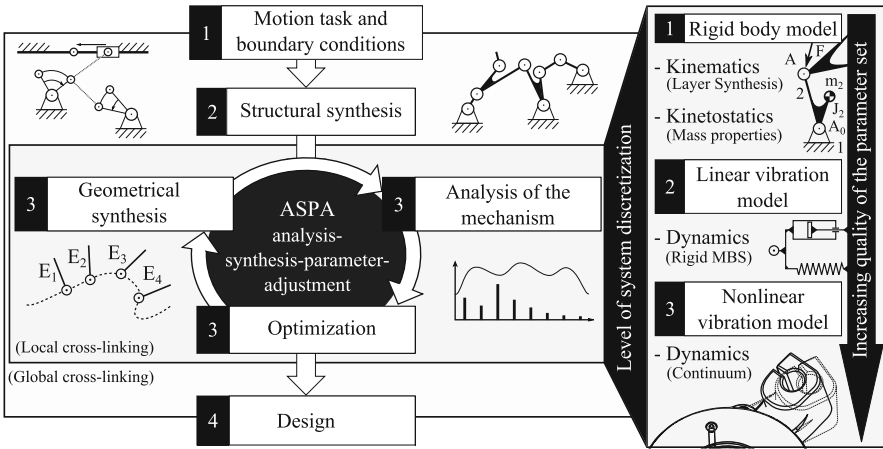


Fig. 1. Principle of an interactive analysis-synthesis-parameter-adjustment

A holistic mechanism synthesis with dynamical boundaries, like changing natural frequencies or reducing the foundation excitation, requires a proper description of all mass properties depending on the level of system discretization (established by Dresig [2]) shown in Fig. 1. Therefore, Sect. 3 offers a suitable way to determine these parameters by approximating data sets gained from design studies of predefined solids or assemblies.

2 Modular Geometrical Synthesis

As mentioned before, it is necessary to create randomly connectable synthesis modules as shown in Fig. 2, that are able to communicate and interact with each other. Furthermore, they have to solve the synthesis and provide all relevant information for the computation of mass properties, explained in Sect. 3.

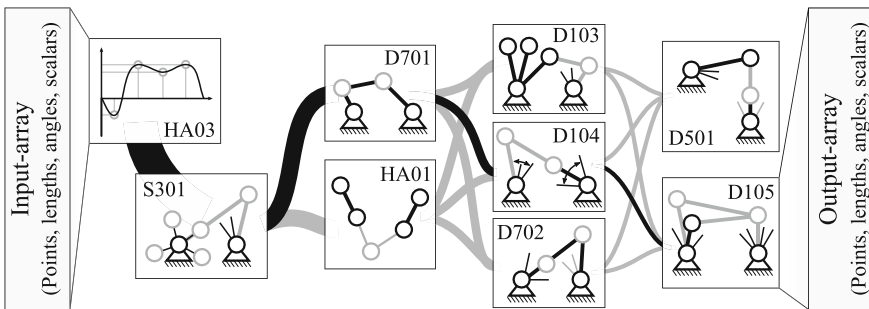


Fig. 2. Exchange of information within a connected modular synthesis

Therefore, each module uses point positions, lengths, angles and scalars to calculate the missing parameters describing every position of each point or plane. Each module returns a standardized data set including the missing positions, lengths, angles or scalars, such as the installation position of a joint point or other design factors. All modules are classified into five categories, shown in Fig. 3. The module V103, for example, is the third (03) variation of the four layer synthesis to compute a revolute joint within a moving frame of reference. This module can be used to find a coupler point on a moving link that is linked to a rocker. Furthermore, this module fulfills the boundary condition that in three out of four linkage positions the rocker does not rotate. Section 4 contains further details on how to use the library.

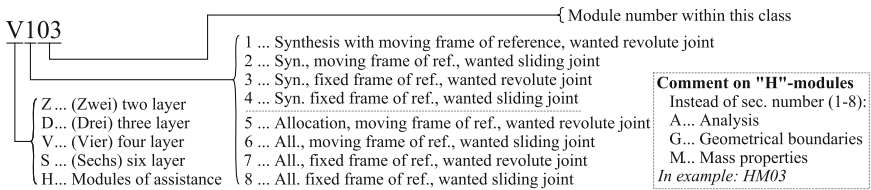


Fig. 3. Classification used within the new modular synthesis library

In order to implement such a library in any MBS or math software, it was necessary to find a suitable way to mathematically describe the solution for a given motion task. Accordingly, the basic approaches were vector analysis and complex numbers. During several studies it appeared that using complex indicators within the program language Modelica, which is the library language used in SimulationX, led to a significant increase of the effective calculation time. Despite this, it is a suitable way to compute the solution with mathematical software (for example Mathcad, Matlab or HyperMath). The following example of a three layer synthesis with a moving frame of reference explains the mathematical description. The module defines the revolute joint B in its three positions shown in Fig. 4.

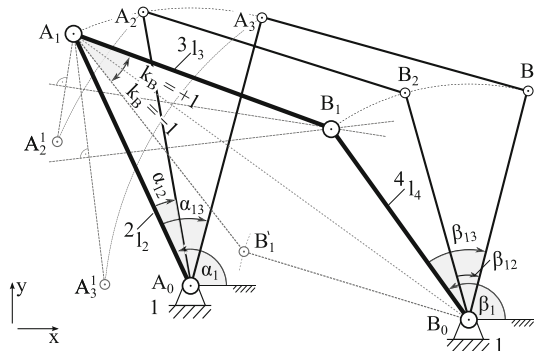


Fig. 4. Input and output of the synthesis module D103

The ingoing parameters of this module are the frame points A_0 and B_0 (given by $x_{A_0}, y_{A_0}, x_{B_0}$ and y_{B_0}), the link length l_2 , the angles $\alpha_1, \alpha_{12}, \alpha_{13}, \beta_{12}$ and β_{13} . A_0 is calculated with complex numbers and so is analogous to Eq. (1) B_0 . The first step is to calculate the positions $A_{1,2,3}$ of the revolute joint point A according to Eqs. (2) and (3). In order to calculate the center point B_1 , it is necessary to transform the positions of A back into position one of the frame of reference which is the rocker 4. Therefore Eq. (4) is used to rotate the points A_2 and A_3 around B_0 .

$$A_0 = x_{A_0} + y_{A_0} \cdot i \quad i = \sqrt{-1} \quad (1)$$

$$A_1 = A_0 + l_2 \cdot e^{(\alpha_1 \cdot i)} \quad (2)$$

$$A_n = A_0 + l_2 \cdot e^{([\alpha_1 + \alpha_{1n}] \cdot i)} \quad n = [2, 3] \quad (3)$$

$$A_n^1 = B_0 + (A_n - B_0) \cdot e^{(-\beta_{1n} \cdot i)} \quad n = [2, 3] \quad (4)$$

The next step is to calculate the position of B_1 as the intersection point using the two perpendicular bisectors on the sides $A_1 - A_2^1$ and $A_1 - A_3^1$ by employing Eq. (5)¹.

$$B_1 = \frac{(A_2^1 - A_3^1)|A_1|^2 + (A_3^1 - A_1)|A_2^1|^2 + (A_1 - A_2^1)|A_3^1|^2}{(A_1 - A_3^1)(A_2^1 - A_1) - (A_1 - A_2^1)(A_3^1 - A_1)} \quad (5)$$

Calculating the positions B_2 and B_3 by rotating them around B_0 as shown in Eq. (6) is a faster way than applying the law of cosine due to the fact that the layer synthesis guarantees the adherence of all the three positions.

$$B_n = B_0 + (B_1 - B_0) \cdot e^{(\beta_{1n} \cdot i)} \quad n = [2, 3] \quad (6)$$

Finally, the missing module outputs are defined through Eqs. (7) to (9). Equation (7) calculates β_1 (start angle) of the rocker. Equation (8) delivers the rocker and link length and Eq. (9) is used to define whether the installation position factor k_B is positive (+1) or negative (-1). This last factor is an important information for the module based analysis of the synthesized linkage according to VDI 2729 [3].

$$\beta_1 = \text{Im}(\ln(B_1 - B_0)) \quad (7)$$

$$l_3 = |B_1 - A_1| \quad l_4 = |B_1 - B_0| \quad (8)$$

$$k_B = \begin{cases} 1, & \text{if } \text{Im}\left(\ln\left[\frac{B_1 - A_1}{B_0 - A_1}\right]\right) > 0 \\ -1, & \text{otherwise} \end{cases} \quad (9)$$

As a result of these calculations, the module D103 returns the exact positions of $A_{1,2,3}$ and $B_{1,2,3}$, the angle β_1 , the link lengths l_3, l_4 and the installation position factor k_B . That information allows the modules to be included in a complex mechanism simulation. Furthermore, it is now possible to compute mass parameters with those synthesis solutions to achieve further analysis.

¹ The vinculum within the denominator is used for the conjugated complex vector.

3 Parameterized Mass Properties

Anticipating nearly exact mass properties during a layer synthesis to determine the dynamical behavior of a drive assembly combined with its optimization leads to the issue dealt within this section. There are several different ways to compute mass properties from solids with or without the CAD environment. Typically, a CAD software continuously calculates the moment of inertia \underline{J} according to Eq. (10) by knowing all the relevant model parameters (constant density ρ , the position vectors \underline{r}) and especially the bounds of integration due to the design process. Bearing that in mind, it would be necessary to create CAD features within typical MBS or math software if it was necessary to compute mass properties in the exact same manner.

$$\underline{J} = \rho \int_V \left((\underline{r} \cdot \underline{r}) \underline{I} - \underline{r} \otimes \underline{r} \right) dV \quad \underline{I} \dots \text{identity tensor} \quad (10)$$

However, there are five ways to describe the unknown mass parameters which can easily be implemented:

1. Co-simulation with parametric models and a continuous exchange of parameters
2. Parameter identification based on a CAD design study
3. Manipulation of triangulated solids from STL files
4. Determination of mass properties by using primitive solids
5. Using discrete mass points for a compensatory moment of inertia

Referring to number 2, links in non linear mechanisms can be standardized by typically used design strategies shown in Fig. 5. Therefore, it is suitable to create a data set through a design study (VC) of predefined solids or assemblies within the CAD environment.

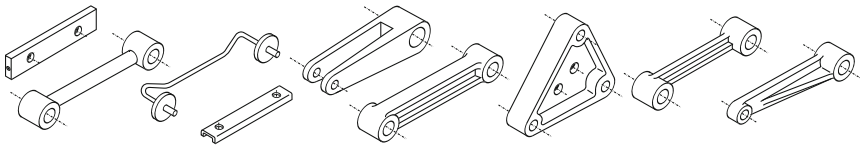


Fig. 5. Typical designs of linkages within mechanisms drawn by Volmer [4]

Such a data set contains the moment of inertia (J_S) about the polar axis, the position of the center of gravity (S) and the mass (m) of the solid. Furthermore, it contains all varied parameters, as for example a length or an angle. It occurs that using the Gauss method of least squares is also a practical way to approximate those mass parameters through a p -dimensional polynomial approach function. A ternary link, for example, can be described by three variable parameters: its two lengths l_{AB} , l_{AC} and the angle γ_{BAC} . This leads to a one, two or three dimensional polynomial approach function depending on the number of used

variables. Equation (11) represents such a p -dimensional polynomial approach function of the order n that can be used for the Gauss method.

$$P_n(x_1, \dots, x_p) = \sum_{n_1 + \dots + n_p < n} b_{n_1, \dots, n_p} \cdot x_1^{n_1} \cdot \dots \cdot x_p^{n_p} \tag{11}$$

Therefore, the minimization problem for a data set with m entries per dimension p is defined by Eq. (12). In this equation, \mathbf{b} represents the coefficient vector, \mathbf{x}_i the i^{th} p -dimensional variable vector from the data set and y_i the attached mass parameter.

$$\min_{\mathbf{b}} \sum_{i=1}^m \left(f(\mathbf{x}_i, \mathbf{b}) - y_i \right)^2 \tag{12}$$

Solving Eq. (12) leads to the polynomial coefficients of a p -dimensional function, in this case an area function as shown in Fig. 6. In this example, the two parameters γ_{BAC} and l_{AC} of the ternary link $A-B-C$ were varied. The polynomial regression led to one area function for each mass parameter vector from the data set.

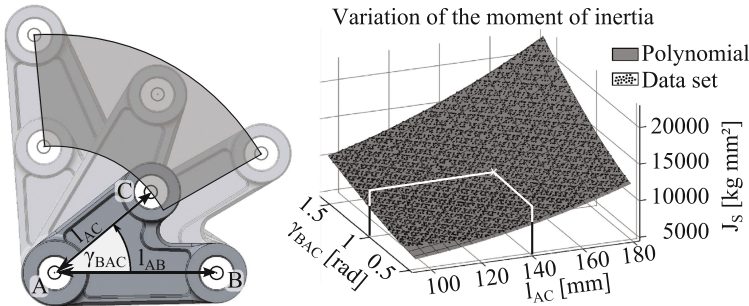


Fig. 6. Example of a design study with a polynomial regression approximating the data

Applying these polynomial functions to describe all the mass parameters gives the opportunity to investigate dynamical characteristics through a modal analysis or the distribution of the total energy of the mechanism.

4 Example of a Parameterized Multilayer Synthesis

This section deals with an example of a synthesis task based on a mechanism promoted by Socha in 1967 [5] that consists of 8 links. In Fig. 7 only the lower, and for this section relevant part of the complex mechanism, is shown. With the help of the introduced modular synthesis and description of link mass parameters it is possible to calculate the system behavior and study sensitivities by varying free parameters. Usually, a geometrical layer synthesis leads to a variety

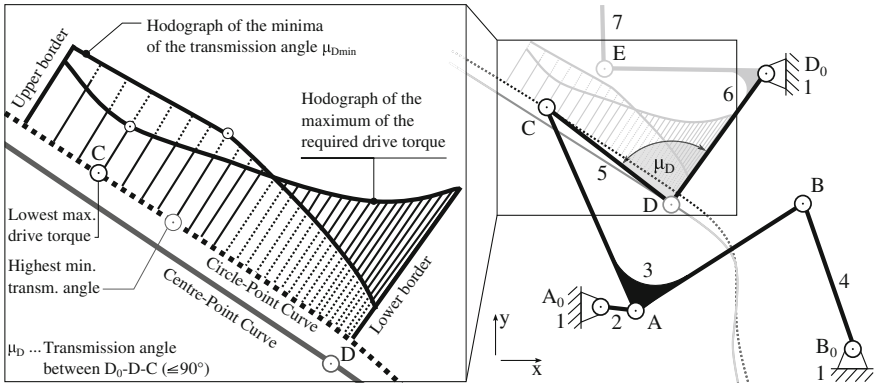


Fig. 7. Section of a coupler mechanism with a position variation on the Burmester curves [6]

of possible link lengths and angles, all fulfilling given motion demands. From such a variety of solutions the designer has to choose his favorable parameter set according to recommendations from the literature. Unfortunately, those are usually based on geometrical parameters like the transmission angle (see Fig. 7) which is not enough for meeting stronger boundary conditions on its dynamical behavior.

A variation of the position of C on the circle-point curve² during the layer synthesis directly affects the required drive torque based on the mass and energy distribution in the mechanism. By having a closer look on the drive torque curves from Fig. 8 it occurs that even within a small interval this variation has a huge impact on the maximum torque. The upper and lower border are defined through the given boundary conditions, that can be looked up in [6].

Comparing the hodograph of the required maximum drive torque with the hodograph of the transmission angle from Fig. 8 shows that a dynamical optimum

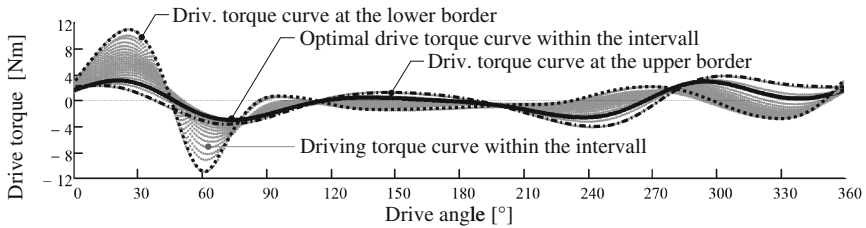


Fig. 8. Torque curves resulting from a parameter study within the given interval in Fig. 7

² The circle- and center-point curves are also known as Burmester curves in a four layer synthesis.

not necessarily has to be a geometrical optimum. The optimal drive torque curve can be reached by choosing a position on the circle-point curve close to the geometrical optimum. Further explanations on this example can be found in [6].

5 Conclusion

Determining a dynamically favorable design of a nonlinear mechanism usually leads to an iterative method based on experience and some imprecise recommendations from the literature. Thus, the classical geometrical layer synthesis often cannot meet the given dynamic boundaries. Referring to Fig. 7, a geometrical based optimization of a linkage could result in a dynamical disadvantageous mechanism. Trying to close the gap between dynamics and classical layer synthesis led to two challenges. The first objective was to develop a modular synthesis library based on algorithms that easily can be implemented in various MBS software. The second and more challenging objective was to find a suitable way to determine mass properties that are necessary for proper modeling. The shown approach of using design studies combined with a polynomial regression provides the opportunity to investigate the dynamical behavior during the synthesis. Based on an exact description of the mechanism mass parameters, it is now possible to improve the mechanism model. Especially when it comes to further studies on the mechanical system behavior, it is inevitable to know the exact moment of inertia (J_S) about the polar axis, the position of the center of gravity (S) and the mass (m). Further investigations on this issue will answer the following questions:

1. How can a variation of a design parameter from the layer synthesis positively influence the interchange of energy between the links, regarding the total amount of energy?
2. How does the variation of design parameters interfere with the response to parametric excitation, based on bearing play or stiffness?

References

1. Heinrich, S., Berger, M.: New concept of continuously interactive analysis-synthesis-parameter-adjustments (ASPA) for nonlinear drive assemblies. In: ITI Symposium, Dresden, 09 November–11 November 2015
2. Dresig, H.: Schwingungen Mechanischer Antriebssysteme. Springer, Heidelberg, Berlin (2014)
3. VDI-guideline 2729 Part 1: Modular analysis of planar linkages with rotating and sliding joints - Kinematic analysis, June 2016
4. Volmer, J., Dresig, H., Modler, K.: Getriebetechnik: Koppelgetriebe VEB Verlag Technik, Berlin, 1. Auflage (1979)
5. Socha, J.: Antriebsprobleme im Wirkmaschinenbau. Industrie-Anzeiger, Giradet, Essen, Germany (1967). <http://www.dmg-lib.org/>. Accessed 28 Jan 2017
6. Heinrich, S., Berger, M.: Modulgestützte Untersuchung der Mittel- und Kreispunktkurve hinsichtlich kinetostatischer Kenngrößen bei Stephenson-Getrieben. 18. VDI Getriebetagung - Bewegungstechnik, Nürtingen, VDI Berichte 2286 (2016). ISBN:978-3-18-092286-7

Theoretical Kinematics

Motion Interpolation in Lie Subgroups and Symmetric Subspaces

J.M. Selig¹(✉), Yuanqing Wu², and Marco Carricato²

¹ School of Engineering, London South Bank University, London SE1 0AA, UK
seligjm@lsbu.ac.uk

² Department of Industrial Engineering, Università di Bologna, Bologna, Italy
{yuanqing.wu,marco.carricato}@unibo.it

Abstract. We show that a map defined by Pfurner, Schröcker and Husty, mapping points in 7-dimensional projective space to the Study quadric, is equivalent to the composition of an extended inverse Cayley map with the direct Cayley map, where the Cayley map in question is associated to the adjoint representation of the group $SE(3)$. We also verify that subgroups and symmetric subspaces of $SE(3)$ lie on linear spaces in dual quaternion representation of the group. These two ideas are combined with the observation that the Pfurner-Schröcker-Husty map preserves these linear subspaces. This means that the interpolation method proposed by Pfurner *et al.* can be restricted to subgroups and symmetric subspaces of $SE(3)$.

Keywords: Motion interpolation · Lie triple systems · Symmetric subspaces · Cayley map

1 Introduction

There is a very large number of methods and procedures for interpolating rigid-body motion as this is an important problem not only in robotics but also in computer graphics. See the review paper by Röschel [6].

Recently [5], a new simple method was presented for interpolating motions based on the embedding of the group of rigid-body displacements $SE(3)$ in the seven dimensional projective space \mathbb{P}^7 as a non-singular quadric, known as the Study quadric Q_S . This method is reminiscent of a method proposed by Belta and Kumar where interpolation was carried out on matrices and then the matrices mapped back to the group of rigid-body displacements, see [9] and references therein.

Here we show that this new interpolation method is equivalent to using the Cayley map associated to the adjoint representation of the group. That is, the rational map, used by Pfurner, Schröcker and Husty to map points in \mathbb{P}^7 to Q_S is equivalent to performing the composition of the inverse Cayley map, extended to all of \mathbb{P}^7 , followed by the Cayley map sending points in \mathbb{P}^6 to the Study quadric.

In another recent work [13], a method for interpolating motions in symmetric subspaces of $SE(3)$ was given. Symmetric subspaces of $SE(3)$ are important in

many practical applications, see [11]. In [14], it was observed that these symmetric subspaces lie in the intersection of the Study quadric with some linear space. Below we make this statement precise. We also verify that the map defined in [5] respects these linear subspaces; a point in \mathbb{P}^7 , not on the Study quadric but lying in a linear subspace which defines a subgroup or symmetric subspace, will be mapped to a point in the intersection of the subspace and Q_S . So the interpolation method of Pfurner, Schröcker and Husty (PSH method) is ideally suited as an interpolation method on the symmetric subspaces. Finally, we give a couple of simple examples of the method.

2 Cayley Maps

Given a matrix representation of $se(3)$, the Lie algebra to the group of rigid-body displacements, we can map the Lie algebra to the group itself using the map,

$$\text{Cay}(A) = (I + A)(I - A)^{-1}, \tag{1}$$

where A is the matrix representing an element in $se(3)$ and I is the identity matrix. The result is a group element in $SE(3)$ represented as a matrix of the same dimension. These maps, unlike the exponential map, depend on the particular representation used. Here, the adjoint representation of $SE(3)$ is used and the corresponding Cayley map will be written Cay_6 .

Now a general dual quaternion is given by,

$$g = (a_0 + a_1i + a_2j + a_3k) + \varepsilon(c_0 + c_1i + c_2j + c_3k) \tag{2}$$

where i, j and k are the unit quaternion generators and ε is the dual unit which commutes with the quaternions and squares to zero, $\varepsilon^2 = 0$.

A rigid-body displacement is given by a dual quaternion with elements satisfying the equation,

$$a_0c_0 + a_1c_1 + a_2c_2 + a_3c_3 = 0. \tag{3}$$

Taking $(a_0 : a_1 : a_2 : a_3 : c_0 : c_1 : c_2 : c_3)$ as homogeneous coordinates in a \mathbb{P}^7 , the above quadratic equation determines the Study quadric Q_S .

In [10] the map Cay_6 and its inverse were described in terms of dual quaternions. An element of $se(3)$ can be written as a pure dual quaternion; $s = (w_1i + w_2j + w_3k) + \varepsilon(v_1i + v_2j + v_3k)$. In the algebra of dual quaternions the Cayley map based on the adjoint representation can be written as,

$$\text{Cay}_6(s) = \frac{1}{2(w_0^2 + \mu^2)^{3/2}} ((2w_0^2 + 3\mu^2)w_0 + (2w_0^2 + 3\mu^2)s + w_0s^2 + s^3), \tag{4}$$

where $\mu^2 = w_1^2 + w_2^2 + w_3^2$. The variable w_0 has been included to make the equation homogeneous. In this way the map can be viewed as a map from the projective space \mathbb{P}^6 , with homogeneous coordinates, $(w_0 : w_1 : w_2 : w_3 : v_1 : v_2 : v_3)$ to Q_S .

In order to give a compact but explicit formula for this map we introduce the following notation. Let,

$$\mathbf{a} = (a_0, a_1, a_2, a_3)^T, \quad \mathbf{c} = (c_0, c_1, c_2, c_3)^T,$$

and also

$$\mathbf{w} = (w_0, w_1, w_2, w_3)^T, \quad \mathbf{v} = (0, v_1, v_2, v_3)^T.$$

Now, the powers of s can be expanded in Eq. (4) and in terms of the above notation the Cayley map can be written,

$$\mathbf{a} = \mathbf{w}(\mathbf{w} \cdot \mathbf{w}), \quad \mathbf{c} = \mathbf{v}(\mathbf{w} \cdot \mathbf{w}) - \mathbf{w}(\mathbf{v} \cdot \mathbf{w}). \tag{5}$$

Note that, since the codomain of the map lies in a projective space, any common factors can be ignored. It is simple to check, using Eq. (3), that the image of the transformation is indeed the Study quadric. The map clearly has degree 3 in the homogeneous coordinates of \mathbb{P}^6 . The exceptional set for the map consists of the 2-plane $w_0 = w_1 = w_2 = w_3 = 0$ and the 4-dimensional intersection of the 2 quadrics $w_0^2 + w_1^2 + w_2^2 + w_3^2 = 0$ and $w_1v_1 + w_2v_2 + w_3v_3 = 0$.

The inverses of these maps were also found in [10]. Given a group element g satisfying (3), the inverse map is,

$$\text{Cay}_6^{-1}(g) = \frac{-1}{2a_0^2}(g^2 - 4a_0g + (3a_0^2 + a_1^2 + a_2^2 + a_3^2)). \tag{6}$$

If we assign $w_0 = -2a_0^2$, the common denominator, then the other coordinates of $s = \text{Cay}_6^{-1}(g)$ are given by expanding the polynomial in g and simplifying using the Study quadric, (3) and cancelling common factors:

$$\mathbf{w} = a_0\mathbf{a}, \quad \mathbf{v} = a_0\mathbf{c} - c_0\mathbf{a}. \tag{7}$$

This is a quadratic transformation with exceptional set consisting of the 5-plane $a_0 = c_0 = 0$ and the 3-plane $a_0 = a_1 = a_2 = a_3 = 0$. The 3-plane is the A-plane of ideal elements in the Study quadric, the points which do not correspond to any rigid-body transformation. The intersection of the 5-plane with the Study quadric is the set of half-turns, that is rotations by π radians about some axis. This pair of maps can be viewed as a birational transformation between the six-dimensional projective space \mathbb{P}^6 and the Study quadric Q_S in \mathbb{P}^7 .

Notice that the definition of the inverse of Cay_6 , can be extended to all points of \mathbb{P}^7 , using the same definition as above. The extended map will be denoted $\widetilde{\text{Cay}}_6^{-1}$.

In [5] Pfurner *et al.* introduced a simple method for interpolating rigid-body motions. The algorithm consists of writing the control points of the motion as dual quaternions and then performing the interpolation in the ambient \mathbb{P}^7 . Finally, the motion is found by projecting the curve into the group. The map given in [5] takes an arbitrary point of \mathbb{P}^7 to Q_S in \mathbb{P}^7 , so let us write the coordinates in the first \mathbb{P}^7 as $\bar{\mathbf{a}}$ and $\bar{\mathbf{c}}$, so the map can be written as,

$$\mathbf{a} = \bar{\mathbf{a}}(\bar{\mathbf{a}} \cdot \bar{\mathbf{a}}), \quad \mathbf{c} = \bar{\mathbf{c}}(\bar{\mathbf{a}} \cdot \bar{\mathbf{a}}) - \bar{\mathbf{a}}(\bar{\mathbf{a}} \cdot \bar{\mathbf{c}}). \tag{8}$$

It is straightforward to check that the image of this map satisfies the equation defining the Study quadric and hence the image of the map is indeed Q_S . Notice that this map is the analogue in \mathbb{P}^7 of the map in \mathbb{P}^5 which maps a screw to its axis: a line in the Klein quadric.

Theorem 1. *The Pfurner-Schröcker-Husty map (PSH map), given in (8), is equivalent to the composite map $\text{Cay}_6 \circ \widetilde{\text{Cay}}_6^{-1}$.*

Proof. The proof is by direct computation. First the effect of the extended inverse Cayley map will be,

$$\mathbf{w} = \bar{a}_0 \bar{\mathbf{a}}, \quad \mathbf{v} = \bar{a}_0 \bar{\mathbf{c}} - \bar{c}_0 \bar{\mathbf{a}} \tag{9}$$

Now we can easily substitute into the definition for the Cayley map to get,

$$\mathbf{a} = \mathbf{w}(\mathbf{w} \cdot \mathbf{w}) = \bar{a}_0^3 \bar{\mathbf{a}}(\bar{\mathbf{a}} \cdot \bar{\mathbf{a}}) \tag{10}$$

and

$$\mathbf{c} = \mathbf{v}(\mathbf{w} \cdot \mathbf{w}) - \mathbf{w}(\mathbf{v} \cdot \mathbf{w}) = \bar{a}_0^3 \bar{\mathbf{c}}(\bar{\mathbf{a}} \cdot \bar{\mathbf{a}}) - \bar{a}_0^3 \bar{\mathbf{a}}(\bar{\mathbf{a}} \cdot \bar{\mathbf{c}}). \tag{11}$$

Clearly, apart from the common factor \bar{a}_0^3 , which is irrelevant in a projective space, this gives the same result as the PSH map. \square

3 Subgroups and Symmetric Subspaces

Loos [3], defines symmetric spaces as spaces with a multiplication defined on the points of the space. The map defined by left-multiplication by a particular point x , is an involutive automorphism of the space with isolated fixed point x . Loos also shows that any Lie group, with Lie multiplication xy , becomes a symmetric space when the multiplication is modified to $\sigma(x, y) = xy^{-1}x$. Here, by a symmetric subspace of $SE(3)$, we mean a proper subspace of $SE(3)$ closed under σ . There is a correspondence between Lie triple system (LTS) of the Lie algebra and symmetric subspaces of the group.

In $SE(3)$ linear subspaces of the Lie algebra are known as screw systems. Screw systems were classified up to rigid-body transformations by Gibson and Hunt [2], see also [1]. The Gibson-Hunt type (GH type) of a screw system distinguishes between type II systems, which contain screws with the same pitch, and type I systems which contain screws with different pitches. The number of infinite pitch screw in the system is given by a letter, A for no infinite pitch screws, B for 1 infinite pitch screw, C for a line of infinite pitch screws, and so forth. These basic classes split into finer classes, characterised by invariants, often a characteristic pitch or set of pitches.

The Lie triple systems of $se(3)$ were classified in [4, 7, 12], details of symmetric subspaces of $SE(3)$ can also be found in [14]. It was observed in [4], that most of the symmetric subspaces of $SE(3)$ are linear spaces or the intersection of the Study quadric Q_s with a linear subspace. We state this as a theorem here.

Theorem 2. *Algebraic subgroups of $SE(3)$ and algebraic symmetric subspaces of $SE(3)$ lie on linear spaces contained in the Study quadric or on the intersection of the Study quadric with a linear subspace of \mathbb{P}^7 .*

By an algebraic subgroup or symmetric subspace we mean a subspace that can be generated by exponentiating linear combinations of only zero pitch or infinite pitch twists.

Proof. The theorem can be proved by straightforward inspection of all possible cases. All possibilities were found in [4, 7, 12]. To find points in the symmetric subspaces we need to be able to exponentiate elements of the Lie triple system. This can be done using the Rodrigues-like formula,

$$e^s = \frac{1}{2}(2 \cos \theta + \theta \sin \theta) - \frac{1}{2\theta}(\theta \cos \theta - 3 \sin \theta)s + \frac{1}{2\theta}(\sin \theta)s^2 - \frac{1}{2\theta^3}(\theta \cos \theta - \sin \theta)s^3. \tag{12}$$

where s is a dual quaternion of the form, $s = (\theta_x i + \theta_y j + \theta_z k) + \varepsilon(u_x i + u_y j + u_z k)$ and $\theta^2 = \theta_x^2 + \theta_y^2 + \theta_z^2$. A derivation of this formula can be found in [10]¹.

So for example, if we take a general twist from a IIB ($p = 0$) 3-system, $s = ai + bj + c\varepsilon k$ the exponential of this is,

$$e^s = \cos \theta + \frac{a}{\theta} \sin \theta i + \frac{b}{\theta} \sin \theta j + \frac{c}{\theta} \sin \theta \varepsilon k \tag{13}$$

where $\theta^2 = a^2 + b^2$. Clearly, whatever the values of the parameters a, b and c , the exponential lies in the 3-plane $a_3 = c_0 = c_1 = c_2 = 0$. This 3-plane is a generator plane of the Study quadric.

In this way, all possible subalgebras and Lie triple systems can be examined. Tables of canonical forms for the possible subalgebras and Lie triple systems can be found in Tables 1 and 2 respectively, together with the linear equations satisfied by the subspaces they generate. □

¹ Note, reference [10] contains a couple of errors. Equation (8.6) for the log of a dual quaternion should read,

$$\log(g) = \frac{1}{4 \sin^3(\theta)} \left((2\theta - \sin(2\theta))g^3 + (2 \sin(3\theta) - 6\theta \cos(\theta))g^2 - (6\theta \cos(\theta) - 2 \sin(3\theta))g - (3\theta \cos(\theta) - \theta \cos(3\theta) + \sin(\theta) - \sin(3\theta)) \right).$$

Thanks to J. Bookshire for pointing this out. The formula in Sect. 5 for the quasi-pitch of the dual quaternion Cayley map should read,

$$h_q = \frac{a \cdot b}{a \cdot a} = \frac{\theta/2}{\sin \theta/2} \left(\frac{p}{2\pi} \right).$$

Table 1. Canonical forms for the connected subgroups of $SE(3)$. GH type denotes the class of the screw system in the Gibson-Hunt classification of screw systems.

Dim	GH type	Subgroup	Sub. Alg. basis	Linear equations	Description
1	IA ($p = 0$)	$SO(2)$	$\{i\}$	$a_2 = a_3 = c_0 = c_1 = c_2 = c_3 = 0$	Line in Q_S
1	IA ($p \neq 0$)	H_p	$\{i + p\epsilon i\}$	Not algebraic	-
1	IIB	\mathbb{R}	$\{\epsilon i\}$	$a_1 = a_2 = a_3 = c_0 = c_2 = c_3 = 0$	Line in Q_S
2	IB^0	$SO(2) \times \mathbb{R}$	$\{i, \epsilon i\}$	$a_2 = a_3 = c_2 = c_3 = 0$	3-plane
2	IIC	\mathbb{R}^2	$\{\epsilon i, \epsilon j\}$	$a_1 = a_2 = a_3 = c_0 = c_1 = 0$	2-plane in Q_S
3	IIA ($p = 0$)	$SO(3)$	$\{i, j, k\}$	$c_0 = c_1 = c_2 = c_3 = 0$	A-plane
3	IIC ($p = 0$)	$SE(2)$	$\{i, \epsilon j, \epsilon k\}$	$a_2 = a_3 = c_0 = c_1 = 0$	A-plane
3	IIC ($p \neq 0$)	$H_p \times \mathbb{R}^2$	$\{i + p\epsilon i, j, k\}$	Not algebraic	-
3	IID	\mathbb{R}^3	$\{\epsilon i, \epsilon j, \epsilon k\}$	$a_1 = a_2 = a_3 = c_0 = 0$	B-plane
4	\overline{IIC}	$SE(2) \times \mathbb{R}$	$\{i, \epsilon i, \epsilon j, \epsilon k\}$	$a_2 = a_3 = 0$	5-plane

Table 2. Canonical forms for the connected symmetric subspaces of $SE(3)$. LTS basis denotes a basis for the Lie triple system.

Dim	GH type	LTS basis	Linear equations	Description
2	IIA ($p = 0$)	$\{i, j\}$	$a_3 = c_0 = c_1 = c_2 = c_3 = 0$	2-plane in Q_S
2	IIB ($p = 0$)	$\{i, \epsilon j\}$	$a_2 = a_3 = c_0 = c_1 = c_3 = 0$	2-plane in Q_S
2	IIB ($p \neq 0$)	$\{i + p\epsilon i, \epsilon j\}$	Not algebraic	-
3	IIB ($p = 0$)	$\{i, j, \epsilon k\}$	$a_3 = c_0 = c_1 = c_2 = 0$	B-plane
3	IC^0	$\{i, \epsilon i, \epsilon j\}$	$a_2 = a_3 = c_3 = 0$	4-plane
4	$\overline{IB^0}$	$\{i, j, \epsilon i, \epsilon j\}$	$a_3 = c_3 = 0$	5-plane
5	\overline{IIB}	$\{i, j, \epsilon i, \epsilon j, \epsilon k\}$	$a_3 = 0$	Hyperplane

4 Interpolation

Finally the two parts can be combined. The idea is to interpolate the motion in the subgroup or symmetric subspace using the Study coordinates. The result may not lie in the Study quadric but will lie in a linear subspace defining the subgroup or symmetric subspace. Now use the PSH map to send the curve back to the Study quadric. For this to work we must check that the PSH map preserves the linear spaces. A point in the linear space, not on the Study quadric must be mapped to a point on Q_S but still in the linear space.

If the linear spaces lies entirely within the Q_s there is nothing to check since points in Q_S are not changed by the map. This leaves 5 cases to check, the cylindrical subgroup (IB^0), the Schönflies subgroup (\overline{IIC}), and the last three rows in Table 2, (IC^0 , $\overline{IB^0}$ and \overline{IIB}). The checks are not difficult and all do satisfy the required condition. For example, the linear space for the canonical Schönflies group is given by $\bar{a}_2 = \bar{a}_3 = 0$, after the PSH map points satisfying these equations will satisfy $a_2 = \bar{a}_2(\bar{\mathbf{a}} \cdot \bar{\mathbf{a}}) = 0$ and similarly for a_3 . For the

canonical cylindrical subgroup $\bar{a}_2 = \bar{a}_3 = \bar{c}_2 = \bar{c}_3 = 0$ and after the PSH map, $a_2 = a_3 = 0$ and also $c_2 = \bar{c}_2(\bar{\mathbf{a}} \cdot \bar{\mathbf{a}}) - \bar{a}_2(\bar{\mathbf{a}} \cdot \bar{\mathbf{c}}) = 0$ and similar for c_3 . Since the results hold for the canonical forms of the subgroups and symmetric subspaces, they hold for all subgroups and symmetric subspaces by symmetry.

As a first example, consider linearly interpolating between the identity in the group and a 2θ screw motion with pitch p , note that linear interpolation was also considered in [5]. We can choose coordinates so that the screw axis is the x -axis and then the group element will be,

$$g_1 = c + si - p\theta s\varepsilon + p\theta c\varepsilon i \tag{14}$$

where $s = \sin(\theta)$ and $c = \cos(\theta)$. Now the interpolated motion will be given in terms of a parameter t as,

$$g(t) = (1 - t) + tg_1. \tag{15}$$

Then the PSH map takes this to a twisted cubic curve in the group,

$$\begin{aligned} PSH(g(t)) = & (1 + 3(c - 1)t + 2(c - 1)(c - 2)t^2 - 2(c - 1)^2t^3) \\ & + st(1 + 2(c - 1)t - 2(c - 1)t^2)i \\ & - p\theta st^2(c + (1 - c)t)\varepsilon + p\theta t(c + (c - 1)^2t - (c - 1)^2t^2)\varepsilon i \end{aligned} \tag{16}$$

The two group elements lie in a cylindrical subgroup, hence so does the twisted cubic curve. So the result is a vertical Darboux motion, in agreement with the results of [10].

Next we look at a slightly more complicated example, we interpolate between three group elements with a conic. The three group elements will be,

$$g_0 = 1, \quad g_1 = \frac{1}{2} + \frac{\sqrt{3}}{2}k - \frac{\pi}{4\sqrt{3}}\varepsilon + \frac{\pi}{12}\varepsilon k, \quad g_2 = \frac{\sqrt{3}}{2} + \frac{1}{2}k + \frac{3}{2}\varepsilon j \tag{17}$$

so that the points lie in the symmetric subspace generated by the IC⁰ 3-system. A conic through these points can be given by,

$$\bar{g}(t) = \frac{1}{2}(1 - t)(2 - t)g_0 + t(2 - t)g_1 - \frac{1}{2}t(1 - t)g_2. \tag{18}$$

Note that there are many other conics through these three points, however, this is the unique conic passing through the knot points at time $t = 0, 1$ and 2 respectively. The PSH map then gives a degree 6 curve in the Study quadric.

5 Conclusion

We were not able to find an algebraic proof that the subgroups and symmetric subspaces lie on linear subspaces in \mathbb{P}^7 . However, it is clear that such an explanations should exist, this fact cannot be a coincidence.

Acknowledgements. Many thanks to the anonymous reviewers whose suggestions have greatly improved this work.

References

1. Donelan, P.S., Gibson, C.G.: On the hierarchy of screw systems. *Acta Appl. Math.* **32**, 267–296 (1993)
2. Gibson, C.G., Hunt, K.H.: Geometry of screw systems. *Mech. Mach. Theory* **25**, 1–27 (1990)
3. Loos, O.: *Symmetric Spaces I*. Benjamin, New York (1969)
4. Löwe, H., Wu, Y., Carricato, M.: Symmetric subspaces of $SE(3)$. *Adv. Geom.* **16**(3), 381–388 (2016)
5. Pfurner, M., Schröcker, H.-P., Husty, M.: Path planning in kinematic image space without the study condition. In: Lenarčič, J., Merlet, J.-P. (eds.) *Advances in Robot Kinematics: Proceedings of the 15th International Conference on Advances in Robot Kinematics*, 27–30 June 2016, Grasse, France. <https://hal.archives-ouvertes.fr/hal-01339423>
6. Röschel, O.: Rational motion design – a survey. *Comput. Aided Des.* **30**(3), 169–178 (1998)
7. Selig, J.M.: A class of explicitly solvable vehicle motion problems. *IEEE Trans. Robot.* **31**(3), 766–777 (2015). doi:[10.1109/TRO.2015.2426471](https://doi.org/10.1109/TRO.2015.2426471)
8. Selig, J.M.: Cayley maps for $SE(3)$. In: *The International Federation for the Promotion of Mechanism and Machine Science 12th World Congress*, Besançon. http://79.6.136.172/iftomm/proceedings/proceedings_WorldCongress/WorldCongress07/articles/article_cd.htm. A corrected version of this work can be found at https://www.researchgate.net/publication/242315171-Cayley_Maps_for_SE3
9. Selig, J.M., Wu, Y.: Interpolated rigid-body motions and robotics. In: *IEEE International Conference on Robotics and Automation*, Beijing, pp. 1086–1091 (2006)
10. Selig, J.M.: Exponential and Cayley maps for dual quaternions. *Adv. Appl. Clifford Algebra* **20**(3–4), 923–936 (2010). doi:[10.1007/s00006-010-0229-5](https://doi.org/10.1007/s00006-010-0229-5)
11. Wu, Y., Liu, G., Löwe, H., Li, Z.: Exponential submanifolds: a new kinematic model for mechanism analysis and synthesis. In: *Proceedings of the IEEE International Conference on Robotics and Automation*, pp. 4177–4182 (2013)
12. Wu, Y., Löwe, H., Carricato, M., Li, Z.: Inversion symmetry of the Euclidean group: theory and application in robot kinematics. *IEEE Trans. Robot.* **32**(2), 312–326 (2016)
13. Wu, Y., Müller, A., Carricato, M.: The 2D orientation interpolation problem: a symmetric space approach. In: Lenarčič, J., Merlet, J.-P. (eds.) *Advances in Robot Kinematics: Proceedings of the 15th International Conference on Advances in Robot Kinematics*, 27–30 June 2016, Grasse, France (2016). <https://hal.archives-ouvertes.fr/hal-01339423>
14. Wu, Y., Carricato, M.: Identification and geometric characterization of Lie triple screw systems and their exponential images. *Mech. Mach. Theory* **107**, 305–323 (2017)

Intrusion, Proximity and Stationary Distance

Paul Zsombor-Murray^(✉)

Department of Mechanical Engineering and Centre for Intelligent Machines,
McGill University, 817 Sherbrooke St. W., Montreal, QC H3A 0C3, Canada
paul@cim.mcgill.ca

Abstract. Computation of intersection of right truncated cylinders of revolution and stationary distances, including least and greatest, between conics and quadrics will be re-examined using classical geometry. Solutions are provided by formulating simultaneous polynomial constraint equations that represent 3D surfaces. Previous investigations in this regard claim that the work is useful in preventing interference between rigid bodies in joint articulated mechanical systems. No such claim is made herein. Indeed the intent was to have fun by indulging in elementary “geometric thinking”.

Keywords: Rigid body · Collision · Conics · Quadrics · Shortest distance

1 Introduction

A great deal has been written about this topic. Not long ago Agarwal, Srivatsan and Bandyopadhyay [1] published the definitive article. There is little that I can add to this and to the literature mentioned in its comprehensive bibliography. Rather I will concentrate on some of the piecemeal sub-problems and expose some not-widely-known, possibly novel, methodology.

- Since our cylinders k_P, k_Q are sectioned by axis-normal planes let us represent a pair by their centreline end points $A\{1 : a_1 : a_2 : a_2\}, B\{1 : b_1 : b_2 : b_3\}$ and $C\{1 : c_1 : c_2 : c_3\}, D\{1 : d_1 : d_2 : d_3\}$ and respective radii r, s .
- A key sub-problem is to find on the cylinder axes, lines \mathcal{P} and \mathcal{Q} , their common normal end points P on AB and Q on CD . The closest distance between surfaces, if lengths are indefinite, is simply $|PQ| - r - s$. Line geometry will be applied.
- To find if an end disc intersects another, these are represented, *e.g.*, the one of four on A , by sphere $k_A : (x_1 - a_1)^2 + (x_2 - a_2)^2 + (x_3 - a_3)^2 - r^2 = 0$ and plane with coordinates $a\{A_0 : b_1 - a_1 : b_2 - a_2 : b_3 - a_3\}$ ¹. Contact or intrusion occurs if the line of intersection between the two planes intersects *both* spheres on real points.

¹ $A_0 = -a_1(b_1 - a_1) - a_2(b_2 - a_2) - a_3(b_3 - a_3)$.

- To find if an end disc intrudes into a cylinder flank, say, $k_{a''} = k_{A''} \cap a''$, and that of $k_{Q''} : x_2^2 + x_3^2 - s^2 = 0$. (") indicates all three elements are displaced so C is on the origin and D on the x_1 axis. Then the four points $X(x_1, x_2, x_3)$ of intersection of $a'' \cap k_{A''} \cap k_{Q''}$, if real, are checked to see if $0 \leq x_1 \leq |CD|$.
- Finally a line geometric approach to finding the octic univariate that describes stationary distances between a pair of spatial circles will be described. One of these is the shortest. Distance criteria were used by Agarwal *et al.* [1] to avoid collision. My three sub-problem collision, as opposed to their four sub-problem distance, method seems simpler and sufficiently secure if actual cylindrical pieces are buffered by increase in length and radius.

2 Common Normal Cylinder Centreline End Points

Cylinder centrelines $\mathcal{P}_r, \mathcal{Q}_r$ are represented by their *radial* Plücker coordinates directly computed with point pairs A, B and C, D (Fig. 1).

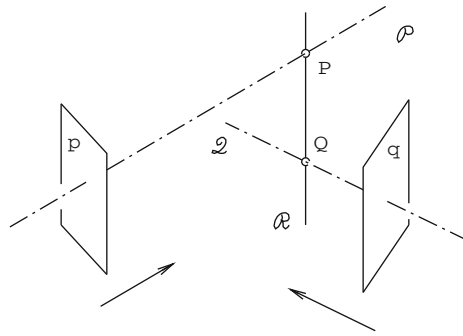


Fig. 1. Common normal \mathcal{R}

$$\mathcal{P}_r\{p_{01} : p_{02} : p_{03} : p_{23} : p_{31} : p_{12}\}, \quad \mathcal{Q}_r\{q_{01} : q_{02} : q_{03} : q_{23} : q_{31} : q_{12}\}$$

Pencils p, q of planes normal to \mathcal{P}, \mathcal{Q} respectively are used to define *axial* line \mathcal{R}_a .

$$p\{P_0 : p_{01} : p_{02} : p_{03}\}, \quad q\{Q_0 : q_{01} : q_{02} : q_{03}\}$$

P_0 and Q_0 are the two unknowns necessary to find end points P and Q of common normal axial line \mathcal{R}_a on lines \mathcal{P}_r and \mathcal{Q}_r using intersections

$$\mathcal{R}_a\{R_{01} : R_{02} : R_{03} : R_{23} : R_{31} : R_{12}\}, \quad \mathcal{P}_r \cdot \mathcal{R}_a = 0, \quad \mathcal{Q}_r \cdot \mathcal{R}_a = 0$$

$P = p \cap \mathcal{P}_r$ and $Q = q \cap \mathcal{Q}_r$, e.g., $p_i = \sum_{j=0}^3 p_{ij} P_j$ thus, where $P_j = p_{0j}$.

$$\begin{aligned} p_0 &= p_{01}P_1 + p_{02}P_2 + p_{03}P_3 \\ p_1 &= -p_{01}P_0 + p_{12}P_2 - p_{31}P_3 \\ p_2 &= -p_{02}P_0 + p_{12}P_1 + p_{23}P_3 \\ p_3 &= -p_{03}P_0 + p_{31}P_1 - p_{12}P_2 \end{aligned} \tag{1}$$

If $|PQ| - r - s \leq 0$ to establish collision we check that P is on either or between A and B and that Q bears similar relation to C and D . This can be done, *e.g.*, directly with A_0 ² and B_0 , the constant coefficients of equations of normal planes on A and B , by verifying that $A_0 \leq P_0 \leq B_0$ or $A_0 \geq P_0 \geq B_0$.

3 Collision or Intersection of Cylinder Ends

To check if cylinder ends on points, say, A, C interfere we apply Eq. 2.

$$\begin{aligned}
 a : A_0 + A_1x_1 + A_2x_2 + A_3x_3 &= 0 \\
 c : C_0 + C_1x_1 + C_2x_2 + C_3x_3 &= 0 \\
 k_A : (x_1 - a_1)^2 + (x_2 - a_2)^2 + (x_3 - a_3)^2 - r^2 &= 0 \\
 k_C : (x_1 - c_1)^2 + (x_2 - a_c)^2 + (x_3 - c_3)^2 - s^2 &= 0
 \end{aligned} \tag{2}$$

Consider Fig. 2. Cylinder end discs will have a line segment, or at least a point, in common if simultaneous solution of the first three of Eq. 2 and the first two and the last *both* yield real X at P and Q . Note how descriptive geometry and judicious choice of view pair provide clear visualization of the process.

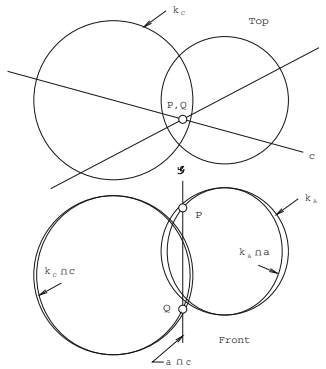


Fig. 2. Line on cylinder end planes intersect both spheres

4 Collision or Intersection of a Cylinder Surface with an End

First the cylinder, radius s , with ends on C, D is displaced so C is on origin O and D is along x_1 -axis, $x_1 > 0$. Then the translation $C \rightarrow O$ is imposed upon plane a and centre A of sphere k_A followed by the rotation necessary to make $A \rightarrow B$ parallel to x_1 -axis. So $a, A, k_A \rightarrow a', A', k_{A'} \rightarrow a'', A'', k_{A''}$.

² In this case, as opposed to that mentioned in the introduction, $A_0 = -p_{01}a_1 - p_{02}a_2 - p_{03}a_3$.

4.1 Translation

$$A \rightarrow A' : \begin{bmatrix} 1 & 0 & 0 & 0 \\ c_1 & 1 & 0 & 0 \\ c_2 & 0 & 1 & 0 \\ c_3 & 0 & 0 & 1 \end{bmatrix} \begin{bmatrix} 1 \\ a_1 \\ a_2 \\ a_3 \end{bmatrix} = \begin{bmatrix} 1 \\ c_1 + a_1 \\ c_2 + a_2 \\ c_3 + a_3 \end{bmatrix} = \begin{bmatrix} 1 \\ a'_1 \\ a'_2 \\ a'_3 \end{bmatrix} \tag{3}$$

Although the translation of point A via Eq. 3 is obvious, plane coordinates, being of dual species, are transformed by the *cofactor* of the translation matrix as in Eq. 4.

$$a \rightarrow a' : \begin{bmatrix} 1 - c_1 & -c_2 & -c_3 \\ 0 & 1 & 0 & 0 \\ 0 & 0 & 1 & 0 \\ 0 & 0 & 0 & 1 \end{bmatrix} \begin{bmatrix} A_0 \\ A_1 \\ A_2 \\ A_3 \end{bmatrix} = \begin{bmatrix} A_0 - c_1 A_1 - c_2 A_2 - c_3 A_3 \\ A_1 \\ A_2 \\ A_3 \end{bmatrix} = \begin{bmatrix} A'_0 \\ A'_1 \\ A'_2 \\ A'_3 \end{bmatrix} \tag{4}$$

4.2 Normed Quaternion and Rotation Matrix

The normed quaternion \mathbf{v} or rotation matrix $[\mathbf{V}]$ that rotates direction $C \rightarrow D$ as required must premultiply A', a' . A neat property of $[\mathbf{V}]$ is that it is identical to its cofactor. \mathbf{v} and $[\mathbf{V}]$ are introduced in Eq. 5.

$$\mathbf{v} = \begin{bmatrix} v_0 \\ v_1 \\ v_2 \\ v_3 \end{bmatrix} = \begin{bmatrix} \cos(\phi/2) \\ \cos \alpha \sin(\phi/2) \\ \cos \beta \sin(\phi/2) \\ \cos \gamma \sin(\phi/2) \end{bmatrix}, \quad [\mathbf{V}] = \begin{bmatrix} r_{00} & 0 & 0 & 0 \\ 0 & r_{11} & r_{12} & r_{13} \\ 0 & r_{21} & r_{22} & r_{23} \\ 0 & r_{31} & r_{32} & r_{33} \end{bmatrix} \tag{5}$$

$$= \begin{bmatrix} v_0^2 + v_1^2 + v_3^2 + v_3^2 & 0 & 0 & 0 \\ 0 & v_0^2 + v_1^2 - v_2^2 - v_3^2 & 2(v_1 v_2 - v_0 v_3) & 2(v_1 v_3 + v_0 v_2) \\ 0 & 2(v_2 v_1 + v_0 v_3) & v_0^2 - v_1^2 + v_2^2 - v_3^2 & 2(v_2 v_3 - v_0 v_1) \\ 0 & 2(v_3 v_1 - v_0 v_2) & 2(v_3 v_2 + v_0 v_1) & v_0^2 - v_1^2 - v_2^2 + v_3^2 \end{bmatrix}$$

Elements v_i of a normed quaternion are also called Euler-Rodrigues parameters. $[\cos \alpha \ \cos \beta \ \cos \gamma]^\top$ is the unit vector –expressed in terms of direction cosines– in the direction of the rotation axis while ϕ is the rotation angle in a right-hand screw sense. To get quaternion from rotation matrix –except for half-turns which I won’t mention here– we use the diagonal elements r_{ii} to get v_i^2 as shown in Eq. 6.

$$\begin{bmatrix} r_{00} & 0 & 0 & 0 \\ 0 & r_{11} & r_{12} & r_{13} \\ 0 & r_{21} & r_{22} & r_{23} \\ 0 & r_{31} & r_{32} & r_{33} \end{bmatrix} \rightarrow \begin{matrix} v_0^2 = (r_{00} + r_{11} + r_{22} + r_{33})/4 \\ v_1^2 = (r_{00} + r_{11} - r_{22} - r_{33})/4 \\ v_2^2 = (r_{00} - r_{11} + r_{22} - r_{33})/4 \\ v_3^2 = (r_{00} - r_{11} - r_{22} + r_{33})/4 \end{matrix} \tag{6}$$

4.3 Rotation

The rotation sought turns $C'D'$, $C' \equiv C'' \equiv O$, onto the x_1 -axis through rotation through ϕ about O via unit vector $\mathbf{n} = [n_1 \ n_2 \ n_3]^T$ into $\mathbf{x} = [1 \ 0 \ 0]^T$. The unit vector $\boldsymbol{\rho}$ in the rotation axis direction is given by Eq. 7.

$$\mathbf{n} = \begin{bmatrix} n_1 \\ n_2 \\ n_3 \end{bmatrix} = \frac{1}{\sqrt{(d_1-c_1)^2+(d_2-c_2)^2+(d_3-c_3)^2}} \begin{bmatrix} d_1 - c_1 \\ d_2 - c_2 \\ d_3 - c_3 \end{bmatrix} \quad (7)$$

$$\boldsymbol{\rho} = \begin{bmatrix} \cos \alpha \\ \cos \beta \\ \cos \gamma \end{bmatrix} = \frac{\mathbf{n} \times \mathbf{x}}{|\mathbf{n} \times \mathbf{x}|} = \begin{bmatrix} n_1 \\ n_2 \\ n_3 \end{bmatrix} \times \begin{bmatrix} 1 \\ 0 \\ 0 \end{bmatrix} / |\mathbf{n} \times \mathbf{x}| = \frac{1}{\sqrt{n_2^2+n_3^2}} \begin{bmatrix} 0 \\ n_3 \\ -n_2 \end{bmatrix}$$

To complete the computation of the quaternion elements *cum* Euler-Rodrigues parameters we need $\cos(\phi/2)$ and $\sin(\phi/2)$. Imagine vectors \mathbf{n} and \mathbf{x} placed tail-to-tail on O , a line segment joining their tips, its mid-point M , the tip of vector \mathbf{m} from O . Consider that $|\mathbf{m}| = \cos(\phi/2)$ and $|\mathbf{x} - \mathbf{m}| = \sin(\phi/2)$. All this is illustrated in Fig. 3.

$$\cos \frac{\phi}{2} = \frac{1}{2} \sqrt{(1 + n_1)^2 + n_2^2 + n_3^2}, \quad \sin \frac{\phi}{2} = \frac{1}{2} \sqrt{(1 - n_1)^2 + n_2^2 + n_3^2} \quad (8)$$

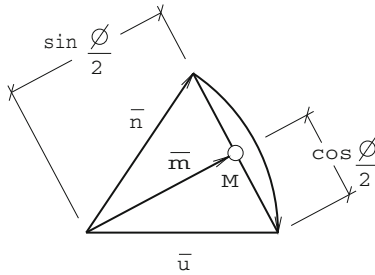


Fig. 3. Rotation and significance of half-angle sine and cosine

As an exercise the reader may reformulate the problem of Eq. 9 as $a \cap k_A \cap k_Q$ by displacing $k_Q'' \rightarrow k_Q$ instead of $a \rightarrow a''$ and $k_A \rightarrow k_{A''}$.

4.4 Constraint Equations

The implicit equations of plane a'' , sphere $k_{A''}$ and the cylinder $k_{Q''}$, to be solved simultaneously to yield points X , appear in Eq. 9.

$$\begin{aligned}
 a'' &: A_0'' + A_1''x_1 + A_2''x_2 + A_3''x_3 = 0 \\
 k_{A''} &: (x_1 - a_1'')^2 + (x_2 - a_2'')^2 + (x_3 - a_3'')^2 - r^2 = 0 \\
 k_{Q''} &: x_2^2 + x_3^2 - s^2 = 0
 \end{aligned}
 \tag{9}$$

Figure 4 contains two views showing the plane a'' in edge or line view at upper left and the circle of cylinder $k_{P''}$ circular end disc together with the elliptical plane section of cylinder $k_{Q''}$. The existence of real points X indicate encroachment of the surfaces. If radius r is so small as to place the disc entirely within $k_{Q''}$ without triggering the common normal length criterion this condition is checked via the distance between disc centre point A and centre line \mathcal{Q} on CD being less than radius s .

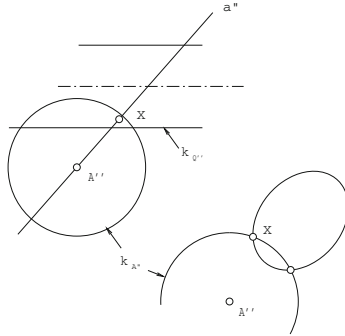


Fig. 4. Line on cylinder end planes intersect both spheres

5 Stationary Distances Between Spatial Circles

In the article [1] the shortest distance between two circles is made use of to account for impending contact between cylinder end edges and an octic solution is referred to. Although the approach introduced in Sect. 3 handles this situation automatically it is of interest to reveal how these distances can be computed using a line \mathcal{R} that intersects circle axis lines \mathcal{M} and \mathcal{N} on respective points M, N . \mathcal{R} will be defined by points P, Q on circles k_a and k_c , respectively, as shown in Fig. 5. Line \mathcal{R} , shown in Fig. 5, depicts a typical line belonging to two line congruences. One contains all lines on points on circle k_a and normal to the circle tangent at that point, P . This property is ensured by the intersections $P \in k_a, P \in \mathcal{R}, M \in \mathcal{R}, M \in \mathcal{M}$, i.e., $\exists \mathcal{M} \cap \mathcal{R}$ and $\exists \mathcal{N} \cap \mathcal{R}$. The other congruence on circle k_c gives rise to similar relationships, viz., $Q \in k_c, Q \in \mathcal{R}, N \in \mathcal{R}, N \in \mathcal{N}$. Dissecting these relations yields six equations, Eq. 10, in six Cartesian points coordinates, $P(p_1, p_2, p_3), Q(q_1, q_2, q_3)$.

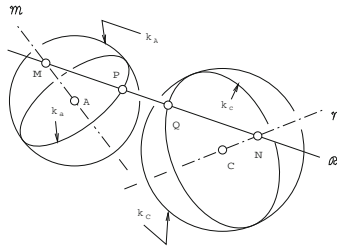


Fig. 5. Congruence of normal lines on circles

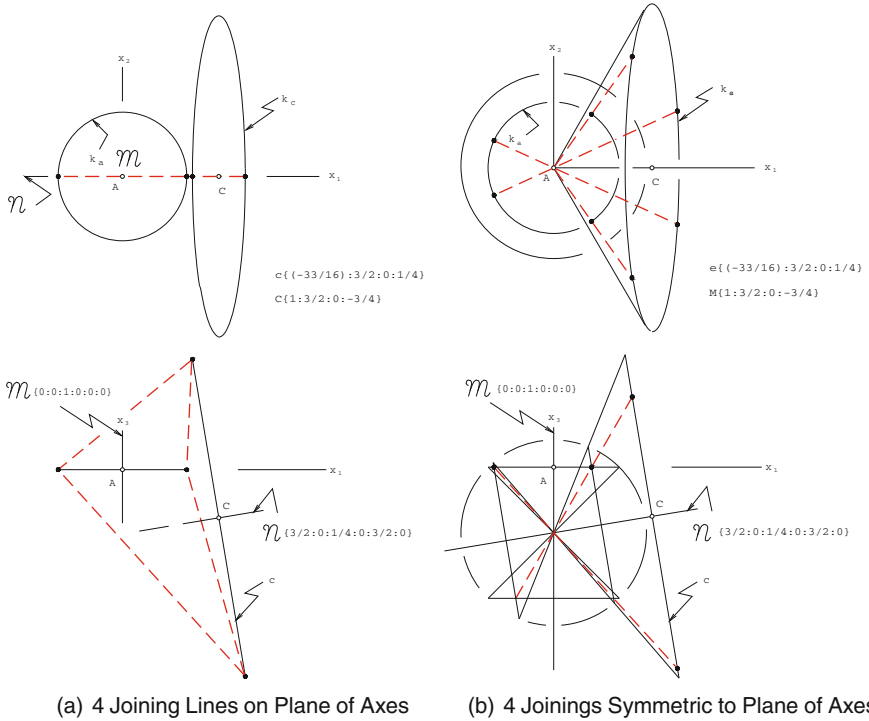


Fig. 6. Eight connections between circles

Using Gröbner basis and an arbitrary pair of spatial circles these simultaneous equations yield an octic univariate in one of the p_i, q_i and the basis provides a systematic way to compute the remaining five. *I.e.*, each successive basis polynomial contains one linear unknown in terms of those already evaluated. In general, there are only four real stationary distances among the eight solutions. Are there circle dispositions that admit eight real solutions? Again, geometric thinking and descriptive geometry reveal in Fig. 6 eight connecting segments that satisfy Eq. 10.

$$\begin{aligned}
 &k_a = k_A \cap a, \quad P \in k_a, \quad k_c = k_C \cap c, \quad Q \in k_c \\
 &A_0 + A_1 p_1 + A_2 p_2 + A_3 p_3 = 0 \\
 &(p_1 - a_1)^2 + (p_2 - a_2)^2 + (p_3 - a_3)^2 - r^2 = 0 \\
 &C_0 + C_1 q_1 + C_2 q_2 + C_3 q_3 = 0 \\
 &(q_1 - c_1)^2 + (q_2 - c_2)^2 + (q_3 - c_3)^2 - s^2 = 0 \\
 &\exists M = \mathcal{M} \cap \mathcal{R}, \quad \exists N = \mathcal{N} \cap R \\
 &m_{01}R_{01} + m_{02}R_{02} + m_{03}R_{03} + m_{23}R_{23} + m_{31}R_{31} + m_{12}R_{12} = 0 \\
 &n_{01}R_{01} + n_{02}R_{02} + n_{03}R_{03} + n_{23}R_{23} + n_{31}R_{31} + n_{12}R_{12} = 0 \\
 &\mathcal{M}_r\{A_1 : A_2 : A_3 : a_2 A_2 - a_3 A_2 : a_3 A_1 - a_1 A_3 : a_1 A_2 - a_2 A_1\} \\
 &\mathcal{N}_r\{C_1 : C_2 : C_3 : c_2 C_2 - c_3 C_2 : c_3 C_1 - c_1 C_3 : c_1 C_2 - c_2 C_1\} \\
 &\mathcal{R}_a\{p_2 q_3 - p_3 q_2 : p_3 q_1 - p_1 q_3 : p_1 q_2 - p_2 q_1 \\
 &\quad : p_0 q_1 - p_1 q_0 : p_0 q_2 - p_2 q_0 : p_0 q_3 - p_3 q_0\}
 \end{aligned} \tag{10}$$

6 Conclusions

Using implicit sphere, plane and cylinder equations, some geometric thinking and descriptive geometry I've tried to unify the computational sub-problems pertinent to collision and intrusion between two cylinders and use a consistent nomenclature among them. Have any special cases been overlooked? Yes, a small end disc can intrude into a large cylinder undetected. Do you see how to overcome this using sphere centre A'' ? Was this case covered in [1]? Apologies for my, in places, didactic tone. Furthermore why should I cite more than one article? If it's the right one, clutter is undesirable.

Acknowledgements. Jean-Pierre Merlet taught me in 1995 when he was at the second CK in Milano –the first was at Schloß Dagstuhl in 1993– that if you can formulate an algebraic problem with eight solutions, an upper bound, and can construct an example, a lower bound, with that number the issue is then settled.

Reference

1. Agarwal, S., Srivatsan, R.A., Bandyopadhyay, S.: Analytical determination of the proximity of two right-circular cylinders in space. Adv. Robot. 8(4), 1–11 (2015). JMR-15-1218 Bandyopadhyay. doi:[10.1115/1.4032211](https://doi.org/10.1115/1.4032211)

A Novel Geometric Analysis of the Kinematics of the 3-RPS Manipulator

Teja Krishna Mamidi, Aravind Baskar, and Sandipan Bandyopadhyay^(✉)

Department of Engineering Design, Indian Institute of Technology Madras,
Chennai 600 036, India

tejaiiit27@gmail.com, krishna.arvind91@gmail.com, sandipan@iitm.ac.in

Abstract. This paper looks at the forward kinematics problem of the 3-RPS manipulator from a geometric perspective. It shows that the problem is equivalent to finding the intersection of a pair of quad-circular octic curves with a circle. The results explain all the known algebraic results in this regard, and provide an intuitive insight into the nature of the solutions, as regards the operation modes, and the assembly modes inside each. The theoretical results are illustrated with a numerical example, where all the 16 assembly modes are real.

Keywords: 3-RPS manipulator · Forward Kinematic Univariate (FKU) · Operation modes · Constraint surfaces · Quad-circular octic curve

1 Introduction

Forward kinematic (FK) problem of the 3-RPS manipulator has been studied in detail in the past [2, 7]. In a recent contribution, Schadlbauer et al. present a detailed algebraic analysis using the Study parameter representation of $\mathbb{SE}(3)$, leading to the identification of the two operation modes of the manipulator. In this paper, a novel geometric approach to the problem is proposed, in which the manipulator is decomposed into two kinematic sub-chains, namely, a spatial RSSR chain, and a planar RP chain. The FK problem reduces to the intersection of the circle generated by the second chain with the surface generated by the first one, once all the inputs are given. While this idea has been mentioned in [3], the authors were not able to find any published reports using this approach. The authors retrieve the fact that there are up to 16 possible assembly modes, counting the pair-wise mirrored modes at the base plane. Also, the two operation modes reported in [6] show up in these results, in a new and interesting manner. The geometric interpretation of the FK could lead to an intuitive understanding of the singularities of the manipulator, which is yet to be studied.

The rest of the paper is organised as follows: the geometric formulation of the FK problem, followed by a numerical example is presented in Sect. 2. The new results are interpreted geometrically and corroborated with the existing results in Sect. 3. Finally, the conclusions are presented in Sect. 4.

2 Geometric Formulation of the FK Problem

The FK problem is formulated below, as a geometric problem of finding the intersections of a surface and a circle in \mathbb{R}^3 .

2.1 Geometry of the 3-RPS Manipulator

The 3-RPS manipulator consists of three legs, each of which is an RPS-serial chain connected to the fixed platform $\mathbf{b}_1\mathbf{b}_2\mathbf{b}_3$ by a revolute joint, and to the moving platform $\mathbf{p}_1\mathbf{p}_2\mathbf{p}_3$ by a spherical joint, as shown in Fig. 1a. The said platforms are equilateral triangles in shape, with circumradii b and a respectively. The manipulator has three degrees-of-freedom (DoF), which are activated by the prismatic actuators denoted by $\mathbf{l} = [l_1, l_2, l_3]^\top$, while the revolute joints are *passive*. These joint angles, denoted by $\boldsymbol{\phi} = [\phi_1, \phi_2, \phi_3]^\top$ form the unknowns to be obtained as a result of the FK problem. The fixed frame of reference $\{A\}$, given by $\mathbf{o}_A\text{-}\mathbf{X}_A\mathbf{Y}_A\mathbf{Z}_A$, is attached to the centre of the base platform, while the moving frame of reference $\{B\}$, by $\mathbf{o}_B\text{-}\mathbf{X}_B\mathbf{Y}_B\mathbf{Z}_B$, is attached at the centre of the moving platform. The vertices of the fixed and moving platforms are found as: ${}^A\mathbf{b}_1 = [b, 0, 0]^\top$, ${}^A\mathbf{b}_2 = \left[-\frac{b}{2}, \frac{\sqrt{3}b}{2}, 0\right]^\top$, ${}^A\mathbf{b}_3 = \left[-\frac{b}{2}, -\frac{\sqrt{3}b}{2}, 0\right]^\top$; and ${}^A\mathbf{p}_1 = {}^A\mathbf{b}_1 + [-l_1 \cos \phi_1, 0, l_1 \sin \phi_1]^\top$, ${}^A\mathbf{p}_2 = {}^A\mathbf{b}_2 + \left[\frac{l_2}{2} \cos \phi_2, -\frac{\sqrt{3}l_2}{2} \cos \phi_2, l_2 \sin \phi_2\right]^\top$, ${}^A\mathbf{p}_3 = {}^A\mathbf{b}_3 + \left[\frac{l_3}{2} \cos \phi_3, \frac{\sqrt{3}l_3}{2} \cos \phi_3, l_3 \sin \phi_3\right]^\top$, respectively.

The objective of the FK problem is to determine the position and orientation of the moving platform. This can be achieved if the unknown passive angles, ϕ_i , can be obtained from the knowledge of the inputs l_j . Three *independent* equations need to be formed, relating ϕ_i to l_j , which is accomplished below using the concept of kinematic sub-chains.

2.2 Derivation of the Constraints

The manipulator is hypothetically decomposed into two sub-chains, by removing the spherical joint at point \mathbf{p}_1 , as shown in Fig. 1. This leads to two hypothetically distinct points: \mathbf{p}_{s_1} , which is a *coupler point* of the spatial RSSR mechanism $\mathbf{b}_2\mathbf{p}_2\mathbf{p}_3\mathbf{b}_3$; and \mathbf{p}_{c_1} , which is the tip of the serial chain $\mathbf{b}_1\mathbf{p}_1$. Obviously, the points \mathbf{p}_{s_1} and \mathbf{p}_{c_1} *must* coincide to form the original point \mathbf{p}_1 in the manipulator. Equivalently, the locus of \mathbf{p}_{s_1} , which is a surface, must intersect the locus of \mathbf{p}_{c_1} , i.e., a circle in the plane $\mathbf{o}_A\mathbf{b}_1\mathbf{p}_1$ (see Fig. 1).

2.2.1 Derivation of the coupler surface, $\mathbf{S} = \mathbf{0}$

Let ${}^A\mathbf{p}_{s_1} = {}^A\mathbf{p}_{c_1} = {}^A\mathbf{p}_1 = [x, y, z]^\top$. Once the inputs l_2, l_3 are frozen, the locus of \mathbf{p}_{s_1} , which can be interpreted as the *coupler surface* of the said RSSR chain, is described in terms of five unknown variables, namely, ϕ_2, ϕ_3, x, y, z . These variables need to satisfy the following constraints:

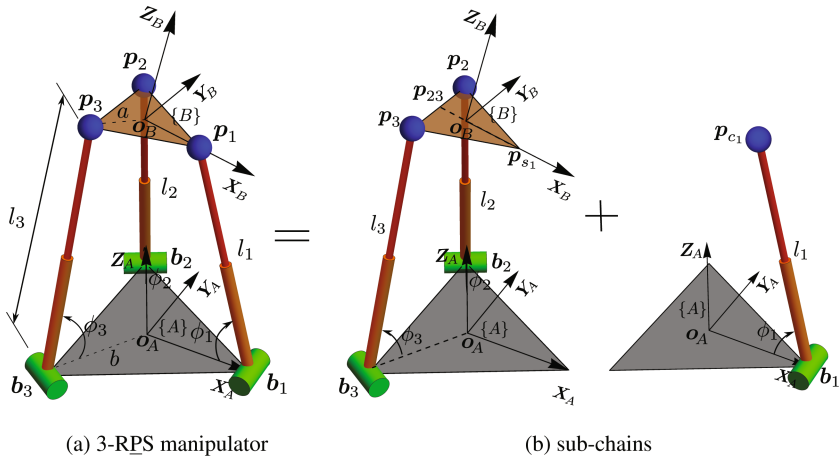


Fig. 1. 3-RPS manipulator decomposition into sub-chains

- The first constraint is derived from the closure of the RSSR loop. This is equivalent of noting that the distance between ${}^A\mathbf{p}_2$ and ${}^A\mathbf{p}_3$ is equal to $\sqrt{3}a$:

$$g_1(\phi_2, \phi_3, x, y, z) \triangleq ({}^A\mathbf{p}_3 - {}^A\mathbf{p}_2) \cdot ({}^A\mathbf{p}_3 - {}^A\mathbf{p}_2) - 3a^2 = 0. \quad (1)$$

- The other two constraints are derived from the fact that the locus of \mathbf{p}_{s_1} , with respect to the points $\mathbf{p}_2\mathbf{p}_3$, is a circle, in a plane that bisects $\mathbf{p}_2\mathbf{p}_3$ perpendicularly. In effect, this defines a *virtual rigid link* $\mathbf{p}_{23}\mathbf{p}_{s_1}$, which has a rotary joint at \mathbf{p}_{23} , with an axis aligned with $\mathbf{p}_2\mathbf{p}_3$. Orthogonality of the virtual link to $\mathbf{p}_2\mathbf{p}_3$ is captured by the constraint:

$$g_2(\phi_2, \phi_3, x, y, z) \triangleq ({}^A\mathbf{p}_{23} - {}^A\mathbf{p}_{s_1}) \cdot ({}^A\mathbf{p}_3 - {}^A\mathbf{p}_2) = 0. \quad (2)$$

Rigidity of the virtual link leads to the third and final constraint:

$$g_3(\phi_2, \phi_3, x, y, z) \triangleq ({}^A\mathbf{p}_{23} - {}^A\mathbf{p}_{s_1}) \cdot ({}^A\mathbf{p}_{23} - {}^A\mathbf{p}_{s_1}) - \frac{9a^2}{4} = 0. \quad (3)$$

The unknown ϕ_2 is easily eliminated from Eqs. (1, 3), which are linear in $\sin \phi_2$ and $\cos \phi_2$. This leads to the eliminant $h_1(\phi_3, x, y, z) = 0$, while substitution of $\sin \phi_2$ and $\cos \phi_2$ into Eq. (2) leads to $h_2(\phi_3, x, y, z) = 0$. The function h_1 is of degree four in $\cos \phi_3, \sin \phi_3$, while h_2 is linear in these. Converting $h_i = 0$ to their algebraic forms in $t_3 = \tan(\phi_3/2)$ one obtains the equations $s_i(t_3, x, y, z) = 0$, $i = 1, 2$. The equation of the coupler surface, $S(x, y, z) = 0$, which is of degree 20 in x, y, z and even powered in z , is obtained by eliminating t_3 between the last two equations. The process of elimination is depicted in schematic (4) below:

$$\left. \begin{aligned} h_1(\phi_3, x, y, z) = 0 &\xrightarrow{\phi_3 \rightarrow t_3} s_1(t_3, x, y, z) = 0 \\ h_2(\phi_3, x, y, z) = 0 &\xrightarrow{\phi_3 \rightarrow t_3} s_2(t_3, x, y, z) = 0 \end{aligned} \right) \xrightarrow{\times t_3} S(x, y, z) = 0. \quad (4)$$

The symbol ‘ $\xrightarrow{\phi_3 \rightarrow t_3}$ ’ denotes the conversion of the equations preceding it, into their algebraic form in $t_3 = \tan(\phi_3/2)$. The symbol ‘ $\xrightarrow{\times t_3}$ ’ represents the elimination of the variable t_3 from the equations preceding it.

2.2.2 Derivation of the Circular Constraint, $C = 0$

The point \mathbf{p}_{c_1} describes a circle in the plane $\mathbf{o}_A \mathbf{b}_1 \mathbf{p}_1$, by virtue of the rotary joint at \mathbf{b}_1 . This can be captured in terms of algebraic equations as follows.

- Rigidity of leg 1 (given the input l_1), expressed in terms of the leg-length constraint, describes a *sphere* of radius l_1 , centered at \mathbf{b}_1 :

$$\zeta_1(x, y, z) \triangleq ({}^A \mathbf{p}_{c_1} - {}^A \mathbf{b}_1) \cdot ({}^A \mathbf{p}_{c_1} - {}^A \mathbf{b}_1) - l_1^2 = 0. \tag{5}$$

- Axis of the rotary joint at \mathbf{b}_1 is along $\mathbf{e}_{Y_A} = [0, 1, 0]^T$, which leads to the *planarity constraint*:

$$\zeta_2(y) \triangleq ({}^A \mathbf{p}_{c_1} - {}^A \mathbf{b}_1) \cdot \mathbf{e}_{Y_A} = 0 \tag{6}$$

$$\Rightarrow y = 0. \tag{7}$$

The locus of the point \mathbf{p}_{c_1} is established as a circle of radius l_1 centered at \mathbf{b}_1 , by cutting the sphere in Eq. (5) by the plane $y = 0$. The equation of the circle, denoted as $C(x, z) = 0$, is obtained by substituting $y = 0$ in Eq. (5).

2.3 Derivation of the Forward Kinematic Univariate (FKU)

The FK problem may be solved by computing the intersections of the surface $S = 0$ with the circle $C = 0$. However, the same may also be reduced by first cutting the surface $S = 0$ by the plane $y = 0$ to obtain the curve $C' = 0$ in the $\mathbf{X}_A \mathbf{Z}_A$ plane, and then obtaining the intersections of $C' = 0$ with $C = 0$. An advantage of this approach is that the curve $C' = 0$ decomposes into three components (see Fig. 2 for an illustration, and Sect. 3 for a detailed interpretation of the same), as shown in schematic (8):

$$S(x, y, z) = 0 \xrightarrow{y \rightarrow 0} C'(x, z) = C'_0(x, z)C'_1(x, z)C'_2(x, z) = 0. \tag{8}$$

The component $C'_0(x, z) = ((x + 2b)^2 + z^2)^2 = 0$ admits a real solution *iff* $x = -2b$ and $z = 0$. For these values of x, z the constraint equations given by Eqs. (1, 2, 3, 5) in Sects. 2.2.1 and 2.2.2 are consistent *iff* the input parameters satisfy the following conditions:

$$l_2^2 = l_3^2 = 3a^2 - 3b^2, \quad l_1^2 = 9b^2. \tag{9}$$

The conditions in Eq. (9) correspond to the finite self-motion of the manipulator reported in [5]. Hence, the factor C'_0 is ignored in the following analysis. The implications of the said factor in relevance to the sub-chains have been discussed in [1]. The components $C'_i, i = 1, 2$ are of degree 8 in x, z and they describe the

two *operation modes* of the manipulator. Bézout limit puts the possible number of intersections with a circle at 16. However, the components of C'_i describe very special octic curves—these are quad-circular in nature. Therefore, 4 pairs of points of intersection lie in the plane at infinity, thus limiting the number of finite complex solutions to only 8, per mode.

Vanishing of the resultant of $C'_1(x, z)$ with $C(x, z)$ w.r.t. x leads to the desired FKU equation, namely, $\xi_1(z) = 0$, for the mode 1.

$$\left. \begin{matrix} C'_1(x, z) = 0 \\ C(x, z) = 0 \end{matrix} \right) \xrightarrow{\times x} \xi_1(z) = 0, \quad \left. \begin{matrix} C'_2(x, z) = 0 \\ C(x, z) = 0 \end{matrix} \right) \xrightarrow{\times x} \xi_2(z) = 0.$$

A similar computation leads to $\xi_2(z) = 0$, the FKU equation for the second mode. These equations have been derived in closed-form, whereupon it is observed that the FKUs are both of degree four in z^2 , and they maintain the relationship:

$$\xi_1(a) = \xi_2(-a), \tag{10}$$

where a is the circumradius of the moving platform.

2.4 Numerical Example

The formulation presented above is illustrated for the following set of numerical values: $a = 1/2$, $b = 1$, $l_1 = 11/5$, $l_2 = 23/10$ and $l_3 = 12/5$.

The length dimensions are scaled by the radius of the circum-circle of the base triangle, b , rendering them unit-less, while all angles are measured in radians.

Table 1. Sixteen real solutions to forward kinematics problem

Operation mode	Assembly mode	z	x	ϕ_1	ϕ_2	ϕ_3	x_0	x_1
Mode 1	1	2.197	0.889	1.520	0.899	0.860	0	-0.268
	2	-2.197	0.889	-1.520	-0.899	-0.860	0	-0.268
	3	1.721	-0.371	0.898	1.465	0.831	0	-0.393
	4	-1.721	-0.371	-0.898	-1.465	-0.831	0	-0.393
	5	1.660	-0.443	0.855	0.829	1.386	0	-0.540
	6	-1.660	-0.443	-0.855	-0.829	-1.386	0	-0.540
	7	1.627	-0.480	0.833	0.853	0.912	0	-0.987
	8	-1.627	-0.480	-0.833	-0.853	-0.912	0	-0.987
Mode 2	1	2.178	0.687	1.428	0.781	1.264	-0.469	0
	2	-2.178	0.687	-1.428	-0.781	-1.264	-0.469	0
	3	2.165	0.609	1.392	1.298	0.754	-0.400	0
	4	-2.165	0.609	-1.392	-1.298	-0.754	-0.400	0
	5	2.139	0.485	1.335	1.355	1.355	-0.993	0
	6	-2.139	0.485	-1.335	-1.355	-1.355	-0.993	0
	7	1.597	-0.513	0.812	1.390	1.320	-0.565	0
	8	-1.597	-0.513	-0.812	-1.390	-1.320	-0.565	0

It may be noted that the rational values of the numeric parameters help in retaining the *exact* nature of the computation up to the values of the coefficients of the FKU equations. The monic forms of these, for the given values, are¹:

$$\begin{aligned} \xi_1 &= u^4 - 13.193u^3 + 63.689u^2 - 134.113u + 104.347, \\ \xi_2 &= u^4 - 16.554u^3 + 101.072u^2 - 268.351u + 259.275, \text{ where } u = z^2. \end{aligned}$$

Each operation mode contains 8 real assembly modes for these numbers. The results have been tabulated in Table 1. The solutions are visualised as the points of intersection of the constraint curves $C'_i = 0$ and $C = 0$, as seen in Fig. 2.

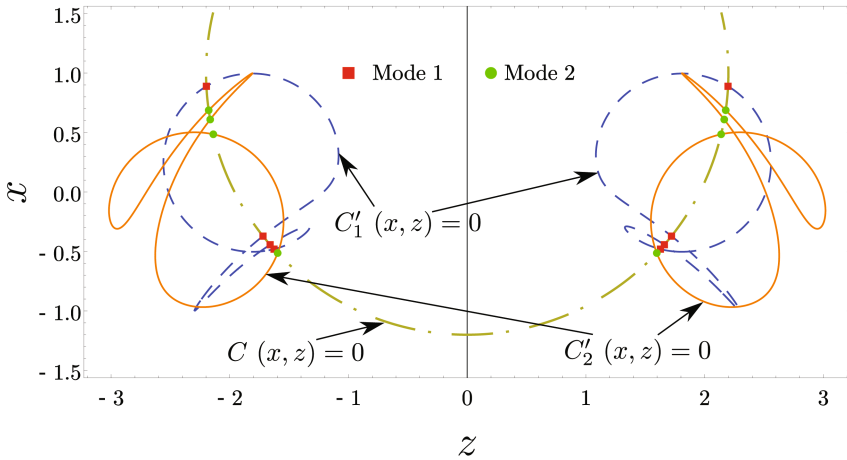


Fig. 2. Constraint geometries in the plane $X_A Z_A$: $C'_i = 0$ and $C = 0$

3 Interpretation of the Results and Correlation with Existing Ones

The algebraic properties of the FKU of the 3-RPS manipulator have been studied and reported at length. Yet, there has been no attempt to bring out the coherence between these results, and to visualise them geometrically. For instance, [6] reports the two operational modes, each characterised by the vanishing of one of the two Study parameters, x_1 and x_0 . In physical terms, this means that in the latter case, the moving platform rotates through π about a horizontal axis. In [4], the FKU is derived from the constraint equations in the joint-space, and it is found that the FKU factors in two components, g_1 and g_2 , where $g_1(a) = g_2(-a)$, a being the circum-radius of the moving platform. It may be noted that this is *consistent* with the findings in [6], since a going to $-a$ is

¹ Though the coefficients are obtained as exact rational numbers, their real approximations are presented here for the want of space.

identical in effect with the *flipping* of the moving platform *up-side down*, which is same as the π -*screw* motion described in [6]—in either case, a CCW distribution of the vertices $\mathbf{p}_1, \mathbf{p}_2, \mathbf{p}_3$ changes into a CW one.

The results of the present work corroborate and unify all of the results on FK reported in [4, 6]. The relationship with the results in [4] is captured by Eq. (10), where ξ_i play the roles of g_i in [4]. Also, the FKU is found to have only the even powers in either mode, signifying the manipulator poses are reflected pairwise at the base platform. On the other hand, as seen in Table 1, the vanishing of x_0 and x_1 in one of the two modes confirm the corroboration with the results of [6].

Figure 2 presents a visual summary of the algebraic results, which can be considered as a new contribution of the present work. The curve $C'(x, z) = 0$ decomposes into its components $C'_1(x, z) = 0$ and $C'_2(x, z) = 0$, signifying the two modes. Also, the reflections of each mode at the $z = 0$ line are obvious in the figure. Thus, these pictures provide a complete understanding of all the operations modes, and the assembly modes therein. These interpretations can be extended easily into the domain of singularity analysis and design.

4 Conclusion

This paper presents a geometric analysis of the 3-RPS manipulator. The manipulator is decomposed into two kinematic sub-chains, and the forward kinematic problem is formulated as the geometric problem of finding the intersections of the constraint varieties generated by the individual sub-chains. A new result is revealed in the process, that the problem is equivalent to the intersection of a circle with a pair of quad-circular octic curves in the plane of the circle. All the existing algebraic results reported in [4, 6, 7] are explained from the same geometric perspective. The results show striking similarities with those known in the case of the planar 3-RRR manipulator, whose forward kinematic problem is equivalent to the intersection of a tri-circular sextic curve with a circle. On the other hand, other spatial manipulators, such as the 3-RRS, which have architectural similarities with the 3-RPS, may be analysed in the same geometric framework, leading, hopefully, to analogous results. Also, these geometric interpretations may lead to a better understanding of the singularities of these manipulators, which is to be studied next.

Acknowledgment. The last author expresses his sincere gratitude to Professor Manfred L. Husty, University of Innsbruck, Austria, for all the learnings he has received from the latter through various formal and informal interactions, without which this work would not have been possible!

References

1. Bandyopadhyay, S., Mamidi, T.K., Baskar, A.: Kinematic analysis of the 3-RPS manipulator using the geometry of plane curves. Submitted for presentation in Proceedings of the International Symposium of Mechanism and Machine Science, Azerbaijan Technical University, Baku, Azerbaijan (2017)
2. Ghosal, A.: Robotics: Fundamental Concepts and Analysis. Oxford University Press, New Delhi (2006)
3. Gosselin, C.: Kinematic analysis, optimization and programming of parallel robotic manipulators. Ph.D. thesis, Department of Mechanical Engineering, McGill University, Montreal, Canada (1988)
4. Rangaprasad, A.S., Bandyopadhyay, S.: Analysis of constraint equations and their singularities. In: Lenarcic, J., Khatib, O. (eds.) *Advances in Robot Kinematics*, pp. 429–436. Springer International Publishing, Switzerland (2014)
5. Schadlbauer, J., Husty, M.L., Caro, S., Wenger, P.: Self-motions of 3-RPS manipulators. *Front. Mech. Eng.* **8**(1), 62–69 (2013)
6. Schadlbauer, J., Walter, D.R., Husty, M.L.: The 3-RPS parallel manipulator from an algebraic viewpoint. *Mech. Mach. Theory* **75**, 161–176 (2014)
7. Tsai, L.W.: *Robot Analysis: The Mechanics of Serial and Parallel Manipulators*. Wiley, New York (1999)

Constraint Equations of Inverted Kinematic Chains

Thomas Stigger and Manfred L. Husty^(✉)

Unit Geometry and CAD, University of Innsbruck, Innsbruck, Austria
{thomas.stigger,manfred.husty}@uibk.ac.at

Abstract. A lot of different kinematic chains have been investigated focusing on constraint equations, singularities, assembly modes and motion capabilities. The approach to obtain constraint equations via inverted chains however is rarely considered. We provide a detailed look on the constraint varieties of inverted chains, beginning with the basics of quaternion conjugation. The transformation of the Denavit- Hartenberg parameters needed for the quaternion conjugation is discussed in the paper. The quaternion conjugation is a fast way to obtain the variety corresponding to the inverted kinematic chain. Geometrically the conjugation is a reflection in the kinematic image space \mathbb{P}^7 with respect to a line and a five- dimensional subspace. Some examples of constraint equations of kinematic chains and their inverted chains complete the paper.

Keywords: Kinematic chains · Inverted kinematic chains · Constraint equations · Dual quaternion conjugation

1 Introduction

In recent years the description of kinematic chains and parallel or serial mechanisms by systems of polynomial equations has become more and more popular because of its success in describing the direct and inverse kinematics, a global analysis of singularities, workspaces and operation modes (see e.g. [4, 6, 10, 11]). The main reason for this success is the availability of more and more sophisticated algebraic manipulation systems that can deal with large systems of polynomial equations, the advance in the implementation of algorithms developed in algebraic geometry in such systems, but also the advances in the global numerical solution methods of these equations (see e.g. [13]). Therefore it makes sense to search for polynomial descriptions of all thinkable kinematic chains with the goal to use these descriptions in the synthesis and analysis of mechanisms and robots that are designed by combinations of different kinematic chains. This is the goal of a joint research program between IRCyNN Nantes and the University of Innsbruck. In the course of this project the question arose how the constraint equations of a kinematic chain change when base and endeffector are interchanged. A quick - but wrong- answer to this problem would be that one obtains the inverse of the motion and this yields the same motion. The mistake in this assumption can be seen immediately when one studies simple planar

motions like the Cardan and its inverse, the Oldham motion. It is well known that the degree of these two motions differ. How the two simple motions are linked was already discussed in [1]. That inverted parallel manipulators behave quite differently was recently shown in [6].

When displacements are described in Study parameters or dual quaternions, then it is well known that the inverse displacement can be described by simple conjugation of the dual quaternion. The effect of inverting the motion of a mechanism - like a parallel manipulator - on its set of polynomial constraint equations is less known. It is the goal of this paper to shed some light on this issue with the basic idea to simplify the necessary work in finding the constraint equations of inverted kinematic chains. In [15], the so called implicitization algorithm was developed, which always can be used to derive the constraint equations of a kinematic chain. This algorithm essentially computes the implicit constraint equations by eliminating the motion parameters of the classical forward kinematics of the chain. It is obvious that this algorithm could be applied to the inverted chain to obtain the constraint equations. But it is desirable to avoid this computationally laborious algorithm whenever possible. It will be shown explicitly in this paper that quaternion conjugation of the set of constraint equations yields the same result as the implicitization algorithm.

The paper is organized as follows: In Sect. 2 the geometric interpretation of quaternion conjugation in the kinematic image space will be discussed, in Sect. 3 the effect on the design parameters (Denavit-Hartenberg parameters) of the chain is studied, which is necessary to compare the implicitization algorithm with the conjugation of the set of constraint equations. In Sects. 4 and 5 the theory is applied to RP - (revolute-prismatic-chains) and PR - as well as RRP - and PRR -chains.

2 Conjugation of Quaternions

In the following 3D-Euclidean displacements ($SE(3)$) are described in a point model, which is obtained via kinematic mapping¹. In this mapping every Euclidean displacement corresponds to a point with homogeneous projective coordinates $(x_0 : x_1 : x_2 : x_3 : y_0 : y_1 : y_2 : y_3)$ located on the Study quadric $S_6^2 : x_0y_0 + x_1y_1 + x_2y_2 + x_3y_3 = 0$, which is a six dimensional quadric in a seven dimensional projective space \mathbb{P}^7 . This space is called kinematic image space, sometimes also Soma space. The projective point coordinates can also be interpreted as the components of a dual quaternion. Both interpretations will be used simultaneously in the following.

The scope of this chapter is to investigate the constraint equations of an inverted serial chain without using the implicitization algorithm but with the use of conjugate quaternions. Before this can be done some basic properties of kinematic chains and the image space \mathbb{P}^7 must be recalled. The kinematics of a serial chain is described with respect to (arbitrarily chosen) coordinate frames in the base and the end-effector. All possible locations of the end-effector with

¹ Due to space limitation this mapping cannot be explained in detail, but a comprehensive introduction can be found in [4] or [3].

respect to the base correspond to algebraic varieties which are described by sets of polynomial equations in \mathbb{P}^7 . Coordinate transformations in the base and the end-effector frame induce linear mappings T in \mathbb{P}^7 that preserve several interesting geometric objects:

1. the *Study quadric* S_6^2 ,
2. the *Null cone* defined by $\mathcal{N} : x_0^2 + x_1^2 + x_2^2 + x_3^2 = 0$, which is quadric in \mathbb{P}^7 , that has only complex points with exception of its 3-dimensional vertex space $\mathcal{E} : x_0 = x_1 = x_2 = x_3 = 0$. \mathcal{E} is entirely contained in S_6^2 and is called *exceptional generator space*,
3. the *exceptional quadric* $\mathcal{Y} : y_0^2 + y_1^2 + y_2^2 + y_3^2 = 0 \in \mathcal{E}$,
4. all quadrics $\mathcal{Q} = \lambda S_6^2 + \mu \mathcal{N}, \lambda, \mu \in \mathbb{R}$ in the pencil spanned by the Study quadric and the Null cone.

A detailed derivation and proofs for these statements and some interesting examples can be found in [9]. The invariant objects essentially govern the kinematics of 3D-Euclidean displacements². The mapping of a dual quaternion with components $[x_0, x_1, x_2, x_3, y_0, y_1, y_2, y_3]$ to $[x_0, -x_1, -x_2, -x_3, y_0, -y_1, -y_2, -y_3]$ implies a mapping in \mathbb{P}^7 which does not effect the line $(s : 0 : 0 : 0 : t : 0 : 0 : 0)$ with projective parameters s and t nor the five-dimensional subspace $(0 : t_1 : t_2 : t_3 : 0 : t_5 : t_6 : t_7)$ with projective parameters t_i . These properties can be shown as follows: The conjugation of a quaternion corresponds to a linear mapping, more precisely a collineation, in \mathbb{P}^7 described with the matrix

$$\mathbf{A} = \begin{pmatrix} 1 & 0 & 0 & 0 & 0 & 0 & 0 & 0 \\ 0 & -1 & 0 & 0 & 0 & 0 & 0 & 0 \\ 0 & 0 & -1 & 0 & 0 & 0 & 0 & 0 \\ 0 & 0 & 0 & -1 & 0 & 0 & 0 & 0 \\ 0 & 0 & 0 & 0 & 1 & 0 & 0 & 0 \\ 0 & 0 & 0 & 0 & 0 & -1 & 0 & 0 \\ 0 & 0 & 0 & 0 & 0 & 0 & -1 & 0 \\ 0 & 0 & 0 & 0 & 0 & 0 & 0 & -1 \end{pmatrix} \tag{1}$$

The characteristic equation $(1 - \lambda)^2(-1 - \lambda)^6 = 0$ of \mathbf{A} yields the double eigenvalue $\lambda_1 = 1$ and a sixfold eigenvalue $\lambda_2 = -1$. The corresponding eigenspaces v ($\lambda_1 = 1$) and w ($\lambda_2 = -1$) are simply found to be

$$v = \begin{bmatrix} 1 \\ 0 \\ 0 \\ 0 \\ 0 \\ 0 \\ 0 \\ 0 \end{bmatrix} t + \begin{bmatrix} 0 \\ 0 \\ 0 \\ 1 \\ 0 \\ 0 \\ 0 \\ 0 \end{bmatrix} s, \quad w = \begin{bmatrix} 0 \\ 1 \\ 0 \\ 0 \\ 0 \\ 0 \\ 0 \\ 0 \end{bmatrix} t_1 + \begin{bmatrix} 0 \\ 0 \\ 1 \\ 0 \\ 0 \\ 0 \\ 0 \\ 0 \end{bmatrix} t_2 + \dots + \begin{bmatrix} 0 \\ 0 \\ 0 \\ 0 \\ 0 \\ 0 \\ 0 \\ 1 \end{bmatrix} t_6, \text{ with } t, s, t_1, t_2, \dots, t_6 \in \mathbb{R} \tag{2}$$

² The kinematic images of planar and spherical displacements subordinate completely to this description because both cases are obtained by three dimensional sub-spaces of \mathbb{P}^7 . The corresponding geometry of their image spaces and the algorithms to derive these geometries can be found in [1] p. 393ff. resp. [5] p. 60ff.

Equation 2 shows that v can be characterized by the relations $x_1 = x_2 = x_3 = y_1 = y_2 = y_3 = 0$ which define a line in \mathbb{P}^7 and the second eigenspace w is given by $x_0 = y_0 = 0$ which is a five-dimensional subspace of \mathbb{P}^7 . The intersection of the line v and S_6^2 yields two characteristic points, namely the point $I = (1 : 0 : 0 : 0 : 0 : 0 : 0 : 0)$ which corresponds to the identity in $SE(3)$ and an ideal point $I_d = (0 : 0 : 0 : 0 : 1 : 0 : 0 : 0)$ in the exceptional space \mathcal{E} . It is obvious that the identity is fixed under quaternion conjugation. The line v is a fiber in the fiber projectivity φ defined in [8,9], that can be used to define a non-injective “extended kinematic map”. The second eigenspace w is the span of the six points $P_1 = (0 : 1 : 0 : 0 : 0 : 0 : 0 : 0), \dots, P_6 = (0 : 0 : 0 : 0 : 0 : 0 : 0 : 1)$. Intersecting w with S_6^2 yields the quadric $\mathcal{P} : x_1y_1 + x_2y_2 + x_3y_3 = 0$. Points on this quadric are characterized by the equations $x_0 = y_0 = 0$ and define displacements which have the property that the inverse of the displacement is the same as the displacement itself. These displacements are well known in the kinematics, Study ([14], p. 178) calls them “Umwendungen” (π -turns). In the one parametric case (curves on \mathcal{P}) the corresponding motions are called line-symmetric motions and have been studied by Krames synthetically (see [1], Chap. 9, Sect. 7) and analytically in [12].

The planar kinematic mapping and also the effect of conjugation was developed in [1] (Chap. 11, Sect. 14). To show how the planar case fits into the theory developed above, let's have a brief look into this case. Planar displacements are characterized by the equations $x_2 = x_3 = y_0 = y_1 = 0$. The intersection of these four hyperplanes yields a three-dimensional subspace $E \subset \mathbb{P}^7$, which is a generator space of S_6^2 . The intersection of E with the Null cone \mathcal{N} yields the quadric $x_0^2 + x_1^2 = 0$ which can be factorized into

$$V_1 : x_0 + ix_1 = 0, \quad V_2 : x_0 - ix_1 = 0, \quad i \dots \text{complex unit.} \tag{3}$$

V_1 and V_2 are two complex conjugate 2-planes intersecting in a real line u . On the other hand this line intersects the exceptional quadric in two complex conjugate points $J_1 = (0 : 0 : 1 : i)$ and $J_2 = (0 : 0 : 1 : -i)$. Alternatively one could provide the following arguments: According to the dimension formula ($dim(v \cap E) = dim(v) + dim(E) - dim(\mathbb{P}^7) = 5 + 3 - 7 = 1$) the 5-dim subspace w and the 3-space E must intersect in a one dimensional linear subspace which is of course the line u . The intersection of the fixed space v (Eq. (2)), the Study quadric and the three-dimensional subspace T yields an intersection point, which is exactly the origin $[1,0,0,0]$ of the planar displacements. Applying the linear map

$$[x_0, x_1, y_2, y_3] \mapsto [x_0, -x_1, -y_2, -y_3] \tag{4}$$

to the 2-planes $x_0 \pm ix_1 = 0$ one can see that they are interchanged $x_0 \mp ix_1 = 0$ fixing their intersection line u . The linear map (Eq.(4)) also does not effect the origin. The map is a reflection into the origin. These results are exactly the same as in the classical planar case but within the bigger setting of spatial kinematic mapping ([1], p. 433).

3 Denavit-Hartenberg Parameters

The investigation of inverse kinematic chains and a comparison of their constraint equations obtained by different methods requires an adaption of their Denavit- Hartenberg parameters when base and end-effector coordinate systems are interchanged (Fig. 1). This change has to be observed when one wants to compare the constraint equations obtained by simple dual quaternion conjugation and the constraint equations obtained by applying the implicitization to the forward kinematics equations of the inverted chain. A simple considerations shows that the transformation can be written as

$$\begin{aligned}
 T_{DH} : \quad & a_{0+j} \rightarrow -a_{n-j} && a, d, \alpha \dots \text{DH- parameters,} \\
 & d_{0+j} \rightarrow -d_{n-j} && j < n \dots \text{number of the joint to be changed} \\
 & \alpha_{0+j} \rightarrow -\alpha_{n-j} && n \dots \text{total number of joints} \quad (5)
 \end{aligned}$$

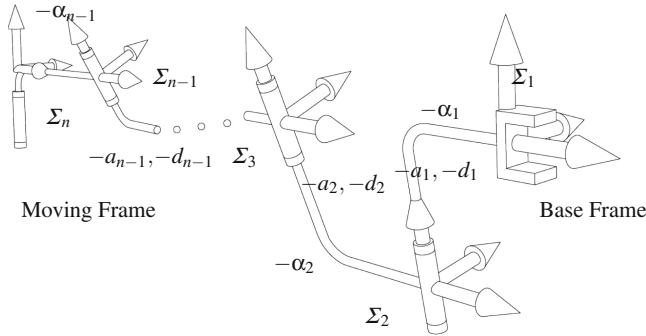


Fig. 1. Interchanged frames [7, p. 49]

Interchanging base and end-effector frames and applying the transformation T_{DH} on the DH- parameters one can now apply quaternion conjugation and thereby obtain the constraint equations of the inverse kinematic chain having the former end-effector frame as base frame. It is easy to see that this general method also can be used when a manipulator is composed of several (even different) kinematic chains. In the next sections this method will be used to obtain the constraint equations of some kinematic chains and compare it with the results of the linear implicitization algorithm (LIA).

4 RP- and the PR-chains

To show that LIA and quaternion conjugation followed by the T_{DH} transformation yield the same solution set (the same variety), the constraint equations for

the RP- and the inverse PR-chain are computed at first via LIA. For both chains the Gröbner bases of the ideal corresponding to the set of constraint equations are computed and denoted by B_1 and B_2 . Onto one set of constraint equations, for example B_1 , the quaternion conjugation and T_{DH} are applied resulting in a set of equations \bar{B}_1 . Then one has to show that the variety represented by B_2 is the same as the one of \bar{B}_1 . Note that the ideals (the set of equations) do not necessarily have to be identical but the represented varieties have to be identical. To check if the same variety is represented by the two different ideals, the radical membership has to be checked.

According to Cox, Little and O’Shea [2] the necessary and sufficient condition can be formulated,

“Let k be an arbitrary field and let $I = \langle f_1, \dots, f_s \rangle \subset k[x_1, \dots, x_n]$ be an ideal. Then $f \in \sqrt{I}$ if and only if the constant polynomial 1 belongs to the ideal $\tilde{I} = \langle f_1, \dots, f_s, 1 - yf \rangle \subset k[x_1, \dots, x_n, y]$ (in which case, $\tilde{I} = k[x_1, \dots, x_n, y]$).”

This algorithm is applied to the ideals B_2 and \bar{B}_1 . Taking a polynomial f_1 of one basis, adding $1 - yf_1$ to the second basis and computing the Gröbner bases of the ideal yields in general a remainder. If there is no remainder the polynomial f_1 is already included in the first basis. This has to be done with all polynomials of the first basis and then the same procedure is applied reversely. As expected the computation shows that the varieties of the RP- and the conjugated PR-chain are identical because no single remainder shows up. Although the equations describing the variety of the RP-chain as well as the conjugated set of constraints describing the PR-chain are simple, they still differ in some signs, as it can be seen in Eqs.(6) and (7). But the application of the radical membership test shows immediately that they are describing the same variety.

$$\begin{aligned}
 Cm_{RP-con} = [& (\alpha_1^2 a_1 - a_1) x_3 - 2 y_2 - 2 \alpha_1 y_3, (\alpha_1^2 a_1 - a_1) x_2 - 2 \alpha_1 y_2 - 2 \alpha_1^2 y_3, \\
 & (\alpha_1^2 a_1 - a_1) x_1 + 2 \alpha_1^2 y_0 - 2 \alpha_1 y_1, (\alpha_1^2 a_1 - a_1) x_0 - 2 \alpha_1 y_0 + 2 y_1, \\
 & \alpha_1 y_0^2 + (-\alpha_1^2 - 1) y_0 y_1 + \alpha_1 y_1^2 + \alpha_1 y_2^2 + (\alpha_1^2 + 1) y_2 y_3 + \alpha_1 y_3^2]
 \end{aligned} \tag{6}$$

$$\begin{aligned}
 Cm_{PR} = [& (\alpha_1^2 a_1 - a_1) x_3 + 2 y_2 - 2 \alpha_1 y_3, (\alpha_1^2 a_1 - a_1) x_2 - 2 \alpha_1 y_2 + 2 \alpha_1^2 y_3, \\
 & (\alpha_1^2 a_1 - a_1) x_1 - 2 \alpha_1^2 y_0 - 2 \alpha_1 y_1, (\alpha_1^2 a_1 - a_1) x_0 - 2 \alpha_1 y_0 - 2 y_1, \\
 & \alpha_1 y_0^2 + (\alpha_1^2 + 1) y_0 y_1 + \alpha_1 y_1^2 + \alpha_1 y_2^2 + (-\alpha_1^2 - 1) y_2 y_3 + \alpha_1 y_3^2]
 \end{aligned} \tag{7}$$

5 RRP- and the PRR-chains

The investigation of the relation between the RRP- and its inverse, the PRR-chain is not as straightforward as in the previous section. The used computer system Maple is not able to compute the radical membership for the RRP- and the PRR-chain in general coordinates. But it is possible to provide an alternative, remarkably simple algorithm. The LIA comes up in both cases with a set of nine constraint equations, which are quadratic in x_i and y_i . These sets are denoted

by H_1 and H_2 . Four out of the nine equations are linear in y_i and are used to solve for these parameters. Because of lack of space only one of the resulting y_i is displayed, all the others look similar

$$y_0 = -\frac{a_1(\alpha_1\alpha_2 - 1)(\alpha_1\alpha_2 + 1)x_1^2}{2\alpha_1(\alpha_2^2 + 1)x_0} - \frac{(\alpha_1^2\alpha_2 a_1 - \alpha_1\alpha_2^2 a_2 - a_2\alpha_1 + \alpha_2 a_1)x_1}{2\alpha_1(\alpha_2^2 + 1)} - \frac{a_1(\alpha_1\alpha_2 - 1)(\alpha_1\alpha_2 + 1)x_2^2}{2\alpha_1(\alpha_2^2 + 1)x_0} - \frac{(\alpha_1^2 + 1)\alpha_2 a_1 x_2 x_3}{\alpha_1(\alpha_2^2 + 1)x_0} + \frac{\alpha_2 d_2 x_2}{\alpha_2^2 + 1} + 2\frac{\alpha_2^2 d_2(\alpha_1^2 + 1)x_3}{(\alpha_1^2 - \alpha_2^2)(\alpha_2^2 + 1)} \tag{8}$$

Back substitution into H_1 results in only one quadratic equation in each set. Applying the dual quaternion conjugation and the T_{DH} transformation yields exactly the equation \bar{H}_1 describing the rotation capability of the inverted chain and this equation is identical to the equation H_2 obtained by performing the LIA on PRR-chain

$$H_1 : (\alpha_1^2\alpha_2^2 - 1)(x_1^2 + x_2^2) + 2(\alpha_1^2\alpha_2 + \alpha_2)(x_2 x_3 + x_1) + (\alpha_1^2 - \alpha_2^2)(x_3^2 + 1) = 0$$

$$\bar{H}_1 = H_2 : (\alpha_1^2\alpha_2^2 - 1)(x_1^2 + x_2^2) - 2(\alpha_2^2\alpha_1 + \alpha_1)(x_2 x_3 - x_1) + (\alpha_2^2 - \alpha_1^2)(x_3^2 + 1) = 0 \tag{9}$$

Figure 2 shows the two quadrics H_1 and H_2 and one point and its inverse connected by a mirroring line colored in blue for the parameter values $a_2 = -5, a_1 = -7, d_2 = -3, d_1 = 0, \alpha_1 = -3/2, \alpha_2 = -7/5$ (α_i denote the algebraic values of the angles).

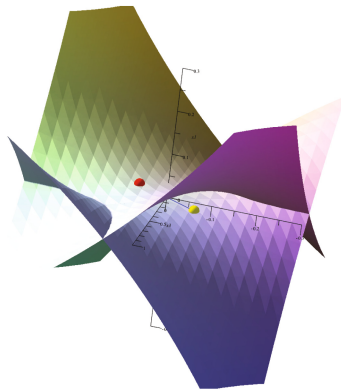


Fig. 2. Quadrics, points and connection line (Color figure online)

6 Conclusion

In the paper it was shown that the constraint equations of an inverted kinematic chain can be obtained by simply applying quaternion conjugation to the constraint equations of the original chain. The effect of quaternion conjugation

in the kinematic image space was shown to be a reflection with respect to a line and a five-dimensional subspace. Furthermore it was explicitly shown, that quaternion conjugation and the much more complicated linear implicitization algorithm yield the same result. Those displacements that are fixed in conjugation are on the intersection of a five-dimensional space $x_0 = y_0 = 0$ with the Study quadric. The provided algorithm can be applied not only to any thinkable kinematic chain but also to any mechanism and its inverted which are composed of (even different) kinematic chains.

Acknowledgements. The authors acknowledge the support of the FWF project I 1750-N26 “Kinematic Analysis of Lower-Mobility Parallel Manipulators Using Efficient Algebraic Tools”.

References

1. Bottema, O., Roth, B.: Theoretical Kinematics, 1st edn. North-Holland Publishing Company, Amsterdam (1979)
2. Cox, D.A., Little, J., O’Shea, D.: Ideals, Varieties, and Algorithms: An Introduction to Computational Algebraic Geometry and Commutative Algebra, 3rd edn. Springer, Heidelberg (2007)
3. Husty, M., Schröcker, H.P.: Kinematics and algebraic geometry. In: 21st Century Kinematics, pp. 85-123. Springer (2012)
4. Husty, M.L., Pffurner, M., Schröcker, H.P., Brunthaler, K.: Algebraic methods in mechanism analysis and synthesis. *Robotica* **25**, 661–675 (2007)
5. Müller, H.R.: Sphärische Kinematik. VEB Deutscher Verlag der Wiss, Berlin (1962)
6. Nayak, A., Nurahmi, L., Wenger, P., Caro, S.: Comparison of 3-RPS and 3-SPR Parallel Manipulators Based on Their Maximum Inscribed Singularity-Free Circle, pp. 121-130. Springer International Publishing, Cham (2017)
7. Pffurner, M.: Analysis of spatial serial manipulators using kinematic mapping. Doctoral thesis, University Innsbruck (2006)
8. Pffurner, M., Schröcker, H.P., Husty Manfred, L.: Path planning in kinematic image space without the Study condition. In: Merlet, J.P., Lenarcic, J. (eds.) *Advances in Robot Kinematics* (2016). <https://hal.archives-ouvertes.fr/hal-01339423>
9. Rad, T.D., Scharler, D., Schröcker, H.P.: The kinematic image of RR, PR and RP Dyads. In: [arXiv:1607.08119v1](https://arxiv.org/abs/1607.08119v1) [csRO], 27 Jul 2016
10. Schadlbauer, J.: Algebraic methods in kinematics and line geometry. Doctoral thesis, University Innsbruck (2014)
11. Schadlbauer, J., Walter, D.R., Husty, M.L.: The 3-RPS parallel manipulator from an algebraic viewpoint. *Mechanism Mach. Theory* **75**, 161–176 (2014)
12. Selig, J., Husty, M.: Half-turns and line symmetric motions. *Mechanism Mach. Theory* **46**(2), 156–167 (2011)
13. Sommese, A.J., Wampler, C.W.: The Numerical Solution of Systems of Polynomials Arising in Engineering and Science. World Scientific, Singapore (2005)
14. Study, E.: *Geometrie der Dynamen: die Zusammensetzung von Kräften und verwandte Gegenstände der Geometrie*. Teubner, Leipzig (1903)
15. Walter, D.R., Husty, M.L.: On implicitization of kinematic constraint equations. *Mach. Des. Res.* **26**, 218–226 (2010)

Local and Full-Cycle Mobility Analysis of a 3-RPS-3-SPR Series-Parallel Manipulator

Abhilash Nayak¹, Stéphane Caro^{2(✉)}, and Philippe Wenger²

¹ École Centrale de Nantes,
Laboratoire des Sciences du Numérique de Nantes (LS2N),
1 rue de la Noë, 44321 Nantes, France
Abhilash.Nayak@ircyn.ec-nantes.fr

² CNRS, Laboratoire des Sciences du Numérique de Nantes (LS2N),
École Centrale de Nantes, 1 rue de la Noë, UMR CNRS 6004, 44321 Nantes, France
{Stephane.Caro,Philippe.Wenger}@ls2n.fr

Abstract. This paper aims to shed light on the determination of the true mobility for a 3-RPS-3-SPR series-parallel manipulator, which was claimed to be six in [6] without any proof, and shown to be five in [3,4] with an erroneous proof. Screw theory is used to derive the kinematic Jacobian matrix and the twist system of the mechanism, leading to the determination of its local mobility. It turns out that this local mobility is found to be six in several arbitrary configurations, which indicates a full-cycle mobility equal to six. This full-cycle mobility is confirmed by calculating the Hilbert dimension of the ideal made up of the set of constraint equations. It is also shown that the mobility drops to five in some particular configurations, referred to as impossible output singularities.

Keywords: Series-parallel manipulator · Mobility analysis · Jacobian matrix · Screw theory · Hilbert dimension

1 Introduction

A series-parallel manipulator (S-PM) is composed of parallel manipulators mounted in series and has merits of both serial and parallel manipulators. The 3-RPS-3-SPR S-PM is such a mechanism with the proximal module being composed of the 3-RPS parallel mechanism and the distal module being composed of the 3-SPR PM. Hu *et al.* [6] analyzed the workspace of this manipulator. Hu formulated the Jacobian matrix for S-PMs as a function of Jacobians of the individual parallel modules [5]. In the former paper, it was assumed that the number of local dof of the 3-RPS-3-SPR mechanism is equal to six, whereas Gallardo *et al.* found out that it is equal to five [3,4]. As a matter of fact, it is not straightforward to find the local mobility of this S-PM due to the third-order twist systems of each individual module. It is established that the 3-RPS PM performs a translation and two non pure rotations about non fixed axes, which induce two translational parasitic motions [7]. The 3-SPR PM also has the

same type of dof [12]. In addition, these mechanisms are known as zero-torsion mechanisms. When they are mounted in series, the axis about which the torsional motion is constrained, is different for a general configuration of the S-PM. Gallardo *et al.* failed to consider this fact but only those special configurations in which the axes coincide resulting in a mobility equal to five. This paper aims at clarifying that the full-cycle mobility of the 3-RPS-3-SPR S-PM is equal to six with the help of screw theory and some algebraic geometry concepts. Although the considered S-PM has double spherical joints and two sets of three coplanar revolute joint axes, the proposed methodology to calculate the mobility of the manipulator at hand is general and can be applied to any series-parallel manipulator.

The paper is organized as follows: The manipulator under study is described in Sect. 2. The kinematic Jacobian matrix of a general S-PM with multiple modules is expressed in vector form in Sect. 3. Section 4 presents some configurations of the 3-RPS-3-SPR S-PM with the corresponding local mobility. Section 5 deals with the full-cycle mobility of the 3-RPS-3-SPR S-PM.

2 Manipulator Under Study

The architecture of the 3-RPS-3-SPR S-PM under study is shown in Fig. 1. It consists of a proximal 3-RPS PM module and a distal 3-SPR PM module. The 3-RPS PM is composed of three legs each containing a revolute, a prismatic and a spherical joint mounted in series, while the legs of the 3-SPR PM have these lower pairs in reverse order. Thus, the three equilateral triangular shaped platforms are the fixed base, the coupler and the end effector, coloured brown, green and blue, respectively. The vertices of these platforms are named A_i , B_i and C_i , $i = 0, 1, 2$. Here after, the subscript 0 corresponds to the fixed base, 1 to the coupler platform and 2 to the end-effector. A coordinate frame \mathcal{F}_i is attached to each platform such that its origin O_i lies at its circumcenter. The coordinate axes, x_i points towards the vertex A_i , y_i is parallel to the opposite side B_iC_i and by the right hand rule, z_i is normal to platform plane. Besides, the circum-radius of the i -th platform is denoted as h_i . \mathbf{p}_i and \mathbf{q}_i , $i = 1, \dots, 6$ are unit vectors along the prismatic joints while \mathbf{u}_i and \mathbf{v}_i , $i = 1, \dots, 6$ are unit vectors along the revolute joint axes.

3 Kinematic Modeling of Series-Parallel Manipulators

Keeping in mind that the two parallel mechanisms are mounted in series, the end effector twist (angular velocity vector of a body and linear velocity vector of a point on the body) for the 3-RPS-3-SPR S-PM with respect to base can be represented as follows:

$${}^0\mathbf{t}_{2/0} = {}^0\mathbf{t}_{2/0}^{PROX} + {}^0\mathbf{t}_{2/1}^{DIST} \implies \begin{bmatrix} {}^0\omega_{2/0} \\ {}^0\mathbf{v}_{O_2/0} \end{bmatrix} = \begin{bmatrix} {}^0\omega_{2/0}^{PROX} \\ {}^0\mathbf{v}_{O_2/0}^{PROX} \end{bmatrix} + \begin{bmatrix} {}^0\omega_{2/1}^{DIST} \\ {}^0\mathbf{v}_{O_2/1}^{DIST} \end{bmatrix} \quad (1)$$

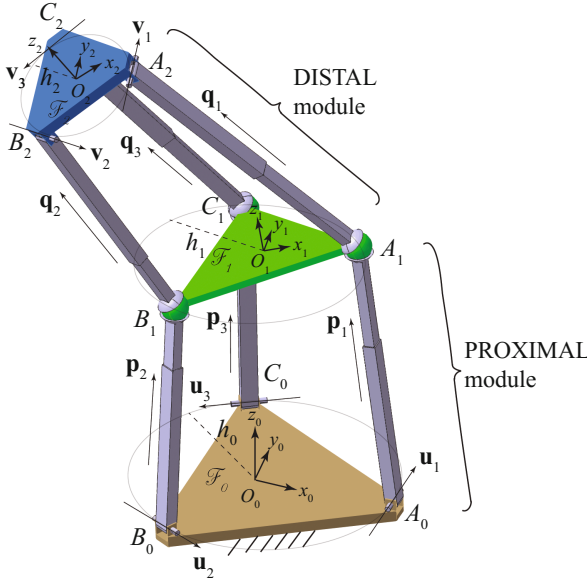


Fig. 1. A 3-RPS-3-SPR series-parallel manipulator

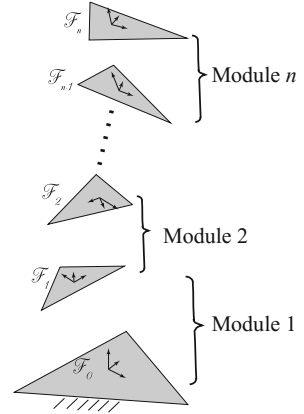


Fig. 2. n parallel mechanisms (named modules) arranged in series

where ${}^0\mathbf{t}_{2/0}^{PROX}$ is the end effector twist with respect to the base (2/0) due to the proximal module motion and ${}^0\mathbf{t}_{2/1}^{DIST}$ is the end effector twist with respect to the coupler (2/1) due to the distal module motion. These twists are expressed in the base frame \mathcal{F}_0 , hence the left superscript. The terms on right hand side of Eq. (1) are not known, but can be expressed in terms of the known twists using screw transformations. To do so, the known twists are first noted down. If the proximal and distal modules are considered individually, the twist of their respective moving platforms with respect to their fixed base will be expressed as a function of the actuated joint velocities:

$$\mathbf{A}_{PROX} {}^0\mathbf{t}_{1/0}^{PROX} = \mathbf{B}_{PROX} \dot{\rho}_{13} \implies \begin{bmatrix} ({}^0\mathbf{r}_{O_1A_1} \times {}^0\mathbf{p}_1)^T & {}^0\mathbf{p}_1^T \\ ({}^0\mathbf{r}_{O_1B_1} \times {}^0\mathbf{p}_2)^T & {}^0\mathbf{p}_2^T \\ ({}^0\mathbf{r}_{O_1C_1} \times {}^0\mathbf{p}_3)^T & {}^0\mathbf{p}_3^T \\ ({}^0\mathbf{r}_{O_1A_1} \times {}^0\mathbf{u}_1)^T & {}^0\mathbf{u}_1^T \\ ({}^0\mathbf{r}_{O_1B_1} \times {}^0\mathbf{u}_2)^T & {}^0\mathbf{u}_2^T \\ ({}^0\mathbf{r}_{O_1C_1} \times {}^0\mathbf{u}_3)^T & {}^0\mathbf{u}_3^T \end{bmatrix} \begin{bmatrix} {}^0\omega_{1/0}^{PROX} \\ {}^0\mathbf{v}_{O_1/0}^{PROX} \end{bmatrix} = \begin{bmatrix} \mathbf{I}_{3 \times 3} \\ \mathbf{0}_{3 \times 3} \end{bmatrix} \begin{bmatrix} \dot{\rho}_1 \\ \dot{\rho}_2 \\ \dot{\rho}_3 \end{bmatrix} \quad (2)$$

$$\mathbf{A}_{DIST} {}^1\mathbf{t}_{2/1}^{DIST} = \mathbf{B}_{DIST} \dot{\rho}_{46} \implies \begin{bmatrix} ({}^1\mathbf{r}_{O_2A_1} \times {}^1\mathbf{q}_1)^T & {}^1\mathbf{q}_1^T \\ ({}^1\mathbf{r}_{O_2B_1} \times {}^1\mathbf{q}_2)^T & {}^1\mathbf{q}_2^T \\ ({}^1\mathbf{r}_{O_2C_1} \times {}^1\mathbf{q}_3)^T & {}^1\mathbf{q}_3^T \\ ({}^1\mathbf{r}_{O_2A_1} \times {}^1\mathbf{v}_1)^T & {}^1\mathbf{v}_1^T \\ ({}^1\mathbf{r}_{O_2B_1} \times {}^1\mathbf{v}_2)^T & {}^1\mathbf{v}_2^T \\ ({}^1\mathbf{r}_{O_2C_1} \times {}^1\mathbf{v}_3)^T & {}^1\mathbf{v}_3^T \end{bmatrix} \begin{bmatrix} {}^1\omega_{2/1}^{DIST} \\ {}^1\mathbf{v}_{O_2/1}^{DIST} \end{bmatrix} = \begin{bmatrix} \mathbf{I}_{3 \times 3} \\ \mathbf{0}_{3 \times 3} \end{bmatrix} \begin{bmatrix} \dot{\rho}_4 \\ \dot{\rho}_5 \\ \dot{\rho}_6 \end{bmatrix} \quad (3)$$

where, ${}^0\mathbf{t}_{1/0}^{PROX}$ is the twist of the coupler with respect to the base expressed in \mathcal{F}_0 and ${}^1\mathbf{t}_{2/1}^{DIST}$ is the twist of the end effector with respect to the coupler expressed in \mathcal{F}_1 . \mathbf{A}_{PROX} and \mathbf{A}_{DIST} are called forward Jacobian matrices and they incorporate the actuation and constraint wrenches of the 3-RPS and 3-SPR PMs, respectively [9]. \mathbf{B}_{PROX} and \mathbf{B}_{DIST} are called inverse Jacobian matrices and they are the result of the reciprocal product between wrenches of the mechanism and twists of the joints for the 3-RPS and 3-SPR PMs, respectively. $\dot{\rho}_{13} = [\dot{\rho}_1, \dot{\rho}_2, \dot{\rho}_3]^T$ and $\dot{\rho}_{46} = [\dot{\rho}_4, \dot{\rho}_5, \dot{\rho}_6]^T$ are the prismatic joint velocities for the proximal and distal modules, respectively. ${}^k\mathbf{r}_{PQ}$ denotes the vector pointing from a point P to point Q expressed in frame \mathcal{F}_k . Considering Eq. (1), the unknown twists ${}^0\mathbf{t}_{2/0}^{PROX}$ and ${}^0\mathbf{t}_{2/1}^{DIST}$ can be expressed in terms of the known twists ${}^0\mathbf{t}_{1/0}^{PROX}$ and ${}^1\mathbf{t}_{2/1}^{PROX}$ using the following screw transformation matrices [2, 11].

$$\begin{bmatrix} {}^0\omega_{2/0}^{PROX} \\ {}^0\mathbf{v}_{O_2/0}^{PROX} \end{bmatrix} = {}^2\mathbf{Ad}_1 \begin{bmatrix} {}^0\omega_{1/0}^{PROX} \\ {}^0\mathbf{v}_{O_1/0}^{PROX} \end{bmatrix} \quad (4)$$

$$\text{with } {}^2\mathbf{Ad}_1 = \begin{bmatrix} \mathbf{I}_{3 \times 3} & \mathbf{0}_{3 \times 3} \\ -{}^0\hat{\mathbf{r}}_{O_1O_2} & \mathbf{I}_{3 \times 3} \end{bmatrix}, \quad {}^0\hat{\mathbf{r}}_{O_1O_2} = \begin{bmatrix} 0 & -{}^0z_{O_1O_2} & {}^0y_{O_1O_2} \\ {}^0z_{O_1O_2} & 0 & -{}^0x_{O_1O_2} \\ -{}^0y_{O_1O_2} & {}^0x_{O_1O_2} & 0 \end{bmatrix}$$

${}^2\mathbf{Ad}_1$ is called the adjoint matrix. ${}^0\hat{\mathbf{r}}_{O_1O_2}$ is the cross product matrix of vector ${}^0\mathbf{r}_{O_1O_2} = [{}^0x_{O_1O_2}, {}^0y_{O_1O_2}, {}^0z_{O_1O_2}]$, pointing from point O_1 to point O_2 expressed in frame \mathcal{F}_0 .

Similarly, for the distal module, the velocities ${}^1\omega_{2/1}^{DIST}$ and ${}^1\mathbf{v}_{O_2/1}^{DIST}$ can be transformed from frame \mathcal{F}_1 to \mathcal{F}_0 just by multiplying each of them by the rotation matrix ${}^0\mathbf{R}_1$ from frame \mathcal{F}_0 to frame \mathcal{F}_1 :

$$\begin{bmatrix} {}^0\omega_{2/1}^{DIST} \\ {}^0\mathbf{v}_{O_2/1}^{DIST} \end{bmatrix} = {}^0\overline{\mathbf{R}}_1 \begin{bmatrix} {}^1\omega_{2/1}^{DIST} \\ {}^1\mathbf{v}_{O_2/1}^{DIST} \end{bmatrix} \quad \text{with } {}^0\overline{\mathbf{R}}_1 = \begin{bmatrix} {}^0\mathbf{R}_1 & \mathbf{I}_{3 \times 3} \\ \mathbf{I}_{3 \times 3} & {}^0\mathbf{R}_1 \end{bmatrix} \quad (5)$$

${}^0\overline{\mathbf{R}}_1$ is called the augmented rotation matrix between frames \mathcal{F}_0 and \mathcal{F}_1 . Consequently from Eqs. (4) and (5),

$${}^0\mathbf{t}_{2/0} = {}^2\mathbf{Ad}_1 {}^0\mathbf{t}_{1/0}^{PROX} + {}^0\overline{\mathbf{R}}_1 {}^1\mathbf{t}_{2/1}^{DIST} \quad (6)$$

Note that Eq. (6) amounts to the twist equation derived in [5] whereas Gallardo *et al.* add the twists of individual modules directly without considering the screw transformations. It is noteworthy that Eq. (11) in [4] is incorrect, so are any further conclusions based on this equation. Following Eqs. (2) and (3), with the assumption that the proximal and distal modules are not in a parallel singularity¹ or in other words, matrices \mathbf{A}_{PROX} and \mathbf{A}_{DIST} are invertible,

¹ Parallel singularity can be an actuation singularity, constraint singularity or a compound singularity [1, 10, 13].

$$\begin{aligned}
 {}^0\mathbf{t}_{2/0} &= {}^2\mathbf{Ad}_1 \mathbf{A}_{PROX}^{-1} \mathbf{B}_{PROX} \dot{\rho}_{13} + {}^0\overline{\mathbf{R}}_1 \mathbf{A}_{DIST}^{-1} \mathbf{B}_{DIST} \dot{\rho}_{46} \\
 &= [{}^2\mathbf{Ad}_1 \mathbf{A}_{PROX}^{-1} \mathbf{B}_{PROX} \quad {}^0\overline{\mathbf{R}}_1 \mathbf{A}_{DIST}^{-1} \mathbf{B}_{DIST}] \begin{bmatrix} \dot{\rho}_{13} \\ \dot{\rho}_{46} \end{bmatrix} \\
 &= \mathbf{J}_{S-PM} \begin{bmatrix} \dot{\rho}_{13} \\ \dot{\rho}_{46} \end{bmatrix}
 \end{aligned} \tag{7}$$

\mathbf{J}_{S-PM} is the kinematic Jacobian matrix of the 3-RPS-3-SPR S-PM under study. The rank of this matrix provides the local mobility of the S-PM.

Equations (6), (7) and (8) can be extended to a series-parallel manipulator with n number of parallel mechanisms, named *modules* in this paper, in series as shown in Fig. 2. Thus, the twist of the end effector with respect to the fixed base expressed in frame \mathcal{F}_0 can be expressed as follows:

$${}^0\mathbf{t}_{n/0} = \sum_{i=1}^n {}^0\overline{\mathbf{R}}_{(i-1)} {}^n\mathbf{Ad}_i {}^{(i-1)}\mathbf{t}_{i/(i-1)}^{M_i} = \mathbf{J}_{6 \times 3n} \begin{bmatrix} \dot{\rho}_{M_1} \\ \dot{\rho}_{M_2} \\ \vdots \\ \dot{\rho}_{M_n} \end{bmatrix} \tag{8}$$

$$\text{with } {}^0\overline{\mathbf{R}}_i = \begin{bmatrix} {}^0\mathbf{R}_i & \mathbf{I}_{3 \times 3} \\ \mathbf{I}_{3 \times 3} & {}^0\mathbf{R}_i \end{bmatrix}, \quad {}^n\mathbf{Ad}_i = \begin{bmatrix} \mathbf{I}_{3 \times 3} & \mathbf{0}_{3 \times 3} \\ -{}^{(i-1)}\hat{\mathbf{r}}_{O_i O_n} & \mathbf{I}_{3 \times 3} \end{bmatrix} \text{ and}$$

$$\mathbf{J}_{6 \times 3n} = \begin{bmatrix} {}^n\mathbf{Ad}_1 \mathbf{A}_{M_0}^{-1} \mathbf{B}_{M_0} & {}^0\overline{\mathbf{R}}_1 {}^n\mathbf{Ad}_2 \mathbf{A}_{M_1}^{-1} \mathbf{B}_{M_1} & \dots & {}^0\overline{\mathbf{R}}_n \mathbf{A}_{M_n}^{-1} \mathbf{B}_{M_n} \end{bmatrix}$$

where, $\mathbf{J}_{6 \times 3n}$ is the $6 \times 3n$ kinematic Jacobian matrix of the n -module hybrid manipulator. M_i stands for the i -th module, \mathbf{A}_{M_i} and \mathbf{B}_{M_i} are the forward and inverse Jacobian matrices of M_i of the series-parallel manipulator, respectively. $\dot{\rho}_{M_i}$ is the vector of the actuated prismatic joint rates for the i -th module.

4 Twist System of the 3-RPS-3-SPR S-PM

Each leg of the 3-RPS and 3-SPR parallel manipulators are composed of three joints, but the order of the limb twist system is equal to five and hence there exist five twists associated to each leg. Thus, the constraint wrench system of the i -th leg reciprocal to the foregoing twists is spanned by a pure force \mathcal{W}^i passing through the spherical joint center and parallel to the revolute joint axis. Therefore, the constraint wrench systems of the proximal and distal modules are spanned by three zero-pitch wrenches, namely,

$$\begin{aligned}
 {}^0\mathcal{W}_{PROX} &= \bigoplus_{i=1}^3 {}^0\mathcal{W}_{PROX}^i = \text{span} \left\{ \begin{bmatrix} {}^0\mathbf{u}_1 \\ {}^0\mathbf{r}_{O_2 A_1} \times {}^0\mathbf{u}_1 \end{bmatrix}, \begin{bmatrix} {}^0\mathbf{u}_2 \\ {}^0\mathbf{r}_{O_2 B_1} \times {}^0\mathbf{u}_2 \end{bmatrix}, \begin{bmatrix} {}^0\mathbf{u}_3 \\ {}^0\mathbf{r}_{O_2 C_1} \times {}^0\mathbf{u}_3 \end{bmatrix} \right\} \\
 {}^1\mathcal{W}_{DIST} &= \bigoplus_{i=1}^3 {}^1\mathcal{W}_{DIST}^i = \text{span} \left\{ \begin{bmatrix} {}^1\mathbf{v}_1 \\ {}^1\mathbf{r}_{O_2 A_1} \times {}^1\mathbf{v}_1 \end{bmatrix}, \begin{bmatrix} {}^1\mathbf{v}_2 \\ {}^1\mathbf{r}_{O_2 B_1} \times {}^1\mathbf{v}_2 \end{bmatrix}, \begin{bmatrix} {}^1\mathbf{v}_3 \\ {}^1\mathbf{r}_{O_2 C_1} \times {}^1\mathbf{v}_3 \end{bmatrix} \right\}
 \end{aligned} \tag{9}$$

Due to the serial arrangement of the parallel mechanisms, the constraint wrench system of the S-PM is the intersection of the constraint wrench systems of each module. Alternatively, the twist system of the S-PM is the direct sum (disjoint union) of the twist systems of each module. Therefore, the nullspace of the 3×6 matrix containing the basis screws of ${}^0\mathcal{W}_{PROX}$ and ${}^1\mathcal{W}_{DIST}$ leads to the screws that form the basis of the twist system of each module, ${}^0\mathcal{T}_{PROX} = \text{span}\{{}^0\xi_1, {}^0\xi_2, {}^0\xi_3\}$ and ${}^1\mathcal{T}_{DIST} = \text{span}\{{}^1\xi_4, {}^1\xi_5, {}^1\xi_6\}$, respectively. The augmented rotation matrix derived in Eq. (5) is exploited to ensure that all the screws are expressed in one frame (\mathcal{F}_0 in this case). Therefore, the total twist system of the S-PM can be obtained as follows:

$$\begin{aligned} {}^0\mathcal{T}_{S-PM} &= {}^0\mathcal{T}_{PROX} \oplus {}^0\mathcal{T}_{DIST} \\ &= \text{span}\{{}^0\xi_1, {}^0\xi_2, {}^0\xi_3, {}^0\bar{\mathbf{R}}_1 {}^1\xi_4, {}^0\bar{\mathbf{R}}_1 {}^1\xi_5, {}^0\bar{\mathbf{R}}_1 {}^1\xi_6\} \end{aligned} \quad (10)$$

The order of the twist system ${}^0\mathcal{T}_{S-PM}$ yields the local mobility of the whole manipulator.

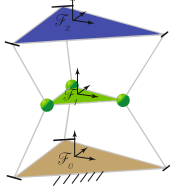
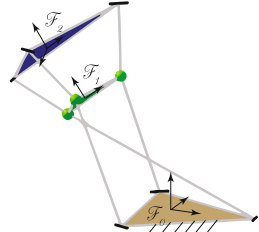
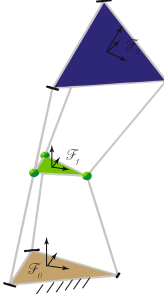
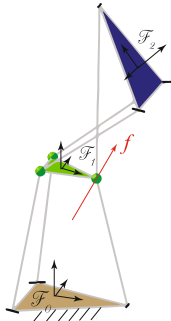
Some general and singular configurations of the 3-RPS-3-SPR S-PM with $h_0 = 2$, $h_1 = 1$ and $h_2 = 2$ are considered and its mobility is listed based on the rank of the Jacobian and the order of the twist system in Table 1. For general configurations like 2 and 3, the mobility is found to be six. The mobility reduces only when some singularities are encountered. For a special configuration when the three platform planes are parallel to each other as shown in the first row of this table, the rotations of the coupler generate translational motions of the end effector. Yet, the torsional axes of both mechanisms coincide and hence, the mechanism cannot perform any rotation about an axis of vertical direction leading to a mobility equal to five.

Moreover, a configuration in which any revolute joint axis in the end effector is parallel to its corresponding axis in the fixed base results in a mobility lower than six for the S-PM. For instance, for the 4th configuration in the table, there exists a constraint force f , parallel to the two parallel revolute joint axes resulting in a five dof manipulator locally. Configurations 1 and 4 are the impossible output singularities as identified by Zlatanov *et al.* [15]. It should be noted that if one of the modules is in a parallel singularity, the motion of the moving-platform of the manipulator becomes uncontrollable. A detailed singularity analysis of series-parallel manipulators will be performed in a future work for a better understanding of their behaviour in singular configurations.

5 Full-Cycle Mobility of the 3-RPS-3-SPR S-PM

The full cycle mobility can be obtained by calculating the Hilbert dimension of the set of constraint equations of the mechanism [8]. Two Study transformation matrices are considered: ${}^0\mathbf{X}_1$ from \mathcal{F}_0 to \mathcal{F}_1 and ${}^1\mathbf{Y}_2$ from \mathcal{F}_1 to \mathcal{F}_2 composed of Study parameters x_i and y_i , $i = 0, 1, \dots, 7$, respectively. Thus, the coordinates of points A_j , B_j and C_j , $j = 0, 1, 2$ and vectors \mathbf{u}_k and \mathbf{v}_k , $k = 1, 2, 3$ can be represented in \mathcal{F}_0 to yield sixteen constraint equations (six for the 3-RPS

Table 1. Mobility of the 3-RPS-3-SPR S-PM in different configurations

Number	Study parameters and configuration	Rank of J_{S-PM}	Order of ${}^0\mathcal{F}_{S-PM}$
1	$x_i = (1 : 0 : 0 : 0 : 0 : 0 : 0 : 0.75)$ $y_i = (1 : 0 : 0 : 0 : 0 : 0 : 0 : 0.8)$ 	5	5
2	$x_i = (0.35 : -0.9 : 0.25 : 0 : 0.57 : 0.27 : -1.76 : -1.33)$ $y_i = (1 : 0 : 0 : 0 : 0 : 0 : 0 : -0.8)$ 	6	6
3	$x_i = (0.99 : 0 : -0.10 : 0 : 0 : 0.21 : 0 : 1.92)$ $y_i = (-0.79 : -0.59 : 0.16 : 0 : -0.16 : -0.13 : -1.25 : -2.04)$ 	6	6
4	$x_i = (0.99 : 0 : -0.10 : 0 : 0 : 0.21 : 0 : 1.92)$ $y_i = (-0.39 : 0 : 0.92 : 0 : 0 : -1.88 : 0 : 0.12)$ 	5	5

PM, six for the 3-SPR PM, Study quadric and normalization equations for each transformations). It was established that the 3-RPS and the 3-SPR parallel mechanisms have two operation modes each, characterized by $x_0 = 0, x_3 = 0$ and $y_0 = 0, y_3 = 0$, respectively [12, 14]. For the S-PM, four ideals of the constraint equations are considered: \mathcal{K}_1 , when $x_0 = y_0 = 0$, \mathcal{K}_2 , when $x_3 = y_0 = 0$, \mathcal{K}_3 , when $x_0 = y_3 = 0$ and \mathcal{K}_4 , when $x_3 = y_3 = 0$. The Hilbert dimension of these ideals over the ring $\mathbb{C}[h_0, h_1, h_2]$ is found to be six² and hence the global mobility of the 3-RPS-3-SPR S-PM.

$$\overline{\dim}\mathcal{K}_i = 6, \quad i = 1, 2, 3, 4. \quad (11)$$

6 Conclusions and Future Work

In this paper, the full-cycle mobility of a 3-RPS-3-SPR PM was elucidated to be six. The kinematic Jacobian matrix of the series-parallel manipulator was calculated with the help of screw theory and the result was extended to n -number of modules. Moreover, the methodology for the determination of the twist system of series-parallel manipulators was explained. The rank of the Jacobian matrix or the order of the twist system gives the local mobility of the S-PM. Global mobility was calculated as the Hilbert dimension of the ideal of the set of constraint equations. In the future, we intend to solve the inverse and direct kinematics using algebraic geometry concepts and to enlist all possible singularities of series-parallel mechanisms. Additionally, it is challenging to consider n -modules ($n > 2$) and to work on the trajectory planning of such manipulators as the number of output parameters is equal to six and lower than the number of actuated joints, which is equal to $3n$.

Acknowledgements. This work was conducted with the support of both the École Centrale de Nantes and the French National Research Agency (ANR project number: ANR-14-CE34-0008-01).

References

1. Amine, S., Mokhiamar, O., Caro, S.: Classification of 3T1R parallel manipulators based on their wrench graph. *ASME J. Mech. Robot.* **9**(1) (2017)
2. Binaud, N., Cardou, P., Caro, S., Wenger, P.: The kinematic sensitivity of robotic manipulators to joint clearances. In: Conference: International Design Engineering Technical Conferences and Computers and Information in Engineering Conference, pp. 1371–1380 (2010)
3. Gallardo-Alvarado, J., Abedinnasab, M.H., Rodríguez-Castro, R., Aguilar-Nájera, C.R.: Kinematics of a series-parallel manipulator with constrained rotations by means of the theory of screws. In: Petrova, V.M. (ed.) *Advances in Engineering Research*. Nova Science Publishers, New York (2016)

² The pdf file of the Maple sheet with calculation of Hilbert dimension can be found here: <https://www.dropbox.com/s/3bqsn45rszvgdax/Mobility3RPS3SPR.pdf?dl=0>.

4. Gallardo-Alvarado, J., Pérez-González, L., Ruiz-Mondragón, G., Rojas-Garduño, H., Villagómez, A.T.: Mobility and velocity analysis of a limited-DOF series-parallel manipulator. In: Conference: XVII COMRob 2015, Mexican Robotics Congress (2015)
5. Hu, B.: Formulation of unified Jacobian for serial-parallel manipulators. *Robot. Comput.-Integr. Manuf.* **30**(5), 460–467 (2014)
6. Hu, B., Lu, Y., Yu, J.J., Zhuang, S.: Analyses of inverse kinematics, statics and workspace of a novel 3-RPS-3-SPR serial-parallel manipulator. *Open Mech. Eng. J.* **6**(Suppl1–M5), 65–72 (2012)
7. Hunt, K.H.: Structural kinematics of in-parallel-actuated robot-arms. *ASME J. Mech. Trans. Autom.* **105**(4), 705–712 (1983)
8. Husty, M.L., Schröcker, H.P.: A Proposal for a New Definition of the Degree of Freedom of a Mechanism, pp. 109–117. Springer, Netherlands, Dordrecht (2011)
9. Joshi, S.A., Tsai, L.W.: Jacobian analysis of limited-DOF parallel manipulators. *ASME Mech. Des. J.* **124**(2), 254–258 (2002)
10. Maraje, S., Nurahmi, L., Caro, S.: Operation modes comparison of a reconfigurable 3-PRS parallel manipulator based on kinematic performance. In: Proceedings of the ASME 2016 International Design Engineering Technical Conferences and Computers and Information in Engineering Conference, pp. 21–24 (2016)
11. Murray, R.M., Sastry, S.S., Zexiang, L.: A Mathematical Introduction to Robotic Manipulation. CRC Press, Boca Raton (1994)
12. Nayak, A., Nurahmi, L., Wenger, P., Caro, S.: Comparison of 3-RPS and 3-SPR parallel manipulators based on their maximum inscribed singularity-free circle. In: *New Trends in Mechanism and Machine Science*, pp. 121–130 (2017)
13. Nurahmi, L., Caro, S.: Dimensionally homogeneous extended jacobian and condition number. In: *The 2nd International Conference on Mechanical Engineering (ICOME 2015)*, pp. 3–5 (2015)
14. Schadlbauer, J., Walter, D., Husty, M.: The 3-RPS parallel manipulator from an algebraic viewpoint. *Mech. Mach. Theory* **75**, 161–176 (2014)
15. Zlatanov, D., Fenton, R.G., Benhabib, B.: A unifying framework for classification and interpretation of mechanism singularities. *ASME Mech. Des. J.* **117**(4), 566–572 (1995)

Application of Intersection Theory to Singularity and Motion Mode Analysis of Mechanisms

Samuli Piipponen¹(✉), Andreas Müller², Eero Hyry¹, and Jukka Tuomela³

¹ School of Information Sciences, University of Tampere, Tampere, Finland
samuli.piipponen@uta.fi

² Institute of Robotics, JKU Johannes Kepler University, Linz, Austria
a.mueller@jku.at

³ Department of Physics and Mathematics,
University of Eastern Finland, Joensuu, Finland
jukka.tuomela@uef.fi

Abstract. Different motion modes of mechanisms often correspond to irreducible components of the configuration space (c-space), and singularities of the c-space often (but not necessarily) happen at the intersections of irreducible components, i.e. motion modes, of the configuration space. Frequently mechanisms are required to perform different tasks on different motion modes of the mechanism *connected by c-space singularities*. This means that in order for the mechanism to switch between motion modes it has to pass through a c-space singularity. Although singularities may not be avoided, it is desirable to design the mechanism in such a way that the transition motion through the singularity is as smooth as possible. In this paper we propose using the theory of intersections of algebraic varieties as a tool from algebraic geometry that allows investigating this situation. Modern computational algebra provides the necessary algorithms. The theory and its implications are demonstrated for two simple examples.

1 Introduction

Most mechanisms comprise ‘algebraic joints’, i.e. kinematic pairs whose geometric constraints can be described by *polynomial equations* $f_1 = 0, \dots, f_k = 0$. These generate the *constraint ideal* $\mathcal{I} = \langle f_1, \dots, f_k \rangle \subset \mathbb{A}$ in the polynomial ring \mathbb{A} . Thus the c-space is an *algebraic variety* $V(\mathcal{I})$, and algebraic geometry and commutative algebra provide a framework for the analysis, and potentially the design, of the c-space. The goal of this paper is to recall the relevant concepts from algebraic geometry facilitating the analysis of c-space singularities of mechanisms and robots. This gives us computational tools to analyze c-space singularities.

In general singularities are not desirable since the differential mobility of a mechanism changes impairing their stability and making their control difficult. However if a mechanism contains closed loops and is designed to go from one motion mode to another it has to go through a singularity. Also the simulation of

the mechanism dynamics becomes difficult since standard numerical integration methods for differential algebraic (DAE) system can not handle singularities. In fact these types of mechanisms and their constraints are often used when testing and comparing different DAE-solvers [7]. If a mechanism is to perform several tasks where each one corresponds to irreducible components/motion modes V_i of the c -space variety V , then the mechanism must pass through a c -space singularity. It is thus important that the singularities and their nature are known a priori. An interesting question in this regard is whether there are tangential intersections of motion modes that allow for smooth transitions between different modes [1, 12].

To study these questions we propose to use the concept of multiplicity. If at a point in the intersection of two varieties the multiplicity of intersection is greater than one, then at the intersection there are at least some common tangent direction to both varieties, and hence a smooth transition between different modes is possible at least in principle. From an engineering perspective it would be desirable to be able to design regular/tangential intersections of mechanisms performing tasks in several motion modes that are connected by singularities since then the mechanism would not have to stop at singularity in order to change to another motion mode. Another interesting aspect about multiplicity is that it may provide a good quantitative model of what has been intuitively called the shakiness of the mechanism. This aspect will be treated more thoroughly in a forthcoming paper. A similar approach is used also in [14]. The singularity analysis is therefore particularly important, but at the same time also a difficult area of mechanism design [2, 3, 8, 11, 13, 16]. The advantage of using algebraic geometry instead of the differential geometric approach is that in algebraic geometry one can obtain global as well as local results.

Computations in this paper were performed with the program `Singular` [10].

2 Mathematical Preliminaries

2.1 Rings, Ideals and Singularities

We recall some basic facts and refer to [5, 9] for more details. The polynomial ring with coefficient field \mathbb{K} and variables x_i is denoted by $\mathbb{A} = \mathbb{K}[x_1, \dots, x_n]$. The following facts about ideals $\mathcal{I} \subset \mathbb{A}$ in \mathbb{A} are fundamental

- (i) Every ideal is *finitely generated*, i.e. it has a basis with a finite number of generators.
- (ii) Every radical ideal can be decomposed to a finite number of prime ideals: This gives the decomposition of the variety into *irreducible components*:

$$V(\mathcal{I}) = V(\sqrt{\mathcal{I}}) = V(I_1) \cup \dots \cup V(I_s).$$

Definition 2.1 (Tangent space). Let $\mathcal{I} = \langle f_1, \dots, f_k \rangle$ be an ideal and let us denote by $f = (f_1, \dots, f_k)$ the map defined by the generators. The differential

(or Jacobian) of f is then denoted by df , and its value at q is df_q . Let us suppose that \mathcal{I} is a prime ideal. Then the tangent space of the variety $V = \mathbb{V}(\mathcal{I})$ at q is

$$T_qV = \{z \in \mathbb{K}^n \mid df_qz = 0\}. \tag{1}$$

Note that by definition T_qV is a vector space, so its dimension is well defined.

Definition 2.2 (Singular points). A point $q \in V$ is singular if $\dim(T_qV) > \dim_q(V)$. Otherwise the point q is regular. The set of singular points of V is denoted by $\Sigma(V)$.

Recall that $\Sigma(V)$ is itself a variety whose dimension is less than $\dim(V)$. Hence almost all points of a variety are regular.

Throughout the paper the constraint ideal (the ideal associated with the constraints) is assumed to be prime.

Let $V = V_1 \cup \dots \cup V_\ell$ be the decomposition to irreducible components. Then there are basically two ways of a point q of a general variety V to be singular: either q is a singularity of an irreducible component V_i or it is an intersection point of two components. That is, the variety of singular points is

$$\Sigma(V) = \bigcup_{i=1}^{\ell} \Sigma(V_i) \cup \bigcup_{i \neq j} V_i \cap V_j. \tag{2}$$

Once we have the irreducible decomposition it is easy to compute the intersections (the second term in (2)). To compute the singular points of irreducible components (the first term in (2)) one needs the concept of *Fitting ideals* [9].

Let M be a matrix of dimension $k \times n$ with entries in \mathbb{A} . The ℓ th Fitting ideal of M , $F_\ell(M)$, is the ideal generated by the $\ell \times \ell$ minors of M . Let now $f = (f_1, \dots, f_k) : \mathbb{K}^n \mapsto \mathbb{K}^k$ be a map corresponding to the prime ideal $\mathcal{I} = \langle f_1, \dots, f_k \rangle$ and let $V = \mathbb{V}(\mathcal{I})$ be the corresponding irreducible variety. Let us suppose that $\dim(V) = n - \ell$.

Theorem 2.1 (Jacobian criterion). The singular variety of V is

$$\Sigma(V) = \mathbb{V}(\mathcal{I} + F_\ell(df)) = \mathbb{V}(\mathcal{I}) \cap \mathbb{V}(F_\ell(df)).$$

In particular if $\mathcal{I} + F_\ell(df) = \mathbb{A}$ then V is smooth.

One can now ask how does the variety ‘look like’ locally. Unlike manifolds varieties don’t have to be smooth or even locally Euclidean. If q is a smooth point then naturally the tangent space T_qV can be thought of as the best local approximation. In case of singular points we need the concept of *tangent cone* [4, 15]. Let us suppose that q is the origin. Then each polynomial $f \in \mathbb{I}(V)$ can be written as a sum of its homogeneous components. Let us denote by $f_{(q,min)}$ the component of lowest degree.

Definition 2.3 (Tangent cone). Suppose that $\mathbb{V}(\mathcal{I}) \subset \mathbb{R}^n$ is an algebraic variety and $\mathcal{I} = \langle h_1, \dots, h_l \rangle$ and let $q \in V$. The Tangent cone of V at q , denoted by $C_q(V)$, is the variety

$$C_q(V) = \mathbb{V}(f_{(q,min)} \mid f \in \mathbb{I}(V)). \tag{3}$$

The tangent cone has the following basic properties:

- q is a smooth point if and only if $C_qV = T_qV$
- $\dim(C_qV) = \dim_q(V)$.

The tangent cone is the *simplest possible approximation* of V in the neighborhood of q and thus $\dim(C_qV) = \dim_q(V)$. The generators of the tangent cone can be obtained efficiently using Gröbner basis techniques.

2.2 Intersection Multiplicity and Singular Points

Let q be a point of a subvariety $V \subset \mathbb{K}^m$. We denote by $\mathcal{O}_{V,q}$ the local ring of V at q . Consider an ideal $\mathcal{I} \subset \mathcal{O}_{V,q}$ with $\dim_{\mathbb{K}}(\mathcal{O}_{V,q}/\mathcal{I}) < \infty$. Then the Hilbert-Samuel function of \mathcal{I} is

$$H_{\mathcal{I}}(n) = \dim_{\mathbb{K}}(\mathcal{O}_{V,q}/\mathcal{I}^n) \quad (n \in \mathbb{N}). \tag{4}$$

It is known that there exists a polynomial $P_{\mathcal{I}}(n)$ such that $H_{\mathcal{I}}(n)$ and $P_{\mathcal{I}}(n)$ coincide for large n . This polynomial is called the Hilbert-Samuel polynomial of \mathcal{I} . It is of degree $d = \dim \mathcal{O}_{V,q}$. The leading coefficient is $e(\mathcal{I})/d!$, where $e(\mathcal{I})$ is an integer. We say that $e(\mathcal{I})$ is the Hilbert-Samuel multiplicity of \mathcal{I} .

Let $V_1, V_2 \subset \mathbb{K}^n$ be subvarieties. Then one can define the intersection multiplicity of V_1 and V_2 at an irreducible component of the intersection $V_1 \cap V_2$. We restrict to the special case where the irreducible component is a point $q \in V_1 \cap V_2$. The definition is based on the idea of ‘reduction to the diagonal’ [6]. Let us define the diagonal embedding and the ideal corresponding to it:

$$\begin{aligned} \Delta: \mathbb{K}^n &\rightarrow \mathbb{K}^n \times \mathbb{K}^n \quad , \quad (a_1, \dots, a_n) \mapsto (a_1, \dots, a_n, a_1, \dots, a_n) \\ \delta &= (x_1 - y_1, \dots, x_n - y_n) \subset \mathbb{K}[x, y] \quad , \quad \mathcal{V}(\delta) = \Delta(\mathbb{K}^n) \end{aligned}$$

In this way we have an isomorphism $V_1 \cap V_2 \cong \Delta(\mathbb{K}^n) \cap (V_1 \times V_2)$. We now consider δ as an ideal of the local ring $\mathcal{O}_{V_1 \times V_2, (q,q)}$.

Definition 2.4 (Intersection multiplicity). *The intersection multiplicity of V_1 and V_2 at q is*

$$i_q(V_1, V_2) = e(\delta). \tag{5}$$

A fundamental theorem connecting multiplicities of points of V to its tangent cone says that the tangent cone C_qV and the variety V have the same multiplicity at q . The tangent cone gives the geometric picture of the variety near its singular points.

Gröbner basis techniques can be extended to local rings, hence the multiplicity can actually be computed. The drawback with this approach is that the number of variables is artificially doubled, making the computations potentially very time consuming. However, it is possible to do the computations in such a way that this inconvenience is avoided. This will be explored in another paper.

3 Examples

3.1 Slider-Crank Mechanism with Circular Constraints

Figure 1(a) shows a planar slider-crank mechanism whose slider is constrained to move on the union of two circles with radius $1/2$ and centers at $(1, 1/2)$ and $(1, -1/2)$, respectively (This can also be regarded as a planar 2R serial manipulator that must perform motion on the circles). The constraint equations are $p_i = 0, i = 1 \dots 5$ where

$$p_1 = c_1 + c_2 - x, \quad p_2 = s_1 + s_2 - y, \quad p_3 = c_1^2 + s_1^2 - 1 = 0, \quad p_4 = c_2^2 + s_2^2 - 1$$

$$p_5 = ((x - 1)^2 + (y - 1/2)^2 - 1/4)((x - 1)^2 + (y + 1/2)^2 - 1/4)$$

where $s_i := \sin x_i, c_i := \cos x_i$. The equation $p_5 = 0$ restricts the slider to move on the circles. Analyzing the constraint ideal $\mathcal{I} = \langle p_1, p_2, p_3, p_4, p_5 \rangle$ yields

$$\mathcal{I} = \sqrt{\mathcal{I}} = \mathcal{I}_1 \cap \mathcal{I}_2 \subset \mathbb{Q}[c_1, s_1, c_2, s_2, x, y]$$

The singular points of $V(\mathcal{I})$ are the intersections of two modes $V(\mathcal{I}_1) = V_1$ and $V(\mathcal{I}_2) = V_2$ which represent the motion where the end effector is constrained to move on either circles. Checking the Jacobian criterion proves that both modes, $V(\mathcal{I}_1)$ and $V(\mathcal{I}_2)$, are smooth. The singular points are thus

$$\Sigma(V) = V(\mathcal{I}_1 \cap \mathcal{I}_2) = V(\mathcal{I}_1 + \mathcal{I}_2)$$

$$= V(y, x - 1, 4s_2^2 - 3, 2c_2 - 1, s_1 + s_2, c_1 + c_2 - 1) = q_+ \cup q_-$$

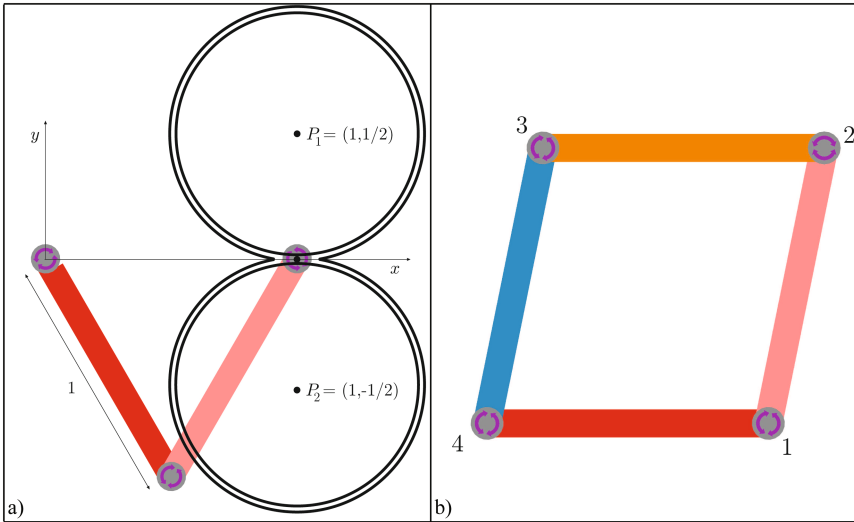


Fig. 1. (a) Slider-Crank mechanism with circular constraints. (b) 4-bar linkage with equal link lengths

where $q_{\pm} = (1/2, \mp\sqrt{3}/2, 1/2, \pm\sqrt{3}/2, 1, 0)$. Now we make a coordinate transformation so that q_+ is the origin and then double the number of variables. In this way the ideals corresponding to \mathcal{I}_1 and \mathcal{I}_2 to can be written as

$$\begin{aligned} i_1 &= \langle b_1 + b_2 - y_1, a_1 + a_2 - z_1, y_1^2 + z_1^2 - y_1, \\ &\quad 2b_2y_1 + 2a_2z_1 + 2a_2 - (\sqrt{3} + 1)y_1 - z_1, a_2^2 + b_2^2 + a_2 - \sqrt{3}b_2 \rangle \\ i_2 &= \langle e_1 + e_2 - y_2, d_1 + d_2 - z_2, y_2^2 + z_2^2 + y_2, \\ &\quad 2e_2y_2 + 2d_2z_2 + 2d_2 - (\sqrt{3} - 1)y_2 - z_2, d_2^2 + e_2^2 + d_2 - \sqrt{3}e_2 \rangle \end{aligned}$$

Hence the sum $\mathcal{J} = i_1 + i_2$ is an ideal in the ring

$$\mathbb{A} = \mathbb{Q}(\sqrt{3})[a_1, b_1, a_2, b_2, d_1, e_1, d_2, e_2, z_1, y_1, z_2, y_2]$$

Let us now consider the quotient ring \mathbb{A}/\mathcal{J} corresponding to the variety $V = \mathbb{V}(\mathcal{J})$. This construction is needed when one does actual computations in the local ring $\mathcal{O}_{V,q}$. Hence the ideal in Definition 2.4 is now also interpreted as

$$\delta = \langle a_1 - d_1, b_1 - e_1, a_2 - d_2, b_2 - e_2, y_1 - y_2, z_1 - z_2 \rangle \subset \mathbb{A}/\mathcal{J}.$$

The Hilbert polynomial of δ is now $P_{\delta}(n) = 1 + 2n$ and hence the multiplicity is $i_{q_+}(\mathbb{V}_1, \mathbb{V}_2) = 2$. Since \mathbb{V}_1 and \mathbb{V}_2 are smooth we must have tangential intersection of modes V_1 and V_2 at q_+ .

The tangent cone at q_+ can be computed as

$$C_0V = \mathbb{V}(a_1 + a_2 - z, b_1 + b_2 - y, 2a_2 - z - \sqrt{3}y, 6b_2 - \sqrt{3}z - 3y, y^2) = (L_1)^2$$

which is a ‘doubled’ tangent line $y^2 = 0$ in the plane

$$T = \mathbb{V}(6b_2 - \sqrt{3}z, 2a_2 - z, 6b_1 + \sqrt{3}z, 2a_1 - z),$$

and indicates the same result, i.e. that the multiplicity is two.

3.2 Four-Bar Mechanism with Equal Link Lengths

The constraint equations for the mechanism in Fig. 1(b) can be formulated by using joint 4 as cut-joint as

$$\begin{aligned} p_4 &= c_1 + c_2 + c_3 - 1 = 0, \quad p_5 = s_1 + s_2 + s_3 = 0 \\ p_i &= c_i^2 + s_i^2 - 1, \quad i = 1, 2, 3. \end{aligned}$$

Analyzing the constraint ideal $\mathcal{I} = \langle p_1, p_2, p_3, p_4, p_5 \rangle$ leads to

$$\mathcal{I} = \sqrt{\mathcal{I}} = \mathcal{I}_1 \cap \mathcal{I}_2 \cap \mathcal{I}_3 \subset \mathbb{Q}[c_1, s_1, c_2, s_2, c_3, s_3].$$

The singular points are again intersections of three smooth motion modes $\mathbb{V}(\mathcal{I}_1)$, $\mathbb{V}(\mathcal{I}_2)$ and $\mathbb{V}(\mathcal{I}_3)$. The singular points then consists of three points:

$$\Sigma(V) = \mathbb{V}(\mathcal{I}_1 \cap \mathcal{I}_2 \cap \mathcal{I}_3) = \mathbb{V}(\mathcal{I}_1 + \mathcal{I}_2 + \mathcal{I}_3) = \{q_0, q_1, q_2\}.$$

The mechanism is, for example, analyzed at the point

$$q_0 = (1, 0, -1, 0, 1, 0) = \mathcal{V}(\mathcal{I}_1) \cap \mathcal{V}(\mathcal{I}_2) = V_1 \cap V_2.$$

A coordinate transformation such that q_0 is the origin yields the ideals

$$\begin{aligned} i_1 &= \langle a_2^2 + b_2^2 - 2a_2, b_3, a_3, b_1 + b_2 + b_3, a_1 + a_2 + a_3 \rangle \\ i_2 &= \langle d_3^2 + e_3^2 + 2e_3, d_2 + d_3, e_2 + e_3, d_1 + d_2 + d_3, e_1 + e_2 + e_3 \rangle, \end{aligned}$$

corresponding to \mathcal{I}_1 and \mathcal{I}_2 after the transformation. As above the sum $\mathcal{J} = i_1 + i_2$ is considered in the ring

$$\mathbb{A} = \mathbb{Q}[a_1, b_1, a_2, b_2, a_3, b_3, d_1, e_1, d_2, e_2, d_3, e_3]$$

and then we need to consider the quotient ring \mathbb{A}/\mathcal{J} . Computing as before we obtain in this case $i_{q_0}(\mathcal{V}_1, \mathcal{V}_2) = 1$. Hence the intersection is not tangential in this case as expected. If we compute the tangent cone at q_0 we get

$$\begin{aligned} C_{q_0}V &= \mathcal{V}(a_1 + a_2 + a_3, b_1 + b_2 + b_3, 2a_2, 2a_3, 2b_2b_3 + 2b_3^2) \\ &= \mathcal{V}(a_1, b_1 + b_2, a_2, a_3, b_3) \cup \mathcal{V}(a_1, b_1, b_2, a_3, b_2 + b_3) = L_1 \cup L_2 \subset \mathbb{R}^6 \end{aligned}$$

Now L_1 and L_2 clearly represent two *different* lines in \mathbb{R}^6 :

$$L_1 \cup L_2 = \{t(0, -1, 0, 1, 0, 0) \mid t \in \mathbb{R}\} \cup \{t(0, 0, 0, 1, 0, -1) \mid t \in \mathbb{R}\}$$

The lines intersect at a nonzero angle which implies that multiplicity is one.

4 Conclusion

The ability to treat the c-spaces of mechanisms and robots as algebraic varieties has many advantages. Most importantly essential properties, like singularities and mobility, can be algorithmically computed and possibly designed. In this paper we have introduced the concept of intersection multiplicity in order to investigate the ‘order of tangency’ of intersections of different motion modes of a mechanism. This is demonstrated for two simple examples. The presented method has been applied to larger systems as well that cannot be presented here. It was observed that the complexity scales up well. Tangential intersections in particular are of practical importance since a mechanism could transit regularly between motion modes, i.e. not have to stop when switching between motion modes, which also reduces constraint forces.

References

1. Arponen, T., Müller, A., Piipponen, S., Tuomela, J.: Kinematical of overconstrained and underconstrained mechanisms by means of computational algebraic geometry. *Meccanica* **49**(4), 843–862 (2014)
2. Arponen, T., Piipponen, S., Tuomela, J.: Analysis of singularities of a benchmark problem. *Multibody Syst. Dyn.* **19**(3), 227–253 (2008)
3. Bandyopadhyay, S., Ghosal, A.: Analysis of configuration space singularities of closed-loop mechanisms and parallel manipulators. *Mech. Mach. Theory* **39**(5), 519–544 (2004)
4. Cox, D., Little, J., O’Shea, D.: *Ideals, Varieties and Algorithms*, 3rd edn. Springer, Berlin (2007)
5. Decker, W., Lossen, C.: Computing in algebraic geometry. In: *Algorithms and Computation in Mathematics*, vol. 16. Springer-Verlag, Berlin (2006)
6. Flenner, H., Carroll, L.O., Vogel, W.: *Joins and Intersections*. Springer, Heidelberg (1999)
7. González, M., Dopico, D., Lugrís, U., Cuadrado, J.: A benchmarking system for MBS simulation software. *Multibody Syst. Dyn.* **16**(2), 179–190 (2006)
8. Gosselin, C., Angeles, J.: Singularity analysis of closed loop kinematic chains. *IEEE J. Robot. Automation.* **6**(3), 119–132 (1990)
9. Greuel, G.-M., Pfister, G.: *A Singular Introduction to Commutative Algebra*. Springer, Berlin (2002)
10. Greuel, G.-M., Pfister, G., Schönemann, H.: *Singular 3.1.6. A Computer Algebra System for Polynomial Computations*, Centre for Computer Algebra, Uni. Kaiserslautern (2012)
11. Müller, A.: Geometric characterization of the configuration space of rigid body mechanisms in regular and singular points. In: *Proceedings of IDETC/CIE 2005, ASME 2005*, pp. 1–14, Long Beach, California, USA, 22–28 September 2005
12. Müller, A., Piipponen, S.: On regular kinematotropies. In: *14th World Congress in Mechanism and Machine Science*, pp. 1–8. IFToMM, Taipei, Taiwan, 25–30 October 2015
13. Sefrioui, J., Gosselin, C.: Singularity analysis and representation of planar parallel manipulators. *J. Robot. Auton. Syst.* **10**, 209–224 (1993)
14. Wampler, C., Hauenstein, J., Sommese, A.: Mechanism mobility and a local dimension test. *Mech. Mach. Theor.* **46**(9), 1193–1206 (2011)
15. Whitney, H.: Local properties of analytic varieties. In: *Differential and Combinatorial Topology: Symposium in Honor of M. Morse*. Princeton University Press (1965)
16. Wolf, A., Ottaviano, E., Shoham, M., Ceccarelli, M.: Application of line geometry and linear complex approximation to singularity analysis of the 3-dof capaman parallel manipulator. *Mech. Mach. Theor.* **39**(1), 75–95 (2004)

Rational Parametrization of Linear Pentapod's Singularity Variety and the Distance to It

Arvin Rasoulzadeh^(✉) and Georg Nawratil

Center for Geometry and Computational Design,
Vienna University of Technology, Vienna, Austria
{rasoulzadeh,nawratil}@geometrie.tuwien.ac.at

Abstract. A linear pentapod is a parallel manipulator with five collinear anchor points on the motion platform (end-effector), which are connected via SPS legs to the base. This manipulator has five controllable degrees-of-freedom and the remaining one is a free rotation around the motion platform axis (which in fact is an axial spindle). In this paper we present a rational parametrization of the singularity variety of the linear pentapod. Moreover we compute the shortest distance to this rational variety with respect to a suitable metric. Kinematically this distance can be interpreted as the radius of the maximal singularity free-sphere. Moreover we compare the result with the radius of the maximal singularity free-sphere in the position workspace and the orientation workspace, respectively.

Keywords: Pentapod · Kinematic singularity · Rational variety · Singularity-free zone

1 Introduction

The Stewart-Gough platform (sometimes called simply Stewart platform) can be defined as a six degree-of-freedom (DOF) parallel manipulator (PM) with six identical spherical-prismatic-spherical (SPS) legs, where only the prismatic joints are active. This parallel robot is merely used in *flight simulation* where a replica cockpit plays the role of the moving platform.

Although the Stewart platform is the most celebrated PM, some of its sub-assemblies with a lower number of legs are of interest from theoretical and practical points of view. Sometimes these sub-assemblies are referred to as *components* [9]. In this paper we study the so-called *line-body component*, which is a rigid sub-assembly of a Stewart PM consisting of a linear motion platform (end-effector) named ℓ and five SPS legs, where the base anchor points can have position in \mathbb{R}^3 . Here this component is referred to as *linear pentapod*, which is an alternative to serial robots for handling axis-symmetric tools (see Fig. 1). Moreover we use the following notations:

1. The position of ℓ is given by the vector $\mathbf{p} = (p_x, p_y, p_z)^T$ and the orientation of ℓ is defined by a unit-vector $\mathbf{i} = (u, v, w)^T$.

2. The coordinate vector \mathbf{b}_j of the platform anchor point of the j th leg is described by the equation $\mathbf{b}_j = \mathbf{p} + r_j \mathbf{i}$ for $j = 1, \dots, 5$.
3. The base anchor point of the j -th leg has coordinates $\mathbf{a}_j = (x_j, y_j, z_j)^T$.

Note that all vectors are given with respect to a fixed reference frame, which can always be chosen and scaled in a way that the following conditions hold:

$$x_1 = y_1 = z_1 = y_2 = z_2 = z_3 = 0 \quad \text{and} \quad x_2 = 1. \tag{1}$$

According to [13, Theorem 12] one possible point-model for the configuration space \mathcal{C} of the linear pentapod reads as follows: *There exists a bijection between \mathcal{C} and all real points $\mathfrak{C} = (u, v, w, p_x, p_y, p_z) \in \mathbb{R}^6$ located on the singular quadric $\Gamma : u^2 + v^2 + w^2 = 1$.* Based on this notation we study the singularity loci of linear pentapods and the distance to it in the paper at hand, which is structured as follows:

We close Sect. 1 by a review on the singularity analysis of linear pentapods and recall the implicit equation of the singularity variety. In Sect. 2 we give a brief introduction to rational varieties and present a rational parametrization of the singularity loci of linear pentapods. In Sect. 3 we compute the minimal distance to the singularity variety with respect to a novel metric in the ambient space \mathbb{R}^6 of the configuration space \mathcal{C} . We also compute the closest singular configuration under the constraint of a fixed orientation and a fixed position, respectively. Finally a conclusion and a plan for future research is given.

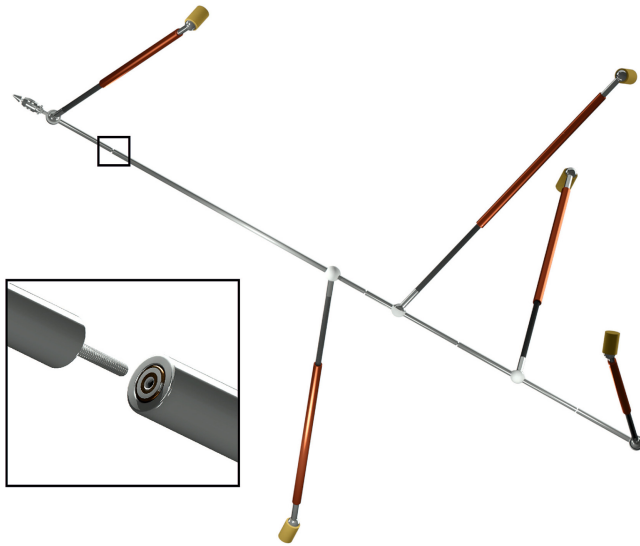


Fig. 1. Linear pentapod with the following architectural parameters: $\mathbf{a}_1 = (0, 0, 0)^T$, $\mathbf{a}_2 = (5, 0, 0)^T$, $\mathbf{a}_3 = (-4, -3, 0)^T$, $\mathbf{a}_4 = (3, 7, -6)^T$, $\mathbf{a}_5 = (9, -5, 4)^T$, $(r_1, r_2, r_3, r_4, r_5) = (0, 2, 4, 5, 10)$. Moreover it should be noted that in the illustrated design the linear platform ℓ consists of five parts, which are joined by four passive rotational joints (a zoom of this detail is given in the box). This construction enlarges the workspace by compensating some joint limits of the platform S-joints.

1.1 Singularity Variety of the Pentapod

Singularity analysis plays an important role in motion planning of PMs. For linear pentapods the singularities as well as the singular-invariant leg-rearrangements have been studied in [5] for a planar base and in [3] for a non-planar one. A complete list of architectural singular designs of linear pentapods is given in [14], where also non-architecturally singular designs with self-motions are classified (see also [12]).

Kinematical singularities occur whenever the Jacobian matrix \mathbf{J} becomes rank deficient, where \mathbf{J} can be written as follows (cf. [3]):

$$\mathbf{J} = \begin{pmatrix} \hat{\mathbf{l}}_1 & \dots & \hat{\mathbf{l}}_5 \end{pmatrix}^T \text{ with } \mathbf{l}_j = \begin{pmatrix} p_x + r_j u - x_j \\ p_y + r_j v - y_j \\ p_z + r_j w - z_j \end{pmatrix}, \hat{\mathbf{l}}_j = \begin{pmatrix} z_j(p_y + r_j v) - y_j(p_z + r_j w) \\ x_j(p_z + r_j w) - z_j(p_x + r_j u) \\ y_j(p_x + r_j u) - x_j(p_y + r_j v) \end{pmatrix}.$$

This 5×6 Jacobian matrix \mathbf{J} has a rank less than five whenever the determinants of all its 5×5 sub-matrices vanish. So by naming the determinant of the 5×5 sub-matrix, which results from excluding the j th column, with F_j the singularity loci equals $V(F_1, \dots, F_6)$; i.e. the variety of the ideal spanned by the polynomials F_1, \dots, F_6 . It can easily be checked by direct computations that this variety equals the zero-set of the greatest common divisor F of F_1, \dots, F_6 . This singularity polynomial F has the following structure:

$$\begin{aligned} F := & (A_1 p_y + A_2 p_z)u^2 + [(A_3 p_x + A_4 p_y + A_5 p_z + A_6)v + (A_7 p_x + A_8 p_y \\ & + A_9 p_z + A_{10})w + (A_{11} p_y + A_{12} p_z)p_x + A_{13} p_y^2 + (A_{14} p_z + A_{15})p_y \\ & + A_{16} p_z^2 + A_{17} p_z]u + (A_{18} p_x + A_{19} p_z + A_{20})v^2 + [(A_{21} p_x + A_{22} p_y \\ & + A_{23} p_z + A_{24})w + A_{25} p_x^2 + (A_{26} p_y + A_{27} p_z + A_{28})p_x + (A_{29} p_z \\ & + A_{30})p_y + A_{31} p_z^2 + A_{32} p_z]v + (A_{33} p_x + A_{34} p_y + A_{35})w^2 + [A_{36} p_x^2 \\ & + (A_{37} p_y + A_{38} p_z + A_{39})p_x + A_{40} p_y^2 + (A_{41} p_z + A_{42})p_y + A_{43} p_z]w \end{aligned} \quad (2)$$

where the coefficients A_i belong to the ring $\mathbb{R} = \mathbb{R}[x_3, x_4, x_5, y_3, y_4, y_5, z_4, z_5, r_1, \dots, r_5]$ which evidently makes F a polynomial with the total-degree of 3 belonging to $\mathbb{R}[u, v, w, p_x, p_y, p_z]$. Note that for a specified orientation (u, v, w) the equation $F = 0$ determines only a quadric surface $\Omega(u, v, w)$ in the space of positions. This property is of great importance later on.

Remark 1. It can easily be checked that the polynomial F is identical with the determinant of a 7×7 matrix given in [3, Eq. (4)]. \diamond

2 Rational Parametrization of the Singularity Variety

In this section we rationally parametrize the singularity variety, which is given by the implicit equation $F = 0$. But before stepping into the computations, the presentation of a formal definition of this parametrization seems necessary.

Definition 1. Let \mathbb{K} be a field and $V \subset \mathbb{K}^m$ and $W \subset \mathbb{K}^n$ be irreducible affine varieties. A *rational mapping* from V to W is a function ϕ represented by

$$\phi : V \dashrightarrow W \quad \text{with} \quad \phi(x_1, \dots, x_m) = \left(\frac{f_1(x_1, \dots, x_m)}{g_1(x_1, \dots, x_m)}, \dots, \frac{f_n(x_1, \dots, x_m)}{g_n(x_1, \dots, x_m)} \right) \quad (3)$$

where $\frac{f_i}{g_i} \in \mathbb{K}(x_1, \dots, x_m)$ and satisfies the following properties:

1. ϕ is defined at some point of V .
2. For every $(a_1, \dots, a_m) \in V$ where ϕ is defined, $\phi(a_1, \dots, a_m) \in W$.

Definition 2. Two irreducible varieties V and W are said to be *birationally equivalent* if there exist rational mappings $\phi : V \dashrightarrow W$ and $\psi : W \dashrightarrow V$ such that $\phi \circ \psi$ and $\psi \circ \phi$ be equal to id_W and id_V respectively.

Definition 3. A *rational variety* is a variety that is *birationally equivalent* to \mathbb{K}^n .

One can find the extensive discussion of above definitions in [16, Chaps. 1 and 2].

Having a rational parametrization of a variety has numerous advantages: If the coefficients of the polynomials f_i and g_i of Eq. (3) belong to \mathbb{Q} and if (x_1, \dots, x_m) is an element of \mathbb{Q}^m , then one obtains points with rational coordinates on the singularity variety [16, p. 3]. This is a matter, which is of high importance to computer aided designs, as computers can calculate rational coordinates at a much faster rate.

Moreover the rationality of the singularity variety implies that it is *path connected*, which means that every singular pose can be connected to any other singular pose by a continuous singular motion [7]. This property can be used for a computationally efficient approximation of the singularity-free workspace by hierarchical structured hyperboxes, where only their boundaries have to be checked to be free of singularities. Beside the rationally parametrized singularity loci of the planar 3-RPR PM [7], only the one of Stewart PMs with planar platform and planar base [6] (see also [1, 2]) are known to the authors (in the context of PMs of Stewart-Gough type).

For the computation of the rational parametrization of the linear pentapod, we exploit the idea used in [6]: By homogenizing the singularity polynomial F of Eq. (2) by the extra variable p_0 with respect to the position variables p_x, p_y and p_z , we obtain a homogeneous polynomial $F_h \in \mathbb{R}(u, v, w)[p_x, p_y, p_z, p_0]$ in the projective 3-space \mathbb{P}^3 with homogeneous coordinates $(p_x : p_y : p_z : p_0)$. It turns out that the point \mathbf{B} with homogeneous coordinates $(u : v : w : 0)$ is a point of the singularity variety; i.e. $\mathbf{B} \in \mathbb{V}(F_h) \subset \mathbb{P}^3$. Note that \mathbf{B} is the ideal point of the linear platform ℓ with orientation vector \mathbf{i} .

The side condition on the vector $\mathbf{i} = (u, v, w)^T$ to be of unit-length, can be avoided by using the *stereographic parametrization* of the unit-sphere S^2 :

$$\mathbf{x} : (t_3, t_4) \mapsto \left(\frac{2 t_3}{t_3^2 + t_4^2 + 1}, \frac{2 t_4}{t_3^2 + t_4^2 + 1}, \frac{t_3^2 + t_4^2 - 1}{t_3^2 + t_4^2 + 1} \right). \quad (4)$$

Based on this we can parametrize the lines of the bundle \mathcal{B} with vertex \mathbf{B} in the finite space \mathbb{R}^3 of positions with coordinates (p_x, p_y, p_z) as follows:

$$\mathcal{B} : \begin{pmatrix} p_x \\ p_y \\ p_z \end{pmatrix} = a\mathbf{x}(t_3, t_4) + t_1 \frac{\partial \mathbf{x}(t_3, t_4)}{\partial t_3} + t_2 \frac{\partial \mathbf{x}(t_3, t_4)}{\partial t_4}. \tag{5}$$

Note that the bituple (t_1, t_2) fixes the line of the bundle \mathcal{B} and the parameter a determines the point on this line. By varying $(t_1, t_2) \in \mathbb{R}^2$ and setting $a = 0$ one obtains the plane through the origin, which is orthogonal to \mathbf{i} .

Plugging $\mathcal{B}(a, t_1, t_2, t_3, t_4)$ into $F = 0$ shows that the resulting expression is only linear in a , as the ideal point \mathbf{B} is always one of the two intersection points of a line belonging to \mathcal{B} with the quadric $\Omega(\mathbf{x}(t_3, t_4))$. By solving this linear condition we get $a(t_1, t_2, t_3, t_4)$. Now the singular configurations $\mathfrak{X} = (\xi_1, \dots, \xi_6) \in \mathbb{R}^6$ of the linear pentapod can be rationally parametrized by $(\xi_1, \xi_2, \xi_3) := \mathbf{x}(t_3, t_4)$ and

$$\begin{aligned} \xi_4 &= 2 \frac{a(t_1, t_2, t_3, t_4) t_3}{t_3^2 + t_4^2 + 1} - 2 \frac{t_1(t_3^2 - t_4^2 - 1)}{(t_3^2 + t_4^2 + 1)^2} - 4 \frac{t_2 t_3 t_4}{(t_3^2 + t_4^2 + 1)^2}, \\ \xi_5 &= 2 \frac{a(t_1, t_2, t_3, t_4) t_4}{t_3^2 + t_4^2 + 1} - 4 \frac{t_1 t_3 t_4}{(t_3^2 + t_4^2 + 1)^2} + 2 \frac{t_2(t_3^2 - t_4^2 + 1)}{(t_3^2 + t_4^2 + 1)^2}, \\ \xi_6 &= \frac{a(t_1, t_2, t_3, t_4)(t_3^2 + t_4^2 - 1)}{t_3^2 + t_4^2 + 1} + 4 \frac{t_1 t_3}{(t_3^2 + t_4^2 + 1)^2} + 4 \frac{t_2 t_4}{(t_3^2 + t_4^2 + 1)^2}. \end{aligned} \tag{6}$$

This parametrization covers the singular variety with exception of two low-dimensional sub-variety: A missing 3-dimensional sub-variety is defined by the denominator of $a(t_1, t_2, t_3, t_4)$. In this case the residual intersection point $\in \mathbb{R}^3$ of the line belonging to \mathcal{B} with $\Omega(\mathbf{x}(t_3, t_4))$ is not determined uniquely; i.e. the complete line belongs to $\Omega(\mathbf{x}(t_3, t_4))$. As the orientation $(0, 0, 1)$ cannot be obtained by the *stereographic parametrization*, also the 2-dimensional sub-variety $\Omega(0, 0, 1)$ is missing.

Moreover for a given singular pose $\mathfrak{X} = (\xi_1, \dots, \xi_6) \in \mathbb{R}^6$ we can trivially compute t_1, \dots, t_4 in a rational way from ξ_1, \dots, ξ_6 , thus the singularity variety is a rational one (according to the Definitions 1, 2 and 3).

3 Distance to the Singularity Variety

In singularities the number of DOFs of the mechanism changes instantaneously and becomes uncontrollable. Additionally the actuator forces can become very large and cause the break down of the platform [10]. Henceforth knowing the distance of a given pose $\mathfrak{G} = (g_1, \dots, g_6) \in \mathbb{R}^6$ from the singularity variety is of great importance.

Fixed Orientation: We ask for the closest singular configuration \mathfrak{D} having the same orientation (g_1, g_2, g_3) as the given pose \mathfrak{G} . As \mathfrak{G} and \mathfrak{D} only differ by a translation, we can define the distance between these two poses by the length of the translation vector. Therefore \mathfrak{D} has to be a pedal-point on $\Omega(g_1, g_2, g_3)$ with respect to the point

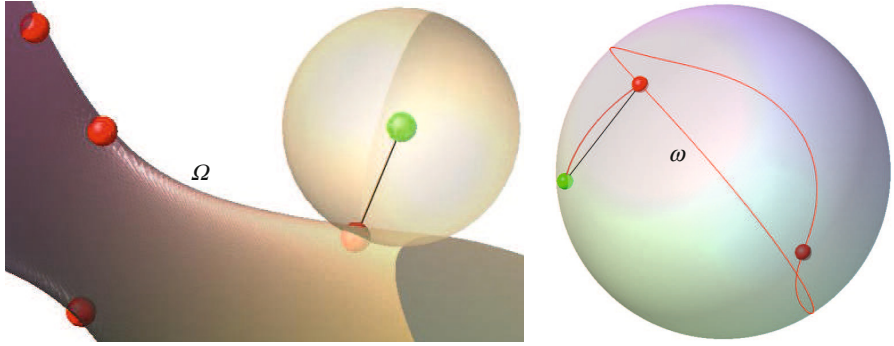


Fig. 2. Illustrations are done for $\mathfrak{G} = (\frac{3}{5}, \frac{4}{5}, 0, 2, 3, 4)$ of the linear pentapod displayed in Fig. 1. Fixed orientation (Left): \mathcal{O} has only four real solutions where the closest one $\mathfrak{D} = (\frac{3}{5}, \frac{4}{5}, 0, 2.5517, 2.6374, 0.1144)$ has a distance of 3.9412 units. Fixed position (right): \mathcal{P} has only two real solutions where the closest one $\mathfrak{B} = (0.3701, 0.5523, 0.7468, 2, 3, 4)$ has a spherical distance of 48.4178° .

(g_4, g_5, g_6) . The set \mathcal{O} of all these pedal-points equals the variety $V(\frac{\partial L}{\partial p_x}, \frac{\partial L}{\partial p_y}, \frac{\partial L}{\partial p_z}, \frac{\partial L}{\partial \lambda})$ where λ is the Lagrange multiplier of the Lagrange equation

$$L(p_x, p_y, p_z, \lambda) = (p_x - g_4)^2 + (p_y - g_5)^2 + (p_z - g_6)^2 + \lambda F. \tag{7}$$

It is well known (see [15, Appendix A]) that in general \mathcal{O} consists of six points over \mathbb{C} , where the closest one to (g_4, g_5, g_6) implies \mathfrak{D} (see Figs. 2 and 3).

Fixed Position: Now we ask for the closest singular configuration \mathfrak{B} , which has the same position (g_4, g_5, g_6) as the given pose \mathfrak{G} . As \mathfrak{G} and \mathfrak{B} only differ in orientation, the angle $\in [0, \pi]$ enclosed by these two directions can be used as distance function. Note that this angle is the spherical distance function on S^2 .

By intersecting the singularity surface for the given position (g_4, g_5, g_6) with S^2 we obtain a spherical curve $\omega(g_4, g_5, g_6)$ of degree 4. Then \mathfrak{B} has to be a spherical pedal-point on $\omega(g_4, g_5, g_6)$ with respect to the point $(g_1, g_2, g_3) \in S^2$ (see Fig. 2). By replacing the underlying spherical distance by the Euclidean metric of the ambient space \mathbb{R}^3 , one will not change the set \mathcal{P} of pedal-points on $\omega(g_4, g_5, g_6)$ with respect to (g_1, g_2, g_3) . Therefore \mathcal{P} can be computed as the variety $V(\frac{\partial L}{\partial u}, \frac{\partial L}{\partial v}, \frac{\partial L}{\partial w}, \frac{\partial L}{\partial \lambda_1}, \frac{\partial L}{\partial \lambda_2})$ where λ_1 and λ_2 are the Lagrange multipliers of the Lagrange equation

$$L(u, v, w, \lambda_1, \lambda_2) = (u - g_1)^2 + (v - g_2)^2 + (w - g_3)^2 + \lambda_1 F + \lambda_2 G \tag{8}$$

with $G = u^2 + v^2 + w^2 - 1$. It can easily be proved (see [15, Appendix B]) that in general \mathcal{P} consists of 8 points over \mathbb{C} , where the one with the shortest spherical distance to (g_4, g_5, g_6) implies \mathfrak{B} (see Fig. 3).

Remark 2. For the practical application of this spherical distance to the singularity, we recommend to locate the position vector \mathbf{p} in the tool-center-point of ℓ . \diamond

General Case: In contrast to the two special cases discussed above, the general case deals with mixed (translational and rotational) DOFs, thus the question of a suitable

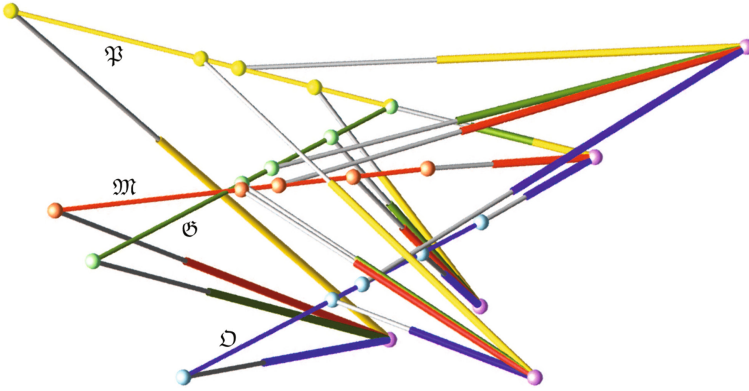


Fig. 3. Comparison of the different configurations \mathfrak{G} (green), \mathfrak{D} (blue), \mathfrak{P} (yellow) and the red-colored $\mathfrak{M} = (0.5559, 0.7274, 0.4021, 2.2966, 3.4794, 1.8357)$ with $d(\mathfrak{M}, \mathfrak{G}) = 1.4791$. In contrast $d(\mathfrak{D}, \mathfrak{G}) = 3.9412$ and $d(\mathfrak{P}, \mathfrak{G}) = 4.4142$. For this example only 16 out of 80 pedal-points are real. (Color figure online)

distance function arises. As the configuration space \mathcal{C} equals the space of oriented line-elements, we can adopt the object dependent metrics discussed in [13] for our mechanical device as follows:

$$d(\mathfrak{L}, \mathfrak{L}')^2 := \frac{1}{5} \sum_{j=1}^5 \|\mathbf{b}_j - \mathbf{b}'_j\|^2 \tag{9}$$

where \mathfrak{L} and \mathfrak{L}' are two configurations and \mathbf{b}_j and \mathbf{b}'_j denote the coordinate vectors of the corresponding platform anchor points. Note that the ambient space \mathbb{R}^6 (of \mathcal{C}) equipped with the metric d of Eq. (9) is a Euclidean space (cf. [13]).

With respect to this metric d we can compute the closest singular configuration \mathfrak{M} to \mathfrak{G} in the following way: We determine the set \mathcal{M} of pedal-points on the singularity variety with respect to \mathfrak{G} as the variety $V(\frac{\partial L}{\partial u}, \frac{\partial L}{\partial v}, \frac{\partial L}{\partial w}, \frac{\partial L}{\partial p_x}, \frac{\partial L}{\partial p_y}, \frac{\partial L}{\partial p_z}, \frac{\partial L}{\partial \lambda_1}, \frac{\partial L}{\partial \lambda_2})$ where λ_1 and λ_2 are the Lagrange multipliers of the Lagrange equation

$$L(u, v, w, p_x, p_y, p_z, \lambda_1, \lambda_2) := d(\mathfrak{M}, \mathfrak{G})^2 + \lambda_1 G + \lambda_2 F. \tag{10}$$

Random examples (see [15, Appendix C]) indicate that \mathcal{M} consists of eighty points over \mathbb{C} , where the one with the shortest distance d to \mathfrak{G} equals \mathfrak{M} (see Fig. 3).

Remark 3. Note that these minimal distances can be seen as the radii of maximal singularity-free hyperspheres [10] in the position workspace (see also [11]), the orientation workspace (see also [8]) and the complete configuration space. Moreover the distance $d(\mathfrak{M}, \mathfrak{G})$ to the singularity variety can also be interpreted as quality index thus it is an alternative to the value of F proposed in [4]. \diamond

4 Conclusions and Future Research

We presented a rational parametrization of the singularity variety of linear pentapods in Sect. 2 and computed the distance to it in Sect. 3 with respect to the novel metric

given in Eq. (9), which can easily be adopted for e.g. Stewart PMs as well. As this distance is of interest for many tasks (e.g. quality index for path planning, radius of the maximal singularity-free hypersphere, ...) a detailed study of it (e.g. efficient computation of \mathfrak{M} , proof of $\#\mathcal{M} = 80, \dots$) is dedicated to future research.

Acknowledgements. The first author is funded by the Doctoral College *Computational Design* of the Vienna University of Technology. The second author is supported by Grant No. P 24927-N25 of the Austrian Science Fund FWF within the project *Stewart Gough platforms with self-motions*.

References

1. Aigner, B., Nawratil, G.: Planar Stewart Gough platforms with quadratic singularity surface. In: Wenger, P., Flores, P. (eds.) *New Trends in Mechanisms Science - Theory and Industrial Applications*, pp. 93–102. Springer, Heidelberg (2016)
2. Bandyopadhyay, S., Ghosal, A.: Geometric characterization and parametric representation of the singularity manifold of a 6–6 Stewart platform manipulator. *Mech. Mach. Theory* **41**(11), 1377–1400 (2006)
3. Borràs, J., Thomas, F.: Singularity-invariant leg substitutions in pentapods. In: *IEEE/RSJ International Conference on Intelligent Robots and Systems*, Taipei, Taiwan, 18–22 October 2010
4. Borràs, J., Thomas, F., Ottaviano, E., Ceccarelli, M.: A reconfigurable 5-DOF 5-SPU parallel platform. In: *ASME/IFToMM International Conference on Reconfigurable Mechanisms and Robots*, King's College of London, London, UK, 22–24 June 2009
5. Borràs, J., Thomas, F., Torras, C.: Singularity-invariant families of line-plane 5-SPU platforms. *IEEE Trans. Robot.* **27**(5), 837–848 (2011)
6. Coste, M., Moussa, S.: On the rationality of the singularity locus of a Gough-Stewart platform - biplanar case. *Mech. Mach. Theory* **87**, 82–92 (2015)
7. Husty, M., Gosselin, C.: On the singularity surface of planar 3-RPR parallel mechanisms. *Mech. Des. Struct. Mach.* **36**, 411–425 (2008)
8. Jiang, Q., Gosselin, C.M.: Determination of the maximal singularity-free orientation workspace for the Gough-Stewart platform. *Mech. Mach. Theory* **44**(6), 1281–1293 (2009)
9. Kong, X., Gosselin, C.M.: Classification of 6-SPS parallel manipulators according to their components. In: *Proceedings of ASME Design Technical Conferences, DETC2000/MECH-14105*, Baltimore, USA, 10–13 September 2000
10. Li, H., Gosselin, C.M., Richard, M.J.: Determination of the maximal singularity-free zones in the six-dimensional workspace of the general Gough-Stewart platform. *Mech. Mach. Theory* **42**(4), 497–511 (2007)
11. Nag, A., Reddy, V., Agarwal, S., Bandyopadhyay, S.: Identifying singularity-free spheres in the position workspace of semi-regular Stewart platform manipulators. In: Lenarcic, J., Merlet, J.-P. (eds.) *Advances in Robot Kinematics*, pp. 427–435. HAL (2016)
12. Nawratil, G.: On the line-symmetry of self-motions of linear pentapods. In: Lenarcic, J., Merlet, J.-P. (eds.) *Advances in Robot Kinematics*, pp. 149–157. HAL (2016)
13. Nawratil, G.: Point-models for the set of oriented line-elements - a survey. *Mech. Mach. Theory* **111**, 118–134 (2017)

14. Nawratil, G., Schicho, J.: Self-motions of pentapods with linear platform. *Robotica* (accepted) doi:[10.1017/S0263574715000843](https://doi.org/10.1017/S0263574715000843)
15. Rasoulzadeh, A., Nawratil, G.: Rational parametrization of linear pentapod's singularity variety and the distance to it. Extended version on [arXiv:1701.09107](https://arxiv.org/abs/1701.09107) (2017)
16. Shafarevich, I.R.: *Basic Algebraic Geometry 1: Varieties in Projective Space*. Springer, Heidelberg (2013)

Inverse Kinematics of Anthropomorphic Arms Yielding Eight Coinciding Circles

B. Bongardt^(✉)

Robotics Innovation Center, DFKI GmbH,
Robert-Hooke-Str. 1, 28359 Bremen, Germany
bertold.bongardt@dfki.de

Abstract. In this paper it is demonstrated that the solution space of the inverse kinematic problem of an anthropomorphic, redundant 7R chain for a given pose does consist of eight different coinciding circles instead of a single circle that has been reported as of today. By modeling the structure using the convention by Sheth and Uicker, the displacements within the kinematics of the chain are partitioned in time-invariant displacements along rigid links and time-variant displacements along the seven rotative joints. In particular, the subchains of shoulder, elbow, and wrist are preserved. By respecting the ‘flips’ of these three substructures the eight-fold occupancy of the redundancy circle is obtained. The result corresponds to the eight IK solutions for regional-spherical arms and provides a prerequisite for using all capabilities of respective robots in practical applications.

Keywords: Kinematic analysis · Anthropomorphic robot arm · Redundant manipulator · Cyclic law of cosines · Virtual joints

1 Introduction

The inverse kinematic problem (IKP) of a redundant robot is seeking for an infinite set of joint configurations for a given orientation and position of its endeffector. Since robotic chains with seven degree of freedom (DOF) possess a kinematic redundancy of degree one in the six-dimensional space of poses $SE(3)$ the solution space of the IKP of chains with seven rotative joints (7R) is characterized by one-dimensional manifolds: each containing ∞^1 points representing certain joint configurations. Kinematic 7R chains with intersecting axes of the first and the last three joints (*shoulder* and *wrist*) are called anthropomorphic arms. Their structure can be grouped in two spherical submechanisms and one rotative (*elbow*) element and thus be called an SRS structure. The *self-motions* [5,9] or *null-space motions* [7] – those joint configuration changes that let the endeffector’s pose remain constant – of an anthropomorphic 7R arm can be characterized by the *redundancy circle* [1,6,9]. The solution set for a given pose has been computed [12] as specific interval sets for the redundancy angle (circle segments for the elbow position) that depend on minimally and maximally feasible values of the seven joints.

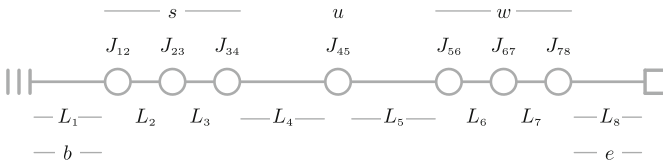


Fig. 1. Overview of used notation for links, joints, and joint groups of the 7R chain.

The approach of this paper is based on the works by Shimizu et al. [12]: the robot redundancy is parametrized by the elbow angle with respect to redundancy circles. The modeling here employs the kinematic convention by Sheth and Uicker [11], instead of the convention by Denavit and Hartenberg [8]. Due to the advantageous properties of this convention [4], the kinematic SRS structure of the robot is well reflected and the analytic solution procedure is simplified. As main contribution, the approach yields the insight that a complete solution of the inverse kinematics does not incorporate *one* but *eight* different one-parameter sets in parameter space which each represent eight circles coinciding in \mathbb{R}^3 , the Euclidean workspace [2,3].¹

The structure of the paper reads as follows: In Sect. 2 the robot model is introduced and the forward kinematics is computed. Section 3 presents geometric analysis within three planes of the robot’s geometry. Section 4 contains the computation of the inverse kinematics, including a brief example. The paper is concluded in Sect. 5.

2 Forward Kinematics

The eight links of the 7R chain are enumerated by a simple index from the index set $\mathcal{S}_L = (1, 2, \dots, 8)$. The seven joints are equipped with a double index from $\mathcal{S}_J = ((1, 2), (2, 3), \dots, (7, 8))$. The first and the last three joints are referred by *s* (shoulder) and by *w* (wrist). The elbow is denoted by *u* (cubital). The reference location at the first link is called *b* (basis) and the reference location of the last link is called *e* (endeffector), see the sketch in Fig. 1.

The description of the geometry of an anthropomorphic arm (Mitsubishi PA10) is given in Table 1 in terms of its Sheth–Uicker parameters. The values $b = 0$ in each row reflect that each sequential pair of joint axes is intersecting. The spherical constellation of the first three and last three joint axes is reflected by zeros of the translative parameters in the rows 2–3 and 6–7. The reference posture of the robot in Table 1 represents a fully-stretched configuration (as displayed in Fig. 4a).

¹ In terminology of [12], the complete solution reported here incorporates the inversion of the three cosine-type into the solution procedure. In comparison to the recent work [10] which employs a parametrization with respect to the second joint, the parametrization via the redundancy angle permits the direct interpretation as eight coinciding elbow circles.

Table 1. Sheth–Uicker parameters of an anthropomorphic 7R arm with sequentially-orthogonal joint axes. The numerical lengths *base–shoulder*, *shoulder–elbow*, *elbow–wrist*, and *wrist–effector* are $l_{bs} = 31.7$ cm, $l_{su} = 38.0$ cm, $l_{uw} = 48.0$ cm, and $l_{we} = 12.28$ cm for the Mitsubishi PA10.

Link	q_{ij}	d_{ij}	γ_j	c_j	β_j	b_j	α_j	a_j
1	–	–	–	$l_{bs}/2$	–	–	–	$l_{bs}/2$
2	q_{12}	–	–	–	$-\pi/2$	–	–	–
3	q_{23}	–	–	–	$+\pi/2$	–	–	–
4	q_{34}	–	–	$l_{su}/2$	$-\pi/2$	–	–	$l_{su}/2$
5	q_{45}	–	–	$l_{uw}/2$	$+\pi/2$	–	–	$l_{uw}/2$
6	q_{56}	–	–	–	$-\pi/2$	–	–	–
7	q_{67}	–	–	–	$+\pi/2$	–	–	–
8	q_{78}	–	–	$l_{we}/2$	–	–	–	$l_{we}/2$

By means of the Sheth–Uicker specification, the forward kinematics of the 7DOF kinematic chain for a configuration vector $\mathbf{q} = (q_{12}, q_{23}, q_{34}, q_{45}, q_{56}, q_{67}, q_{78})$, with $\mathbf{q} = \mathbf{q}^{(t)}$ for a certain time t , as the chain of matrix multiplications

$$\mathbf{D}_{be} = \text{FK}(\mathbf{q}) = \underline{\mathbf{L}}_1 \cdot \mathbf{J}_{12} \cdot \underline{\mathbf{L}}_2 \cdot \mathbf{J}_{23} \cdot \underline{\mathbf{L}}_3 \cdot \mathbf{J}_{34} \cdot \underline{\mathbf{L}}_4 \cdot \mathbf{J}_{45} \cdot \underline{\mathbf{L}}_5 \cdot \mathbf{J}_{56} \cdot \underline{\mathbf{L}}_6 \cdot \mathbf{J}_{67} \cdot \underline{\mathbf{L}}_7 \cdot \mathbf{J}_{78} \cdot \underline{\mathbf{L}}_8. \quad (1)$$

Each link displacement $\underline{\mathbf{L}}_k$ is given as a time-invariant displacement parametrized by a dual Euler angle $(\tilde{\gamma}_k, \tilde{\beta}_k, \tilde{\alpha}_k)$ as $\underline{\mathbf{L}}_k = \underline{\mathbf{L}}(\gamma_k, c_k, \beta_k, b_k, \alpha_k, a_k)$ for all $k \in \mathcal{S}_L$ and each joint displacement $\mathbf{J}_{ij} = \mathbf{J}(q_{ij}) = \mathbf{D}_z(q_{ij})$ is given as time-variant z -rotation for all $(i, j) \in \mathcal{S}_J$ [2, 4].

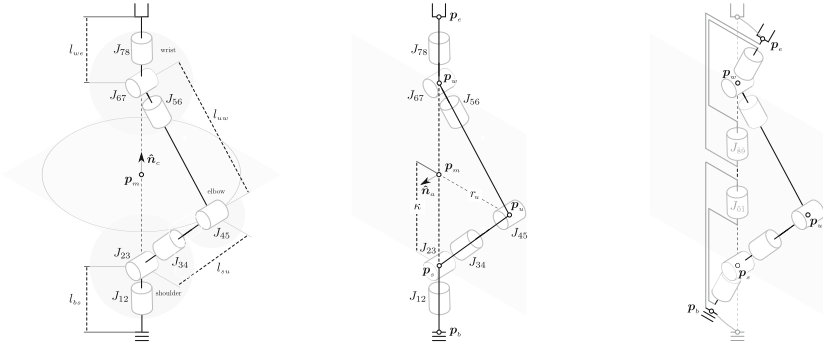
For the rotative part $\mathbf{R}_{be} = \mathbf{E}_e$ of $\mathbf{D}_{be} = \begin{pmatrix} \mathbf{R}_{be} & \mathbf{t}_{be} \\ \mathbf{0} & 1 \end{pmatrix} = \begin{pmatrix} \mathbf{P}_e & \mathbf{p}_e \\ \mathbf{0} & 1 \end{pmatrix} = \mathbf{P}_e$, the forward kinematics of Eq. 1 is simplified to

$$\begin{aligned} \mathbf{R}_{be} &= \underbrace{\underline{\mathbf{R}}_1}_{=\mathbf{I}} \cdot \underbrace{\mathbf{Z}_{12} \cdot \underline{\mathbf{R}}_2 \cdot \mathbf{Z}_{23} \cdot \underline{\mathbf{R}}_3 \cdot \mathbf{Z}_{34}}_{=:\mathbf{S}_{14}} \cdot \underline{\mathbf{R}}_4 \cdot \mathbf{Z}_{45} \cdot \underline{\mathbf{R}}_5 \cdot \underbrace{\mathbf{Z}_{56} \cdot \underline{\mathbf{R}}_6 \cdot \mathbf{Z}_{67} \cdot \underline{\mathbf{R}}_7 \cdot \mathbf{Z}_{78}}_{=:\mathbf{S}_{58}} \cdot \underbrace{\underline{\mathbf{R}}_8}_{=\mathbf{I}} \\ &= \mathbf{I} \cdot \mathbf{S}_{14} \cdot \underline{\mathbf{R}}_4 \cdot \mathbf{Z}_{45} \cdot \underline{\mathbf{R}}_5 \cdot \mathbf{S}_{58} \cdot \mathbf{I} = \mathbf{S}_{14} \cdot \underline{\mathbf{R}}_4 \cdot \mathbf{Z}_{45} \cdot \underline{\mathbf{R}}_5 \cdot \mathbf{S}_{58}. \end{aligned} \quad (2)$$

Here, the simplifications $\underline{\mathbf{R}}_1 = \mathbf{I}$ and $\underline{\mathbf{R}}_8 = \mathbf{I}$ follow from the first and last row in Table 1 and the compact forms \mathbf{S}_{14} and \mathbf{S}_{58} represent the spherical subchains.

3 Geometry

Three planes are introduced to describe the possible postures of an SRS arm with a specific end-effector pose: the circle plane \mathcal{H}_c orthogonal to the shoulder-wrist vector \mathbf{d}_{sw} contains the current elbow position; the elbow plane \mathcal{H}_b is that affine subspace containing the positions of shoulder, elbow, and wrist; one of the elbow planes is distinguished as the reference (anchor) plane \mathcal{H}_a . See Fig. 2 for three-dimensional sketches.



The circle of redundancy lays in the plane \mathcal{H}_c with unit normal vector $\hat{\mathbf{n}}_c$ passing through the midpoint \mathbf{p}_m . Triangle geometry in the reference plane \mathcal{H}_a (or elbow plane \mathcal{H}_b) with normal direction $\hat{\mathbf{n}}_a$ (or $\hat{\mathbf{n}}_b$). Illustrated virtual joints J_{01} and J_{89} for covering the redundancy circle while keeping final pose and real joints constant.

Fig. 2. Sketches of an anthropomorphic 7R arm.

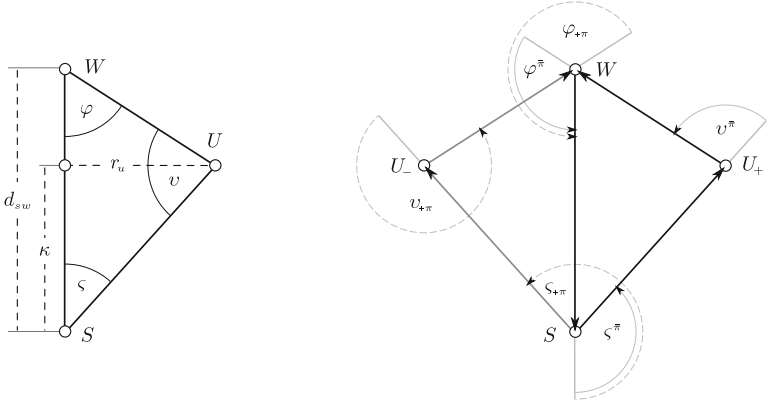
Circle plane \mathcal{H}_c . For one endeffector pose $\mathbf{D}_{be} = \begin{pmatrix} \mathbf{R}_{0e} & \mathbf{t}_{be} \\ \mathbf{0} & 1 \end{pmatrix}$, the wrist $\mathbf{p}_w = \mathbf{p}_s + \mathbf{d}_{sw}$ is constant since shoulder $\mathbf{p}_s = (0, 0, l_{bs})^T$ and \mathbf{d}_{sw} are constant:

$$\begin{aligned} \mathbf{d}_{sw} &= \mathbf{p}_w - \mathbf{p}_s = (\mathbf{p}_e - \mathbf{d}_{we}) - \mathbf{d}_{bs} = (\mathbf{d}_{be} - [\mathbf{R}]_{be} \cdot [\mathbf{d}_{we}]_e) - \mathbf{d}_{bs} \\ &= \mathbf{t}_{be} - \mathbf{R}_{be} \cdot \begin{pmatrix} 0 \\ 0 \\ l_{we} \end{pmatrix} - \begin{pmatrix} 0 \\ 0 \\ l_{bs} \end{pmatrix}. \end{aligned} \quad (3)$$

Thus, a redundant arm motion only involves the elbow position. Since l_{su} and l_{uw} are constant, the elbow is constrained to a circle given as the intersection of the shoulder sphere $\mathcal{S}_s = (\mathbf{p}_s, l_{su})$ and the wrist sphere $\mathcal{S}_w = (\mathbf{p}_w, l_{uw})$. The intersecting circle $\mathcal{C}_u = \mathcal{S}_s \cap \mathcal{S}_w$ is called the circle of redundancy. The situation is indicated in Fig. 2a. The normal direction $\hat{\mathbf{n}}_c$ of the plane \mathcal{H}_c containing the redundancy circle $\mathcal{C}_u \subset \mathcal{H}_c$ is contained is given as $\hat{\mathbf{n}}_c = \mathbf{d}_{sw} / \|\mathbf{d}_{sw}\|$. The circle midpoint \mathbf{p}_m is computed by solving the Pythagorean relations $\kappa^2 + r_u^2 = l_{su}^2$ and $(\|\mathbf{d}_{sw}\| - \kappa)^2 + r_u^2 = l_{uw}^2$ of the triangle $\Delta = \Delta(\mathbf{p}_s, \mathbf{p}_u, \mathbf{p}_w)$ for $\kappa = \frac{1}{2 \cdot \|\mathbf{d}_{sw}\|} \cdot (\|\mathbf{d}_{sw}\|^2 + l_{su}^2 - l_{uw}^2)$. The center \mathbf{p}_m of the redundancy circle \mathcal{C}_u is then determined as $\mathbf{p}_m = \mathbf{p}_s + \kappa \cdot \hat{\mathbf{n}}_c$. Via κ , the radius r_u of the circle is computed with $r_u = \sqrt{l_{su}^2 - \kappa^2}$ (see Fig. 3a).

Elbow plane \mathcal{H}_b . In contrast to $\Delta = \Delta(S, U, W)$ (Fig. 3a), the two triangles, $\Delta_+ = \Delta(S, U_+, W)$ and $\Delta_- = \Delta(S, U_-, W)$, in Fig. 3b reflect the orientation of the axis of the elbow joint J_{45} . For such oriented triangles, the cyclic form of the law of cosines [2] can be applied providing the trigonometric identities

$$\begin{aligned} \cos(\gamma) &= +\cos(\alpha) \cdot \cos(\beta) - \sin(\alpha) \cdot \sin(\beta) \\ \sin(\gamma) &= -\sin(\alpha) \cdot \cos(\beta) - \cos(\alpha) \cdot \sin(\beta), \end{aligned} \quad (4)$$



Sketch of triangle $\Delta(S,U,W)$ spanned by shoulder S , elbow U , and wrist W with interior, undirected angles, ζ , v , ϕ , height r_u , and edge section κ .

Two directed triangles $\Delta_+ = \Delta(S,U_+,W)$ and $\Delta_- = \Delta(S,U_-,W)$ with exterior, directed angles in counter-clockwise orientation, and directed edges directed edges d_{sw} , d_{wu} , and d_{ws} .

Fig. 3. Triangles spanned by shoulder, elbow, and wrist.

which are used to compute to determine the oriented² angles $v_{+\pi}$ and $v_{-\pi}$. The solutions for elbow joint q_{45+} and q_{45-} are then derived [2] with the oriented triangles Δ_+ and Δ_- with the compact expression

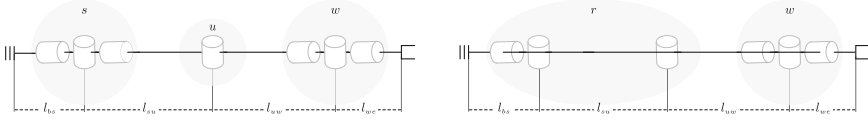
$$q_{45+}, q_{45-} = \pm \text{acos}(\cos(\phi) \cdot \cos(\zeta) - \sin(\phi) \cdot \sin(\zeta)). \quad (5)$$

The trigonometric values for ϕ are given with $\sin(\phi) = r_u / l_{uw}$ and $\cos(\phi) = (\|d_{sw}\| - \kappa) / l_{uw}$ (Fig. 3a). The values for ζ are given with $\sin(\zeta) = r_u / l_{su}$ and $\cos(\zeta) = \kappa / \|l_{su}\|$. Using the previously computed expressions, $\kappa = \frac{1}{2 \cdot \|d_{sw}\|} \cdot (\|d_{sw}\|^2 + l_{su}^2 - l_{uw}^2)$ and $r_u = \sqrt{l_{su}^2 - \kappa^2}$, and simplifying the terms, the two possible elbow angles from Eq. 5 are determined as³

$$q_{45+}, q_{45-} = \pm \text{acos}\left(\frac{l_{su}^2 + l_{uw}^2 - \|d_{sw}\|^2}{2 \cdot l_{su} \cdot l_{uw}}\right). \quad (6)$$

² Given the triangle Δ in Fig. 3a with interior angles $\zeta, v, \phi \in [0, \pi]$, the oriented angles of the positive-elbow triangle Δ_+ on the right hand side of Fig. 3b are given as the supplementary angles $\phi_{+\pi}, \zeta_{+\pi}, v_{+\pi}$ (with $\phi_{+\pi} := \pi - \phi$). The angles of the negative-elbow triangle Δ_- on the left hand side of Fig. 3b are given as the π -shifted angles $\phi_{-\pi}, \zeta_{-\pi}, v_{-\pi}$ (with $\phi_{-\pi} := \pi + \phi$).

³ In [12] only one solution is reported. Note, that the two solutions are not covered by an elbow rotation of π : while rotating along the circle, the elbow angle remains constant. However, the elbow configuration q_{45-} is the negative of the configuration q_{45+} : apart from any ‘stretched-out’ posture, where the two values coincide $q_{45+} = q_{45-} = 0$, they differ in general postures. In Fig. 3b, this distinction is reflected by the counter-clockwise orientations of all six angles.



Reference posture corresponding to the Sheth-Uicker specification in Table 1.

Decoupled regional-spherical 6R arm obtained by deactivating the third joint.

Fig. 4. Two sketches of arms in reference posture.

Reference plane \mathcal{H}_a . Each of the two triangles, Δ_+ and Δ_- , can be rotated around the axis $(\mathbf{p}_s, \mathbf{d}_{sw})$. For parametrization of all points on the (two instances of the) redundancy circle, the angle ψ is defined. While the rotation axis is defined with $\hat{\mathbf{n}}_c = \mathbf{d}_{sw}^\oplus$, an ‘ x -axis’ is not given a priori by the manipulator’s geometry. As shown in the article [12], by fixing q_{34} to zero – for a given target pose \mathbf{P}_e and a deduced elbow configuration q_{45} – values, q_{12} and q_{23} , for the first two shoulder joints, J_{12} and J_{23} , can be determined by means of using the rotative forward kinematics from Eq. 2 and \mathbf{d}_{sw} from Eq. 3 by solving

$$\begin{aligned} \mathbf{d}_{sw} &= \mathbf{p}_w - \mathbf{p}_s = (\mathbf{p}_s + \mathbf{d}_{su} + \mathbf{d}_{uw}) - \mathbf{p}_s = [\mathbf{R}]_{14} \cdot [\mathbf{d}_{su}]_4 + [\mathbf{R}]_{15} \cdot [\mathbf{d}_{uw}]_5 \\ &= \mathbf{S}_{14}(q_{12}, q_{23}, 0) \cdot \left(\begin{pmatrix} 0 \\ 0 \\ l_{su} \end{pmatrix} + \mathbf{R}_4 \cdot \mathbf{Z}(q_{45}) \cdot \begin{pmatrix} 0 \\ 0 \\ l_{uw} \end{pmatrix} \right). \end{aligned} \tag{7}$$

The position of the elbow joint $\mathbf{p}_u = \mathbf{p}_s + \mathbf{d}_{su}$ for the reference angles q_{12}^* and q_{23}^* , fulfilling Eq. 7, is used to define $\psi = 0$. According to Eq. 6, two elbow positions in the elbow plane \mathcal{H}_b realize the endeffector pose. For ensuring uniqueness, the elbow position \mathbf{p}_{u+} for the positive value q_{45+} is selected to define direction of the ‘ x -axis’ and the circle angle $\psi = 0$. The elbow plane \mathcal{H}_b is thus equipped with an interior, oriented basis by the indicator axis $\hat{\mathbf{b}}_x = (\mathbf{p}_{u+} - \mathbf{p}_m) / \|\mathbf{p}_{u+} - \mathbf{p}_m\|$ and by the normal direction $\hat{\mathbf{b}}_y = \hat{\mathbf{n}}_c = (\mathbf{p}_w - \mathbf{p}_s) / \|\mathbf{p}_w - \mathbf{p}_s\|$, providing its oriented normal direction, $\hat{\mathbf{n}}_c := \hat{\mathbf{b}}_x \times \hat{\mathbf{b}}_y$ (see Fig. 2b). The reference plane \mathcal{H}_a is defined as the elbow plane \mathcal{H}_b in this specific configuration. While the orientation of ψ is induced by the normal direction of the circle plane $\hat{\mathbf{n}}_c \cong \mathbf{d}_{sw}$, its identity $\psi = 0$ is fixated by the introduced reference plane \mathcal{H}_a .

4 Inverse Kinematics

In the first step of the inverse kinematics computation, the IKP is solved for a given endeffector pose \mathbf{P}_e with a ‘reference configuration’ for the joints. In the second step, the modifications of this configuration for (i) swapping to a different instances of the circle and (ii) letting the elbow travel along the redundancy circle are outlined.

First Step. A feasible elbow angle q_{45}^* can be selected from Eq. 6. A feasible reference configuration for $q_{12}^*, q_{23}^*, q_{34}^*$ is determined with Eq. 7. For such selected four angles $q_{12}^*, q_{23}^*, q_{34}^*, q_{45}^*$, a configuration for the joints of the spherical shoulder,

J_{56}, J_{67}, J_{78} , can be computed by solving Eq. 2 for

$$\mathbf{S}_{58}(q_{56}, q_{67}, q_{78}) = \underline{\mathbf{R}}_5^T \cdot \mathbf{Z}^T(q_{45}^*) \cdot \underline{\mathbf{R}}_4^T \cdot \mathbf{S}_{14}^T(q_{12}^*, q_{23}^*, q_{34}^*) \cdot \underline{\mathbf{R}}_{be}. \quad (8)$$

In total, one feasible solution $\mathbf{q}^* = (q_{12}^*, q_{23}^*, q_{34}^*, q_{45}^*, q_{56}^*, q_{67}^*, q_{78}^*)^T$ to the Inverse Kinematics Problem is obtained.

Second Step. Given a feasible configuration \mathbf{q}^* selected in the first step, the second step consists of modifying this configuration in such way that the elbow travels along (one of the eight instances of) the redundancy circle. The selected reference configuration \mathbf{q}^* fulfills the forward kinematics Eq. 1, and in particular, the rotative pendant $\underline{\mathbf{R}}_{be} = \mathbf{S}_{14}^* \cdot \underline{\mathbf{R}}_4 \cdot \mathbf{Z}_{45}^* \cdot \underline{\mathbf{R}}_5 \cdot \mathbf{S}_{58}^*$, Eq. 2, with the shoulder matrix $\mathbf{S}_{14}^* = \mathbf{S}_{14}^*(q_{12}^*, q_{23}^*, q_{34}^*) = \mathbf{Z}(q_{12}^*) \cdot \underline{\mathbf{R}}_2 \cdot \mathbf{Z}(q_{23}^*) \cdot \underline{\mathbf{R}}_3 \cdot \mathbf{Z}(q_{34}^*)$, the elbow matrix $\mathbf{Z}_{45}^* = \mathbf{Z}(q_{45}^*)$, and the wrist matrix $\mathbf{S}_{58}^* = \mathbf{S}_{58}^*(q_{56}^*, q_{67}^*, q_{78}^*) = \mathbf{Z}(q_{56}^*) \cdot \underline{\mathbf{R}}_2 \cdot \mathbf{Z}(q_{67}^*) \cdot \underline{\mathbf{R}}_3 \cdot \mathbf{Z}(q_{78}^*)$. The change of the elbow position on the redundancy circle is expressed by introducing the virtual joints $J_{0\bar{1}}$ and $J_{\bar{8}9}$ into the chain (Fig. 2c) as

$$\underline{\mathbf{R}}_{be} = \underline{\mathbf{R}}_0 \cdot \mathbf{Z}_{0\bar{1}}(\psi) \cdot \underline{\mathbf{R}}_{\bar{1}} \cdot \mathbf{S}_{14}^* \cdot \underline{\mathbf{R}}_4 \cdot \mathbf{Z}_{45}^* \cdot \underline{\mathbf{R}}_5 \cdot \mathbf{S}_{58}^* \cdot \underline{\mathbf{R}}_{\bar{8}} \cdot \mathbf{Z}_{\bar{8}9}(-\psi) \cdot \underline{\mathbf{R}}_9.$$

Here, $\underline{\mathbf{R}}_0$ maps the z -axis of the base frame to the direction $\hat{\mathbf{n}}_c$, and $\underline{\mathbf{R}}_{\bar{1}}$ describes the inverse rotation $\underline{\mathbf{R}}_{\bar{1}} = \underline{\mathbf{R}}_0^T$. Similarly, $\underline{\mathbf{R}}_{\bar{8}}$ maps the z -axis of the endeffector frame to the direction $\hat{\mathbf{n}}_c$, and $\underline{\mathbf{R}}_9$ describes the inverse rotation $\underline{\mathbf{R}}_9 = \underline{\mathbf{R}}_{\bar{8}}^T$ (Fig. 2c).

A configuration \mathbf{q} that realizes a certain redundancy angle ψ is computed by ‘pushing’ the displacement of the two virtual joints into the joint configuration \mathbf{q}^* . A shoulder configuration (q_{12}, q_{23}, q_{34}) is computed so that the wrist displacement $\mathbf{S}_{14} = \mathbf{S}_{14}(q_{12}, q_{23}, q_{34})$ compensates for the rotation $\mathbf{Z}_{0\bar{1}}(\psi)$ of the virtual joint $J_{0\bar{1}}$ as

$$\mathbf{S}_{14} = \underline{\mathbf{R}}_0 \cdot \mathbf{Z}_{0\bar{1}}(\psi) \cdot \underline{\mathbf{R}}_{\bar{1}} \cdot \mathbf{S}_{14}^* = \exp(\psi \cdot \hat{\mathbf{n}}_c^{\otimes}) \cdot \mathbf{S}_{14}^* \quad (9)$$

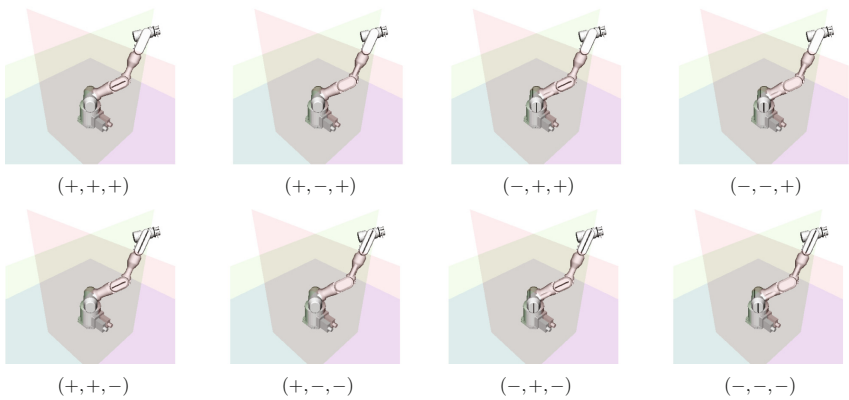


Fig. 5. Example of eight different joint configurations corresponding one endeffector pose and one elbow position. The links of the robot are marked with black lines to distinguish the postures.

Table 2. Matrix-to-zyz-angle conversion method**Algorithm 1** Euler angle computation (zyz-convention)

(in) Rotation matrix $\mathbf{R} = \mathbf{R}_z(\gamma) \cdot \mathbf{R}_y(\beta) \cdot \mathbf{R}_z(\alpha)$	7:	$\gamma_+ \leftarrow \text{atan}_2(+\mathbf{R}_{[2,3]}, +\mathbf{R}_{[1,3]}/s)$
(out) Euler angles $(\gamma_+, \beta_+, \alpha_+), (\gamma_-, \beta_-, \alpha_-)$	8:	$\gamma_- \leftarrow \text{atan}_2(-\mathbf{R}_{[2,3]}, -\mathbf{R}_{[1,3]}/s)$
1: function ROTMAT-2-EA-ZYZ(\mathbf{R})	9:	else # Singular
2: $\beta_+ \leftarrow \text{acos}(\mathbf{R}_{[3,3]}), \beta_- \leftarrow -\beta_+$	10:	$\alpha_+ \leftarrow \text{atan}_2(\mathbf{R}_{[1,2]}, \mathbf{R}_{[1,1]})$
3: $s \leftarrow \sin(\beta_+)$	11:	$\alpha_- \leftarrow 0$
4: if $s \neq 0$ then # Regular	12:	$\gamma_+ \leftarrow 0$
5: $\alpha_+ \leftarrow \text{atan}_2(+\mathbf{R}_{[3,2]}/s, -\mathbf{R}_{[3,1]}/s)$	13:	$\gamma_- \leftarrow \text{atan}_2(\mathbf{R}_{[1,2]}, \mathbf{R}_{[1,1]})$
6: $\alpha_- \leftarrow \text{atan}_2(-\mathbf{R}_{[3,2]}/s, +\mathbf{R}_{[3,1]}/s)$	14:	return $(\gamma_+, \beta_+, \alpha_+), (\gamma_-, \beta_-, \alpha_-)$

with $\mathbf{a}^\otimes := \begin{pmatrix} 0 & -a_3 & a_2 \\ a_3 & 0 & -a_1 \\ -a_2 & a_1 & 0 \end{pmatrix}$. For the wrist, a spherical displacement $\mathbf{S}_{58} = \mathbf{S}_{58}(q_{56}, q_{67}, q_{78})$ compensating for the rotation $\mathbf{Z}_{\delta\delta}(-\psi)$ of the virtual joint $J_{\delta\delta}$ is computed with

$$\begin{aligned} \mathbf{S}_{58} &= \mathbf{S}_{58}^* \cdot \underline{\mathbf{R}}_3 \cdot \mathbf{Z}_{\delta\delta}(-\psi) \cdot \underline{\mathbf{R}}_9 = \mathbf{S}_{58}^* \cdot [\mathbf{R}]_{eb} \cdot \exp(-\psi \cdot \hat{\mathbf{n}}_c^\otimes) \cdot [\mathbf{R}]_{be} \\ &= \mathbf{S}_{58}^* \cdot [\exp(-\psi \cdot \hat{\mathbf{n}}_c^\otimes)]_{ee}. \end{aligned} \quad (10)$$

For augmenting the computation with the second solution,⁴ the modeling via Sheth–Uicker parameters (Table 1) offers a straightforward approach: The link displacement rotations $\underline{\mathbf{R}}_2$, $\underline{\mathbf{R}}_3$, $\underline{\mathbf{R}}_6$, and $\underline{\mathbf{R}}_7$, defined by β_2 , β_3 and β_6 , β_7 from Table 1, are quarter-turn matrices with coordinates

$$\underline{\mathbf{R}}_2 = \underline{\mathbf{R}}_6 = \mathbf{R}_x(-\frac{\pi}{2}) = \begin{pmatrix} 1 & 0 & 0 \\ 0 & 0 & +1 \\ 0 & -1 & 0 \end{pmatrix} \quad \underline{\mathbf{R}}_3 = \underline{\mathbf{R}}_7 = \mathbf{R}_x(+\frac{\pi}{2}) = \begin{pmatrix} 1 & 0 & 0 \\ 0 & 0 & -1 \\ 0 & +1 & 0 \end{pmatrix}.$$

With these properties and $\mathbf{R}_x(-\pi/2) \cdot \mathbf{R}_x(+\pi/2) = \mathbf{I}$, it is observed that the shoulder displacement $\mathbf{S}_{14} = \mathbf{Z}(q_{12}) \cdot \underline{\mathbf{R}}_2 \cdot \mathbf{Z}(q_{23}) \cdot \underline{\mathbf{R}}_3 \cdot \mathbf{Z}(q_{34})$ and the wrist displacement $\mathbf{S}_{58} = \mathbf{Z}(q_{56}) \cdot \underline{\mathbf{R}}_6 \cdot \mathbf{Z}(q_{67}) \cdot \underline{\mathbf{R}}_7 \cdot \mathbf{Z}(q_{78})$ feature the shape of an Euler rotation matrix in zyz-convention. For this reason, the joint configurations for the matrices \mathbf{S}_{14} and \mathbf{S}_{58} ,

$$\mathbf{S}_{14} = \exp(\psi \cdot \hat{\mathbf{n}}_c^\otimes) \cdot \mathbf{S}_{14}^* \quad \mathbf{S}_{58} = \mathbf{S}_{58}^* \cdot [\exp(-\psi \cdot \hat{\mathbf{n}}_c^\otimes)]_{ee}, \quad (11)$$

from Eqs. 9 and 10 can be computed with Table 2. Since the conversion method returns two solution for the shoulder triplet (q_{12}, q_{23}, q_{34}) and for the wrist triplet

⁴ For determining the shoulder angles and wrist angles from the matrices \mathbf{S}_{14} and \mathbf{S}_{58} , the method in [12] is based on orthogonal decomposition of rotation matrices and solving for (q_{12}, q_{23}, q_{34}) and (q_{56}, q_{67}, q_{78}) , by coefficient comparison with respect to ψ . For the shoulder, the equation

$$\mathbf{S}_{14}(q_{12}, q_{23}, q_{34}) = \exp(\psi \cdot \hat{\mathbf{n}}_c^\otimes) \cdot \mathbf{S}_{14}^* = \underbrace{\sin(\psi) \cdot \hat{\mathbf{n}}_c^\otimes \cdot \mathbf{S}_{14}^*}_{=: \mathbf{A}_s} + \underbrace{\cos(\psi) \cdot (-\hat{\mathbf{n}}_c^\otimes)^2 \cdot \mathbf{S}_{14}^*}_{=: \mathbf{B}_s} + \underbrace{\hat{\mathbf{n}}_c^\otimes \cdot \mathbf{S}_{14}^*}_{=: \mathbf{C}_s},$$

with $\mathbf{a}^\otimes := \mathbf{a} \cdot \mathbf{a}^T$, and the coefficients of \mathbf{S} are analyzed. For the wrist, a similar approach is chosen. In both cases, the coefficient analysis only reports one of the two feasible solutions.

(q_{56}, q_{67}, q_{78}) , and considering the two solutions for the elbow joint q_{45} (Eq. 6), the size of the solution space (for a nonsingular configuration) is determined as

$$|\text{CONFIGS}| = |\text{SHOULDER}| \cdot |\text{ELBOW}| \cdot |\text{WRIST}| \cdot |\text{CIRCLE}| = 2 \cdot 2 \cdot 2 \cdot (\infty^1) = 8 \cdot (\infty^1)$$

coherent to eight IKP solutions of a corresponding regional-spherical arm (Fig. 4b).

Example. An example for solutions to the inverse kinematics problem on eight different circles is shown in Fig. 5. The signum triplets in the captions indicate the flips of the subchains shoulder, elbow, and wrist.

5 Conclusion and Outlook

The paper documents eight coinciding circles with $8 \cdot (\infty^1)$ solutions for the inverse kinematics problem of anthropomorphic arms and provides an essential step for using all capabilities of such manipulators. For this goal, the interval analysis [12] can be combined with the presented modeling and computation in the future.

Acknowledgements. The work was performed within the projects *Capio* and *Recupera*, funded with federal funds from the German Federal Ministry of Education and Research (BMBF) (Grant 01-IW-10001 and 01-IM-14006A). The author would like to thank Sankaranarayanan Natarajan, Wiebke Drop, and Arnaud Sengers for their contributions.

References

1. Asfour, T., Dillmann, R.: Human-like motion of a humanoid robot arm based on a closed-form solution of the inverse kinematics problem. In: International Conference on Intelligent Robots and Systems (IROS) (2003)
2. Bongardt, B.: Analytic Approaches for Design and Operation of Haptic Human-Machine Interfaces. Ph.D. thesis. Universität Bremen (2015)
3. Bongardt, B.: New Solutions for the Null-Space of Anthropomorphic 7R Arms (Extended Abstract). In: IFToMM D-A-CH, February 2016
4. Bongardt, B.: Sheth-Uicker convention revisited. *Mech. Mach. Theory* **69**, 200–229 (2013)
5. Burdick, J.W.: On the inverse kinematics of redundant manipulators: characterization of the self-motion manifolds. In: International Conference on Robotics and Automation (ICRA) (1989)
6. Dahm, P., Joubin, F.: Closed form solution for the inverse kinematics of a redundant robot arm. Technical report. IRINI 97-08 (1997)
7. Dietrich, A., Ott, C., Albu-Schäffer, A.: An overview of null space projections for redundant, torque-controlled robots. *Int. J. Robot. Res.* **34**(11), 1385–1400 (2015)
8. Hartenberg, R.S., Denavit, J.: A kinematic notation for lower-pair mechanisms based on matrices. *J. Appl. Mech.* **22**, 215–221 (1955)

9. Hollerbach, J.M.: Optimum kinematic design for a seven degree of freedom manipulator. In: International Symposium on Robotics Research (1985)
10. Pffurner, M.: Closed form inverse kinematics solution for a redundant anthropomorphic robot arm. *Comput. Aided Geom. Des.* **47**, 163–171 (2016)
11. Sheth, P.N., Uicker, J.J.: A generalized symbolic notation for mechanisms. *J. Eng. Ind. Ser. B* **93**(1), 102–112 (1971)
12. Shimizu, M., Kakuya, H., Yoon, W.-K., Kitagaki, K., Kosuge, K.: Analytical inverse kinematic computation for 7-DOF redundant manipulators with joint limits and its application to redundancy resolution. *IEEE Trans. Robot.* **24**(5), 1131–1142 (2008)

Optimal Synthesis of Overconstrained 6R Linkages by Curve Evolution

Tudor-Dan Rad^(✉) and Hans-Peter Schröcker

Unit Geometry and CAD, University of Innsbruck,
Technikerstraße 13, 6020 Innsbruck, Austria
{tudor-dan.rad,hans-peter.schroecker}@uibk.ac.at

Abstract. The paper presents an optimal synthesis of overconstrained linkages, based on the factorization of rational curves (representing one parametric motions) contained in Study's quadric. The group of Euclidean displacements is embedded in a affine space where a metric between motions based on the homogeneous mass distribution of the end effector is used to evolve the curves such that they are fitted to a set of target poses. The metric will measure the distance (in Euclidean sense) between the two resulting vectors of the feature points displaced by the two motions. The evolution is driven by the normal velocity of the curve projected in the direction of the target points. In the end we present an example for the optimal synthesis of an overconstrained 6R linkage by choosing a set of target poses and explaining in steps how this approach is implemented.

Keywords: Optimal mechanism synthesis · Curve evolution · Kinematic mapping · Motion factorization · Overconstrained linkage

1 Introduction

A linkage is a mechanism which generates a complex motion. The synthesis of a linkage means determining its geometric structure such that it generates a predetermined motion or trajectory and satisfies some structural restrictions. Fulfilling the previous requirements puts a lot of limitations on the linkage. This gave rise to optimal synthesis which aims at approximating these requirements. Some of the optimization techniques used in optimal synthesis of linkages are: interior-point methods [13], Gauss constraint methods [11], genetic algorithms [3] and evolution [12].

The paper also takes an evolutionary approach to synthesis. The novelty consists in using the factorization of motion polynomials [4] synthesis process. We demonstrate that it is particularly well-suited for evolution techniques because it allows to construct (overconstrained) linkages directly from a given approximated rational motion.

The factorization of motion polynomials is a process that generates a linkage which performs a one parametric motion (the functions of the joint angles share the same parameter). This motion must be defined by a rational curve in the

kinematic image space. The motion curve is constructed by starting from a set of target points in this space that resemble the poses needed to be achieved by the linkage. Using curve evolution methods [1], the initial motion curve will converge and approximate the specified poses.

For the evolution process to work for such curves the group of Euclidean displacements $SE(3)$ is embedded in 12-dimensional affine space \mathbb{R}^{12} . A *metric* between two motions is used by equipping the end effector of the linkage with a homogeneous mass distribution or a set of “feature points” whose barycenter is the tool center point (TCP) [8]. The metric will measure the distance (in Euclidean sense) between the two resulting vectors of the feature points displaced by the two motions.

The paper is structured as follows Sect. 2 explains the Euclidean metric in the affine space \mathbb{R}^{12} and offers a quick glimpse into motion factorization and overconstrained linkage construction, Sect. 3 presents the evolutionary design of the motion curve. Section 4 follows up with an example and in Sect. 5 some conclusions are drawn.

2 Preliminaries

The group of special Euclidean displacements $SE(3)$ represents rigid body displacements and is used to map a point \mathbf{p} to a new position \mathbf{p}' in Euclidean three-dimensional space:

$$\gamma: \mathbb{R}^3 \rightarrow \mathbb{R}^3, \quad \mathbf{p}' = \mathbf{A}\mathbf{p} + \mathbf{a}. \quad (1)$$

The matrix \mathbf{A} is a 3×3 special orthogonal matrix representing an element of the rotation group $SO(3)$ and the vector \mathbf{a} is a translation vector. Because displacements incorporate multiple distance concepts defining a metric between them can be problematic. In the past the concept was addressed for example by [10] but due to the nature of motion design used in this paper we have chosen the method proven in motion design by [6]. This approach embeds $SE(3)$ in a 12-dimensional affine space by mapping the entries of \mathbf{A} and \mathbf{a} to a 12-dimensional vector. In an object oriented metric the gripper is given by a set of “feature points” \mathbf{fp}_i and the Euclidean metric is defined by the inner product $\langle \alpha, \beta \rangle := \sum_i \langle \alpha(\mathbf{fp}_i), \beta(\mathbf{fp}_i) \rangle$ for any $\alpha, \beta \in SE(3)$. The corresponding squared distance is $\|\alpha - \beta\|^2 = \langle \alpha - \beta, \alpha - \beta \rangle$. It is well-known [8] that this metric only depends on the barycenter and the inertia tensor of the set of feature points and is capable of representing more general mass distributions in a computationally simple way.

Motion factorization is a method developed by Hegedüs, Schicho and Schröcker in [4] and can be used to synthesize linkages with one degree of freedom joints whose end link motion is defined by a rational curve on Study’s quadric. By combining multiple factorizations overconstrained linkages can be constructed as was demonstrated in [4].

For further understanding of the synthesis process a quick introduction to the kinematic image space and Study’s quadric is necessary. Study’s kinematic

mapping maps the group SE(3) to a quadric in seven dimensional projective space \mathbb{P}^7 with the equation $x_0y_0 + x_1y_1 + x_2y_2 + x_3y_3 = 0$ called Study’s quadric and denoted by \mathcal{S} . A more detailed explanation is given by Husty and Schröcker in [9]. The points of \mathbb{P}^7 are represented by the skew ring of dual quaternions \mathbb{DH} , denoted as $q = x_0 + x_1\mathbf{i} + x_2\mathbf{j} + x_3\mathbf{k} + \varepsilon(y_0 + y_1\mathbf{i} + y_2\mathbf{j} + y_3\mathbf{k})$ with the multiplication properties:

$$\varepsilon^2 = 0, \quad \mathbf{i}^2 = \mathbf{j}^2 = \mathbf{k}^2 = \mathbf{ijk} = -1, \quad \varepsilon\mathbf{i} = \mathbf{i}\varepsilon, \quad \varepsilon\mathbf{j} = \mathbf{j}\varepsilon, \quad \varepsilon\mathbf{k} = \mathbf{k}\varepsilon.$$

The conjugate of a dual quaternion is given by replacing \mathbf{i}, \mathbf{j} and \mathbf{k} with $-\mathbf{i}, -\mathbf{j}$, and $-\mathbf{k}$, respectively. A dual quaternion on \mathcal{S} is characterized by $q\bar{q} \in \mathbb{R}$.

The motion factorization algorithm of [4] starts with a rational curve of degree n on \mathcal{S} given by the polynomial $P(t) = c_0t^n + c_1t^{n-1} + \dots + c_n$ where $c_\ell \in \mathbb{DH}$ and $P\bar{P} \in \mathbb{R}[t]$. Generically (only generic cases are relevant for evolution based synthesis), it can be factored as $P(t) = (t - h_1) \cdot \dots \cdot (t - h_n)$. The linear factors $t - h_\ell$ are computed by polynomial division over the dual quaternions using the quadratic irreducible factors M_i of $P\bar{P} = M_1M_2 \cdot \dots \cdot M_n$ one at a time in the following manner: By polynomial division, polynomials P_{n-1}, R are attained with $P_n = P_{n-1}M_i + R$ and $R = r_1t + r_2$. In [4] it was proven that the unique dual quaternion zero $h_n = -r_1^{-1}r_2$ of R gives the rightmost factor $t - h_n$ in a possible factorization of P_n . To obtain the remaining linear factors, another quadratic factor M_k is chosen and the process is repeated with P_{n-1} instead of P_n .

Each of the n linear factors represent a revolute displacement around an axis and by consecutive multiplication to the right they form a linkage whose leftmost factor is the fixed joint and the rightmost factor is the distal joint. There are, in general, $n!$ different possibilities for the selection order of the M_ℓ ’s. This leads to the synthesis of $n!$ different open chains that perform the same motion. As it was shown in [4] an overconstrained linkage can be constructed by combining multiple kinematic chains to form a closed structure.

3 Curve Evolution on Study’s Quadric

Curve evolution is a widely used procedure in image processing and design and of late is also used in motion generation [7]. Our evolutionary approach is based on curve fitting to a set of data points driven by the normal velocity of the curve in the direction of the target points [2]. By mapping the desired poses to \mathcal{S} is obtained the set of target points TP_m which need to be approximated by a rational curve C also contained in \mathcal{S} , that is, satisfying $C\bar{C} \in \mathbb{R}[t]$. The validity of this condition is ensured throughout the evolution process by writing C in factorized form $C = (t - h_1) \cdot \dots \cdot (t - h_n)$ where each linear factor represents a rotation about an axis in space. The linear factors are defined in (2) where the Plücker coordinates of the revolute axes are $(\mathbf{d}_i, \mathbf{m}_i)$:

$$t - h_i = \frac{t - h_{0i} - \mathbf{d}_i - \varepsilon\mathbf{m}_i}{\|\mathbf{d}_i\|}. \tag{2}$$

By fluctuating the shape parameters Sp_1, \dots, Sp_k (coefficients of C) in time a family of curves C_k is obtained such that the target points TP_1, \dots, TP_m are optimally approximated. The moving velocity of a curve point $C(t_j)$ is given by the amount of change in time of the shape parameters Sp_k :

$$v_{C_j} = \sum_{l=1}^k \frac{\partial C(t_j)}{\partial Sp_l} \dot{Sp}_l \tag{3}$$

We are interested in moving the points on $C(t)$ which are closest to the target points. These points are computed as the foot-normals between the TP_m and $C(t)$ using the Euclidean structure given by the inner product defined in Sect. 2:

$$\langle TP_m - C(t), C'(t) \rangle = 0 \rightsquigarrow \{t_{m1}, \dots, t_{ml}\}, \tag{4}$$

$$t_m = \arg \min(\|TP_m - C(t_{mi})\|^2 : i \in \{1, \dots, l\}). \tag{5}$$

Note that the involved computations essentially boils down to finding the zeros of a univariate polynomials because the motion is given by a polynomial C . This is one of the advantages inherent to our approach.

The foot-points $FP_m = C(t_m)$ are computed using relations (4) and (5) and so the ideal velocity vector \mathbf{d} of the foot-points should be $TP_m - FP_m$. Comparing coefficients of both vectors in an orthonormal basis (with respect to the given scalar product) and using (3) results in an overconstrained system of linear equations for \dot{Sp}_l that can be solved in least square sense. The new shape parameters of the curve are computed as: $Sp_l = \dot{Sp}_l + \lambda \dot{Sp}_l$ where λ is a scaling parameter used such that the curve doesn't overshoot. In time as the distance between the curve $C(t)$ and the target points TP_m decreases, the system will converge to a local minimum.

4 Numeric Example

For the example, a set of 11 target poses is chosen as shown in Table 1. Without loss of generality, the first pose is the identity. A cubic curve $C(t) = (t - \mathbf{x})(t - \mathbf{y})(t - \mathbf{z})$ is chosen to approximate the target poses. We limit ourselves to polynomials of degree three because the end goal of the example is to construct a 6R overconstrained linkage. More explicitly, the linear factor $t - \mathbf{x}$ is of the shape

$$\frac{t - x_0 + x_1\mathbf{i} + x_2\mathbf{j} + x_3\mathbf{k} - \varepsilon((x_2x_7 - x_3x_6)\mathbf{i} + (x_3x_5 - x_1x_7)\mathbf{j} + (x_1x_6 - x_2x_5)\mathbf{k})}{\sqrt{x_1^2 + x_2^2 + x_3^2}}, \tag{6}$$

and similar for $t - \mathbf{y}$ and $t - \mathbf{z}$, resulting in a total of 21 shape parameters. The special shape of (6) is crucial. It ensures validity of the Study condition for each factor and hence also for $C(t)$ throughout the whole evolution process.

Table 1. Target poses

TP	Study parameters
1	1
2	$\mathbf{i}(-(\frac{337}{7})\varepsilon - \frac{79}{968}) + \mathbf{j}((\frac{22}{379})\varepsilon + \frac{3}{5066}) + \mathbf{k}((\frac{67}{161})\varepsilon + \frac{55}{509}) - (\frac{108}{53})\varepsilon + \frac{79}{41}$
3	$\mathbf{i}(-(\frac{2533}{19})\varepsilon - \frac{73}{328}) + \mathbf{j}((\frac{92}{105})\varepsilon + \frac{8}{3103}) + \mathbf{k}((\frac{46}{89})\varepsilon + \frac{41}{128}) - (\frac{313}{29})\varepsilon + \frac{119}{44}$
4	$\mathbf{i}(-(\frac{949}{4})\varepsilon - \frac{30}{77}) + \mathbf{j}((\frac{163}{43})\varepsilon + \frac{7}{815}) + \mathbf{k}(-(\frac{51}{128})\varepsilon + \frac{153}{245}) - (\frac{528}{19})\varepsilon + \frac{95}{29}$
5	$\mathbf{i}(-(\frac{1696}{5})\varepsilon - \frac{110}{201}) + \mathbf{j}((\frac{247}{21})\varepsilon + \frac{11}{456}) + \mathbf{k}(-(\frac{89}{24})\varepsilon + \frac{906}{907}) - (\frac{660}{13})\varepsilon + \frac{165}{46}$
6	$\mathbf{i}(-(\frac{2939}{7})\varepsilon - \frac{79}{119}) + \mathbf{j}((\frac{1279}{46})\varepsilon + \frac{19}{358}) + \mathbf{k}(-(\frac{1449}{145})\varepsilon + \frac{100}{71}) - (\frac{816}{11})\varepsilon + \frac{18}{5}$
7	$\mathbf{i}(-461\varepsilon - \frac{487}{682}) + \mathbf{j}((\frac{575}{11})\varepsilon + \frac{10}{101}) + \mathbf{k}(-(\frac{557}{32})\varepsilon + \frac{135}{76}) - (\frac{185}{2})\varepsilon + \frac{257}{78}$
8	$\mathbf{i}(-(\frac{1364}{3})\varepsilon - \frac{115}{167}) + \mathbf{j}((\frac{864}{11})\varepsilon + \frac{31}{212}) + \mathbf{k}(-(\frac{347}{14})\varepsilon + \frac{291}{145}) - (\frac{705}{7})\varepsilon + \frac{191}{70}$
9	$\mathbf{i}(-(\frac{1226}{3})\varepsilon - \frac{44}{73}) + \mathbf{j}((\frac{957}{10})\varepsilon + \frac{181}{1018}) + \mathbf{k}(-(\frac{817}{27})\varepsilon + \frac{75}{37}) - (\frac{694}{7})\varepsilon + \frac{390}{191}$
10	$\mathbf{i}(-(\frac{1713}{5})\varepsilon - \frac{85}{173}) + \mathbf{j}((\frac{1921}{20})\varepsilon + \frac{20}{109}) + \mathbf{k}(-(\frac{713}{22})\varepsilon + \frac{106}{57}) - (\frac{715}{8})\varepsilon + \frac{38}{27}$
11	$\mathbf{i}(-(\frac{8831}{32})\varepsilon - \frac{77}{201}) + \mathbf{j}((\frac{248}{3})\varepsilon + \frac{52}{311}) + \mathbf{k}(-(\frac{458}{15})\varepsilon + \frac{73}{46}) - (\frac{1476}{19})\varepsilon + \frac{109}{119}$

The linear factors are normalized to avoid numeric fluctuation of $C(t)$ without any geometric change.

A suitable initial guess for the shape parameter can be found by interpolating four poses [5] or, as we did in our example, by assigning random values to the shape parameters. Several attempts might be necessary in order to ensure good convergence. Once the evolution runs smoothly little effect on the local minimum has been observed. In the first iterations, the scaling factor λ needs to be small enough in order to compensate for large amount of changes Sp_l in the shape parameters. For the evolution to have a good flow, we found $\lambda := \max\{10\|\text{Sp}_l\|_\infty^{-1}, 1\}$ to be a good choice. With this initial setup we arrive at the computation of the foot points on $C(t)$ as described in the previous section. From relation (4) we obtain an equation of degree at most 10. Its zeros are found numerically and we can use (5) to find the parameter value of the closest point. Here, we also impose some constraints on the foot point computation in order to ensure that the poses are visited in successive order. To achieve this, after a provisional curve is evolved, two target points are chosen which are approximated best. Next interval constraints are applied to the remaining foot points such that their respective parameter values t_m are in successive order. If the computed values of foot points do not fit the constraint interval, the boundary point with the minimal distance is chosen.

The evolution rule consists of comparing coordinates of the curve velocity (3) with respect to some orthonormal basis of \mathbb{R}^{12} with the coordinates of the difference vector from foot point to target point. This produces an overconstrained system which is solved in least square sense. Hence the shape parameters Sp_{p_l} approximately change with the corresponding amount and the process

Table 2. Final shape parameters

x_0	x_1	x_2	x_3	x_5	x_6	x_7
5.822	-0.213	0.2	-0.337	-329.055	82.644	-100.544
y_0	y_1	y_2	y_3	y_5	y_6	y_7
6.084	0.051	-0.244	0.287	-8.987	-749.392	937.288
z_0	z_1	z_2	z_3	z_5	z_6	z_7
4.926	0.061	0.181	0.384	-99.5	-423.666	34.386

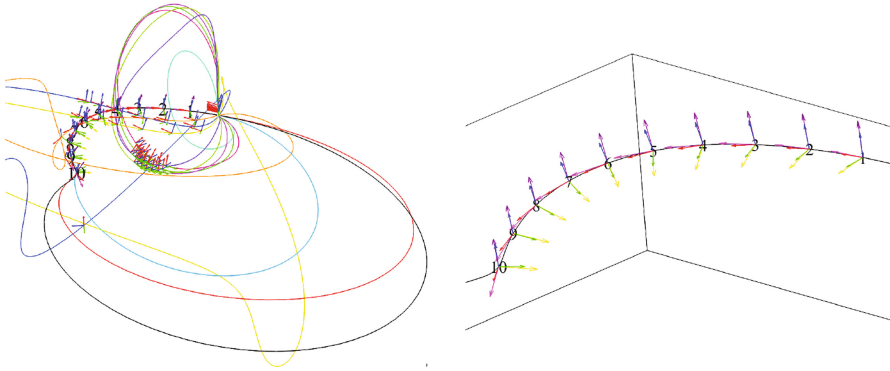


Fig. 1. TCP trajectory and orientation during the evolution process

Table 3. Variation of angle (in radians) and distance

TP _s	TP ₁	TP ₂	TP ₃	TP ₄	TP ₅	TP ₆	TP ₇	TP ₈	TP ₉	TP ₁₀
ϕ	0.061	0.102	0.125	0.139	0.124	0.106	0.08	0.061	0.151	0.421
t	0.922	1.488	1.38	1.182	1.522	2.689	4.914	8.26	3.736	4.336

is repeated again starting with the foot point computation. The final results are presented in Table 2 with a three decimal digit precision. The evolution process itself is visualized in Fig. 1. The target poses are labelled from 1 to 10, the angles and distances to the respective target poses are given in Table 3. It can be seen that the distances are quite good while the orientation seems to be hard to match. The reasons for this are under investigation. We conjecture an inappropriate distribution of feature points.

After the motion curve $C(t) = (t - \mathbf{x})(t - \mathbf{y})(t - \mathbf{z})$ is obtained we can start the synthesis of the overconstrained 6R linkage using motion factorization [4] as explained in Sect. 2. First the quadratic factors M_i are computed by multiplying the curve with it's quaternion conjugate:

$$C\bar{C} = (t^2 - 12.165t + 37.143)(t^2 - 11.648t + 34.116)(t^2 - 9.853t + 24.456) \quad (7)$$

By selecting the first quadratic factor from (7) polynomial division (a variant of Euclid’s algorithm taking into account the non-commutativity of quaternion multiplication) is used to divide $C(t)$ and single out the remainder

$$\begin{aligned}
 &(-59.057i\epsilon - 0.191i - 9.9j\epsilon + 0.036j - 13.531k\epsilon + 0.134k - 16.841\epsilon \\
 &\quad + 0.352)t + 347.317i\epsilon + 1.143i + 70.062j\epsilon - 0.222j + 80.891k\epsilon \quad (8) \\
 &\quad - 0.667k + 94.976\epsilon - 2.208
 \end{aligned}$$

The constant term h_{13} in the rightmost factor is computed as a unique root of this linear remainder polynomial:

$$h_{13} = i(30.463\epsilon + 0.135) + j(16.643\epsilon + 0.135) + k(19.361\epsilon - 0.329) + 6.084 \quad (9)$$

After the first root is computed $C(t)$, is divided by $t - h_{13}$ and the process is iterated with the quotient and with one of the remaining quadratic factors from (7). After the second root is computed the quotient will be the last linear factor. All the possible combinations in which the quadratic factor can be chosen will produce six different open 3R kinematic chains. Suitable combinations [4] then give overconstrained 6R linkages. Four examples are depicted in Fig. 2.

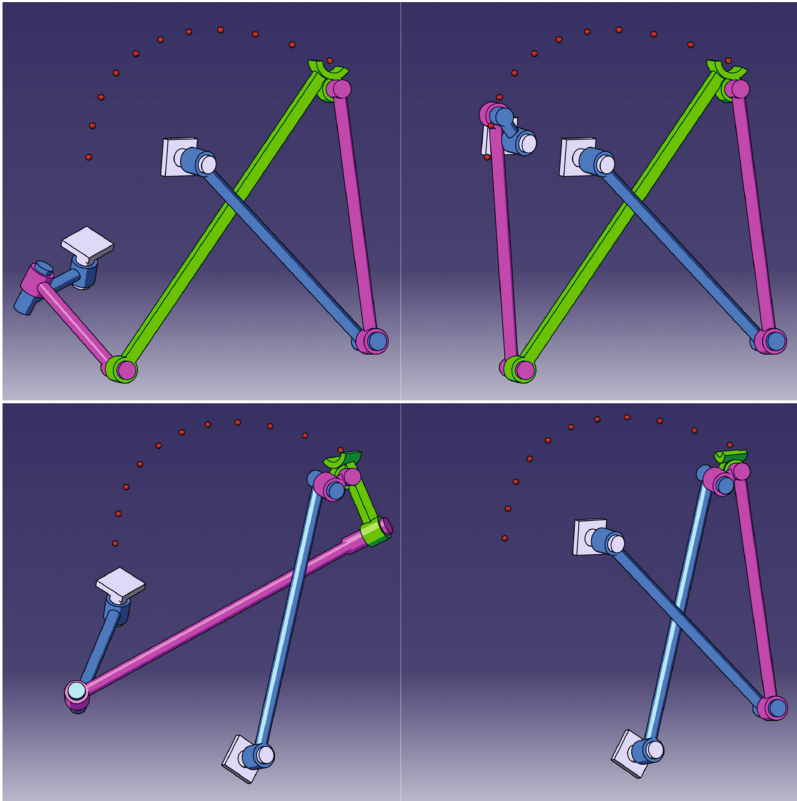


Fig. 2. Four different 6R linkages obtained

5 Conclusions

We used properties of the factorized representation of rational motions to set-up an evolution process for optimal design of corresponding linkages. The evolution gives an open kinematic chain that, if desired, can be combined with other chains obtained from different factorizations to produce overconstrained linkages. From a mechanical point of view, overconstrained linkages are robust, need minimal control elements and they are ideal for repetitive motions in an interval. In Sect. 4 we illustrated this process for an overconstrained 6R linkage. So far, position matching is good while matching orientations should be improved.

The construction relies on the factorized representation which helps to ensure validity of the Study condition throughout the evolution and automatically relates the rational motion to kinematic chains. Moreover, rationality allows efficient and stable computation of footpoints which is a crucial part in any evolution based mechanism synthesis.

Acknowledgements. The research was supported by the Austrian Science Fund (FWF): P 26607 (Algebraic Methods in Kinematics: Motion Factorisation and Bond Theory).

References

1. Aigner, M., Šír, Z., Jüttler, B.: Evolution-based least-squares fitting using Pythagorean hodograph spline curves. *Comput. Aided Geom. Des.* **24**(6), 310–322 (2007)
2. Aigner, M., Jüttler, B.: Hybrid curve fitting. *Computing* **79**(2), 237–247 (2007)
3. Cabrera, J.A., Simon, A., Prado, M.: Optimal synthesis PF mechanisms with genetic algorithms. *Mech. Mach. Theory* **37**(10), 1165–1177 (2002)
4. Hegedüs, G., Schicho, J., Schröcker, H.-P.: Factorization of rational curves in the study quadric and revolute linkages. *Mech. Mach. Theory* **69**(2), 142–152 (2013)
5. Hegedüs, G., Schicho, J., Schröcker, H.-P.: Four-pose synthesis of angle-symmetric 6R linkages. *J. Mech. Robot.* **7**(4), 50–57 (2015)
6. Hofer, M., Pottmann, H.: Energy-minimizing splines in manifolds. *Trans. Graphics* **23**(3), 284–293 (2004). *Proceedings of ACM SIGGRAPH 2004*
7. Hofer, M., Pottmann, H., Ravani, B.: From curve design algorithms to the design of rigid body motions. *Vis. Comput.* **20**(5), 279–297 (2004)
8. Hofer, M., Pottmann, H., Ravani, B.: Geometric design of motions constrained by a contacting surface pair. *Comput. Aided Geom. Des.* **20**(8), 523–547 (2003)
9. Husty, M.L., Schröcker, H.-P.: Algebraic geometry and kinematics. In: *Nonlinear Computational Geometry*, pp. 85–107 (2009)
10. Larochelle, P.M., Murray, A.P., Angeles, J.: SVD and PD based projection metrics on $SE(n)$. In: Lenarčič, J., Galetti, C. (eds.) *On Advances in Robot Kinematics*, pp. 13–22. Kluwer Academic Publishers, Dordrecht (2004)
11. Paradis, M.J., Willmert, K.D.: Optimal mechanism design using the Gauss constrained method. *J. Mech. Trans. Autom.* **105**(2), 187–196 (1983)

12. Schröcker, H.-P., Jüttler, B., Aigner, M.: Evolving four-bars for optimal synthesis. In: Proceedings of the Second European Conference on Mechanism Science, EUROMES 2008, pp. 109–116 (2009)
13. Zhang, X., Zhou, J., Ye, Y.: Optimal mechanism design using interior-point methods. *Mech. Mach. Theory* **31**(1), 83–98 (2000)

The Instantaneous Screw Axis of Motions in the Kinematic Image Space

Martin Pfurner^(✉) and Josef Schadlbauer

Unit Geometry and CAD, University of Innsbruck, Innsbruck, Austria
{martin.pfurner, josef.schadlbauer}@uibk.ac.at

Abstract. In the velocity analysis of mechanisms the instantaneous screw axes and the corresponding axodes play an important role. The instantaneous screw axis is computed via the velocity operator, this is the skew-symmetric matrix $\dot{\mathbf{A}}\mathbf{A}^T$, where \mathbf{A} is the transformation matrix. From this operator the Plücker coordinates of the instantaneous screw axis are known. When the Study parameters of a one parametric motion are given a direct computation of the instantaneous screw axis would be more convenient. Without computing \mathbf{A} and its derivative first, this paper shows a way of computing the instantaneous screw axis directly from the Study parameterization of the one parametric motion.

Keywords: Kinematic mapping · Axodes · Plücker coordinates · Velocity operator

1 Introduction

In kinematics the velocity operator for a given motion in Euclidean three-space is a well-known concept. In some applications it is important to determine the velocity distribution and the axodes, these are the ruled surfaces representing the instantaneous screw axis in the fixed and the moving frame of one parametric motions. Let $\mathbf{A}(t)$ be the homogeneous 4×4 matrix description of such a one parametric motion in \mathbb{E}^3 . The matrix representation of the velocity operator is then given by the skew-symmetric 4×4 matrix

$$\Omega = \mathbf{A}\dot{\mathbf{A}} = \begin{pmatrix} 0 & 0 & 0 & 0 \\ \tau_x & 0 & -\omega_z & \omega_y \\ \tau_y & \omega_z & 0 & -\omega_x \\ \tau_z & -\omega_y & \omega_x & 0 \end{pmatrix}. \quad (1)$$

The matrix representation in Eq. (1) is often rearranged to the vector notation, the so-called velocity screw $\mathbf{v} = (\omega_x, \omega_y, \omega_z, \tau_x, \tau_y, \tau_z)^T$, as stated by Bottema and Roth [2] or Husty et al. [4]. Its entries determine the linear and angular velocities.

In the last centuries Study parameters, a point model for Euclidean displacements, were of great benefit in the investigation of kinematic properties of

mechanisms [5]. In this model one parameter motions are curves in the so-called Study quadric S_6^2 , which carries all points in the kinematic image space that correspond to Euclidean displacements. Recently it turned out that S_6^2 can be neglected for some problems [6], for example for motion design in P^7 .

To the best of the authors knowledge until now there exists no such velocity operator in the kinematic image space, not for curves on nor off the Study quadric. Therefore one has to map the curve from P^7 back to the matrix description in \mathbb{E}^3 and compute the velocity screw and the axodes there.

The scope of this paper is to investigate an operator that acts on the Study parameters directly to compute the linear and angular velocities and furthermore the instantaneous screw axes. These facts are shown for some examples.

The paper is organized as follows: In Sect. 2 a brief introduction to the used notations and theories will be stated, which will be applied in Sect. 2.1 for curves in the Study quadric and Sect. 2.2 for curves not included in the Study quadric. The final Sect. 3 will show examples, such as the well-known $RPRP$ and the Bennett mechanism, and finally for a motion given by a line not included in the Study quadric, which corresponds to a vertical Darboux motion.

2 Velocity Operator in Kinematic Image Space

Let the coordinates in kinematic image space P^7 be denoted by the homogeneous coordinates $(\mathbf{x}, \mathbf{y})^\top$, with $\mathbf{x} = (x_0, x_1, x_2, x_3)^\top$ and $\mathbf{y} = (y_0, y_1, y_2, y_3)^\top$. For the following computations $(\mathbf{x}, \mathbf{y})^\top$ is defined as column vector. Since [6] it is known that curves in kinematic image space correspond to Euclidean motions in the task space \mathbb{E}^3 , nevertheless if they are in the Study quadric, which can be written as

$$x_0y_0 + x_1y_1 + x_2y_2 + x_3y_3 = 0 \iff \langle \mathbf{x}, \mathbf{y} \rangle = \mathbf{x}^\top \cdot \mathbf{y} = 0 \tag{2}$$

or off the Study quadric.

In the following $\mathbf{m}(t) = (\mathbf{p}(t), \mathbf{q}(t))^\top$, where $\mathbf{p}(t) = (p_0(t), \dots, p_3(t))^\top$ and $\mathbf{q}(t) = (q_0(t), \dots, q_3(t))^\top$, should describe a curve (or a one parameter motion) in P^7 . For brevity the parameter t is avoided in the notation and $\dot{\mathbf{m}}$ denotes the derivative with respect to t . The curve $\mathbf{m}_\infty = (\mathbf{0}, \mathbf{p})^\top$ lies in the exceptional generator of the Study quadric, this is the three space represented by $x_0 = x_1 = x_2 = x_3 = 0$ and is connected with the original curve via the fibrization in [6]. A fiber through an arbitrary point $(x_0 : \dots : y_3)$ outside the exceptional generator is defined by the straight line

$$(x_0 : x_1 : x_2 : x_3 : y_0 + tx_0 : y_1 + tx_1 : y_2 + tx_2 : y_3 + tx_3), \tag{3}$$

where t is the parameter of the line. The intersection points with the Study quadric correspond to the parameter values $t_1 = \infty$ and $t_2 = -\langle \mathbf{x}, \mathbf{y} \rangle / \langle \mathbf{x}, \mathbf{x} \rangle$. Note that the point of intersection with $t = \infty$ lies in the exceptional generator.

For the following inspections we use normalized coordinates, which means that $x_0^2 + x_1^2 + x_2^2 + x_3^2 = 1$, which is no loss of generality.

2.1 Curves in the Study Quadric

At first we restrict the curve $\mathbf{m} = (\mathbf{p}, \mathbf{q})^\top$ to be contained in the Study quadric. Then it is straight forward to compute the operator Σ by collecting the coefficients of the derivatives in the vectorial version of the velocity screw $\mathbf{A}\dot{\mathbf{A}}$. It can be written as

$$\Sigma = \begin{pmatrix} -p_1 & p_0 & -p_3 & p_2 & 0 & 0 & 0 & 0 \\ -p_2 & p_3 & p_0 & -p_1 & 0 & 0 & 0 & 0 \\ -p_3 & -p_2 & p_1 & p_0 & 0 & 0 & 0 & 0 \\ q_1 & -q_0 & q_3 & -q_2 & p_1 & -p_0 & p_3 & -p_2 \\ p_2 & -q_3 & -q_0 & q_1 & p_2 & -p_3 & -p_0 & p_1 \\ q_3 & q_2 & -q_1 & -q_0 & p_3 & p_2 & -p_1 & -p_0 \end{pmatrix} = \begin{pmatrix} \mathbf{P} & \mathbf{0} \\ \mathbf{Q} & -\mathbf{P} \end{pmatrix} \tag{4}$$

and this yields via

$$\mathbf{v} = \Sigma \cdot \dot{\mathbf{m}} = (\omega_x, \omega_y, \omega_z, \tau_x, \tau_y, \tau_z)^\top \tag{5}$$

the velocity screw. Using the notation $\mathbf{v}_\infty = (0, 0, 0, \omega_x, \omega_y, \omega_z)^\top$ the Plücker coordinates of the instantaneous screw axis can be written as

$$S_I = \mathbf{v} - \frac{\langle \dot{\mathbf{p}}, \dot{\mathbf{q}} \rangle}{\langle \dot{\mathbf{p}}, \dot{\mathbf{p}} \rangle} \cdot \mathbf{v}_\infty \tag{6}$$

where the coefficient $\langle \dot{\mathbf{p}}, \dot{\mathbf{q}} \rangle / \langle \dot{\mathbf{p}}, \dot{\mathbf{p}} \rangle$ is the instantaneous pitch, which is zero for instantaneous rotations. Combining Eqs. (4), (5) and (6) yields

$$S_I = \Phi \cdot \dot{\mathbf{m}} = \begin{pmatrix} \mathbf{P} & \mathbf{0} \\ \mathbf{Q} - \frac{\langle \dot{\mathbf{p}}, \dot{\mathbf{q}} \rangle}{\langle \dot{\mathbf{p}}, \dot{\mathbf{p}} \rangle} \mathbf{P} & -\mathbf{P} \end{pmatrix} \cdot \dot{\mathbf{m}}. \tag{7}$$

Equation (7) yields an operator, which computes the Plücker coordinates of the instantaneous screw axes in the fixed frame using the motion \mathbf{m} and its derivative $\dot{\mathbf{m}}$, as long as \mathbf{m} lies in the Study quadric. The matrix Φ is a 6×8 matrix. Geometrically S_I are the Plücker coordinates of the fixed axode. Note that S_I really represent Plücker coordinates [8], because they fulfill the Plücker relation. Using the embedding of those line coordinates of P^5 in the kinematic image space P^7 like described in [9] the moving axode can be computed with the inverse transformation.

2.2 Curves Not Contained in the Study Quadric

Lets consider $\mathbf{m}^* = (\mathbf{p}^*, \mathbf{q}^*)^\top$ to be a curve in $P^7 \notin S_6^2$, i.e. $\langle \mathbf{p}^*, \mathbf{q}^* \rangle \neq 0$. The derivative of \mathbf{m}^* with respect to t is denoted by $\dot{\mathbf{m}}^*$. Because of the fibrization shown in Eq. (3) the curve \mathbf{m}^* and its derivative $\dot{\mathbf{m}}^*$ are pulled onto S_6^2 and its tangent space, respectively, by

$$\mathbf{m} = \Pi \cdot \mathbf{m}^*, \quad \dot{\mathbf{m}} = \overline{\Pi} \cdot \dot{\mathbf{m}}^* \tag{8}$$

where

$$\Pi = \begin{pmatrix} \mathbf{I}_4 & \mathbf{0}_4 \\ -\langle \mathbf{p}^*, \mathbf{q}^* \rangle \mathbf{I}_4 & \mathbf{I}_4 \end{pmatrix} \tag{9}$$

and

$$\overline{\Pi} = \begin{pmatrix} \mathbf{I}_4 & \mathbf{0}_4 \\ \langle \mathbf{p}^*, \mathbf{q}^* \rangle (2\mathbf{p}^* \cdot \mathbf{p}^{*\top} - \mathbf{I}_4) - \mathbf{p}^* \cdot \mathbf{q}^{*\top} \mathbf{I}_4 - \mathbf{p}^* \cdot \mathbf{p}^{*\top} & \end{pmatrix}. \tag{10}$$

Note, that $\Pi = \overline{\Pi} = \mathbf{I}_8$ if $\mathbf{m}^* \in S_6^2$. This can be computed by using the equation $\langle \mathbf{p}^*, \mathbf{q}^* \rangle + \langle \dot{\mathbf{p}}^*, \mathbf{q}^* \rangle = 0$, which is the derivative of $\langle \mathbf{p}^*, \mathbf{q}^* \rangle$.

To compute the instantaneous screw axes S_I of the motion given by \mathbf{m}^* , Eq. (7) has to be applied to the projected curve \mathbf{m} and the projected derivative $\dot{\mathbf{m}}$ computed in Eq. (8).

3 Examples

To illustrate this process, the fixed and the moving axode will be computed for some one parametric motions.

3.1 The RPRP Mechanism

The RPRP is a single-loop four bar mechanism with two revolute (R) and two prismatic (P) joints (see for example [3]). The motion of the coupler [7] is given by

$$\mathbf{m} = \frac{1}{\Delta} \left(0, -6t, 6, 0, 0, \sqrt{3}(12t + 5\sqrt{3}), \sqrt{3}t(12t + 5\sqrt{3}), -12(t^2 + 1) \right)^\top \tag{11}$$

where $\Delta = (-2 + \sqrt{3})/\sqrt{(7 - 4\sqrt{3})(t^2 + 1)}$, which is a curve in S_6^2 . Therefore we can use the theory in Sect. 2.1 to compute

$$\Phi = \frac{1}{\Delta} \begin{pmatrix} t & 0 & 0 & 1 & 0 & 0 & 0 & 0 \\ -1 & 0 & 0 & t & 0 & 0 & 0 & 0 \\ 0 & -1 & -t & 0 & 0 & 0 & 0 & 0 \\ \frac{1}{6}\sqrt{3}\delta_1 & 0 & -2t^2 - 2 & -\frac{1}{6}\sqrt{3}\delta_2 & -t & 0 & 0 & -1 \\ \frac{1}{6}\sqrt{3}\delta_2 & 2t^2 + 2 & 0 & \frac{1}{6}\sqrt{3}\delta_1 & 1 & 0 & 0 & -t \\ -2t^2 - 2 & \frac{1}{6}\sqrt{3}\delta_2 & -\frac{1}{6}\sqrt{3}\delta_1 & 0 & 0 & 1 & t & 0 \end{pmatrix} \tag{12}$$

with $\delta_1 = (-12t^3 + 5\sqrt{3})$ and $\delta_2 = (24t^2 + 12 + 5t\sqrt{3})$. Then the instantaneous screw axis, and therefore the Plücker coordinates of the fixed axode are

$$S_I = \Phi \cdot \dot{\mathbf{m}} = (0, 0, 1, 4t, 2(t^2 - 1), 0)^\top. \tag{13}$$

The moving axode can be computed via the inverse transformation and can be written as

$$(0, 0, t^2 + 1, 4(t^3 - t^2s + ts^2 + s), 2(t^2s^2 - 3t^2 + 4ts - s^2 - 1), 0)^\top \tag{14}$$

where t is the parameter of the motion and s is the parameter on the surface. Figure 1 shows the fixed axode and some discrete copies of the moving axode (in the base frame) during the motion.

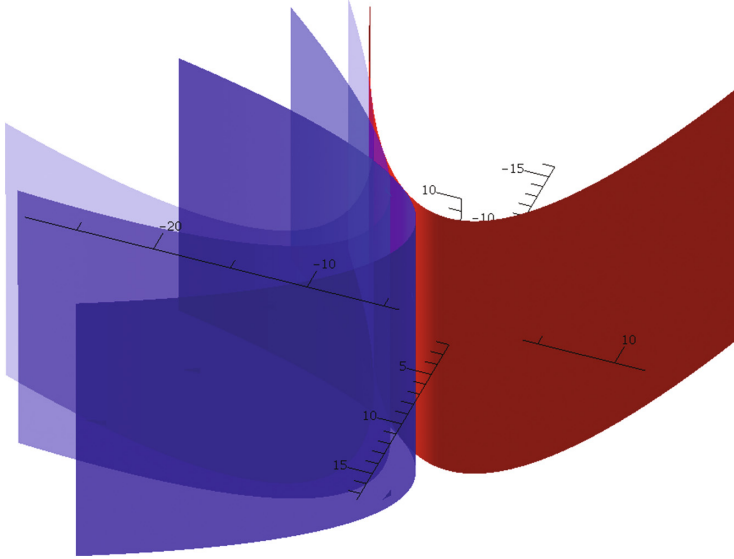


Fig. 1. Fixed axode (red) and some discrete copies of the moving axode (blue) of the RPRP (Color figure online)

3.2 Bennett Mechanism

Despite the spherical or planar four-bar, the Bennett mechanism is the only spatial single-loop closed four bar with revolute joints only [1]. The motion of the coupler [7] is given by

$$\mathbf{m} = \frac{1}{\Delta\sqrt{t^2 + 1}} \begin{pmatrix} 0 \\ (2 - \sqrt{2})t \\ \sqrt{2}/2(t^2 - 2\sqrt{2} + 3) \\ -1/2(\sqrt{3}\sqrt{2} - 2\sqrt{3} - 2\sqrt{2} + 2)(t^2 + 1) \\ 0 \\ 3/2(\sqrt{3}\sqrt{2} - 2\sqrt{3} - 2\sqrt{2} + 2)t \\ 3/4(3\sqrt{3}\sqrt{2} - 4\sqrt{3} - 4\sqrt{2} + 6)(t^2 + 2\sqrt{2} + 3) \\ -3/4(2 - \sqrt{2})(t^2 + 1) \end{pmatrix} \tag{15}$$

with $\Delta = \sqrt{(t^2 + 1)(3\sqrt{3}\sqrt{2} - 4\sqrt{3} - 5\sqrt{2} + 8) - 6\sqrt{2} + 8}$ and the instantaneous screw axis is

$$S_I = \begin{pmatrix} -8(\sqrt{2} + \sqrt{3})t \\ -4(\sqrt{2} + \sqrt{3})(t^2 - 1) \\ -4(1 + \sqrt{2})((\sqrt{2} - 1)^2 - t^2) \\ -6/\delta((\sqrt{3} + 1)^2 - 2t^2)((\sqrt{2} - 1)^2 - t^2)t \\ -3/\delta((\sqrt{3} + 1)^2 - 2t^2)((\sqrt{2} - 1)^2 - t^2)(t^2 - 1) \\ 3/\delta((\sqrt{3} + 1)^2 - 2t^2)(\sqrt{3}\sqrt{2} - \sqrt{3} - \sqrt{2} + 2)(t^2 + 1)^2 \end{pmatrix} \tag{16}$$

with $\delta = \sqrt{3}\sqrt{2}t^2 + t^4 - \sqrt{3}t^2 + \sqrt{2}t^2 - 2\sqrt{3}\sqrt{2} - t^2 + 3\sqrt{3} - 4\sqrt{2} + 6$.

Although computation with the operator Φ is quite simple the expressions, also in this simple example, are too complicated to be displayed here. The corresponding axodes are plotted in Fig. 2.

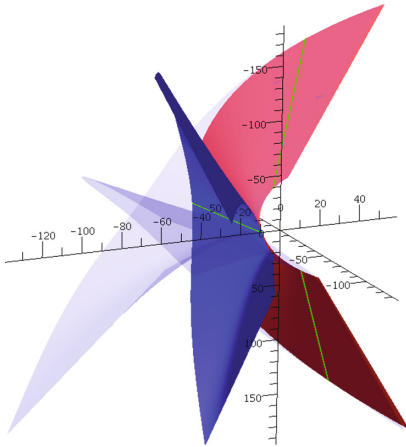


Fig. 2. Fixed axode (red) and some discrete copies of the moving axode (blue) of the Bennett (Color figure online)

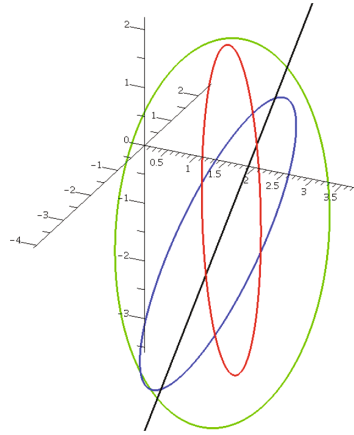


Fig. 3. Some point paths during the motion given by \mathbf{m}^*

3.3 Straight Line in P^7

As an example for a curve not included in the Study quadric, consider the connecting line $\mathbf{m} = \mathbf{a}_1 \vee \mathbf{a}_2$ of the two arbitrarily chosen points $\mathbf{a}_1 = (5, 6, 7, 8, 13, 7, 9, 2)^\top$ and $\mathbf{a}_2 = (9, 3, 1, 7, 13, 5, 13, 17)^\top$. A parameterization of this line is given by

$$\mathbf{m}^*(t) = \frac{1}{\Delta}(-4t + 9, 3t + 3, 6t + 1, t + 7, 13, 2t + 5, -4t + 13, -15t + 17)^\top, \quad (17)$$

with $\Delta = \sqrt{62t^2 - 28t + 140}$.

As an example of a curve not contained in S_6^2 the theory developed in Sect. 2.2 is applied. At first the line \mathbf{m}^* has to be pulled to the Study Quadric using Π of Eq. (9). This yields

$$\mathbf{m} = \begin{pmatrix} (9 - 4t)/\Delta \\ 3(t + 1)/\Delta \\ (6t + 1)/\Delta \\ (t + 7)/\Delta \\ -(132t^3 - 923t^2 - 1097t + 556)/\Delta^3 \\ (223t^3 + 488t^2 - 517t - 92)/\Delta^3 \\ -(50t^3 - 1221t^2 + 2463t - 1556)/\Delta^3 \\ -(897t^3 - 1750t^2 + 2525t - 532)/\Delta^3 \end{pmatrix} \quad (18)$$

with $\Delta = \sqrt{62t^2 - 28t + 140}$.

In the second step $\dot{\mathbf{m}}^*$ has to be mapped to the tangent space of $S_{\mathfrak{g}}^2$ using $\overline{\Pi}$ of Eq. (10) to compute

$$\dot{\mathbf{m}} = \begin{pmatrix} -2(251t + 217)/\Delta^3 \\ -6(38t - 77)/\Delta^3 \\ -2(73t - 427)/\Delta^3 \\ -14(32t - 17)/\Delta^3 \\ -2(25841t^3 + 102195t^2 - 188607t - 65114)/\Delta^5 \\ -2(19811t^3 - 75468t^2 - 73257t + 38122)/\Delta^5 \\ -18(4089t^3 - 14851t^2 - 999t + 15526)/\Delta^5 \\ -2(35413t^3 + 44070t^2 - 177849t + 165578)/\Delta^5 \end{pmatrix}. \quad (19)$$

As shown in [6] the resulting motion \mathbf{m} is a vertical Darboux motion, i.e. a rotation around a fixed axis combined with a harmonic oscillation along the same axis. In this motion all point paths are ellipses, as shown in Fig. 3 for some points. Therefore the fixed and moving axodes have to be fixed lines in this example. They can be written as

$$S_I = (-1414, 53732, 36764, -2560, -70279, 102617)^T. \quad (20)$$

4 Conclusions

This article shows how to compute the instantaneous screw axis directly from curves on the Study quadric. Furthermore it was shown how to pull a curve and its derivative onto the Study quadric and its tangent space, respectively, via a fibrization of the kinematic image space.

A developed operator in this publication can be used to directly compute the axodes of a given motion in P^7 .

The benefit of this work is that all the operators can be used on normalized Study parameters and there is no need to use the matrix representation of Euclidean displacements.

References

1. Bennett, G.: A new mechanism. *Engineering* **76**, 777–778 (1903)
2. Bottema, O., Roth, B.: *Theoretical Kinematics*. North-Holland Publishing Company, New York (1979)
3. Grünwald, A.: Die kubische Kreisbewegung eines starren Körpers. *Z. Math. Phys.* **55**, 264–296 (1907)
4. Husty, M.L., Karger, A., Sachs, H., Steinhilper, W.: *Kinematik und Robotik*. Springer, Berlin (1997)
5. Husty, M.L., Schröcker, H.P., Pfurner, M.: Algebraic methods in mechanism analysis and synthesis. *Robotica* **25**(6), 661–675 (2007)
6. Pfurner, M., Schröcker, H.P., Husty, M.L.: Path planning in kinematic image space without the study condition. In: Lenarčič, J., Merlet, J.P. (eds.) *Advances in Robot Kinematics*, France, pp. 290–297 (2016). <https://hal.archives-ouvertes.fr/hal-01339423>

7. Pffurner, M., Stigger, T., Husty, M.L.: Overconstrained single loop four link mechanisms with revolute and prismatic joints. In: Wenger, P., Flores, P. (eds.) Mechanism and Machine Science, New Trends in Mechanism and Machine Science, Theory and Industrial Applications, Nantes, France, vol. 43 (2016)
8. Pottmann, H., Wallner, J.: Computational Line Geometry. Springer, Heidelberg (2001)
9. Schadlbauer, J.: Algebraic methods in kinematics and line geometry. Ph.D. thesis, University of Innsbruck (2014). <http://geometrie.uibk.ac.at/cms/datastore/schadlbauer/phd-thesis.pdf>

A New Insight into the Coupler Curves of the RCCC Four-Bar Linkage

Federico Thomas¹(✉) and Alba Pérez-Gracia²

¹ Institut de Robòtica I Informàtica Industrial (CSIC-UPC),
08028 Barcelona, Spain
fthomas@iri.upc.edu

² Department of Mechanical Engineering,
Idaho State University, Pocatello, ID 83209, USA
perealba@isu.edu

Abstract. Based on the condition for four points to lie on the unit sphere, derived using Distance Geometry, a new mathematical formulation for the coupler curves of the RCCC linkage is presented. The relevance of this formulation is not only its simplicity, but the elegant way in which we can obtain the derivative of any variable with respect to any other, and the simple way in which intervals of monotonicity can be detected. All these results are compactly expressed in terms of Gramians and, as a consequence, they have a direct geometric meaning contrarily to what happens with previous approaches based on kinematic loop equations.

Keywords: RCCC linkage · Coupler curves · Distance geometry

1 Introduction

The RCCC linkage is the most general spatial four-bar linkage with mobility one [1]. This linkage has been proved to be a good testbed in which to try and evaluate new ideas concerning the analysis of spatial linkages [2]. The spatial coupler curves of the RCCC linkage were studied in [3] using an analytic approach based on 3×3 orthogonal transformation matrices with dual number elements. This approach has become the standard formulation in most subsequent analysis of this linkage [4, 5].

In Fig. 1 shows a CCCC linkage from which an RCCC linkage can be derived by blocking the sliding motion of any of its cylindrical joints. In this linkage, the two parameters which describe the kinematics of the joint i ; namely, the angular displacement denoted as θ_i and the joint offset denoted as d_i , can be combined into the dual angle $\hat{\theta}_i = \theta_i + \varepsilon d_i$. The two parameters describing the geometry of link i ($i = 1, \dots, 4$), namely, the twist angle denoted as $\theta_{i,i+1}$ and the link length denoted as $d_{i,i+1}$, can be combined into the dual angle $\hat{\theta}_{i,i+1} = \theta_{i,i+1} + \varepsilon d_{i,i+1}$ where ε stands for the dual unit which is defined as $\varepsilon^2 = 0$, $\varepsilon \neq 0$. Observe that $\theta(d)$, with only a subindex, denotes the angular

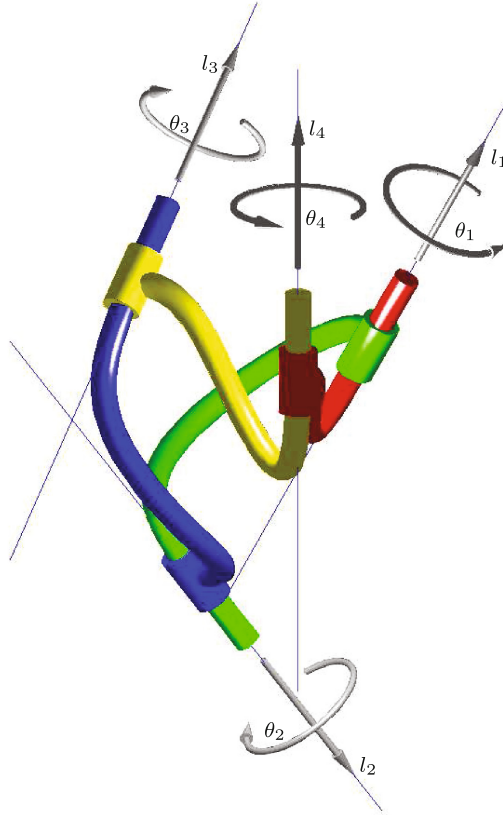


Fig. 1. Notation associated with the joints of a CCCC linkage.

displacement (joint offset) of the joint defined by the subindex; and, with two subindices, denotes the twist angle (link length) between the two axes defined by the two subindices. This notation does not comply with the standard, but it simplifies the formulation given below and avoids possible confusions between standard and modified DH parameters. The axes I_1 , I_2 , and I_3 , and I_4 can be transferred to the dual space as the four points P_1 , P_2 , P_3 and P_4 , respectively, all lying on the dual unit sphere. Therefore, the position analysis of the CCCC linkage in the Euclidean space is equivalent to solving the position analysis of the corresponding single-dof spherical four-bar linkage in the dual unit sphere. To this end, it is possible to derive the loop equation of this spherical four-bar linkage as the product of 3×3 orthogonal transformation matrices with dual number elements. By developing this matrix product, a system of nine nonlinear equations in four unknowns ($\theta_i, i = 1, \dots, 4$) is obtained [3, 6, 7]. Alternatively, we could also use dual quaternions in which case we would get four equations. Nevertheless, only three independent scalar equations are required to solve this position analysis because a four-bar linkage on the sphere has 1 dof. In this

paper we depart from these standard formulations based on a loop equation by deriving, using Distance Geometry on the sphere [8,9], a single scalar equation in two unknowns. The relevance of this equation is not only its simplicity, but the elegant way in which we can obtain the derivatives of any of the variables with respect to any other, including the geometric interpretation of local extrema, in terms of Gramians.

The rest of this paper is organized as follows. Section 2 concisely describes the new formulation and its basic properties. Section 3 gives the main clues on how this new formulation can be applied to a particular example. Finally, Sect. 4 gives some conclusions and prospects for future research.

2 Deriving a Single Scalar Closure Condition

In spherical geometry, the shortest distance between two points, also known as the geodesic distance, is the length of an arc of a great circle containing both points. This great circle is the result of intersecting the plane passing through the origin and the two points with the sphere. Then, the distance between two points on the unit sphere is $d(P_i, P_j) = \cos^{-1} \langle \mathbf{p}_i, \mathbf{p}_j \rangle$, the angle between the vectors from the origin to the points P_i and P_j which will be denoted by $\theta_{i,j}$. Here $\langle \mathbf{p}_i, \mathbf{p}_j \rangle$ is the standard Euclidean inner product.

The triangle inequality between three points on a sphere holds provided that the distance between any two points is the lowest of the two arcs of great circle with them as endpoints. Then, if we assume that $0 \leq \theta_{i,j} < \pi$, the mapping between $\theta_{i,j}$ and $\cos \theta_{i,j}$ becomes one-to-one. Observe that a link with twist angle $\theta_{i,j}$ is kinematically equivalent to a link with twist angle $2\pi - \theta_{i,j}$. Therefore, in what follows and as a matter of convenience, we will indistinctly use θ_{ij} or $\cos \theta_{ij}$ when referring to the distance between P_i and P_j .

Given the location vectors, $\mathbf{p}_1, \dots, \mathbf{p}_n$, of points P_1, \dots, P_n , the Gram determinant, or Gramian, is the determinant defined as

$$G(1, \dots, n) = \begin{vmatrix} \langle \mathbf{p}_1, \mathbf{p}_1 \rangle & \langle \mathbf{p}_1, \mathbf{p}_2 \rangle & \dots & \langle \mathbf{p}_1, \mathbf{p}_n \rangle \\ \langle \mathbf{p}_2, \mathbf{p}_1 \rangle & \langle \mathbf{p}_2, \mathbf{p}_2 \rangle & \dots & \langle \mathbf{p}_2, \mathbf{p}_n \rangle \\ \vdots & \vdots & \ddots & \vdots \\ \langle \mathbf{p}_n, \mathbf{p}_1 \rangle & \langle \mathbf{p}_n, \mathbf{p}_2 \rangle & \dots & \langle \mathbf{p}_n, \mathbf{p}_n \rangle \end{vmatrix}, \tag{1}$$

which, in the particular case in which all points lie on the unit sphere, reduces to

$$G(1, \dots, n) = \begin{vmatrix} 1 & \cos \theta_{1,2} & \dots & \cos \theta_{1,n} \\ \cos \theta_{1,2} & 1 & \dots & \cos \theta_{2,n} \\ \vdots & \vdots & \ddots & \vdots \\ \cos \theta_{1,n} & \cos \theta_{2,n} & \dots & 1 \end{vmatrix}. \tag{2}$$

Gramians are zero if, and only if, the involved coordinate vectors are linearly dependent, and strictly positive otherwise [10, p. 251]. Negative Gramians only arise in those situations in which the given interpoint distances do not correspond

to any configuration of real points. Since we limit our analysis to a sphere in three dimensions, a Gramian of four points necessarily vanishes. For the same reason, a Gramian of three points lying on a great circle also vanishes. Next, we analyze the four-point case in more detail.

If we have four points, say P_i, P_j, P_k and P_l , then

$$G(i, j, k, l) = \begin{vmatrix} 1 & \cos \theta_{i,j} & \cos \theta_{i,k} & \cos \theta_{i,l} \\ \cos \theta_{i,j} & 1 & \cos \theta_{j,k} & \cos \theta_{j,l} \\ \cos \theta_{i,k} & \cos \theta_{j,k} & 1 & \cos \theta_{k,l} \\ \cos \theta_{i,l} & \cos \theta_{j,l} & \cos \theta_{k,l} & 1 \end{vmatrix} \tag{3}$$

vanishes if, and only if, the four points lie on the three-dimensional unit sphere. Then, in what follows, $G(i, j, k, l)$ will be referred to as the *closure condition* for P_i, P_j, P_k and P_l .

Using a computer algebra system, it can be verified that (see [11] for details)

$$G(i, j)G(i, j, k, l) = -(G(i, j) \cos(\theta_{k,l}) + B(i, j, k, l))^2 + G(i, j, k)G(i, j, l), \tag{4}$$

where

$$B(i, j, k, l) = \begin{vmatrix} 1 & \cos \theta_{i,j} & \cos \theta_{i,k} \\ \cos \theta_{i,j} & 1 & \cos \theta_{j,k} \\ \cos \theta_{i,l} & \cos \theta_{j,l} & 0 \end{vmatrix}. \tag{5}$$

Now, since $G(i, j, k, l) = 0$, we can easily conclude that

$$\cos \theta_{k,l} = \frac{-B(i, j, k, l) + \sigma_{k,l} \sqrt{G(i, j, l)G(i, j, k)}}{G(i, j)}, \tag{6}$$

where

$$\sigma_{k,l} = \begin{cases} -1, & \text{if } P_k \text{ and } P_l \text{ lie on the two different hemispheres defined by} \\ & \text{the great circle containing } P_i \text{ and } P_j \\ +1, & \text{otherwise} \end{cases} \tag{7}$$

If $G(i, j, k)G(i, j, l) = 0$, there is only one solution for $\theta_{k,l}$. Clearly, this only happens when any of the two triangles $P_i P_j P_k$ and $P_i P_j P_l$ degenerate (i.e., when either P_k or P_l lies on the great circle defined by P_i and P_j) (Fig. 2).

If we derive (4) with respect to $\cos \theta_{k,l}$, we conclude, using (6), that

$$\frac{\partial G(i, j, k, l)}{\partial \cos \theta_{k,l}} = 2 \sigma_{k,l} G(i, j, k)G(i, j, l). \tag{8}$$

Similar expressions are obtained when deriving $G(i, j, k, l)$ with respect to the cosine of any other angle. Then, since $G(i, j, k, l) = 0$, using the theorem of implicit differentiation, we have, for example, that

$$\frac{\partial \cos \theta_{i,j}}{\partial \cos \theta_{k,l}} = -\frac{\partial G(i, j, k, l) / \partial \cos \theta_{k,l}}{\partial G(i, j, k, l) / \partial \cos \theta_{i,j}} = -\sigma_{i,j} \sigma_{k,l} - \sigma_{i,j} \sigma_{k,l} \sqrt{\frac{G(i, j, l)G(i, j, k)}{G(i, k, l)G(j, k, l)}}. \tag{9}$$

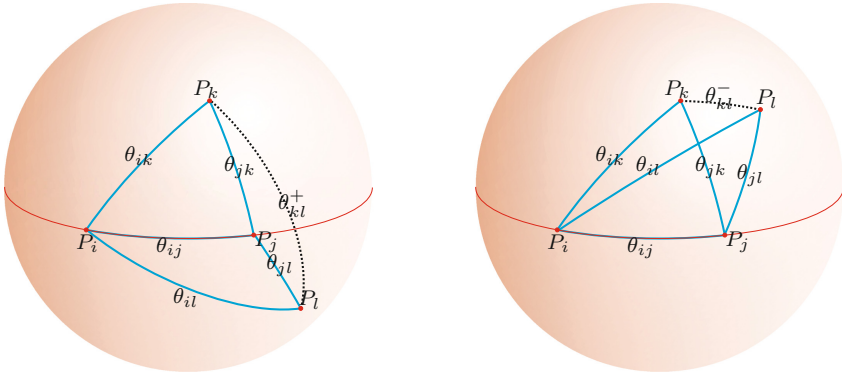


Fig. 2. Given four points on the unit sphere, P_i , P_j , P_k , and P_l , the distance between, say P_k and P_l , is determined by all other interpoint distances. In general, two solutions are possible which corresponds to the cis (left) and trans configuration (right).

It follows from this expression that the variation of $\theta_{i,j}$ with respect to that of $\theta_{k,l}$ is monotone provided that no three points involved in the Gramians inside the squared root get aligned (they lie on a great circle).

The derivative in (8) is also very helpful to obtain the dual component of the closure condition $G(i, j, k, l) = 0$ when extending it to dual angles. Let us denote this extension as $\widehat{G}(i, j, k, l) = 0$. Then, $\widehat{G}(1, 2, 3, 4) = 0$, in the dual variables $\hat{\theta}_{i,j} = \theta_{i,j} - \varepsilon d_{i,j}$, for $1 \leq i < j \leq 4$, can be expressed using the chain rule as follows:

$$\widehat{G}(1, 2, 3, 4) = G(1, 2, 3, 4) + \varepsilon \sum_{1 \leq i < j \leq 4} d_{i,j} \frac{\partial G(1, 2, 3, 4)}{\partial \cos \theta_{i,j}} \frac{\partial \cos \theta_{i,j}}{\partial \theta_{i,j}}. \tag{10}$$

This allows us to conclude, using (8), that the dual component of the closure condition can be expressed as

$$\sum_{1 \leq i < j \leq 4} \sigma_{i,j} d_{i,j} \sin \theta_{i,j} \sqrt{G(\{1, 2, 3, 4\} \setminus i) G(\{1, 2, 3, 4\} \setminus j)} = 0, \tag{11}$$

an elegant expression for the dual component of $\widehat{G}(1, 2, 3, 4) = 0$ of great compactness when compared with the results obtained using loop equations.

3 Example

Let us consider the CCCC linkage in Fig. 1 for which we want to obtain the coupler curve relating θ_4 as a function of θ_1 . This problem corresponds to the second example in [3]. In this particular case,

$$\hat{\theta}_{1,2} = 30^\circ + \varepsilon 2\text{cm}, \quad \hat{\theta}_{2,3} = 120^\circ + \varepsilon 3\text{cm}, \quad \hat{\theta}_{3,4} = 105^\circ + \varepsilon 4\text{cm}, \quad \hat{\theta}_{1,4} = 45^\circ + \varepsilon 3.5\text{cm},$$

and where the input joint offset, d_1 , is set to 6 cm.

If we only consider the real part of the closure condition $\widehat{G}(1, 2, 3, 4) = 0$, i.e. $G(1, 2, 3, 4) = 0$, we can readily plot θ_{13} as a function of θ_{24} using (6). The result appears in Fig. 3. In this plot, the Cartesian region defined by $[-1, 1] \times [-1, 1]$ can be divided into subregions attending to the signs of the Gramians resulting from taking all subsets of three points. Only the part of the curve inside the

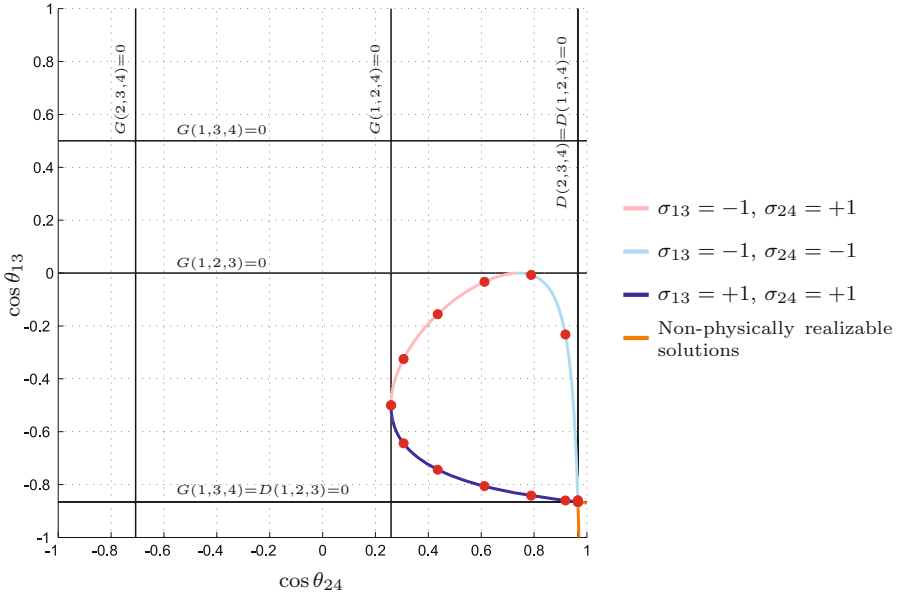


Fig. 3. Plot of $\cos \theta_{1,3}$ as a function of $\cos \theta_{2,4}$ (it can also be seen as the root locus of $G(1, 2, 3, 4) = 0$). The dots in red correspond to the linkage configurations reported in [3]. (Color figure online)

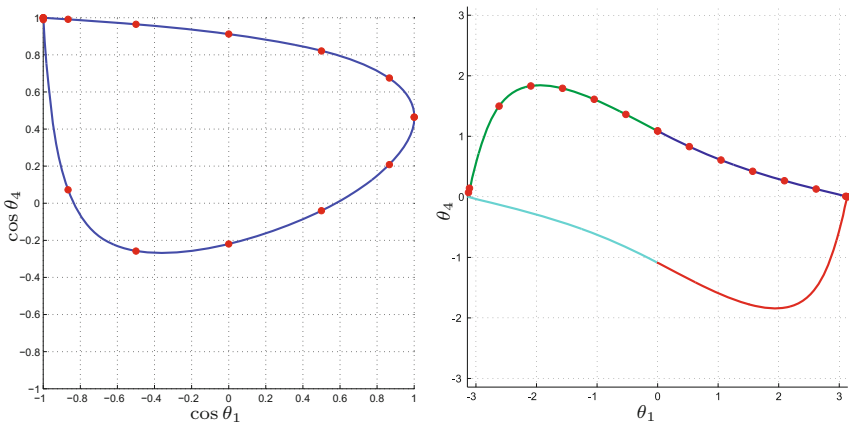


Fig. 4. Left: Curve relating $\cos \theta_4$ and $\cos \theta_1$ obtained from the curve in Fig. 3 using (13) and (12). Right: Coupler curve relating θ_1 and θ_4 . Again, the dots in red correspond to the linkage configurations reported in [3]. (Color figure online)

region where all these Gramians are positive has physical meaning. The boundaries between all these regions correspond to configuration where three points get aligned. The curve itself can also be subdivided into monotonic segments attending to the signs of $\sigma_{1,3}$ and $\sigma_{2,4}$. The points separating these segments also correspond to points where three points get aligned. As a consequence, these points are necessarily located on the boundary of the feasibility region. In general, we can have up to four such segments, but in this particular example we just have three because this mechanism has a configuration in which $G(1, 3, 4) = G(1, 2, 3) = 0$ which corresponds to the limiting position reported in [3]. At this position $\theta_1 = \pi$ and the coupler link and the output link are collinear, i.e., $\theta_3 = \pi$ (see [3] for more details). This mechanism has no configurations where $\sigma_{1,3} = +1$ and $\sigma_{2,4} = -1$, that is, configurations where P_1 and P_3 are located on the same hemisphere defined with respect to the great circle containing P_2 and P_4 , and where P_2 and P_4 are located on different hemispheres defined with respect to the great circle containing P_1 and P_3 .

Each point of the obtained curve gives a value for $\cos \theta_{24}$ and $\cos \theta_{13}$ from which we can obtain the values of $\cos \theta_i$, $i = 1, \dots, 4$, using the law of cosines for supplementary angles. In the particular case of $\cos \theta_1$ and $\cos \theta_4$ we have that:

$$\begin{aligned} \cos \theta_1 &= (-\cos \theta_{2,4} + \cos \theta_{1,4} \cos \theta_{1,2}) / (\sin \theta_{1,4} \sin \theta_{1,2}) \\ &= (-\cos \theta_{2,4} + 0.61237) / 0.35355 \end{aligned} \quad (12)$$

$$\begin{aligned} \cos \theta_4 &= (-\cos \theta_{1,3} + \cos \theta_{3,4} \cos \theta_{1,4}) / (\sin \theta_{3,4} \sin \theta_{1,4}) \\ &= (-\cos \theta_{1,3} - 0.18301) / 0.68301 \end{aligned} \quad (13)$$

Now, we can obtain the plot expressing $\cos \theta_4$ as a function of $\cos \theta_1$ that appears in Fig. 4(left). Since (12) and (13) are affine relations, the monotonicity of the three segments is preserved.

Finally, the coupler curve relating θ_4 and θ_1 can be obtained by computing the $\pm \arccos$ of both coordinates of each point of the curve in Fig. 4(left). This is a 1-to-4 mapping. Two of these images are not solutions of the problem because they do not satisfy the original kinematic constraints, i.e. the signs of $\theta_{1,2}$, $\theta_{2,3}$, $\theta_{3,4}$, and $\theta_{1,4}$. As with many problems solved in a distance space, when mapping the obtained solutions to an Euclidean space, they should be checked to satisfy some consistency constraints [12].

4 Conclusion

The position analysis of a RCCC linkage in the Euclidean space is equivalent to solving the position analysis of a spherical four-bar linkage in the dual unit sphere. If we try to solve this problem using Distance Geometry directly in the Euclidean space using Cayley-Menger determinants, the formulation becomes quite involved. In this paper, we have shown how the problem can be solved using Distance Geometry in the dual unit sphere. This result opens the possibility of using Cayley-Menger determinants with dual arguments to compactly formulate other geometric problems. This is a point that certainly deserves further attention.

Acknowledgements. This work has been partially supported by the Spanish Ministry of Economy and Competitiveness under project DPI2014-57220-C2-2-P, and by the National Science Foundation under Grant No. 1208385. The content of this paper is solely the authors' responsibility.

References

1. Yang, A.T., Freudenstein, F.: Application of dual-number quaternion algebra to the analysis of spatial mechanisms. *ASME J. Appl. Mech. Series E* **2**, 300–308 (1964)
2. Jamalov, R.I., Litvin, F.L., Roth, B.: Analysis and design of RCCC linkages. *Mech. Mach. Theory* **19**(4–5), 397–407 (1984)
3. Marble, S.D., Pennock, G.N.: Algebraic-geometric properties of the coupler curve of the RCCC spatial four-bar mechanism. *Mech. Mach. Theory* **35**(5), 675–693 (2000)
4. Bai, S., Angeles, J.: A unified input-output analysis of four-bar linkages. *Mech. Mach. Theory* **43**(2), 240–251 (2008)
5. Figliolini, G., Rea, P., Angeles, J.: The synthesis of the axodes of RCCC linkages. *ASME J. Mech. Robot.* **8**(2), 9 pages (2015). paper 021011
6. Thomas, F.: On the n-bar mechanism, or how to find global solutions to redundant single loop spatial kinematic chains. In: *IEEE International Conference on Robotics and Automation*, vol. I, pp. 403–408 (1992)
7. Fischer, I.S.: *Dual-Numer Methods in Kinematics, Statics and Dynamics*. CRC Press, New York (1998)
8. Audet, D.: Déterminants sphérique et hyperbolique de Cayley-Menger. *Bulletin de l'Association Mathématique du Québec* **51**(2), 45–52 (2011)
9. Maehara, H.: On spherical four-point-spaces. *J. Geom.* **107**(1), 1–8 (2016)
10. Gantmakher, F.R.: *The Theory of Matrices*, vol. 1. Chelsea Pub Co, New York (1984)
11. Porta, J.M., Thomas, F.: Distance-bound smoothing on the sphere. In: *IEEE International Conference on Robotics and Automation*, Singapore (2017)
12. Rojas, N.: *Distance-Based Formulations for the Position Analysis of Kinematic Chains*, Technical University of Catalonia, Spain (2012)

A Forward Kinematics Data Structure for Efficient Evolutionary Inverse Kinematics

Sebastian Starke^(✉), Norman Hendrich, and Jianwei Zhang

Department of Informatics, Group TAMS
(Technical Aspects of Multimodal Systems),
University of Hamburg, 22527 Hamburg, Germany
{starke,hendrich,zhang}@informatik.uni-hamburg.de

Abstract. Various approaches to solving inverse kinematics implicitly rely on computing forward kinematics in order to obtain an approximate solution. This work proposes an optimised data structure to efficiently compute these equations by avoiding redundant transformations and calculations. This is particularly relevant for highly articulated kinematic models and multiple end effectors with shared joints along their kinematic chains. By integrating the developed OFKT (Optimised Forward Kinematics Tree), less computation time within each iteration is required, which contributes to a significant speedup in convergence. Experiments were conducted using a novel evolutionary approach which was designed for handling complex kinematic geometries.

Keywords: Forward kinematics · Inverse kinematics · Data structures · Computational efficiency · Evolutionary optimisation · Robotics · Character animation

1 Introduction

A rigid body kinematic system can be described by a set of kinematic chains, each consisting of a consecutive set of segments and joints from the root to the end effectors. Each end effector results in a certain Cartesian configuration \mathcal{X} given a specific joint variable configuration θ . Together, the motion axes of the joints define the DOF (Degree of Freedom) and thus the computational complexity of the whole kinematic system. [1]

While forward kinematics (FK) is straightforward to compute by a consecutive set of coordinate transformations, obtaining solutions for inverse kinematics (IK) in contrast is not as easy. For any given IK query, a varying or even infinite number of solutions can exist, and it is not generally clear which one to prefer. However, IK takes an important role in various applications such as robotics, including object manipulation and grasping with anthropomorphic hands, as well as for character animation in computer graphics. Since analytical approaches to this problem are not generally available as they must be derived individually for specific kinematic structures, numerical algorithms for obtaining approximate solutions have become more popular. In order to optimise an appropriate solution for IK, such methods rely on calculating the FK equations using the known

kinematic structure. Then, sampling-based joint variable updates are generated using gradient-based or probabilistic techniques, and the Cartesian end effector configurations are calculated individually for each objective. Multiple end effector systems—such as the finger tips of an arm—usually contain many shared joints along their kinematic chains, and the FK equations then become partially equivalent. As a result, most computation time is typically required for repeated FK computation, and many transformations become redundant when only small joint variable changes are applied. This is especially the case for evolutionary approaches, for which the genetic operators—such as recombination and mutation—cause most joint variable configurations to be only slightly modified within each generation. Given the joint variables which correspond to the genes of an individual, the resulting end effector configurations $\mathcal{X}_{1,\dots,k}$ can be obtained by evaluating the FK function. Based on this, it is then possible to define the multi-objective fitness function Ω to be minimised as the root-mean-square error over all individually weighted objectives $\mathcal{L}_{1,\dots,k}$ with end effector targets $\mathcal{Y}_{1,\dots,k}$.

$$\phi = \Omega(x) = \sqrt{\frac{1}{k} \sum_{i=1}^k w_i \mathcal{L}_i^2(\mathcal{X}_i, \mathcal{Y}_i)} \quad (1)$$

Repeated evaluation of the fitness ϕ of each individual within the population then drives the evolutionary optimisation. Hence, efficient computation of the FK is essential for the overall performance and convergence of the IK algorithm. Figure 1 demonstrates solving articulated IK of the Kyle humanoid, with the OFKT (Optimised Forward Kinematics Tree) data structure integrated to achieve higher computational efficiency for repeated and only slightly varying joint variable queries.

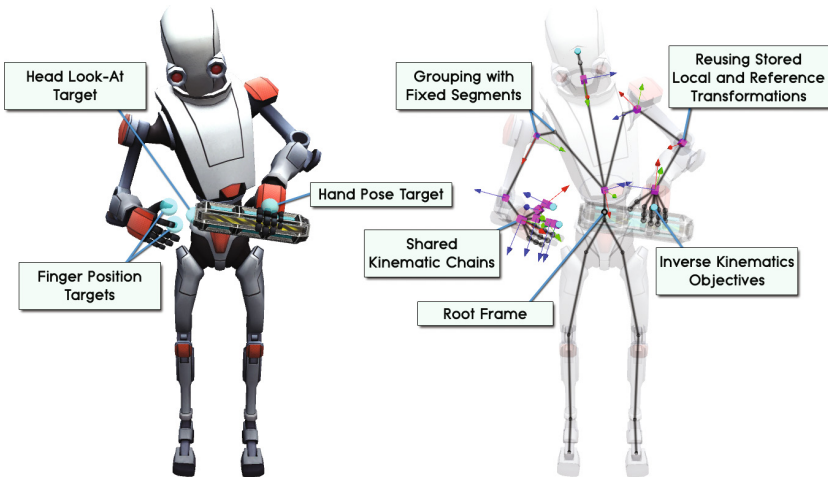


Fig. 1. Kinematic geometry from the pelvis to the head and finger tips of the Kyle humanoid (28 DOF). Inverse kinematics is solved by evolutionary computation while efficiently calculating forward kinematics using the OFKT data structure.

2 Background and Related Work

Solving IK is a fundamental problem which is relevant in very different fields of research, such as robotics, computer graphics or human-computer interaction. Typical scenarios include control of virtual characters and runtime manipulation of underlying animations, grasping with anthropomorphic hands, teleoperation tasks as well as motion planning and trajectory generation. Therefore, numerous sophisticated approaches have been developed that tackle the problem by the specific requirements of their applications, typically regarding computational efficiency, accuracy or flexibility. The numerical methods can be categorised into four groups: gradient-based, probabilistic, geometric or learning. In this work, we will primarily focus on the former two as they require generating FK samples for IK optimisation.

Considering the FK calculation for a given a kinematic structure, homogeneous coordinate transformations in robotics are commonly represented using Denavit-Hartenberg parameters, which can achieve a considerable reduction in the required amount of calculations [4,5]. Implementing rotations by quaternions rather than matrices is slightly more efficient from a computational perspective, and also offers a unique representation for the resulting orientations. Furthermore, information about axis alignments in serial or parallel mechanisms can be incorporated [2,3]. However, those computational optimisations are only appropriate for specific geometries and must be derived individually. It is also possible to learn the FK equations by neural networks which can be used to create a functional relation between joint and Cartesian space [6]. Nevertheless, this method introduces an additional inaccuracy for the numerical IK optimisation due to the inherent learning error.

Gradient-based Jacobian or SQP methods optimise an IK solution by slightly modifying each joint variable to obtain the gradient [7–9]. These methods are often applied in robotics as they can achieve a fast convergence, but can suffer from multiple local extrema in the search space. In this regard, genetic algorithms (GA) perform a more robust search space exploration by means of biologically inspired probabilistic optimisation, and offer better scalability for higher DOF [10,11]. The key idea is to encode joint variable configurations as individuals, and to iteratively evolve new solutions until convergence. The fitness is obtained by the resulting end effector errors using the FK equations. However, traditional methods require many parameters to be tuned, or the required computation time or attainable accuracy might remain insufficient. In our prior work, a novel evolutionary hybridisation of GA and swarm intelligence achieved promising results both in accuracy and computation time, with adaptive parameter control for varying dimensionality and kinematic geometries [12,13]. As each fitness evaluation for every individual requires a FK pass in order to obtain the resulting errors in position and orientation, it was observed that most of the computation time was due to the required coordinate transformations. More specifically, many of those were redundant as with increasing accuracy, fewer genetic mutations were applied, and partially shared kinematic chains for multiple end effectors were computed repeatedly.

3 Algorithmic Approach

The main purpose of our OFKT data structure is to avoid calculating repeating or redundant consecutive transformations. Given a single joint variable configuration $\theta = (\theta_1, \dots, \theta_n)$ as input, the individual Cartesian transformations for end effectors $\mathcal{X}_{1, \dots, k}$ can be obtained as denoted by (2). Hence, calculating FK becomes processing a tree of single kinematic chains with either individual or partially shared joints.

$$f(\theta) = \mathcal{X}_{1, \dots, k} \tag{2}$$

For each kinematic chain (3), the end effector configuration is computed by consecutive transformations starting from its root.

$${}^{root}T_{ee} = {}^{root}T_1 {}^1T_2 \dots {}^{n-1}T_{ee} \tag{3}$$

According to (4), these transformations between the single relevant segments can be grouped into *reference* and *local* transformations, R_i and L_i respectively.

$$R_i = R_{i-1} L_i \quad L_i = S_i T(\theta_j) \tag{4}$$

However, not every segment of the kinematic chains is necessarily connected to a joint. Thus, the *static* transformation S_i denotes the constant transformation between the segment’s preceding non-static segment to the segment’s local transformation with $\theta_j = 0$. Note that S_i only needs to be computed once, and is then stored to avoid recalculating non-changing transformations. The OFKT itself is then represented by a linked list of segments, one for each moveable part of the kinematic structure. Within each node, R_i and L_i are individually computed and stored, together with the currently assigned corresponding joint variable θ_j . While the former depends on the preceding reference and the current local transformation, the latter is calculated using the segment’s static transformation S_i modified by θ_j . Algorithm 1 summarises building the OFKT data structure which can then be used for efficiently processing multiple successive FK queries.

Algorithm 1. Building the Optimised Forward Kinematics Tree

```

Input : Geometry, Root, End Effectors
1 OFKT = CreateLinkedList(Root, End Effectors);
2 Chains = GetChains(Root, End Effectors);
3 foreach Segment in Chains do
4   if Segment.HasJoint() then
5     Node = OFKT.Insert(Segment);
6     Node.ComputeAndStoreStaticTransformation();
7     Node.StoreJointVariable();
8     Node.ComputeAndStoreLocalTransformation();
9     Node.ComputeAndStoreReferenceTransformation();
10  end
11 end

```

When performing a FK query, a joint variable configuration is given as input to the OFKT. The goal is to perform kinematic queries efficiently by using the stored variables for the current transformation and the joint value within each node. As described by Algorithm 2, the update procedure is started at the root node of the linked list, and is recursively called for all childs. Also, a boolean parameter is recursively passed which initially assumes that no update would be required. The flag is set in case of joint variable changes, as otherwise the stored local transformation can be reused. As soon as one local update occurred during the FK calculation, a relative update is also necessary for all subsequent nodes. Note that transformation updates in local and reference space are treated independently by propagating the boolean flag. After the tree traversal, the resulting end effector transformations can be returned in world space using (5), where the additional ${}^{world}T_{root}$ transformation is prepended to handle movement in world space. Thus, the OFKT keeps all transformations in reference to the kinematic model while representing only non-static connections.

$$W_i = {}^{world}T_{root} R_i \quad (5)$$

Algorithm 2. Querying the Optimised Forward Kinematics Tree

Input : Joint Variable Configuration

Output: End Effector Transformations

```

1 Function UpdateFK(Node, RequireUpdate):
2   if HasJointVariableChanged() then
3     Node.StoreJointVariable();
4     Node.ComputeAndStoreLocalTransformation();
5     RequireUpdate = true
6   end
7   if RequireUpdate then
8     Node.ComputeAndStoreReferenceTransformation();
9   end
10  foreach Child of Node do
11    UpdateFK(Child, RequireUpdate);
12  end
13  return ;
14 UpdateFK(OFKT.Root, false);
15 foreach End Effector Node do
16   return Node.ComputeWorldTransformation();
17 end

```

Intuitively, the OFKT data structure is optimised to efficiently process multiple FK queries by caching transformations from preceding calculations, assuming that only a few joint values will change between successive queries. Considering the genetic evolutionary IK algorithm which was our original motivation, only some genes (joint angles) of an individual are usually modified during one generation, and many reference as well as local transformations can be reused, resulting in a large performance increase.

4 Evaluation and Results

First, a theoretical evaluation for the OFKT data structure is done regarding the total required transformations in four scenarios, summarised in Table 1. Given a n -dimensional serial joint variable configuration, one FK pass requires calculating n local transformations which are then concatenated by n transformations, and 1 further from world to root — this will be used as baseline for performance comparison.

1. *FK computation by updating a (random) number of values along a serial kinematic chain:* This is the typical query after evolving the genes of an individual. In general, $2n + 1$ calculations would be needed for independent FK queries. Using the OFKT, previous results can be reused efficiently, and the required amount of local transformation updates becomes equivalent to the number of changed joint values $j < n$. Traversing the single segments then results in $n - i$ instead of n reference transformations, where i is the first modified index along the serial kinematic chain.
2. *Predicting the end effector world transformation by modifying exactly one joint value:* This is helpful for determining or estimating the error gradient. Only 1 local L'_i as well as 3 further transformations $R_{i-1} L'_i R_i^{-1} R_{ee}$ are necessary for calculating the end effector transformation, followed by 1 additional world transformation. In particular, the required transformations of the single segments are already available, and enable to directly obtain the relative end effector change.
3. *Iteratively updating exactly one joint value while maintaining information about all segment transformations:* This is particularly important for enabling efficient further computation of relative transformations within the kinematic tree. n queries are performed iteratively, requiring $n(2n + 1)$ calculations. Using the OFKT, each of the n queries automatically avoids recalculating unchanged transformations, resulting in n local updated segments and a total of $\frac{n(n+1)}{2}$ calculations for the affected reference transformations.
4. *FK calculations on different chains with multiple end effectors of an anthropomorphic arm:* This is relevant in terms of scalability for complex geometries. A 27 DOF anthropomorphic geometry is considered, starting with a 7 DOF arm and splitting up into a hand with five 4 DOF fingers — giving rise to $k = 5$ chains with 11 DOF each. Hence, calculating all end effectors individually would require $k(2n + 1)$ transformations, while the OFKT automatically avoids recalculating the shared $s = 7$ joints along the arm.

Table 1. Comparison of the required amount of transformations in different scenarios.

Scenario	Standard	OFKT
Random modifications	$2n + 1$	$n - i + j + 1$
End effector computation	$2n + 1$	5
Single iterative modifications	$2n^2 + n$	$\frac{n^2}{2} + \frac{5n}{2}$
Multiple end effectors	$k(2n + 1)$	$k(2n + 1) - 2(k - 1)s$

In order to put the previous FK evaluations into practical context, experiments were conducted in performing IK on an articulated 10DOF kinematic model using the presented algorithm in [12, 13]. It was observed that $\approx 10^3$ generations in average were required for solution convergence. In this regard, Fig. 2 demonstrates the computational improvement at each generation during one IK query (left) and in average for increasing DOF (right) when using the OFKT. In particular, note that less computation time per generation is required since fewer genetic changes are applied as the population scores progress over several generations. It can be observed that this computational improvement scales significantly for more complex geometries, reaching a cost reduction per generation by a factor of ≈ 8 for 30 DOF.

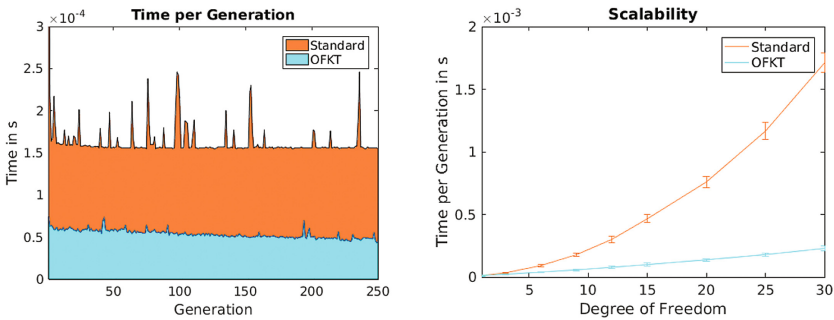


Fig. 2. Computational cost per generation for one IK query (left) and for increasing DOF (right).

Ultimately, we investigated the speedup in solving evolutionary IK on different robot geometries of 6 to 10 DOF. The results are shown in Fig. 3 and are averaged over 10.000 randomly generated samples using full pose objectives. In particular,

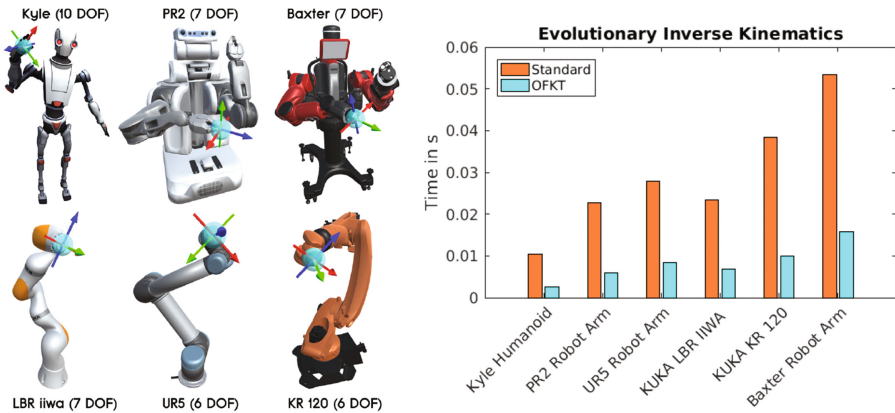


Fig. 3. Computational cost in solving random reachable IK queries on different robots.

a considerable computational improvement can be observed by requiring approximately one third of the original time for convergence on all tested kinematic models.

5 Conclusions

This work proposed a method to efficiently compute the FK equations for multiple consecutive queries with only slightly varying joint variable configurations. The developed OFKT data structure caches results that were computed in preceding calls, and only updates the transformations along the kinematically affected segments within the whole kinematic tree. Hence, the required amount of costly calculations for sampling-based IK optimisation on complex and multiple end effector geometries can be reduced. Integrating the OFKT into our evolutionary IK algorithm, one third of the original computation time for solving full poses on typical lower DOF industrial robots was required, with significantly larger improvements obtained for increasing DOF. This work will be further investigated applied to dexterous manipulation, humanoid robots and character animation.

Acknowledgements. This research was funded by the German Research Foundation (DFG) and the National Science Foundation of China (NSFC) in project Crossmodal Learning, TRR-169.

References

1. Kathib, O., Siciliano, B.: Handbook of Robotics. Springer, Heidelberg (2008)
2. Wu, P., Wu, C., Yu, L.: An method for forward kinematics of stewart parallel manipulators. In: Proceedings of the IEEE International Conference on Intelligent Robotics and Applications, 171–178 (2008)
3. Song, S., Kwon, D.: Efficient formulation approach for the forward kinematics of 3-6 parallel mechanisms. *Adv. Robot.* **16**(2), 191–215 (2002)
4. Denavit, J., Hartenberg, R.: A kinematic notation for lower-pair mechanisms based on matrices. *Trans. ASME J. Appl. Mech.* **23**, 215–221 (1955)
5. Denavit, J., Hartenberg, R.: Kinematic Synthesis of Linkages. McGraw-Hill Series in Mechanical Engineering, p. 435. McGraw-Hill, New York (1965)
6. Sadjadian, H., Taghirad, H.D., Fatehi, A.: Neural networks approaches for computing the forward kinematics of a redundant parallel manipulator. *Int. J. Comput. Electr. Autom. Control Inf. Eng.* **2**(5), 1664–1671 (2008)
7. Beeson, P., Ames, B.: TRAC-IK: an open-source library for improved solving of generic inverse kinematics. In: Proceedings of the IEEE RAS Humanoids Conference (2015)
8. Kim, I., Oh, J.: Inverse kinematic control of humanoids under joint constraints. *Int. J. Adv. Robot. Syst.* **10** (2012)
9. Lee, D., An, S.: Prioritized inverse kinematics with multiple task definitions. In: IEEE International Conference on Robotics and Automation (2015)
10. Tabandeh, S., Clark, C.M., Melek, W.W.: An adaptive niching genetic algorithm approach for generating multiple solutions of serial manipulator inverse kinematics with applications to modular robots. *Robotica* **28**, 493–507 (2010)

11. González Uzcátegui, C.E.: A Memetic Approach to the Inverse Kinematics Problem for Robotic Applications. Doctoral Thesis, Carlos III University of Madrid (2014)
12. Starke, S.: A Hybrid Genetic Swarm Algorithm for Interactive Inverse Kinematics. Master Thesis, University of Hamburg (2016)
13. Starke, S., Hendrich, N., Magg, S., Zhang, J.: An efficient hybridization of genetic algorithms and particle swarm optimization for inverse kinematics. In: Proceedings of the IEEE International Conference on Robotics and Biomimetics (2016)

Adaptation of the Geometric Model of a 6 dof Serial Robot to the Task Space

Jose Gutiérrez^(✉), Helene Chanal, Severine Durieux,
and Emmanuel Duc

Université Clermont Auvergne, CNRS, SIGMA Clermont, Institut Pascal,
63000 Clermont-Ferrand, France

{jose-javier.gutierrez-tapia, helene.chanal,
severine.durieux, emmanuel.duc}@sigma-clermont.fr

Abstract. This work presents the results concerning the modeling and sensitivity analysis of the serial ABB IRB 6660 robot in a dedicated workspace. In this sense, this study is a first step to define a geometrical modeling method. The proposed method is based on the introduction of one parameter for each defect which affects the orientation and position of each robot joint and end-effector. Then, the parameters selection is realized with a sensitivity analysis with regard to the workspace and needed accuracy. This work is illustrated on an ABB IRB 6660 robot. The final aim of this approach is to improve the accuracy of a robot during the following of a tool path in a given workspace.

Keywords: Sensitivity analysis · Direct kinematic analysis · Serial robot · Geometric modeling

1 Introduction

The use of serial robots for machining operations has become a robot development issue in recent years. The aim is to propose an alternative to machine tools. Thus, 6-axis heavy-duty robots are offered by robot manufacturers and designers. However, developed robots have toolpath following accuracy only near 0.1 mm, although their stiffness has been improved compared to robots used for less demanding operations. Indeed, the geometrical, static and dynamic behaviors of these robots do not allow machining to be performed with great accuracy and, finally, only 3% to 4% of industrial robots are dedicated to machining [1, 2].

The geometric model is the mathematical description of the geometrical behavior of the robot. This model expresses the pose of the center of the tool in the robot coordinate system with regard to the pose of the active joints [3]. The geometric models of robots are generally based on a set of mathematical equations allowing computing the pose of the final end-effector with regard to the values of the articular variables and geometric parameters. The most widely used modeling methods are generally based on the Denavit-Hartenberg (DH) formalism [4]. This formalism is enriched by various scientific works in order to be more adapted to the studied structure behavior [5]. However, the complexity of the models developed does not guarantee the improvement of robot geometric accuracy. Indeed, the addition of geometric parameters makes the

model more sensitive to identification errors [6]. It is necessary to limit the number of geometric parameters to influential and identifiable parameters.

Similarly, in order to improve the accuracy of task realisation, it is necessary to study the influence of each geometrical parameter on the task and to identify its parameters under the conditions of realization of the task [6]. The objective is not to guarantee absolute accuracy of the robot throughout its working space but to focus on the task accuracy. In other words, it is necessary to focus only on the end-effector poses which have an influence on the accuracy of task realization in the task workspace. In the case of machining, the accuracy of the machined part is linked to the robot accuracy during the toolpath following in the part coordinate system.

We propose in this work to make a contribution on the definition of the number and the nature of the geometric parameters of a serial robot equipped with a spindle with regard to the needed workspace.

First, we introduce the ABB IRB 6660 robot and its characteristics. Then, methods for geometric modeling are presented. Finally, we perform the sensitivity analysis to select the most influential parameters and proposed a geometrical model adapted to a given workspace.

2 Presentation of the ABB IRB 6660 Robot

The robot IRB 6660 is composed of a serial structure with a parallelogram structure to improve the overall rigidity of the robot [7, 8]. The robot is composed of six motorized joints (from 1 to 6) and three passive joints (7, 8 and 9) (Fig. 1). Axes 3, 7, 8 and 9 composed the parallelogram structure.

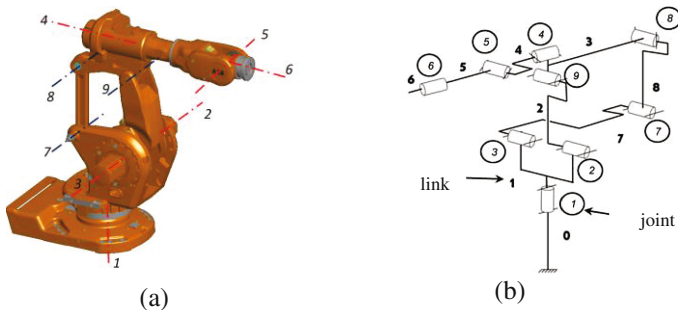


Fig. 1. (a) Joints of the ABB IRB 6660 robot. (b) Kinematic diagram of the robot.

This robot is a 6 dof serial robot with a simple closed kinematic chain. It is thus considered by Khalil as a complex robot [5] because it has at least one solid positioned by more than two joints.

The robot studied is also equipped with a spindle fixed at the last joint in order to carry out pre-machining operations. This spindle is a spindle MFW-1412 from Precise France Fisher.

A first analysis of the architecture of the robot is realised in order to determine the overconstrained degree of the mechanism [9]. The aim is to determine the dimensional and geometrics constraints which ensure to guarantee good working condition of the system [10].

According to this study, the robot IRB 6660 has an overconstrained degree of 3 [9]. This overconstrained degree is due to the parallelogram mechanism behavior. Indeed, the mechanism is in parallelogram the axes of joint 3, 7, 8, and 9 have to be parallel to transmit the movement from joint 3 to joint 9.

This mechanical constraint must be taken into account during the definition of the geometric parameters used in the geometric model of the robot. Thus, we consider that the orientation defect between the joints 3, 7, 8, and 9 are not taken into account in the geometrical model of the robot as their parallelism is controlled by the manufacturing and assembly constraints and we also considered joint 2 is independent of joint 3, 7, 8 and 9.

This first analysis of the structure of the robot ensure us to realize geometric models closer to the mechanical behavior of the architecture of the robot.

3 Direct Kinematic Model Analysis

The initial realized model is a 6-parametric model defined from DH method for serial robot (Fig. 2). This model does not take into account the transformation of motion generated by the parallelogram mechanism and it is composed with the minimal number of parameters. The coordinate system linked to each active joint is defined and noted $R_i(\mathbf{X}_i, \mathbf{Y}_i, \mathbf{Z}_i)$ except for joint 9 which is $R_3(\mathbf{X}_3, \mathbf{Y}_3, \mathbf{Z}_3)$. The DH parameters are then: $R_{L1}, d_2, d_3, d_4, R_{L4}, R_{L6}$.

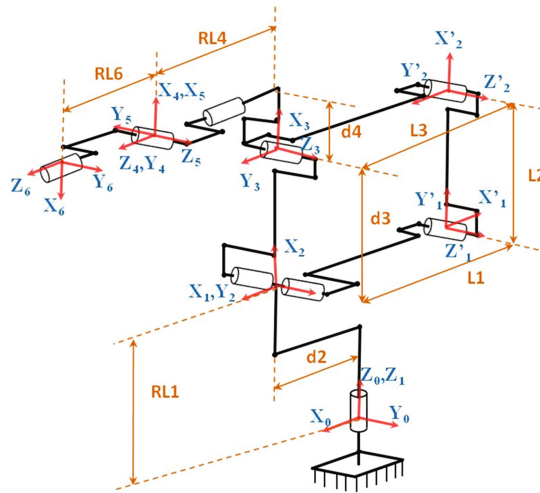


Fig. 2. Geometrical model of the robot.

However, this model has to be completed by taking into account the parallelogram mechanism behavior in the movement transmission between joint 3 to joint 9.

Figure 2 presented the parameters used to described the geometrical behavior of the parallelogram mechanism.

The articular variable q_3 is located at the articulation 3, the relation between q_3 , the geometrical parameters of the parallelogram and the angle θ_3 of the articulation 9 must then be determined.

Figure 3 illustrates the modeling of the parallelogram mechanism and the relationship between the values of the articular variables q_2, q_3, θ_3 and the introduced geometrical parameters (L_1, L_2, L_3) of the parallelogram. We assume from the over-constrained analysis that the system is plane and that all the axes of the bonds are parallel. Thus, the modelling hypothesis are consistent with the hypotheses of the Denavit-Hartenberg method.

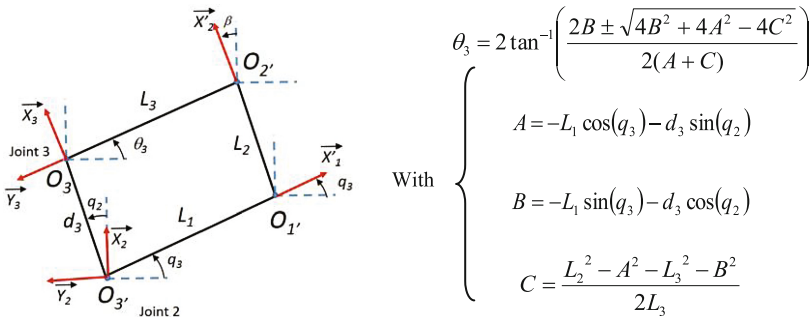


Fig. 3. Parameter relations of the parallelogram.

This model is thus completed to express geometric models taking into account each defect between non-overconstrained joints and the spindle coordinate system. Thus, 6 parameters are taken into account to express the position and orientation of i th joint coordinate system with regard to $(i-1)$ th joint coordinate system:

$${}^0\mathbf{T}_6 = {}^0\mathbf{T}_1 {}^1\mathbf{T}_2 {}^2\mathbf{T}_3 {}^3\mathbf{T}_4 {}^4\mathbf{T}_5 {}^5\mathbf{T}_6 \tag{1}$$

$$\begin{aligned}
 {}^0\mathbf{T}_1 &= \begin{bmatrix} \cos(q_1) & -\sin(q_1) & 0 & 0 \\ \sin(q_1) & \cos(q_1) & 0 & 0 \\ 0 & 0 & 1 & RL_1 \\ 0 & 0 & 0 & 1 \end{bmatrix} &
 {}^1\mathbf{T}_2 &= \begin{bmatrix} \cos(q_2 - \pi/2) & -\sin(q_2 - \pi/2) & 0 & d_2 \\ 0 & 0 & 1 & 0 \\ -\sin(q_2 - \pi/2) & -\cos(q_2 - \pi/2) & 0 & 0 \\ 0 & 0 & 0 & 1 \end{bmatrix} \\
 {}^2\mathbf{T}_3 &= \begin{bmatrix} \cos(\theta_3 - q_2) & -\sin(\theta_3 - q_2) & 0 & d_3 \\ \sin(\theta_3 - q_2) & \cos(\theta_3 - q_2) & 0 & 0 \\ 0 & 0 & 1 & 0 \\ 0 & 0 & 0 & 1 \end{bmatrix} &
 {}^3\mathbf{T}_4 &= \begin{bmatrix} \cos(q_4) & -\sin(q_4) & 0 & d_4 \\ 0 & 0 & 1 & RL_4 \\ -\sin(q_4) & -\cos(q_4) & 0 & 0 \\ 0 & 0 & 0 & 1 \end{bmatrix} \\
 {}^4\mathbf{T}_5 &= \begin{bmatrix} \cos(q_5) & -\sin(q_5) & 0 & 0 \\ 0 & 0 & -1 & 0 \\ \sin(q_5) & -\cos(q_5) & 0 & 0 \\ 0 & 0 & 0 & 1 \end{bmatrix} &
 {}^5\mathbf{T}_6 &= \begin{bmatrix} \cos(q_6 + \pi) & -\sin(q_6 + \pi) & 0 & 0 \\ 0 & 0 & 1 & RL_6 \\ -\sin(q_6 + \pi) & -\cos(q_6 + \pi) & 0 & 0 \\ 0 & 0 & 0 & 1 \end{bmatrix}
 \end{aligned}$$

Where ${}^{j-1}\mathbf{T}_j$ is the homogeneous transformation matrix to i articulation to j articulation. Then, 3 parameters are added to define the position and orientation of the spindle coordinate system with regard to the 6th joint coordinate system (x_{ef} , y_{ef} and z_{ef}) J_{tool} is the length of the tool used:

$${}^6\mathbf{T}_{spindle} \begin{bmatrix} 0 & 0 & 1 & x_{ef} = x_{spindle} + J_{tool} \\ 0 & 1 & 0 & y_{ef} = y_{spindle} \\ -1 & 0 & 0 & z_{ef} = z_{spindle} \\ 0 & 0 & 0 & 1 \end{bmatrix} \quad (2)$$

A model with 45 parameters are then considered by taking into account errors of position and orientation of the coordinate systems of each non-overconstrained joints and the parallelogram mechanism parameters, these 45 parameters takes into account the position and orientation errors of each pivot link (6×6 parameters), the position and orientation errors of the final effector (6 parameters) and the 3 parameters of the parallelogram. These parameters are named t_{ix} , t_{iy} and t_{iz} for translations errors on the x, y and z axe respectively of the i link; tit_i , psi_i and alf_i for angulars errors on the x, y and z axe respectively of the i link i ; t_{bx} , t_{by} and t_{bz} for translations errors on spindle and tit_b , psi_b and alf_b for angulars errors on spindle.

4 Sensitivity Analysis

The sensitivity analysis will enable us to evaluate the influence of the geometric parameters on the position of the end effector of the robot. It will also allow us to discuss the number of optimum parameters to introduce. In the case of our study, we carry out the sensitivity analysis on the most complete model, the geometric model with 45 parameters. The MGD is represented by:

$$\mathbf{X} = MGD(\mathbf{Q}, \xi) \quad (3)$$

Where \mathbf{X} is the pose vector which corresponds to the coordinates of the piloted point of the robot end-effector and its orientation in the robot base coordinate system and ξ the 45 parameters.

\mathbf{Q} is the vector of the articular variables of the robot (q_1 , q_2 , q_3 , q_4 , q_5 and q_6).

In our case, we study the influence of the geometric parameters on the position of the tool for given values of the motor set points. Thus, if we consider the articular instruction to be perfectly repeatable, the sensitivity matrix \mathbf{S} is then:

$$\mathbf{S} = \frac{d\mathbf{X}}{d\xi} = \frac{\partial MGD(\mathbf{Q}, \xi)}{\partial \xi} \quad (4)$$

The matrix of sensitivity is a matrix of 3×45 elements where the term S_{ij} represents the influence of the parameter i on the coordinate j of the tool position.

In this first part we will carry out the sensitivity analysis on a given workspace which is used to realize the identification (Fig. 4). After an analysis of the sensitivity matrix transformed with the Gaussian pivot method, we observe that the parameters $t2z$, $t3z$, $t4z$, $t5z$, $t6z$, tbx , tby , tbz and $psi5$ are redundant parameters and we can establish relations between these parameters and the model parameters (Associated parameters). The maximum influence in this space is shown in Fig. 5.

On the basis of these results, we propose a new model without the redundant and zero parameters, that is to say without the parameters $t2z$, $t3z$, $t4z$, $t5z$, $t6z$, tbx , tby , tbz , $alf6$, $titb$, $psib$ and $alfb$. The new model contains 33 parameters.

5 Identification of Geometric Parameters

To see, the impact of this model adapted to the workspace, a process of identification is realized. The identification phase of the robot consists of determining the values of the geometrical parameters related to the structure of the robot and the spindle.

For the identification of the 33 parameters model, the identification of the proposed model is carried out with 60 positions measured with a Laser Tracker measurement system, Leica ATD-901 with accurate performance measurement of the position of the test pattern of $\pm 15 \mu\text{m} + 6 \mu\text{m}/\text{m}$ and compared with the positions simulated with the direct kinematic model (Fig. 6). Thus, by minimizing the cost function with Matlab's *lsqnonlin* function, we obtain the identified geometric parameters of the model.

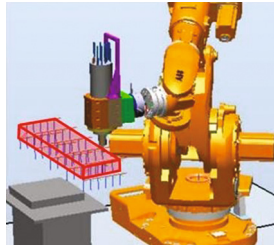


Fig. 4. Workspace used to the identification.

After the measurement of 60 points the maximum residual error values are: 0.09566 mm on the X-axis, 0.1222 mm on the Y-axis and 0.09191 mm on the Z-axis, with a maximum spatial position error of 0.1803 mm for the model with 33 parameters sans compensation de la gravité.

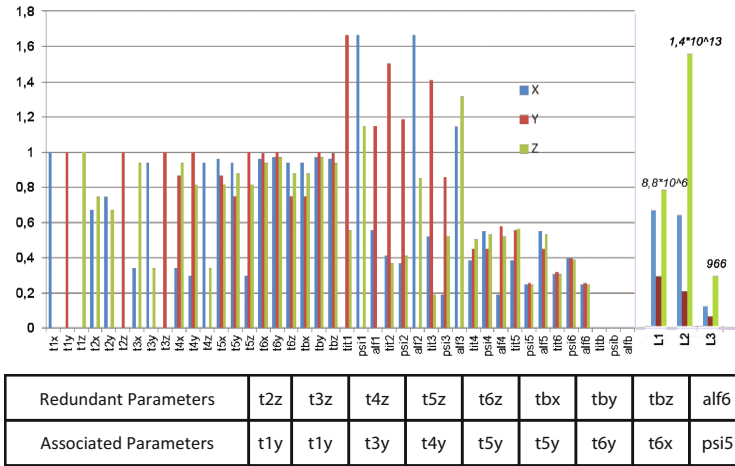


Fig. 5. Maximum influence of parameters in the X, Y and Z axis for 60 points and the redundant parameters and associated parameters.

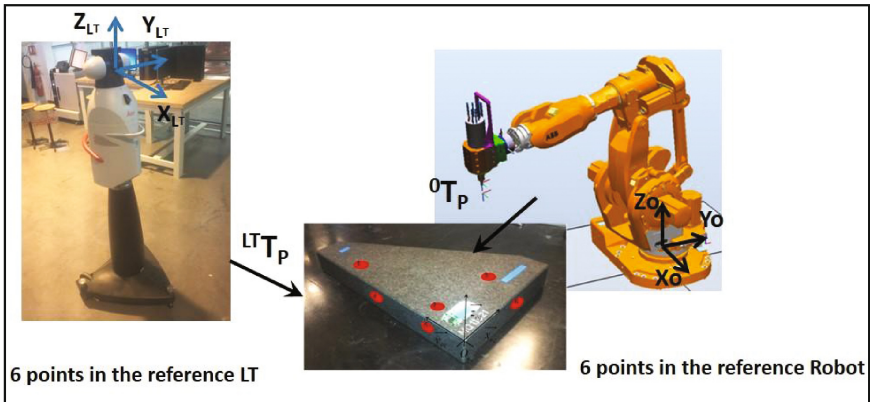


Fig. 6. Reconfiguration of reference system.

6 Conclusions

The goal of this study is to analyze the influence of the geometrical parameters use to define the ABB IRB 6660. A new approach for the identification of the influential geometric parameters of a serial robot is developed. Despite the sensitivity study and the reduction of the model of 45 parameter to 33 parameters the error of position remains always important. Indeed, taking into account parameters of a different nature in the parameter model can explain this deviation as well as the fixed orientation of the tool in the space under consideration. However, the proposed modeling method can be applied to different working spaces in position and orientation.

References

1. Milutinovic, D., Glavanjik, M., Slavkovic, N., Dimic, Z., Zinanovic, S., Kokotovic, B., Tanovic, L.: Reconfigurable robotic machining system controlled and programmed in a machine tool manner. *Int. J. Adv. Manuf. Technol.* **53**, 1217–1229 (2010). London
2. Denkena, B., Litwinski, K., Schönherr, M.: Innovative drive concept for machining robots. In: 2ème CIRP Global Web Conference, pp. 67–72 (2013)
3. Ginani, L., Motta, J.: Theoretical and practical aspects of robot calibration with experimental verification. *J. Braz. Soc. Mech. Sci. Eng.* **33**, 15–21 (2011)
4. Denavit, J., Hartenberg, R.S.: A kinematic notation for lower pair mechanisms based on matrices. *Trans. ASME, J. Appl. Mech.* **22**, 215–221 (1955)
5. Khalil, W., Dombre, E.: Modeling identification and control of robots. Ed. Hermes, Paris (1999)
6. Chanal, H., Paccot, F., Duc, E.: Sensitivity analysis of an overconstrained parallel structure machine tool, the Tripteor X7. *Appl. Mech. Mater.* **162**, 394–402 (2012)
7. ABB. <http://new.abb.com/products/robotics>
8. Guo, Y., Shibin, Y., Yongjie, R., Jigui, Z., Shourui, Y., Shenghua, Y.: A multilevel calibration technique for an industrial robot with parallelogram mechanism. *Precis. Eng.* **40**, 261–272 (2015)
9. Gutierrez, J., Chanal, H., Duc, E., Durieux S.: Analyse de l'influence du modèle géométrique d'un robot 6 axes sur la précision géométrique atteinte. In: *Machines et Usinage à Grande Vitesse 2014 (MUGV)* (2014)
10. Schneider, F.: Tolérancement géométrique- Interprétation. Université de Metz (1999)

Differentiation-Free Taylor Approximation of Finite Motion in Closed Loop Kinematics

J.J. de Jong¹(✉), A. Müller², J. van Dijk¹, and J.L. Herder¹

¹ University of Twente, Enschede, The Netherlands
j.j.dejong@utwente.nl

² Johannes Kepler University, Linz, Austria
a.mueller@jku.at

Abstract. Higher-order derivatives of kinematic mappings give insight into the motion characteristics of complex mechanisms. Screw theory and its associated Lie group theory have been used to find these derivatives of loop closure equations up to an arbitrary order. However this has not been extended to the higher-order derivatives of finite motion as given by the inverse or forward kinematic model of closed loop mechanisms. In this paper, a recursive algorithm is presented, consisting solely of matrix multiplications, which is capable of giving these higher-order derivatives of kinematic models of closed loop linkages. It depends on a simplified representation of the higher-order derivatives of an open chain. From these higher-order derivatives a Taylor expansion of a finite motion becomes available. The evaluation of this method on a Taylor approximation (up to 5th order) of the inverse kinematic model of a 5-bar mechanism shows a good approximation in a large part of workspace around the evaluation point.

Keywords: Higher-order kinematics · Taylor approximation · Screw theory · 5-bar mechanism

1 Introduction

Geometric insight of infinitesimal motion of spatial kinematics can be obtained with the differential analysis of screw theory. This theory gives the kinematic relations between the general velocities of bodies (twists) and general constraint forces (constraint wrenches) acting on a system. This instantaneous analysis is only available in the pose of inspection, and in general does not give an understanding of the possible finite motion of a mechanism. For synthesis and analysis purposes, attempts have been made to extend the infinitesimal screw analysis. The finite forward kinematic model of open loop chains is given by Brockett's products of exponents (POE) [1]. It consists of the products of exponential matrices of the instantaneous screw axes. Derivatives up to an arbitrary order of loop closure equations can be found by taking Lie brackets of instantaneous screw axes, which can be expressed as matrix multiplications of twists [2, 3].

This paves the way for an algorithmic differentiation-free derivatives of the loop closure equations [4].

However, higher-order derivatives and approximations of the finite motion of these closed loop mechanisms were not yet found. These higher-order derivatives of finite motion can be used for finding conditions for invariant properties of kinematics and dynamics such as required for balancing, synthesis and analysis of rigid body motions. Moreover, such an approximation is advantageous since closed form kinematic mappings are not always available for the more complex mechanisms. Unfortunately, processing these higher-order, multivariate derivatives require elaborate bookkeeping, as can be seen in the implementation of the higher-order chain rule, the Faa di Bruno’s rule [5].

In this paper a simplified representation of the higher-order derivatives of the screw systems is presented which has a structure similar to the Brockett’s POE. With Veters method for managing higher order matrix derivatives [6] this enables us to obtain a recursive, differentiation-free algorithm for higher-order derivatives of the solution to the closure equations. Using the resulting higher-order closure Jacobians, a Taylor approximation of the closed loop kinematics is performed. The steps taken are exemplified with an approximation of the inverse kinematic model of a 5-bar mechanism.

Before we introduce the higher-order derivatives of the loop closure solution, the screw algebra theory is revisited and applied to an open chain. Based on this a simplified representation of higher-order derivatives of an open chain is presented Sect. 2.2. After this the loop closure equations and the matrix derivatives are revisited Sects. 2.3 and 2.4. Using these rules finally the algorithm for determining the higher-order derivatives and its Taylor expansion is presented Sect. 2.5 and its implementation shown for a 5-bar mechanism Sect. 2.6.

2 Method

2.1 Concepts and Notation

In the notation of screw theory as used in this paper, a reference frame (ψ_i) is associated to each rigid body i . Points in space (\mathbf{a}) can be expressed with respect to this reference frame (denoted with superscript \mathbf{a}^i). A change of reference frame follows from the homogeneous transformation matrix which consists of a rotation matrix (\mathbf{R}) and a translation vector (\mathbf{o}). In the homogeneous representation the \mathbf{a}^i -vector is appended with a 1.

$$\mathbf{a}^j = \mathbf{H}_i^j \mathbf{a}^i \quad \mathbf{H}_i^j = \begin{bmatrix} \mathbf{R}_i^j & \mathbf{o}_i^j \\ \mathbf{0} & 1 \end{bmatrix} \quad \dot{\mathbf{H}}_i^j = \begin{bmatrix} [\boldsymbol{\omega}_i^j \times] & \mathbf{v}_i^j \\ \mathbf{0} & 0 \end{bmatrix} \quad \mathbf{H}_i^j = [\mathbf{t}_i^{j,j} \times] \mathbf{H}_i^j \quad (1)$$

The time derivative of the transformation matrix is given by the twist ($\mathbf{t}_i^{k,j}$), the generalized velocity, of body i with respect to body j expressed in frame k . For clarity reasons the subscript and second superscript are omitted when possible. The twist is a vector containing the angular ($\boldsymbol{\omega}$) and translational (\mathbf{v}) velocity. The $[\boldsymbol{\omega} \times]$ denotes the skew symmetric matrix form of $\boldsymbol{\omega}$. The twist’s frame of

expression changes with the adjoint transformation matrices here denoted with $Ad(\mathbf{H}_i^j)$.

$$\mathbf{t}^j = Ad(\mathbf{H}_i^j)\mathbf{t}^i \quad Ad(\mathbf{H}_i^j) = \begin{bmatrix} \mathbf{R}_i^j & \mathbf{0} \\ [\mathbf{o}_i^j \times] & \mathbf{R}_i^j \end{bmatrix} \quad (2)$$

The time derivative of adjoint transformation matrix is given in terms of instantaneous transformation matrix $ad(\mathbf{t})$.

$$\frac{d}{dt} \left(Ad(\mathbf{H}_i^j) \right) = ad(\mathbf{t}_i^{j,j}) Ad(\mathbf{H}_i^j) \quad ad(\mathbf{t}) = \begin{bmatrix} [\boldsymbol{\omega} \times] & \mathbf{0} \\ [\mathbf{v} \times] & [\boldsymbol{\omega} \times] \end{bmatrix} \quad (3)$$

This matrix itself can be expressed in an other reference frame according to a nested transform:

$$ad(\mathbf{t}^j) = ad\left(Ad(\mathbf{H}_i^j)\mathbf{t}^i \right) = Ad(\mathbf{H}_i^j) ad(\mathbf{t}^i) Ad(\mathbf{H}_j^i) \quad (4)$$

Using these twists, a concise formulation for the forward kinematic mapping of an open chain is available in the form of Brockett's product of exponentials [1]:

$$Ad(\mathbf{H}_n^0(\mathbf{q})) = \prod_{i=1}^n Ad(\mathbf{H}_i^{i-1}(q_i)) = \prod_{i=1}^n e^{ad(\hat{\mathbf{t}}_i^i)q_i} Ad(\mathbf{H}_n^0(0)) \quad (5)$$

In here, the instantaneous screw vector $i0$, denoted with a hat, specifies the amount of twist generated by the instantaneous motion of joint i , and is therefore a pure geometric entity. As this screw vector is always with respect to the previous body in the chain, the second superscript is omitted. The instantaneous screw vector of lower kinematic pairs are constant when expressed in the connecting frames e.g. $\frac{d}{dt}(\hat{\mathbf{t}}_i^{i-1}) = \frac{d}{dt}(\hat{\mathbf{t}}_i^i) = \mathbf{0}$.

2.2 Derivatives of Twist Systems (open Chain)

For an open chain, the higher-order partial derivatives can be found using the transformations of the previous section. A chain of transformations can be decomposed into constant and varying part of which the derivative is available. The nested transform (4) of the twist gives a concise formulation of the derivative of a chain, provided that $i \leq n$.

$$\frac{d}{dq_i} \left(Ad(\mathbf{H}_n^0) \right) = Ad(\mathbf{H}_{i-1}^0) \frac{d}{dq_i} \left(Ad(\mathbf{H}_i^{i-1}) \right) Ad(\mathbf{H}_n^i) \quad (6)$$

$$= Ad(\mathbf{H}_{i-1}^0) ad(\hat{\mathbf{t}}_i^{i-1}) Ad(\mathbf{H}_i^{i-1}) Ad(\mathbf{H}_n^i) \quad (7)$$

$$= ad(\hat{\mathbf{t}}_i^0) Ad(\mathbf{H}_n^0) \quad (8)$$

For the second-order, such a concise representation also exists. For the consecutive derivative with respect to joint j there exist two possibilities, either it is after body i in the chain (case 1.) or before i in the chain (case 2).

1. Case 1. ($i \leq j$) In the case that joint j is higher in the chain than i , the twist is unaffected ($\frac{d}{dq_j} (ad(\hat{\mathbf{t}}_i^0)) = 0$). Therefore, the second partial derivative becomes:

$$\frac{d}{dq_j} \frac{d}{dq_i} (Ad(\mathbf{H}_n^0)) = ad(\hat{\mathbf{t}}_i^0) ad(\hat{\mathbf{t}}_j^0) Ad(\mathbf{H}_n^0) \tag{9}$$

2. Case 2. ($i \geq j$) In the case that j is below i in the chain we use the nested transform property to split the chain into a dependent and independent part. It may be verified that $\frac{d}{dq_j} (ad(\hat{\mathbf{t}}_i^j) Ad(\mathbf{H}_n^j)) = 0$. Therefore:

$$\frac{d}{dq_j} \frac{d}{dq_i} (Ad(\mathbf{H}_n^0)) = \frac{d}{dq_j} (Ad(\mathbf{H}_j^0) ad(\hat{\mathbf{t}}_i^j) Ad(\mathbf{H}_n^j)) \tag{10}$$

$$= \frac{d}{dq_j} (Ad(\mathbf{H}_j^0)) ad(\hat{\mathbf{t}}_i^j) Ad(\mathbf{H}_n^j) \tag{11}$$

Using (8) a matrix chain can be found and collected again using the nested transform:

$$\frac{d}{dq_j} \frac{d}{dq_i} (Ad(\mathbf{H}_n^0)) = ad(\hat{\mathbf{t}}_j^0) ad(\hat{\mathbf{t}}_i^0) Ad(\mathbf{H}_n^0) \tag{12}$$

Leaves us with an expression similar to (9), with the difference that sequence of multiplication is swapped. This also follows from the symmetry (commutativity) property of mixed partial derivatives: $\frac{d}{dq_j} \frac{d}{dq_i} (Ad(\mathbf{H}_n^0)) = \frac{d}{dq_i} \frac{d}{dq_j} (Ad(\mathbf{H}_n^0))$.

A consecutive application of (9), and (12) gives us the geometrical higher-order partial derivatives for any order, supplied in multi-index α^1 , which is ordered from the base to the end-effector.

$$D_q^{(\alpha)} (Ad(\mathbf{H}_n^0)) = \prod_{i=1}^n ((ad(\hat{\mathbf{t}}_i^0))^{\alpha(i)}) Ad(\mathbf{H}_n^0) \tag{13}$$

This result is similar to that of [3], with the difference that the index ranges to distinguish between the sequence of derivatives are taken into account by the ordering of α . From the commutative property of mixed partial derivatives it follows that for whatever sequence of differentiation the same results are obtained. Furthermore, it can be seen that (13) resembles the structure of the Brockett's formula (5) in the sense that the matrix multiplications follow the physical ordering of the chain.

2.3 Loop Closure Equations

The open-loop chain derivatives (13) can be used for closed loops, as a closed loop can be seen as a connection of multiple open-loops. E.g., a simple loop

¹ $D_x^{(k)}(\mathbf{A})$ denotes the matrix collection of all k -th order partial derivatives of \mathbf{A} with respect to \mathbf{x} . $D_x^{(\alpha)}(\mathbf{A})$ denotes the mixed partial derivative with respect to the elements of \mathbf{x} . A sequence of derivatives to each \mathbf{x}_i with an order of the corresponding α_i value. This assumes that the mixed partial derivative are commutative.

can be seen as a open chain of with the last link fixed to the base. The loop closure equation (f) states how the members of the loop are constrained. It can be written in terms of independent (\mathbf{u}) and dependent coordinates (\mathbf{v}), also termed input and output, respectively. The total set of coordinates we call $\mathbf{s}^\top = [\mathbf{u}^\top \ \mathbf{v}^\top]$. The solution to this problem is denoted by c , which can be the inverse, forward, or any other kinematic model giving an exact relation between independent and dependent coordinates.

$$f(\mathbf{u}, \mathbf{v}) = \mathbf{0} \qquad \mathbf{v} = c(\mathbf{u}) \qquad (14)$$

The solution (c) to the loop closure is usually not available for complex mechanisms. Therefore, we are looking for a Taylor expansion using higher-order derivatives of the constraint formulation using the open loop derivatives of Sect. 2.2. We start with the first order. This reads:

$$\mathbf{0} = D_t(f) = D_{\mathbf{u}}(f) \dot{\mathbf{u}} + D_{\mathbf{v}}(f) \dot{\mathbf{v}} = \mathbf{U}\dot{\mathbf{u}} + \mathbf{V}\dot{\mathbf{v}} \qquad (15)$$

This gives rise to the Jacobians (\mathbf{C}) and (\mathbf{K}), respectively linking $\dot{\mathbf{v}}$ and $\dot{\mathbf{w}}$ to $\dot{\mathbf{u}}$.

$$\dot{\mathbf{v}} = -\mathbf{V}^{-1}\mathbf{U}\dot{\mathbf{u}} = \mathbf{C}\dot{\mathbf{u}} = D_{\mathbf{u}}(c) \dot{\mathbf{u}} \qquad \dot{\mathbf{s}} = \mathbf{K}\dot{\mathbf{u}} = \begin{bmatrix} \mathbf{C} \\ \mathbf{I} \end{bmatrix} \dot{\mathbf{u}} \qquad (16)$$

We already have seen that closure equations can be written as a function of transformation matrices of the open chain. Therefore, the higher-order partial derivatives of $D_{\mathbf{s}}^{(\alpha)}(\mathbf{U})$ and $D_{\mathbf{s}}^{(\alpha)}(\mathbf{V})$ are available. Now we are looking for a method of writing the higher-order closure Jacobian $\mathbf{C}_k = D_{\mathbf{u}}^{(k)}(c)$.

2.4 Multivariate Matrix Derivatives Using Kronecker Product

The higher-order partial derivatives of matrices can be managed with the use of the Kronecker product [6]. Here the partial derivative version of the product rule, the chain rule and the inverse matrix derivative are given.

- Product rule of $\mathbf{A}(\mathbf{x}) \in \mathbb{R}^{n \times m}$, $\mathbf{B}(\mathbf{x}) \in \mathbb{R}^{m \times q}$, for $\mathbf{x} \in \mathbb{R}^r$, and \mathbf{I} is an identity matrix:

$$D_{\mathbf{x}}(\mathbf{A}\mathbf{B}) = [D_{\mathbf{x}}(\mathbf{a}_1)\mathbf{B} \dots D_{\mathbf{x}}(\mathbf{a}_m)\mathbf{B}] + \mathbf{A}D_{\mathbf{x}}(\mathbf{B}) \qquad (17)$$

$$= D_{\mathbf{x}}(\mathbf{A})(\mathbf{B} \otimes \mathbf{I}_r) + \mathbf{A}D_{\mathbf{x}}(\mathbf{B}) \qquad (18)$$

- Chain rule:

$$D_{\mathbf{c}}(\mathbf{A}(\mathbf{b}(\mathbf{c}))) = D_{\mathbf{b}}(\mathbf{A})(\mathbf{I}_m \otimes D_{\mathbf{c}}(\mathbf{b})) \qquad (19)$$

- Derivative of matrix inversion:

$$D_{\mathbf{x}}(\mathbf{A}^{-1}) = -\mathbf{A}^{-1}D_{\mathbf{x}}(\mathbf{A})(\mathbf{A}^{-1} \otimes \mathbf{I}_r) \qquad (20)$$

Recursive applications of these rules allow the extension of these derivatives to higher orders.

2.5 Higher-Order Closure Jacobians and Taylor Approximation

Using the rules of the previous section, the second-order derivatives (Hessian) of the solution to the constraint equations are found. This is done by consecutive application of the chain rule, the product rule, and the inverse matrix derivative to the Jacobian (16).

$$D_u(C_1) = C_2 = -[D_s(V^{-1})(U \otimes I) - V^{-1}D_s(U)](I \otimes K) \quad (21)$$

$$= -V^{-1}[D_s(V)(C_1 \otimes I) + D_s(U)](I \otimes K) \quad (22)$$

After reordering and combination of the Kronecker products, we can find a concise formulation of the Hessian matrix.

$$C_2 = -V^{-1} [D_s(V) D_s(U)] (K \otimes K) = -V^{-1} F_2 G_2 \quad (23)$$

A further derivation is applied to show that a similar structure as the Hessian can be found for the 3rd derivative. For higher orders this process can be repeated until the desired order is reached, giving us a recursive algorithm.

$$D_u(C_2) = -V^{-1} [D_s(V) D_s(F_2) F_2] \begin{bmatrix} C_2 \otimes K \\ G_2 \otimes K \\ D_u(G_2) \end{bmatrix} = -V^{-1} F_3 G_3 \quad (24)$$

This algorithm consist of three steps: (1) The higher-order derivatives of V , and U are filled into the proper location of F_k . These can be found a priori by higher-order screw derivatives of the open-loop equivalent. (2) The G_k matrix is filled with precursory, lower-order results. (3) The combination of the three matrices give the subsequent partial derivative of the closure Jacobian (C_k). The derivatives of the G_k matrix involves permutation for the derivatives of the Kronecker product [6]. The exact nature of this permutation is outside the scope of this paper.

The Taylor approximation of the loop closure solution can now be written using the partial derivatives of the closure Jacobians up to the k -th order. We assume that at the evaluation point the closure constraint is satisfied, and that $s = \mathbf{0}$ such that the Taylor series becomes a Maclaurin series. The input for the independent variables is given as a power (denoted with the \otimes^i) of Kronecker products [6]:

$$v(u) = \mathbf{0} + C_1 u + \frac{1}{2!} C_2 (u \otimes u) + \frac{1}{3!} C_3 (u \otimes u \otimes u) + \dots \approx \sum_{i=1}^k \frac{1}{i!} C_i u^{\otimes i} \quad (25)$$

2.6 Approximate Solution of a 5-Bar Mechanism

The higher-order derivatives and Taylor expansion is applied to approximate the inverse kinematic model of a 5-bar mechanism. We choose to describe the 5-bar as a connection of two open chains (a , and b) with joints q_1, q_2 and q_3, q_4 respectively. The connection point is the end-effector x^0 . This point has to satisfy

the constraint equation from both sides (a, b) calculated using the connection point in the local frame (\mathbf{x}^2 and \mathbf{x}^4). The closure equation can be written as:

$$\mathbf{x}_a^0 = \mathbf{H}_2^0(\mathbf{q}_{1,2})\mathbf{x}^2 \quad \mathbf{x}_b^0 = \mathbf{H}_4^0(\mathbf{q}_{3,4})\mathbf{x}^4 \quad f : \mathbf{0} = \begin{bmatrix} \mathbf{x}^0 - \mathbf{x}_a^0 \\ \mathbf{x}^0 - \mathbf{x}_b^0 \end{bmatrix} \quad (26)$$

Using the end-effector coordinates ($\mathbf{u} = \mathbf{x}^0$) as input and the 4 joint angles ($\mathbf{v} = [q_1 \dots q_4]^\top$) as output, the first-order partial derivatives of the closure equation become:

$$D_{\mathbf{u}}(f) = \mathbf{U} = \begin{bmatrix} \mathbf{I} \\ \mathbf{I} \end{bmatrix} \quad D_{\mathbf{v}}(f) = \mathbf{V} = \begin{bmatrix} [\hat{t}_1^0 \times] \mathbf{x}_a^0 & [\hat{t}_2^0 \times] \mathbf{x}_a^0 & \mathbf{0} & \mathbf{0} \\ \mathbf{0} & \mathbf{0} & [\hat{t}_3^0 \times] \mathbf{x}_b^0 & [\hat{t}_4^0 \times] \mathbf{x}_b^0 \end{bmatrix} \quad (27)$$

The higher-order partial derivatives can be found by using the twist derivatives of Sect. 2.2 and recursive equations of Sect. 2.5.

3 Results

The Taylor approximation, up to the 5-th order, is done for 200 positions of the end-effector (\mathbf{x}^0) forming 4 trajectories through the workspace with the aim to find an approximation of the corresponding joint displacement of the joints ($q_1 \dots q_4$). For evaluation of the quality of the Taylor approximation, the end-effector position approximation from the left (\mathbf{x}_a^0) and right (\mathbf{x}_b^0) side are plotted together with input trajectories.

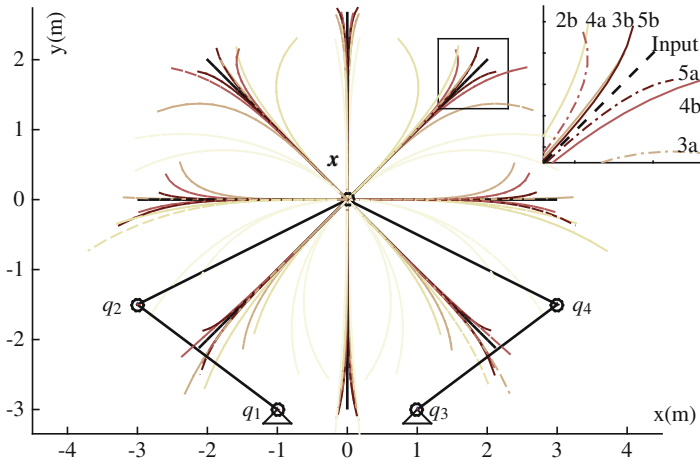


Fig. 1. The Taylor approximation of the IKM of a 5-bar (solid black) around evaluation point at $\mathbf{x}^0 = [0,0]$ up to the 5th order for 4 different trajectories. It shows the left (solid colored) and right (dashed colored) estimation of end-effector trajectory (dashed black). The insert shows convergence for higher-order estimation far from the evaluation point.

The result of the Taylor approximation (Fig. 1) shows that in a large portion of the workspace around the evaluation point ($\mathbf{x}^0 = \mathbf{0}$) the approximation converges to input indicating a correct estimation of finite joint displacement. However, further from the evaluation point the accuracy is less as can be seen in the insert.

4 Discussion and Conclusion

For the calculation of higher-order partial derivatives, this method uses Kronecker products of matrices, which can lead to very large matrices for larger systems and higher orders. This possibly poses practical limits on applicability of this procedure. Sparse matrices and the aggregation of mixed partial derivatives can be used to mitigate the memory usage and reduce the number of matrix operations. It is worth investigating what determines the validity of the Taylor approximations in kinematics, such as the radius of convergence and the closeness to singularities.

In this paper, a recursive method was presented which gives the higher-order partial derivatives of closure Jacobians of open and closed loop mechanisms consisting of lower kinematic pairs. This method relied on a simplified representation of the higher-order twist derivatives, also presented here, and the matrix derivatives of Vetter [6]. This enabled the Taylor approximation of a kinematic mapping over a given trajectory, as exemplified the 5-bar mechanism.

References

1. Brockett, R.W.: Robotic manipulators and the product of exponentials formula. In: *Mathematical Theory of Networks and Systems SE - 9*, vol. 58, pp. 120–129 (1984)
2. Rico, J.M., Gallardo, J., Duffy, J.: Screw theory and higher order kinematic analysis of open serial and closed chains. *Mech. Mach. Theory* **34**(4), 559–586 (1999)
3. Müller, A.: Higher derivatives of the kinematic mapping and some applications. *Mech. Mach. Theory* **76**, 70–85 (2014)
4. Müller, A.: Recursive higher-order constraints for linkages with lower kinematic pairs. *Mech. Mach. Theory* **100**, 33–43 (2016)
5. Tsoy, W.M.: Higher chain formula proved by combinatorics. *Electron. J. Comb.* **16**(1), 1–7 (2009)
6. Vetter, W.J.: Matrix calculus operations and Taylor expansions. *SIAM review* **15**(2), 352–369 (1973)

A New Direct Position Analysis Solution for an Over-Constrained Gough-Stewart Platform

Luca Luzi¹(✉), Nicola Sancisi^{1,2}, and Vincenzo Parenti Castelli^{1,2}

¹ Department of Industrial Engineering (DIN), University of Bologna,
Viale del Risorgimento 2, 40136 Bologna, Italy

{luca.luzi3,nicola.sancisi,vincenzo.parenti}@unibo.it

² Health Sciences and Technologies,

Interdepartmental Centre for Industrial Research (HSTICIR),
University of Bologna, Viale del Risorgimento 2, 40136 Bologna, Italy

Abstract. Recently, the authors presented a new over-constrained manipulator with six degrees of freedom, based on a modified Gough-Stewart platform, and a solution for its direct position analysis. In this paper, a different solution is proposed based on a different parameterization that leads to a reduced system of four closure equations. The new method simplifies the analytical derivation and the geometrical interpretation of the results.

Keywords: Modified Gough-Stewart platform · Direct position analysis · Reduced equation system

1 Introduction

Several types of Gough-Stewart (GS) platforms were proposed in the literature [1]. A new mechanism has been recently presented [2], together with its direct position analysis (DPA). The new manipulator is an evolution of a previous type of GS platform [3] and has several interesting characteristics [2] with respect to the classic GS: it features a lower number of kinematic pairs thus simplifying the mechanical design; it is an over-constrained mechanism, giving the opportunity to remove clearance in kinematic pairs; it features a larger workspace, free from kinematic singularities for practical mechanism dimensions.

In this paper a new solution of the DPA is presented. The closure equations of the mechanism have been found relying upon a technique, known as “open loop chain”, that was presented in [4] and used to solve the DPA of many mechanisms.

Differently from the classical approach, we show in this paper that the core of the DPA can be reduced to a system of four equations in four unknowns. The full analytical derivation is reported here and the new solution is discussed.

2 Modified Gough-Stewart Manipulator

A full description of the new mechanism and of its characteristics is presented in [2]: only its general features are reported here for the sake of clarity. The mechanism (Fig. 1) is composed of a mobile platform (1) (defined by the points C_i , $i = 1, 2, 3$, that define the plane σ), with six degrees-of-freedom with respect to the fixed base (2) (defined by the points $A_{i,j}$, $i = 1, 2, 3$, $j = 1, 2$), that are connected by means of three kinematic chains $i = 1, 2, 3$ (Fig. 2), defined by the points $A_{i,1}, A_{i,2}, B_{i,2}, B_{i,1}$. The mobile platform is connected to the upper link $B_{i,2}B_{i,1}$ of each kinematic chain by the universal joints centered at points C_i . The two axes of the universal joint must not be parallel to the normal to the plane γ_i passing through the points $C_i, A_{i,1}, A_{i,2}$, as to avoid redundancy. In each kinematic chain, $B_{i,j}$ and $A_{i,j}$ denote the connection points of the linear actuators with the upper link and the fixed base, by revolute and universal joints respectively. These joints must comply with some geometrical conditions: the revolute joint axes and the mobile axes of two universal joints must be parallel, while the other universal joint axes must be collinear (Fig. 2). Because of the linear constraints, the i -th kinematic chain lies on the plane γ_i for any configuration of the mobile platform.

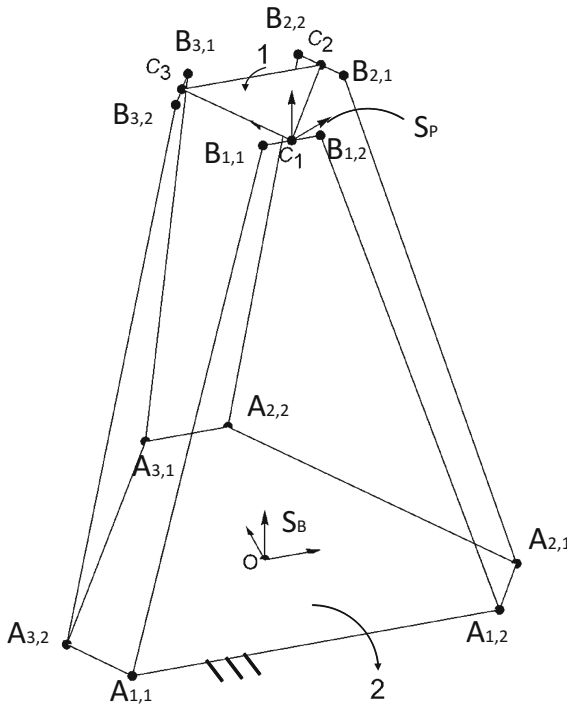


Fig. 1. Schematic representation of the manipulator.

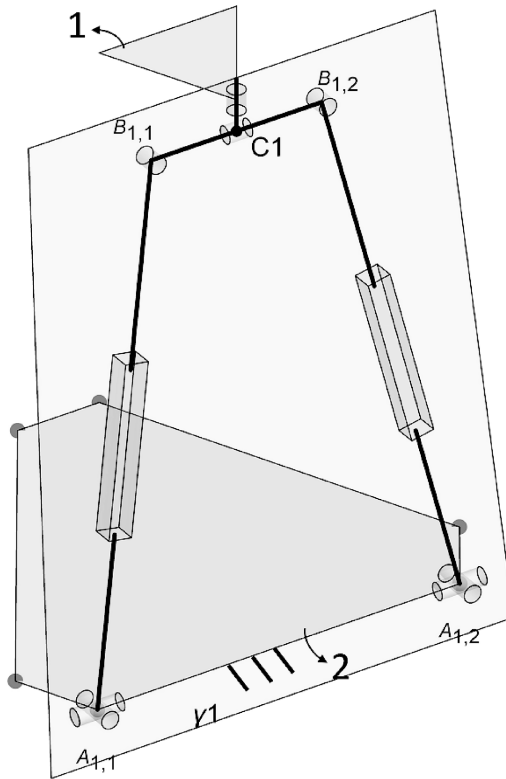


Fig. 2. Detailed representation of the first kinematic chain.

3 Direct Position Analysis

The DPA problem is to find the configuration of the mobile platform, given the lengths of the legs. For the sake of simplicity, the points $A_{i,j}$ of the base will be considered on the same plane, though the mechanism allows a more general geometry also. However, the DPA presented in this paper can be easily generalized to the general geometry by a few adjustments. Two Cartesian coordinate systems are defined (Fig. 1). The first one (S_B) is attached to the fixed base: its center is located at the centroid O of the fixed base, x axis parallel to the vector $\mathbf{A}_{1,1}\mathbf{A}_{1,2}$, z axis orthogonal to the plane on which the fixed base lies, y axis as a consequence. The second coordinate system (S_P) is attached to the mobile platform: it has center on the point C_1 , y axis coincident with the direction $\mathbf{C}_1\mathbf{C}_3$, z axis orthogonal to the plane σ , x axis as a consequence. The mechanism geometry is defined as follows: $\mathbf{a}_{i,j}$ is the position vector of the point $A_{i,j}$ in S_B ; \mathbf{c}_i is the position vectors of the point C_i in S_P ; \mathbf{r}_i is the vector that identifies the frame link of the i -th kinematic chain (i.e., $\mathbf{r}_i = \mathbf{A}_{i,2}\mathbf{A}_{i,1}$); $l_{i,j}$ is the length of the j -th link of the i -th kinematic chain (i.e., $l_{i,j} = \|\mathbf{A}_{i,j}\mathbf{B}_{i,j}\|$); \mathbf{k} is the unit vector normal to the plane σ (i.e., the unit vector of the z axis of the S_P); \mathbf{u}_i is the unit vector normal to the plane γ_i ; \mathbf{t}_i is the

unit vector that defines the direction of the vector $\mathbf{B}_{i,1}\mathbf{B}_{i,2}$ (i.e., $\mathbf{t}_i = \mathbf{B}_{i,1}\mathbf{B}_{i,2}/\|\mathbf{B}_{i,1}\mathbf{B}_{i,2}\|$), and l is its norm (i.e., $l = \|\mathbf{B}_{i,1}\mathbf{B}_{i,2}\|$).

The position of the points C_1 and $B_{1,j}$ can be described with respect to the S_B by the four parameters ψ_i ($i = 1,2,3,4$) (Fig. 3): ψ_1 is the angle between the vector \mathbf{r}_1 and the vector $\mathbf{A}_{1,1}\mathbf{B}_{1,1}$, ψ_2 is the angle between the plane γ_1 and the plane identified by the fixed base, ψ_3 is the angle between the vectors \mathbf{k} and \mathbf{u}_1 , and ψ_4 is the angle between the unit vector obtained as the cross product between the vector \mathbf{k} and \mathbf{t}_1 and the y axis of the S_p . In particular, the position of the point C_1 can be expressed as a function of ψ_1 and ψ_2 and the lengths $l_{1,1}$ and $l_{1,2}$ only, as it will be clarified further on. Moreover, it is worth noting that the kinematic chain $A_{1,1}B_{1,1}B_{1,2}A_{1,2}$ is a four bar mechanism if the prismatic joints are locked, and the angle θ (i.e., the angle between the upper and the lower links) can be expressed as a function of the angle ψ_1 and the lengths $l_{1,1}$ and $l_{1,2}$, according to the well-known relation [5]:

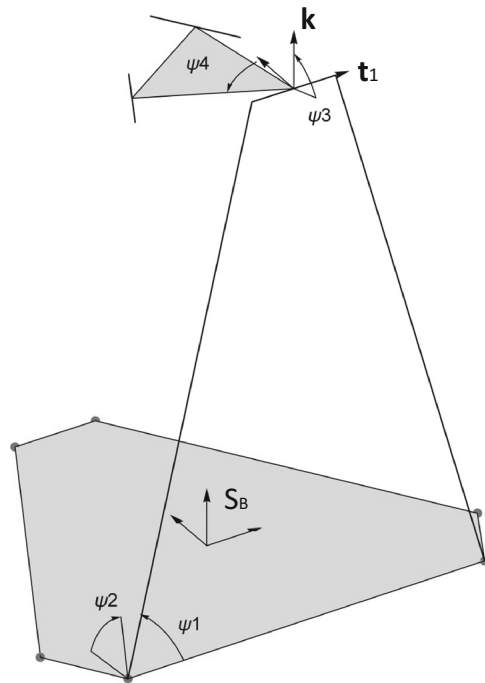


Fig. 3. Representation of the four parameters used for the DPA.

$$\theta = 2 \tan^{-1} \left(\frac{-b - \sqrt{b^2 - 4ac}}{2a} \right) \tag{1}$$

where

$$\begin{aligned} a &= -h_1 + (1 + h_2) \cos(\psi_1) + h_4 \\ b &= -2 \sin(\psi_1) \\ c &= h_1 - (1 - h_2) \cos(\psi_1) + h_4 \end{aligned} \tag{2}$$

and

$$h_1 = \frac{r_1}{l_1}, \quad h_2 = \frac{r_1}{l}, \quad h_4 = \frac{-r_1^2 - l_1^2 - l^2 + l_2^2}{2 \cdot l \cdot l_1} \tag{3}$$

The position vector of the point C_1 can be thus written as:

$$\mathbf{OC}_1 = \mathbf{a}_{1,1} + \mathbf{A}_{1,1} \mathbf{B}_{1,1} + \frac{\mathbf{B}_{1,1} \mathbf{B}_{1,2}}{2} \tag{4}$$

Where the vector $\mathbf{B}_{1,1} \mathbf{B}_{1,2}$, can be express in S_B as:

$${}^B(B_{1,1}B_{1,2}) = l \begin{pmatrix} \cos \theta \\ \sin \theta \cos \psi_2 \\ \sin \theta \sin \psi_2 \end{pmatrix}, \quad {}^B(A_{1,1}B_{1,1}) = l_{1,1} \begin{pmatrix} \cos \psi_1 \\ \sin \psi_1 \cos \psi_2 \\ \sin \psi_1 \sin \psi_2 \end{pmatrix} \tag{5}$$

The position vector \mathbf{OC}_i ($i = 2, 3$) can be expressed as a function of the four parameters as follows:

$${}^B(OC_i) = {}^B(OC_1) + {}^B\mathbf{R}_P^P c_i \quad i = 2, 3 \tag{6}$$

where

$${}^B\mathbf{R}_P = \mathbf{R}_{r_1}(\psi_2) \mathbf{R}_{u_1}(\theta) \mathbf{R}_{t_1}(\psi_3) \mathbf{R}_k(\psi_4) \tag{7}$$

In (7), each \mathbf{R} is the 3×3 orthonormal matrix that represents a rotation defined by the angle in brackets about the axis specified in the subscript.

The expression of the point $B_{i,j}$ ($i = 2, 3; j = 1, 2$) with respect to the S_B can be determined without adding new variables. In particular, it is worth noting that the direction \mathbf{t}_i is obtained as the intersection between the two planes σ and γ_i (Fig. 4). In fact, the joint centered in C_i allows the upper link of the i -th kinematic chain to rotate about the axis \mathbf{k} , so as the direction \mathbf{t}_i lies on the plane σ . Furthermore, the direction \mathbf{t}_i lies on the plane γ_i , since the vector $\mathbf{B}_{i,1} \mathbf{B}_{i,2}$ identifies the upper link of the i -th kinematic chain. Thus, the vector \mathbf{t}_i can be found as the cross product between \mathbf{k} and \mathbf{u}_i :

$$\mathbf{t}_i = \frac{\mathbf{k} \times \mathbf{u}_i}{|\mathbf{k} \times \mathbf{u}_i|} \tag{8}$$

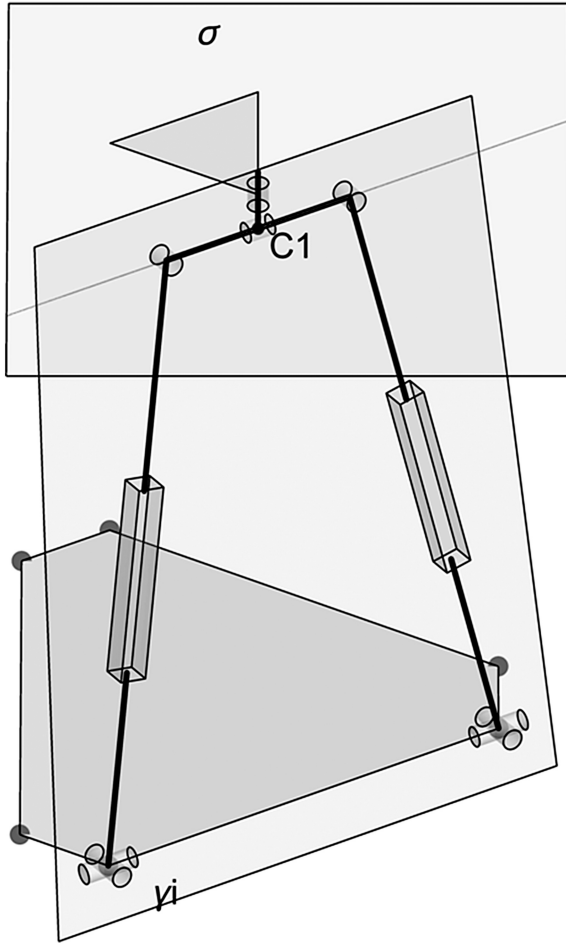


Fig. 4. Definition of the line that passes through the upper link of the kinematic chain

Since:

$$\mathbf{u}_i = \frac{\mathbf{r}_i \times \mathbf{A}_{i,1} \mathbf{C}_i}{|\mathbf{r}_i \times \mathbf{A}_{i,1} \mathbf{C}_i|} \tag{9}$$

Finally, \mathbf{t}_i can be expressed without adding new variables:

$$\mathbf{t}_i = \frac{\mathbf{k} \times (\mathbf{r}_i \times \mathbf{A}_{i,1} \mathbf{C}_i)}{|\mathbf{k} \times (\mathbf{r}_i \times \mathbf{A}_{i,1} \mathbf{C}_i)|} \tag{10}$$

where

$$\mathbf{A}_{i,1}\mathbf{C}_i = \mathbf{OC}_i - \mathbf{a}_{i,1} \tag{11}$$

The position vector $\mathbf{B}_{i,j}$ with respect to the S_B can be written as:

$$\mathbf{OB}_{i,j} = \mathbf{a}_{i,j} + \mathbf{A}_{i,j}\mathbf{B}_{i,j} = \mathbf{OC}_i \pm l \frac{\mathbf{t}_i}{2} \tag{12}$$

Thus, a system of four equations in the four unknowns ψ_n , $n = 1, \dots, 4$, can be obtained:

$$(\mathbf{A}_{i,j}\mathbf{B}_{i,j})^T(\mathbf{A}_{i,j}\mathbf{B}_{i,j}) = l_{i,j}^2 = (\mathbf{OC}_i \pm l \frac{\mathbf{t}_i}{2} - \mathbf{a}_{i,j})^T(\mathbf{OC}_i \pm l \frac{\mathbf{t}_i}{2} - \mathbf{a}_{i,j}) \tag{13}$$

$i = 2, 3; j = 1, 2;$

This system represents the final solution of the DPA, since it makes it possible to obtain the values of the parameters ψ_n that describe the platform pose, when the mechanism geometry and the actuator lengths are given.

4 Numerical Example

As an example, a specific geometry of the mechanism is considered in this section and its configuration is determined with the proposed DPA method for three representative combinations of actuator lengths (Table 1). The points $A_{i,j}$ are on a circle with diameter $d_b = 840$ mm; position vectors of consecutive points $A_{i,j}$ belonging to different kinematic chains form an angle of $\varphi = \pi/9$ (Fig. 5); the points C_i of the mobile platform form an equilateral triangle inscribed in a circumference of diameter $d_p = 280$ mm; the length of the upper link is $l = 100$ mm. In the first considered combination the actuators have all the same length (corresponding to the initial configuration of the platform); in

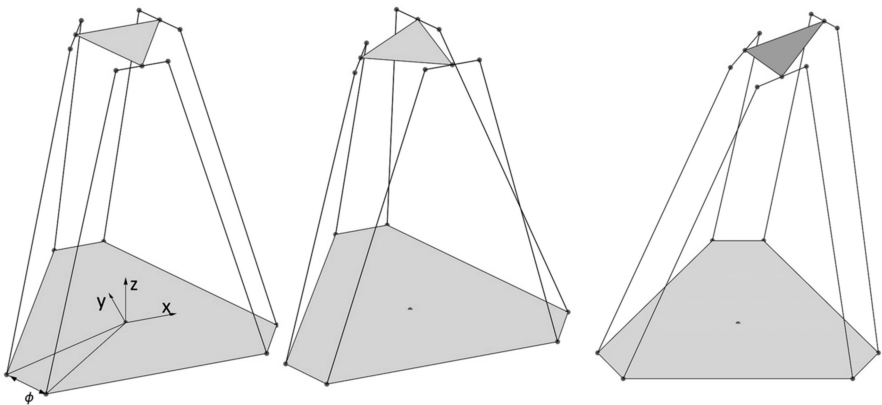


Fig. 5. The three considered mechanism configurations.

the second one, the actuators have the same length three by three that provide a configuration in which the platform is rotated about the z axis); in the third configuration, the actuators have length that provide a configuration in which the platform is rotated about the y axis.

Table 1. Actuator lengths and corresponding values of the configuration parameters at the three considered mechanism poses.

$[l_{1,1} \ l_{1,2} \ l_{2,1} \ l_{2,2} \ l_{3,1} \ l_{3,2}]$	Ψ_1	Ψ_2	Ψ_3	Ψ_4
[958.6, 958.6, 958.6, 958.6, 958.6, 958.6]	1.33736	1.43097	-1.43097	0.523599
[891.6, 847.8, 891.6, 847.8, 891.6, 847.8]	1.21866	1.37925	-1.37925	1.183130
[973.3, 969.8, 1004.2, 1002.9, 939.5, 941.6]	1.17517	1.43822	-1.47862	0.438011

5 Conclusions

In this paper, a new solution for the DPA of a recently proposed over-constrained parallel manipulator is presented. The mechanism is a modified version of the Gough-Stewart manipulator, in which the platform is connected to the base by three kinematic chains that behave as four bar linkages when the actuator lengths are fixed. The new DPA solution is based on a parameterization that leads to a system of four equations in four unknowns, thus reducing the classic system of six equations in six unknowns. This parameterization makes it possible to represent the platform pose through the configuration of a single kinematic chain, thus simplifying the analytical derivation and the geometrical interpretation of the results.

References

1. Dasgupta, B., Mruthyunjaya, T.S.: The Stewart platform manipulator - a review. *Mech. Mach. Theory* **35**, 15–40 (2000)
2. Luzi, L., Sancisi, N., Parenti-Castelli, V.: Design and direct kinematic analysis of a new over-constrained modified Gough-Stewart platform (Under review)
3. Akeel, H.A.: Programmable positioner for the stress-free assembly of components, US005987726A (1996)
4. Innocenti, C., Parenti-Castelli, V.: Direct position analysis of the Stewart platform mechanism. *Mech. Mach. Theory* **25**, 611–621 (1990)
5. Hunt, K.H.: *Kinematic Geometry of Mechanisms*. Oxford University Press, Oxford (1990)

A Study on Constraints Violation in Dynamic Analysis of Spatial Mechanisms

P. Flores^(✉)

Department of Mechanical Engineering, University of Minho,
Campus of Azurém, 4804-533 Braga, Portugal
pflores@dem.uminho.pt

Abstract. The main goal of this work is present a comparative study on several methodologies to solve the equations of motion of constrained spatial multibody systems taking into account the problem of constraints violation. In the sequel of this process, the two main categories of methods to eliminate or reduce constraints violation are revisited, namely those that are based on constraint stabilization approaches and direct correction formulations. Particular attention is given to the most popular approaches, that is, Baumgarte stabilization formulation, penalty method, Augmented Lagrangian formulation and a direct correction approach. Finally, several examples of application are considered to compare the accuracy and efficiency of the different methods used throughout this study.

Keywords: Constraints violation · Baumgarte method · Penalty approach · Augmented Lagrangian formulation · Direct correction · Multibody dynamics

1 Introduction

By and large, the methods to deal with the problem of constraints violation for dynamics of constrained multibody mechanical systems can be divided into three main groups, namely: (i) constraint stabilization approaches; (ii) coordinate partitioning methods and (iii) direct correct formulations [1]. The constraint stabilization approaches are the most popular due to their simplicity and easiness for computational implementation [2]. The coordinate partitioning methods have the great merit of allowing the rigorous resolution of the constraint equations at the position, velocity and acceleration levels. However, they suffer from poor numerical efficiency due to the requirement for the iterative solution for dependent generalized coordinates in the Newton-Raphson method [3]. Finally, the direct formulations have physical meaning, computational efficiency, but they can exhibit some numerical instability [4].

The main focus of this study, which closely follows the recent work by Flores and his coauthors [1], is on the elimination of the constraints violation in dynamic analysis of spatial mechanisms. For this, body coordinates formulation is utilized to describe the system components and the kinematic joints. The equations governing the dynamic behavior of the systems incorporate corrective terms that are added to the position and velocity vectors in order to satisfy the corresponding constraint equations. These corrective terms are expressed in terms of the Jacobian matrix and kinematic constraint

equations. The corrective terms are added and considered during the numerical resolution of the dynamic equations of motion. Results for spatial mechanisms are presented and utilized to discuss the assumptions and procedures adopted throughout this work.

2 Methods to Handle Constraints Violation

The translational and rotational equations of motion for dynamic analysis of constrained spatial mechanisms can be expressed in the form [5]

$$\begin{bmatrix} \mathbf{M} & \mathbf{D}^T \\ \mathbf{D} & \mathbf{0} \end{bmatrix} \begin{Bmatrix} \dot{\mathbf{v}} \\ \boldsymbol{\lambda} \end{Bmatrix} = \begin{Bmatrix} \mathbf{g} \\ \boldsymbol{\gamma} \end{Bmatrix} \quad (1)$$

Applying any method suitable for the resolution of linear algebraic equations can solve this linear system of equations. The existence of null elements in the main diagonal of the leading matrix and the possibility of ill-conditioned matrices suggest that methods using partial or full pivoting are preferred. In a simple way, Eq. (1) is solved for the accelerations then, the velocities and positions can be obtained by numerical integration. This procedure must be repeated until the final time of analysis is reached. This manner to solve the dynamic equations of motion is commonly referred to as the standard Lagrange multipliers method [5].

It is known that Eq. (1) does not use explicitly the position and velocity equations associated with the kinematic constraints. Consequently, during the simulations, the constraint equations start to be violated. In order to keep the constraint violations under control, the Baumgarte stabilization method can be considered [2]. This method allows constraints to be slightly violated before corrective actions can take place, in order to force the violation to vanish. Thus, using the Baumgarte approach, the equations of motion for a system subjected to kinematic constraints can be stated in the following form

$$\begin{bmatrix} \mathbf{M} & \mathbf{D}^T \\ \mathbf{D} & \mathbf{0} \end{bmatrix} \begin{Bmatrix} \dot{\mathbf{v}} \\ \boldsymbol{\lambda} \end{Bmatrix} = \begin{Bmatrix} \mathbf{g} \\ \boldsymbol{\gamma} - 2\boldsymbol{\alpha}\dot{\boldsymbol{\Phi}} - \boldsymbol{\beta}^2\boldsymbol{\Phi} \end{Bmatrix} \quad (2)$$

If α and β are chosen as positive constants, the stability of the general solution of Eq. (2) is guaranteed. Baumgarte [2] highlighted that the suitable choice of the parameters α and β can be performed by numerical experiments. Hence, the Baumgarte method has some ambiguity in determining optimal feedback gains. The improper choice of these parameters can lead to unacceptable results in the dynamic analysis of the multibody systems [6].

The penalty method constitutes an alternative way to solve the dynamic equations of motion. In this method, the equations of motion are modeled as a linear second-order differential equation that can be written in the form [7]

$$m_c \ddot{\boldsymbol{\Phi}} + d_c \dot{\boldsymbol{\Phi}} + k_c \boldsymbol{\Phi} = \mathbf{0} \quad (3)$$

Taking into account the second derivative of the algebraic constraint equations, then Eq. (3) yields

$$m_c(\mathbf{D}\dot{\mathbf{v}} + \dot{\mathbf{D}}\mathbf{v}) + d_c\dot{\Phi} + k_c\Phi = \mathbf{0} \tag{4}$$

Pre-multiplying Eq. (4) by the transpose of Jacobian matrix, \mathbf{D}^T , and after mathematical treatment, results in

$$m_c\mathbf{D}^T\mathbf{D}\dot{\mathbf{v}} = -\mathbf{D}^T(m_c\dot{\mathbf{D}}\mathbf{v} + d_c\dot{\Phi} + k_c\Phi) \tag{5}$$

Let consider now the Newton-Euler equations of motion for a system of unconstrained system and written here as [5]

$$\mathbf{M}\dot{\mathbf{v}} = \mathbf{g} \tag{6}$$

Summation of Eqs. (5) and (6), and after some basic mathematical manipulations yields

$$(\mathbf{M} + \alpha\mathbf{D}^T\mathbf{D})\dot{\mathbf{v}} = \mathbf{g} - \alpha\mathbf{D}^T(-\gamma + 2\mu\omega\dot{\Phi} + \omega^2\Phi) \tag{7}$$

where

$$\alpha = m_c, \quad d_c = 2\mu\omega m_c \quad \text{and} \quad k_c = \omega^2 m_c \tag{8}$$

Equation (8) is solved for the accelerations. This method gives good results if α tends to infinity. Typical values of α , ω and μ are 1×10^7 , 10 and 1, respectively [9]. It should be noted that with this penalty method, multibody systems with redundant constraints or kinematic singular configurations could be easily solved.

The augmented Lagrangian formulation penalizes the constraints violation, in the same form as the Baumgarte stabilization method. This is an iterative procedure that presents a number of advantages relative to other methods because it involves the solution of a smaller set of equations, handles redundant constraints and still delivers accurate results in the vicinity of singular configurations [7]. The augmented Lagrangian formulation consists of solving the system equations of motion by an iterative process. Let index i denote the i -th iteration. The evaluation of the system accelerations in a given time step starts as

$$\mathbf{M}\dot{\mathbf{v}}_i = \mathbf{g}, \quad (i = 0) \tag{9}$$

The iterative process to obtain the accelerations proceeds with the evaluation of the following equations obtaining the accelerations

$$(\mathbf{M} + \alpha\mathbf{D}^T\mathbf{D})\dot{\mathbf{v}}_{i+1} = \mathbf{M}\dot{\mathbf{v}}_i - \alpha\mathbf{D}^T(-\gamma + 2\mu\omega\dot{\Phi} + \omega^2\Phi) \tag{10}$$

This iterative process continues until

$$\|\dot{\mathbf{v}}_{i+1} - \dot{\mathbf{v}}_i\| = \varepsilon \tag{11}$$

Where ε is a specified tolerance.

In what follows, an approach to deal with the elimination of the constraints violation at both position and velocity levels is briefly described [1]. For this, let consider that during the numerical resolution of the dynamic equations of motion, the vector of generalized coordinates needs to be corrected due to the constraints violation. Thus, the corrected positions can be expressed in the form

$$\mathbf{q}^c = \mathbf{q}'' + \delta\mathbf{q} \tag{12}$$

where \mathbf{q}'' denotes the uncorrected positions and $\delta\mathbf{q}$ is the set of corrections that eliminates the constraints violation. This means that the corrective term has to be added to vector \mathbf{q}'' in order to ensure that the constraint equations are satisfied, i.e.

$$\Phi(\mathbf{q}^c) = \Phi(\mathbf{q}'') + \delta\Phi = \mathbf{0} \tag{13}$$

The term $\delta\Phi$ in Eq. (13) can be understood as the variation of the constraint equations and can be expressed as [8]

$$\delta\Phi = \frac{\partial\Phi}{\partial\mathbf{q}_1}\delta\mathbf{q}_1 + \frac{\partial\Phi}{\partial\mathbf{q}_2}\delta\mathbf{q}_2 + \dots + \frac{\partial\Phi}{\partial\mathbf{q}_n}\delta\mathbf{q}_n = \mathbf{D}\delta\mathbf{q} \tag{14}$$

Combining now Eqs. (13) and (14) yields

$$\Phi(\mathbf{q}'') + \mathbf{D}\delta\mathbf{q} = \mathbf{0} \tag{15}$$

which ultimately leads to

$$\delta\mathbf{q} = -\mathbf{D}^{-1}\Phi(\mathbf{q}'') \tag{16}$$

In general, the Jacobian matrix, \mathbf{D} , is not square, therefore, \mathbf{D}^{-1} does not exist. However, the concept of the Moore-Penrose generalized inverse matrix, \mathbf{D}^+ , can be employed as [1]

$$\mathbf{D}^+ = \mathbf{D}^T(\mathbf{D}\mathbf{D}^T)^{-1} \tag{17}$$

such that

$$\mathbf{D}\mathbf{D}^+\mathbf{D} = \mathbf{D} \quad \mathbf{D}^+\mathbf{D}\mathbf{D}^+ = \mathbf{D}^+ \tag{18}$$

and both $\mathbf{D}^+\mathbf{D}$ and $\mathbf{D}\mathbf{D}^+$ are symmetric matrices. Consequently, it is possible to establish the following mathematical relation [1]

$$\mathbf{D}^T(\mathbf{D}\mathbf{D}^T)^{-1} = \mathbf{D}^T(\mathbf{D}^+)^T\mathbf{D}^+ = (\mathbf{D}^+\mathbf{D})^T\mathbf{D}^+ = \mathbf{D}^+\mathbf{D}\mathbf{D}^+ = \mathbf{D}^+ \quad (19)$$

Thus, Eq. (16) can be rewritten in the following form

$$\delta\mathbf{q} = -\mathbf{D}^T(\mathbf{D}\mathbf{D}^T)^{-1}\Phi(\mathbf{q}^u) \quad (20)$$

Finally, introducing Eq. (20) into Eq. (15) yields

$$\mathbf{q}^c = \mathbf{q}^u - \mathbf{D}^T(\mathbf{D}\mathbf{D}^T)^{-1}\Phi(\mathbf{q}^u) \quad (21)$$

that represents the corrected generalized coordinates in each integration time step. It must be noticed that the kinematic constraint equations at the position level are, in general, nonlinear, then Eq. (21) must be solved iteratively by employing a numerical algorithm, such as the Newton-Raphson method.

A similar analysis can be performed at the velocity level, resulting in

$$\mathbf{v}^c = \mathbf{v}^u - \mathbf{D}^T(\mathbf{D}\mathbf{D}^T)^{-1}\dot{\Phi}(\mathbf{q}^c, \mathbf{v}^u) \quad (22)$$

that represents the corrected generalized velocities in each integration time step.

The described methodology can be easily incorporated in the standard method to solve the dynamic equations of motion. The approach described above does not consider weighting factors to the coordinates and velocities variables. In order to take into account different weighting factors, some works have been proposed to include inertia of bodies, which allow for the adjustments to be made in an inverse manner to the system inertia. The basic idea of this approach is that the more massive bodies are moved the least if the constraints allow that [8].

3 Results and Discussion

In order to examine the effectiveness of the approaches briefly presented in the previous section, a spatial four bar mechanisms is considered as an example of application. Figure 1 depicts the initial configuration of this mechanism, which includes three moving bodies, a non-moving body (the ground), two revolute joints and two spherical joints. The revolute joint that connects the crank to the ground is along the x -axis, while the revolute joint that connects the follower to the ground is in the xy plane and makes a 45° angle with the y -axis. At the initial time, the crank is along the z -axis and the other two moving bodies are in the yz plane. A spring element is also considered in this multibody system model in which the spring stiffness and the natural length are equal to 50 N/m and 0.8 m, respectively. Governing properties of the four bar mechanism are presented in Table 1. The initial conditions necessary to characterize this multibody model are obtained from a kinematic analysis for an input constant crank speed equal to 2π rad/s.

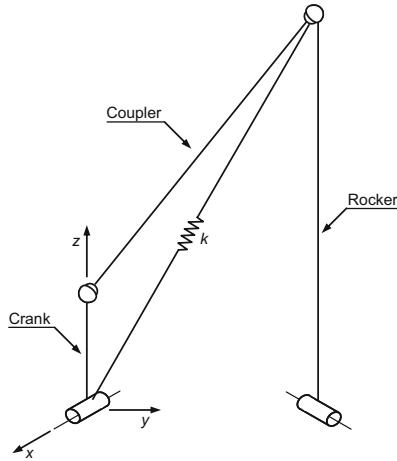


Fig. 1. Spatial four bar mechanism modeled

Table 1. Governing properties for the four bar linkage

Body	Length [m]	Mass [kg]	Moment of inertia [kgm ²]		
			$I_{\xi\xi}$	$I_{\eta\eta}$	$I_{\zeta\zeta}$
Crank	0.020	0.50	0.03	0.03	0.03
Coupler	0.064	1.50	0.02	0.02	0.02
Rocker	0.070	0.15	0.02	0.02	0.02

Long time computational simulations are performed to test and compare the accuracy and efficiency of use different methods to solve the dynamic equations of motion. For this purpose, five approaches are considered, namely the standard method based on the technique of Lagrange multipliers, the Baumgarte method, the penalty method, the augmented Lagrangian formulation and the described methodology. The quantitative measure of the efficiency of these approaches is drawn from the constraints violation as $\Phi^T \Phi$, as well as from the computation time of the dynamic simulations. Table 2 gives the parameters used for the different models, necessary to characterize the problem.

Figure 2 shows the constraints violation at the position level for the four bar mechanism. It should be noticed that different scales are used for the results plotted in Figs. 2a–b, in order to clearly observe the effect of the method used to solve the system dynamics on the constraints violation. By analyzing the diagrams of Figs. 2, it can be observed that when the standard method is utilized the violation of the constraint equations grows indefinitely with time. As it was expected, the standard method based on the Lagrange multipliers technique produces unacceptable results because the kinematic constraint equations are rapidly violated due to the inherent errors and instability that develop during computations. With the stabilization methods, the

Table 2. Parameters used for the dynamic simulations

Final time of simulation	5.0 s	Baumgarte - α	5
Integrator algorithm	ode45	Baumgarte - β	5
Reporting time step	0.02 s	Penalty - α	1×10^7
Relative tolerance	1×10^{-6}	Penalty - ω	10
Absolute tolerance	1×10^{-9}	Penalty - μ	1

behavior of the different methods is significantly different, in the measure that the level of the constraints violation is kept under control during the dynamic simulations. Indeed, with the Baumgarte approach, the penalty method and the augmented Lagrangian formulation experience tells that the numerical results do not diverge from the exact solution, but oscillate around it. Magnitude and frequency of the oscillations depend on the values of the penalty parameters used. Finally, when the described methodology is utilized to solve the dynamic equations of motion, the constraints violation is eliminated as it can be observed in Figs. 2. In fact, with the described approach the average of the constraints violation is of order 1.0×10^{-16} .

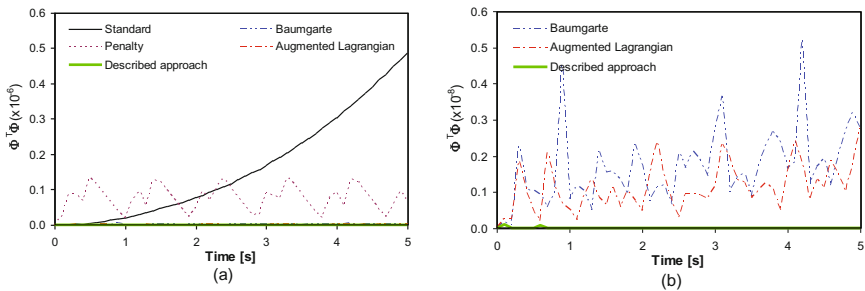


Fig. 2. Constraints violation $\Phi^T \Phi$ of the four bar mechanism

Figure 3 depicts the computation time consumed in dynamic simulations for the four bar mechanism, which can be used to have an idea about the computational efficiency of the different methods used to solve the system dynamics. The most efficient method to deal with the constraints violation is the Baumgarte approach. It can be observed that the described approach does not penalize the total amount of computation time when compared with the other methods to solve the dynamic equations of motion. It must be stated that the standard method is, in fact, the most efficient approach, however, it does not take into account the problem associated with the constraints violation.

The efficiency of the described method can be understood by its nature, in the measure that the two additional blocks are added to the standard solution of the equations of motion [1]. The elimination of the constraints violation for positions needs an iterative scheme, because the corrective terms are dependent on the positions.

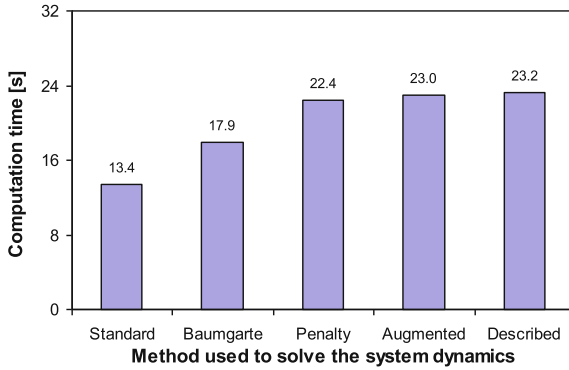


Fig. 3. Computation time for the four bar mechanism

However, based on the computational tests performed, this process requires at most three iterations to eliminate the constraints violation at the position to an acceptable level. The constraints violation for velocities are eliminated with a single step, since constraints at the velocity level are linear and the corrective terms are computed as function of the corrected positions performed previously.

4 Conclusions

A comparative study on the several methodologies to handle the problem of constraints violation in forward dynamics of constrained spatial mechanical systems has been presented in this work. For this, the most commonly used method to deal with resolution of the equations of motion and constraints violation have been revisited, namely the Baumgarte stabilization method, the penalty approach and the augmented Lagrangian formulation. In addition, an alternative approach to eliminate the violation of the kinematic constraint equations in the framework of forward dynamics of constrained multibody systems has been described. The basic idea of the described approach is to add corrective terms to the position and velocity vectors with the intent to satisfy the corresponding kinematic constraint equations. These corrective terms are evaluated as function of the Moore-Penrose generalized inverse of the Jacobian matrix and of the kinematic constraint equations. Finally, a spatial four bar mechanism has been considered as a demonstrative example of application to show that the effectiveness of the several approaches utilized in this study. From the obtained results, it can be drawn that the described approach is effective in eliminate the constraints violation at both positions and velocities levels without penalizing the computational efficiency.

Acknowledgments. This work has been supported by FCT with the reference project UID/EEA/04436/2013, by FEDER funds through the COMPETE 2020 – *Programa Operacional Competitividade e Internacionalização* (POCI) with the reference project POCI-01-0145-FEDER-006941.

References

1. Marques, F., Souto, A.P., Flores, P.: On the constraints violation in forward dynamics of multibody systems. *Multibody Syst. Dyn.* **39**(4), 385–419 (2017)
2. Baumgarte, J.: Stabilization of constraints and integrals of motion in dynamical systems. *Comput. Methods Appl. Mech. Eng.* **1**, 1–16 (1972)
3. Wehage, R.A., Haug, E.J.: Generalized coordinate partitioning for dimension reduction in analysis of constrained systems. *J. Mech. Des.* **104**, 247–255 (1982)
4. Fiset, P., Vaneghem, B.: Numerical integration of multibody system dynamic equations using the coordinate partitioning method in an implicit Newmark scheme. *Comput. Methods Appl. Mech. Eng.* **135**, 85–105 (1996)
5. Nikravesh, P.E.: *Computer-Aided Analysis of Mechanical Systems*. Prentice Hall, Englewood Cliffs (1988)
6. Flores, P., Machado, M., Seabra, E., Silva, M.T.: A parametric study on the Baumgarte stabilization method for forward dynamics of constrained multibody systems. *J. Comput. Nonlinear Dyn.* **6**(1), 1–9 (2011)
7. Jalón, J.G., Bayo, E.: *Kinematic and Dynamic Simulations of Multibody Systems: The Real-time Challenge*. Springer Verlag, New York (1994)
8. Flores, P.: A methodology for quantifying the position errors due to manufacturing and assemble tolerances. *J. Mech. Eng.* **57**(6), 457–467 (2011)

A Generalized and Analytical Method to Solve Inverse Kinematics of Serial and Parallel Mechanisms Using Finite Screw Theory

T. Sun¹(✉), S.F. Yang¹, T. Huang^{1,2}, and J.S. Dai³

¹ Key Laboratory of Mechanism Theory and Equipment Design
of Ministry of Education, Tianjin University, Tianjin 300350, China
stao@tju.edu.cn

² School of Engineering, The University of Warwick,
Coventry CV4 7AL, UK

³ Centre for Robotics Research, King's College London,
University of London, London WC2R 2LS, UK

Abstract. Inverse kinematics is a very important issue in the field of mechanisms and robotics, which is the fundamental problem in kinematical analysis, design and synthesis for both serial mechanisms (SMs) and parallel mechanisms (PMs). The objective of inverse kinematics is to formulate computable kinematic equation at the given pose of end-effector of a SM or moving platform of a PM and then solve all the joint parameters (variables). Solving analytical solution of inverse kinematics is the prerequisite for trajectory planning, precise control and manipulation of mechanisms. This paper presents a generalized method to analytically do inverse kinematics of PMs using finite screw theory. Firstly, the kinematic equation of PM is algebraically formulated through describing finite motions generated by the PM, its limbs and joints employing finite screws. Then, the general procedures to analytically solve the finite screw based kinematic equation are given. Finally, a PM with three translational and one rotational Schoenflies motion is taken as an example to verify the validity of the proposed method.

Keywords: Parallel mechanisms · Inverse kinematics · Screw theory · Finite screw

1 Introduction

Inverse kinematics, which is also called inverse position problem, is aimed at formulating kinematic equation of a mechanism at the given pose and solving all the joint parameters (variables). It is a fundamental problem in kinematical analysis, design and synthesis for both serial mechanisms (SMs) and parallel mechanisms (PMs) [3, 7]. Solving analytical solution of inverse kinematics is the prerequisite for trajectory planning, precise control and manipulation of mechanisms. Because all the joint parameters of a PM can be obtained through solving the joint parameters in each of its limbs sharing the same moving platform, inverse kinematics of a PM can be decomposed into several inverse kinematics problems of SMs. According to the mathematical

tools that are used to formulate kinematic equations, the existing methods to deal with inverse kinematics can be classified into two categories, i.e., vector chain based method and exponential matrix based method.

In vector chain based method, three-dimensional position vectors are used to formulate the kinematic equations through building the mapping between the positions and orientations of the given pose. In the formulated position equations, all joint parameters are independent and decoupled. Hence, the equations can be solved by means of elimination. The vector chain based method can be traced back to the early research of theoretical kinematics, and detailedly discussed and concluded by Wampler [8] and Craig [1]. Based upon this, inverse kinematics of SMs constituted by six revolute (R) joints are solved by Raghavan and Roth [5] through engine value and vector analysis of several univariate polynomial equation with high-order. Because lower mobility SM can be regarded as the sub-chain of six degree-of-freedom (DoF) SM, and six DoF SM can be regarded as the sub-chain of SM with higher DoFs, this method can be extended to solve any SM. It should be noted that nonlinear equations relating the joint parameters and the given orientations needed to be solved when the number of DoFs of the SM is more than three. This brings huge difficulties to analytical solution of inverse kinematics. Thus, numerical methods are usually needed when solving higher DoF SMs.

Using exponential matrix with joint parameter to describe pose transformation between adjacent links, the kinematic equation can be obtained by multiplying these matrices together. In the formulated kinematic equation, all the joint parameters are in the exponents, the algebraic operations can only be carried out using Baker-Campbell-Hausdorff formula or Taylor series expansion. Because there are too many terms in the expanded matrix polynomials, the kinematic equations are hard to be analytically solved. Thus, solution of inverse kinematics mostly relies on numerical methods [2]. For the kinematic equations formulated by exponential matrix based method, inverse kinematics can also be solved by geometrical methods. Based upon Kahan's research work, Paden [4] decomposed the inverse kinematics of SMs into several typical sub-problems through concluding the common structure units of SMs. The analytical solution of each sub-problem is given by geometrical and algebraic derivations. It should be noted that the Paden-Kahan sub-problems do not cover all the possible structure units of SMs. Hence, some SMs cannot be solved applying these sub-problems.

From the above analysis, it can be concluded that the existing methods cannot obtain analytical solution of inverse kinematics for arbitrary SMs because of the mathematical tools used. Both vector chain and exponential matrix have some limitations in describing finite motions and formulating kinematic equations of mechanisms. Hence, the clear algebraic mapping between all the joint parameters and the given pose has not been built. As the concise and non-redundant description of finite motions with analytical composition screw triangle product [6], finite screw has the potential to overcome the limitations of vector chain and exponential matrix. As shown in the authors' previous work [6, 9, 10], the algebraic structures of finite screws were revealed and the derivative mapping between finite and instantaneous screws was built, resulting in a general and consistent method to unify type synthesis and kinematic analysis under the umbrella of screw theory. In this paper, inverse kinematics will be

carried out employing finite screws, which leads to a systematic and thorough theoretical framework that unifies topological, position and orientation (pose), velocity modeling and analysis together.

Based upon the authors’ previous work, this paper presents a generalized method to analytically do inverse kinematics of PMs using finite screw theory. The paper is organized as follows. Having a brief review of the state-of-the-art of the existing methods for inverse kinematics in Sect. 1, Sect. 2 presents the new method to algebraically formulate kinematic equations of a PM and its limbs employing finite screws. In Sect. 3, the general procedures to analytically solve the finite screw based kinematic equation are given. A PM with three translational and one rotational Schoenflies motion is taken as an example to verify the validity of the proposed method in Sect. 4 before the conclusions are drawn in Sect. 5.

2 Finite Screw Based Kinematic Equations

A finite motion of a rigid body from its initial pose to arbitrary pose can be presented as a rotation about the Chasles’ axis followed by a translation along that axis, which can be described by a finite screw S_f in quasi-vector [6] form as

$$S_f = 2 \tan \frac{\theta}{2} \begin{pmatrix} s_f \\ r_f \times s_f \end{pmatrix} + t \begin{pmatrix} \mathbf{0} \\ s_f \end{pmatrix} \tag{1}$$

where s_f and r_f denote the unit vector and position vector of the finite motion axis, θ and t are the angular and linear displacement about/along that axis.

A SM constituted by n one-DOF joints (R joints and prismatic (P) joints) is shown in Fig. 1. Using finite screws to describe the finite motions generated by R and P joints, the finite motions realized by the end-effector can be expressed by screw triangle product [6]. Thus, the kinematic equation of a SM at a given pose can be formulated as

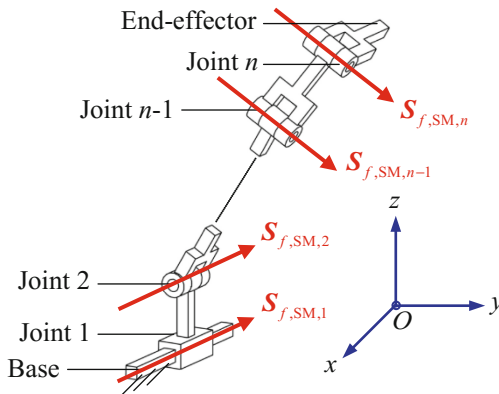


Fig. 1. Finite motions of a SM

$$\mathbf{S}_{f,SM,n} \Delta \mathbf{S}_{f,SM,n-1} \Delta \cdots \Delta \mathbf{S}_{f,SM,1} = \mathbf{S}_{f,SM} \tag{2}$$

$$\mathbf{S}_{f,SM,k} = \begin{cases} 2 \tan \frac{\theta_{SM,k}}{2} \begin{pmatrix} \mathbf{s}_{SM,k} \\ \mathbf{r}_{SM,k} \times \mathbf{s}_{SM,k} \end{pmatrix} & \text{R joint} \\ t_{SM,k} \begin{pmatrix} \mathbf{0} \\ \mathbf{s}_{SM,k} \end{pmatrix} & \text{P joint} \end{cases}, k = 1, 2, \dots, n$$

where $\mathbf{S}_{f,SM}$ denotes the given pose of the SM, the denotations of the symbols in Eq. (2) can be referred to those in Eq. (1).

For a PM composed of l limbs, each limb is a SM sharing the same end-effector, i.e. the moving platform of the PM. Hence, all the joint parameters can be obtained through solving l kinematic equations relating l limbs in form of Eq. (2).

$$\mathbf{S}_{f,i,n_i} \Delta \mathbf{S}_{f,i,n_i-1} \Delta \cdots \Delta \mathbf{S}_{f,i,1} = \mathbf{S}_{f,PM}, i = 1, 2, \dots, l \tag{3}$$

where $\mathbf{S}_{f,i,k}$ ($k = 1, 2, \dots, n_i$) denotes the finite screw generated by the k th joint in the i th limb, $\mathbf{S}_{f,PM}$ is the given pose of the PM.

Equation (3) can be equivalently rewritten using screw triangle product, resulting in clear algebraic mappings between the joint parameters $\theta_{i,k}$, $t_{i,k}$ and the given pose $\mathbf{S}_{f,PM}$. In this way, the joint parameters can be solved by algebraic derivations.

3 Generalized Method to Solve Kinematic Equations

According to Reference [6], the resultant finite screw composited by several finite screws has the quasi-vector form of Eq. (1). Thus, the left side of Eq. (3) can always be rewritten into the following form

$$\mathbf{S}_{f,i,n_i} \Delta \mathbf{S}_{f,i,n_i-1} \Delta \cdots \Delta \mathbf{S}_{f,i,1} = 2 \tan \frac{\theta_i}{2} \begin{pmatrix} \mathbf{s}_{f,i} \\ \mathbf{r}_{f,i} \times \mathbf{s}_{f,i} \end{pmatrix} + t_i \begin{pmatrix} \mathbf{0} \\ \mathbf{s}_{f,i} \end{pmatrix} \tag{4}$$

where $\mathbf{s}_{f,i}$, $\mathbf{r}_{f,i}$, θ_i and t_i of the i th limb are functions of the joint parameters $\theta_{i,k}$, $t_{i,k}$ of that limb.

If the pose of the PM is given as

$$\mathbf{S}_{f,PM} = 2 \tan \frac{\theta_{PM}}{2} \begin{pmatrix} \mathbf{s}_{f,PM} \\ \mathbf{r}_{f,PM} \times \mathbf{s}_{f,PM} \end{pmatrix} + t_{PM} \begin{pmatrix} \mathbf{0} \\ \mathbf{s}_{f,PM} \end{pmatrix} \tag{5}$$

the following equations can be derived based upon Eqs. (3)–(5)

$$\tan \frac{\theta_i}{2} = \tan \frac{\theta_{PM}}{2}, \mathbf{s}_{f,i} = \mathbf{s}_{f,PM} \tag{6}$$

$$\mathbf{r}_{f,i} \times \mathbf{s}_{f,i} + \frac{t_i}{2 \tan \frac{\theta_i}{2}} \mathbf{s}_{f,i} = \mathbf{r}_{f,PM} \times \mathbf{s}_{f,PM} + \frac{t_{PM}}{2 \tan \frac{\theta_{PM}}{2}} \mathbf{s}_{f,PM} \tag{7}$$

Equation (6) is the mapping between the joint parameters relating rotational motions of the *i*th limb and the orientation of the moving platform. Equation (7) is the mapping between the joint parameters relating translational motions of the limb and the position of the moving platform. When $S_{f,PM}$ is given, all joint parameters can be analytically solved using Eqs. (6) and (7). The detailed steps of inverse kinematics for PMs are listed as follows:

- Step 1: Formulate kinematic equations of each limb as Eq. (3) (Eqs. (6) and (7));
- Step 2: Solve rotational parameters of each limb using Eq. (6);
- Step 3: Solve translational parameters of each limb using Eq. (7).

4 Examples

A PM with Schoenflies motion is for example, this PM is composed of four limbs in which every two limbs placed oppositely have the same structures, i.e., $P_1P_2P_3R_aR_b$ and $P_1P_2R_aR_c$. Given $S_{f,PM}$, we solve one limb $P_1P_2P_3R_aR_b$ and one limb $P_1P_2R_aR_c$ in this Section.

Limb $P_1P_2P_3R_aR_b$:

The kinematic equation can be formulated by Eqs. (3), (6) and (7)

$$2 \tan \frac{\theta_b}{2} \begin{pmatrix} s_b \\ \mathbf{r}_b \times s_b \end{pmatrix} \Delta 2 \tan \frac{\theta_a}{2} \begin{pmatrix} s_a \\ \mathbf{r}_a \times s_a \end{pmatrix} \Delta t_{P_3} \begin{pmatrix} \mathbf{0} \\ s_{P_3} \end{pmatrix} \Delta t_{P_2} \begin{pmatrix} \mathbf{0} \\ s_{P_2} \end{pmatrix} \Delta t_{P_1} \begin{pmatrix} \mathbf{0} \\ s_{P_1} \end{pmatrix} = S_{f,PM} \tag{8}$$

$$\tan \frac{\theta_{ba}}{2} = \frac{|\tan \frac{\theta_a}{2} s_a + \tan \frac{\theta_b}{2} s_b + \tan \frac{\theta_a}{2} \tan \frac{\theta_b}{2} (s_a \times s_b)|}{1 - \tan \frac{\theta_a}{2} \tan \frac{\theta_b}{2} s_a^T s_b} = \tan \frac{\theta_{PM}}{2},$$

$$s_{ba} = \frac{\tan \frac{\theta_a}{2} s_a + \tan \frac{\theta_b}{2} s_b + \tan \frac{\theta_a}{2} \tan \frac{\theta_b}{2} (s_a \times s_b)}{|\tan \frac{\theta_a}{2} s_a + \tan \frac{\theta_b}{2} s_b + \tan \frac{\theta_a}{2} \tan \frac{\theta_b}{2} (s_a \times s_b)|} = s_{f,PM} \tag{9}$$

$$p_{ba} + \frac{\mathbf{t} \times s_{ba}}{2} + \frac{\mathbf{t}}{2 \tan \frac{\theta_{ba}}{2}} = \mathbf{r}_{f,PM} \times s_{f,PM} + \frac{t_{PM}}{2 \tan \frac{\theta_{PM}}{2}} s_{f,PM} \tag{10}$$

where

$$p_{ba} = \frac{\tan \frac{\theta_a}{2} (\mathbf{r}_a \times s_a) + \tan \frac{\theta_b}{2} (\mathbf{r}_b \times s_b) + \tan \frac{\theta_a}{2} \tan \frac{\theta_b}{2} (s_a \times (\mathbf{r}_b \times s_b) + (\mathbf{r}_a \times s_a) \times s_b)}{|\tan \frac{\theta_a}{2} s_a + \tan \frac{\theta_b}{2} s_b + \tan \frac{\theta_a}{2} \tan \frac{\theta_b}{2} (s_a \times s_b)|},$$

$$\mathbf{t} = t_{P_1} s_{P_1} + t_{P_2} s_{P_2} + t_{P_3} s_{P_3}$$

The two rotational parameters θ_a and θ_b can be solved from Eq. (9) as

$$\theta_a = 2 \arctan \left(\frac{s_{f,PM}^T (s_a \times s_b)}{s_{f,PM}^T s_b - s_a^T s_b s_{f,PM}^T s_a} \right), \theta_b = 2 \arctan \left(\frac{s_{f,PM}^T (s_a \times s_b)}{s_{f,PM}^T s_a - s_a^T s_b s_{f,PM}^T s_b} \right) \tag{11}$$

The three translational parameters t_{P_1} , t_{P_2} and t_{P_3} can be solved from Eq. (10) as

$$t_{P_1} = \frac{\mathbf{t}^T(\mathbf{s}_{P_2} \times \mathbf{s}_{P_3})}{\mathbf{s}_{P_1}^T(\mathbf{s}_{P_2} \times \mathbf{s}_{P_3})}, t_{P_2} = \frac{\mathbf{t}^T(\mathbf{s}_{P_1} \times \mathbf{s}_{P_3})}{\mathbf{s}_{P_2}^T(\mathbf{s}_{P_1} \times \mathbf{s}_{P_3})}, t_{P_3} = \frac{\mathbf{t}^T(\mathbf{s}_{P_1} \times \mathbf{s}_{P_2})}{\mathbf{s}_{P_3}^T(\mathbf{s}_{P_1} \times \mathbf{s}_{P_2})} \quad (12)$$

where

$$\mathbf{t} = \left(\frac{\mathbf{E}_3}{2 \tan \frac{\theta_{ba}}{2}} - \frac{\tilde{\mathbf{s}}_{ba}}{2} \right)^{-1} \left(\mathbf{r}_{f,PM} \times \mathbf{s}_{f,PM} + \frac{t_{PM}}{2 \tan \frac{\theta_{PM}}{2}} \mathbf{s}_{f,PM} - \mathbf{p}_{ba} \right),$$

\mathbf{E}_3 is a unit matrix of order three, $\tilde{\mathbf{s}}_{ba}$ is the skew matrix of \mathbf{s}_{ba} .

Limb $P_1P_2R_aR_bR_c$:

The kinematic equation can be formulated

$$2 \tan \frac{\theta_c}{2} \begin{pmatrix} \mathbf{s}_c \\ \mathbf{r}_c \times \mathbf{s}_c \end{pmatrix} \Delta 2 \tan \frac{\theta_{a_2}}{2} \begin{pmatrix} \mathbf{s}_a \\ \mathbf{r}_{a_2} \times \mathbf{s}_a \end{pmatrix} \Delta 2 \tan \frac{\theta_{a_1}}{2} \begin{pmatrix} \mathbf{s}_a \\ \mathbf{r}_{a_1} \times \mathbf{s}_a \end{pmatrix} \Delta t_{P_2} \begin{pmatrix} \mathbf{0} \\ \mathbf{s}_{P_2} \end{pmatrix} \Delta t_{P_1} \begin{pmatrix} \mathbf{0} \\ \mathbf{s}_{P_1} \end{pmatrix} = \mathbf{s}_{f,PM} \quad (13)$$

The two rotational parameters $\theta_{a_1} + \theta_{a_2}$ and θ_b can be solved in the similar manner as Eqs. (9) and (11). The three translational parameters θ_{a_1} , t_{P_1} and t_{P_2} can be solved from the position part of Eq. (13)

$$\mathbf{t} = \left(\frac{\mathbf{E}_3}{2 \tan \frac{\theta_{ca}}{2}} - \frac{\tilde{\mathbf{s}}_{ca}}{2} \right)^{-1} \left(\mathbf{r}_{f,PM} \times \mathbf{s}_{f,PM} + \frac{t_{PM}}{2 \tan \frac{\theta_{PM}}{2}} \mathbf{s}_{f,PM} - \mathbf{p}_{ca} \right) \quad (14)$$

where

$$\mathbf{p}_{ca} = \frac{\begin{pmatrix} \tan \frac{\theta_{a_1} + \theta_{a_2}}{2} (\mathbf{r}_{a_2} \times \mathbf{s}_a) + \tan \frac{\theta_c}{2} (\mathbf{r}_c \times \mathbf{s}_c) \\ + \tan \frac{\theta_{a_1} + \theta_{a_2}}{2} \tan \frac{\theta_c}{2} (\mathbf{s}_a \times (\mathbf{r}_c \times \mathbf{s}_c) + (\mathbf{r}_{a_2} \times \mathbf{s}_a) \times \mathbf{s}_c) \end{pmatrix}}{\left| \tan \frac{\theta_{a_1} + \theta_{a_2}}{2} \mathbf{s}_a + \tan \frac{\theta_c}{2} \mathbf{s}_c + \tan \frac{\theta_{a_1} + \theta_{a_2}}{2} \tan \frac{\theta_c}{2} (\mathbf{s}_a \times \mathbf{s}_c) \right|}$$

$$\mathbf{t} = (\exp(\theta_{a_1} \tilde{\mathbf{s}}_a) - \mathbf{E}_3)(\mathbf{r}_{a_2} - \mathbf{r}_{a_1}) + t_{P_1} \mathbf{s}_{P_1} + t_{P_2} \mathbf{s}_{P_2}$$

The solution of Eq. (14) is

$$\theta_{a_1} = 2 \arctan \left(\frac{A \pm \sqrt{A^2 + B^2 - C^2}}{B + C} \right),$$

$$t_{P_1} = \frac{(\mathbf{t} - (\exp(\theta_{a_1} \tilde{\mathbf{s}}_a) - \mathbf{E}_3)(\mathbf{r}_{a_2} - \mathbf{r}_{a_1}))^T (\mathbf{s}_{P_2} \times (\mathbf{s}_{P_1} \times \mathbf{s}_{P_2}))}{\mathbf{s}_{P_1}^T (\mathbf{s}_{P_2} \times (\mathbf{s}_{P_1} \times \mathbf{s}_{P_2}))},$$

$$t_{P_2} = \frac{(\mathbf{t} - (\exp(\theta_{a_1} \tilde{\mathbf{s}}_a) - \mathbf{E}_3)(\mathbf{r}_{a_2} - \mathbf{r}_{a_1}))^T (\mathbf{s}_{P_1} \times (\mathbf{s}_{P_1} \times \mathbf{s}_{P_2}))}{\mathbf{s}_{P_2}^T (\mathbf{s}_{P_1} \times (\mathbf{s}_{P_1} \times \mathbf{s}_{P_2}))} \quad (15)$$

where

$$A = (s_a \times (r_{a_2} - r_{a_1}))^T (s_{P_1} \times s_{P_2}), B = (r_{a_2} - r_{a_1})^T (s_{P_1} \times s_{P_2})$$

$$C = (t + r_{a_2} - r_{a_1})^T (s_{P_1} \times s_{P_2})$$

In this way, all the joint parameters of this PM can be analytically solved.

5 Conclusions

This paper presents a generalized and analytical method to solve inverse kinematics of SMs and PMs using finite screw theory. The main merits of this method are:

- (1) The method can be applied to get analytical solution of inverse kinematics for arbitrary SMs and PMs.
- (2) The main advantage of this method is accuracy and the analytical solution can be directly used in trajectory planning, precise control of mechanisms.
- (3) United with the authors' previous work, all topological, position and orientation (pose), velocity modeling and analysis can be unified into the systematic and consistent framework of screw theory.

Acknowledgments. This research work is partially supported by Tianjin Research Program of Application Foundation and Advanced Technology under Grant No. 16JCYBJC19300.

References

1. Craig, J.J.: Introduction to Robotics: Mechanics and Control, 2nd edn. Addison-Wesley, Boston (1989)
2. Milenkovic, P.: Series solution for finite displacement of planar four-bar linkages. ASME J. Mech. Robot. **3**, 014501-1–014501-7 (2011)
3. Murray, R., Li, Z.X., Sastry, S.: A Mathematical Introduction to Robotic Manipulation. CRC Press, Boca Raton (1994)
4. Paden, B.: Kinematics and Control Robot Manipulators. Ph.D. thesis, Department of Electrical Engineering and Computer Sciences, University of California, Berkeley (1986)
5. Raghavan, M., Roth, B.: Inverse kinematics of the general 6R manipulator and related linkages. ASME J. Mech. Des. **115**, 502–508 (1993)
6. Sun, T., Yang, S.F., Huang, T., Dai, J.S.: A way of relating instantaneous and finite screws based on the screw triangle product. Mech. Mach. Theory **108**, 75–82 (2017)
7. Tsai, L.W.: Robot Analysis and Design: The Mechanics of Serial and Parallel Manipulators. Wiley, Hoboken (1999)
8. Wampler, C.W.: Manipulator inverse kinematic solutions based on vector formulations and damped least-squares methods. IEEE Trans. Syst. Man Cybern. **16**, 93–101 (1986)
9. Yang, S.F., Sun, T., Huang, T., Li, Q.C., Gu, D.B.: A finite screw approach to type synthesis of three-DOF translational parallel mechanisms. Mech. Mach. Theory **104**, 405–419 (2016)
10. Yang, S.F., Sun, T., Huang, T.: Type synthesis of parallel mechanisms having 3T1R motion with variable rotational axis. Mech. Mach. Theory **109**, 220–230 (2017)